MULTIDISCIPLINARY CENTER FOR EARTHQUAKE ENGINEERING RESEARCH
A National Center of Excellence in Advanced Technology Applications

ISSN 1520-295X

Seismic Response of Reinforced Concrete Bridge Pier Walls in the Weak Direction

by

N. Abo-Shadi, M. Saiidi, and D. Sanders
University of Nevada, Reno
Civil Engineering Department
Reno, Nevada 89557-0030

Technical Report MCEER-00-0006

July 17, 2000

This research was conducted at the University of Nevada, Reno and was supported by the Federal Highway Administration under contract number DTFH61-92-C-00106.

NOTICE

This report was prepared by the University of Nevada, Reno as a result of research sponsored by the Multidisciplinary Center for Earthquake Engineering Research (MCEER) through a contract from the Federal Highway Administration. Neither MCEER, associates of MCEER, its sponsors, the University of Nevada, Reno, nor any person acting on their behalf:

a. makes any warranty, express or implied, with respect to the use of any information, apparatus, method, or process disclosed in this report or that such use may not infringe upon privately owned rights; or

b. assumes any liabilities of whatsoever kind with respect to the use of, or the damage resulting from the use of, any information, apparatus, method, or process disclosed in this report.

Any opinions, findings, and conclusions or recommendations expressed in this publication are those of the author(s) and do not necessarily reflect the views of MCEER or the Federal Highway Administration.

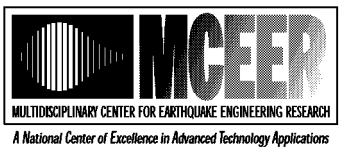

Seismic Response of Reinforced Concrete Bridge Pier Walls in the Weak Direction

by

N. Abo-Shadi[1], M. Saiidi[2], and D. Sanders[3]

Publication Date: July 17, 2000
Submittal Date: January 5, 1999

Technical Report MCEER-00-0006

Task Number 106-E-5.6

FHWA Contract Number DTFH61-92-C-00106

1 Graduate Research Assistant, Department of Civil Engineering, University of Nevada, Reno
2 Professor, Department of Civil Engineering, University of Nevada, Reno
3 Associate Professor, Department of Civil Engineering, University of Nevada, Reno

MULTIDISCIPLINARY CENTER FOR EARTHQUAKE ENGINEERING RESEARCH
University at Buffalo, State University of New York
Red Jacket Quadrangle, Buffalo, NY 14261

Preface

The Multidisciplinary Center for Earthquake Engineering Research (MCEER) is a national center of excellence in advanced technology applications that is dedicated to the reduction of earthquake losses nationwide. Headquartered at the University at Buffalo, State University of New York, the Center was originally established by the National Science Foundation in 1986, as the National Center for Earthquake Engineering Research (NCEER).

Comprising a consortium of researchers from numerous disciplines and institutions throughout the United States, the Center's mission is to reduce earthquake losses through research and the application of advanced technologies that improve engineering, pre-earthquake planning and post-earthquake recovery strategies. Toward this end, the Center coordinates a nationwide program of multidisciplinary team research, education and outreach activities.

MCEER's research is conducted under the sponsorship of two major federal agencies, the National Science Foundation (NSF) and the Federal Highway Administration (FHWA), and the State of New York. Significant support is also derived from the Federal Emergency Management Agency (FEMA), other state governments, academic institutions, foreign governments and private industry.

The Center's FHWA-sponsored Highway Project develops retrofit and evaluation methodologies for existing bridges and other highway structures (including tunnels, retaining structures, slopes, culverts, and pavements), and improved seismic design criteria and procedures for bridges and other highway structures. Specifically, tasks are being conducted to:

- assess the vulnerability of highway systems, structures and components;
- develop concepts for retrofitting vulnerable highway structures and components;
- develop improved design and analysis methodologies for bridges, tunnels, and retaining structures, which include consideration of soil-structure interaction mechanisms and their influence on structural response;
- review and recommend improved seismic design and performance criteria for new highway systems and structures.

Highway Project research focuses on two distinct areas: the development of improved design criteria and philosophies for new or future highway construction, and the development of improved analysis and retrofitting methodologies for existing highway systems and structures. The research discussed in this report is a result of work conducted under the existing highway structures project, and was performed within Task 106-E-5.6, "Evaluation of the Seismic Response of Reinforced Concrete Bridge Pier Walls" of that project as shown in the flowchart on the following page.

The overall objective of this task was to evaluate the behavior and performance of representative pier walls designed in accordance with recent specifications, and to determine the extent and types of retrofitting that may be required for existing pier walls in regions of moderate to high seismicity. The research presented in this report consists of an experimental and an analytical

study. The experimental study focused on the evaluation of out of plane seismic behavior of representative bridge pier walls that exist throughout the U.S. Seven pier wall specimens were tested, and failure was due to either compression of concrete or fracture of vertical reinforcing bars.

In the analytical study, a model to determine the seismic response of bridge pier walls was developed and calibrated. The model showed good agreement with the experimental results when comparing the calculated and measured responses of the pier wall specimens. A parametric study was conducted to extend the seismic response study to bridge pier wall cases that were not tested experimentally using the computer program "PIER." Based on the results of this study, a practical approach to relate the confinement reinforcement in the plastic hinge zones of bridge pier walls to the displacement ductility capacity was developed.

SEISMIC VULNERABILITY OF EXISTING HIGHWAY CONSTRUCTION
FHWA Contract DTFH61-92-C-00106

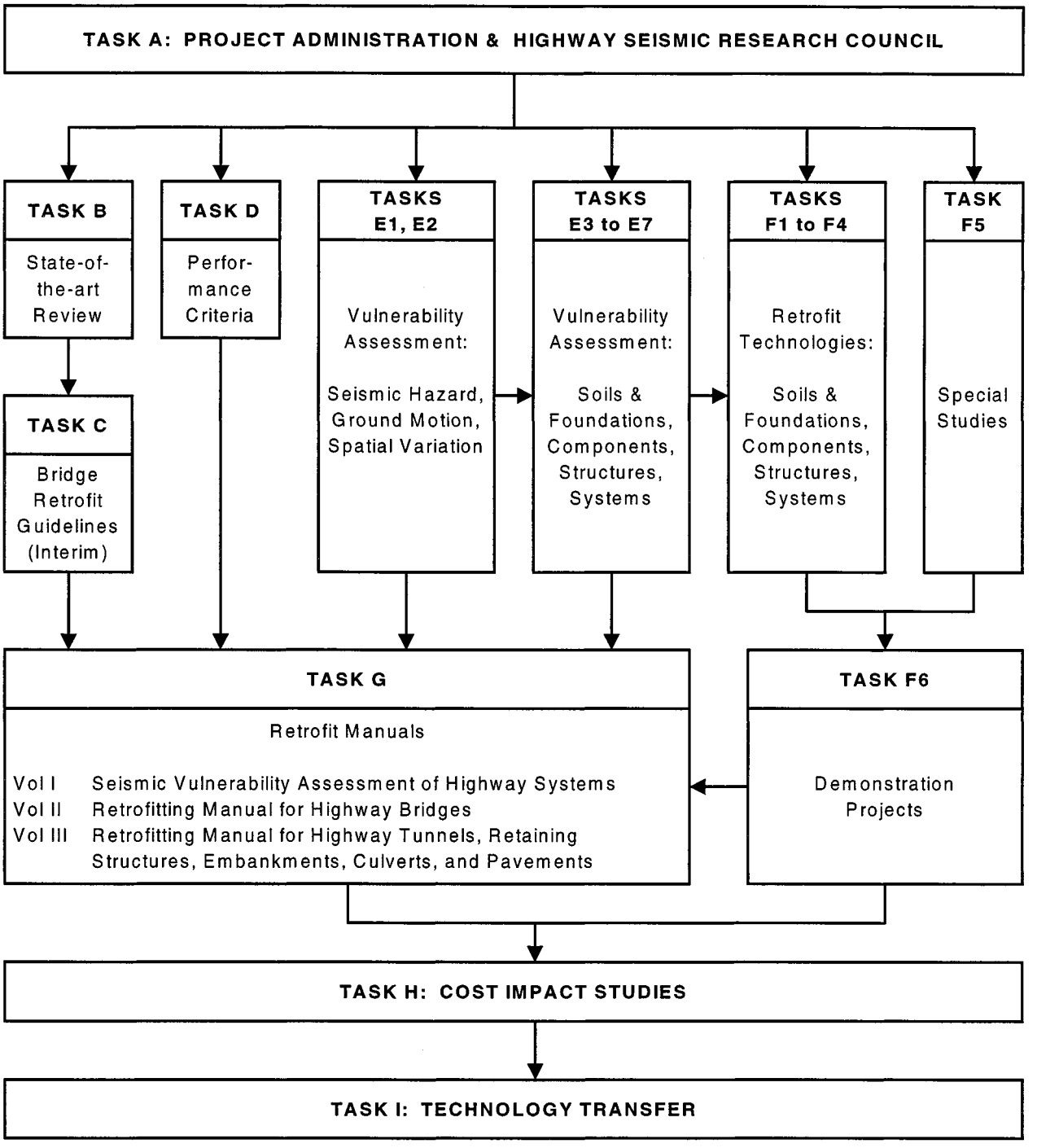

ABSTRACT

The research presented in this report consisted of an experimental and an analytical study. The objective of the experimental study was to evaluate the out-of-plane seismic behavior of representative bridge pier walls that exist in the US. The analytical study had two objectives, the first was to develop and calibrate an analytical model to determine the seismic response of bridge pier walls, while the second was to develop an approach that relates the displacement ductility capacity to the amount of confinement steel.

A comprehensive bridge pier wall survey was conducted to collect information about existing typical pier walls in the US. The data were well distributed geographically and states with full range of seismicity were represented. A statistical analysis was performed on the collected data to select test parameters and specimens. Seven specimens were designed, built, and tested in the experimental study under slow cyclic loads. The failure mode of the wall specimens was either compression failure of the concrete or fracture of the vertical reinforcing bars due to low-cycle fatigue.

An analytical model was developed and calibrated. A computer program called "PIER" was written to implement the analytical model. Good agreement was found when comparing the calculated and measured responses of the pier wall specimens tested in the course of this study and at the University of California at Irvine (UC-Irvine). A parametric study was conducted to extend the seismic response study to bridge pier wall cases that were not tested experimentally using the computer program "PIER". The parameters were the ratio of the wall height to thickness, the vertical steel ratio, the confinement steel ratio, and the axial load index. Pier wall cases that need retrofit were identified based on the expected seismic response.

A practical approach to relate the confinement reinforcement in the plastic hinge zones of bridge pier walls to the displacement ductility capacity was developed based on the results of the parametric study. The proposed approach can be used to design the confinement steel or to estimate the ductility capacity of bridge pier walls for a given confinement steel ratio.

The displacement ductility capacity of six typical pier walls that contained confinement steel designed using the available code provisions was calculated using the proposed approach. A comparison of the resulting ductilities was made to identify design provisions that lead to best level of performance. The displacement ductility capacity of pier walls 29 and 30 in Moribe Viaduct that was severely damaged during the 1995 Hanshin Awaji Earthquake, Japan, was calculated. The damage and the poor seismic performance of these walls, indicated that the actual ductility capacity was lower than those calculated. The likely reason for the poor seismic performance of the walls was discussed.

ACKNOWLEDGMENTS

The research presented in this report was conducted at the University of Nevada, Reno. Financial support for the project was provided by the Multidisciplinary Center for Earthquake Engineering Research (MCEER) at the State University of New York (SUNY) at Buffalo, through the Federal Highway Administration (FHWA) Contract DTFH61-92-C-00106, Task No. 106-E-5.6.

The authors are thankful to Drs. George Lee and Ian Buckle of MCEER for their support. Special appreciation is due Mr. Ian Friedland for his helpful advice in the course of the project. Dr. John Mander is thanked for his many constructive suggestions in selecting the test specimens. Finally gratitude is expressed to the bridge engineering staff from many state departments of transportation for providing information about bridge pier walls in their states.

TABLE OF CONTENTS

SECTION	TITLE	PAGE
1	**INTRODUCTION**	**1**
1.1	Introduction	1
1.2	Objective and Scope	2
1.3	Previous Work	3
2	**PIER WALL SURVEY AND SPECIMEN SELECTION**	**5**
2.1	Introduction	5
2.2	Pier Wall Survey	5
2.3	Statistical Analysis	6
2.4	Selection of Test Specimens	15
2.4.1	Wall Height-to-Thickness Ratio	15
2.4.2	Vertical Steel Ratio	16
2.4.3	Transverse Steel Ratio	16
2.4.4	Crosstie Steel Ratio	16
2.4.5	Lap Splice in Vertical Reinforcing Bars	17
2.4.6	Concrete Compressive Strength	17
2.4.7	Steel Yield Stress	17
2.4.8	Axial Load Index	18
2.5	Number of Specimens	18
3	**EXPERIMENTAL PROGRAM**	**19**
3.1	Introduction	19
3.2	Test Specimens	19
3.2.1	Construction of Test Specimens	21
3.2.2	Material Properties	31
3.2.3	Instrumentation	33
3.3	Test Setup and Testing Program	34
4	**EXPERIMENTAL TEST RESULTS**	**45**
4.1	Introduction	45
4.2	Test Results	45
4.2.1	Performance of Specimen 1	57
4.2.2	Performance of Specimen 2	62
4.2.3	Performance of Specimen 3	67
4.2.4	Performance of Specimen 4	73
4.2.5	Performance of Specimen 5	78
4.2.6	Performance of Specimen 6	83
4.2.7	Performance of Specimen 7	88
4.3	Observations and Remarks	93

TABLE OF CONTENTS (Cont'd)

SECTION	TITLE	PAGE
5	**ANALYTICAL STUDY**	**95**
5.1	Introduction	95
5.2	Deflections and Displacement Ductility of Pier Walls	95
5.2.1	Material Stress-Strain Models	97
5.2.1.1	Unconfined Concrete Model	98
5.2.1.2	Confined Concrete Models	99
5.2.1.2.1	Modified Kent and Park Model	99
5.2.1.2.2	Modified Mander et al. Model	101
5.2.1.2.3	Hoshikuma Model	104
5.2.1.2.4	Comparison of the Confined Concrete Models	107
5.2.1.3	Reinforcing Steel Model	108
5.2.2	Flexural Deflection	111
5.2.2.1	Moment-Curvature Analysis	114
5.2.3	Shear Deflection	116
5.2.4	Bond Slip Deflection	117
5.2.5	Low-Cycle Fatigue	120
5.3	"PIER" Computer Program to Calculate the Deflections and the Ductility	123
5.4	Comparison of Analytical and Experimental Results	123
5.4.1	Analysis of Pier Walls Tested at the University of Nevada, Reno (UNR)	126
5.4.2	Analysis of Pier Walls Tested at UC-Irvine	135
5.5	Concluding Remarks	142
6	**PARAMETRIC STUDY**	**143**
6.1	Introduction	143
6.2	Analysis of the Wall Cases	143
6.3	Results of the Parametric Study	144
6.4	Design Implications	155
6.4.1	Proposed Relationship Between the Confinement Steel and Ductility	155
6.4.2	Transverse Steel Design Methods	158
6.4.2.1	American Concrete Institute (ACI)	158
6.4.2.2	American Association of State Highways and Transportation Officials (AASHTO)	165
6.4.2.3	California Department of Transportation (CALTRANS)	165
6.4.2.4	ACT-32 Method	166
6.4.2.5	Wehbe et al. Equation	166
6.5	Comparison of the Proposed and Wehbe Models	167
6.6	Comparison of the Proposed and the Wehbe Method to Estimate Ductility	168

TABLE OF CONTENTS (Cont'd)

SECTION	TITLE	PAGE
6.7	Evaluation of the Ductility for Pier Walls in Moribe Viaduct, Japan	171
6.8	Concluding Remarks	172
7	**SUMMARY AND CONCLUSIONS**	**175**
7.1	Summary	175
7.2	Conclusions	176
7.2.1	Experimental Conclusions	177
7.2.2	Analytical Conclusions	177
8	**REFERENCES**	**179**
APPENDIX A: Measured Lateral-Load Strain in the Reinforcing Bars		**183**
APPENDIX B: Data and Results for the Parametric Study		**297**

LIST OF ILLUSTRATIONS

FIGURE	TITLE	PAGE
2-1	The Survey Form	6
2-2	States Included in the Database	7
2-3	Percentage of Wall Height/Thickness Ratios	8
2-4	Percentage of Vertical Steel Ratios	8
2-5	Percentage of Transverse Steel Ratios	9
2-6	Percentage of Crosstie Steel Ratios	9
2-7	Percentage of Splice Length/Bar Diameter Ratios	10
2-8	Percentage of Concrete Compressive Strength	10
2-9	Percentage of Steel Yield Stress	11
2-10	Percentage of Axial Load Index	11
2-11	Locations of the Mean, Median and the Mode	13
2-12	Typical Positive and Negative Skewness	13
2-13	Typical Normal, Leptokurtic, and Platykurtic Distributions	13
3-1	Details of Typical Footing	20
3-2	Details of a Typical Top Beam	22
3-3	Details of Specimen 1	24
3-4	Details of Specimen 2	25
3-5	Details of Specimen 3	26
3-6	Details of Specimen 4	27
3-7	Details of Specimen 5	28
3-8	Details of Specimen 6	29
3-9	Details of Specimen 7	30
3-10	Construction of Test Specimens	31
3-11	Locations of Strain Gauges in Specimen 1	36
3-12	Locations of Strain Gauges in Specimen 2	37
3-13	Locations of Strain Gauges in Specimen 3	38
3-14	Locations of Strain Gauges in Specimen 4	39
3-15	Locations of Strain Gauges in Specimen 5	40
3-16	Locations of Strain Gauges in Specimen 6	41
3-17	Locations of Strain Gauges in Specimen 7	42
3-18	Typical Locations of LVDT's for a Test Specimen	43
3-19	Test Setup Elevation	43
3-20	Typical Lateral load-History	44
4-1	Measured Lateral Load-Displacement Hysteresis for Specimen 1	49
4-2	Measured Lateral Load-Displacement Hysteresis for Specimen 2	49
4-3	Measured Lateral Load-Displacement Hysteresis for Specimen 3	50
4-4	Measured Lateral Load-Displacement Hysteresis for Specimen 4	50
4-5	Measured Lateral Load-Displacement Hysteresis for Specimen 5	51
4-6	Measured Lateral Load-Displacement Hysteresis for Specimen 6	51
4-7	Measured Lateral Load-Displacement Hysteresis for Specimen 7	52

LIST OF ILLUSTRATIONS (cont't.)

FIGURE	TITLE	PAGE
4-8	Measured Lateral Load-Displacement Envelopes	52
4-9	Measured Lateral Load-Displacement Ductility Envelopes	53
4-10	Measured Curvature Envelope along Plastic Hinge of Specimen 1	53
4-11	Measured Curvature Envelope along Plastic Hinge of Specimen 2	54
4-12	Measured Curvature Envelope along Plastic Hinge of Specimen 3	54
4-13	Measured Curvature Envelope along Plastic Hinge of Specimen 4	55
4-14	Measured Curvature Envelope along Plastic Hinge of Specimen 5	55
4-15	Measured Curvature Envelope along Plastic Hinge of Specimen 6	56
4-16	Measured Curvature Envelope along Plastic Hinge of Specimen 7	56
4-17	Buckling of the Vertical Bars in Specimen 1	57
4-18	Measured Lateral Load Strain in SG-1 of Specimen 1	58
4-19	Measured Lateral Load Strain in SG-5 of Specimen 1	58
4-20	Measured Lateral Load Strain in SG-9 of Specimen 1	59
4-21	Measured Lateral Load Strain in SG-11 of Specimen 1	59
4-22	Measured Lateral Load Strain in SG-17 of Specimen 1	60
4-23	Measured Lateral Load Strain in SG-19 of Specimen 1	60
4-24	Measured Lateral Load Strain in SG-27 of Specimen 1	61
4-25	Measured Lateral Load Strain in SG-28 of Specimen 1	61
4-26	Spalling of Cover Concrete and Buckling of Vertical Bars in Specimen 2	62
4-27	Measured Lateral Load Strain in SG-1 of Specimen 2	63
4-28	Measured Lateral Load Strain in SG-4 of Specimen 2	63
4-29	Measured Lateral Load Strain in SG-7 of Specimen 2	64
4-30	Measured Lateral Load Strain in SG-10 of Specimen 2	64
4-31	Measured Lateral Load Strain in SG-17 of Specimen 2	65
4-32	Measured Lateral Load Strain in SG-19 of Specimen 2	65
4-33	Measured Lateral Load Strain in SG-28 of Specimen 2	66
4-34	Measured Lateral Load Strain in SG-29 of Specimen 2	66
4-35	Fracture of the Vertical Bars in Specimen 3	67
4-36	Measured Lateral Load Strain in SG-1 of Specimen 3	69
4-37	Measured Lateral Load Strain in SG-3 of Specimen 3	69
4-38	Measured Lateral Load Strain in SG-7 of Specimen 3	70
4-39	Measured Lateral Load Strain in SG-12 of Specimen 3	70
4-40	Measured Lateral Load Strain in SG-19 of Specimen 3	71
4-41	Measured Lateral Load Strain in SG-20 of Specimen 3	71
4-42	Measured Lateral Load Strain in SG-28 of Specimen 3	72
4-43	Measured Lateral Load Strain in SG-30 of Specimen 3	72
4-44	Buckling of the Vertical and the Lateral Bars in Specimen 4	73
4-45	Measured Lateral Load Strain in SG-1 of Specimen 4	74
4-46	Measured Lateral Load Strain in SG-4 of Specimen 4	74
4-47	Measured Lateral Load Strain in SG-7 of Specimen 4	75
4-48	Measured Lateral Load Strain in SG-12 of Specimen 4	75
4-49	Measured Lateral Load Strain in SG-17 of Specimen 4	76

LIST OF ILLUSTRATIONS (cont't.)

FIGURE	TITLE	PAGE
4-50	Measured Lateral Load Strain in SG-19 of Specimen 4	76
4-51	Measured Lateral Load Strain in SG-27 of Specimen 4	77
4-52	Measured Lateral Load Strain in SG-28 of Specimen 4	77
4-53	Vertical Bar Buckling and Opening of the Crossties in Specimen 5	78
4-54	Measured Lateral Load Strain in SG-1 of Specimen 5	79
4-55	Measured Lateral Load Strain in SG-6 of Specimen 5	79
4-56	Measured Lateral Load Strain in SG-7 of Specimen 5	80
4-57	Measured Lateral Load Strain in SG-11 of Specimen 5	80
4-58	Measured Lateral Load Strain in SG-17 of Specimen 5	81
4-59	Measured Lateral Load Strain in SG-19 of Specimen 5	81
4-60	Measured Lateral Load Strain in SG-27 of Specimen 5	82
4-61	Measured Lateral Load Strain in SG-29 of Specimen 5	82
4-62	Vertical Bar Buckling in Specimen 6	83
4-63	Measured Lateral Load Strain in SG-2 of Specimen 6	84
4-64	Measured Lateral Load Strain in SG-6 of Specimen 6	84
4-65	Measured Lateral Load Strain in SG-7 of Specimen 6	85
4-66	Measured Lateral Load Strain in SG-12 of Specimen 6	85
4-67	Measured Lateral Load Strain in SG-19 of Specimen 6	86
4-68	Measured Lateral Load Strain in SG-20 of Specimen 6	86
4-69	Measured Lateral Load Strain in SG-27 of Specimen 6	87
4-70	Measured Lateral Load Strain in SG-28 of Specimen 6	87
4-71	Fracture of a Vertical Bar in Specimen 7	88
4-72	Measured Lateral Load Strain in SG-1 of Specimen 7	89
4-73	Measured Lateral Load Strain in SG-4 of Specimen 7	89
4-74	Measured Lateral Load Strain in SG-9 of Specimen 7	90
4-75	Measured Lateral Load Strain in SG-12 of Specimen 7	90
4-76	Measured Lateral Load Strain in SG-17 of Specimen 7	91
4-77	Measured Lateral Load Strain in SG-20 Specimen 7	91
4-78	Measured Lateral Load Strain in SG-27 of Specimen 7	92
4-79	Measured Lateral Load Strain in SG-28 Specimen 7	92
5-1	Lateral Deflection of Pier Wall	96
5-2	Effect of Confinement on Strength and Ductility of Concrete	97
5-3	The Kent and Park Model for Unconfined Concrete	98
5-4	Modified Kent and Park Model for Confined Concrete	100
5-5	Modified Mander Model for Confined Concrete	103
5-6	Hoshikuma Model for Confined Concrete	106
5-7	Equivalent Confined Section	106
5-8	Comparison of Confined Concrete Models	108
5-9	Stress-Strain Model for Steel	110
5-10	Bending Moment and Idealized Curvature at Yield	113
5-11	Flexural Deflection and Idealized Curvature at Ultimate	113

LIST OF ILLUSTRATIONS (cont't.)

FIGURE	TITLE	PAGE
5-12	Plastic Hinge Coefficient vs. Displacement Ductility	114
5-13	Pier Wall Cross Section Subjected to Axial Load and Bending	115
5-14	Bond Slip of Longitudinal Bars	119
5-15	Typical Strain-Fatigue Life Curve	122
5-16	Typical Plastic Strain Profile	122
5-17(a)	Flow Chart for the Computer Program "PIER"	124
5-17(b)	Flow Chart for the Computer Program "PIER"	125
5-18	Analytical Moment-Curvature Relationship for Specimen 1	128
5-19	Analytical Moment-Curvature Relationship for Specimen 2	128
5-20	Analytical Moment-Curvature Relationship for Specimen 3	129
5-21	Analytical Moment-Curvature Relationship for Specimen 4	129
5-22	Analytical Moment-Curvature Relationship for Specimen 5	130
5-23	Analytical Moment-Curvature Relationship for Specimen 6	130
5-24	Analytical Moment-Curvature Relationship for Specimen 7	131
5-25	Measured and Calculated Lateral load-Displacement for Specimen 1	131
5-26	Measured and Calculated Lateral load-Displacement for Specimen 2	132
5-27	Measured and Calculated Lateral load-Displacement for Specimen 3	132
5-28	Measured and Calculated Lateral load-Displacement for Specimen 4	133
5-29	Measured and Calculated Lateral load-Displacement for Specimen 5	133
5-30	Measured and Calculated Lateral load-Displacement for Specimen 6	134
5-31	Measured and Calculated Lateral load-Displacement for Specimen 7	134
5-32	Details of Wall Specimens Tested at UC-Irvine[8]	138
5-33	Details of Wall Specimens Tested at UC-Irvine[9]	139
6-1	Yield Displacement vs. H/t for $P/(f'_c . A_g)$= 5% and ρ_l&ρ_c= 0.1%	146
6-2	Yield Displacement vs. H/t for $P/(f'_c . A_g)$= 5% and ρ_l&ρ_c= 0.25%	146
6-3	Yield Displacement vs. H/t for $P/(f'_c . A_g)$= 5% and ρ_l&ρ_c= 0.4%	147
6-4	Yield Displacement vs. H/t for $P/(f'_c . A_g)$= 10% and ρ_l&ρ_c= 0.1%	147
6-5	Yield Displacement vs. H/t for $P/(f'_c . A_g)$= 10% and ρ_l&ρ_c= 0.25%	148
6-6	Yield Displacement vs. H/t for $P/(f'_c . A_g)$= 10% and ρ_l&ρ_c= 0.4%	148
6-7	Ultimate Displacement vs. H/t for $P/(f'_c . A_g)$= 5% and ρ_l&ρ_c= 0.1%	149
6-8	Ultimate Displacement vs. H/t for $P/(f'_c . A_g)$= 5% and ρ_l&ρ_c= 0.25%	149
6-9	Ultimate Displacement vs. H/t for $P/(f'_c . A_g)$= 5% and ρ_l&ρ_c= 0.4%	150
6-10	Ultimate Displacement vs. H/t for $P/(f'_c . A_g)$= 10% and ρ_l&ρ_c= 0.1%	150
6-11	Ultimate Displacement vs. H/t for $P/(f'_c . A_g)$= 10% and ρ_l&ρ_c= 0.25%	151
6-12	Ultimate Displacement vs. H/t for $P/(f'_c . A_g)$= 10% and ρ_l&ρ_c= 0.4%	151
6-13	Ductility vs. H/t for $P/(f'_c . A_g)$= 5% and ρ_l&ρ_c= 0.1%	152
6-14	Ductility vs. H/t for $P/(f'_c . A_g)$= 5% and ρ_l&ρ_c= 0.25%	152
6-15	Ductility vs. H/t for $P/(f'_c . A_g)$= 5% and ρ_l&ρ_c= 0.4%	153
6-16	Ductility vs. H/t for $P/(f'_c . A_g)$= 10% and ρ_l&ρ_c= 0.1%	153
6-17	Ductility vs. H/t for $P/(f'_c . A_g)$= 10% and ρ_l&ρ_c= 0.25%	154

LIST OF ILLUSTRATIONS (cont't.)

FIGURE	TITLE	PAGE
6-18	Ductility vs. H/t for $P/(f'_c .A_g)$= 10% and ρ_l&ρ_c= 0.4%	154
6-19	Displacement Ductility vs. ρ_t/ρ_v for $P/(f'_c .A_g)$ = 5% and H/t = 2	159
6-20	Displacement Ductility vs. ρ_t/ρ_v for $P/(f'_c .A_g)$ = 5% and H/t = 4	159
6-21	Displacement Ductility vs. ρ_t/ρ_v for $P/(f'_c .A_g)$ = 5% and H/t = 7	160
6-22	Displacement Ductility vs. ρ_t/ρ_v for $P/(f'_c .A_g)$ = 5% and H/t = 10	160
6-23	Displacement Ductility vs. ρ_t/ρ_v for $P/(f'_c .A_g)$ = 5% and H/t = 15	161
6-24	Displacement Ductility vs. ρ_t/ρ_v for $P/(f'_c .A_g)$ = 10% and H/t = 2	161
6-25	Displacement Ductility vs. ρ_t/ρ_v for $P/(f'_c .A_g)$ = 10% and H/t = 4	162
6-26	Displacement Ductility vs. ρ_t/ρ_v for $P/(f'_c .A_g)$ = 10% and H/t = 7	162
6-27	Displacement Ductility vs. ρ_t/ρ_v for $P/(f'_c .A_g)$ = 10% and H/t = 10	163
6-28	Displacement Ductility vs. ρ_t/ρ_v for $P/(f'_c .A_g)$ = 10% and H/t = 15	163
6-29	Displacement Ductility vs. ρ_t/ρ_v for $P/(f'_c .A_g)$ = 5%	164
6-30	Displacement Ductility vs. ρ_t/ρ_v for $P/(f'_c .A_g)$ = 10%	164
6-31	Displacement Ductility vs. ρ_t/ρ_v (Design Curve)	165
6-32	Evaluated μ_d vs. ρ_v for ρ_t Based on Different Methods at $P/A_g.f'_c$=5%	170
6-33	Evaluated μ_d vs. ρ_v for ρ_t Based on Different Methods at $P/A_g.f'_c$=10%	170
6-34	Damage to Pier Wall 29 in Moribe Viaduct, Japan, Following the 1995 Hanshin-Awaji Earthquake	171

LIST OF TABLES

TABLE	TITLE	PAGE
2-1	Statistical Sampling Analysis of the Bridge Pier Wall Database	14
2-2	Target Reinforcement Ratios for the Test Specimens	18
3-1	Reinforcement Ratios for the Test Specimens	23
3-2	Vertical and the Transverse Reinforcement for the Test Specimens	23
3-3	Crosstie Reinforcement for the Test Specimens	23
3-4	Measured Concrete Slump	32
3-5	Measured Concrete Compressive Strength for the First Set of Specimens, MPa	32
3-6	Measured Concrete Compressive Strength for the Second Set of Specimens, MPa	33
3-7	Measured Steel Properties	33
4-1	Axial Loads Applied to the Pier Wall Specimens, kN	47
4-2	Measured Load-Displacement Data at Key Points	48
4-3	Measured Plastic Hinge	47
5-1	Confinement Coefficient, k_e	102
5-2	Modulus of Elasticity of Concrete Based on Japanese Specifications "Design 1991"[12]	107
5-3	Calculated Unconfined and Confined Concrete Properties	108
5-4(a)	Calculated Yield Displacement Components for UNR Wall Specimens	126
5-4(b)	Calculated Ultimate Displacement Components for UNR Wall Specimens	126
5-5	Comparison of Measured and Calculated Displacement and Displacement Ductility for UNR Wall Specimens	127
5-6	Data for Wall Specimens Tested at UC-Irvine	138
5-7(a)	Calculated Yield Displacement Components for UC-Irvine Wall Specimens	140
5-7(b)	Calculated Ultimate Displacement Components for UC-Irvine Wall Specimens	140
5-8	Comparison of Measured and Calculated Displacement and Displacement Ductility for UC-Irvine Specimens	141
6-1	The Selected Values for the Parameters	144
6-2	Fitting Constants	157
6-3	Confinement Steel Using the Proposed and the Wehbe et al. Methods	167
6-4	The Measured and Calculated μ_d for the Wall Specimens	168
6-5	Calculated Displacement Ductility Capacity for Typical Pier Walls	169

SECTION 1
INTRODUCTION

1.1 Introduction

Recent earthquakes have shown that bridge pier walls generally perform well in the strong direction while the weak direction response could be critical. This was demonstrated by the spectacular failure of several pier walls in a major bridge (the Moribe Viaduct) during the January 1995 Hanshin-Awaji earthquake in Japan[22]. Piers 29 and 30 of the Moribe Viaduct failed catastrophically in shear.

The AASHTO design specifications[2] and California Bridge Design Specifications[6] have no specific provisions to design bridge pier walls. AASHTO[2] requires pier walls to be designed as shear walls in the strong direction and as columns in the weak direction. Caltrans[6] requires bridge pier walls to be designed as columns with certain limits for the reinforcement ratio and spacing. In designing the confinement steel in the plastic hinge zones of bridge pier walls, AASHTO[2] considers the gross and the confined section dimensions, and the material properties. In addition to the parameters considered by AASHTO[2], Caltrans[6] considers the effect of the axial load. None of the two design specifications explicitly consider the displacement ductility capacity of the pier walls.

The practice of designing pier walls in the weak direction based on the provisions for columns is primarily driven by judgment and not actual test data. Whether this practice is appropriate has not been investigated and is yet to be verified by tests. The minimum confinement steel limits also appear to be judgmental and perhaps are approximately based on the minimum shrinkage steel requirements. Comprehensive data and analysis results of the effect of transverse steel on the seismic performance of pier walls for out-of-plane loading are lacking.

1.2 Objective and Scope

This research consists of an experimental and analytical study. The objective of the experimental study was to evaluate the seismic behavior of representative existing bridge pier walls in the U.S. The analytical study had two objectives, the first was to develop an analytical model to determine the seismic response of bridge pier walls, while the second was conduct a parametric study and use the results to develop an approach that relates the displacement ductility capacity to the amount of confinement steel.

A comprehensive bridge pier wall survey was conducted in this study to collect information about typical pier walls that exist in the U.S. The states that responded to the survey were well distributed geographically and represented the full range of seismicity. A statistical analysis was performed on the data to select test parameters and specimens. Seven one-half scale specimens were designed, built, and tested. The parameters included in the experimental study included the steel ratio in the three orthogonal directions of the wall and the axial stress. The walls were tested under cyclic loads. The material properties and loading patterns were not varied.

An analytical model to predict the seismic response of bridge pier walls was developed and calibrated. A computer program named "PIER"[1] that implements the analytical model was used to perform an extensive parametric study. The objective of the parametric study was to extend the seismic response study to bridge pier wall cases that were not tested experimentally. The parameters in this part of the study included those in the tests in addition to the wall height to thickness ratio.

A practical approach to design the confinement steel and to evaluate the displacement ductility capacity of bridge pier walls was developed based on the results of the parametric study. The objective of this approach was to design the confinement steel based on a target displacement ductility level. Conversely, the method can be used to estimate the ductility capacity of an existing wall with a known amount of confinement steel. Depending on the ductility demand, the result can be used to determine if retrofit of the wall is necessary.

1.3 Previous Work

Only a limited number of experimental studies on bridge pier wall specimens subjected to cyclic out-of-plane loads has been conducted. Much of the work has been done at the University of California at Irvine. The UC-Irvine tests[8, 9, 7] were conducted on bridge pier walls with relatively high vertical steel ratios (generally 1.3% to 2.3%). These tests addressed details used in California and were not intended to be a comprehensive evaluation of seismic response of pier walls.

In the first study[8], pier wall specimens representing pre-1971 design specifications were tested. An axial load index of 5% was used in the test. The axial load index is defined as the axial load divided by the product of the gross sectional area of the wall and concrete compressive strength. The specified concrete compressive strength and steel yield stress were 27.6 MPa and 276 MPa, respectively. All the test specimens had a transverse reinforcement ratio of 0.15% with no crossties. The transverse bars were placed inside the vertical bars. The first and second test groups were as-built specimens, while the third group included retrofitted specimens. The walls in the first group consisted of two, ⅓-scale specimens with a vertical steel ratio of 0.6%, and were tested in the strong direction. The two specimens performed well and shear failure was the dominant mode of failure with a large load capacity. The second and third groups were ½-scale specimens with a vertical steel ratio of 0.56% and were tested in the weak direction. Two lap-splice lengths, 16 d_b and 28 d_b (where d_b = the diameter of the vertical reinforcing bars) were tested. Pier walls with longer lap-splices exhibited higher ductility than walls with shorter lap-splices. In the third group, four types of retrofit schemes using steel plates and bolts with different sizes and bolt spacing on each face were investigated. The repair scheme using larger steel plates and smaller bolt spacing showed the most improved performance.

The objective of the second study[9] was to investigate the crosstie performance in bridge pier walls. Six ½-scale wall specimens were constructed and tested. Each specimen was denoted by two letters: the first is either "H" or "L" indicating high or low vertical reinforcement ratio, whereas the second letter ("N", "P", or "U") indicates the crosstie distribution (i.e., no, partially, or uniformly distributed crossties). The low and high vertical steel ratios were 1.3% and 2.3%,

respectively. The lateral steel ratio in all the specimens was 0.25%. The crosstie reinforcement ratio in the U specimens was 0.08%, while it was 0.16% in the P specimens. Deformed wires (D5) were used as crossties with standard 90° and 135° hooks. The specified concrete compressive strength was 27.6 MPa while the steel yield stress for the vertical bars and the deformed wires were 414 MPa, and 620 MPa, respectively. The partially distributed crossties proved to be more efficient than the uniformly distributed crossties because the crosstie ratio in the P specimens was doubled at the plastic hinge zone.

The performance of six repaired pier walls that were remnants of the second study[9] was investigated in the third study[7]. An enhanced crosstie, double crossties, and T-headed crossties were used in the repair schemes. The enhancement in the crossties included increasing the 135° hook length from 44 mm to 88 mm corresponding to 7 and 14 times the crosstie bar diameter, respectively. The length of the 90° hook was kept the same as that in the original specimens. Specimens with double crossties contained sets of two crossties with alternating 90° and 135° hooks provided at each horizontal and vertical bar intersection. This resulted in an increase in the crosstie steel ratio to 0.32%. The T-headed reinforcement consisted of two square metal plates, welded to either end of a section of a standard reinforcing bar. The head of the T-headed reinforcement was a 50-mm x 50-mm square metal plate with a thickness of 13 mm. A standard 16-mm reinforcing bar was used as the stem. The T-headed reinforcement ratio was 1%. The specified material properties were the same as the original specimens[9]. The use of double crossties provided good confinement of the concrete core in the plastic hinge zone. The T-headed crosstie reinforcement performed as well or better than the regular crosstie reinforcement.

Two full-scale pier walls were constructed and tested to investigate the scaling effects on cyclic loading tests[7]. The vertical steel ratio was taken as 1.3%. The crosstie steel ratio in the plastic hinge zone was 0.67% in the first specimen. A pair of 10-mm bars with alternating 90° and 135° hooks, which provided a reinforcement ratio of 0.73%, was used in the second specimen. Good correlation between half-scale and full-scale pier walls was achieved for the displacement ductility and curvatures.

SECTION 2
PIER WALL SURVEY AND SPECIMEN SELECTION

2.1 Introduction

It was essential to obtain information about typical bridge pier walls because the objective of this study was to evaluate the seismic behavior of representative bridge pier walls that exist in the US. A recent survey of bridge construction practice in the Eastern and Western United States[11, 15] has identified typical details of reinforced concrete bridge pier walls. A more comprehensive bridge pier wall survey was conducted in this study to collect information such as the geometry, details of reinforcement, the axial load, and material properties of typical pier walls. A survey form was developed and mailed to all the departments of transportation in the US. Responses were received from 30 states. A statistical analysis was performed on the collected data to select test parameters and specimens. Seven specimens were designed and built for the experimental study. This section describes the survey, the analysis of data obtained from the survey, and selection of variables in the specimens.

2.2 Pier Wall Survey

A survey form was developed and mailed to all 50 state departments of transportation to request information about typical existing bridge pier walls. The data included the material properties, the wall and the footing dimensions, the wall-footing connection type, the vertical steel, the transverse steel, the crosstie steel, the lap-splice length in the vertical rebars, and the axial load index. The axial load index is defined as the axial load divided by the product of the gross sectional area of the wall and the specified concrete compressive strength. Figure 2-1 shows the survey form. Responses and detailed drawings for typical pier walls were received from 30 states. After studying the completed survey forms and the typical details reported in references 11 and 12, a database was formed to include all the information. The states included in the database are shown in figure 2-2. Note that the data are well distributed geographically and that a full range of seismicity is represented.

CONCRETE BRIDGE PIER WALL SURVEY, University of Nevada, Reno
M. Saiid Saiidi (PI), David H. Sanders and Bruce Douglas

Name of Person Filling Out Survey:_____ ☎(__)_____ **Date**_____

Please Provide information on a typical pier wall. If it would be easier to provide details on several pier walls, than do so. Feel free to make copies of the form and provide details for several pier walls.

State		Bridge Name	
Highway		Design Date	

Concrete Strength (Specified)		Measured	
Reinforcement Grade and fy(Specified)		Measured	
Wall-Footing Detail: Fixed or Hinged		Axial Dead Load (%of f'c Ag)	

Wall Dimensions

Height		Thickness		Width	

If it is possible to mention the Reinforcement Ratio for each section, Please do.

Longitudinal Reinforcement connecting the wall to the footing (Dowels or Starter Bars)

No. of Bars		Bar Size		Height extended into the wall	

Is the reinforcement evenly distributed (Yes / No) ***Pls. provide details in case of No***

Pier Wall Longitudinal Reinforcement (Not anchored into the footing)

No. of Bars		Bar Size		Height range from the footing	
No. of Bars		Bar Size		Height range from the footing	

Is the reinforcement evenly distributed (Yes / No) ***Pls. provide details in case of No***

Transverse Reinforcement in the wall

No. of Bars		Bar Size		Height range from the footing	
No. of Bars		Bar Size		Height range from the footing	-

If the reinforcement is not uniform along the wall height, use the second line, ***Pls. provide details.***

Cross Ties in the wall

No. of Bars		Bar Size		Height range from the footing	
No. of Bars		Bar Size		Height range from the footing	-

If the reinforcement is not uniform along the wall height, use the second line, ***Pls. provide details.***

Nagi A. Abo-Shadi
Civil Engr. Dept., UNR
Jan. 2, 1996

The above space for any notes and sketches.

Figure 2-1 Survey Form

2.3 Statistical Analysis

A statistical sampling analysis was performed on the collected data to choose the test parameters and the appropriate number of wall specimens. The selected parameters were the ratio of the height to wall thickness, the vertical steel ratio, the transverse steel ratio, the cross tie steel ratio, the ratio of vertical bar lap-splice length and diameter, the concrete compressive strength, the steel yield stress and the axial load index.

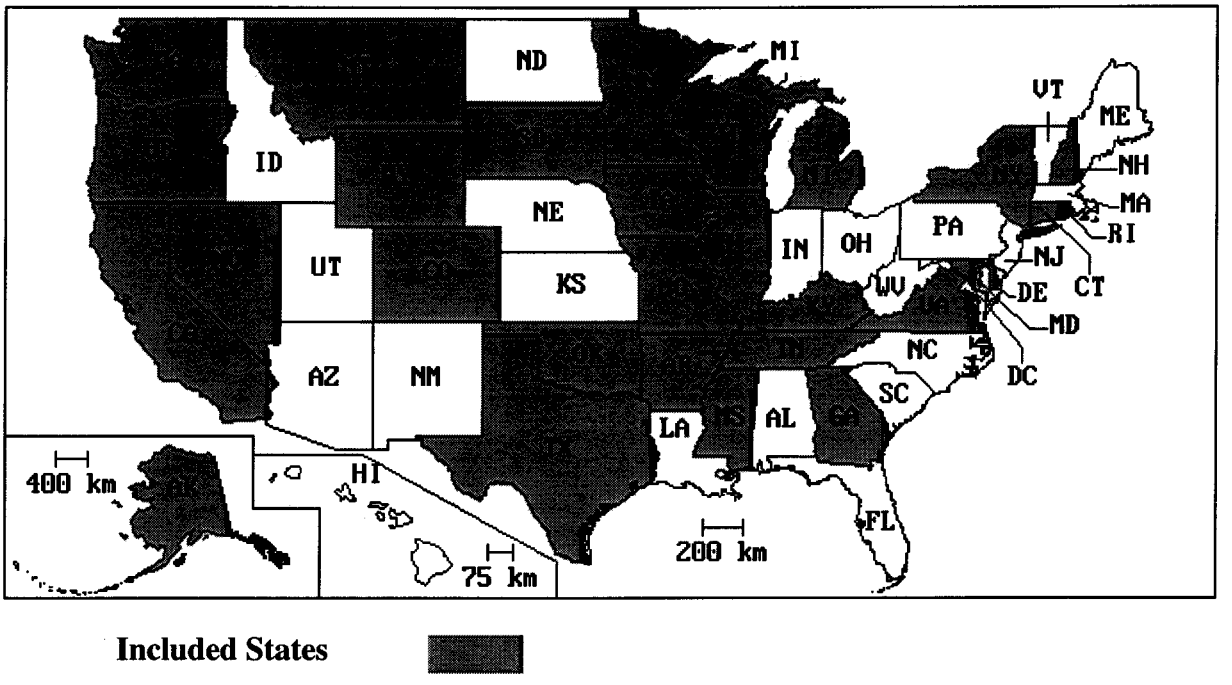

Figure 2-2 States Included in the Database

To identify significant features and patterns of the survey data, the frequency distribution was used. The frequency distribution is an effective and simple tool that organizes and condenses data. Figures 2-3 through 2-10 show the relative frequency distribution of the parameters within the collected data. The circles mark the values selected for the test specimens discussed in Section 2.4.

The frequency distribution reveals the central tendency of the observations. The most important measures of the central tendency are the arithmetic mean, the mode, and the median. The arithmetic mean is the sum of the observations divided by number of observations. The mode is the observation value associated with the largest frequency, which is the most likely or probable observation value. The median is the middle value of an ordered set of observations. If a distribution could be represented by a smooth curve, then the mode is the abscissa of the highest point on the curve. Figure 2-11 shows the location of the mean, median and mode of a moderately skewed distribution. For a symmetrical distribution, all three values coincide. When the median differs considerably from the mean, it is likely that the median is more representative of the observations.

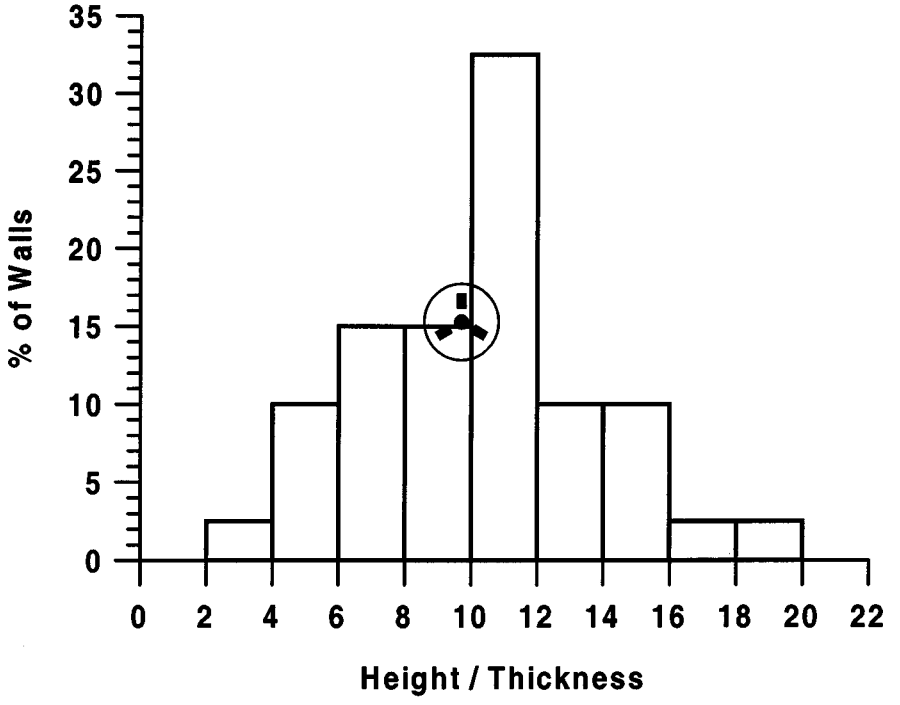

Figure 2-3 Percentage of Wall Height/Thickness Ratios

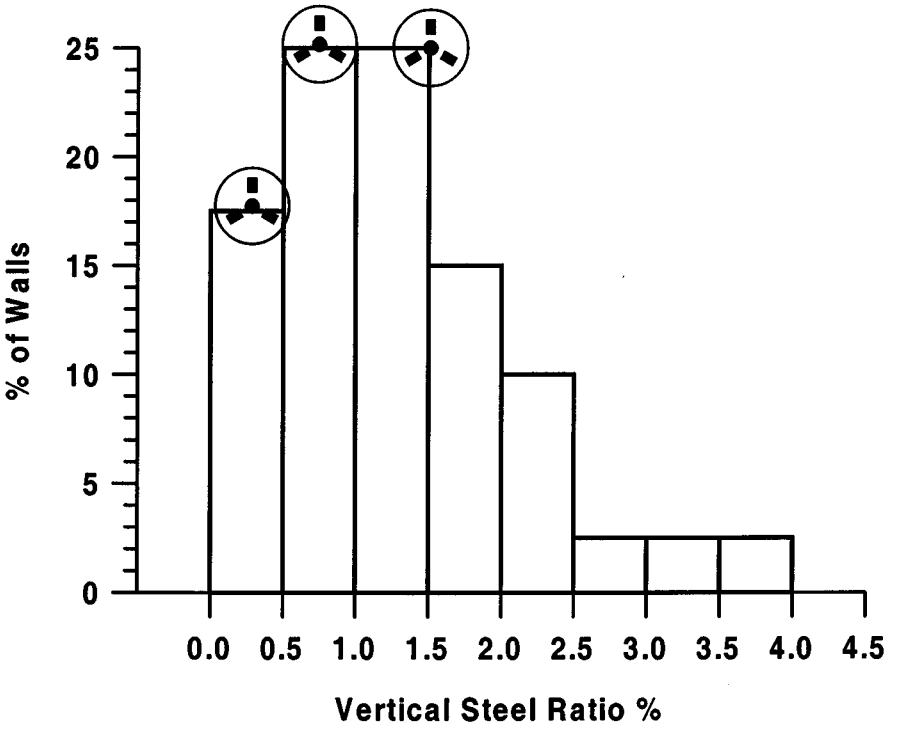

Figure 2-4 Percentage of Vertical Steel Ratios

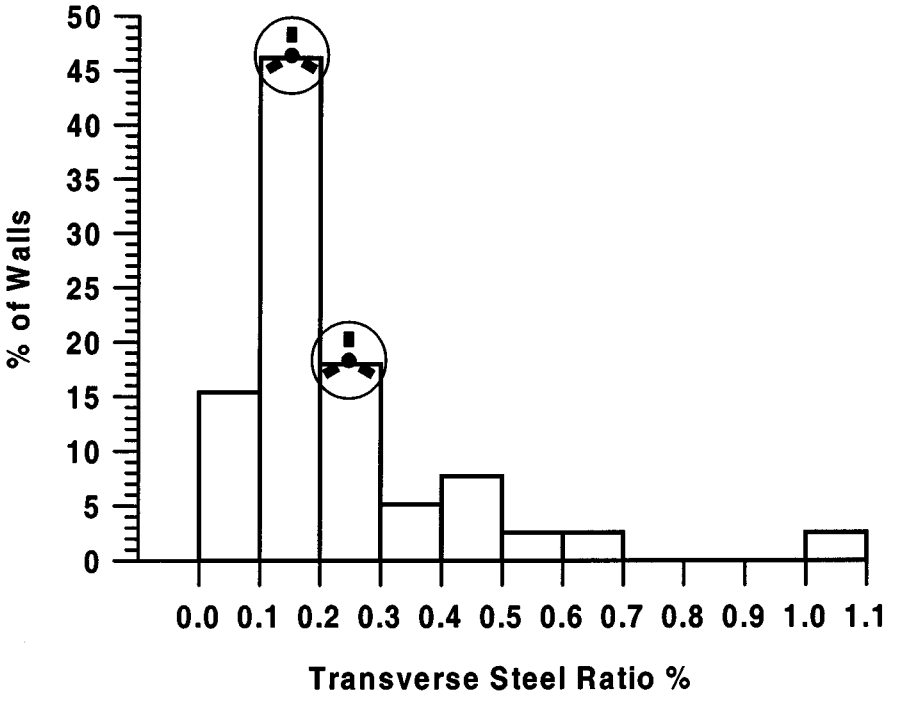

Figure 2-5 Percentage of Transverse Steel Ratios

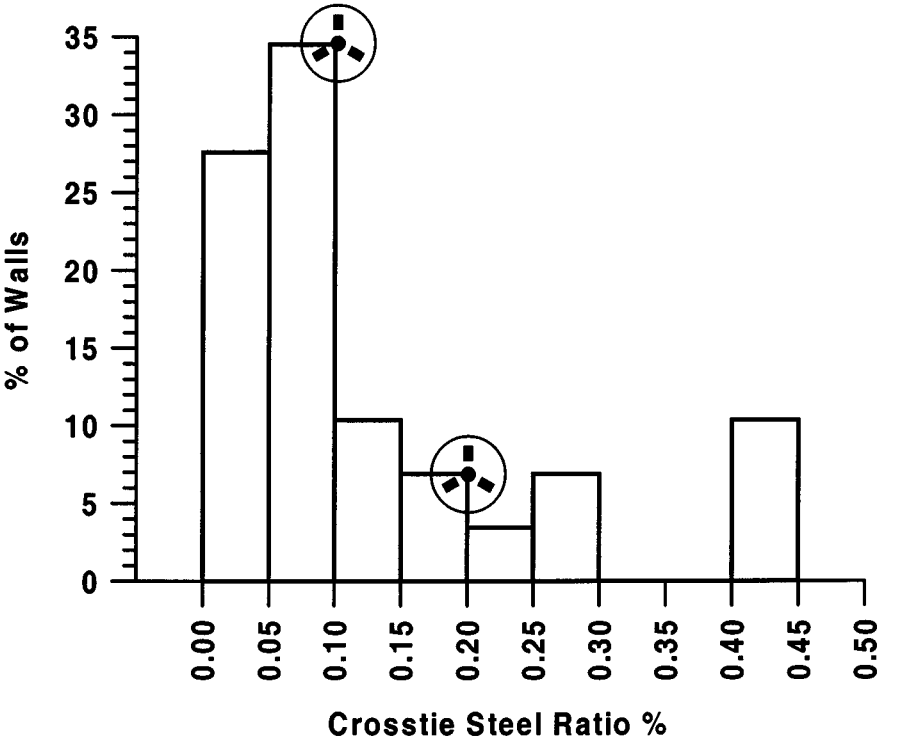

Figure 2-6 Percentage of Crosstie Steel Ratios

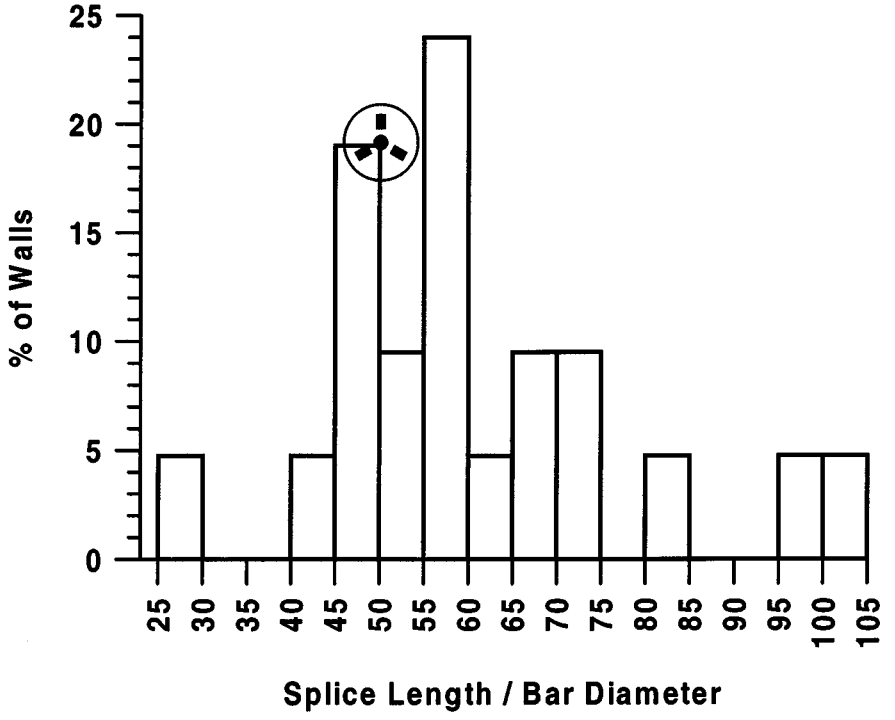

Figure 2-7 Percentage of Splice Length/Bar Diameter Ratios

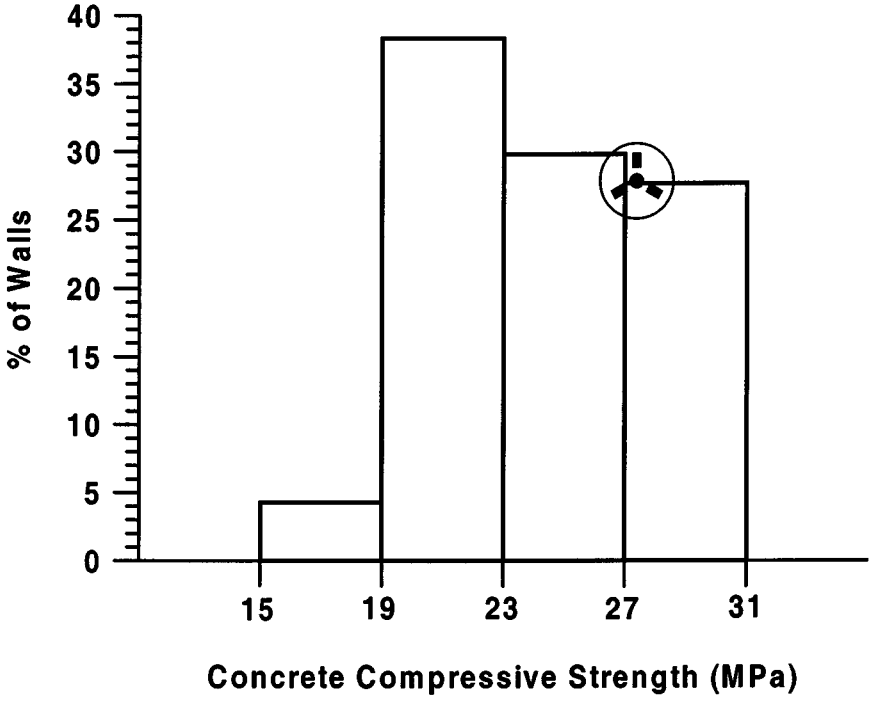

Figure 2-8 Percentage of Concrete Compressive Strength

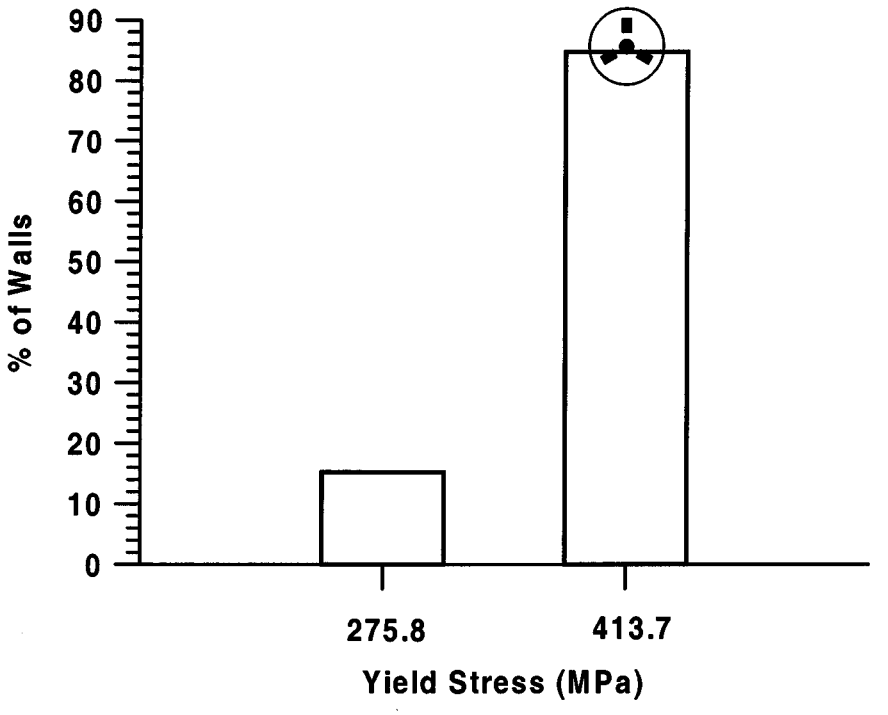

Figure 2-9 Percentage of Steel Yield Stress

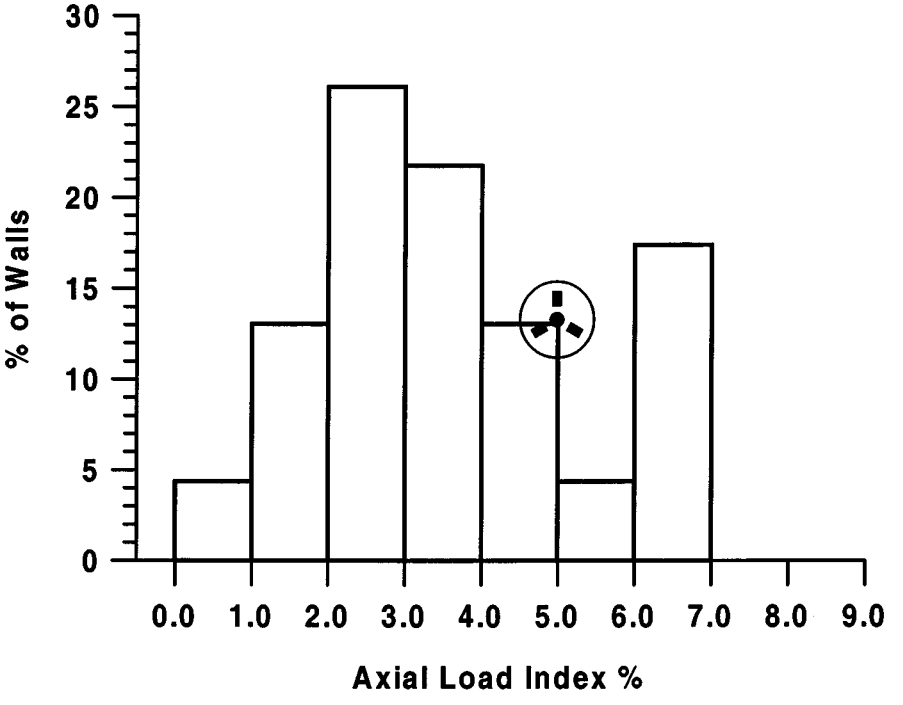

Figure 2-10 Percentage of Axial Load Index

A complete data description results from an evaluation that involves both a measure of average and a measure of variation. Two variation measures were used in the analysis, the range and the standard deviation. The range, which is the difference between the largest and the smallest observation, is the simplest measure of variation. The standard deviation is the most commonly used measure of variation in statistics. It is the square root of the variance, and is determined from the following equation:

$$\sigma^2 = \frac{1}{n-1}\sum_{i=1}^{n}(x_i - \mu)^2 \qquad (2\text{-}1)$$

Where:

σ^2 = Variance

σ = Standard deviation

n = Number of observations

x_i = Observation corresponding to i.

μ = Arithmetic mean

The standard deviation is a superior and more rational measure of variance than the range because the range is based on two extreme observations and ignores the variation exhibited by the interior observations. The coefficient of variance (CV) is defined as the standard deviation divided by the arithmetic mean.

The skewness and the kurtosis are two closely related parameters. The skewness is a measure of symmetry while the kurtosis indicates peakedness or flatness of a distribution relative to the normal distribution.

When the mean and median do not coincide, the distribution is unsymmetric and skewed and one of its tails will be longer than the other. If the mean is greater than (to the right of) the median, the distribution is said to be skewed to the right and has "positive" skewness. In this case, the tail of the distribution points to the right and the majority of data is on the left. Negative skewness occurs when the mean is less than (to the left of) the median, and the distribution is said to be skewed to the left. The larger the skewness absolute value, the more skewed the distribution. Figure 2-12 demonstrates typical normal, positive, and negative skewness.

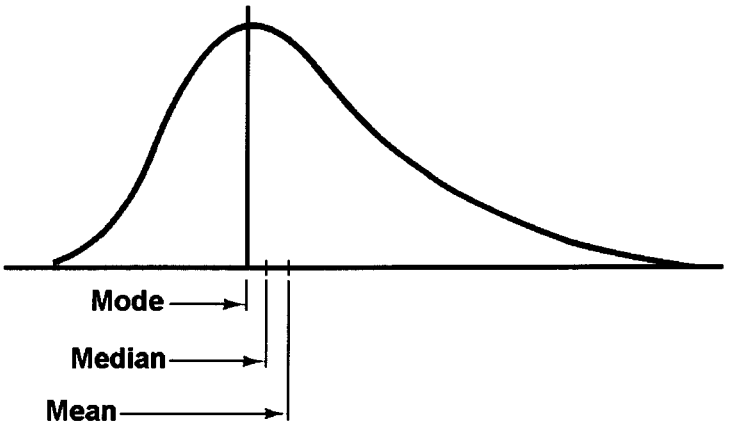

Figure 2-11 Locations of the Mean, Median and Mode

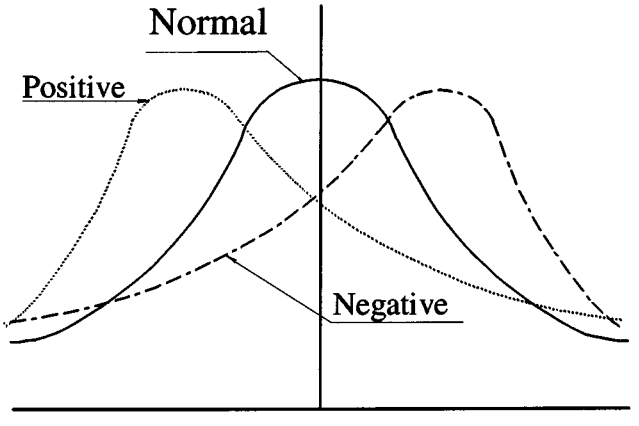

Figure 2-12 Typical Positive and Negative Skewness

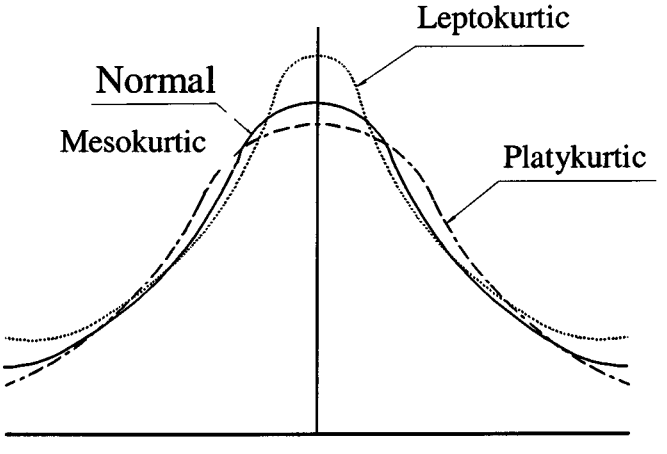

Figure 2-13 Typical Normal, Leptokurtic, and Platykurtic Distributions

Table 2-1 Statistical Sampling Analysis of the Bridge Pier Wall Database

TOTAL OBSERVATIONS: 47

Items	H/T	Vertical Steel	TRANS. Steel	Crosstie Steel	Splice L / D_b	Concrete Comp. Stress	Steel Yield Stress	Axial Load Index
	Ratio	%	%	%	Ratio	f'_c (MPa)	f_y (MPa)	$P/(A_g.f'_c)$%
No. OF CASES	40	40	39	29	21	47	47	23
SUM	410.79	50.58	9.13	3.75	1269.94	1132.10	18477.70	82.06
MEAN	10.27	1.26	0.23	0.13	60.47	24.06	393.13	3.57
MEDIAN	9.90	1.02	0.17	0.07	56.80	24.13	413.70	3.31
MODE	11.00	1.00	0.15	0.08	57.50	22.40	413.70	2.50
MINIMUM	2.75	0.21	0.06	0.01	27.43	16.55	275.80	0.90
MAXIMUM	18.22	3.77	1.02	0.43	101.71	31.00	413.70	6.70
RANGE	15.47	3.56	0.96	0.42	74.28	14.48	137.90	5.80
VARIANCE	10.76	0.74	0.04	0.02	310.29	13.14	2462.56	2.78
STANDARD DEV	3.28	0.86	0.19	0.12	17.62	3.63	49.62	1.67
C.V.	0.32	0.68	0.82	0.94	0.29	0.15	0.13	0.47
SKEWNESS	0.05	0.93	2.28	1.33	0.71	0.19	-1.97	0.53
KURTOSIS	-0.08	0.49	5.89	0.64	0.40	-0.54	1.89	-0.63

The kurtosis measures how flat or peaked the distribution is. In other words, it measures how thin or thick the tails of the distribution are relative to the normal distribution. Leptokurtic distributions are the ones that have thicker tails than normal. Distributions with thinner than normal tails are called Platykurtic distributions. Distributions with normal tails are called Mesokurtic. An increase in the kurtosis value signifies higher peakedness.

The difference between Leptokurtic, Platykurtic, and Mesokurtic distributions are shown in figure 2-13. Table 2-1 shows the results of the statistical sampling analysis. The values in the table were used as a basis to select the parameters in the wall specimens.

2.4 Selection of Test Specimens

The test specimens were intended to represent existing typical pier walls. The wall thickness in the database ranged from 0.3 m to 2.1 m with an average of 0.8 m and a median of 0.75 m. It was decided that a 0.6-m wall thickness represented a full-scale wall because of the positive skewness of the distribution. It was further decided that one-half scale specimens would simulate the actual walls because the walls would be constructed with conventional concrete and steel materials. In selecting the pier wall test specimens the following criteria were used:

i) The values selected should represent a reasonable percentage of the population.
ii) The selected value should be skewed towards the more critical cases.
iii) The kurtosis was used as a guide to choose the number of selected values.
iv) When a single value is used for all the wall specimens, a number close to the average value should be used.
v) The value should be different from those used in walls tested previously.

2.4.1 Wall Height-to-Thickness Ratio

From the statistical analysis of the data, it was found that the wall height-to-thickness ratio ranged from 2.75 to 18.22. (Figure 2-3). The skewness and the kurtosis were very close to zero, which indicated that the frequency distribution was very close to the normal distribution. A ratio

of 9.5, which was nearly the median, was selected because the skewness was positive and because it was slightly more critical than the median value of 9.9.

2.4.2 Vertical Steel Ratio

In the available wall database, the vertical steel ratio ranged from 0.21 % to 3.77 % (Figure 2-4). The positive skewness of the vertical steel ratio emphasized the need for the selected vertical steel ratios to be within the left side of the distribution. The need to have more than one vertical steel ratio came forth due to the positive kurtosis value. Two main vertical steel ratios of 0.75 % and 1.5% were selected because 50% of the observations have a vertical steel ratio ranges from 0.5% to 1.5%. A third vertical steel ratio of 0.21 % was selected to represent lightly reinforced walls. The later value was selected because it is the lowest vertical steel ratio in the database and its relative frequency is more that 17%. Other studies[13] on out-of-plane seismic response of pier walls have included specimens with higher vertical steel ratios.

2.4.3 Transverse Steel Ratio

The ratio of the transverse steel (The reinforcing bars parallel to the strong direction of the wall) in the database ranged from 0.06 % to 1.02 % (Figure 2-5). The frequency distribution of the transverse steel ratio was skewed to the left. This required the selection to be within the left side of the distribution. The high positive kurtosis occurred due to the high transverse steel ratio. This was neglected since the frequency distribution of the high transverse steel ratio was low and discrete. Two ratios were chosen to represent the probable existing ratios. The lower value was taken at 0.14 % since it was close to the median value. The higher ratio was taken at 0.25 %. This value is close to the mean and was the same as the minimum required ratio by AASHTO[2] and Caltrans[6].

2.4.4 Crosstie Steel Ratio

The crosstie steel ratio ranged from 0.01 % to 0.43 % (Figure 2-6). The data showed that when the transverse steel ratio was low, the crosstie steel ratio was also small. Since there were no

cases where the crosstie steel ratio was higher than transverse steel ratio, the selection of crosstie steel ratios was influenced by the selected transverse steel ratios. The skewness and the kurtosis of the frequency distribution of the crosstie steel ratios were moderately positive. Two ratios were selected to represent the range of the crosstie steel ratio of the existing walls. The lower ratio was taken as 0.1% and the higher ratio was taken as 0.2%. The former ratio is slightly greater than the median value, and the latter is close to (but slightly below) the ratio recommended by current seismic codes.

2.4.5 Lap Splice in Vertical Reinforcing Bars

It was found that 54 % of the walls in the survey had a lap splice in the vertical reinforcing bars. The lap splice length ranges from 27 to 102 times the vertical bar diameter (Figure 2-7). However, the ratio for 90 % of the walls exceeded 45. The skewness and the kurtosis of the frequency distribution of the splice length to the bar diameter were considerably low. The splice length was selected so as to be close and slightly less than the median because the very high ratio of the splice length to the bar diameter was impractical and the skewness was positive. A splice length of 50 times the bar diameter was selected to represent the existing splice length and yet to address the more critical cases.

2.4.6 Concrete Compressive Strength

The specified concrete compressive strength ranged from 16.55 MPa to 31 MPa (Figure 2-8). The frequency distribution was nearly symmetrical because the skewness was low. The selected value for the specified compressive strength of the concrete was 27.6 MPa which represents the sum of the mean and the standard deviation to account for time dependent gain in compressive strength.

2.4.7 Steel Yield Stress

Two specified steel yield stress values were found in the database. Approximately 85% of the observations were 413.7 MPa while 15% were 275.8 MPa (Figure 2.9). The high percentage of

walls with 413.7 MPa steel yield stress and the negative skewness of the frequency distribution resulted in the selection of the steel yield stress as 413.7 MPa.

2.4.8 Axial Load Index

The axial load index (defined as the axial load divided by the product of the gross sectional area of the wall and the specified concrete compressive strength) ranged from 0.9% to 6.7% (Figure 2-10) with the majority of the walls having an index of 2% to 5%. The skewness and the kurtosis of the axial load index distribution were low and close to the values of the normal distribution. An axial load index of 5% was selected for the test specimens because it is more critical than the mean value of 3.6% (Table 2-1).

2.5 Number of Specimens

After selecting representative values for the test parameters it was found that there were two main vertical steel ratios, two transverse steel ratios, and two crosstie steel ratios thus leading to eight specimens. The number of test specimens was reduced to six because there were no cases in the database that had high crosstie steel ratio with low transverse steel ratio. A seventh specimen was selected to represent the lowest reinforcement ratio in the database. Table 2-2 presents the selected reinforcement ratios for the test specimens.

Table 2-2 Target Reinforcement Ratios for the Test Specimens

Specimen No.	Vert. Steel Ratio		Trans. Steel Ratio		Crossties Ratio	
	H	L	H	L	H	L
	1.50%	0.75%	0.25%	0.15%	0.20%	0.10%
1		☯		☯		☯
2		☯	☯			☯
3		☯	☯		☯	
4	☯			☯		☯
5	☯		☯			☯
6	☯		☯		☯	
7	0.21%			☯		☯

SECTION 3
EXPERIMENTAL PROGRAM

3.1 Introduction

The experimental study was conducted to evaluate the seismic performance of representative bridge pier walls that exist in the U.S. and to calibrate the analytical model that was used to analyze the pier wall cases in the parametric study. The experimental program involved constructing, instrumenting, and testing seven one-half scale pier wall specimens. All wall specimens had the same overall dimensions. The difference among the wall specimens was the reinforcing steel ratios. Concrete cylinders and bar samples were obtained to measure their mechanical properties. Test data included the lateral displacement and the force along the centerline of the actuator at the top of the wall, the axial and lateral loads, the strains in the instrumented bars, and the curvature in the potential plastic hinge zone. The test setup and testing program were the same for all wall specimens. Each wall specimen was tested cyclically in the weak direction under a constant axial load. This section describes the pier wall test specimens, instrumentation, test setup, and the testing program.

3.2 Test Specimens

All the test specimens had the same overall dimensions. The wall cross section was 300 mm thick by 1500 mm wide. The height measured from the top of the footing to the centerline of the lateral actuator was 2850 mm. The Reinforcing bars in the test specimens were selected from the U.S. customary sizes. Each test specimen had the same geometry and reinforcement for the footing and the top beam (Figure 3-1 to 3-2). The footings of the specimens were designed to be rigid and strong to minimize footing deformation and avoid damage in the footing. The purpose of the footing was to tie the specimen down to the structural floor of the laboratory. Details of a typical footing are shown in figure 3-1. The function of the top beam was to facilitate the application of the axial and the lateral loads (Figure 3-2). The top beam was strengthened by prestressing the longitudinal direction using two 32-mm Dywidag^{TM} bars.

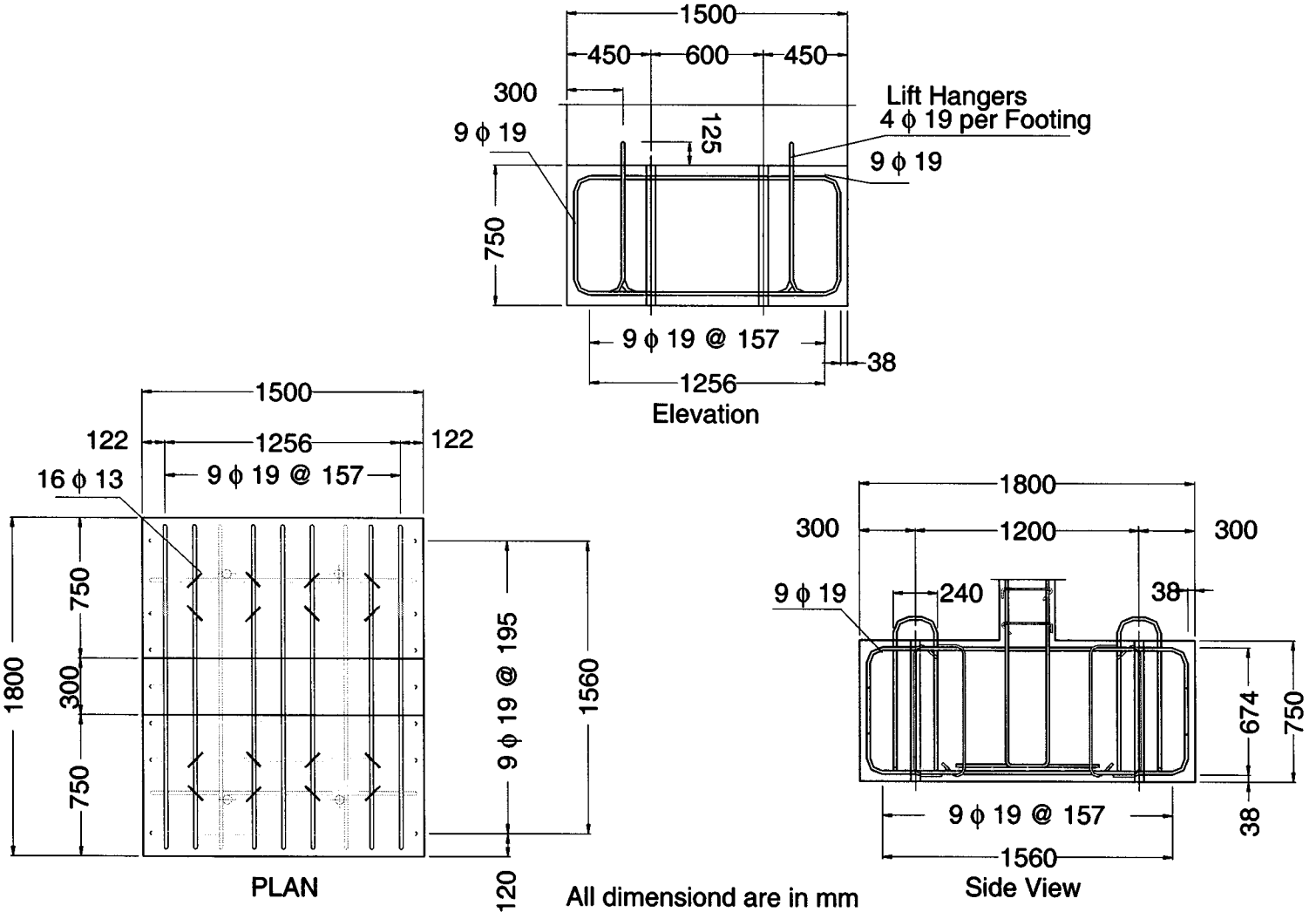

Figure 3-1 Details of Typical Footing

The number and size of the reinforcing bars were selected such that the actual reinforcement ratios would be very close to the selected ratios, as described in Section 2.4. Table 3-1 presents the target and the actual reinforcement ratios. Details of vertical, transverse, and crosstie reinforcements of the wall sections such as the number, the size, and the spacing of the reinforcing bars are described in tables 3-2 and 3-3. Bending lists for the bars were prepared to ensure the accuracy of the dimensions. Figures 3-3 through 3-9 show details of reinforcement of the test specimens. Crossties with standard hooks of 90° and 135° legs were used. The hook extension for all the crossties was 95 mm, which is equivalent to 10 bar diameters.

3.2.1 Construction of Test Specimens

The test specimens were constructed in two sets. The first set included specimens 1, 2, 3, and 7 while the second set included specimens 4, 5, and 6. The procedure for constructing each specimen was the same. The footing was constructed first, then the wall and the top beam. In each set of specimens, the forms of the footings were erected for all specimens. The cages of the footings and the wall dowels were placed inside the forms of the footings. Four 50-mm diameter by 750-mm long plastic sleeves were placed vertically in the footing to enable passage of 32-mm Dywidag ™ bars that were used during the test to tie down the footing to the structural floor.

The concrete was mixed and provided by a local contractor. The target concrete compressive strength and slump were 27.6 MPa and 75 mm, respectively. The concrete was placed and then vibrated mechanically. The concrete surface was smoothed using hand trowels. To measure the concrete compressive strength for the footings, 27 concrete cylinders were taken from the concrete batches. The concrete was kept moist for seven days after construction.

The reinforcement and forms of the walls and the top beams were erected after curing the footings. Subsequently, the steel cages of the top beams were placed into their forms. Plastic sleeves of 50-mm diameter were used in the top beams (Figure 3-2). For each specimen, two 2100-mm long plastic sleeves were placed in the longitudinal direction of the top beam to allow the passage of the prestressing Dywidag ™ bars. Four plastic sleeves with a length of 563 mm were placed in the transverse direction of the top beam to pass the actuator bolts.

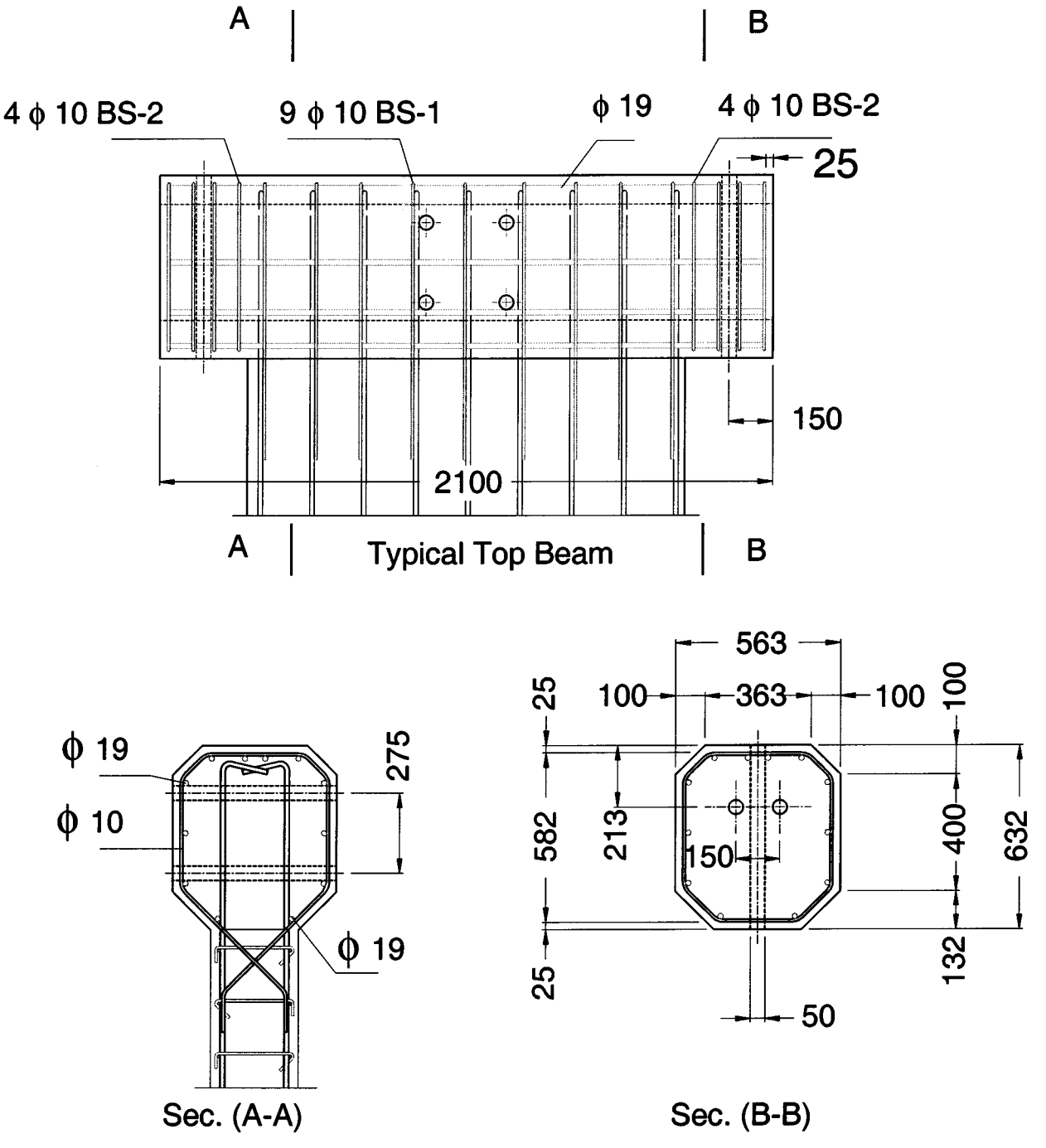

Figure 3-2 Details of a Typical Top Beam

Table 3-1 Reinforcement Ratios for the Test Specimens

Specimen	Vertical Steel Ratio		Transverse Steel Ratio		Crosstie Steel Ratio	
	Target	Actual	Target	Actual	Target	.09%, .1%
1	0.75%	0.78%	0.15%	0.14%	0.10%	0.10%
2	0.75%	0.78%	0.25%	0.25%	0.10%	0.10%
3	0.75%	0.78%	0.25%	0.25%	0.20%	0.20%
4	1.50%	1.47%	0.15%	0.14%	0.10%	0.09%
5	1.50%	1.47%	0.25%	0.25%	0.10%	0.10%
6	1.50%	1.47%	0.25%	0.25%	0.20%	0.20%
7	0.21%	0.28%	0.15%	0.14%	0.10%	0.07%

Table 3-2 Vertical and the Transverse Reinforcement for the Test Specimens

Specimen	Vertical Reinforcement				Transverse Reinforcement			
	No.	Rebar	ρ_v %	S_h (mm)	No.	Rebar	ρ_l %	S_v (mm)
1	18	ϕ16	0.78%	180	16	ϕ10	0.14%	320
2	18	ϕ16	0.78%	180	28	ϕ10	0.25%	182
3	18	ϕ16	0.78%	180	28	ϕ10	0.25%	182
4	24	ϕ19	1.47%	130	16	ϕ10	0.14%	320
5	24	ϕ19	1.47%	130	28	ϕ10	0.25%	182
6	24	ϕ19	1.47%	130	28	ϕ10	0.25%	182
7	10	ϕ13	0.28%	360	16	ϕ10	0.14%	320

Table 3-3 Crosstie Reinforcement for the Test Specimens

Specimen	Lower Crosstie Reinforcement					Upper Crosstie Reinforcement				
	H (mm)	No.	Rebar	ρ_c %	S_v(mm)	H (mm)	No.	Rebar	ρ_c %	S_v(mm)
1	956	21	ϕ10	0.10%	320	63.75	35	ϕ10	0.10%	320
2	910	20	ϕ10	0.10%	182	65.50	36	ϕ10	0.10%	182
3	910	40	ϕ10	0.20%	182	65.50	36	ϕ10	0.10%	182
4	956	18	ϕ10	0.09%	320	63.75	30	ϕ10	0.09%	320
5	910	20	ϕ10	0.10%	182	65.50	36	ϕ10	0.10%	182
6	910	40	ϕ10	0.20%	182	65.50	36	ϕ10	0.10%	182
7	1275	20	ϕ10	0.07%	255	51.00	20	ϕ10	0.07%	255

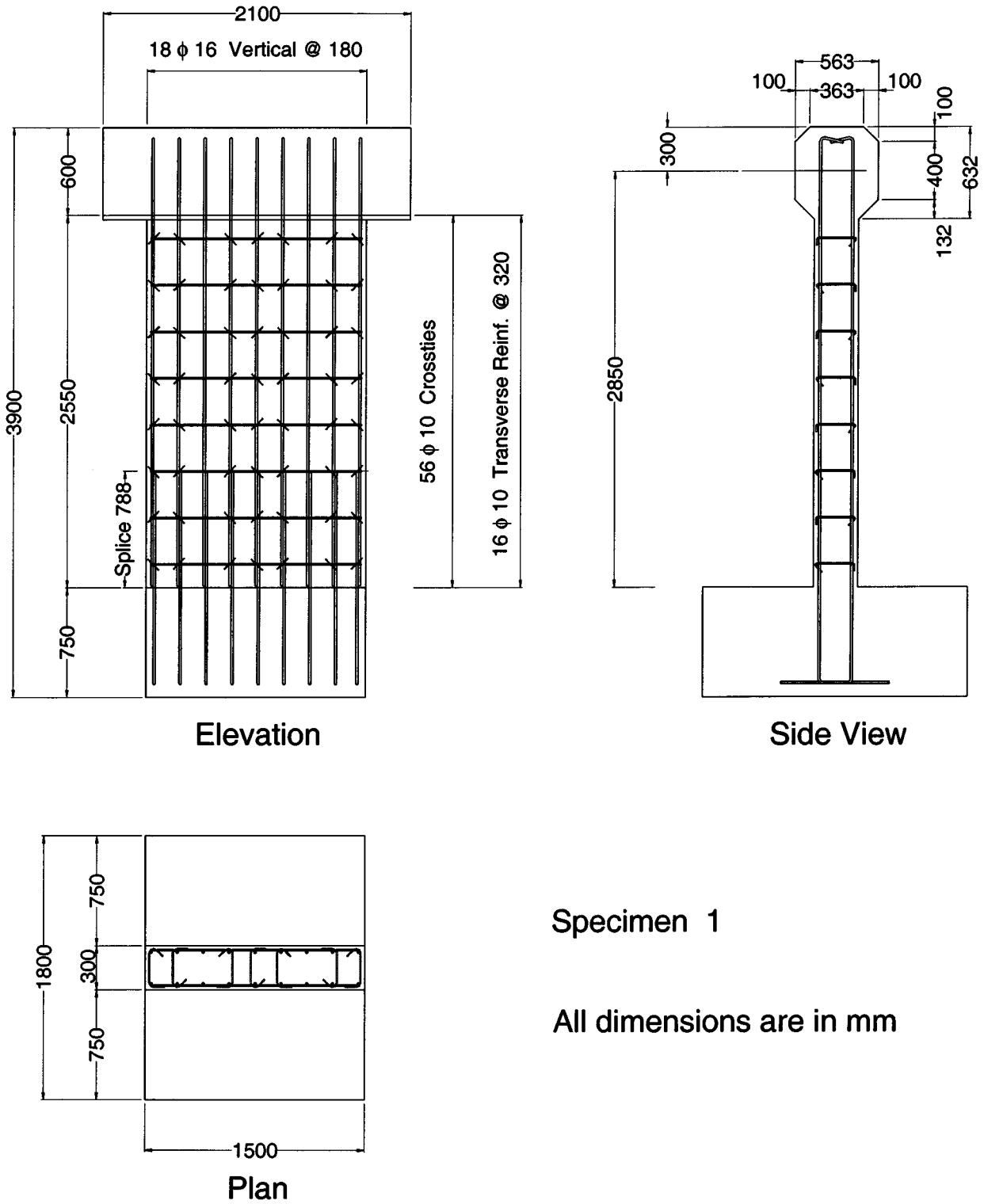

Figure 3-3 Details of Specimen 1

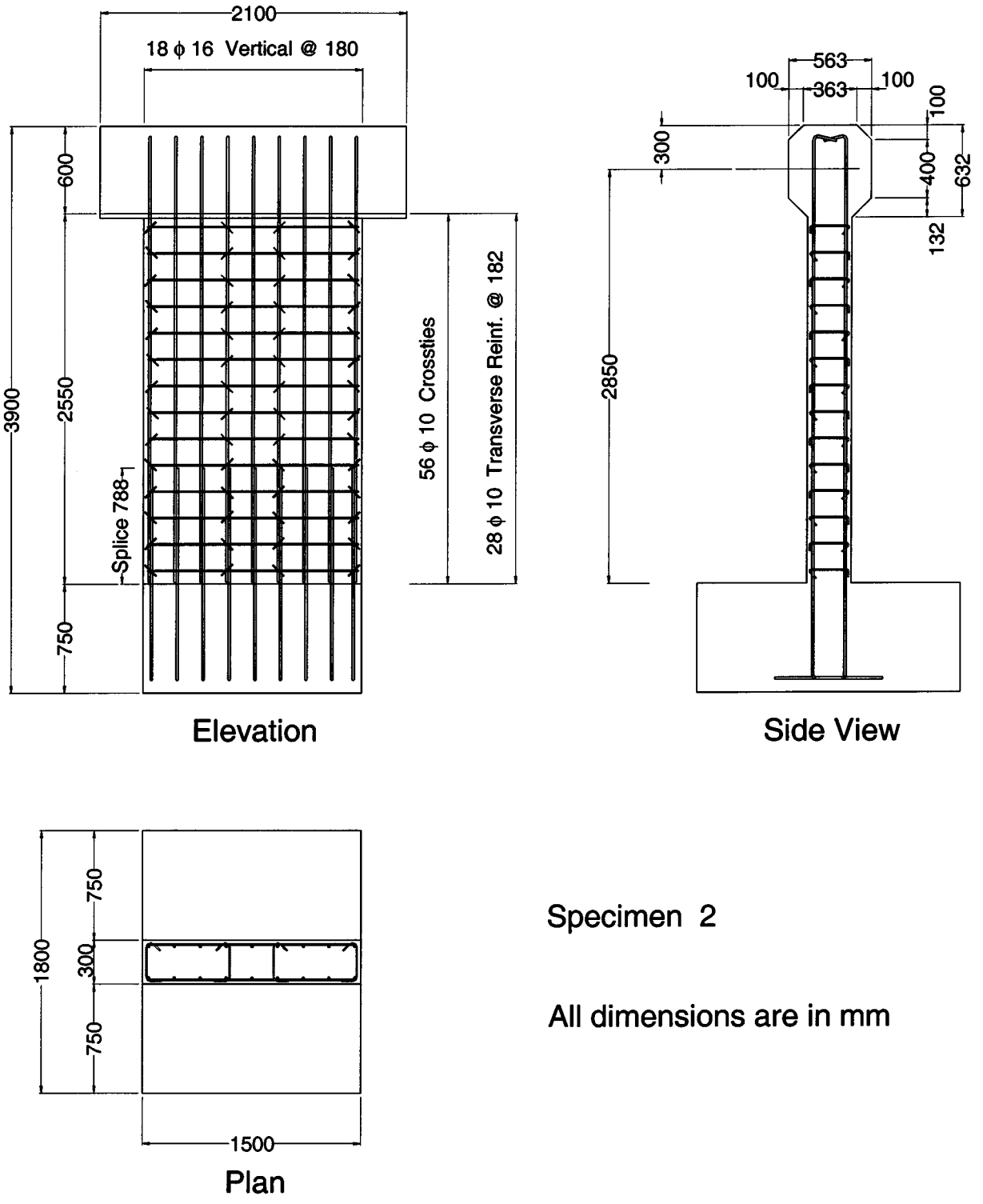

Figure 3-4 Details of Specimen 2

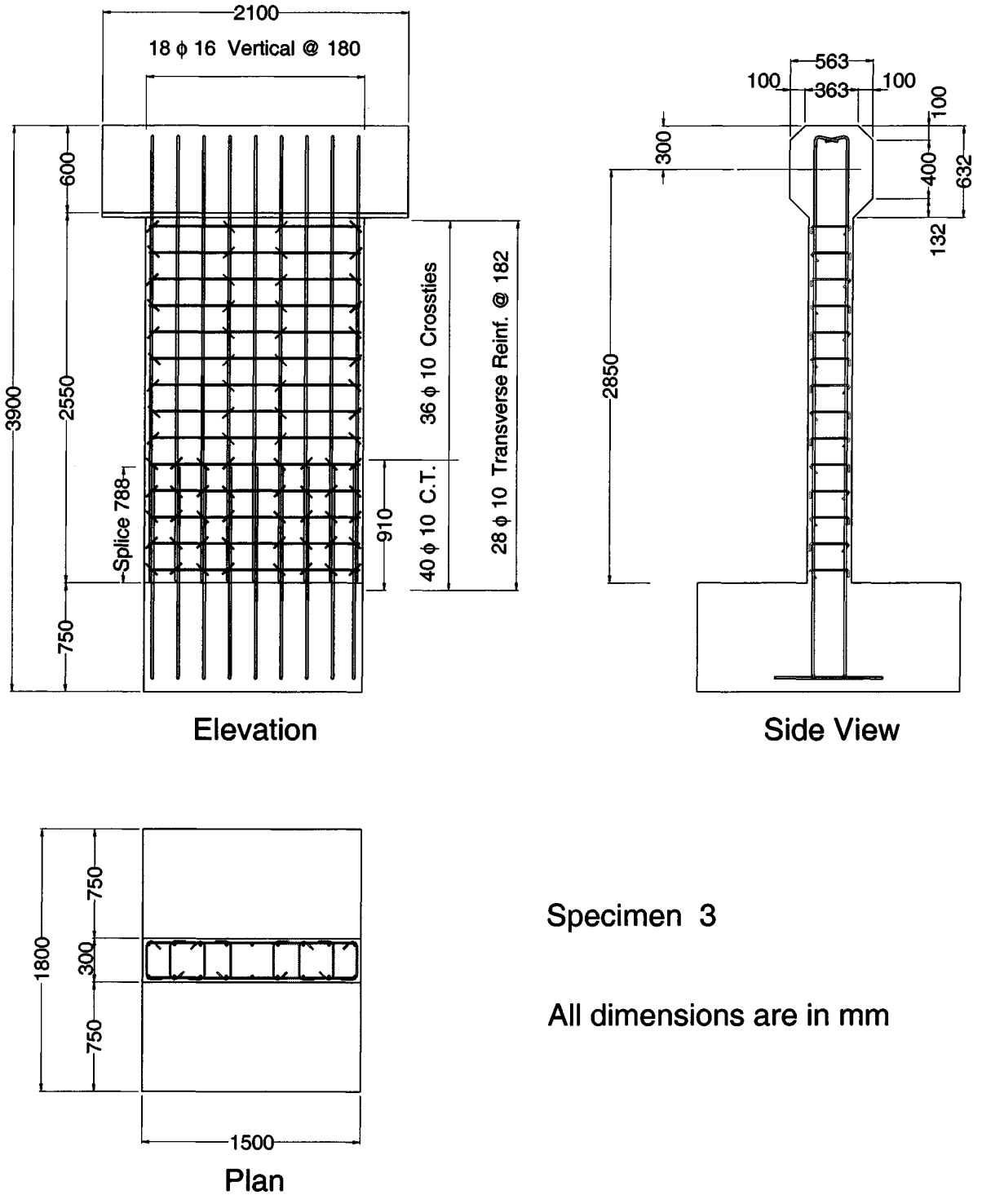

Figure 3-5 Details of Specimen 3

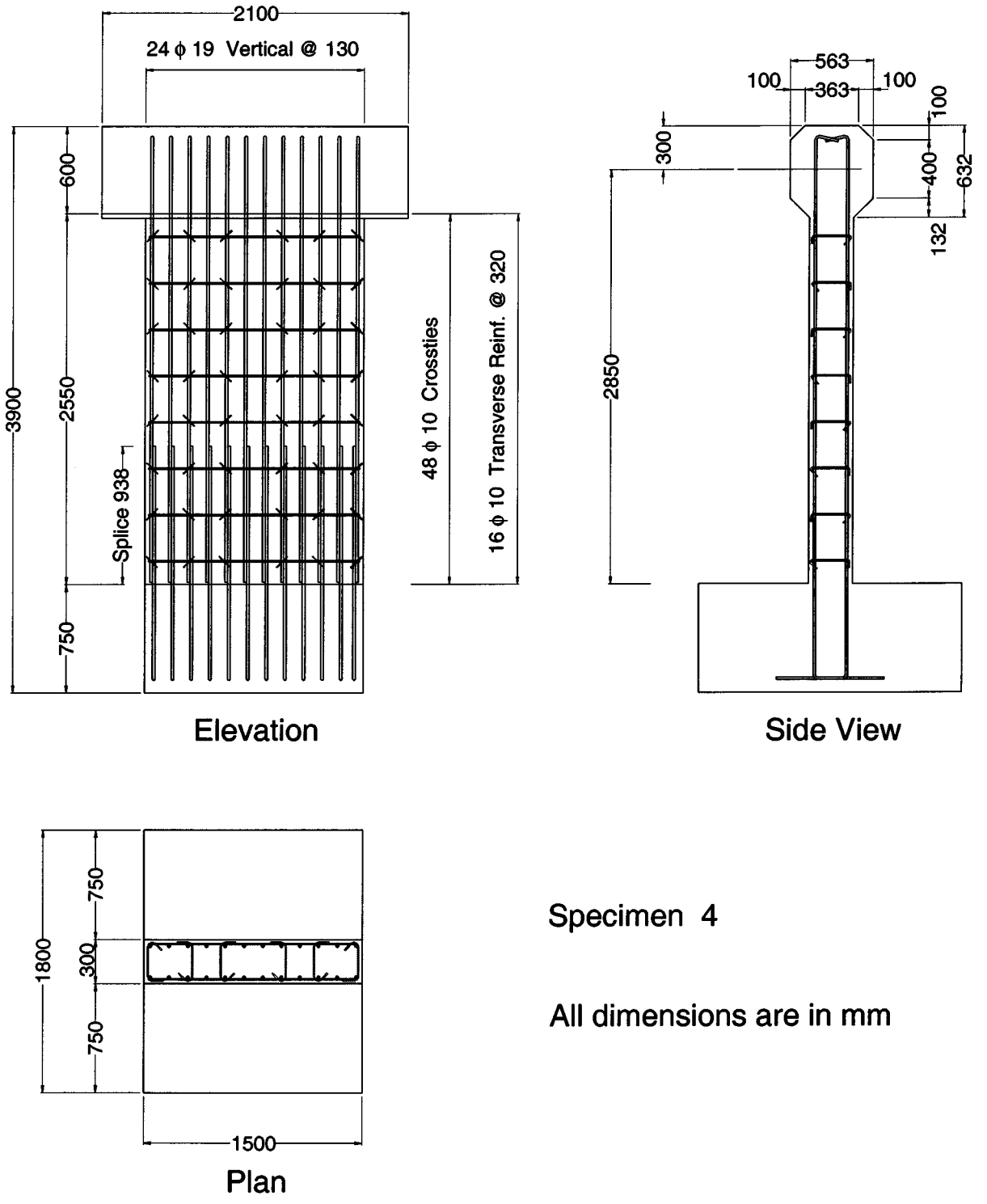

Figure 3-6 Details of Specimen 4

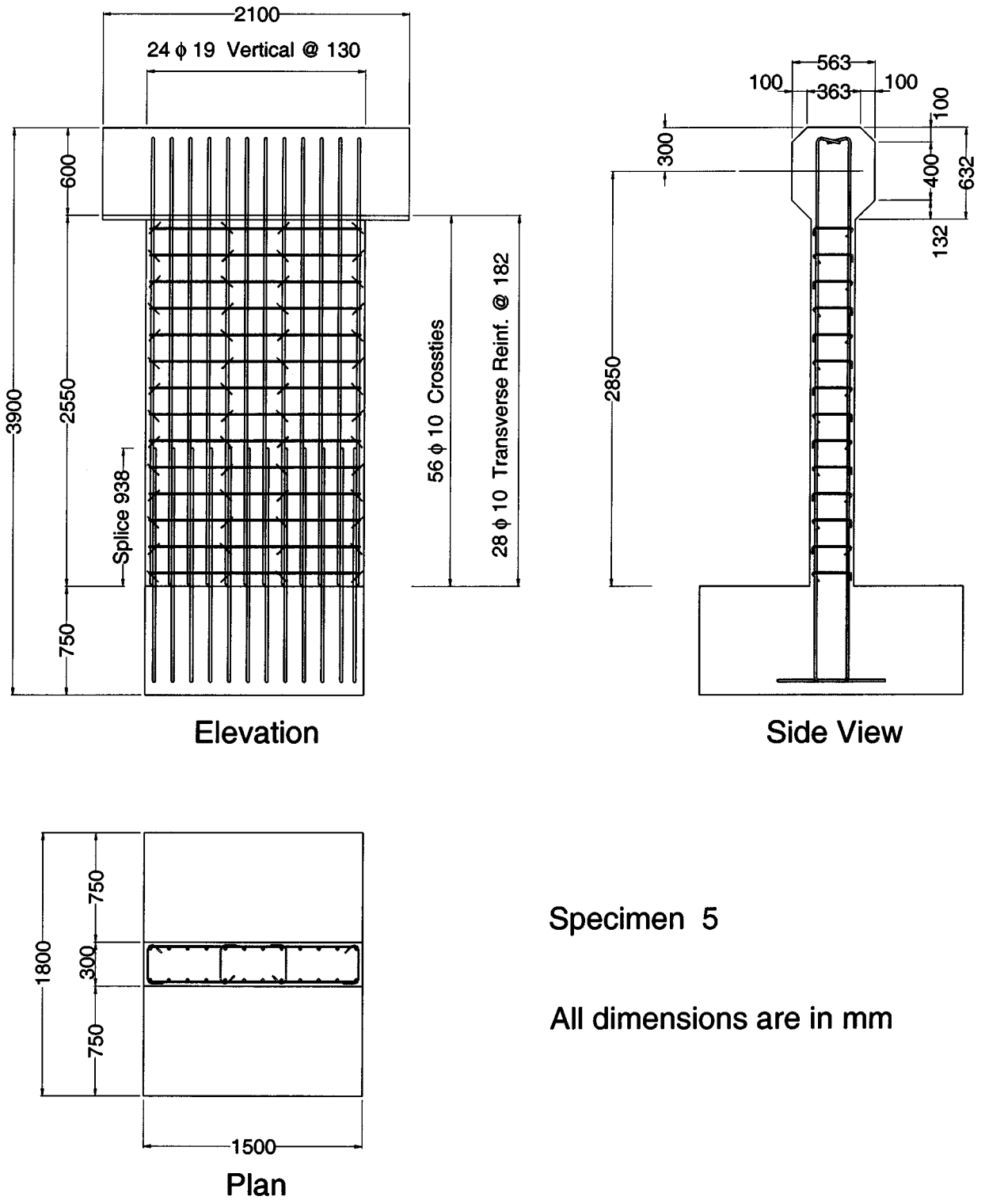

Figure 3-7 Details of Specimen 5

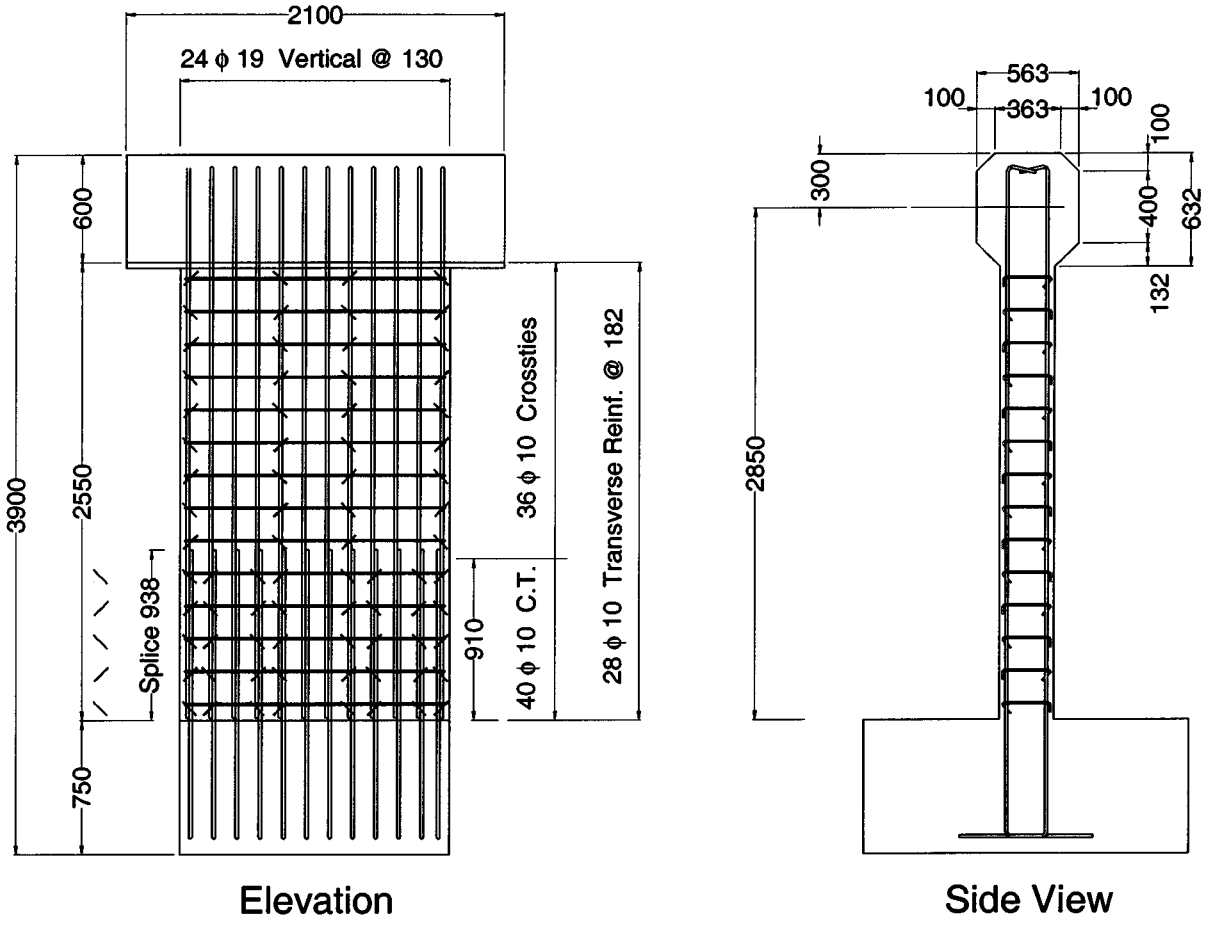

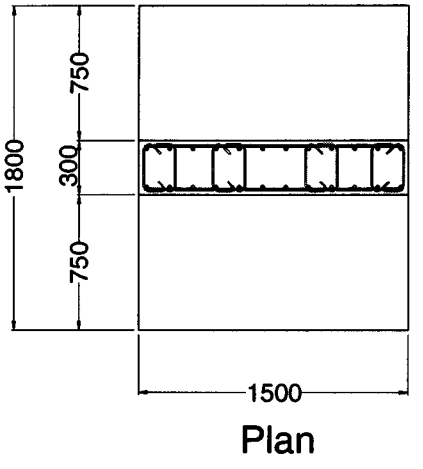

Specimen 6

All dimensions are in mm

Figure 3-8 Details of Specimen 6

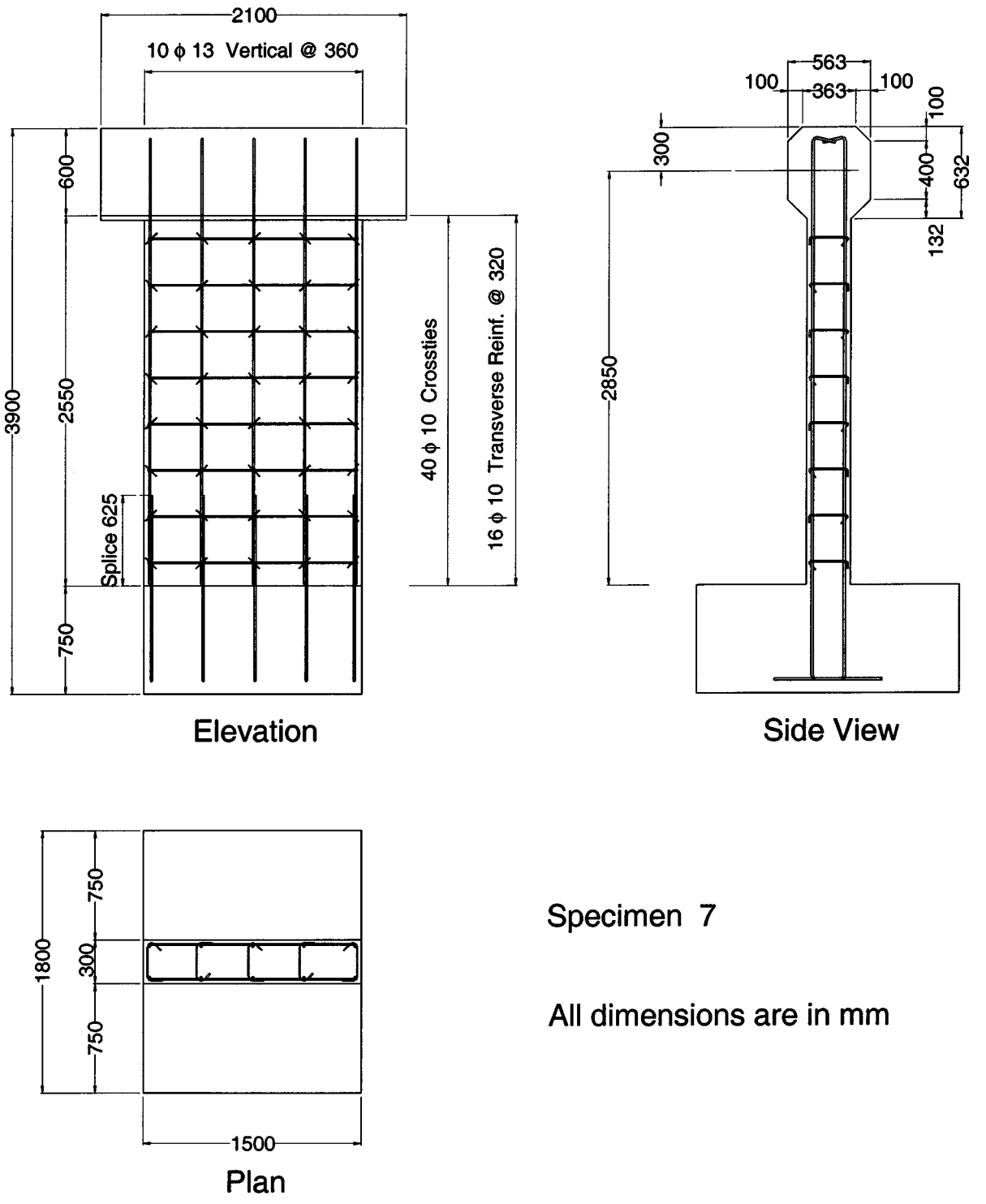

Figure 3-9 Details of Specimen 7

Figure 3-10 Construction of Test Specimens

To allow for the passage of the vertical 32-mm Dywidag bars that were used to apply the vertical axial load, two plastic sleeves with a length of 632 mm were placed in the top beam of each specimen. The forms were closed and fastened, then the walls and the top beams were cast monolithically using a pump and vibrated mechanically. During casting of the walls and top beams, a total of 27 concrete cylinders were taken to measure the compressive strength. The walls were cured for a period of seven days. Figure 3-10 shows the test specimens during construction.

3.2.2 Material Properties

The actual material properties were necessary for the analysis of the pier wall specimens. The concrete cylinders and reinforcing bars were tested to measure their mechanical properties. The target concrete compressive strength was 27.6 MPa while the specified yield stress of the steel reinforcement was 413.7 MPa.

The concrete slump was measured during casting of the concrete. Table 3-4 presents the measured concrete slump for each concrete batch. For each concrete batch, 3 cylinders were

tested at 7 days and another 3 cylinders were tested at 28 days. In addition, for each pier wall specimen, 3 cylinders for the footing and 3 cylinders for the wall were tested on the wall test day. Tables 3-5 and 3-6 show the concrete compressive strength for the wall specimens at 28 days and on the day of the wall tests.

Three specimens of each bar size were tested using an Instron testing machine to measure the mechanical properties of the steel. The average measured properties of the bar specimens are presented in table 3-7. The modulus of elasticity of the steel in the elastic range and in the strain hardening was estimated as 200,000 MPa, and 10,000 MPa, respectively. The strain at the beginning of the strain hardening was estimated as 0.007, while the ultimate strain was estimated as to be 0.15.

Table 3-4 Measured Concrete Slump

Specimens	Location	Slump (mm)
1, 2, 3, and 7	Footings	81
	Walls	88
4, 5, and 6	Footings	83
	Walls	90

Table 3-5 Measured Concrete Compressive Strength for the First Set of Specimens, MPa

Test	Location	Cylinder 1	Cylinder 2	Cylinder 3	Average
At 28 Days	Footing	29.49	29.15	30.10	29.58
At 28 Days	Wall	28.89	28.09	28.49	28.49
Specimen 1	Footing	29.10	30.45	30.30	29.95
	Wall	29.02	29.32	29.14	29.16
Specimen 2	Footing	30.64	28.68	30.35	29.89
	Wall	29.44	28.85	29.10	29.13
Specimen 3	Footing	29.35	31.20	30.59	30.38
	Wall	29.39	32.10	31.60	31.03
Specimen 7	Footing	29.68	29.28	30.38	29.78
	Wall	29.10	29.90	28.39	29.13

Table 3-6 Measured Concrete Compressive Strength for the Second Set of Specimens, MPa

Test	Location	Cylinder 1	Cylinder 2	Cylinder 3	Average
At 28 Days	Footing	29.29	27.23	28.37	28.30
At 28 Days	Wall	24.88	26.67	25.82	25.79
Specimen 4	Footing	29.27	29.76	28.10	29.04
	Wall	27.23	28.92	26.59	27.58
Specimen 5	Footing	29.97	28.02	28.31	28.77
	Wall	24.24	25.24	24.98	24.82
Specimen 6	Footing	31.57	25.29	28.27	28.38
	Wall	25.74	26.81	26.05	26.20

Table 3-7 Measured Steel Properties

Bar Size	Yield Stress f_y (MPa)	Ultimate Stress f_u (MPa)
ϕ10	428.44	520.11
ϕ13	426.75	533.89
ϕ16	424.00	516.59
ϕ19	419.36	553.05

3.2.3 Instrumentation

Each specimen was instrumented with strain gauges, LVDTs (linear variable differential transformers), and load cells. A total of 32 electric resistance strain gauges were used in each specimen. The vertical steel was instrumented with 16 gauges at three levels, and the confinement steel (transverse steel and crossties) was instrumented with 16 gauges. The vertical bars were instrumented to monitor yielding spread in the walls. The gauges on the vertical bars were located at 0, 150, and 470 mm from the top of the footing in specimens 1, 4, and 7, while they were located at 0, 80, and 270 mm in specimens 2, 3, 5, and 6. The gauges immediately above the footings were installed on the dowels while the others were installed on wall bars. The gauges on the transverse bars and crossties were installed to evaluate confinement stresses.

These gauges were located at 160, 480, and 800 mm from the top of the footings in specimens 1, 4, and 7, while they were located at 91, 273, and 455 mm in specimens 2, 3, 5, and 6. Figures 3-11 through 3-17 show the location of the strain gauges.

Each wall specimen was instrumented with 5 LVDTs on each side in the lower 600 mm to measure the curvature in the potential plastic hinge zone. The locations of the LVDTs were identical for all the test specimens (Figure 3-18).

The actuator built-in LVDT and load cell measured the lateral displacement of the wall along the centerline of hydraulic ram and the lateral load. Two load cells were installed under the vertical hydraulic jacks to measure the axial load applied by two vertical 32-mm Dywidag ™ bars. The data from strain gauges, LVDTs and load cells were collected using a data acquisition system (Megadac 5033A) at a rate of one record per second. The data acquisition system was connected to a PC to record and monitor the data instantaneously.

3.3 Test Setup and Testing Program

The test setup was the same for all the pier wall test specimens. The bottom of the specimen footing was set at about 6 mm above the laboratory-testing floor. A mix of gypsum cement was poured to provide a level surface and full contact between the specimen footing and the floor.

Four 32-mm Dywidag ™ bars were used to tie the specimen footing down to the floor. Each bar was stressed to an initial jacking force of 178 kN to prevent rocking of the footing due to the overturning moments generated by the applied lateral load during the test. A gypsum pad was used under each Dywidag ™ bar anchorage of the to level the surface and prevent concentration of the stresses on the specimen footing.

The axial load was applied using two identical hydraulic jacks and two 32-mm Dywidag ™ bars. The jacks were placed on the top beam in each specimen and the Dywidag ™ bars were anchored at the top of the jacks and at the bottom of the laboratory floor. A 44.5-kN pressure accumulator was hooked to the hydraulic system between the pump and the jacks to minimize

axial load fluctuation. To avoid stress concentration on the top of the beam, a gypsum pad and a steel plate were provided underneath each vertical jack. To prevent cracking of the concrete at the top beam due to the applied vertical axial load, the top beam was transversely prestressed using two 32-mm Dywidag ^{TM} bars with a force of 200 kN for each bar.

The lateral load was applied using a 490-kN MTS hydraulic actuator. The actuator was first connected to the reaction wall through a steel plate connector. The actuator was then extended and the head was connected to the top beam of the specimen. A 400-mm x 400-mm bearing plate with a thickness of 19 mm was installed between the actuator head and the specimen to prevent stress concentration and cracking of the concrete. The test setup is shown in figure 3-19.

The testing program was nearly the same for all the seven test specimens. The specimens were tested after the concrete had cured for at least 28 days. The concrete cylinders were tested at approximately 12 hours before each wall specimen test. The cracking lateral load, the yield lateral load, the yield displacement, and the ultimate displacement were calculated before the test.

Each specimen was subjected to a constant axial load and then tested cyclically in the weak direction. The test was load-controlled up to 75% of the yield lateral load, and displacement-controlled from this point up to failure. The axial load was first applied in full to the wall specimen. The lateral load was applied for one cycle at the calculated cracking moment, and one cycle at 75% of the calculated yield lateral load. The first cycle was applied to check the test setup and the instrumentation. The second cycle was applied to estimate the yield displacement by averaging the displacements of the push and the pull directions and then extrapolating the yield displacement.

At the displacement-controlled stage, two full cycles were applied at each displacement ductility level. The specimen was considered to be failed when the lateral load dropped to 80% of its maximum value (capacity) or at rupture of the vertical rebars. Figure 3-20 shows a typical lateral load-history diagram for the test specimens.

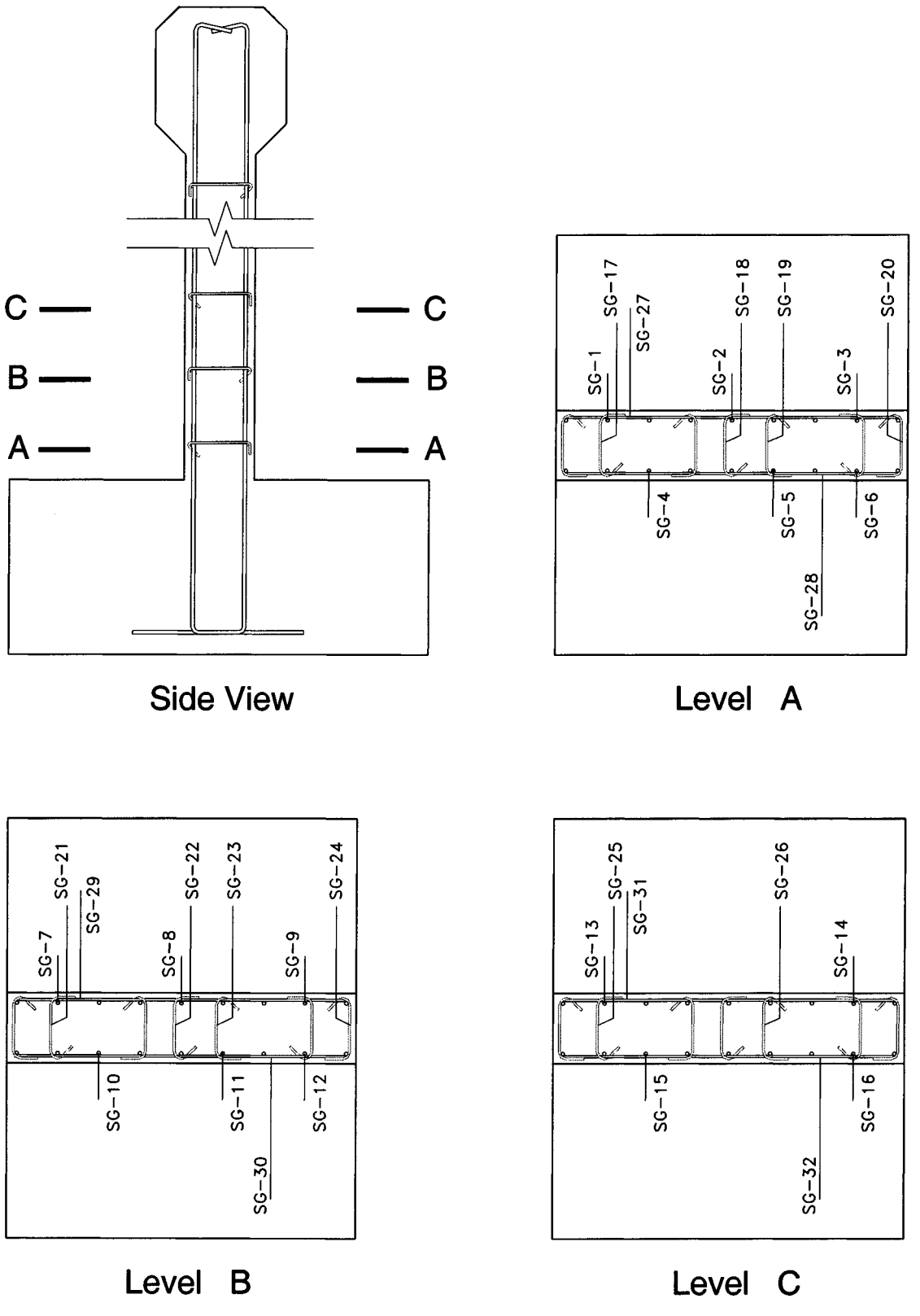

Figure 3-11 Locations of Strain Gauges in Specimen 1

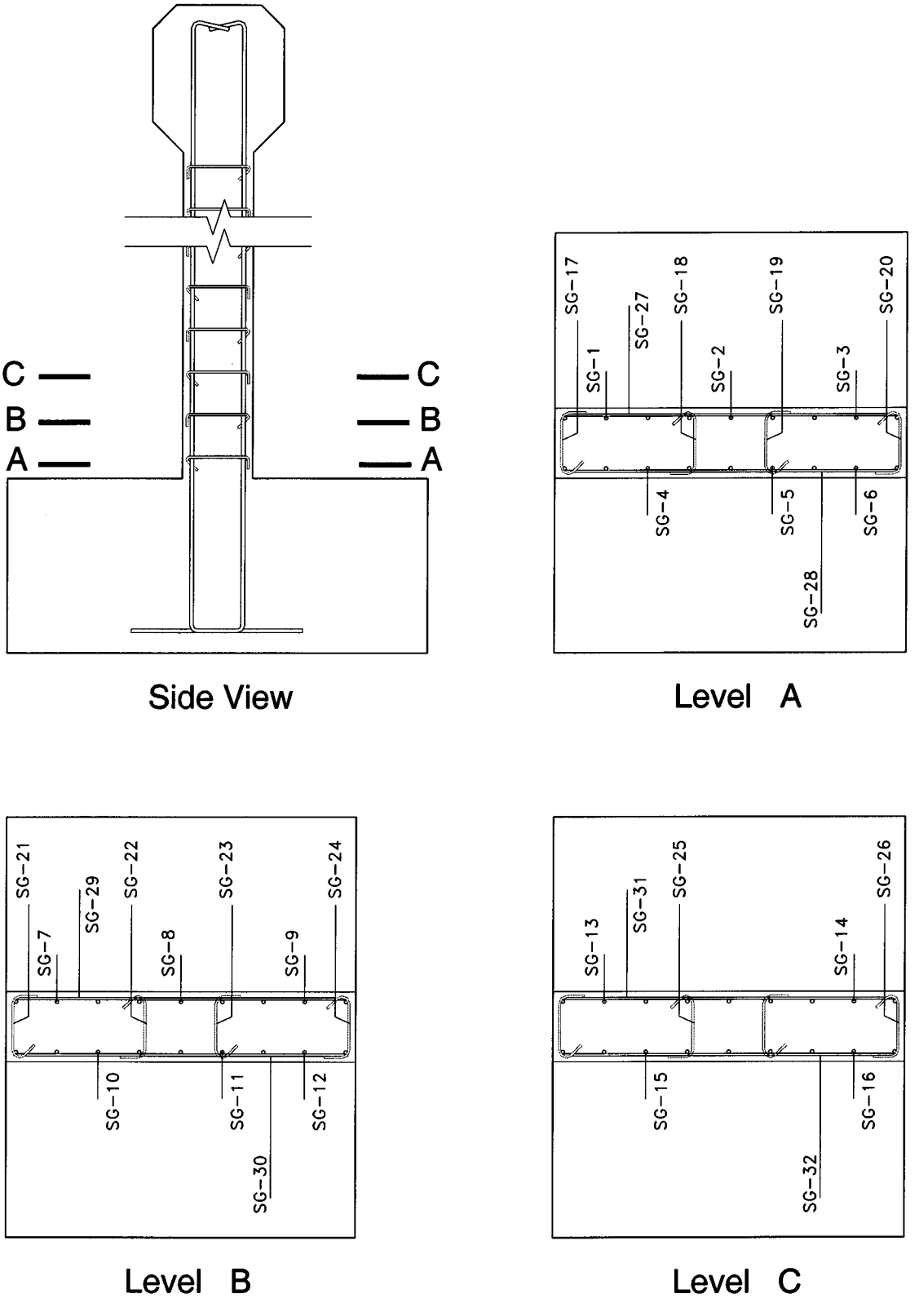

Figure 3-12 Locations of Strain Gauges in Specimen 2

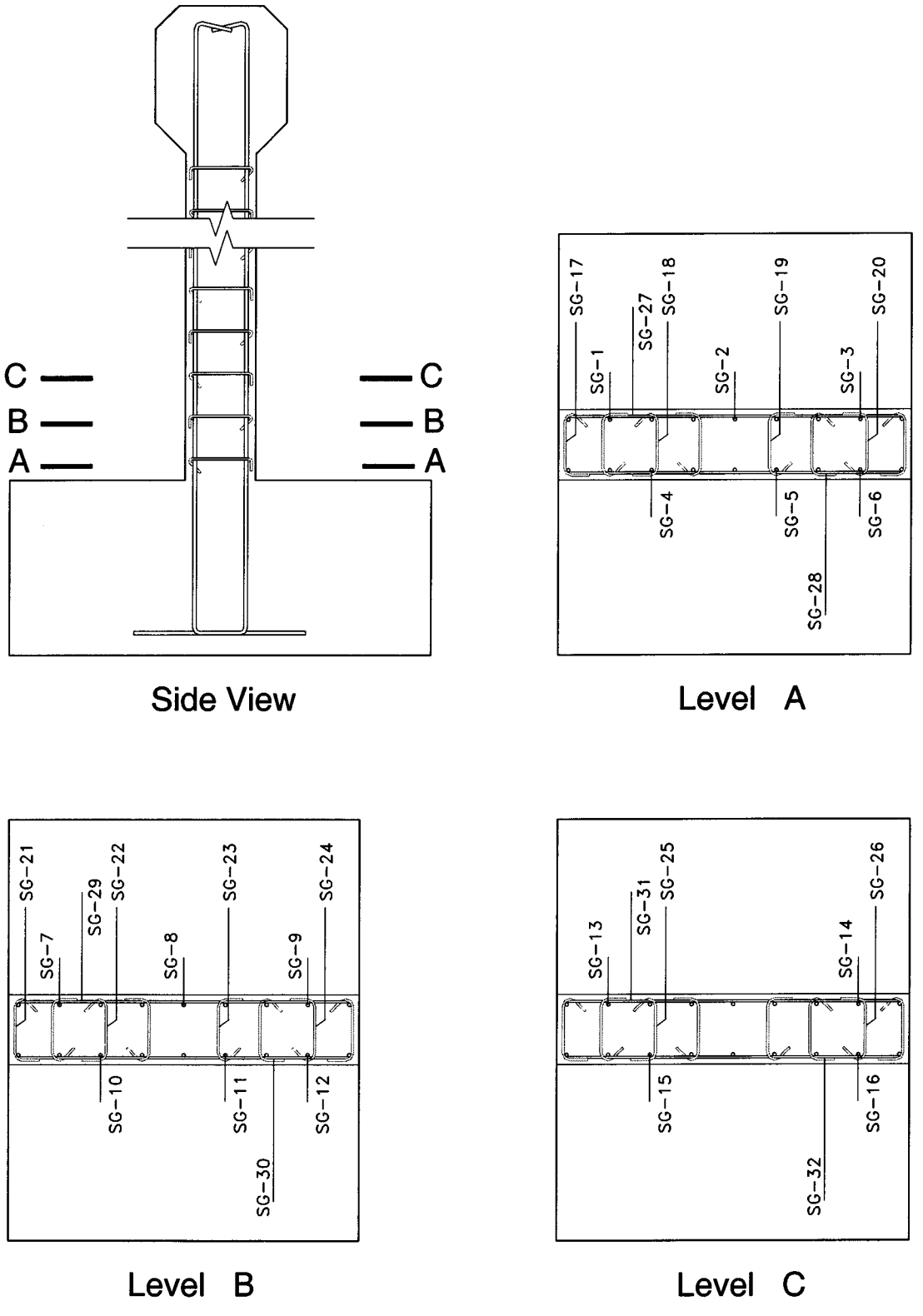

Figure 3-13 Locations of Strain Gauges in Specimen 3

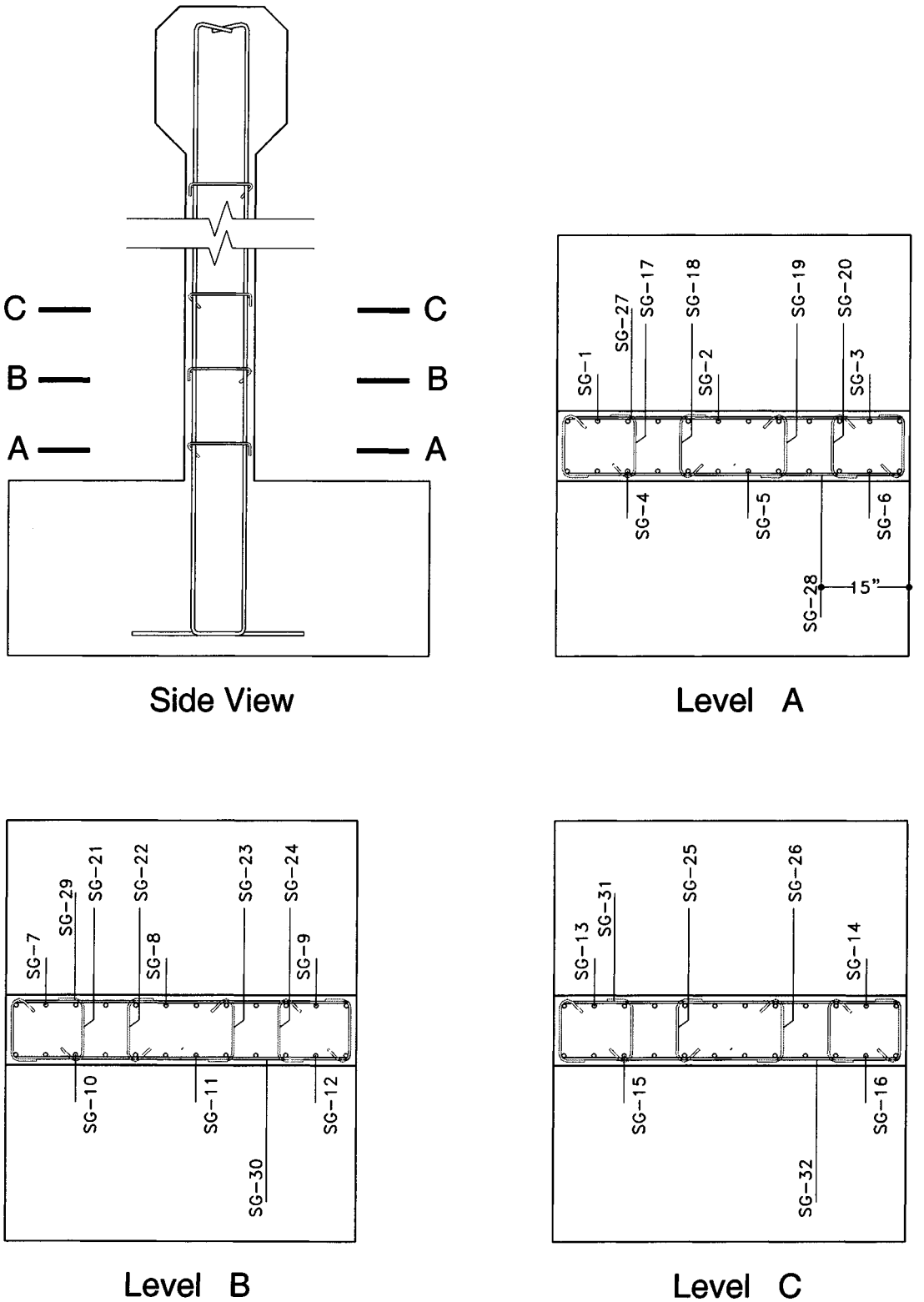

Figure 3-14 Locations of Strain Gauges in Specimen 4

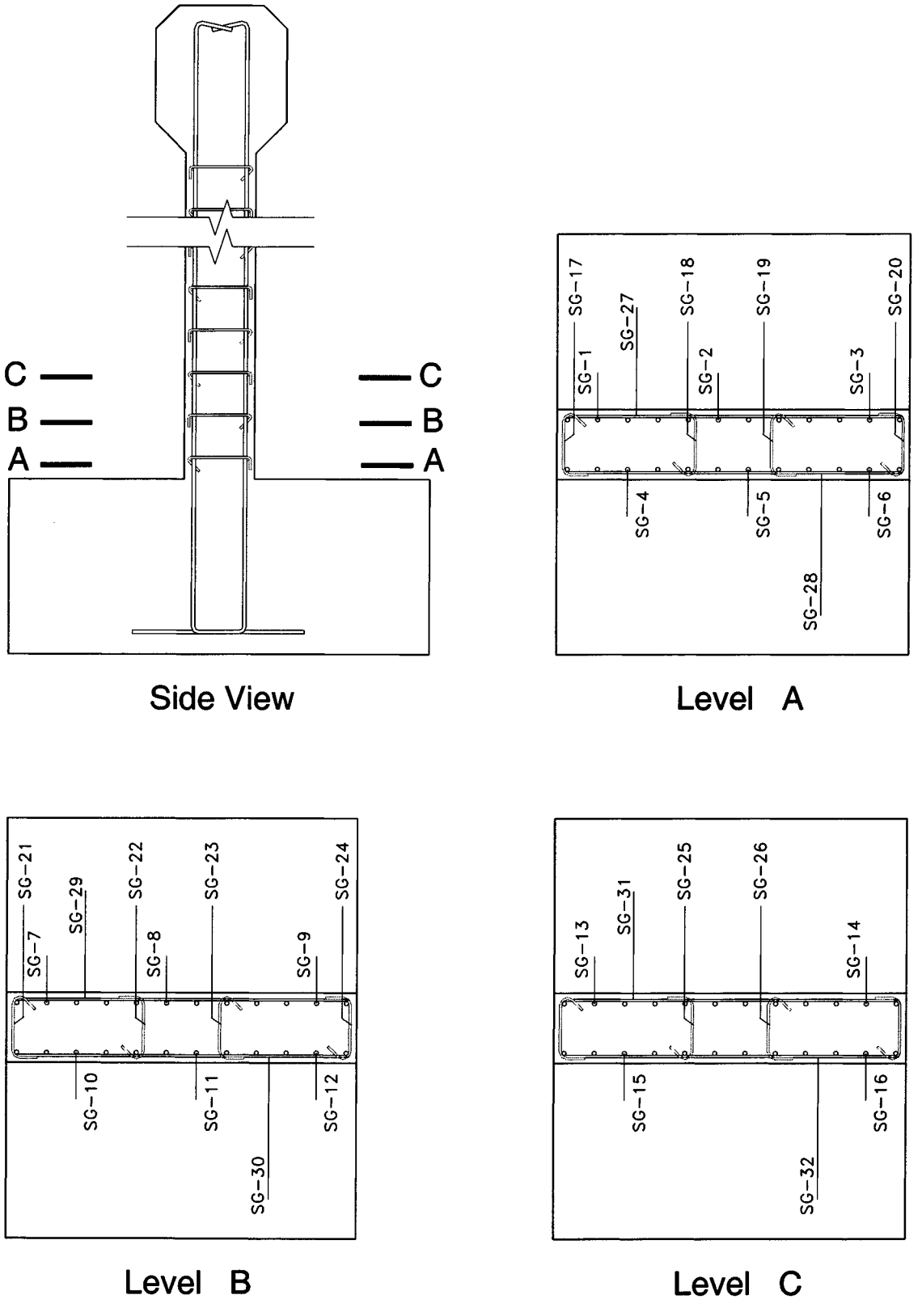

Figure 3-15 Locations of Strain Gauges in Specimen 5

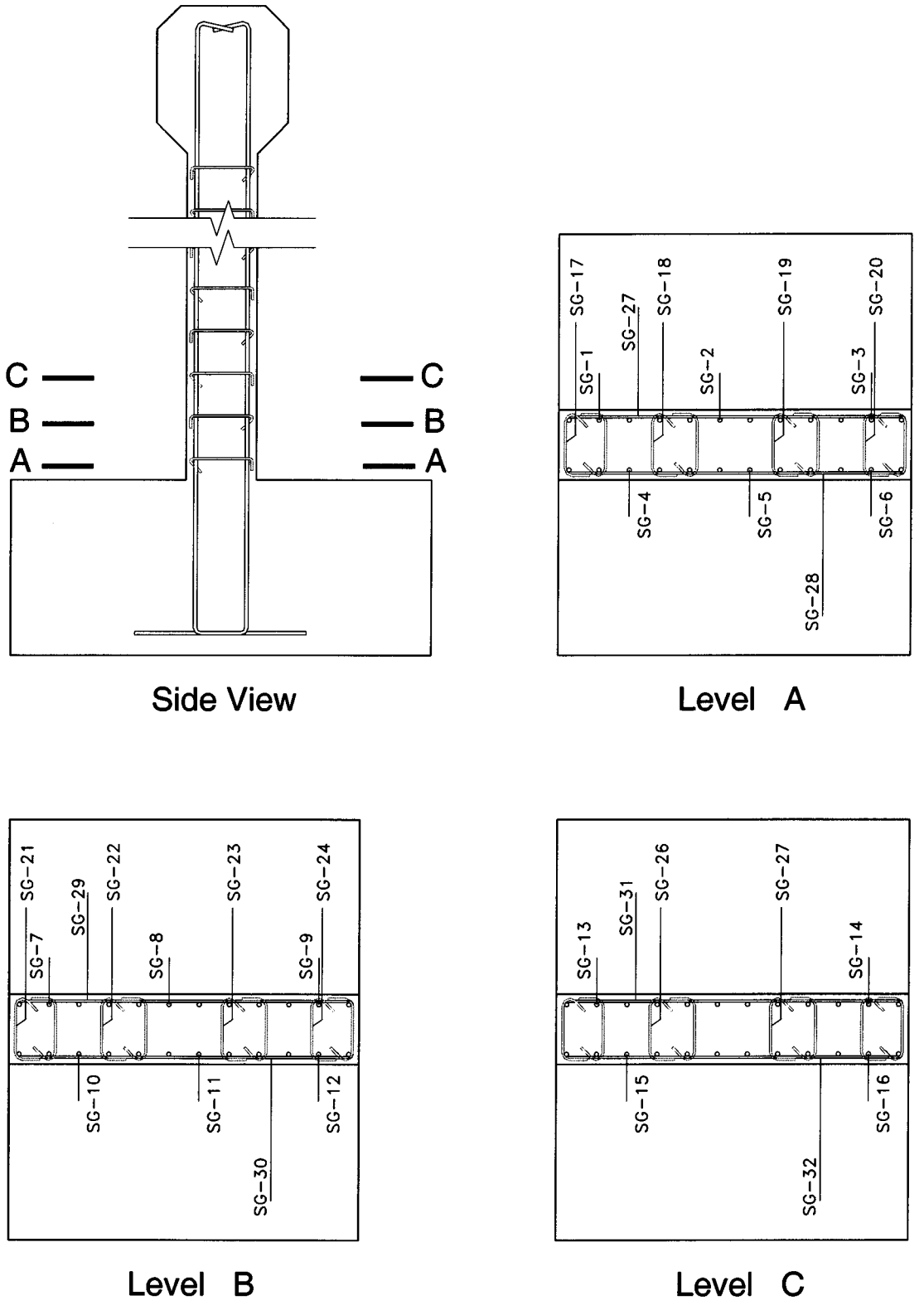

Figure 3-16 Locations of Strain Gauges in Specimen 6

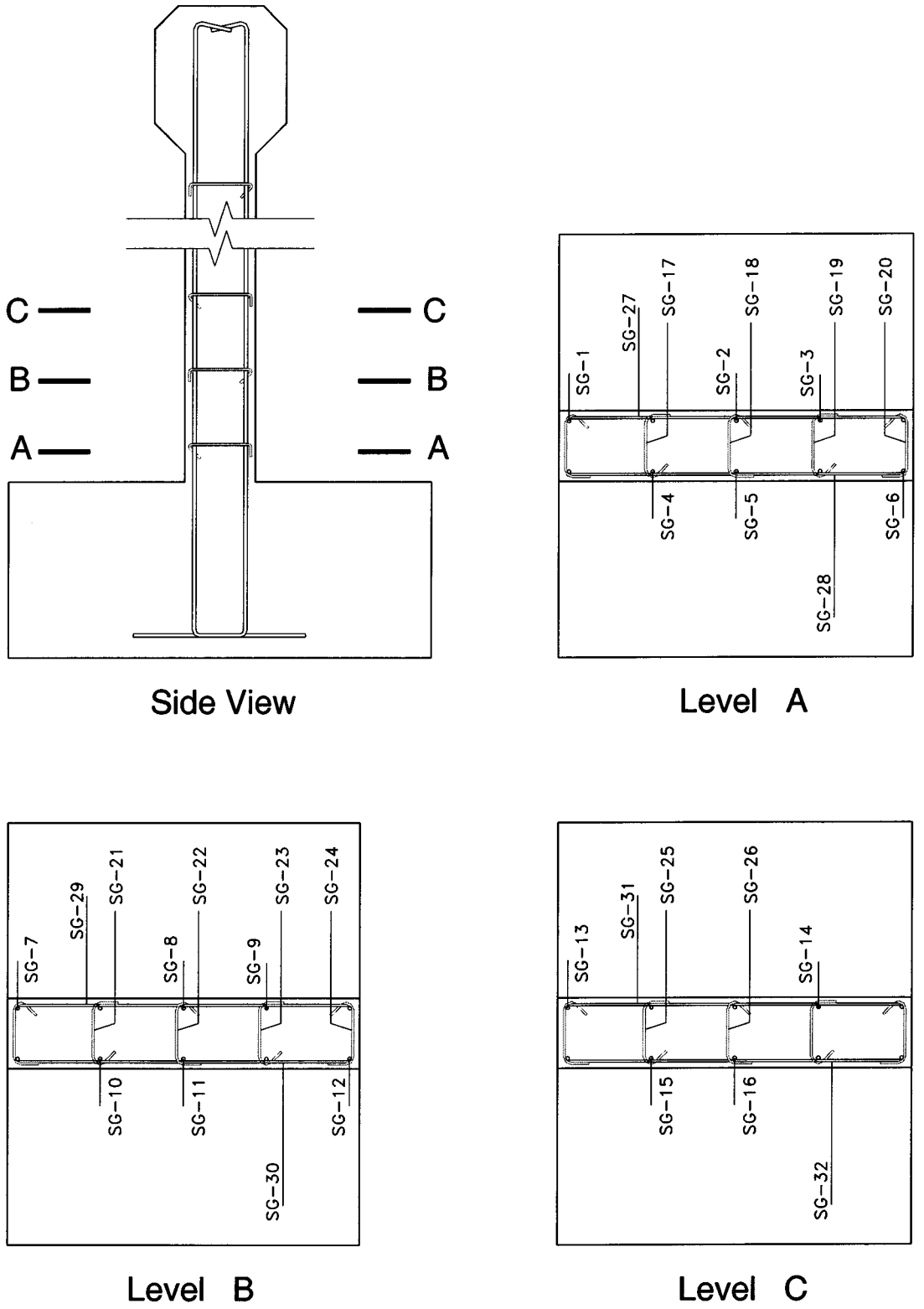

Figure 3-17 Locations of Strain Gauges in Specimen 7

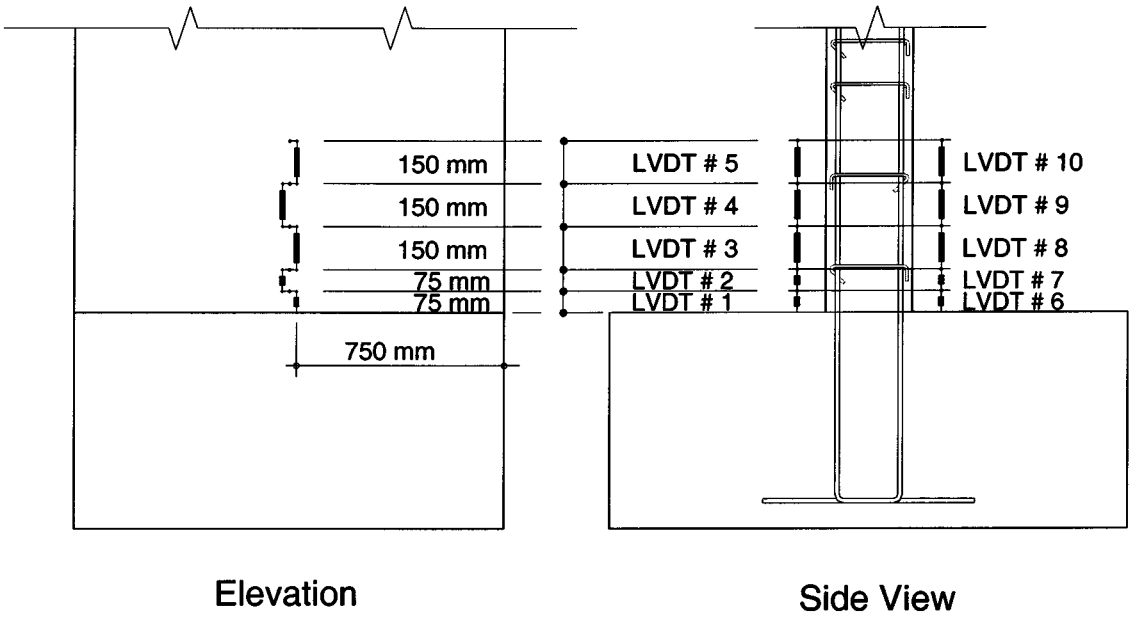

Figure 3-18 Typical Locations of LVDT's for a Test Specimen

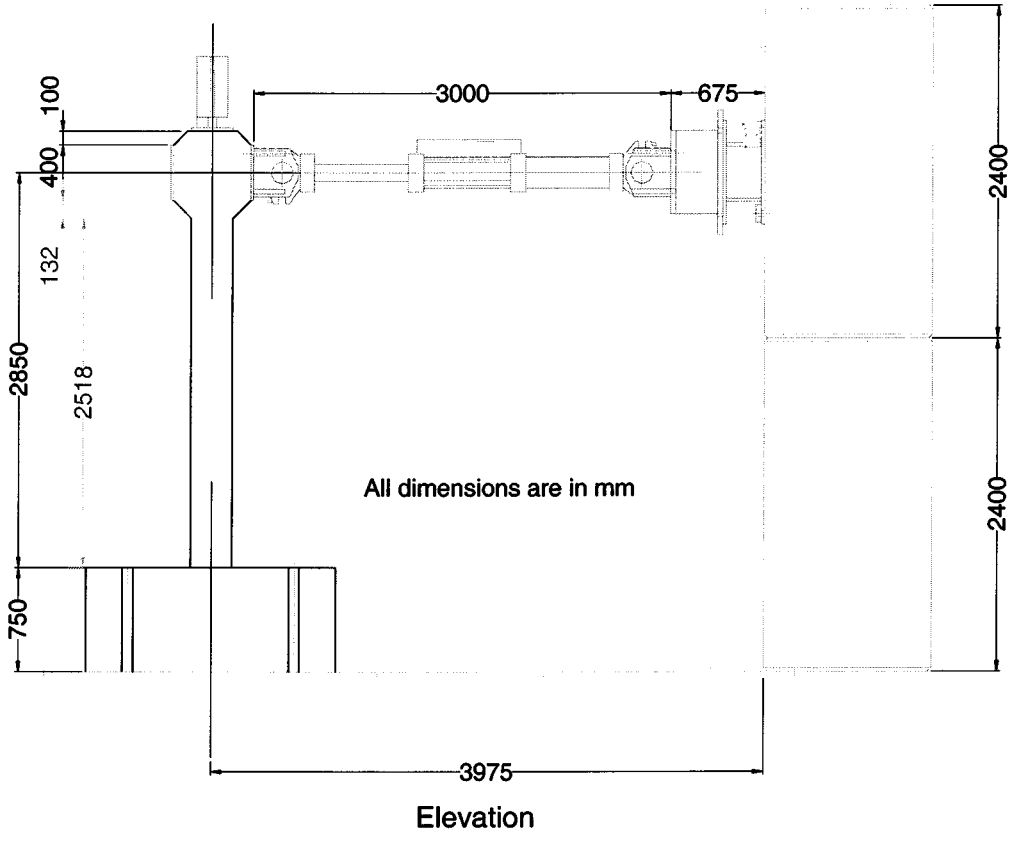

Figure 3-19 Test Setup Elevation

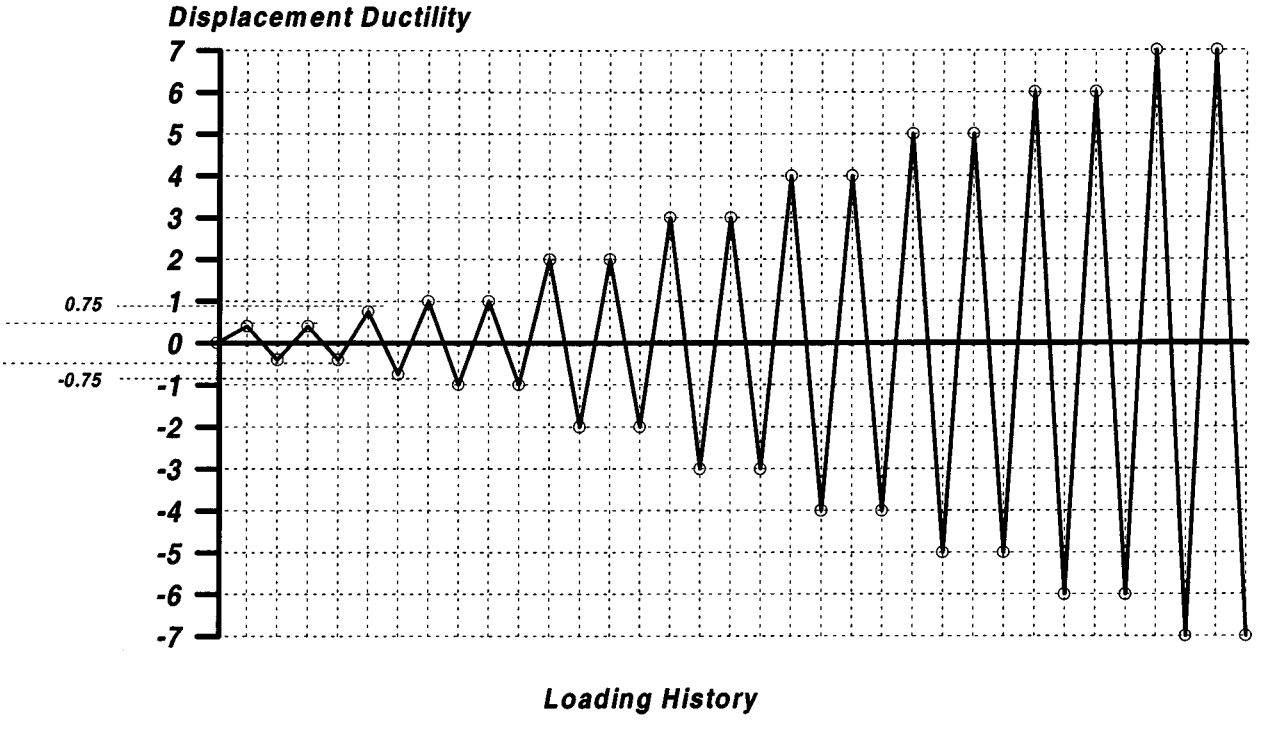

Figure 3-20 Typical Lateral load-History

SECTION 4
EXPERIMENTAL TEST RESULTS

4.1 Introduction

The seven specimens described in Section 3 were tested and data were collected and processed for each. This section presents the more important data that indicate the behavior of the specimens. The measured lateral load-displacement relationships are discussed to examine the overall wall behavior and the ductility capacity of each wall. To study the spread of yielding, lateral load versus longitudinal bar strains are reviewed. The effectiveness of lateral steel to provide confinement is examined by the strain response of the transverse bars and crossties. The LVDT data were used to plot the maximum curvature in the plastic hinge region and estimate the length of the plastic hinges. The most representative data are discussed in this section while other less critical data are shown in Appendix A.

4.2 Test Results

Each specimen was initially subjected to an axial load, which represents an axial load index close to 5 % based on the measured concrete properties. The axial load fluctuated during the test at high lateral displacements even though a pressure accumulator was hooked to the hydraulic system. Initial, minimum, and maximum axial loads applied to the pier wall specimens are presented in table 4.1. The average difference between the target and the minimum axial loads was –10.7%, while it was 7.9% between the target and the maximum axial loads.

The measured yield displacement and lateral load of the wall specimens are presented in table 4.2. The yield displacement was found by monitoring the strain in the tensile longitudinal bars. The displacement at which the bar strains reached the yield value was defined as the measured yield displacement. Figures 4.1 through 4.7 show the lateral load-displacement hysteretic response for the pier wall specimens. When the wall specimen was subjected to high lateral displacements during the test, the resulting inclination along the axial load generated lateral force component opposing the actuator force. This lateral force component was ignored because the angle of inclination was small. The right vertical axis shows the ratio of the lateral load to the nominal capacity. The nominal capacity is defined as the calculated lateral load that will cause

yielding of the steel at the wall-footing interface using the measured material properties. The upper horizontal axis shows the measured displacement ductility factor (μ_d). The displacement ductility factor is defined as the displacement divided by the yield displacement. The overall characteristics of the lateral load-displacement hysteretic response for the wall specimens were nearly the same. The ultimate point was defined as the point at which the lateral load dropped to 80% of its maximum value or at rupture of the vertical reinforcing bars. The ultimate measured displacement ranged between 158 mm and 258 mm. The corresponding maximum distance between the center of the wall section at the wall-footing interface and the line of application of the axial force (the Dywidag^{TM} bars) ranged between 33 mm and 54 mm. The corresponding lateral load to produce the moment due to the P-δ effect was less than 12 kN. Therefore, the P-δ effect was ignored. The summary of the experimental results for the pier wall specimens is presented in table 4.2. The envelopes of the lateral load-displacement and the lateral load-displacement ductility hysteretic response of the pier wall specimens were plotted to compare the response of pier walls (Figures 4.8 and 4.9).

The strain in the vertical reinforcing bars was measured to monitor the yield spread in the walls. To study the effect of the transverse reinforcement and the crossties on the confinement of the plastic hinge zone, the strain in confinement reinforcement was measured. The lateral load-strain hysteretic response of the reinforcing bars is presented in the following subsections for each individual wall specimen.

Curvature was calculated using the LVDT data. Since the LVDTs measure displacement, the strain over each gauge length was computed by dividing the measured displacement by the corresponding LVDT gauge length. The curvature was calculated by assuming a linear strain profile between each pair of LVDTs placed on both sides. The measured curvature envelope was plotted along the lower 600mm of each pier wall specimen and compared with the yield curvature to determine the potential plastic hinge length (Figure 4-10 to 4-16). The measured yield curvature corresponds to a point at which the tensile longitudinal bar reached the yield strain. The intersection of the measured curvature envelope and the measured yield curvature line represents the upper limit of the plastic hinge zone. The curvature ductility factor is equal to unity at the upper limit of the plastic hinge zone. The curvature ductility factor is defined as the curvature divided by the yield curvature. The length of the plastic hinge is considered as the distance

between the wall-footing interface and the upper limit of the plastic hinge. Table 4-3 presents the measured yield curvature and plastic hinge length for the pier wall specimens.

The overall behavior of the wall specimens was nearly the same. Flexural horizontal cracks started along the wall specimen. Minor spalling of the cover concrete occurred on the compression side of the specimen at displacement ductility between 2 and 3. When the wall specimens were tested to higher ductility levels, more spalling of the cover concrete took place revealing the vertical reinforcing bars on both sides of the wall. After that, buckling of the vertical bars began. This induced buckling of the transverse reinforcement and opening of the 90° crosstie hooks. Opening of the hooks increased the unsupported length of the vertical bars, which led to more extensive buckling of the vertical bars. The failure mode of the wall specimens was either compression failure of the concrete or fracture of the vertical reinforcing bars due to low-cycle fatigue. A review of the hysteretic curves (Figures 4-1 through 4-7) shows wide loops and a relatively large energy dissipation capacity for all the specimens.

Table 4-1 Axial Loads Applied to the Pier Wall Specimens, kN

Specimen	Initial Axial Load	Minimum		Maximum	
		Load	Diff. %	Load	Diff. %
1	677.4	606.0	-10.5%	713.2	5.3%
2	676.7	584.6	-13.6%	720.7	6.5%
3	720.8	645.1	-10.5%	721.2	0.0%
4	640.7	571.7	-10.8%	694.0	8.3%
5	576.6	542.8	-5.9%	662.9	15.0%
6	608.6	567.2	-6.8%	676.8	11.2%
7	676.7	565.0	-16.5%	738.5	9.1%
Average			-10.7%		7.9%

Table 4-3 Measured Plastic Hinge

Specimen	Yield Curvature (rad/m)	Plastic Hinge Length (mm)
1	0.0332	178
2	0.0326	179
3	0.0348	181
4	0.0417	175
5	0.0588	180
6	0.0601	190
7	0.0403	110

Table 4-2 Measured Load-Displacement Data at Key Points

Specimen	Yield Point		Peak Point		Ultimate Point		Displacement Ductility Capacity (μ_d)
	Displacement (mm)	Lateral Load (kN)	Displacement (mm)	Lateral Load (kN)	Displacement (mm)	Lateral Load (kN)	
1	32.5	79.7	137.5	111.2	211.3	89.0	6.5
2	27.5	72.4	130.0	110.8	192.5	88.5	7.0
3	25.0	72.6	122.3	111.7	187.5	88.5	7.5
4	41.5	127.3	158.5	177.1	240.7	141.0	5.8
5	42.5	126.3	146.3	169.1	242.3	135.2	5.7
6	42.5	131.6	150.0	173.5	257.7	148.2	6.1
7	17.5	41.9	57.2	59.2	157.5	47.4	9.0

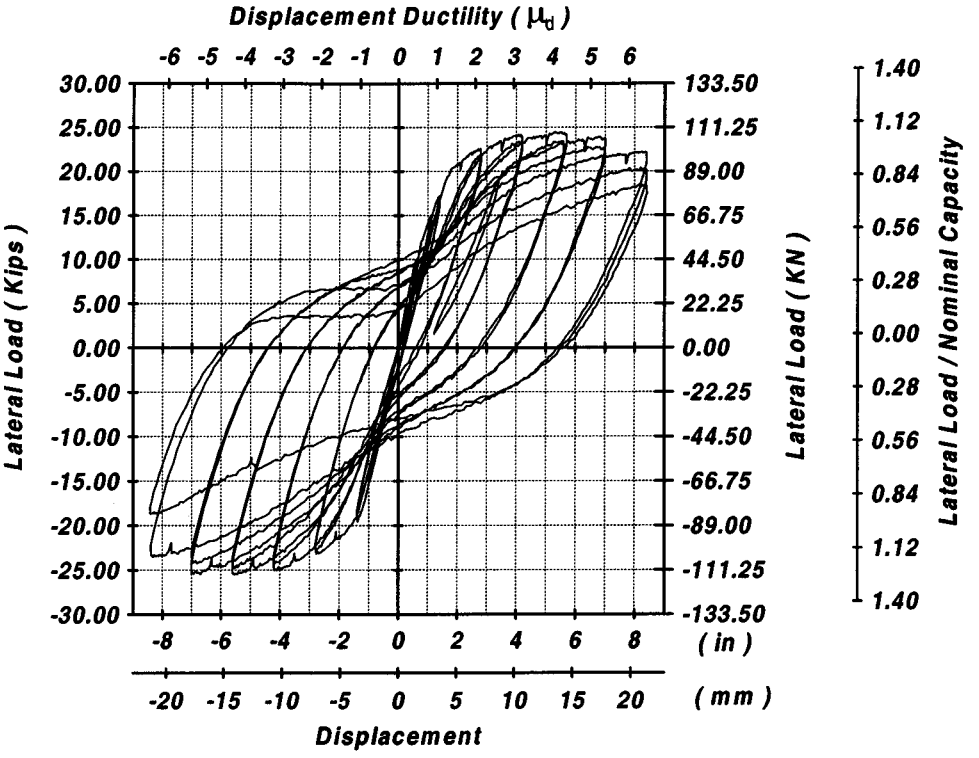

Figure 4-1 Measured Lateral Load-Displacement Hysteresis for Specimen 1

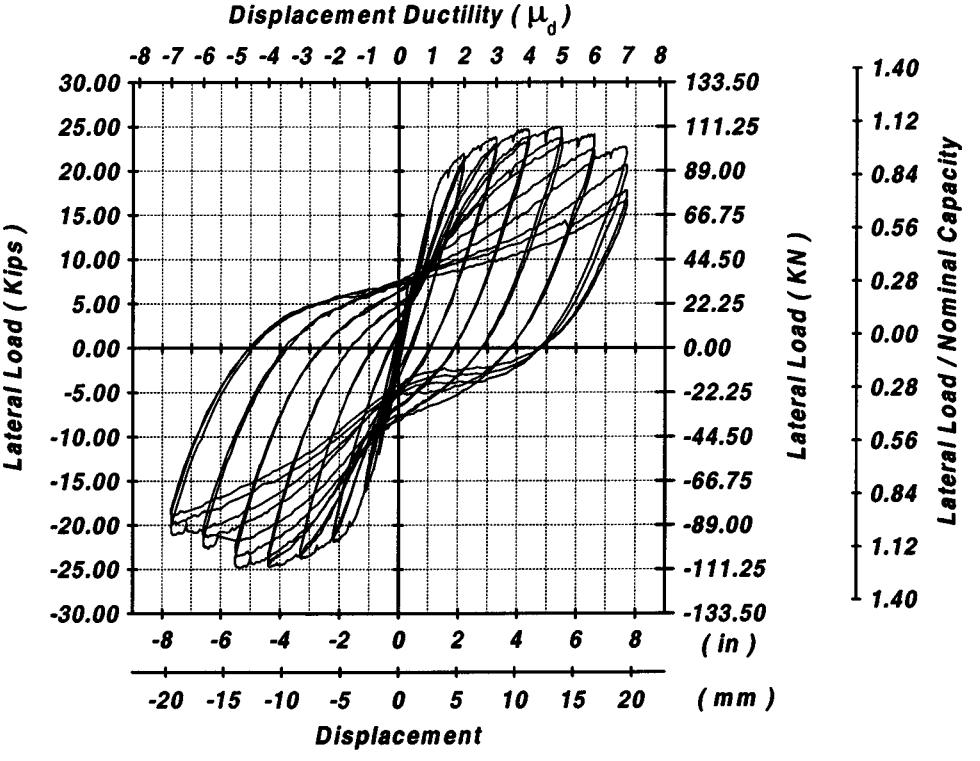

Figure 4-2 Measured Lateral Load-Displacement Hysteresis for Specimen 2

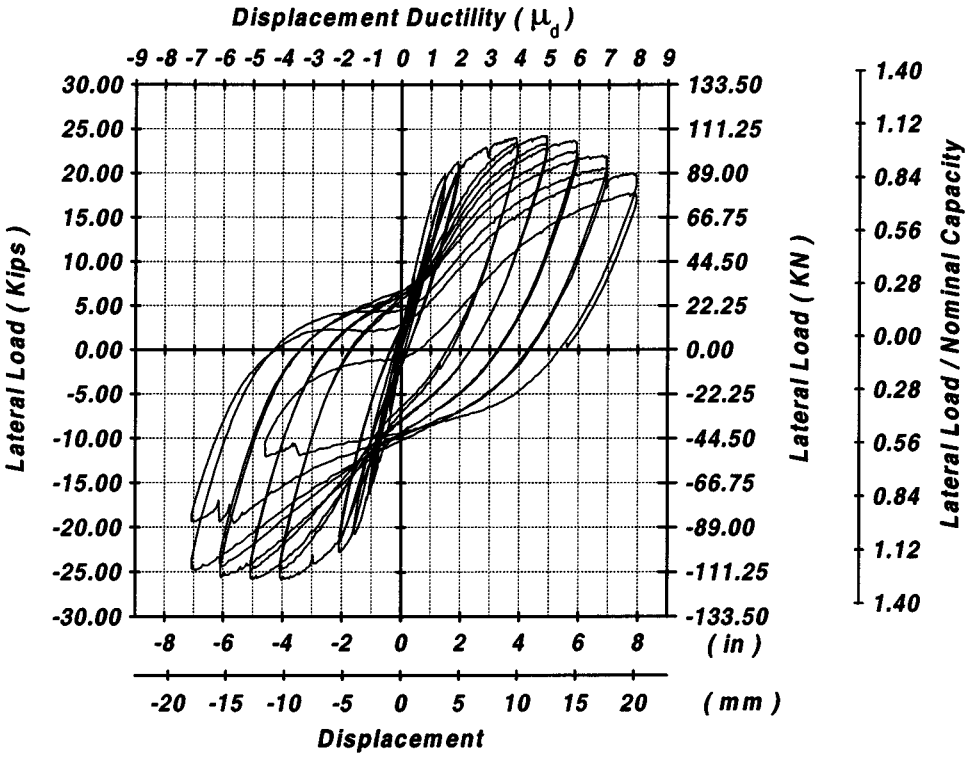

Figure 4-3 Measured Lateral Load-Displacement Hysteresis for Specimen 3

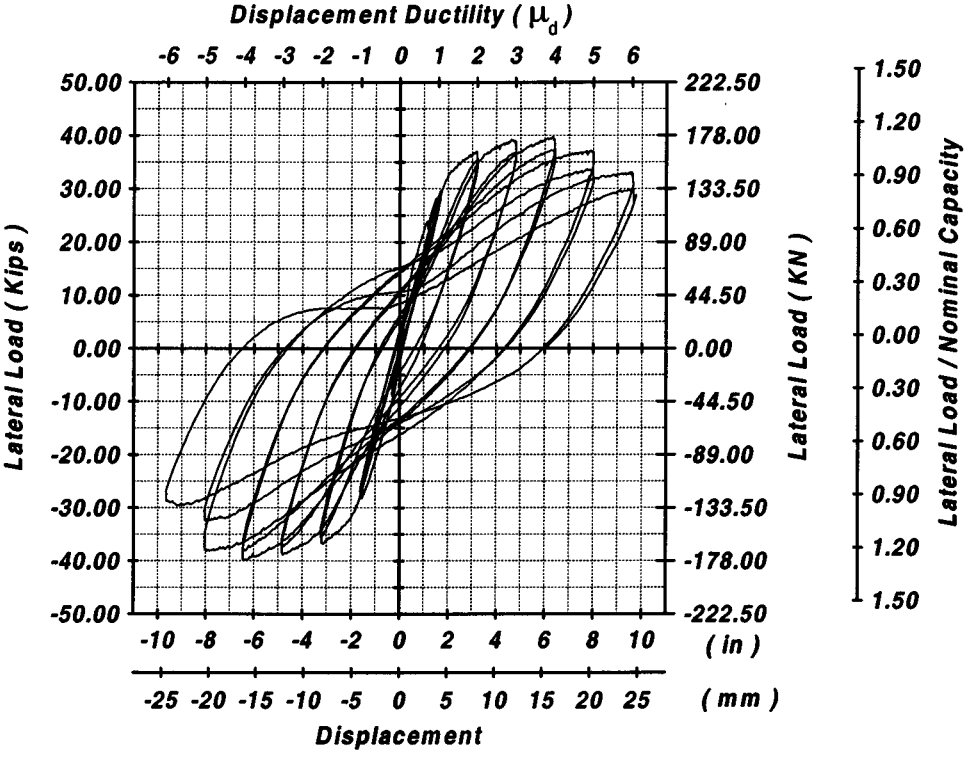

Figure 4-4 Measured Lateral Load-Displacement Hysteresis for Specimen 4

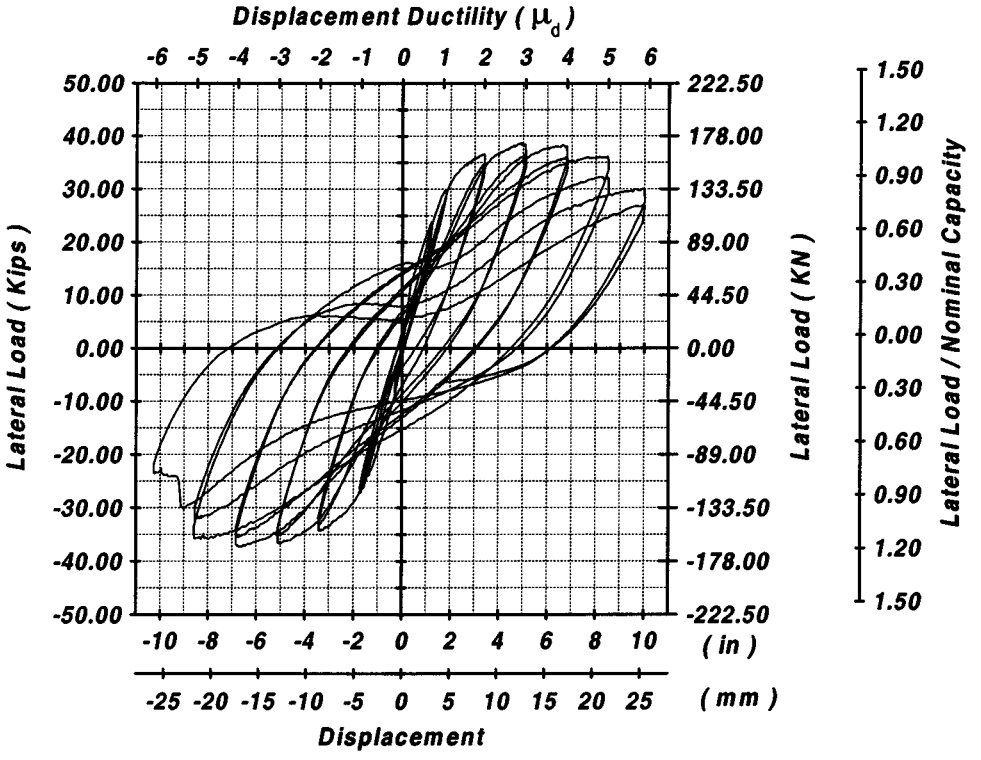

Figure 4-5 Measured Lateral Load-Displacement Hysteresis for Specimen 5

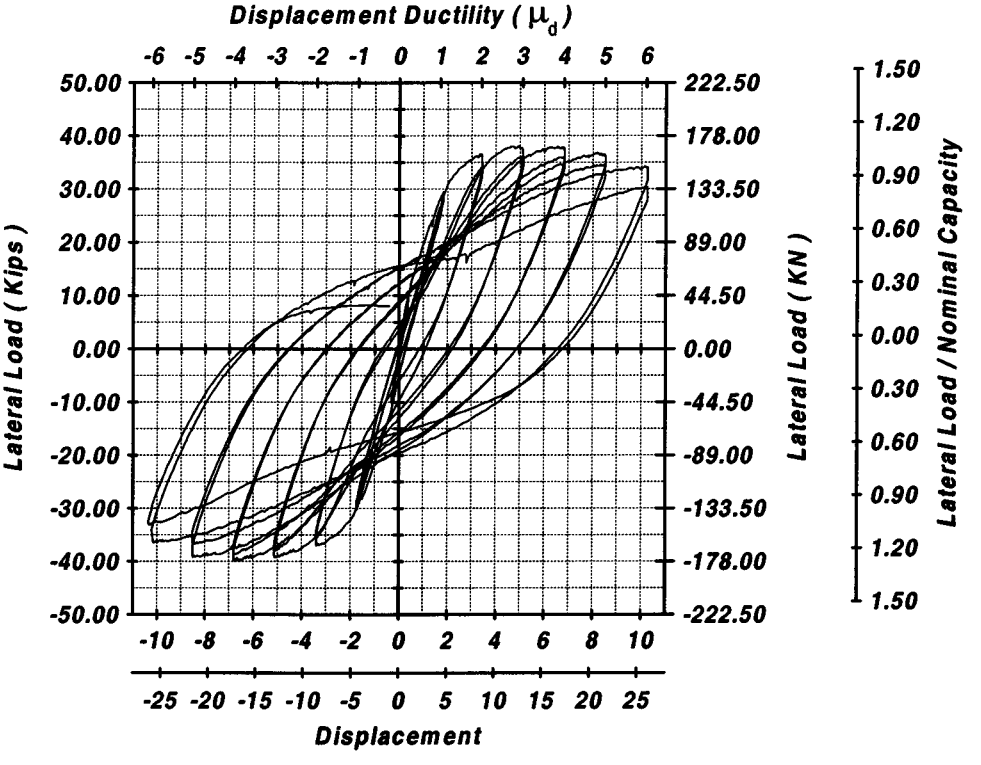

Figure 4-6 Measured Lateral Load-Displacement Hysteresis for Specimen 6

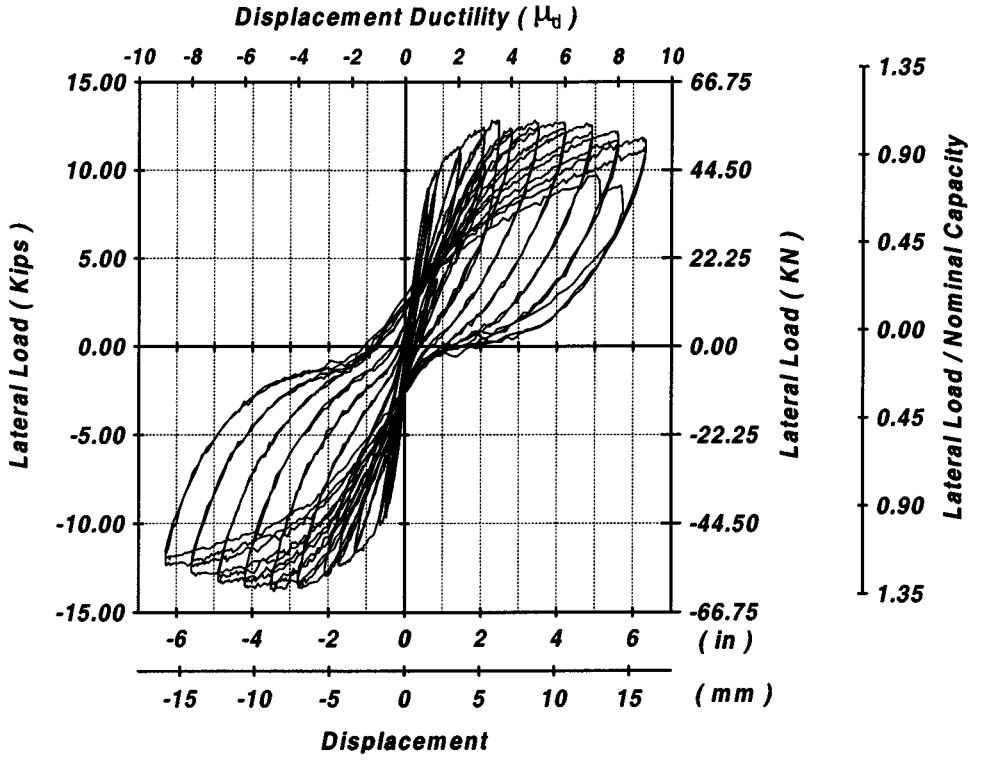

Figure 4-7 Measured Lateral Load-Displacement Hysteresis for Specimen 7

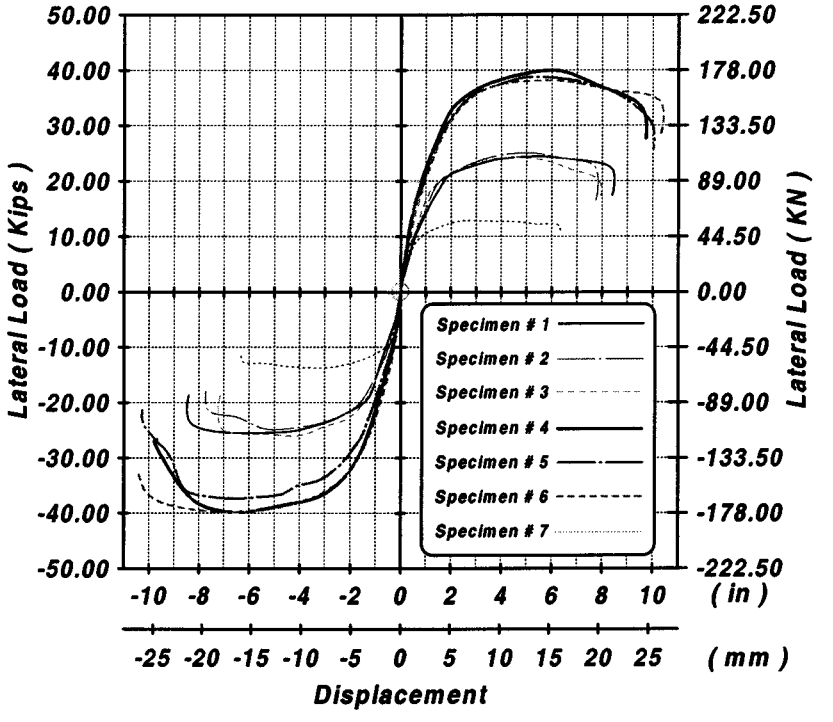

Figure 4-8 Measured Lateral Load-Displacement Envelopes

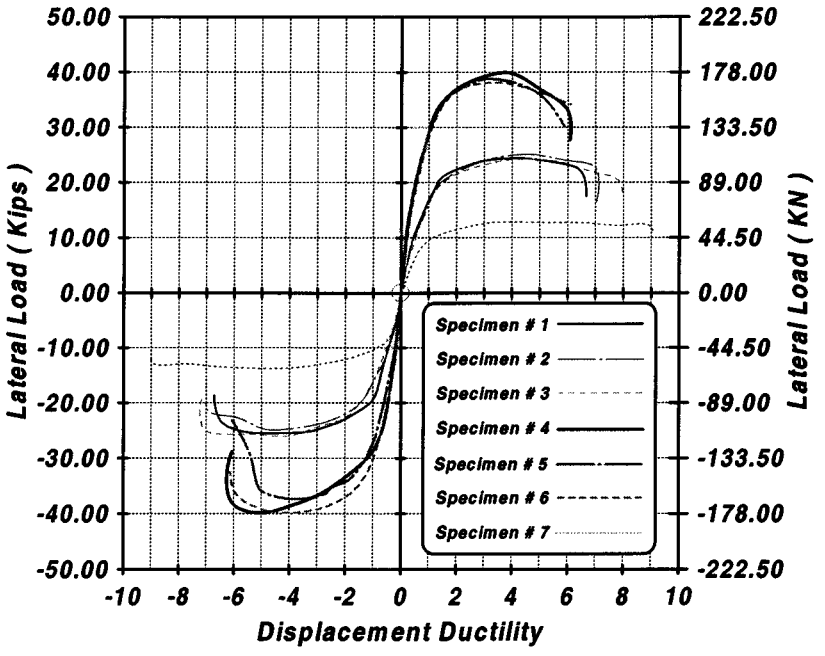

Figure 4-9 Measured Lateral Load-Displacement Ductility Envelopes

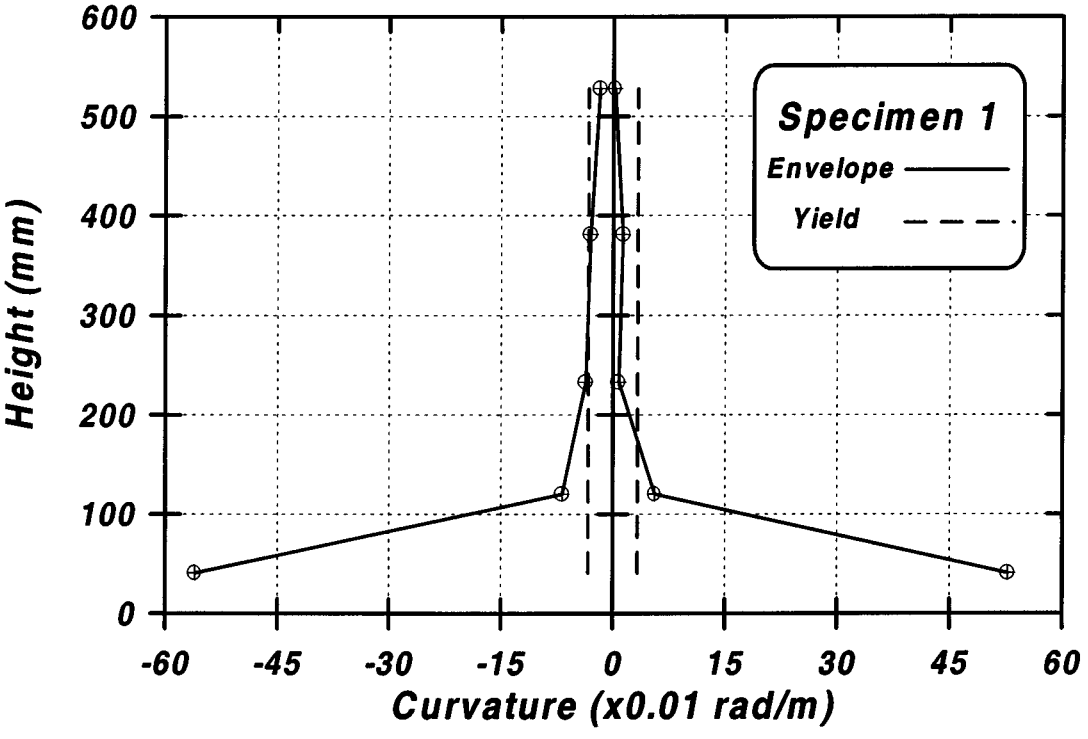

Figure 4-10 Measured Curvature Envelope along Plastic Hinge of Specimen 1

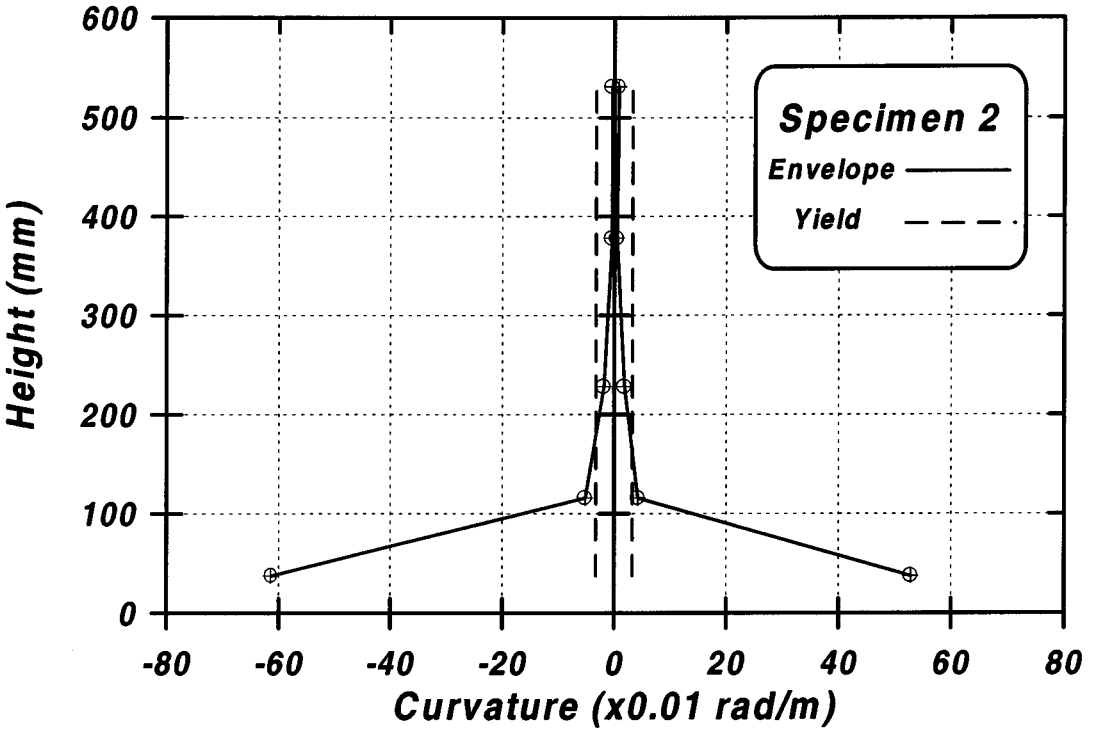

Figure 4-11 Measured Curvature Envelope along Plastic Hinge of Specimen 2

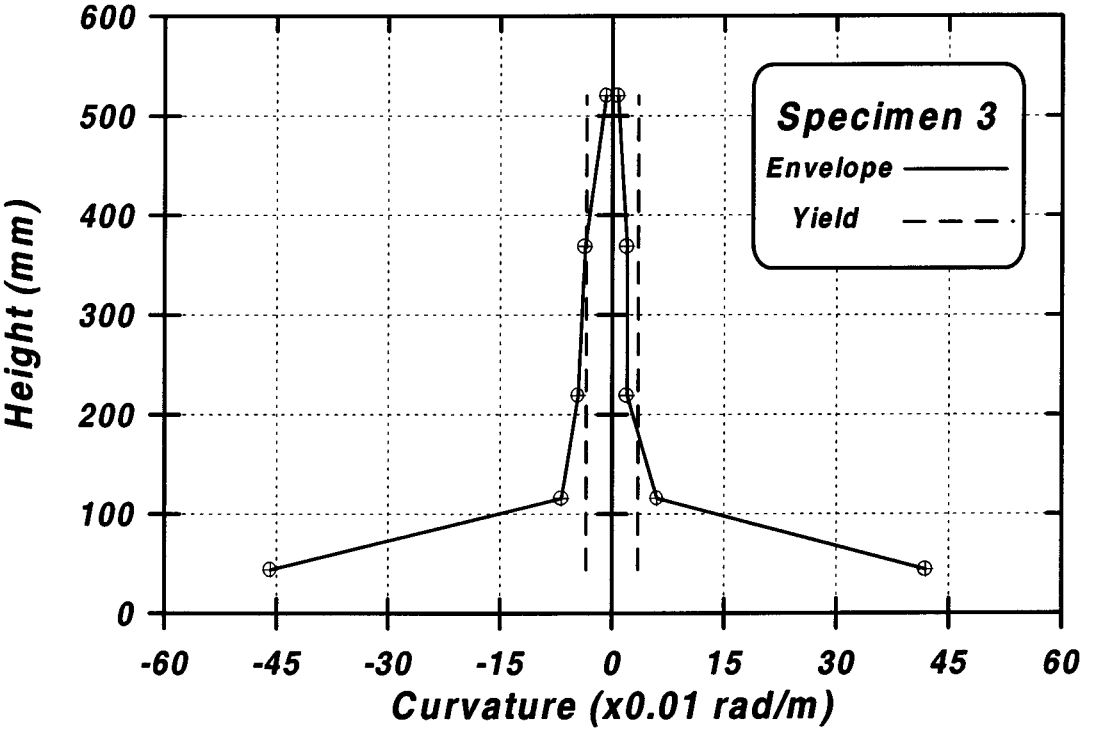

Figure 4-12 Measured Curvature Envelope along Plastic Hinge of Specimen 3

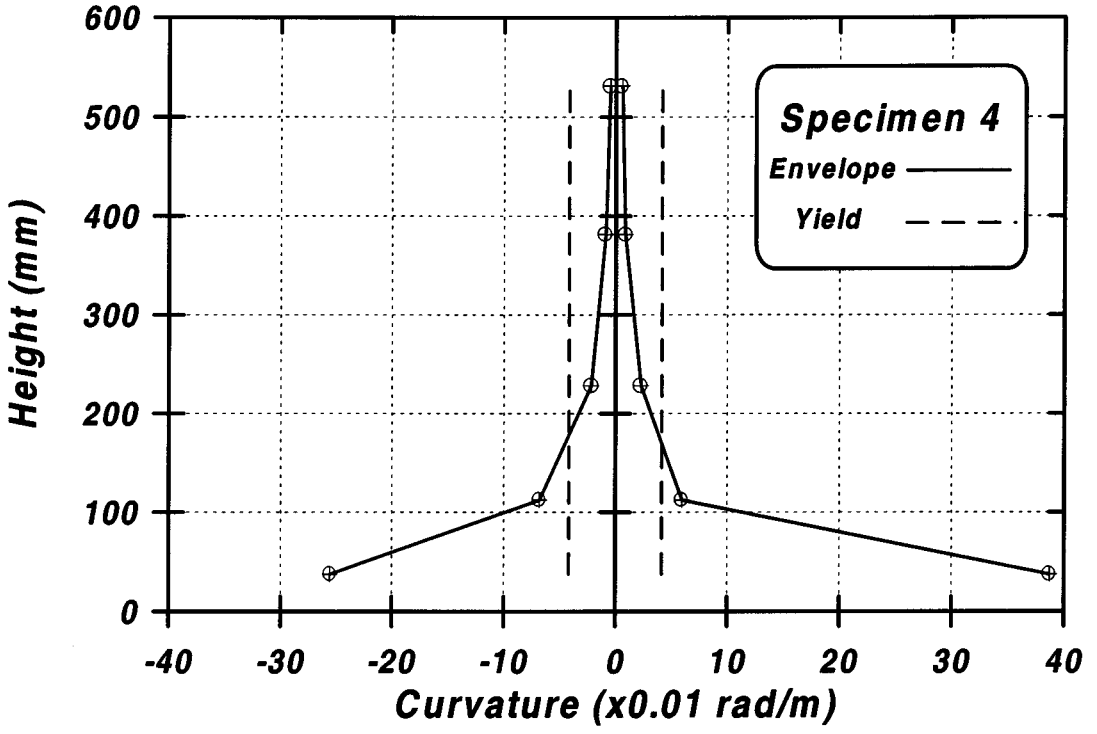

Figure 4-13 Measured Curvature Envelope along Plastic Hinge of Specimen 4

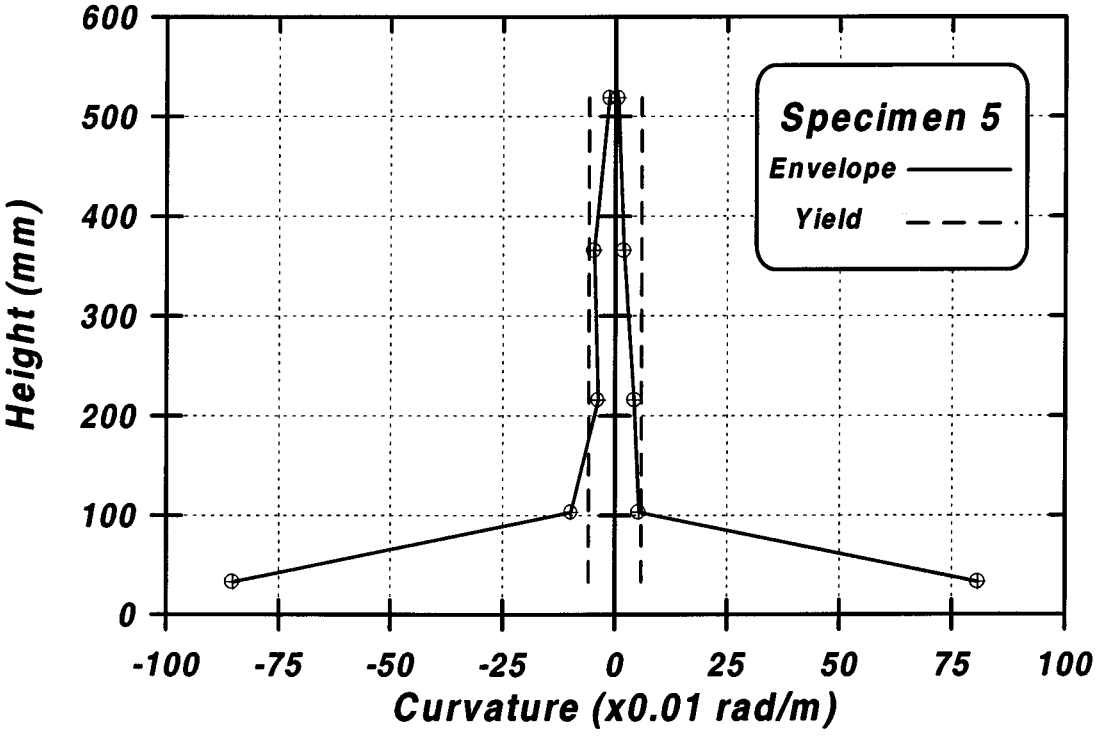

Figure 4-14 Measured Curvature Envelope along Plastic Hinge of Specimen 5

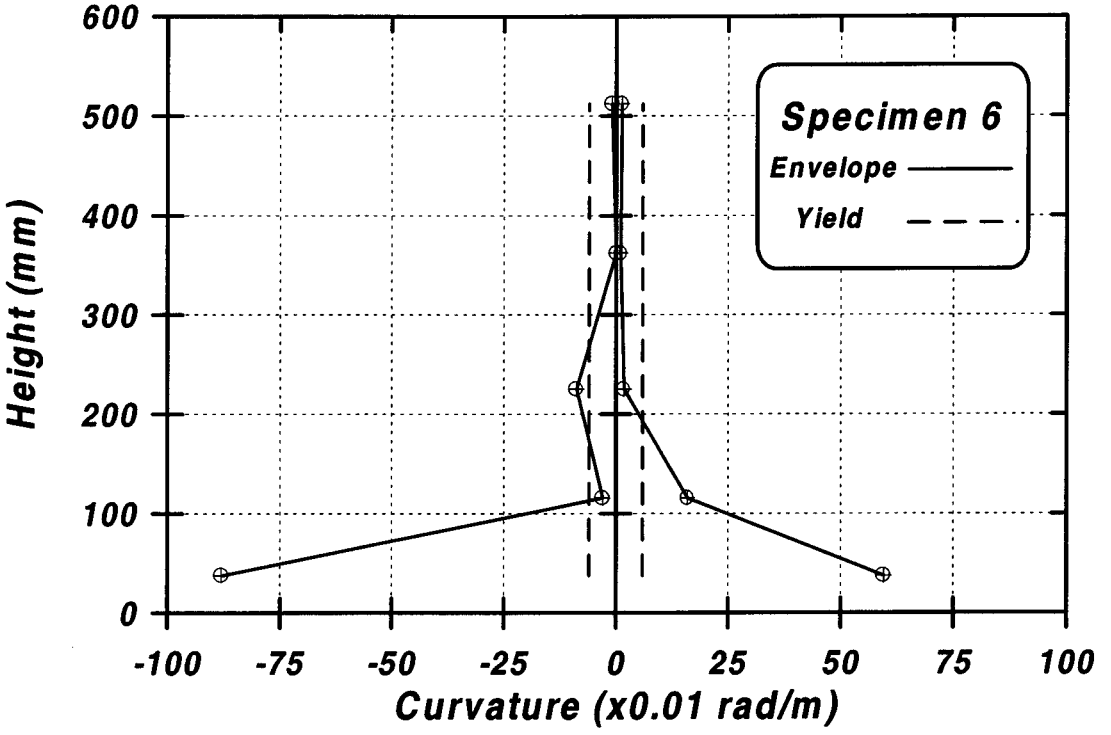

Figure 4-15 Measured Curvature Envelope along Plastic Hinge of Specimen 6

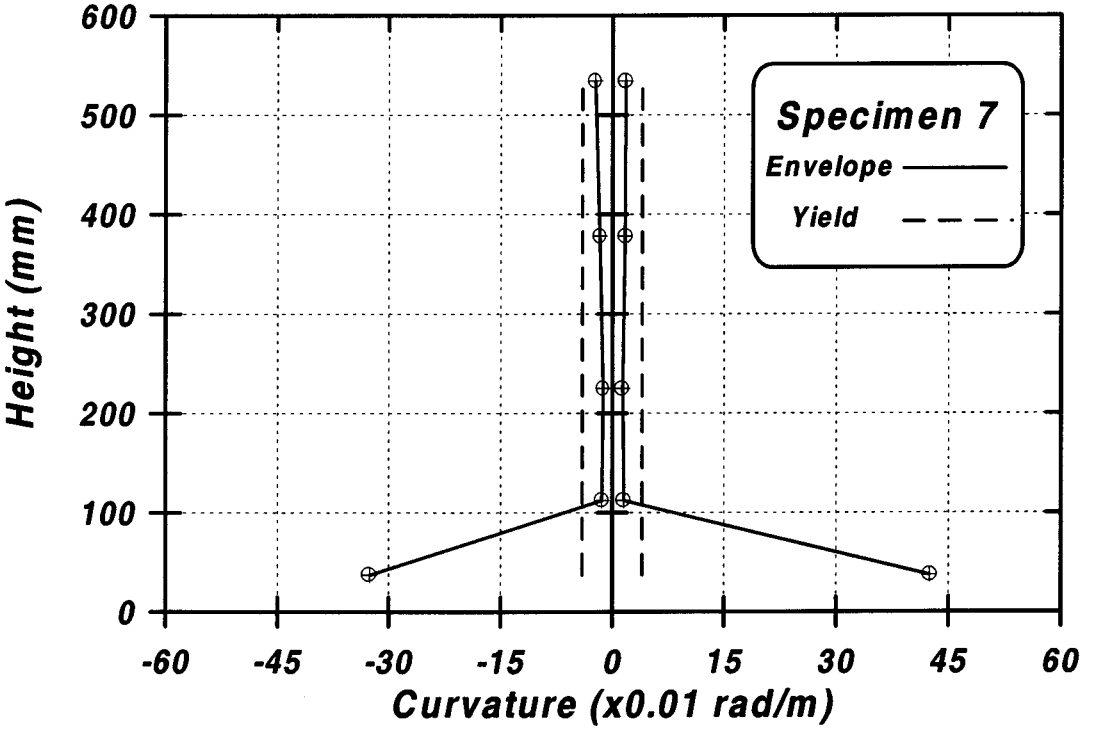

Figure 4-16 Measured Curvature Envelope along Plastic Hinge of Specimen 7

4.2.1 Performance of Specimen 1

Flexural cracks were initiated at a lateral displacement of 13 mm corresponding to a lateral load of 43.74 kN. The lateral load capacity, which is 111.2 kN was reached at a displacement ductility of 4.2. At a displacement of 178 mm (μ_d = 5.5) corresponding to a lateral load of 103.4 kN, extensive spalling of the cover concrete began at the compression side of the wall specimen. As the wall specimen was tested to higher ductility levels, more spalling of the cover concrete and buckling of the vertical bars occurred (Figure 4-17). When the wall was pulled for the second cycle at a displacement ductility of 6, a corner vertical bar was fractured in the tension side at a displacement of 121 mm, corresponding to a lateral load of 56.4 kN. In an attempt to test the wall specimen at higher ductility levels, the lateral load dropped to 81.2 kN (lower than 80% of its lateral load capacity) and the test was stopped.

Figure 4-17 Buckling of the Vertical Bars in Specimen 1

The measured lateral load-strain relationship in the vertical reinforcing bars at the wall-footing interface is presented in figures 4-18 and 4-19. At a height of 160 mm above the top of the footing, the strains in the vertical bars did not reach the yield point (Figure 4-20 and 4-21). The maximum strain in the confinement reinforcement was nearly 60% of the steel yield strain. Figures 4-22 through 4-25 show samples of the lateral load-strain hysteretic response of the transverse reinforcement and the crossties. The strain gauge locations are marked in figure 3-11.

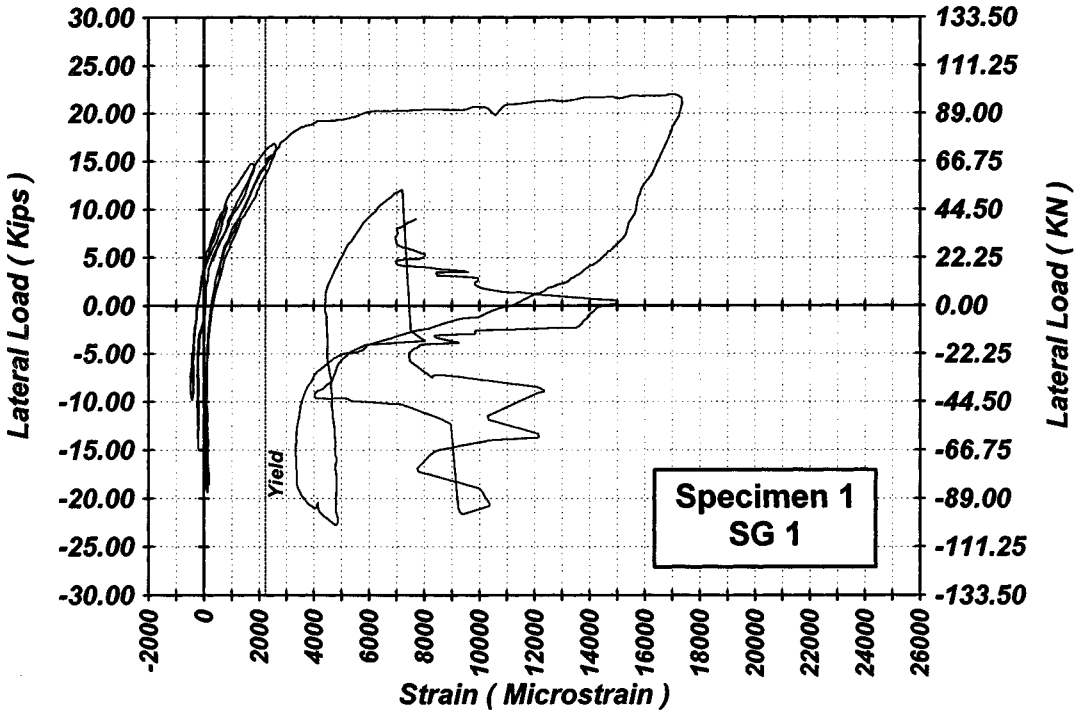

Figure 4-18 Measured Lateral Load Strain in SG-1 of Specimen 1

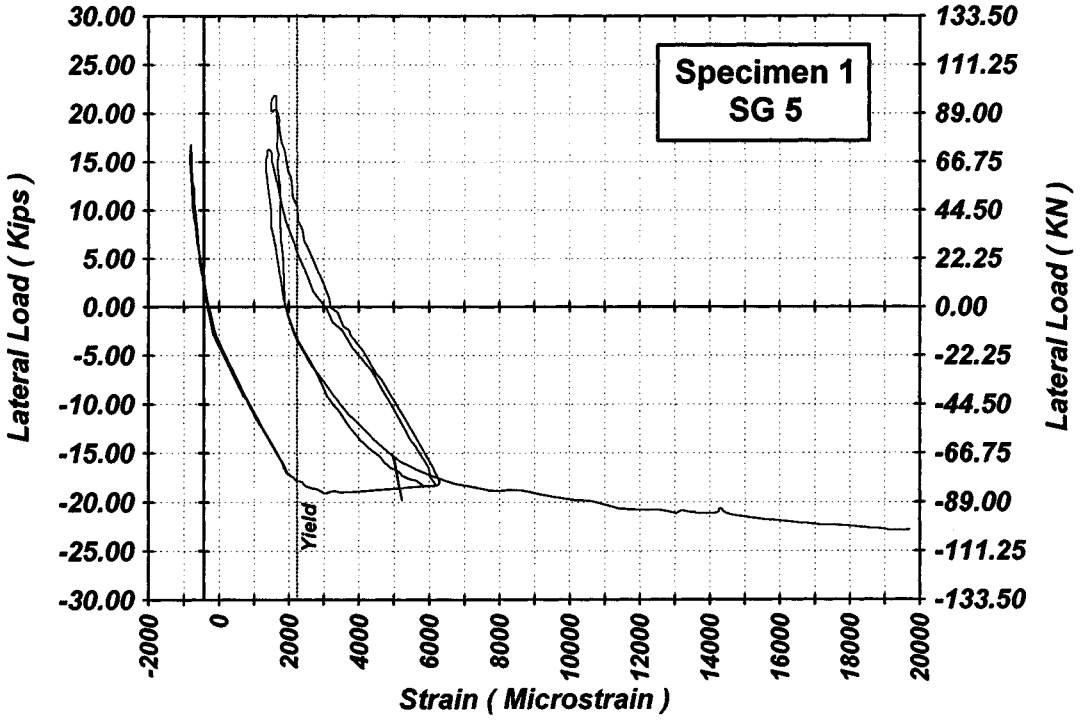

Figure 4-19 Measured Lateral Load Strain in SG-5 of Specimen 1

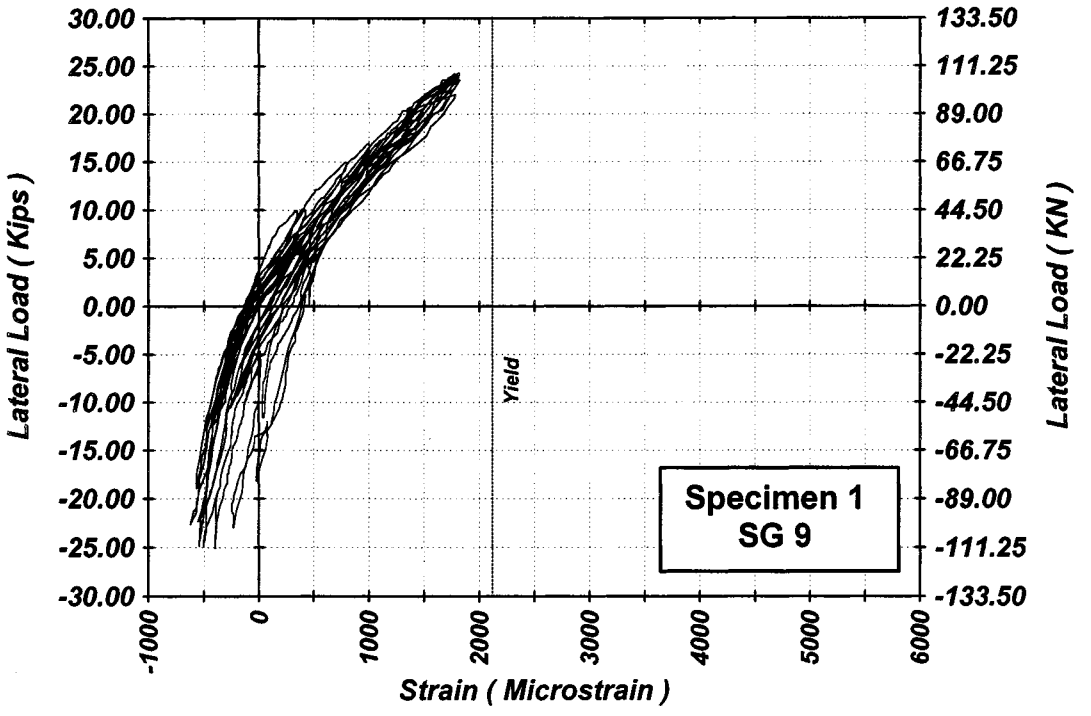

Figure 4-20 Measured Lateral Load Strain in SG-9 of Specimen 1

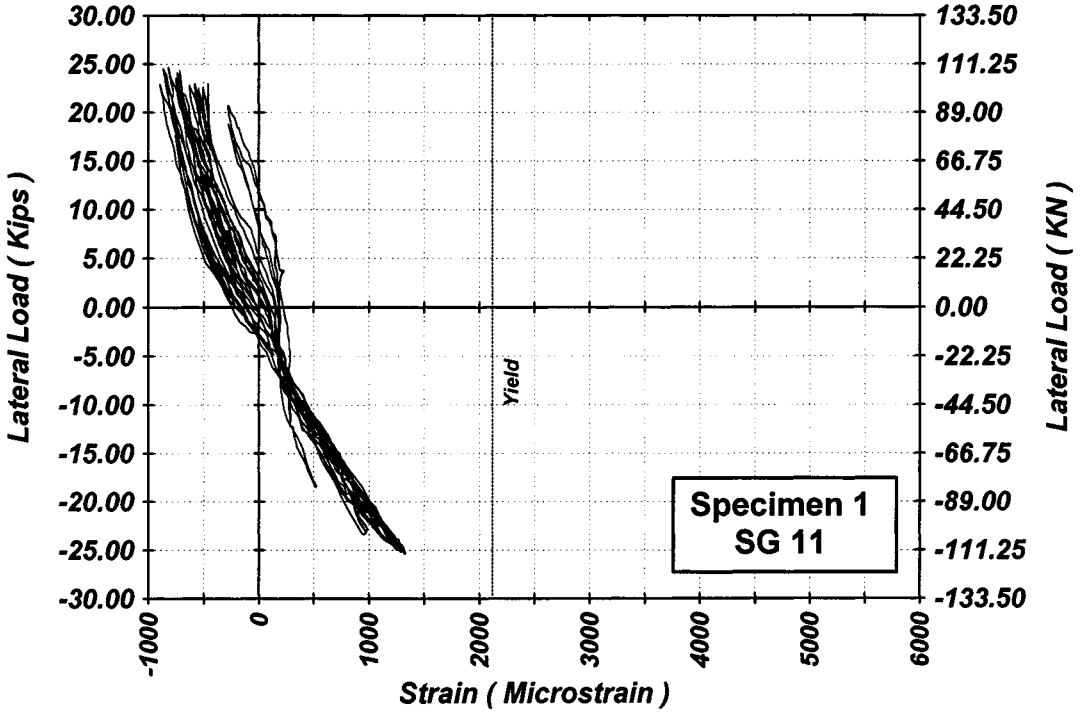

Figure 4-21 Measured Lateral Load Strain in SG-11 of Specimen 1

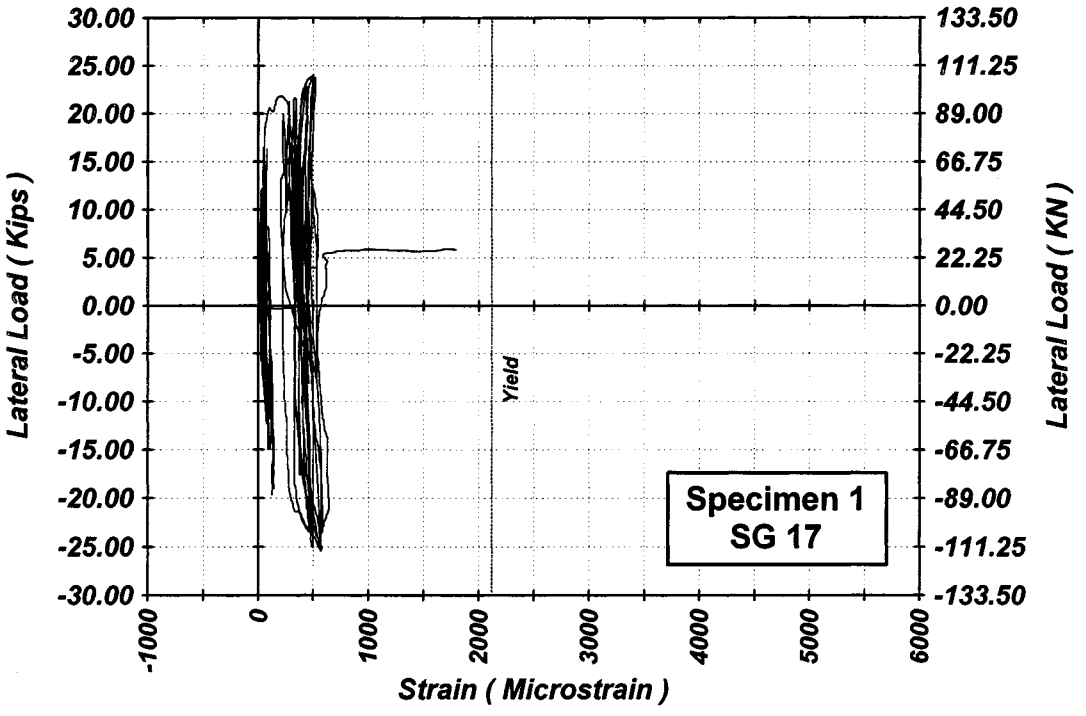

Figure 4-22 Measured Lateral Load Strain in SG-17 of Specimen 1

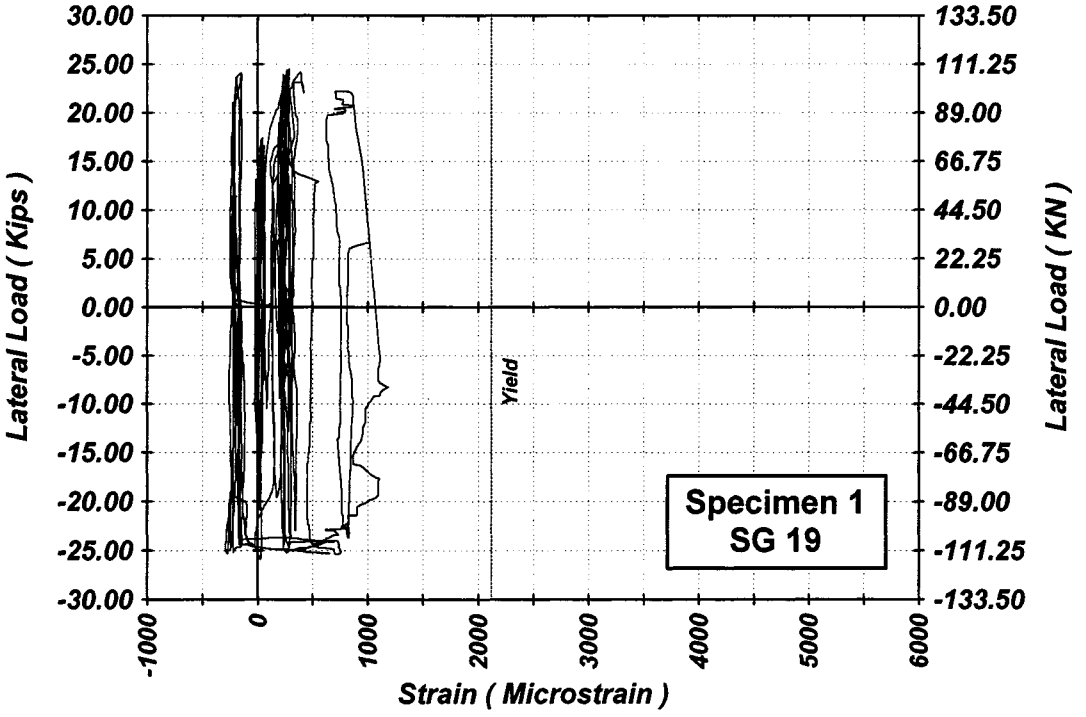

Figure 4-23 Measured Lateral Load Strain in SG-19 of Specimen 1

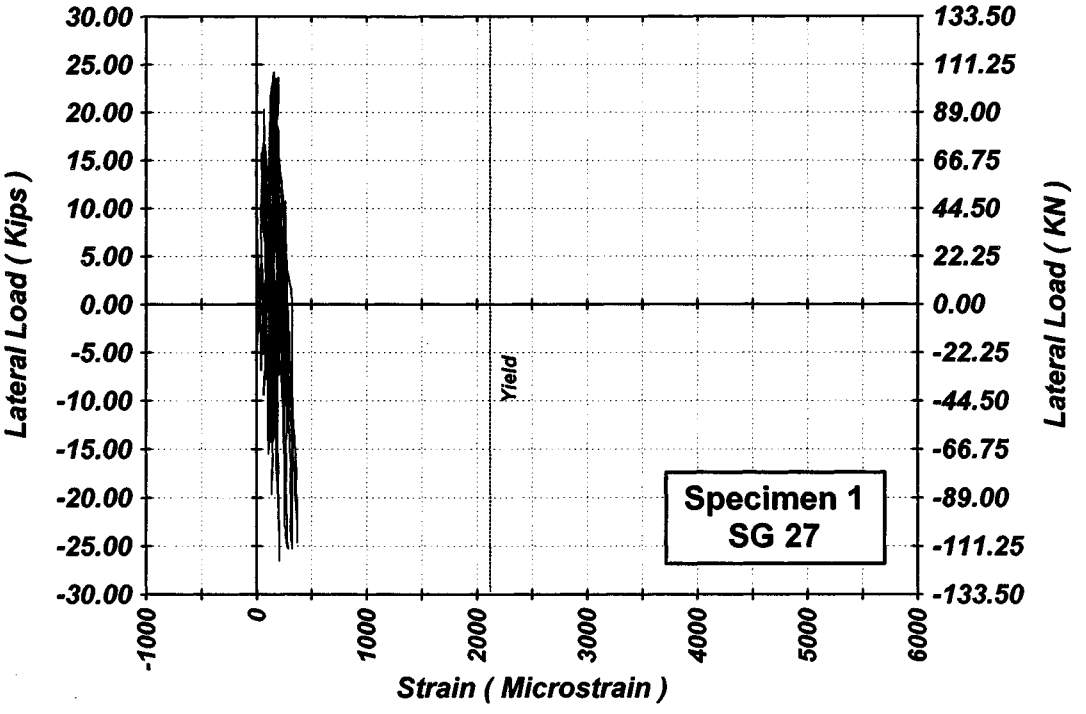

Figure 4-24 Measured Lateral Load Strain in SG-27 of Specimen 1

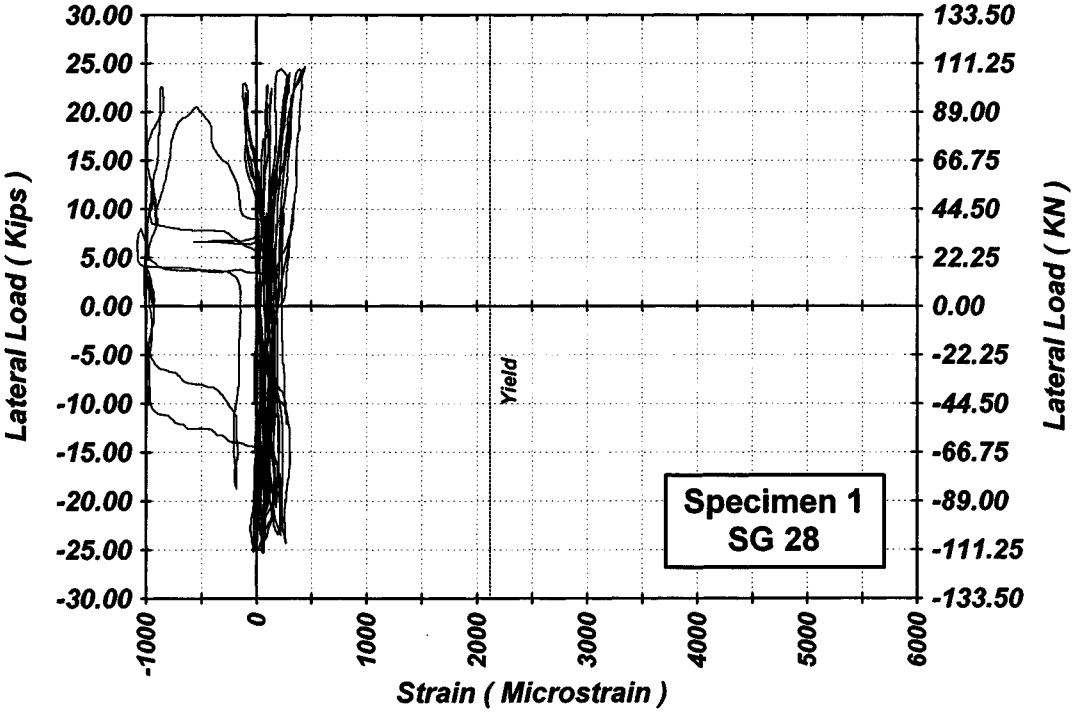

Figure 4-25 Measured Lateral Load Strain in SG-28 of Specimen 1

4.2.2 Performance of Specimen 2

At a displacement of 9 mm corresponding to a lateral load of 34.9 kN, flexural cracks were initiated. More flexural cracks propagated at higher lateral displacements. During the pull in the second cycle at a displacement ductility level of 4, spalling of the cover concrete began at a displacement of 110 mm corresponding to a lateral load of 105.6 kN. Specimen 2 reached its lateral load capacity of 110.8 kN at a displacement ductility of 4.7. As the wall specimen was subjected to two cycles at a displacement ductility of 5, buckling of the vertical bars occurred (Figure 4-26). After applying two full cycles at a displacement ductility level of 7, a vertical reinforcing bar was fractured under tension at a displacement of 193 mm corresponding to 78.4 kN. When the wall specimen was subjected to one more cycle at a displacement ductility of 7, the lateral load was reduced to 73.2 kN. At this point, the wall specimen was considered to have failed and the test was stopped.

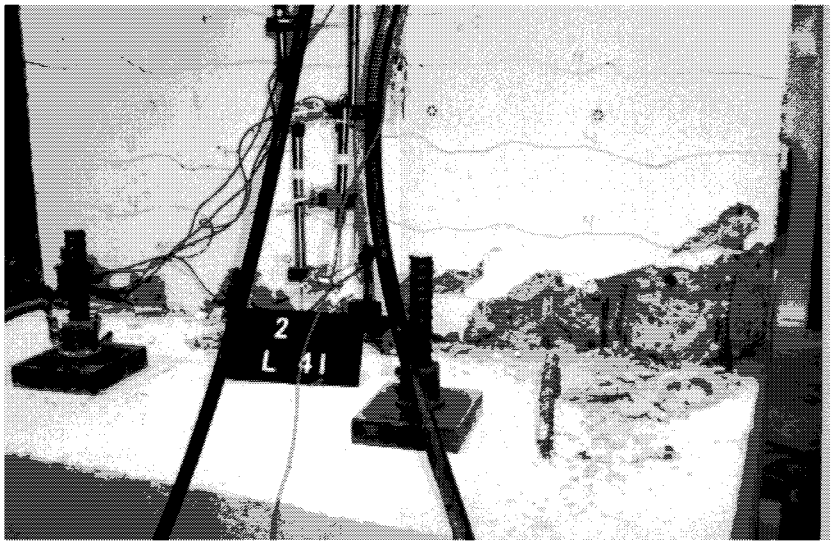

Figure 4-26 Spalling of Cover Concrete and Buckling in Vertical Bars of Specimen 2

The measured lateral load-strain relationship of the vertical reinforcing bars is presented in figures 4-27 through 4-30. The first two figures show the strain in the vertical bars at the wall-footing interface while the second two show the strain at a height of 80 mm from the top of the footing. It is obvious that the yield spread was limited to the lower 80 mm of the wall since the strain in the vertical bars at this height did not reach its yield point. Figures 4-31 through 4-34 show that the maximum strain in the confinement reinforcement was nearly 30% of the steel yield strain.

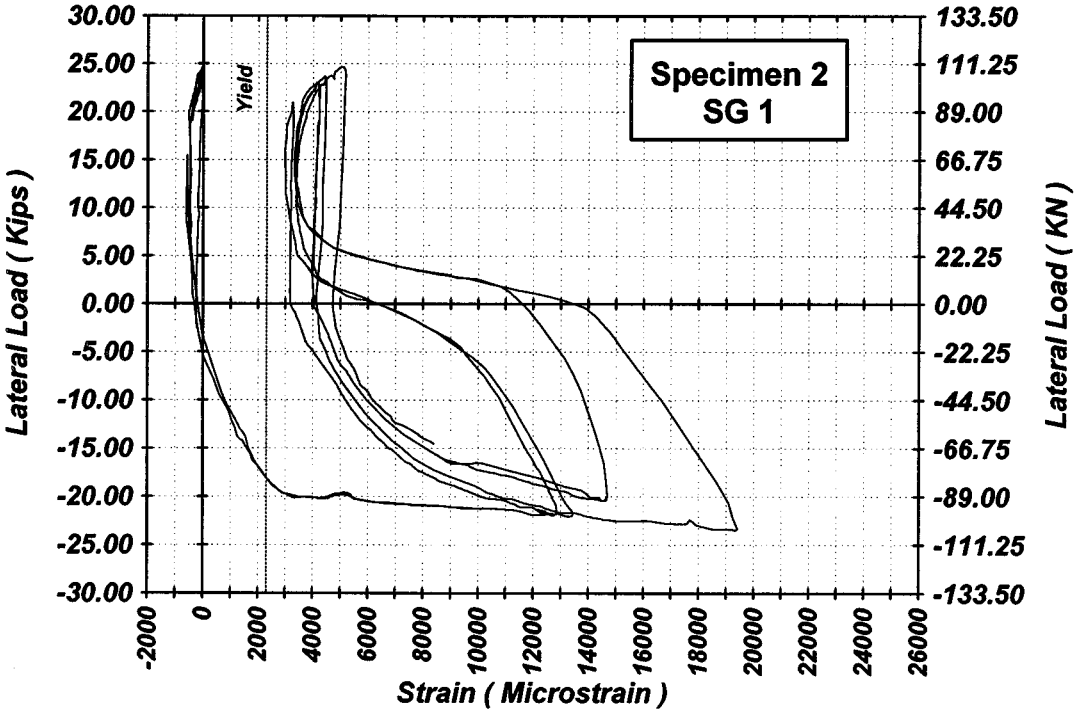

Figure 4-27 Measured Lateral Load Strain in SG-1 of Specimen 2

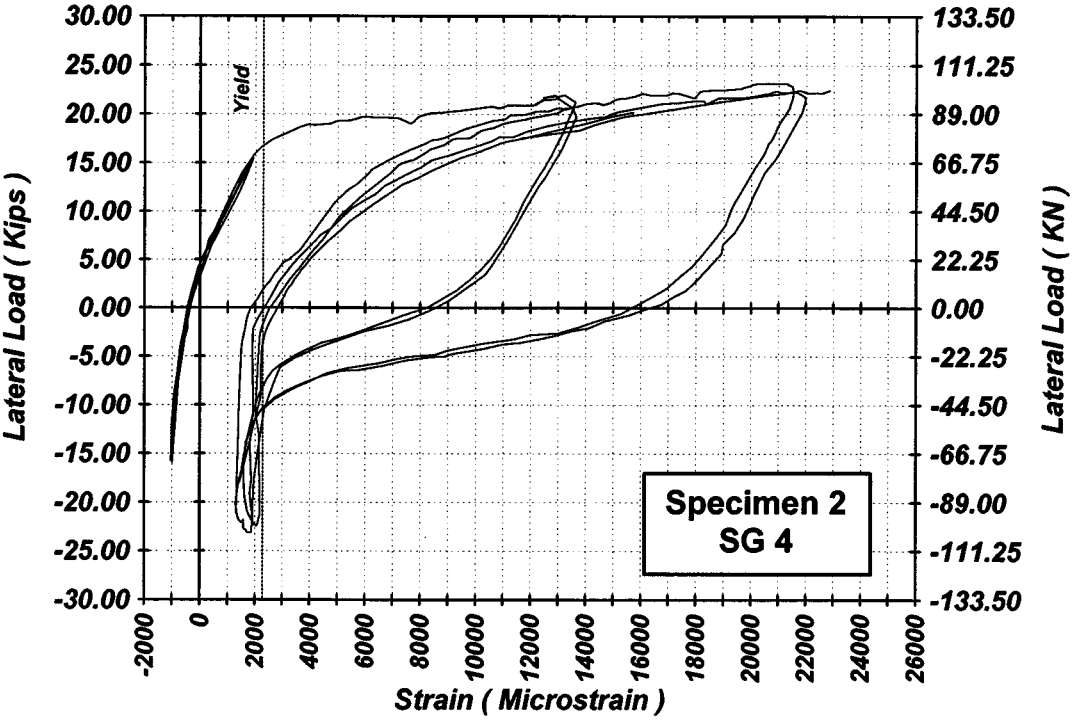

Figure 4-28 Measured Lateral Load Strain in SG-4 of Specimen 2

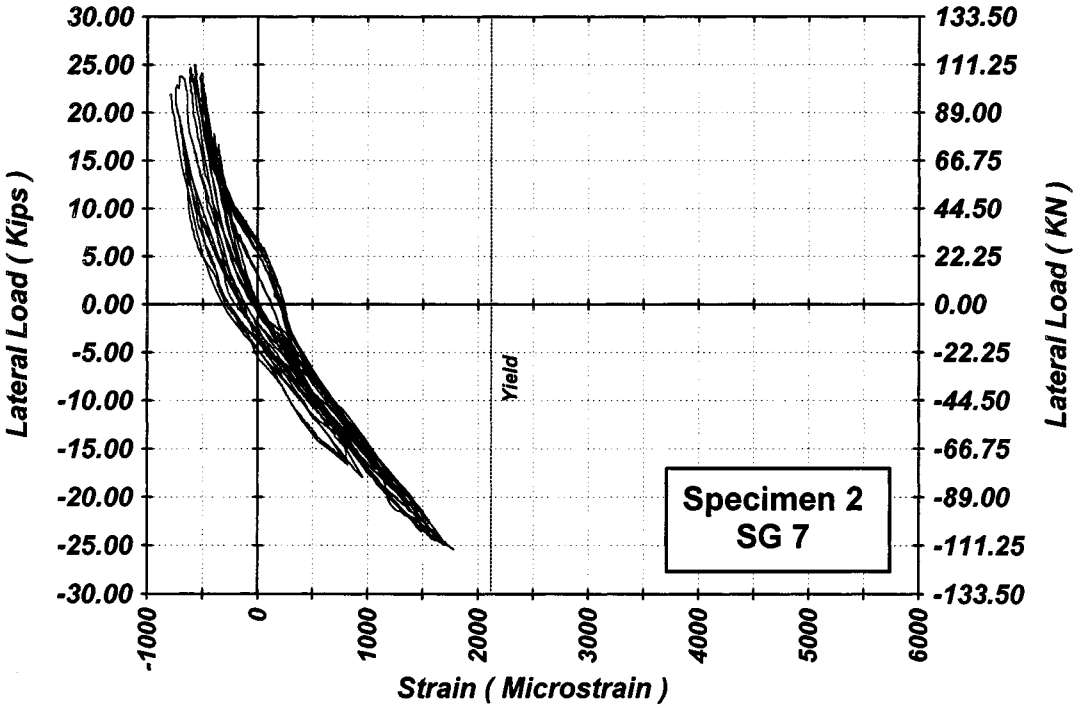

Figure 4-29 Measured Lateral Load Strain in SG-7 of Specimen 2

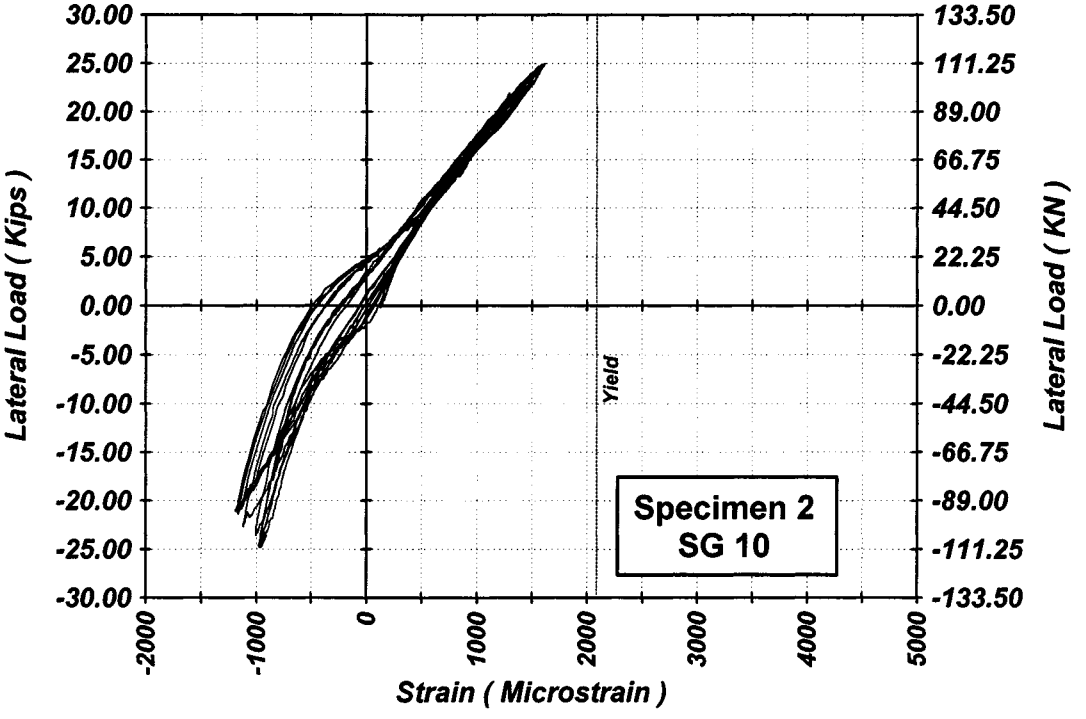

Figure 4-30 Measured Lateral Load Strain in SG-10 of Specimen 2

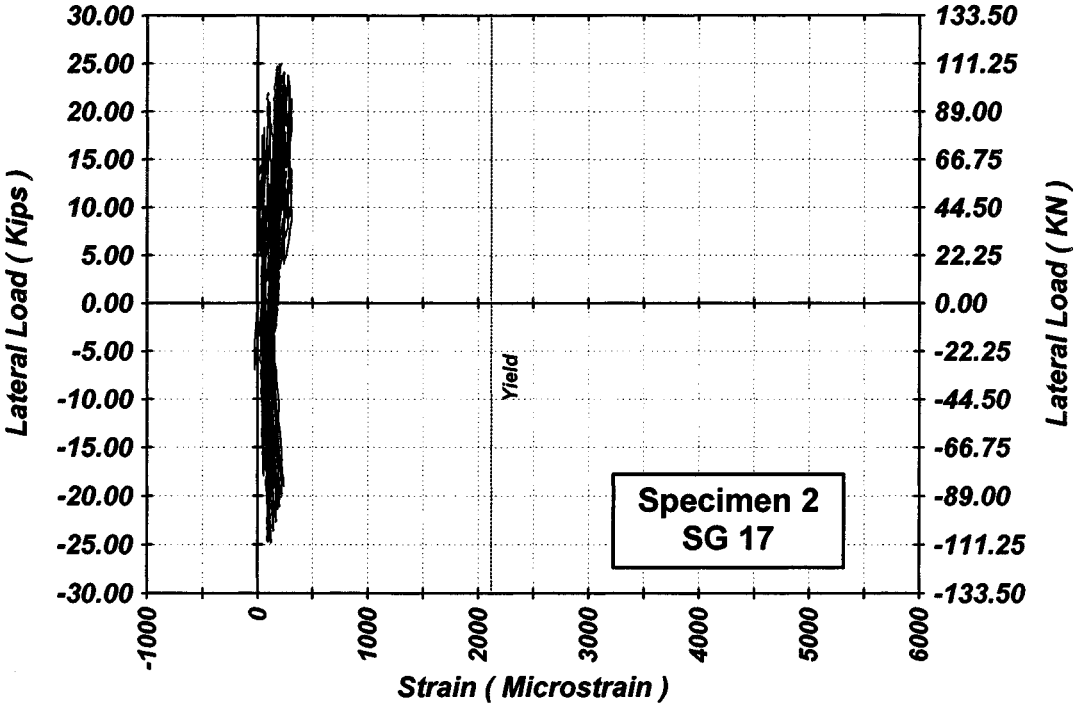

Figure 4-31 Measured Lateral Load Strain in SG-17 of Specimen 2

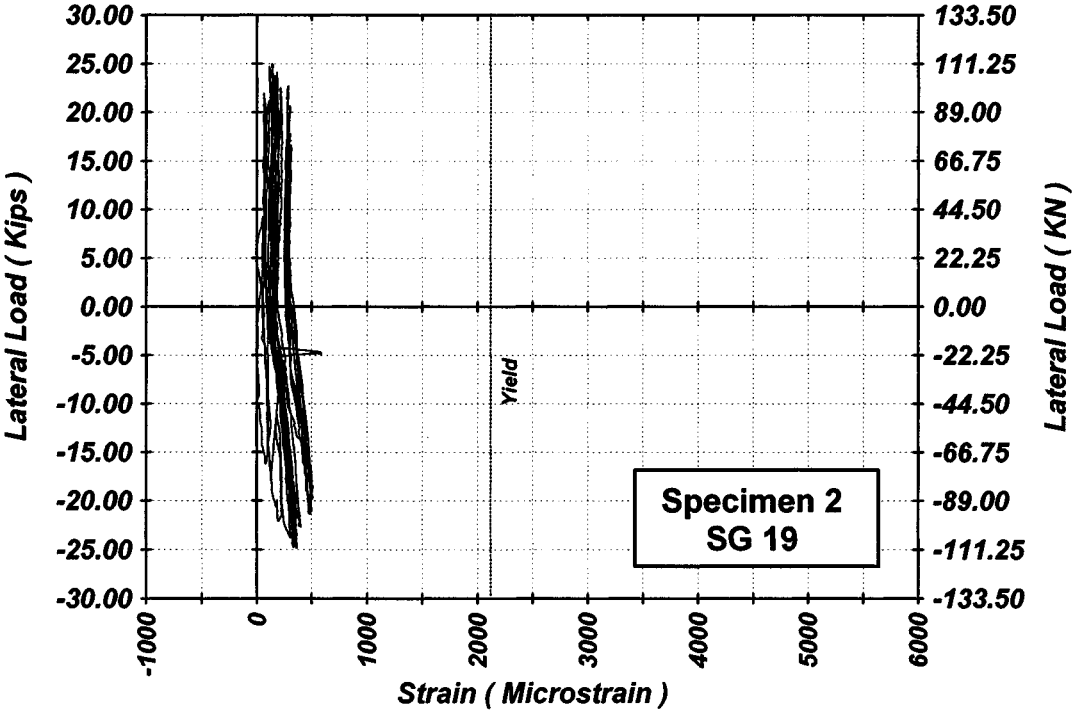

Figure 4-32 Measured Lateral Load Strain in SG-19 of Specimen 2

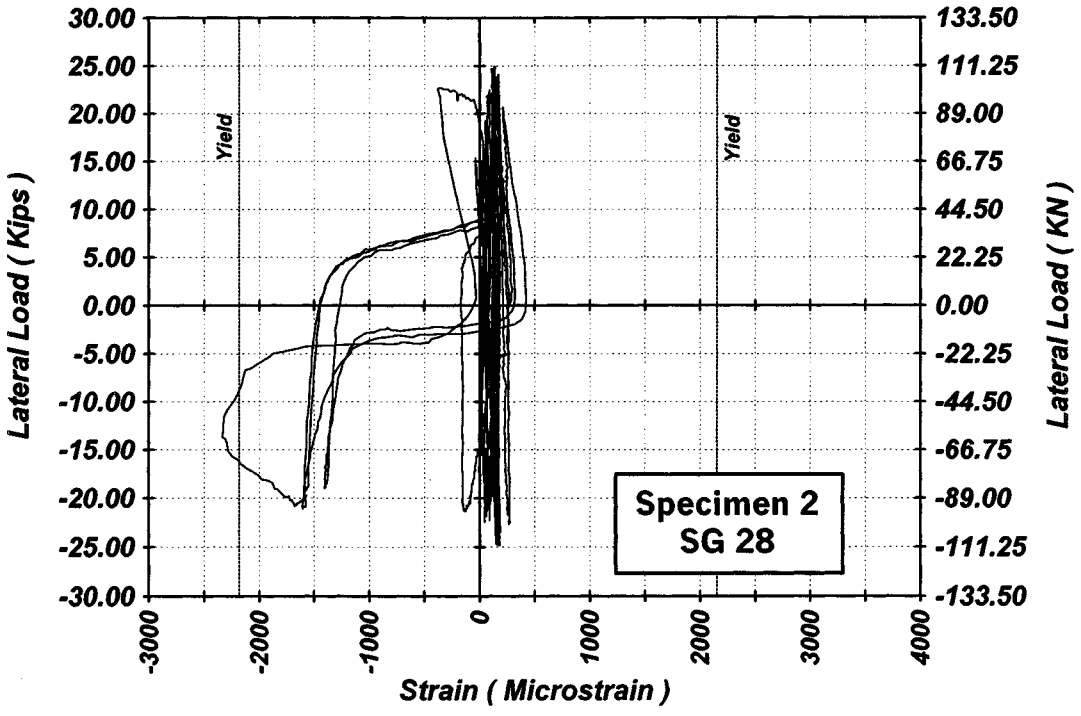

Figure 4-33 Measured Lateral Load Strain in SG-28 of Specimen 2

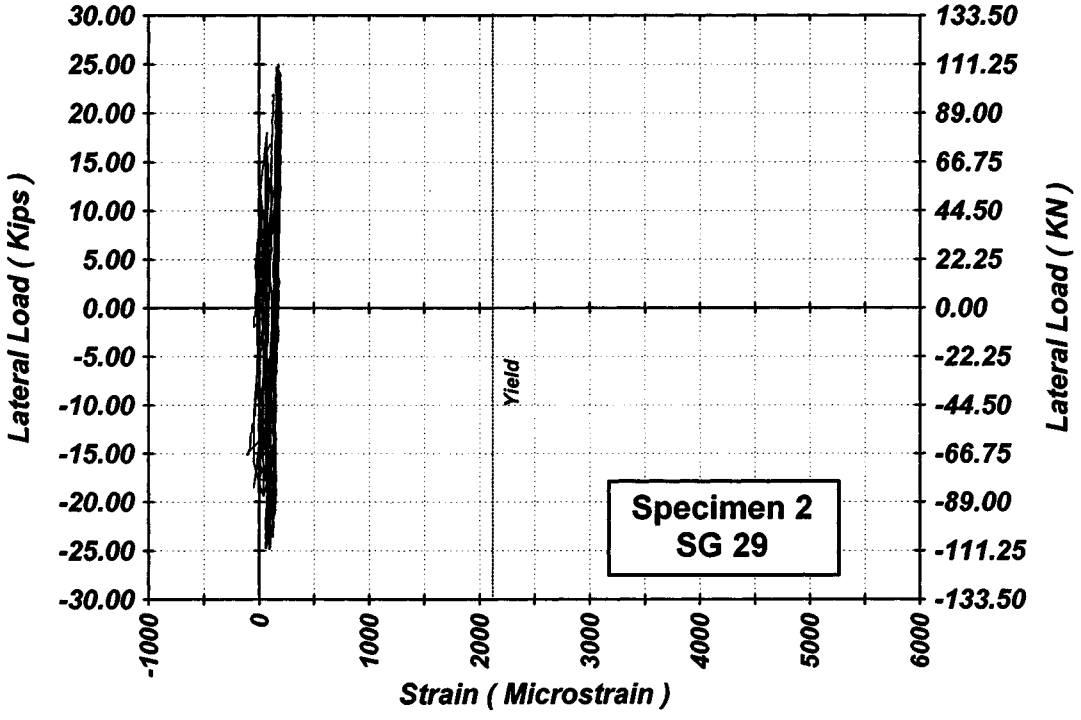

Figure 4-34 Measured Lateral Load Strain in SG-29 of Specimen 2

4.2.3 Performance of Specimen 3

Cracking of Specimen 3 began when it was pushed to a displacement of 11 mm corresponding to a lateral load of 38.6 kN. At the first excursion to a displacement ductility of 4, spalling of the cover concrete started to occur on the compression side. The wall specimen reached its lateral load capacity of 111.7 kN at a displacement ductility of nearly 5. When the specimen was cycled to higher displacements, more cracks appeared and spalling of the cover concrete spread along the plastic hinge zone. This was followed by buckling of the vertical reinforcing bars and opening of the 90° hooks of the crossties at a displacement of 145 mm (μ_d = 6). Before completing the second cycle at a displacement ductility of 7, a vertical bar fractured at a displacement of 148 mm corresponding to a lateral load of 97.65 kN. When the wall specimen was pulled further to complete the second cycle, another vertical bar fractured at a displacement of 154 mm. At this level, the lateral load was reduced to 77.7 kN. During the first pull loop to a displacement ductility of 8, two vertical bars fractured at a displacement of 91 mm and 115 mm, respectively (Figure 4-35). When the wall specimen was pushed for the second cycle at a displacement ductility of 8, the lateral load dropped to 76 kN and the wall specimen was considered to have failed.

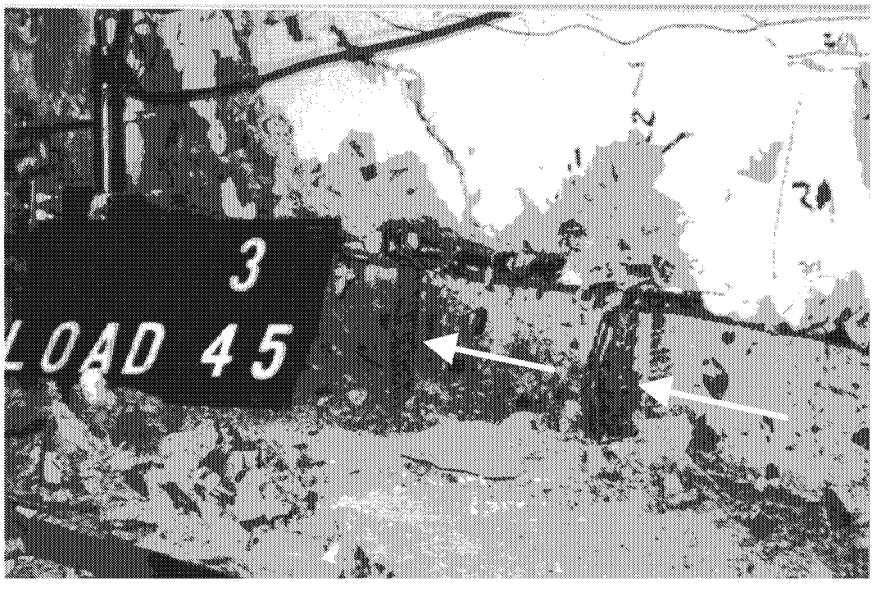

Figure 4-35 Fracture of the Vertical Bars in Specimen 3

Figures 4-36 and 4-37 show the lateral load-strain hysteresis relationships at the wall-footing interface. The strain in the vertical reinforcing bars at a height of 80 mm did not reach its yield point (Figures 4-38 and 4-39). The lateral load-strain relationship in the confinement reinforcement shows that the strain in the transverse bars and the crossties did not exceed 50% of the steel yield strain (Figures 4-40 through 4-43).

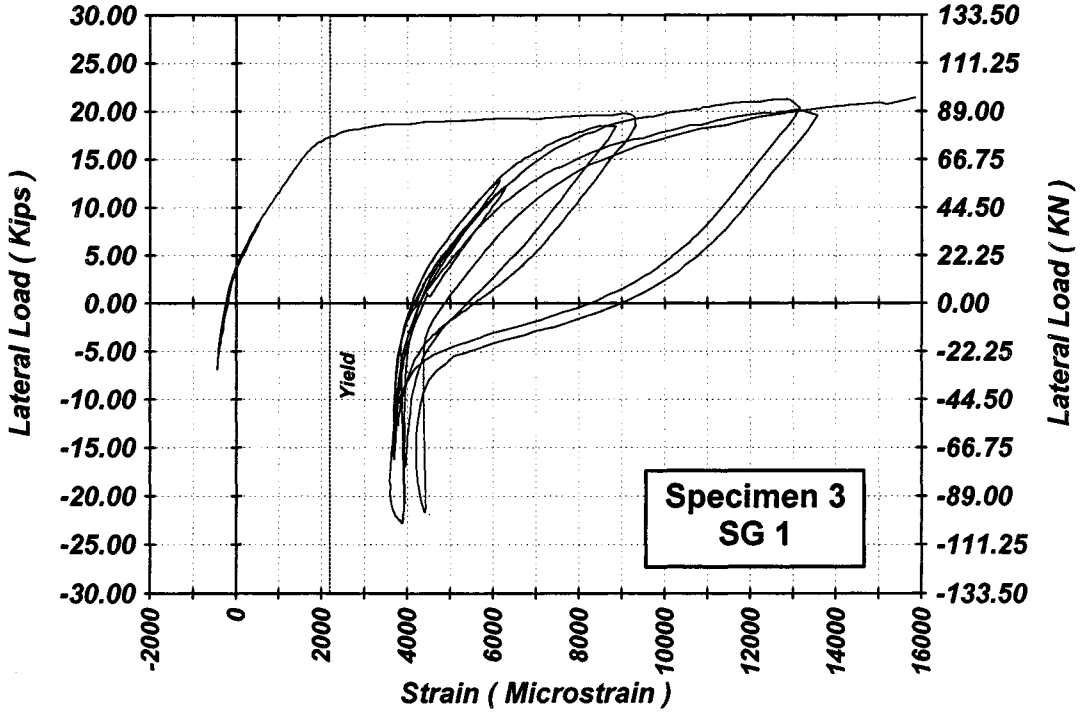

Figure 4-36 Measured Lateral Load Strain in SG-1 of Specimen 3

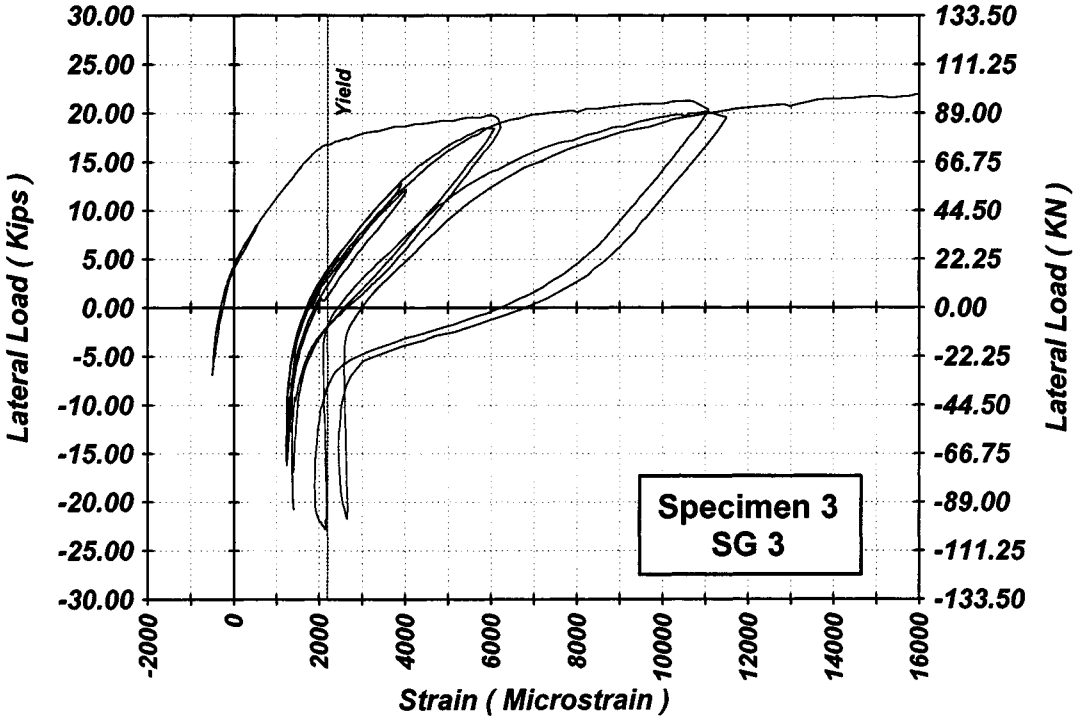

Figure 4-37 Measured Lateral Load Strain in SG-3 of Specimen 3

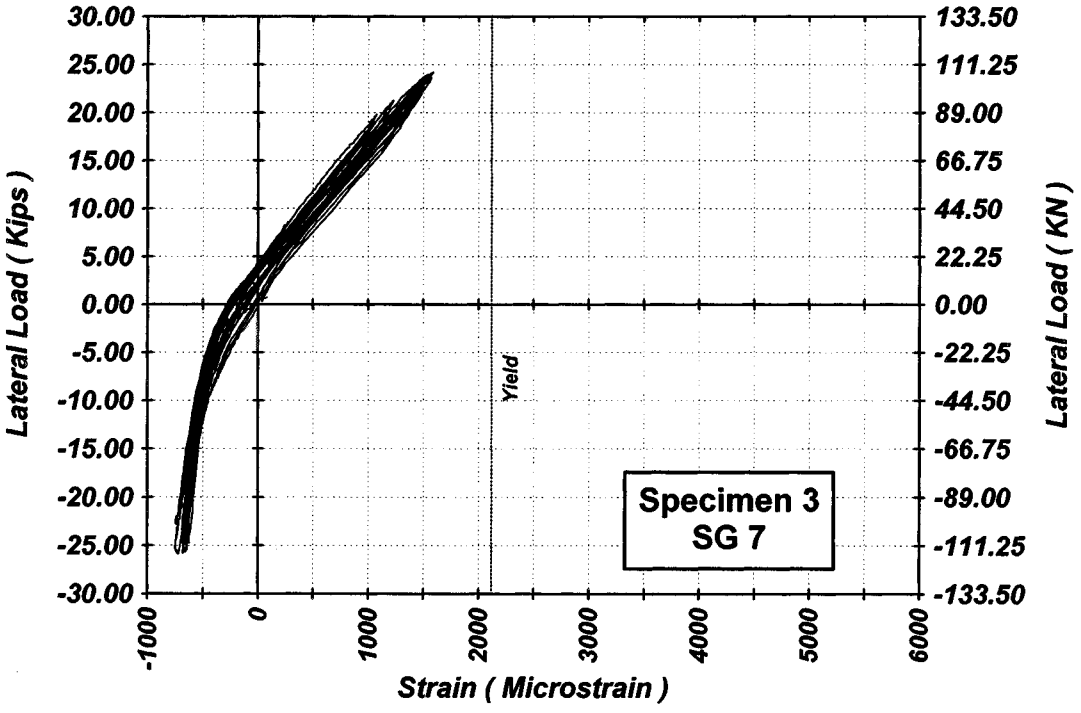

Figure 4-38 Measured Lateral Load Strain in SG-7 of Specimen 3

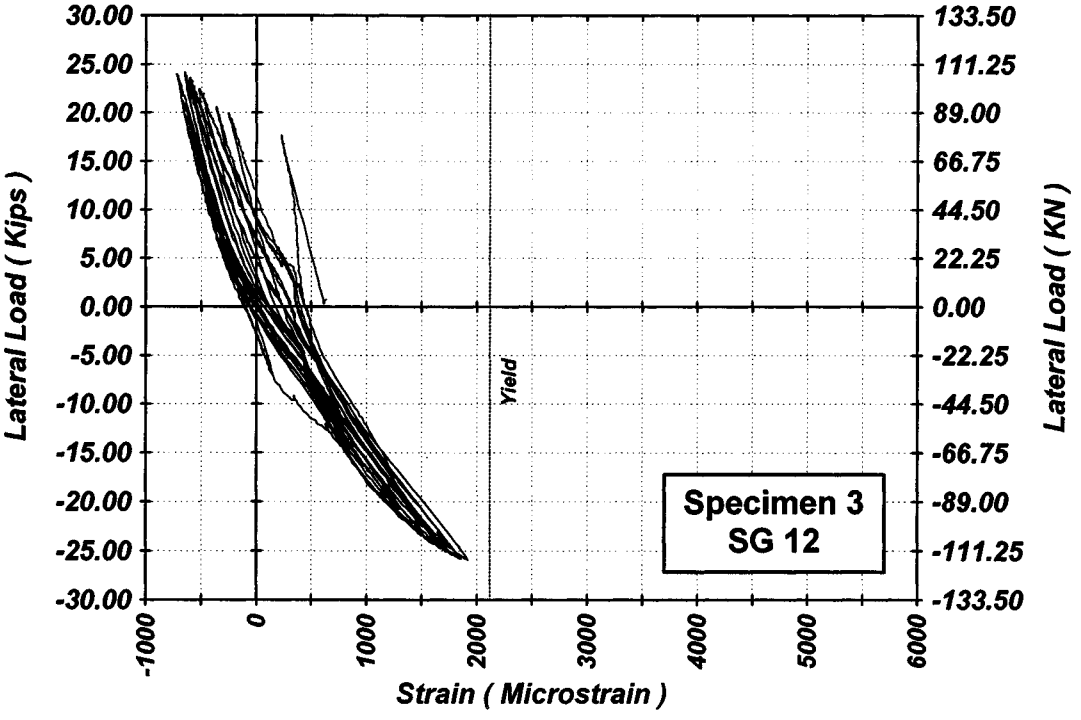

Figure 4-39 Measured Lateral Load Strain in SG-12 of Specimen 3

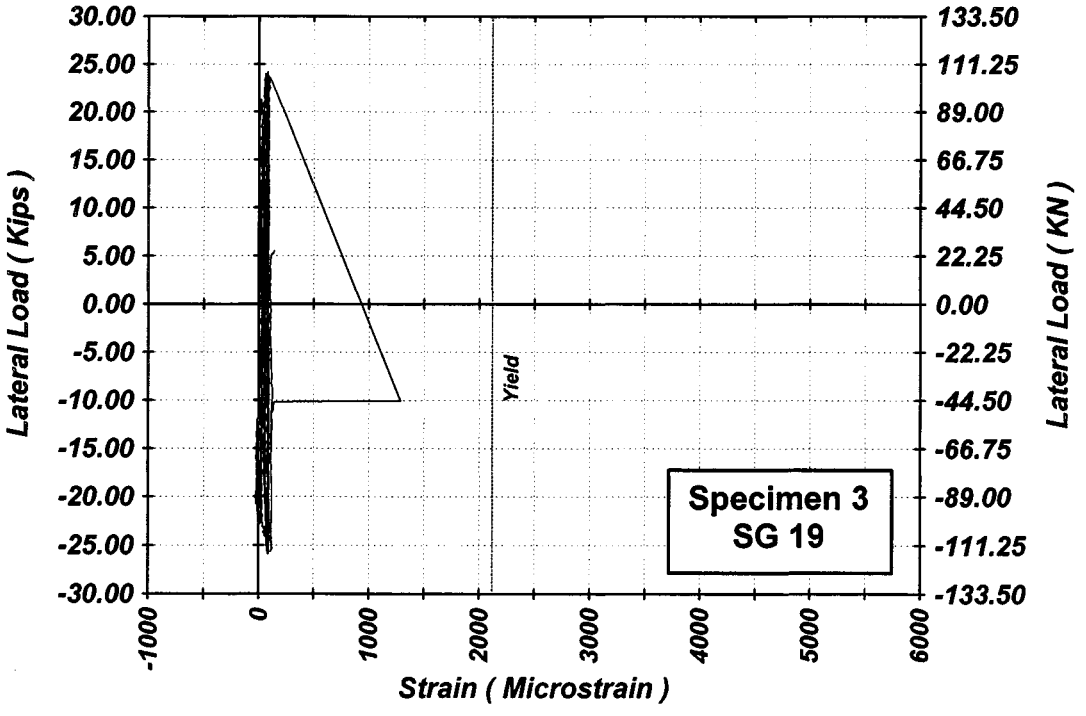

Figure 4-40 Measured Lateral Load Strain in SG-19 of Specimen 3

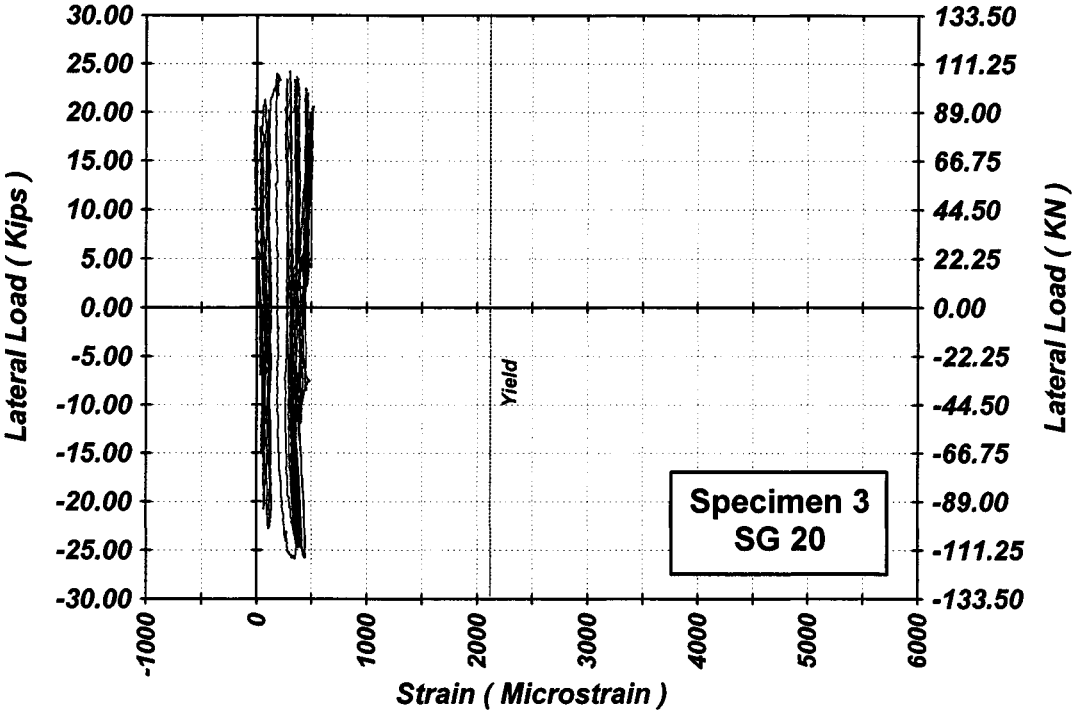

Figure 4-41 Measured Lateral Load Strain in SG-20 of Specimen 3

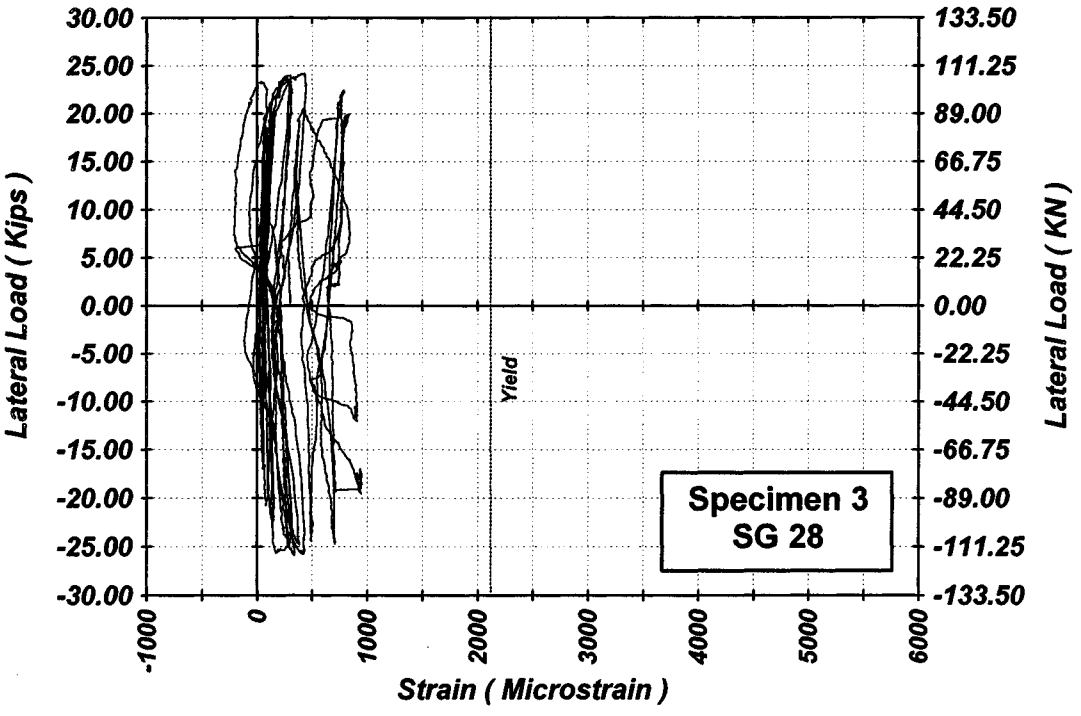

Figure 4-42 Measured Lateral Load Strain in SG-28 of Specimen 3

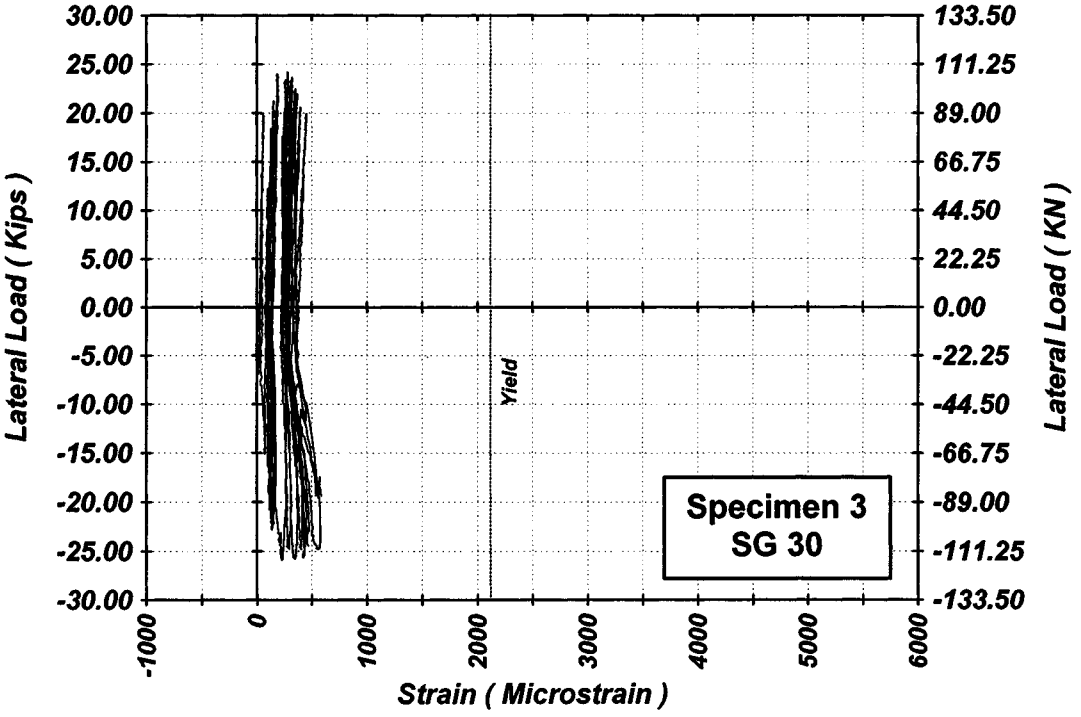

Figure 4-43 Measured Lateral Load Strain in SG-30 of Specimen 3

4.2.4 Performance of Specimen 4

At a displacement of 7.5 mm corresponding to a lateral load of 40.27 kN, flexure cracks were initiated. The maximum lateral load was attained at a displacement ductility of 3.8. As the wall specimen was pulled for the first loop to a displacement ductility of 4, spalling of the cover concrete began on the compression side of the specimen. Buckling of a corner vertical bar occurred when the wall specimen was pulled for the second cycle to a displacement ductility of 7. On the first excursion to a displacement ductility of 5, a 90° hook of a crosstie (located at 160 mm from the wall-footing interface) that held the buckled vertical bar opened at a displacement of 200 mm ($\mu_d = 4.8$). As a result, the unsupported length of the vertical bar increased and more lateral buckling occurred (Figure 4-44). While the wall specimen was cycled to higher ductility levels, more extensive spalling of the cover concrete and buckling of the vertical bars was observed. As the wall was pushed for the second cycle at a displacement ductility of 6, the lateral load dropped to 129.5 kN which is nearly 73% of the lateral load capacity of the wall specimen. The test was stopped at this point.

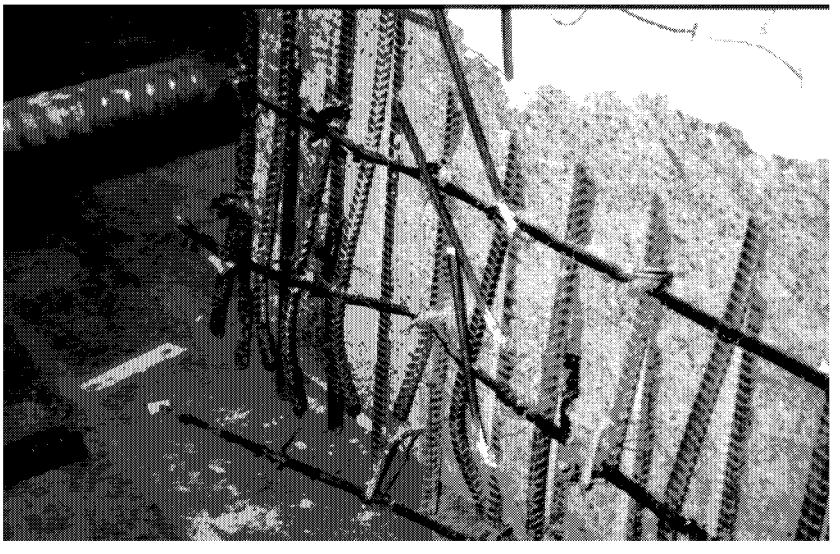

Figure 4-44 Buckling of the Vertical and the Lateral Bars in Specimen 4

The measured lateral load-strain hysteresis of the vertical reinforcing bars indicates that the yield did not spread to the wall sections over 160 mm from the top of the footing (Figures 4-45 through 4-48) and that extensive bar yielding was limited to the wall-footing connection. The highest strain in the confinement reinforcement at the plastic hinge zone was lower than 50 % of the steel yield strain (Figures 4-49 through 4-52).

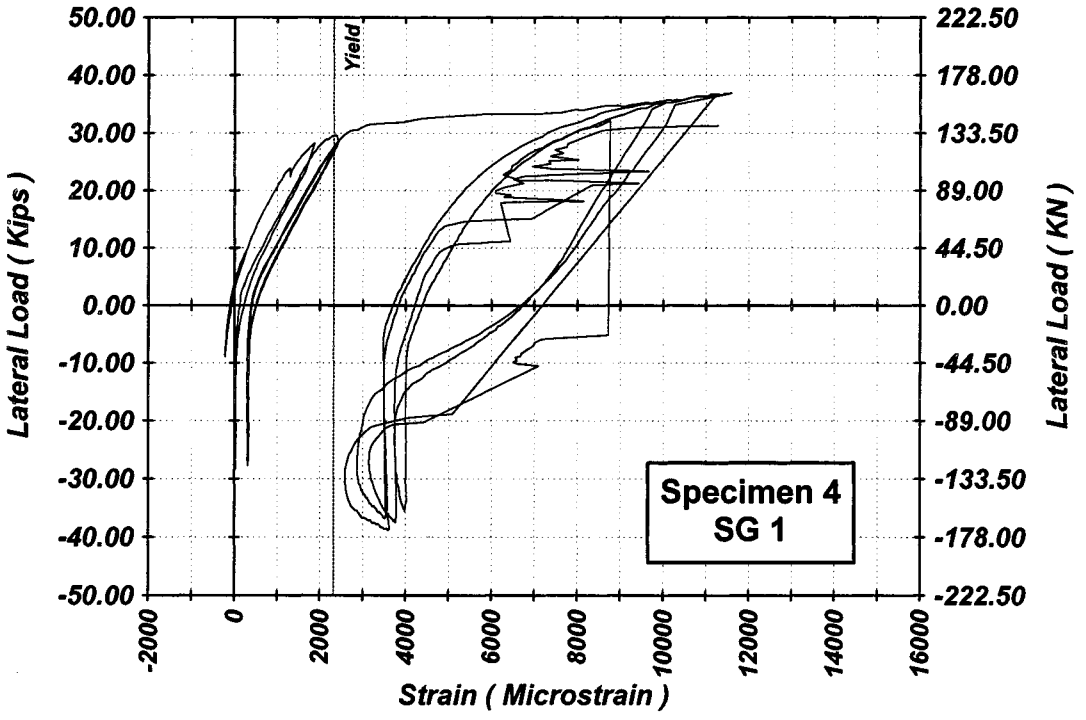

Figure 4-45 Measured Lateral Load Strain in SG-1 of Specimen 4

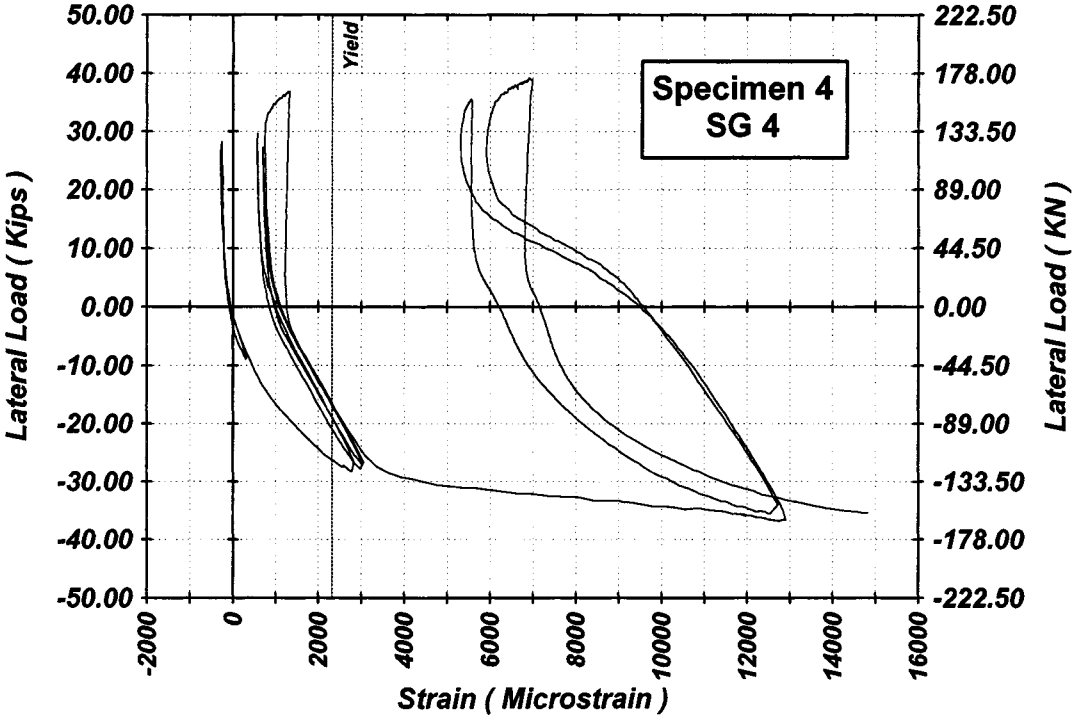

Figure 4-46 Measured Lateral Load Strain in SG-4 of Specimen 4

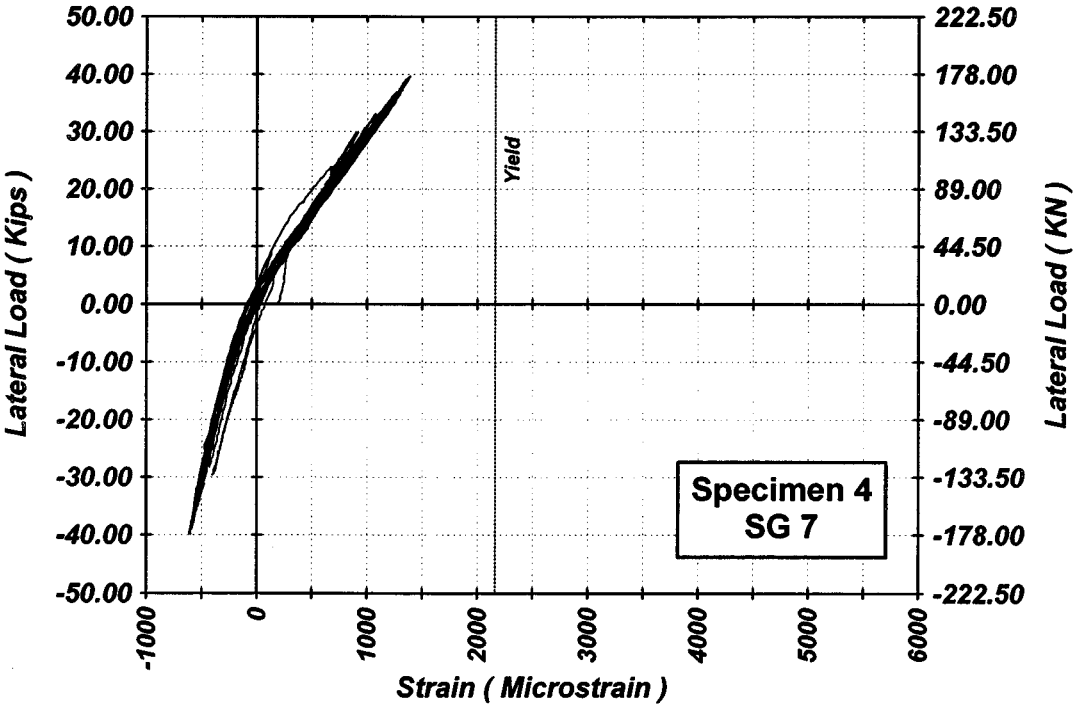

Figure 4-47 Measured Lateral Load Strain in SG-7 of Specimen 4

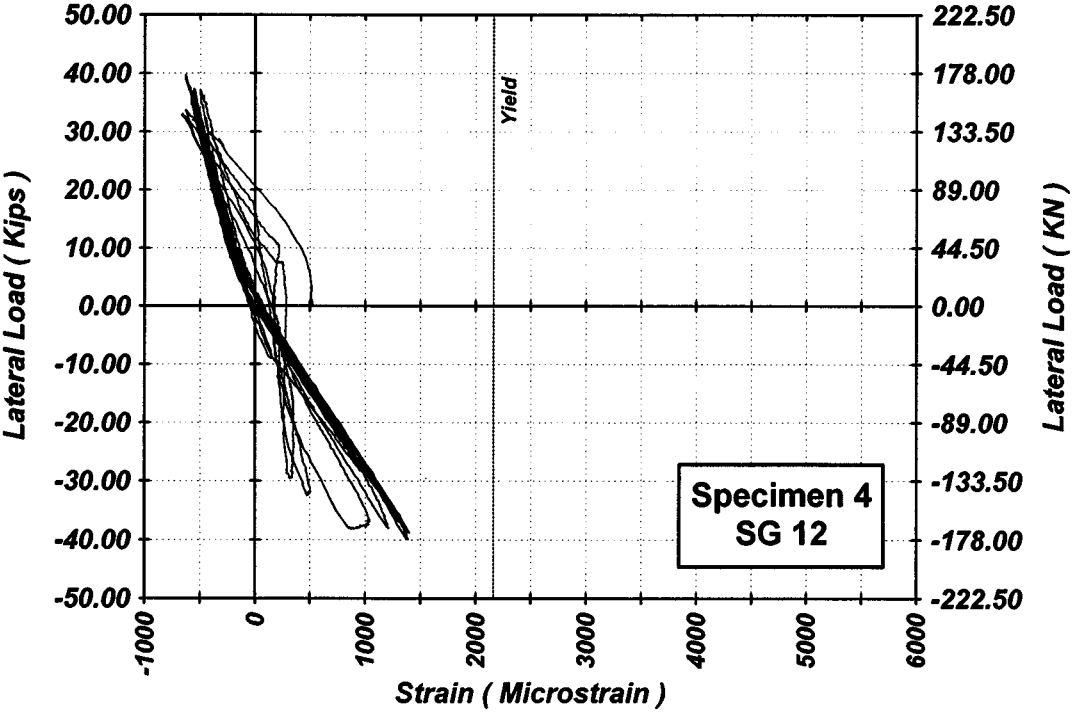

Figure 4-48 Measured Lateral Load Strain in SG-12 of Specimen 4

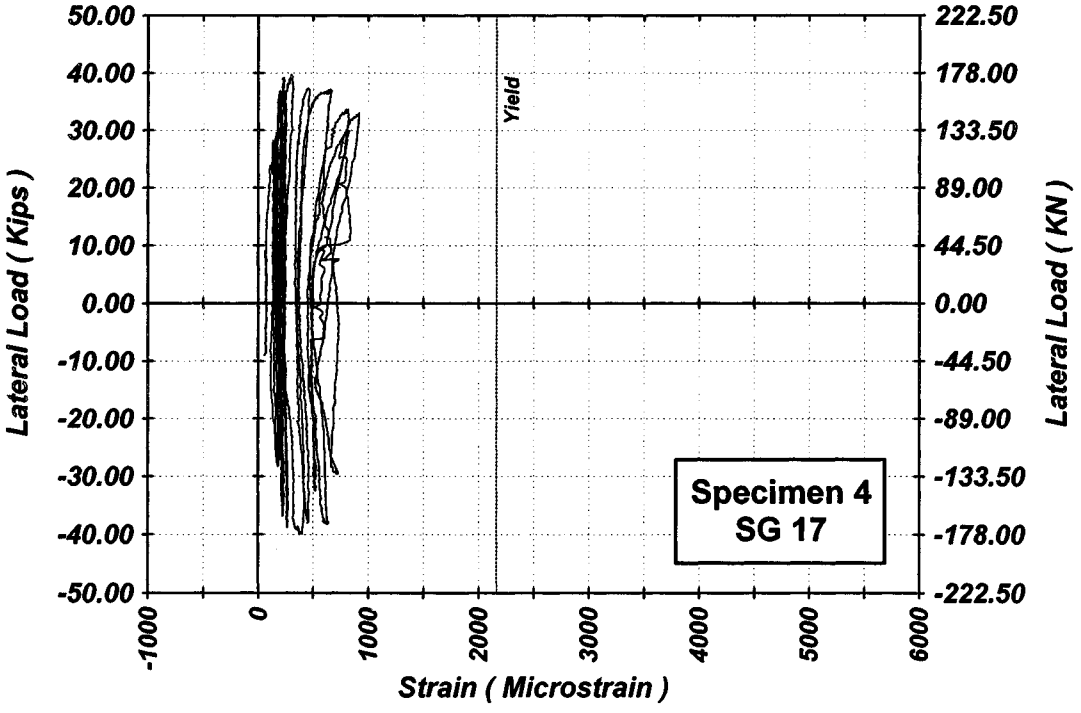

Figure 4-49 Measured Lateral Load Strain in SG-17 of Specimen 4

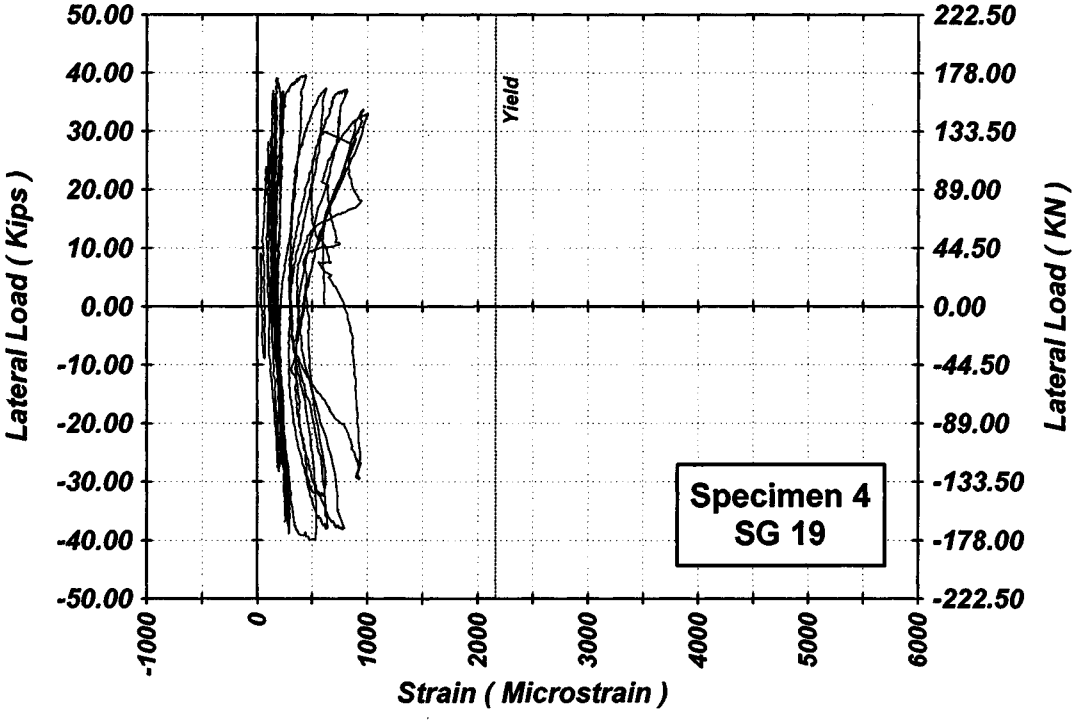

Figure 4-50 Measured Lateral Load Strain in SG-19 of Specimen 4

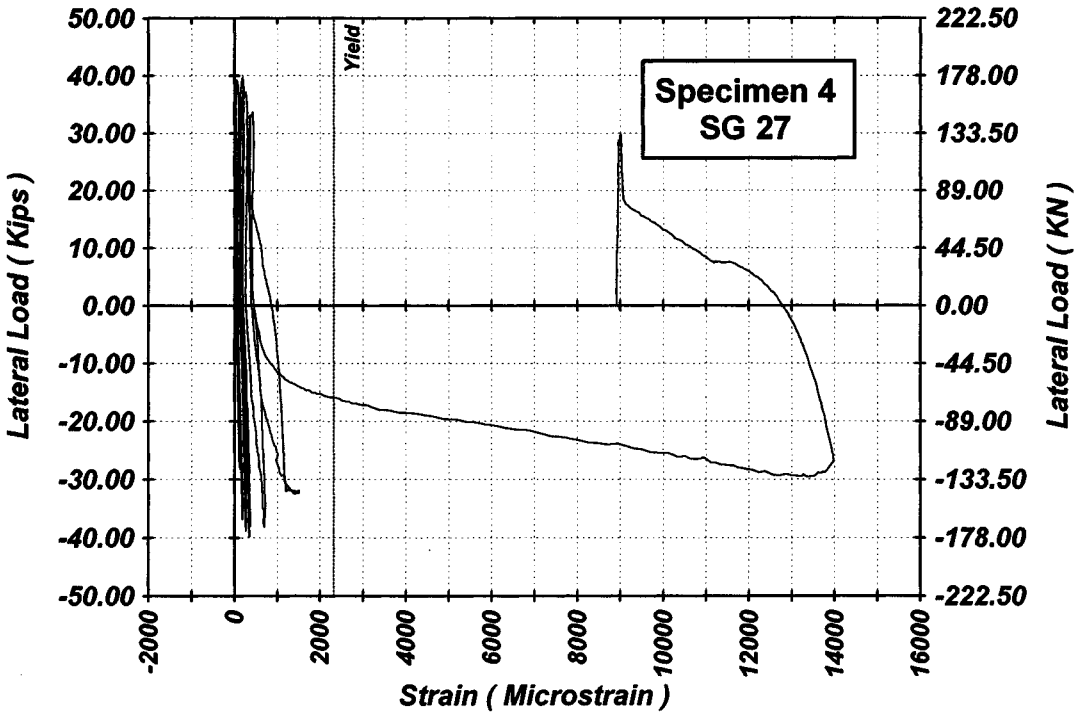

Figure 4-51 Measured Lateral Load Strain in SG-27 of Specimen 4

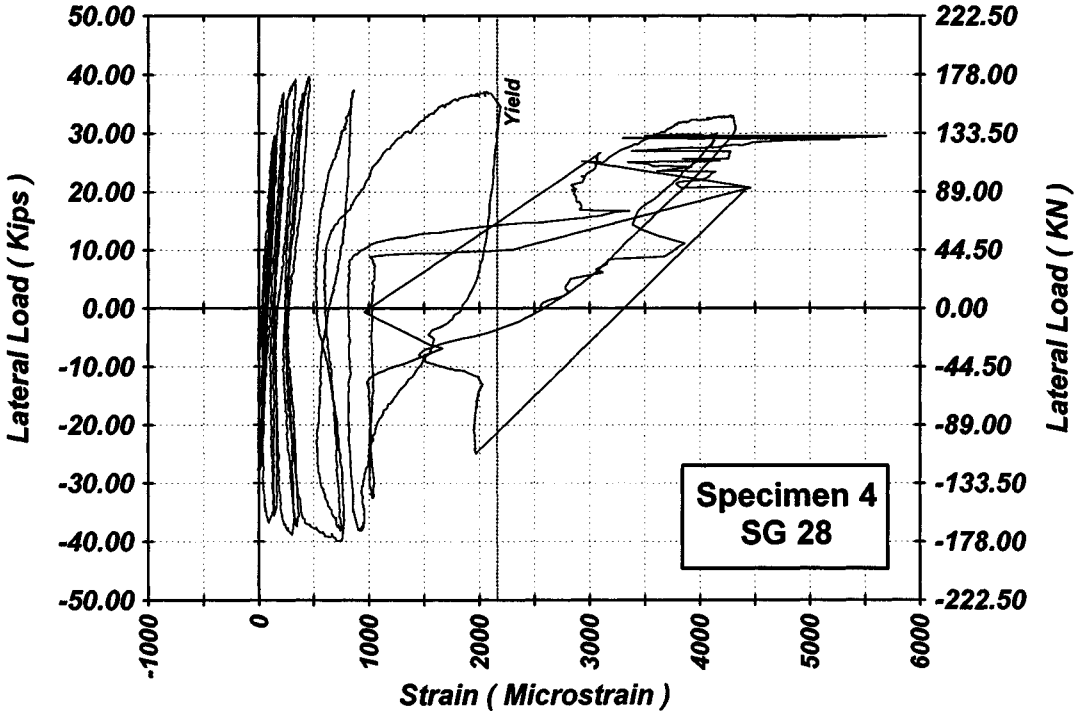

Figure 4-52 Measured Lateral Load Strain in SG-28 of Specimen 4

4.2.5 Performance of Specimen 5

At the wall-footing interface, a horizontal flexural crack was initiated at a lateral displacement of 6 mm corresponding to a lateral load of 34.75 kN. While the wall specimen was pushed for the second cycle at a displacement ductility of 3, spalling of the cover concrete at the compression side started to occur. The wall specimen maintained its lateral load capacity (169.1 kN) at a displacement ductility of 4. Buckling of the vertical reinforcing bars began at a displacement of 212 mm (μ_d = 5). At the second loop of a displacement ductility of 5, opening of the crossties started to occur. When the wall specimen was pulled for the first cycle to a displacement ductility of 6, the lateral load was reduced to 101 kN which is nearly 70% of the lateral load capacity. The test was stopped because the wall was considered to have failed when the lateral load was dropped to 80% of its maximum value. Figure 4-53 shows buckling of the vertical bars and opening of the crossties.

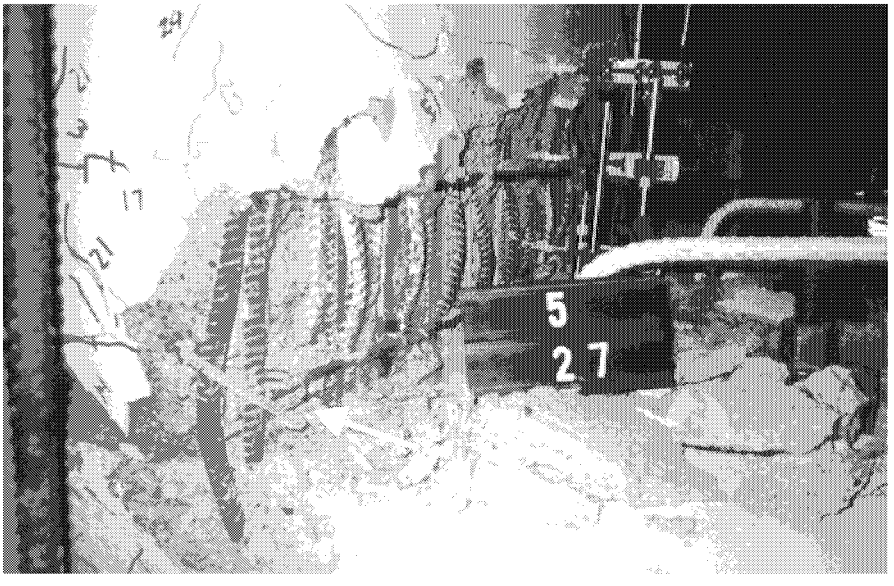

Figure 4-53 Vertical Bar Buckling and Opening of the Crossties in Specimen 5

The measured lateral load-strain hysteresis of the vertical bars at the wall-footing interface is presented in figures 4-54 and 4-55. Figures 4-56 and 4-57 show the strain in the vertical bars at a height of 80 mm from the top of the footing. Only the strain at the wall-footing interface reached the yield point. The maximum measured strain in the confinement reinforcement was 60 % of the steel yield strain (Figures 4-58 through 4-61).

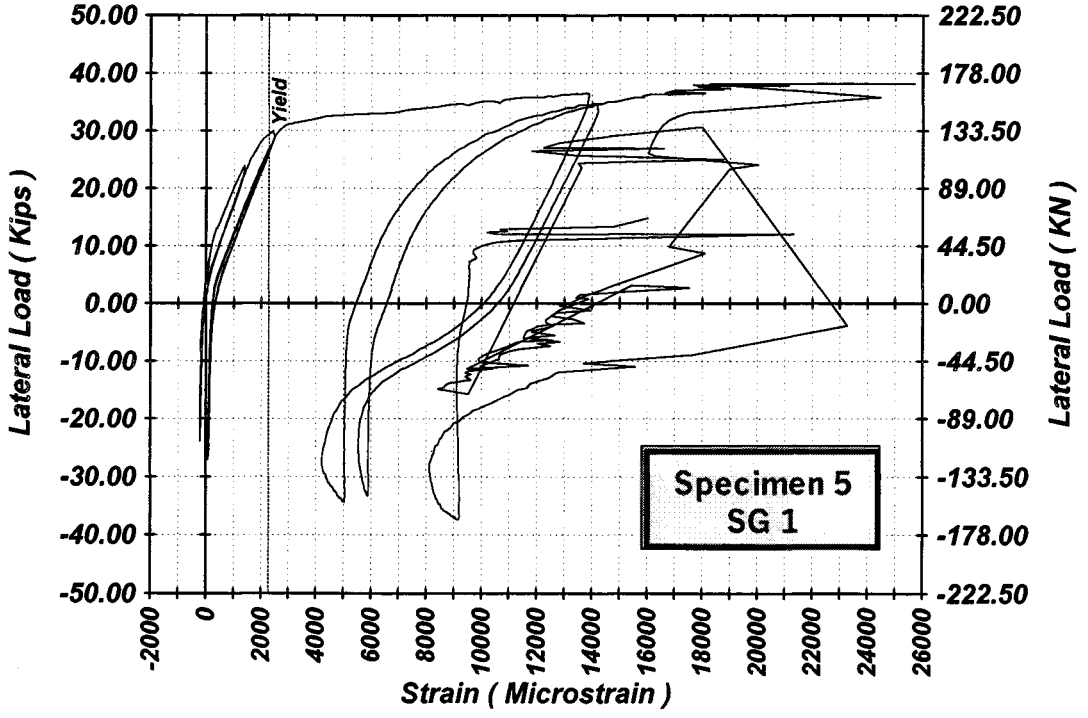

Figure 4-54 Measured Lateral Load Strain in SG-1 of Specimen 5

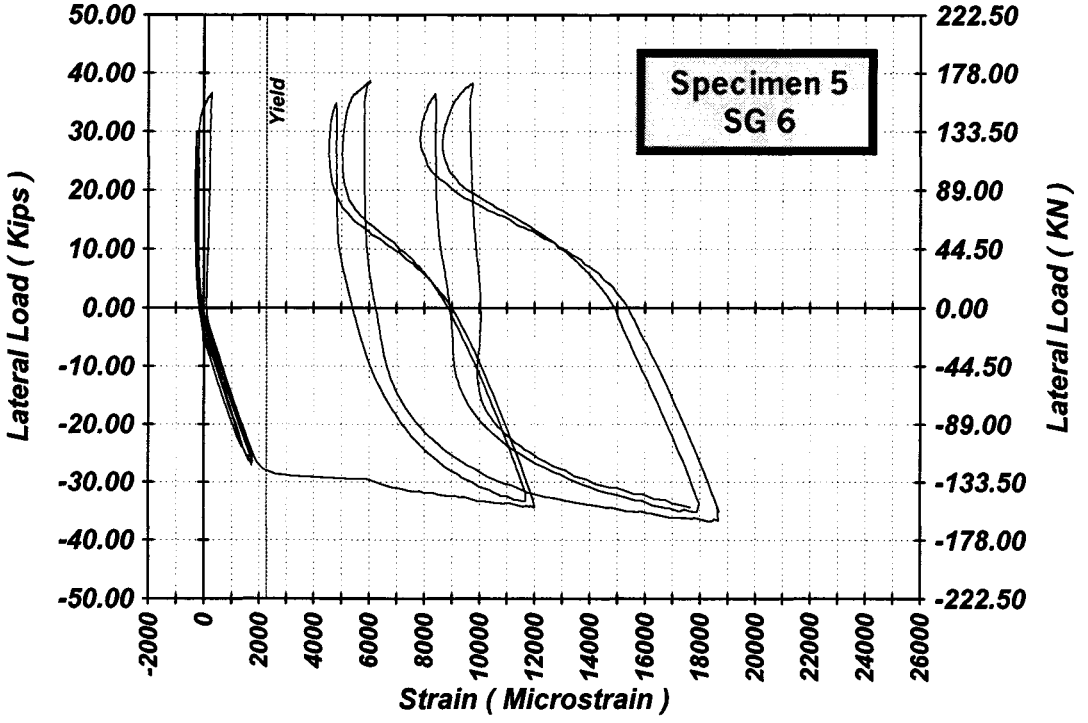

Figure 4-55 Measured Lateral Load Strain in SG-6 of Specimen 5

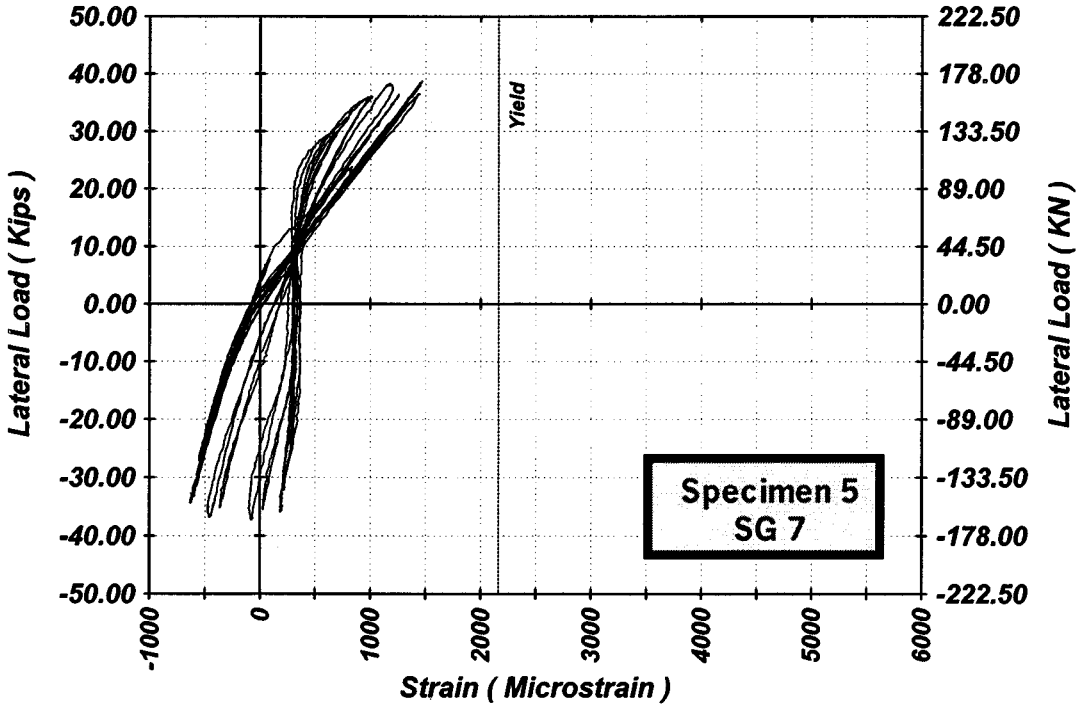

Figure 4-56 Measured Lateral Load Strain in SG-7 of Specimen 5

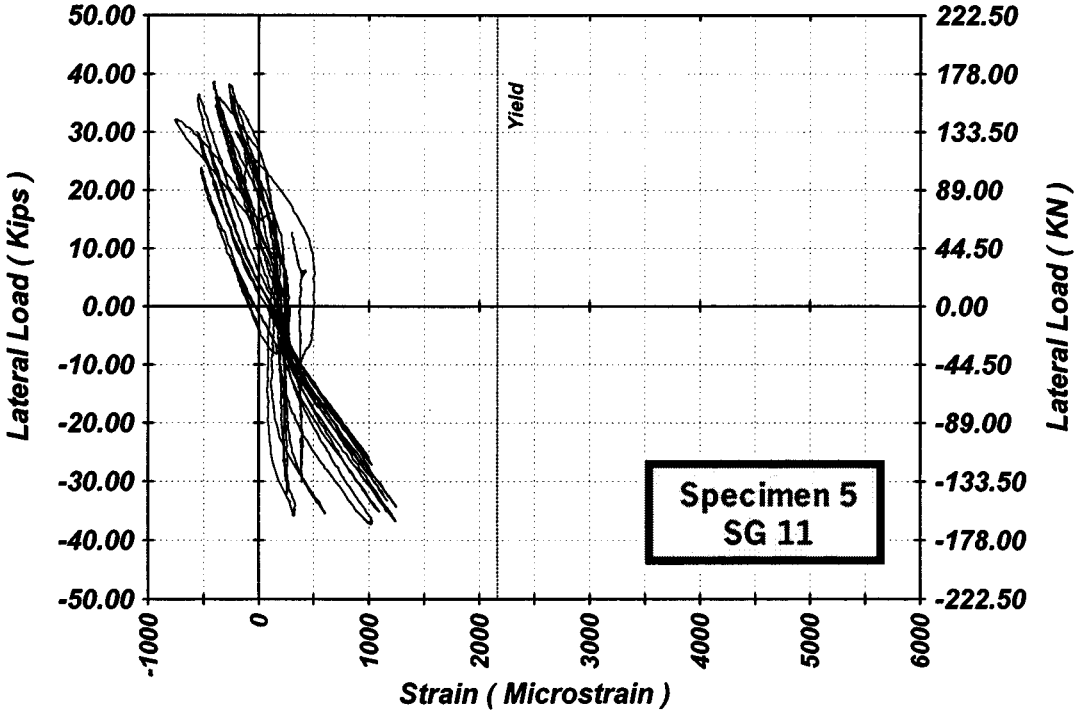

Figure 4-57 Measured Lateral Load Strain in SG-11 of Specimen 5

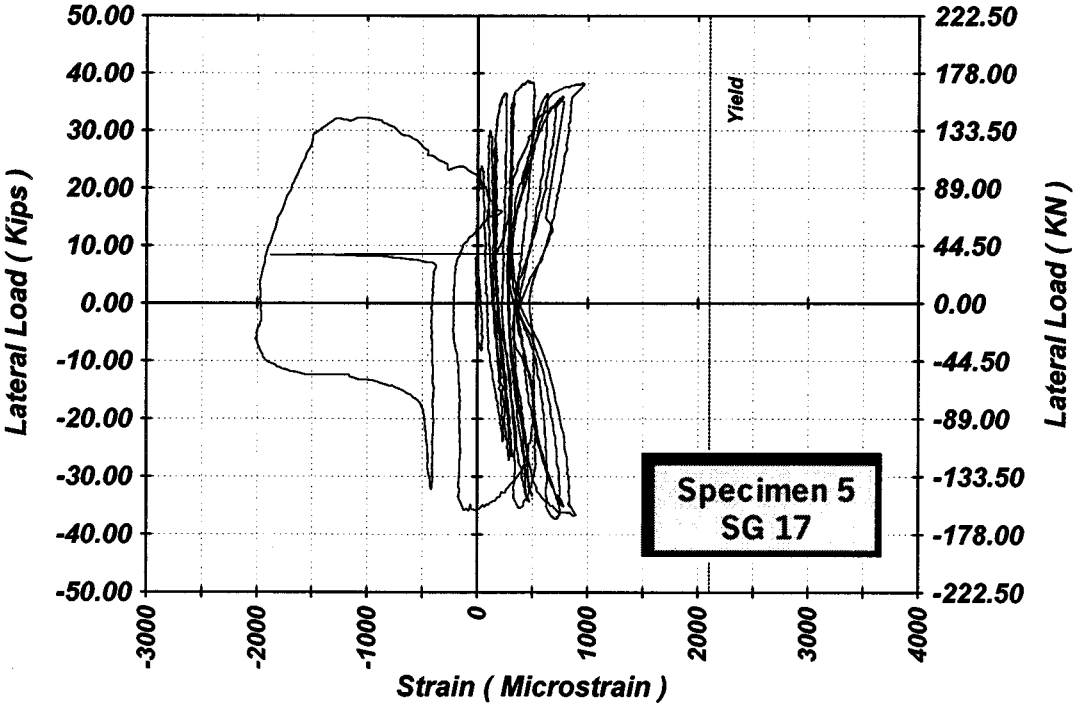

Figure 4-58 Measured Lateral Load Strain in SG-17 of Specimen 5

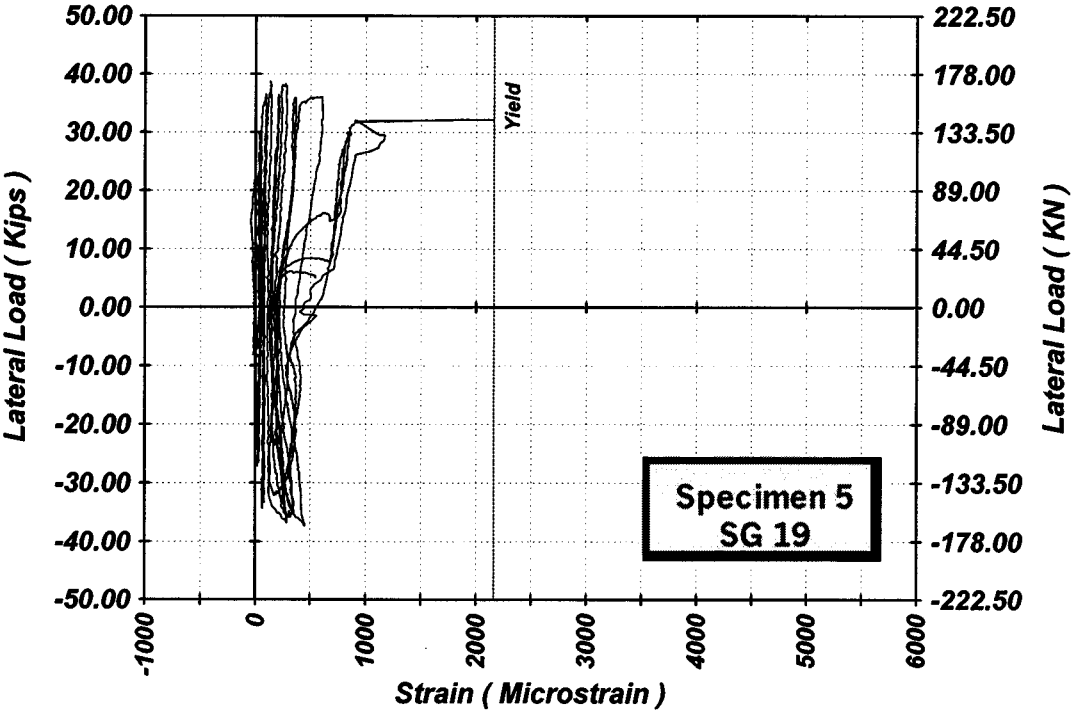

Figure 4-59 Measured Lateral Load Strain in SG-19 of Specimen 5

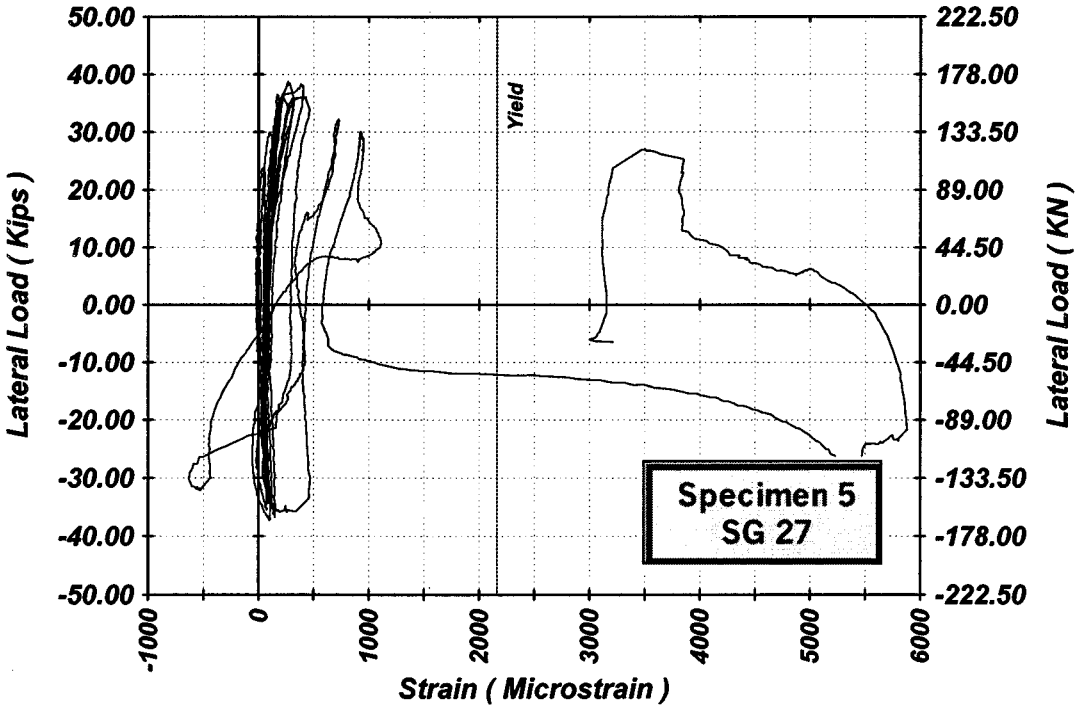

Figure 4-60 Measured Lateral Load Strain in SG-27 of Specimen 5

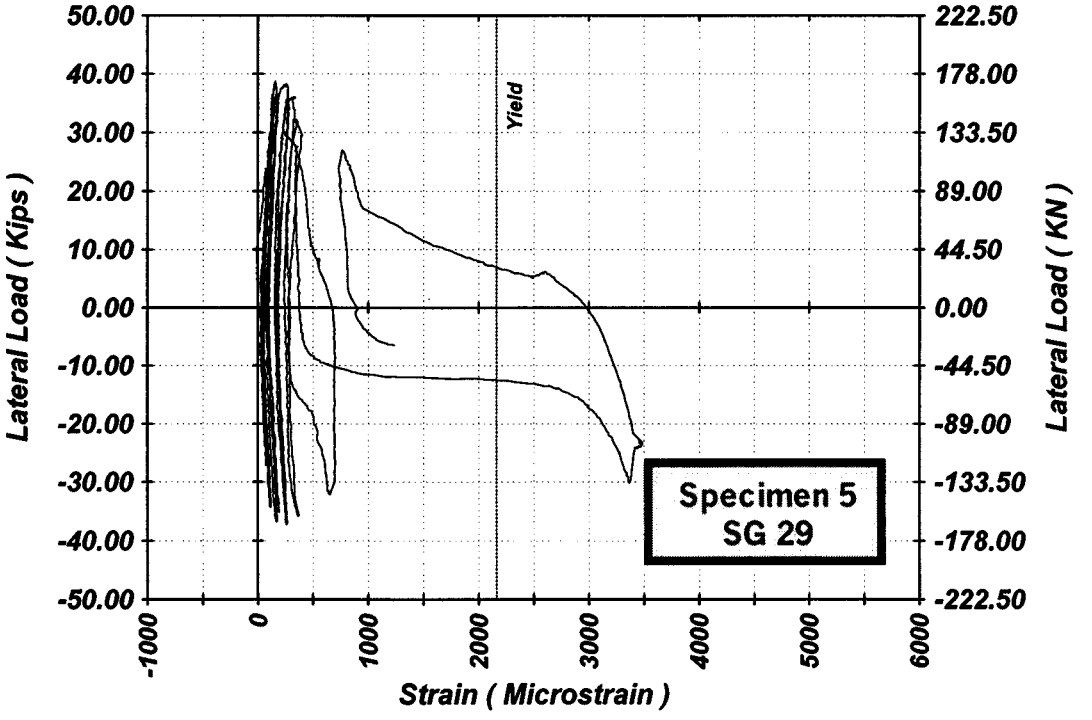

Figure 4-61 Measured Lateral Load Strain in SG-29 of Specimen 5

4.2.6 Performance of Specimen 6

Flexural cracking began with a crack at the wall-footing interface at a displacement of 10 mm corresponding to a lateral load of 43.6 kN. The lateral load capacity was maintained at a displacement ductility of 3.5. As the wall specimen was pulled for the first cycle to a displacement ductility of 4, spalling of the cover concrete at the compression side started to occur. Buckling of the vertical rebars took place during the first cycle at a displacement ductility of 5 (Figure 4-62). A 90° hook of a crosstie opened when the wall specimen was pushed for the second cycle at a displacement ductility of 5. During the first cycle at a displacement ductility of 6, another 90° hook of a crosstie was opened. This led to an increase in the buckling length of the vertical bars. After applying one cycle at a displacement ductility of 6, the lateral load was reduced to 132.9 kN (nearly 77% of the lateral load capacity) corresponding to 255 mm and the test was stopped.

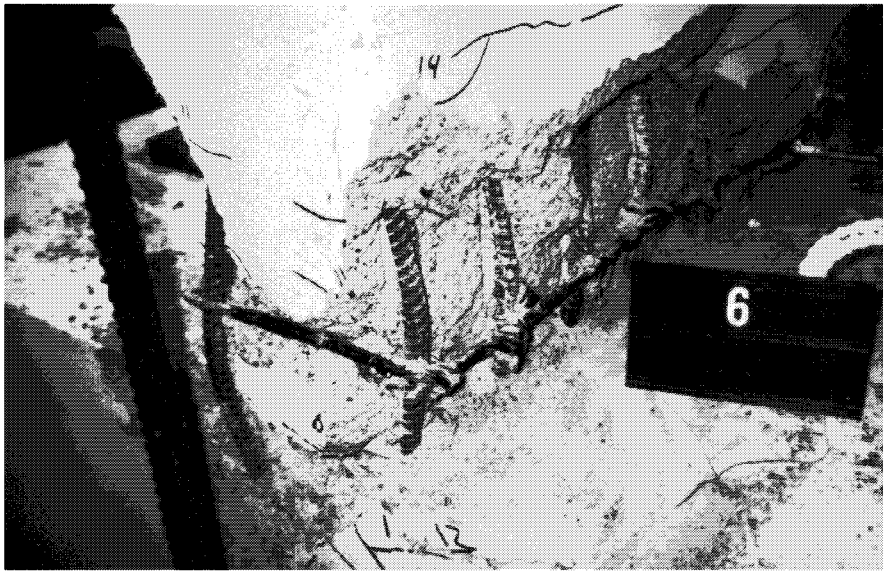

Figure 4-62 Vertical Bar Buckling in Specimen 6

Figures 4-63 and 4-64 show the lateral load-strain in the vertical bars at the wall-footing interface. The maximum strain in the vertical bars at a height of 80 mm from the top of the footing was 70% of the steel yield strain (Figures 4-65 and 4-66). Figures 4-67 through 4-70 show that the strain in the confinement reinforcement did not exceed 60% of the steel yield strain. Similar to the other walls, the maximum lateral steel strain was below the yield strain.

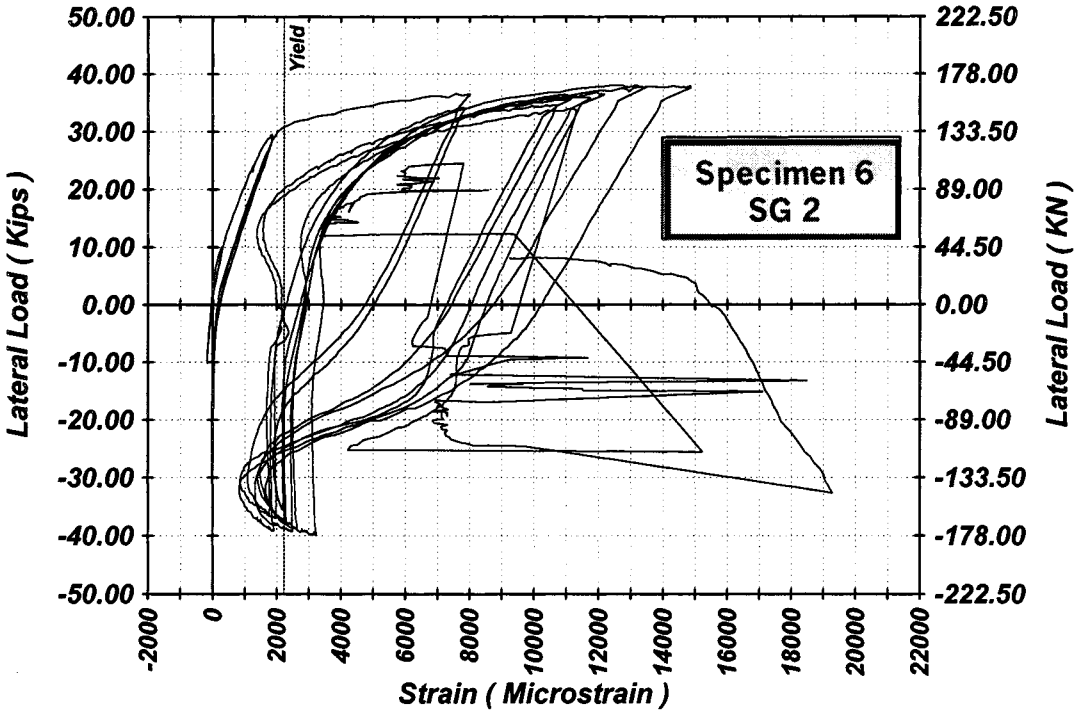

Figure 4-63 Measured Lateral Load Strain in SG-2 of Specimen 6

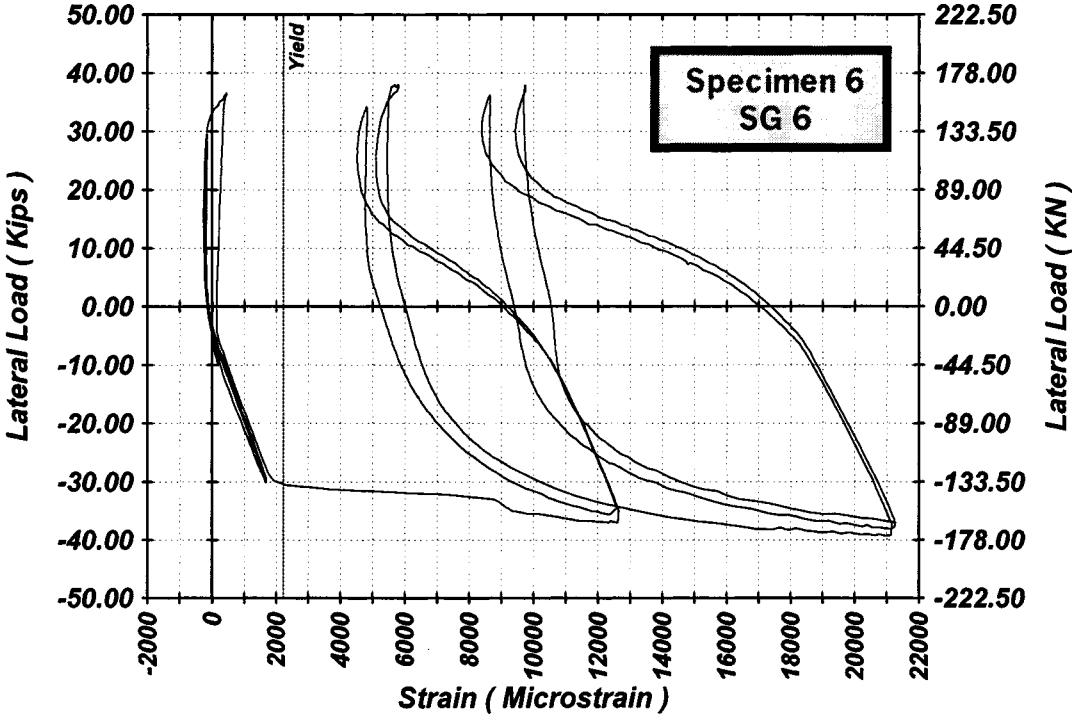

Figure 4-64 Measured Lateral Load Strain in SG-6 of Specimen 6

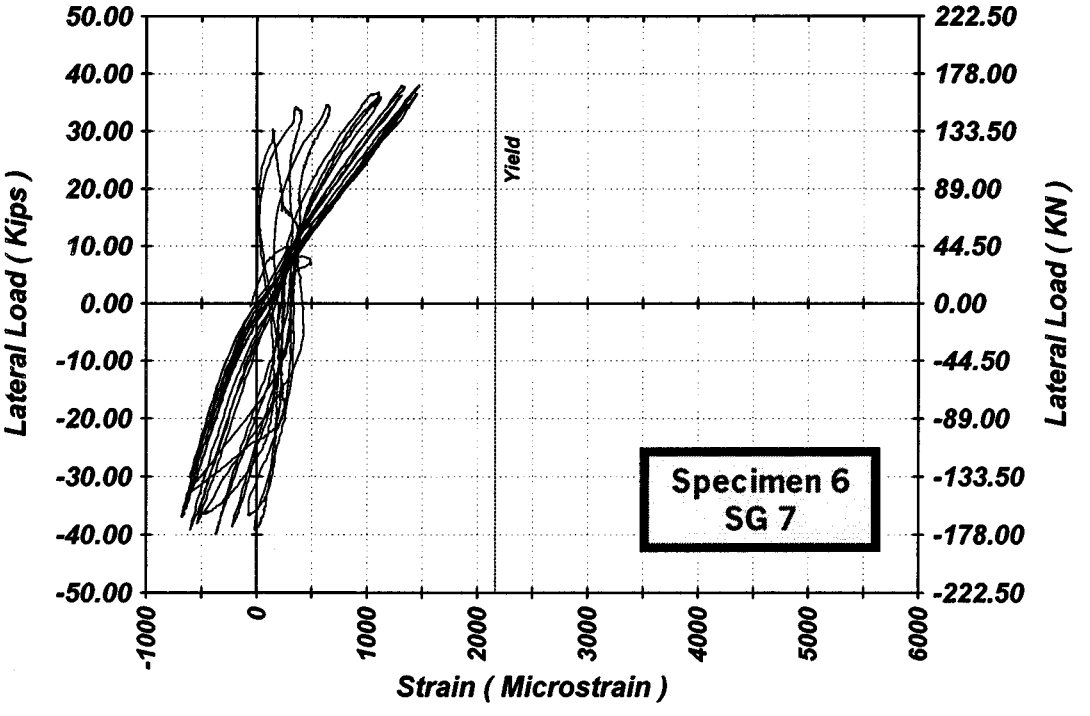

Figure 4-65 Measured Lateral Load Strain in SG-7 of Specimen 6

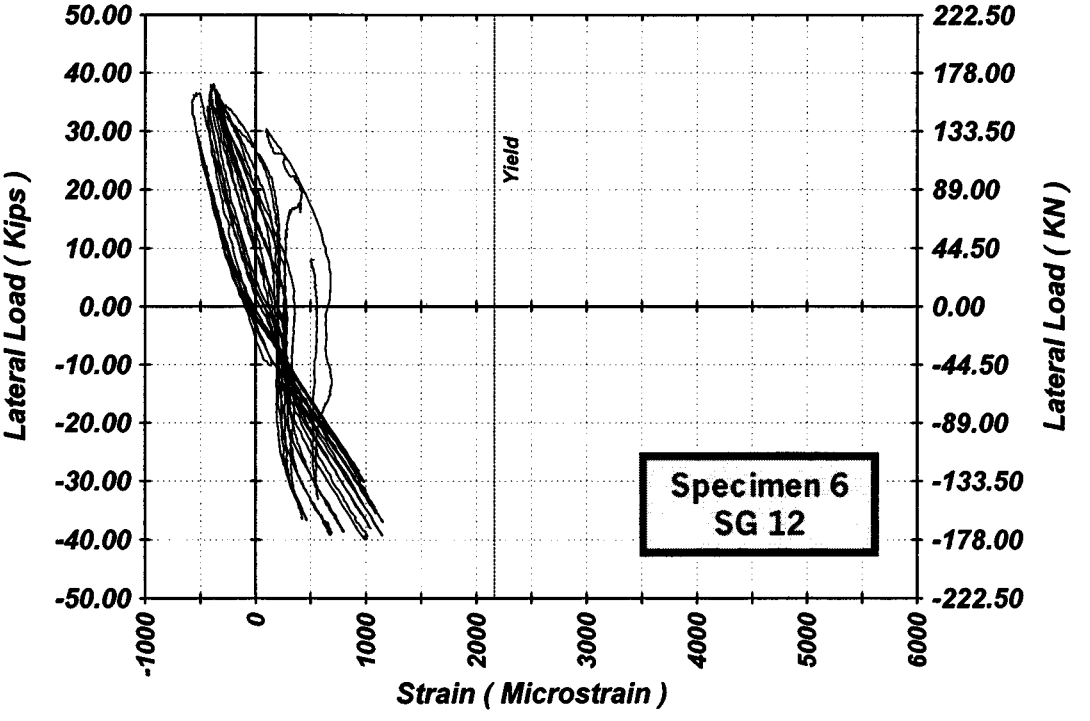

Figure 4-66 Measured Lateral Load Strain in SG-12 of Specimen 6

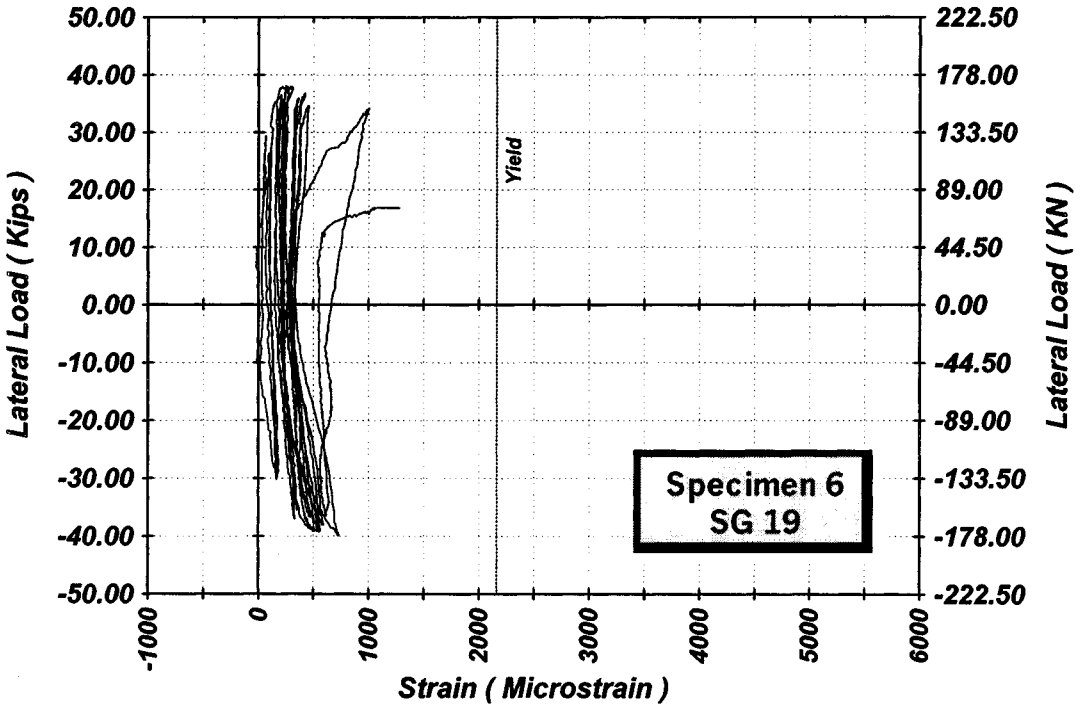

Figure 4-67 Measured Lateral Load Strain in SG-19 of Specimen 6

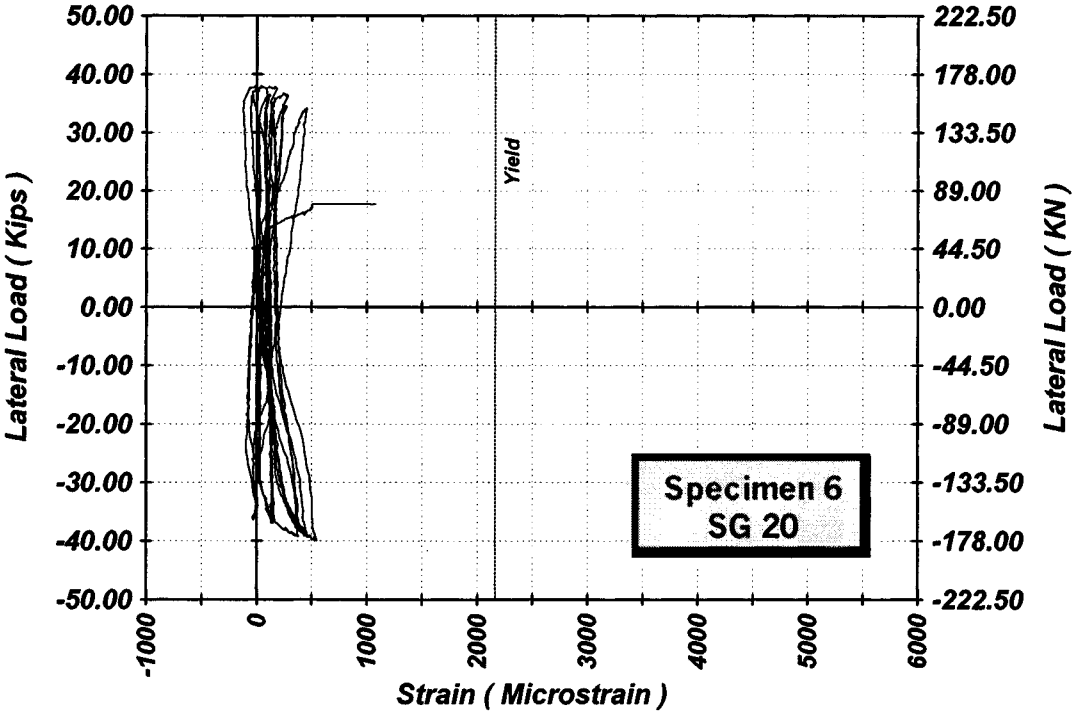

Figure 4-68 Measured Lateral Load Strain in SG-20 of Specimen 6

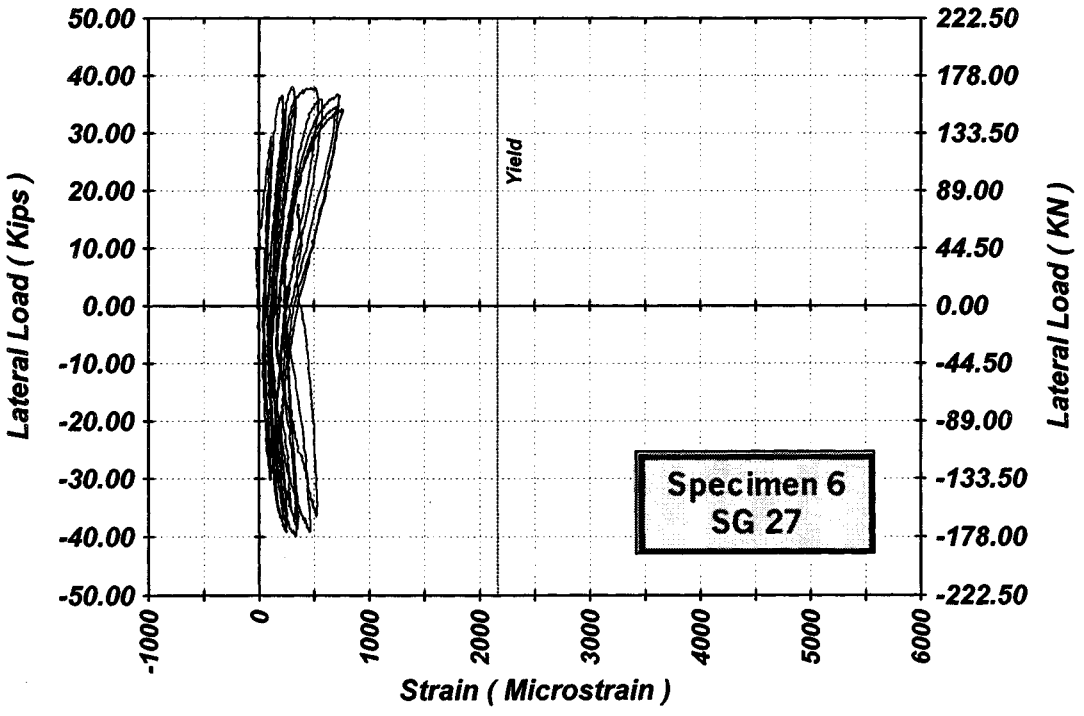

Figure 4-69 Measured Lateral Load Strain in SG-27 of Specimen 6

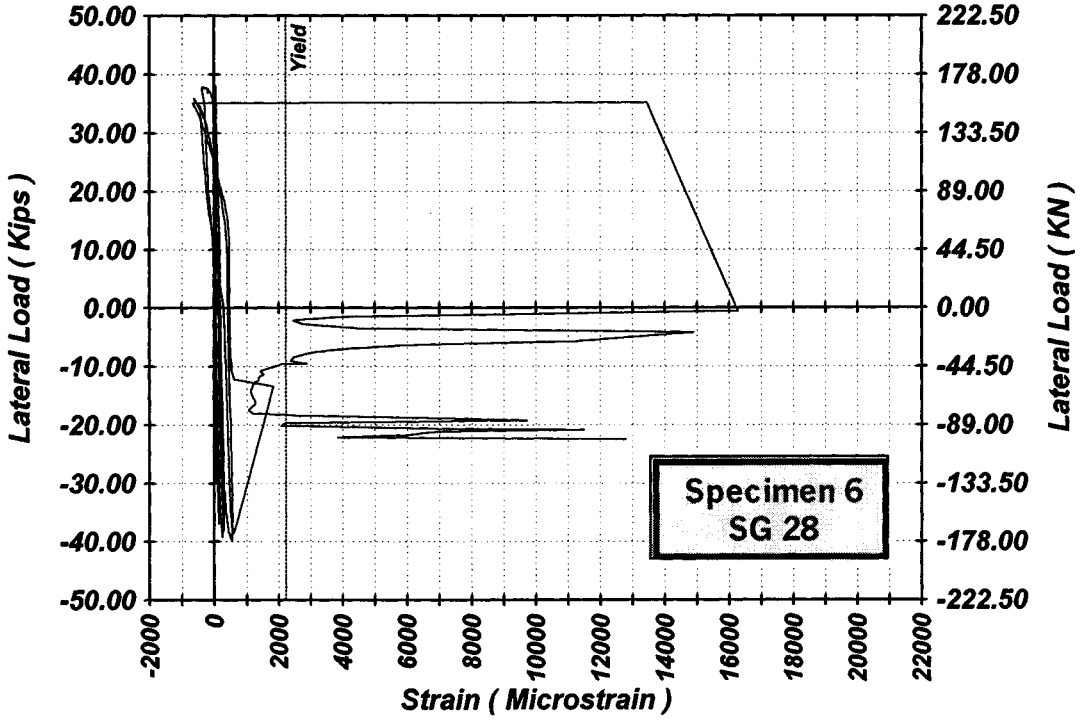

Figure 4-70 Measured Lateral Load Strain in SG-28 of Specimen 6

4.2.7 Performance of Specimen 7

A flexural crack occurred at the wall-footing interface at a displacement of 13 mm corresponding to a lateral load of 35.8 kN. The maximum lateral load was attained at a displacement ductility of 3.3. At the push for the first cycle at a displacement ductility level of 6, spalling of the cover concrete started to occur. When the wall specimen was pulled during the first cycle at a displacement ductility level of 6, buckling of a corner vertical bar began. As the wall specimen was cycled at higher displacement ductility levels, little spalling of the cover concrete occurred. At the pull for the second cycle and at a displacement ductility of 8, a vertical bar fractured. While pushing the wall specimen to a displacement ductility of 10, another vertical bar fractured at a displacement of 133 mm (figure 4-71). As the wall specimen was pushed further to a displacement of 148 mm, a third vertical bar fractured. At this point, the load was reduced to 35.1 kN which is nearly 60 % of the lateral load capacity of the wall specimen. Note that concrete spalling and the apparent damage in Specimen 7 was less extensive than those of the others.

Figure 4-71 Fracture of a Vertical Bar in Specimen 7

The measured lateral load-strain hysteresis of the vertical bars indicates that yielding of the bars occurred only at the wall-footing interface (Figures 4-72 through 4-75). The maximum measured strain in the confinement reinforcement did not exceed 40% of the steel yield strain (Figures 4-76 through 4-79).

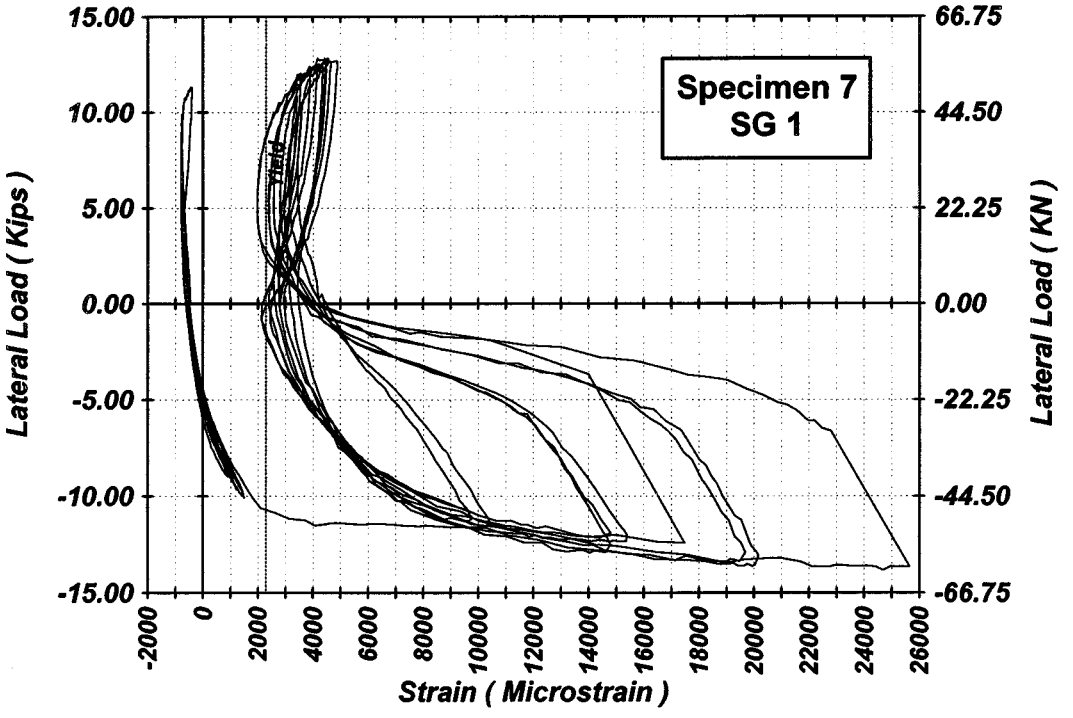

Figure 4-72 Measured Lateral Load Strain in SG-1 of Specimen 7

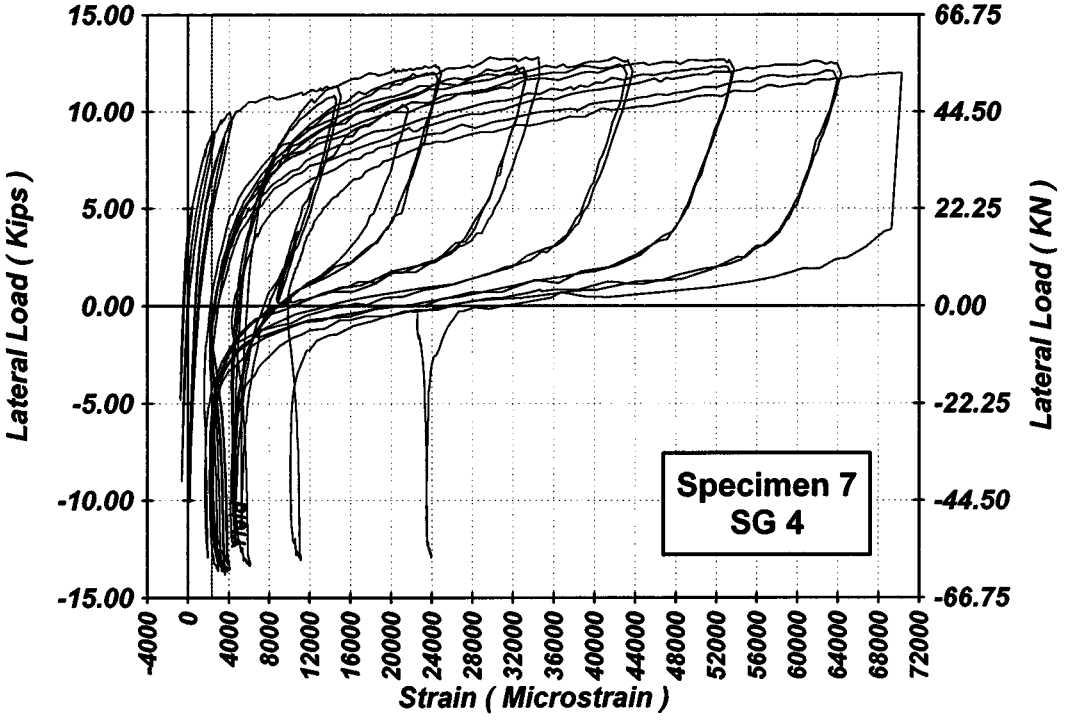

Figure 4-73 Measured Lateral Load Strain in SG-4 of Specimen 7

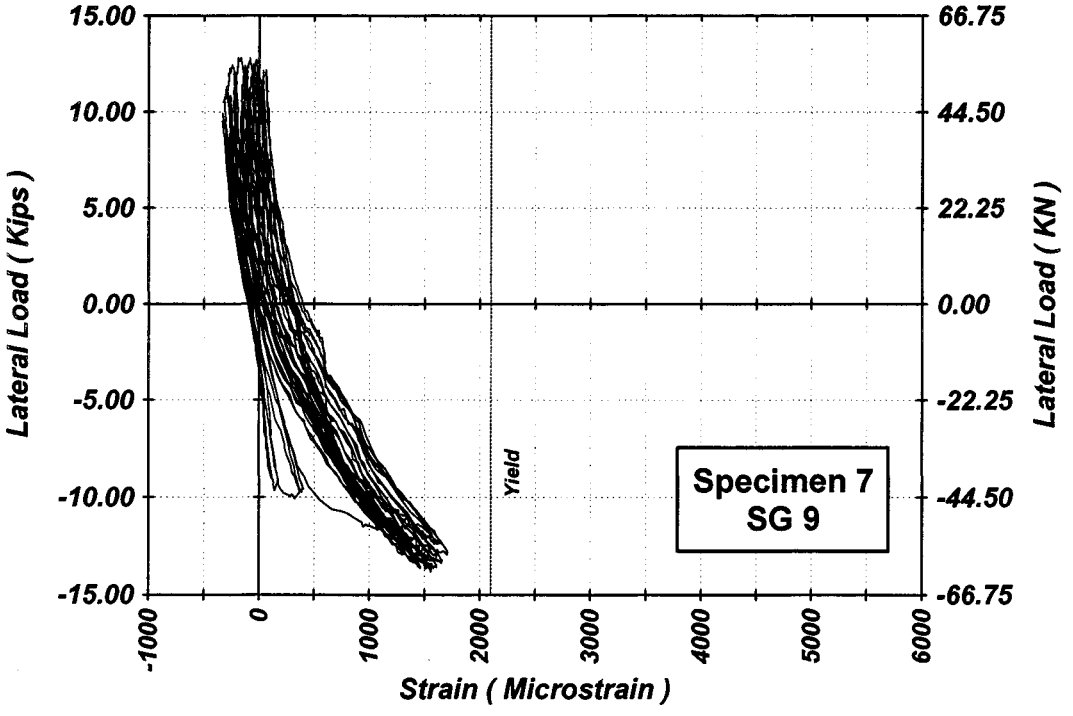

Figure 4-74 Measured Lateral Load Strain in SG-9 of Specimen 7

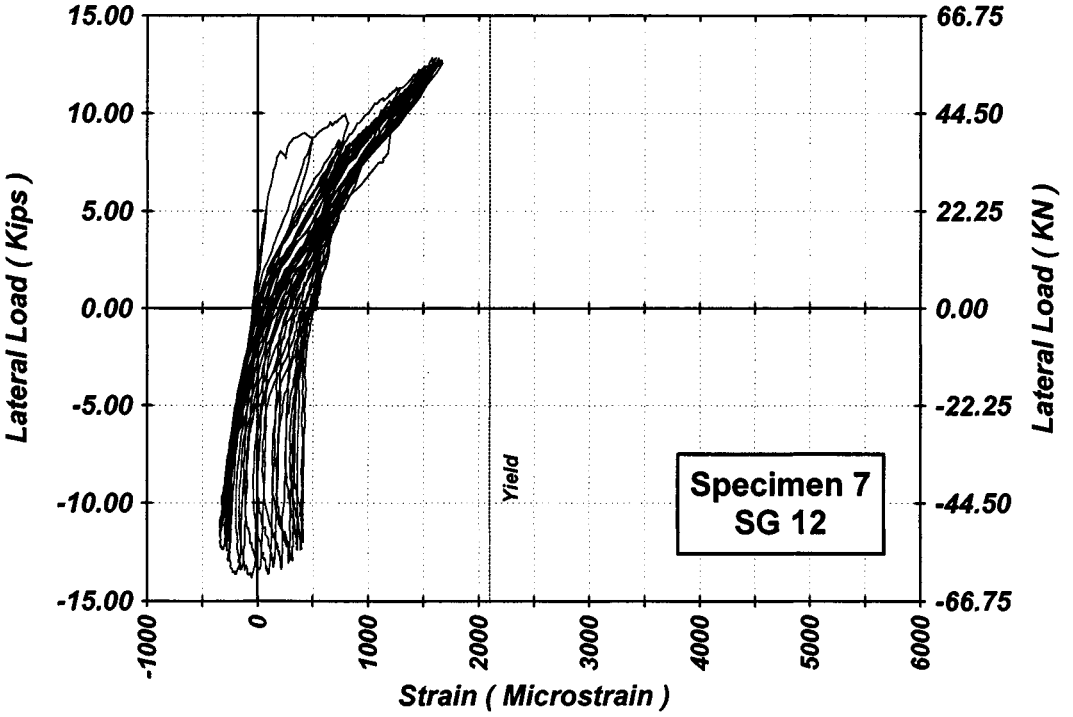

Figure 4-75 Measured Lateral Load Strain in SG-12 of Specimen 7

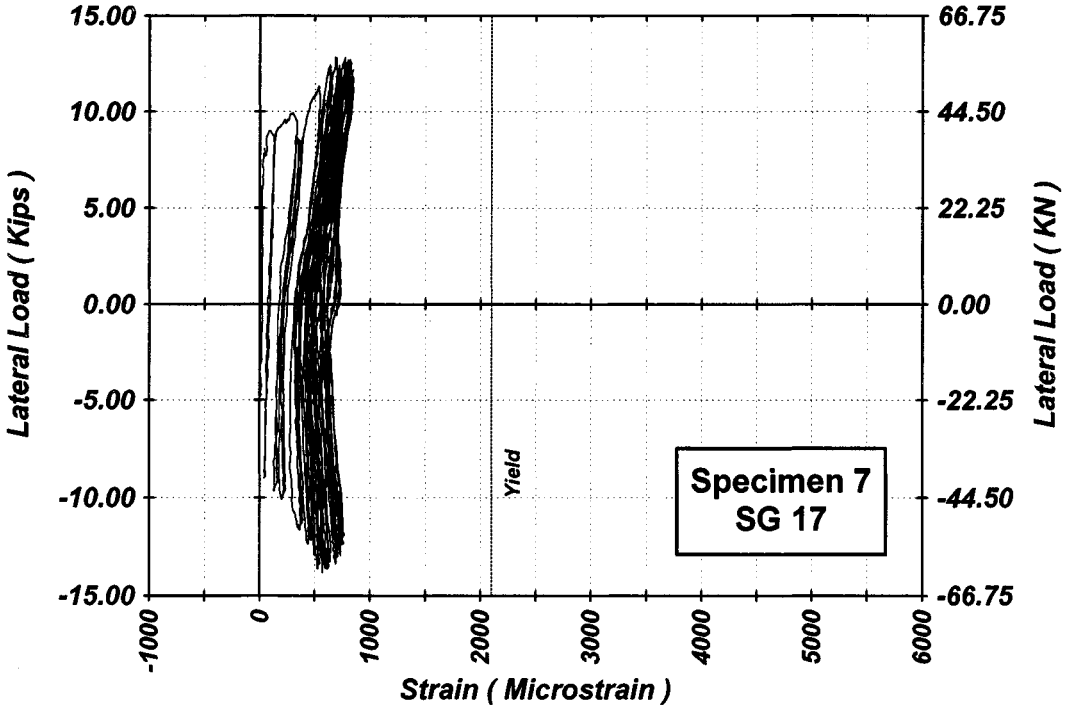

Figure 4-76 Measured Lateral Load Strain in SG-17 of Specimen 7

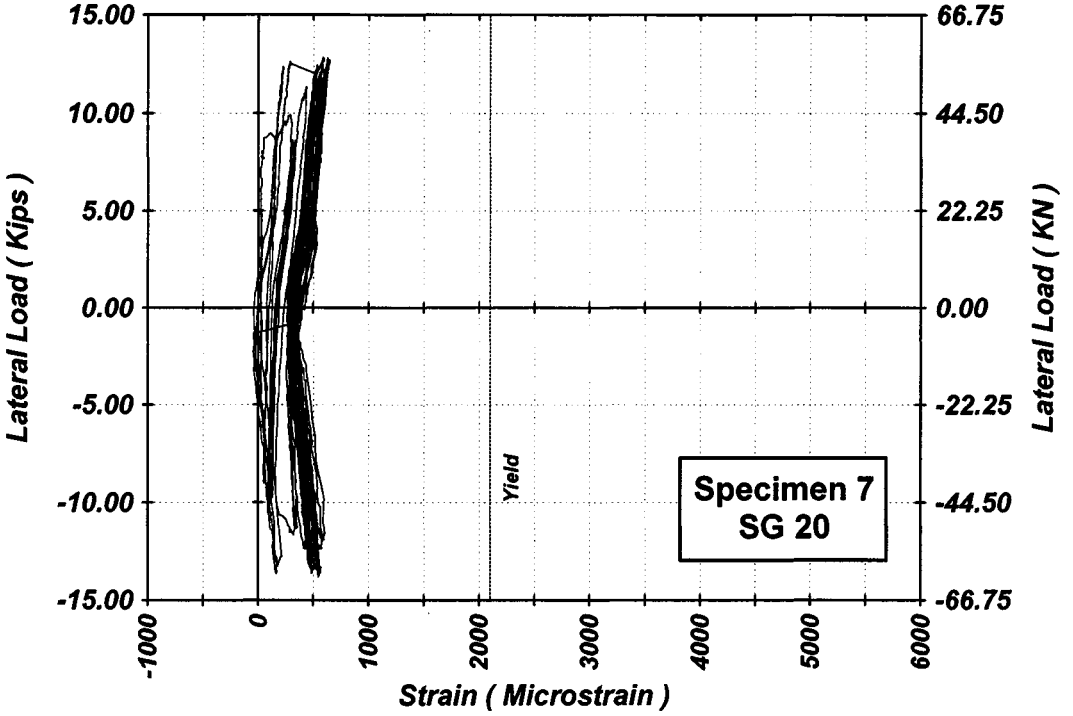

Figure 4-77 Measured Lateral Load Strain in SG-20 Specimen 7

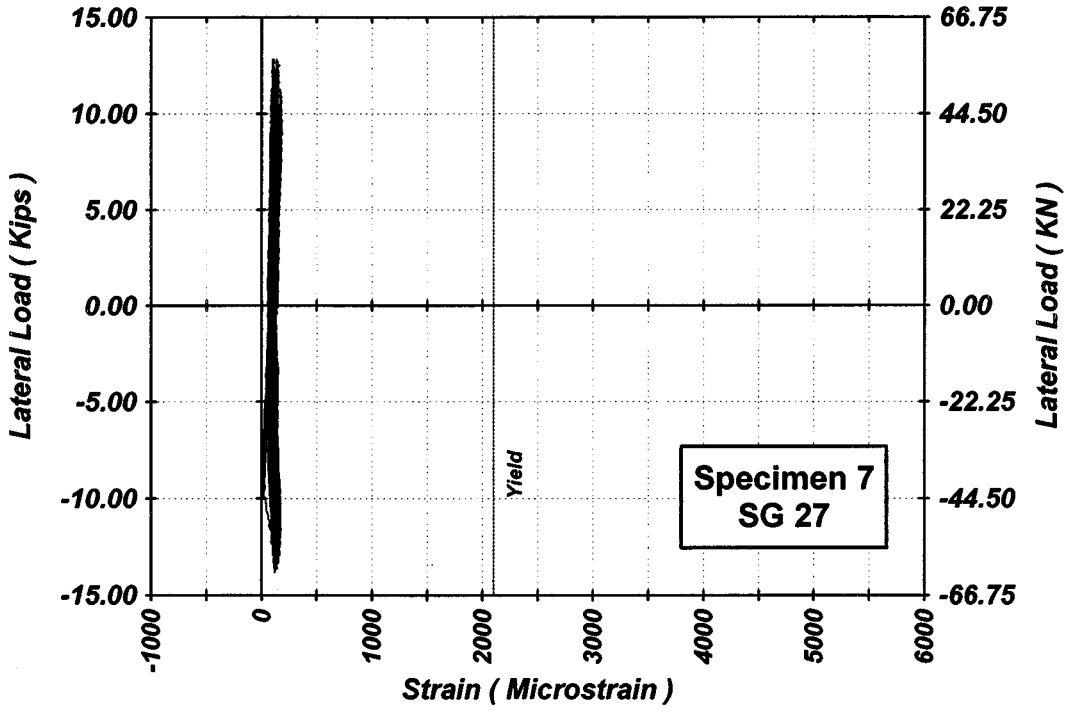

Figure 4-78 Measured Lateral Load Strain in SG-27 of Specimen 7

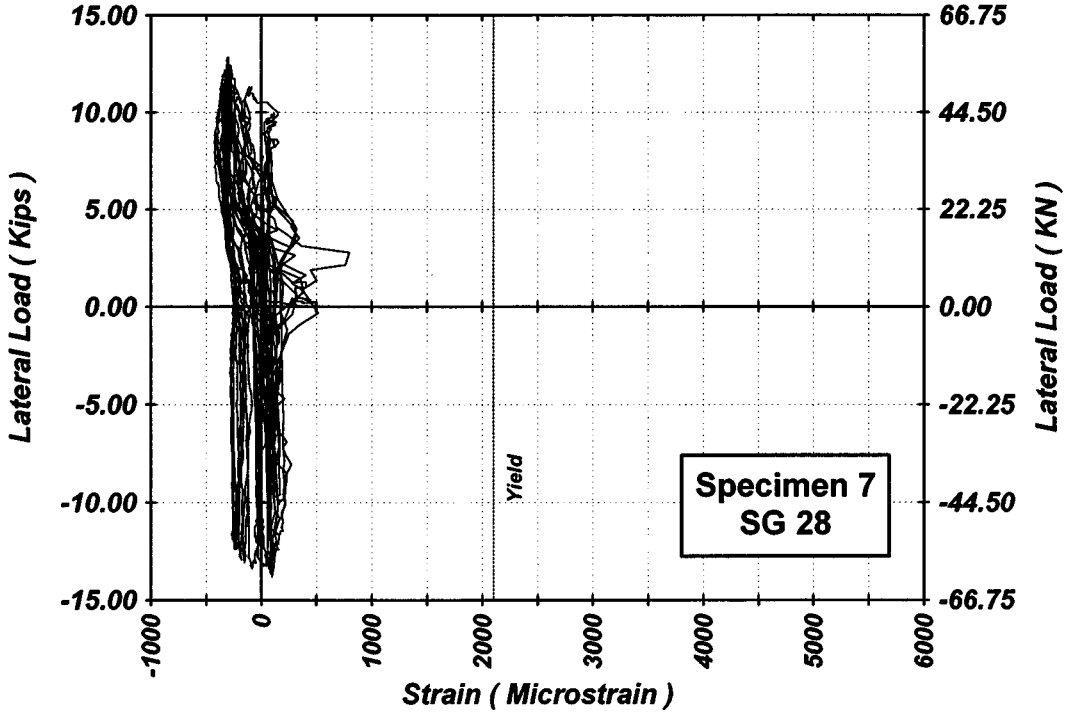

Figure 4-79 Measured Lateral Load Strain in SG-28 Specimen 7

4.3 Observations and Remarks

The lateral load-displacement hysteresis for the first six specimens show that the loops were wide and stable (Figures 4-1 through 4-6). The hysteresis loops of Specimen 7 were pinched, since the vertical steel ratio of this specimen was low (Figure 4-7). The yield displacement was found by monitoring the strain in the tensile longitudinal bars. The displacement at which the bar strain reached the yield value was defined as the measured yield displacement. The ultimate displacement was considered to have been reached when the lateral load dropped to 80% of its maximum value (capacity) or at fracture of the vertical reinforcing bars. The lowest measured displacement ductility among all the wall specimens was 5.8. This implies that pier walls that have axial load indices, H/t ratios, and vertical steel ratios within these of the wall specimens do not have a critical seismic performance even with low confinement steel ratios.

The envelopes of the lateral load-displacement and the lateral load-displacement ductility indicate that wall specimens with higher vertical steel ratios have high lateral load capacity and high displacement capacity, but low displacement ductility capacity, which was expected (Figures 4-8 and 4-9). The lateral load capacity of wall specimens with vertical steel ratio of 1.5% was 1.6 times that of wall specimens with 0.75% and 2.9 times that of wall specimens with 0.28%. The displacement ductility capacity of the specimen with vertical steel ratio of 0.28% was 1.3 times that of wall specimens with 0.75% and 1.5 times that of wall specimens with 1.5%. Wall specimens with higher confinement reinforcement ratios demonstrated only a slightly higher displacement ductility capacity.

The measured strain in the vertical reinforcing bars indicated that yielding of the vertical bars occurred only in the region between the wall-footing interface and a section at 160 mm from the top of the footing in wall specimens 1, 4, and 7. As for specimens 2, 3, 5, and 6, yielding of the vertical bars occurred between the wall-footing interface and a section at 80 mm from the top of the footing. The lateral load-strain hysteresis loops for the transverse reinforcing bars and the crossties show that the maximum strain in the confinement reinforcement was 60% of the steel yield strain. This was used to calibrate the analytical model (see Section 5) by limiting the stress

in the confinement reinforcement to 60% of the steel yield strain. Conventional methods assume full yield of the confinement reinforcement in the plastic hinge zone.

Plastic hinges were formed at the expected critical section (i.e. the interface of the specimen footing and the wall). The intersection of the envelope of the measured curvature and the measured yield curvature defined the length of the plastic hinge (Figures 4-10 through 4-16). The plastic hinge length of the wall specimens 1 through 6 was nearly the same (180 mm) while it was 110 mm for Specimen 7. This is because Specimen 7 had smaller longitudinal bar diameter.

The performance of all wall specimens was nearly similar. Spalling of the cover concrete in the plastic hinge zone followed flexural cracking along the wall specimen. This led to buckling of the vertical reinforcing bars and opening of the 90° hook of the crossties. The latter in turn increased buckling length of the vertical bars. Failure occurred due to either compression of the concrete or fracture of the vertical reinforcing bars due to low-cycle fatigue.

SECTION 5
ANALYTICAL STUDY

5.1 Introduction

The objective of the analytical study was to develop and calibrate an analytical model to determine the response of bridge pier walls. The lateral deflection of a reinforced concrete pier wall includes flexure, bond slip, and shear components. The displacement due to flexure was based on the theoretical moment-curvature analysis, taking into account the confinement effects. Three different confined concrete models were investigated. Deformations due to bond slip were found using a modified version of an existing model. The shear deformations were based on an empirical equation developed by others for cracked reinforced concrete members. The ultimate displacement in the model was controlled by compression failure in the concrete or fatigue of the vertical reinforcing bars. A linear damage model was selected to calculate the damage index, which identifies fracture of the vertical bars due to low cycle-fatigue. A computer program named "PIER" was developed to implement the analytical model.

To calibrate the analytical model, the wall specimens tested in this study (Section 4) and in previous studies[8, 9] were analyzed, and the analytical results were compared with the experimental results. This section includes details of the models used in the analysis, and a comparison between experimental and analytical results of pier walls.

5.2 Deflections and Displacement Ductility of Pier Walls

The lateral displacement of a reinforced concrete cantilever pier wall subjected to a lateral load is composed of flexure, bond slip, and shear components. Figure 5-1 shows a cantilever pier wall subjected to a lateral load, F, at the free end. The total lateral deflection, Δ_t, may be expressed as:

$$\Delta_t = \Delta_f + \Delta_s + \Delta_{sh} \qquad (5\text{-}1)$$

where:

Δ_f = Deflection due to flexure

Δ_s = Deflection due to reinforcement bond slip

Δ_{sh} = Deflection due to shear

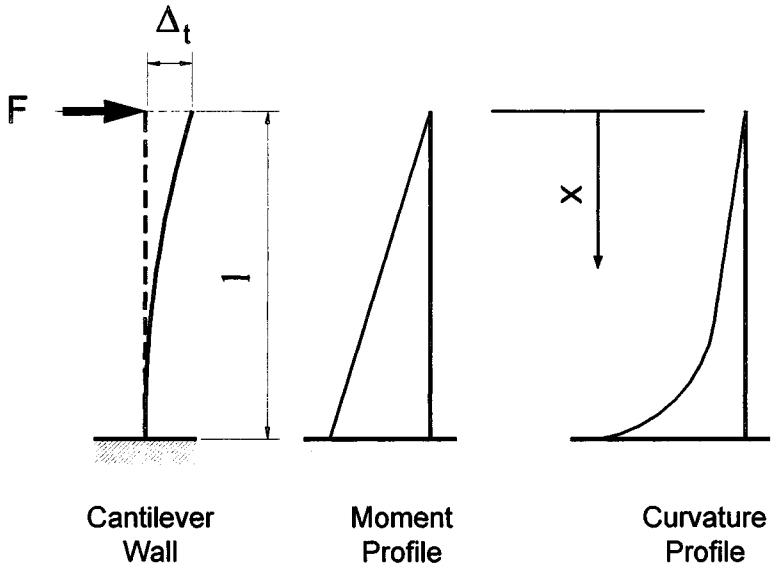

Figure 5-1 Lateral Deflection of Pier Wall

The displacement ductility factor is defined as the displacement divided by the yield displacement while the displacement ductility capacity is defined as the ratio between the ultimate displacement and the yield displacement. The displacement ductility capacity (μ_d) may be written as:

$$\mu_d = \frac{\Delta_u}{\Delta_y} \tag{5-2}$$

where:

Δ_u = Ultimate displacement

Δ_y = Yield displacement

When the tensile strain in the vertical reinforcing bars is equal to the yield strain of the steel, the total lateral deflection of the pier wall is called the yield displacement. The ultimate

displacement is defined as the total lateral deflection at which a limit state is reached. Two possible limit states have been identified: 1) The maximum compression strain in the confined concrete is equal to the ultimate strain of the confined concrete; 2) The damage index of the vertical reinforcing bars is equal to unity (meaning fracture of bars).

During the experimental tests (Section 4), pier wall specimens were subjected to two cycles at each displacement ductility level. To simulate the low cycle fatigue effect on the vertical bars, the displacements and the ductility factors were calculated in the analytical model throughout the loading history.

5.2.1 Material Stress-Strain Models

Constitutive models for steel, unconfined concrete, and confined concrete are required to calculate the displacements of pier walls. The confinement provided by the lateral reinforcement enhances the strength and the ductility of the concrete core[13, 19, 27, 29] (Figure 5-2). The constitutive models for the confined concrete define its enhanced properties and stress-strain relationship.

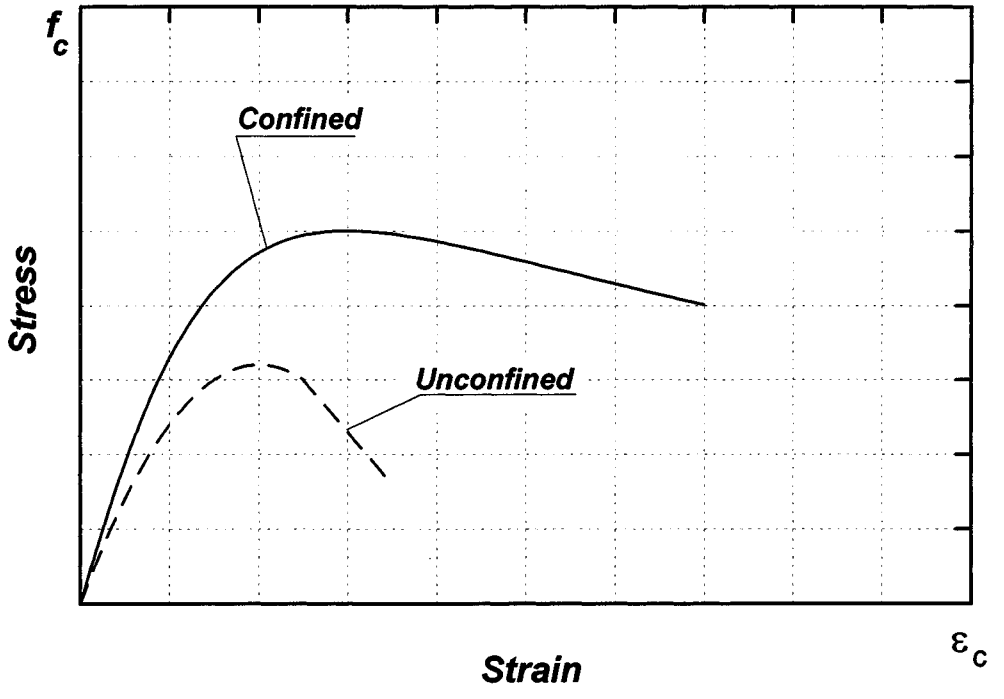

Figure 5-2 Effect of Confinement on Strength and Ductility of Concrete

5.2.1.1 Unconfined Concrete Model

To model the unconfined concrete (cover concrete) the Kent and Park model[23] can be used. The stress-strain relationship for the unconfined concrete using this model consists of two branches, an ascending branch and a descending branch (Figure 5-3). The ascending branch is a second-degree parabola while the descending branch is a straight line. The ascending branch is given by the following expression:

$$f_c = f'_c \left[\frac{2\varepsilon_c}{\varepsilon'_c} - \left(\frac{\varepsilon_c}{\varepsilon'_c} \right)^2 \right] \tag{5-3}$$

where:

f_c = Concrete stress

ε_c = Concrete strain

f'_c = Concrete compressive strength

ε'_c = Strain at concrete compressive strength (assumed as 0.002 for normal weight concrete)

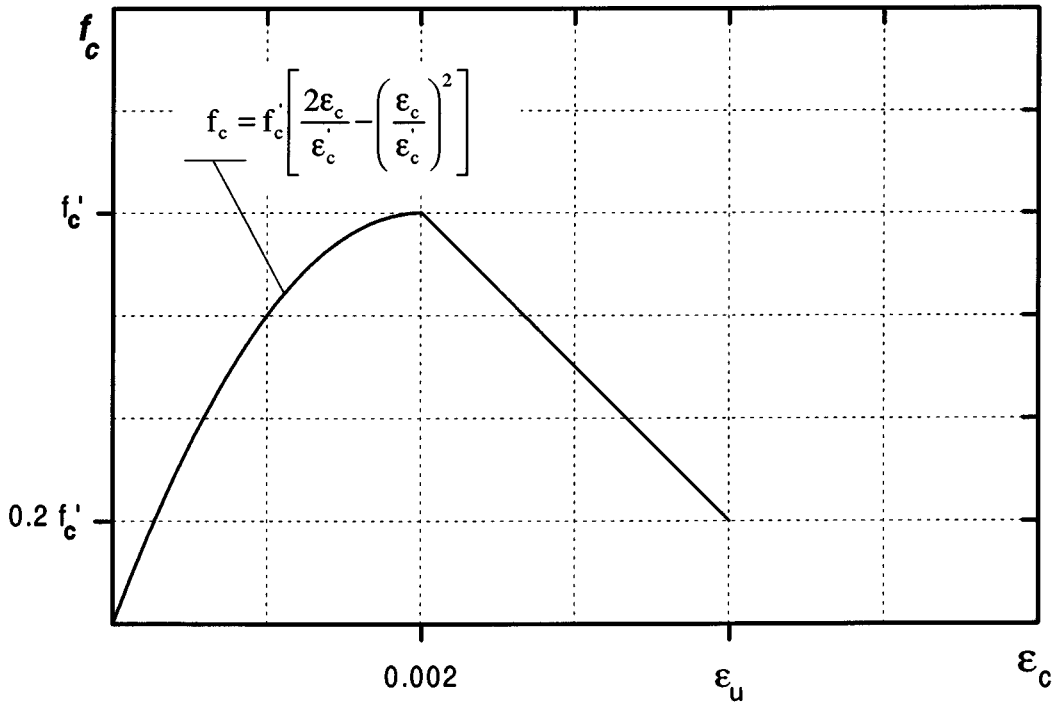

Figure 5-3 The Kent and Park Model for Unconfined Concrete

The descending branch (straight line) starts from the point at which the concrete compressive strength is reached (peak point) and ends at the point with an ultimate strain of ε_u and stress of 0.2 f'_c. Paulay and Priestley[2] recommend $\varepsilon_u = 0.004$ for practical applications.

5.2.1.2 Confined Concrete Models

Three constitutive models for confined concrete were investigated for the purpose of performing the moment-curvature analysis. A comparison of the established stress-strain curves using the models was performed. To calibrate the constitutive models, a value of 60% of the steel yield stress was considered for the confinement reinforcement in calculating the confinement pressure. The stress reduction in the confinement reinforcement was based on the observations during testing the wall specimens in this study (Section 4.3).

5.2.1.2.1 Modified Kent and Park Model

The concrete strength and ductility are enhanced by the effect of the lateral reinforcement. Kent and Park[13] proposed a stress-strain curve for the confined concrete that has the same characteristics as the Kent and Park model[23]. The ascending segment up to the compressive strength and the descending segment to the ultimate strain of the confined concrete are a second-degree parabola and a straight line, respectively (Figure 5-4). Both the unconfined concrete strength and the corresponding strain are magnified by a factor, K (Equation 5-4), which represents the confining effect of the lateral reinforcement. The stress-strain relationship is given by the following equations:

(a) for $\varepsilon_c \leq 0.002K$

$$f_c = Kf'_c \left[\frac{2\varepsilon_c}{0.002K} - \left(\frac{\varepsilon_c}{0.002K} \right)^2 \right] \qquad (5\text{-}4)$$

$$K = 1 + \frac{\rho_s f_{yh}}{f'_c} \qquad (5\text{-}5)$$

(b) for $\varepsilon_c > 0.002K$

$$f_c = Kf_c'[1 - Z_m(\varepsilon_c - 0.002K)] \tag{5-6}$$

$$Z_m = \frac{0.5}{\frac{3 + 0.26f_c'}{145f_c' - 1000} + \frac{3}{4}\rho_s\sqrt{\frac{h''}{s_h}} - 0.002K} \tag{5-7}$$

where:

f_c = Confined concrete stress, MPa

ε_c = Confined concrete strain

f'_c = Unconfined concrete compressive strength, MPa

f_{yh} = Yield stress of the confining steel, MPa

ρ_s = Lateral steel volumetric ratio with concrete volume measured to outside of hoops

h'' = Width of confined concrete core measured to outside of hoops, mm

s_h = Center to center spacing of hoop sets along the member axis, mm

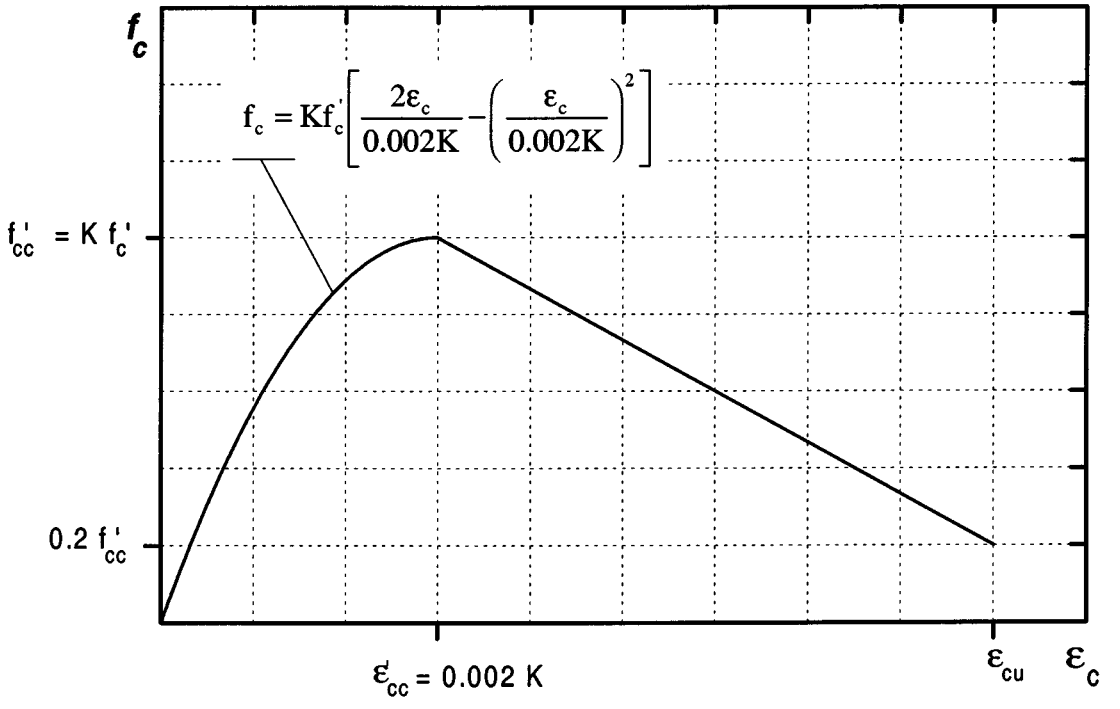

Figure 5-4 Modified Kent and Park Model for Confined Concrete

5.2.1.2.2 Modified Mander et al. Model

In this model[19], the compressive strength of the confined concrete is related to the confining pressure provided by the lateral reinforcement. For circular sections and square sections of equal confining steel in both directions (meaning equal confining pressure), the confined concrete strength and the corresponding strain are given by:

$$f'_{cc} = f'_c\left(-1.254 + 2.254\sqrt{1+\frac{7.94f'_l}{f'_c}} - \frac{2f'_l}{f'_c}\right) \tag{5-8}$$

$$\varepsilon'_{cc} = 0.002\left[1+5\left(\frac{f'_{cc}}{f'_c}-1\right)\right] \tag{5-9}$$

where:

f'_{cc} = Confined concrete compressive strength

f'_l = Confining pressure

ε'_{cc} = Concrete strain at maximum (f'_{cc})

For rectangular sections with unequal lateral reinforcement ratios along the depth and the width of the cross section (x and y directions), the confining pressure in both directions can be found using the following equations:

$$f'_{lx} = K_{ex}\rho_x f_{yh} \tag{5-10}$$

$$f'_{ly} = K_{ey}\rho_y f_{yh} \tag{5-11}$$

where:

K_{ex} = Confinement effectiveness coefficient in the x-direction

K_{ey} = Confinement effectiveness coefficient in the y-direction

ρ_x = Volumetric lateral steel ratio in the x-direction

ρ_y = Volumetric lateral steel ratio in the y-direction

f_{yh} = Yield stress of the confining steel

After finding the confining pressures in both directions, the confined concrete strength can be found using a set of curves. Those curves were based on multiaxial failure criterion and were verified by comparing the solution to triaxial test results.

Mander et al.[19] applied a strain energy approach to find the ultimate strain of confined concrete. The longitudinal concrete compressive strain at failure was considered to be associated with the first fracture in the hoops. To represent the stress-strain relationship of confined concrete under monotonic loading, Paulay and Priestley[24] adopted a modified version of Mander et al. The modification was in the ultimate concrete strain and is given by:

$$\varepsilon_{cu} = 0.004 + \frac{1.4\rho_s f_{yh} \varepsilon_{sm}}{f'_{cc}} \qquad (5\text{-}12)$$

where:

ε_{sm} = Steel strain at maximum tensile stress

Paulay and Priestley suggested a confinement coefficient, k_e, which is based on the cross section geometry (Table 5-1).

Table 5-1 Confinement Coefficient, k_e

Cross Section	k_e
Circular columns	0.95
Rectangular columns	0.75
Rectangular walls	0.60

The stress-strain relationship is based on Popovics[25] equation. The entire stress-strain curve of confined concrete (Figure 5-5) is described using one equation:

$$f_c = \frac{f'_{cc} x r}{r - 1 + x^r} \tag{5-13}$$

where:

$$x = \frac{\varepsilon_c}{\varepsilon'_{cc}}$$

$$r = \frac{E_c}{E_c - E_{sec}}$$

$$E_c = 4734\sqrt{f'_c}, \quad \text{MPa}$$

$$E_{sec} = \frac{f'_{cc}}{\varepsilon'_{cc}}$$

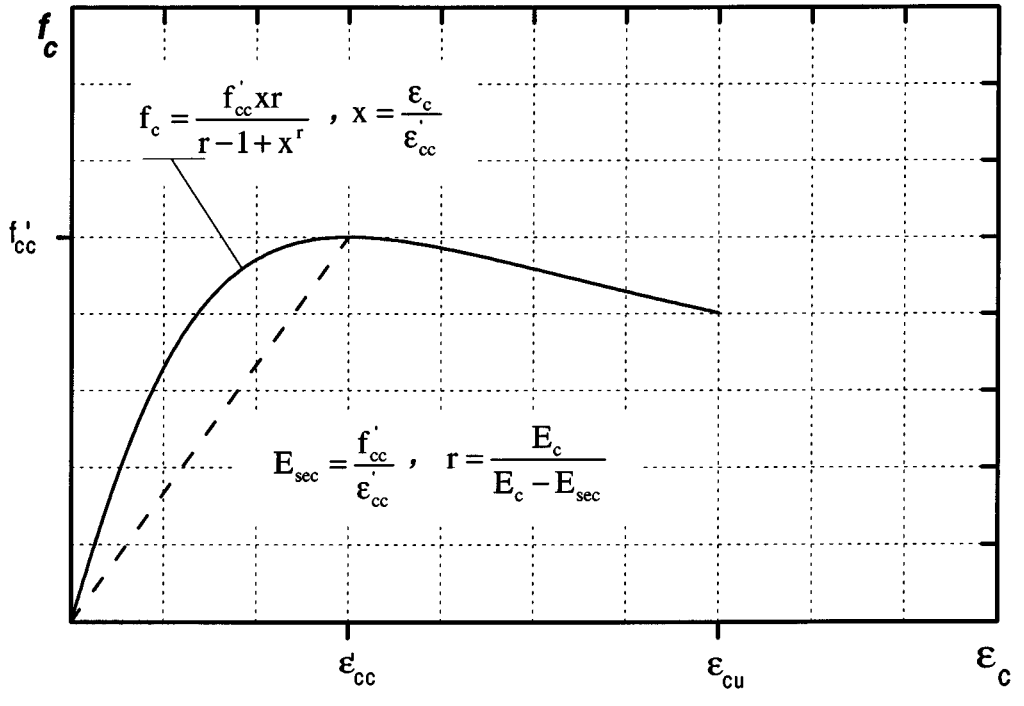

Figure 5-5 Modified Mander Model for Confined Concrete

5.2.1.2.3 Hoshikuma Model

Based on the results of a series of compression loading tests of reinforced concrete column specimens, Hoshikuma[10] developed a stress-strain model for confined concrete. The specimens had circular, square, and wall-type cross sections, with various arrangements of hoop reinforcement. None of the specimens had cover concrete to isolate the effect of cover concrete on confinement. The parameters considered in this model were the volumetric ratio of hoop reinforcement, the yield strength of hoop reinforcement, the strength of unconfined concrete, and the core concrete shape.

The peak stress of the confined concrete (compressive strength), f_{cc}, in the Hoshikuma model is normalized by the strength of the unconfined concrete, f_{co} and is given by the following expressions:

$$\frac{f_{cc}}{f_{co}} = 1.0 + 3.83\frac{\rho_s f_{yh}}{f_{co}} \qquad \text{(for circular sections)} \qquad (5\text{-}14)$$

$$\frac{f_{cc}}{f_{co}} = 1.0 + 0.73\frac{\rho_s f_{yh}}{f_{co}} \qquad \text{(for square sections)} \qquad (5\text{-}15)$$

where:

ρ_s = Volumetric steel ratio of hoop reinforcement

f_{yh} = Yield stress of the confining steel

Hoshikuma proposed an approximation of the ρ_s (f_{yh}/f_{co}) versus ε_{cc} relationship as a linear function using the following equations:

$$\varepsilon_{cc} = 0.00218 + 0.0332\frac{\rho_s f_{yh}}{f_{co}} \qquad \text{(for circular sections)} \qquad (5\text{-}16)$$

$$\varepsilon_{cc} = 0.00245 + 0.0122\frac{\rho_s f_{yh}}{f_{co}} \qquad \text{(for square sections)} \qquad (5\text{-}17)$$

The stress-strain relationship for the confined concrete in this model consists of an ascending branch and descending branch (Figure 5-6). The ascending branch is an nth degree curve while the descending branch is a straight line. The ascending branch is given by the following expression:

$$f_c = E_c \varepsilon_c \left[1 - \frac{1}{n} \left(\frac{\varepsilon_c}{\varepsilon_{cc}} \right)^{n-1} \right] \tag{5-18}$$

where:

$$n = \frac{E_c \varepsilon_{cc}}{E_c \varepsilon_{cc} - f_{cc}}$$

E_c = Modulus of elasticity of concrete, standard values provided by Japanese specifications "Design 1991"[12] are given in table 5-2.

The falling branch which is idealized by a straight line, is formulated as:

$$f_c = f_{cc} - E_{des} (\varepsilon_c - \varepsilon_{cc}) \tag{5-19}$$

where:

$$E_{des} = 11.2 \frac{f_{co}^2}{\rho_s f_{yh}}$$

The deterioration rate, E_{des}, is developed from regression analysis of test data in the range of ε_{cc} to ε_{cu}. It was found that the cross-sectional shape does not significantly influence the deterioration rate. Therefore, a single expression was suggested for both circular and square sections. Hoshikuma defined the ultimate strain, ε_{cu}, as the strain on the descending branch corresponding to 50% of the peak stress (confined compressive strength) f_{cc}. By substituting f_c=0.5 f_{cc}, in Equation 5-19, the ultimate strain, ε_{cu}, is obtained as

$$\varepsilon_{cu} = \varepsilon_{cc} + \frac{f_{cc}}{2E_{des}} \tag{5-20}$$

The relationship between the confinement effectiveness and three factors f_{cc}, ε_{cc}, E_{des} were obtained to evaluate the effect of crossties on the confinement of wall-type cross sections. Based on the test results, it was found that the confinement effect for wall-type sections with crossties may be simply evaluated using equivalent confined sections, as illustrated in figure 5-7. The equivalent section is taken as the spacing between two crossties. The effective confinement steel is one crosstie and two perimeter bars.

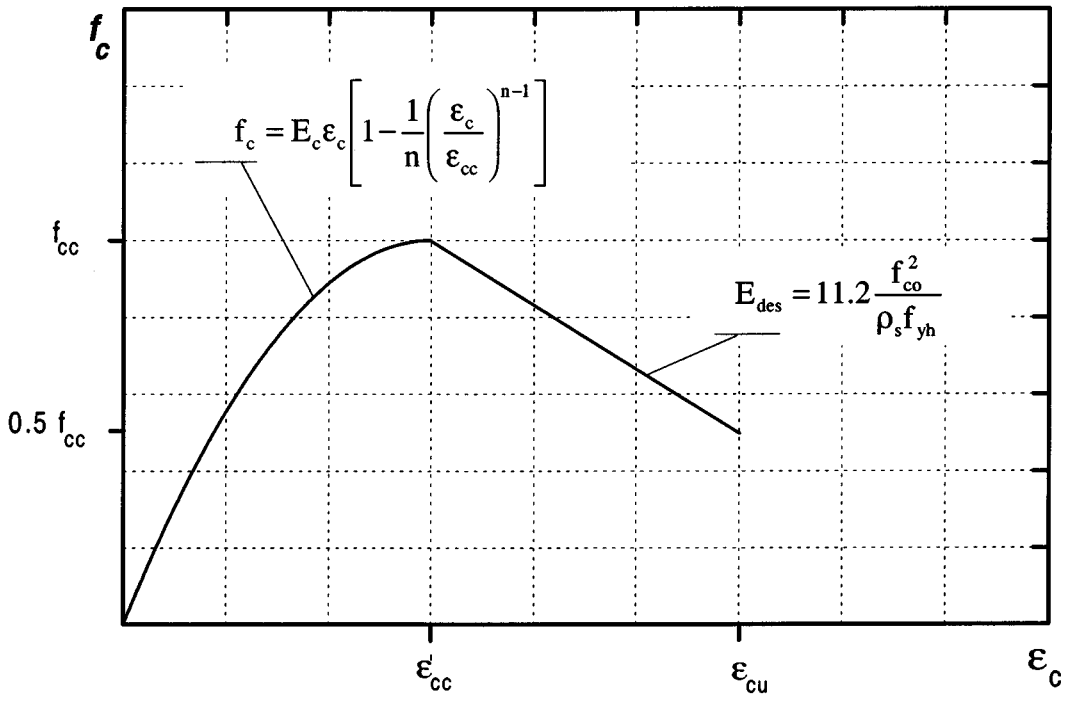

Figure 5-6 Hoshikuma Model for Confined Concrete

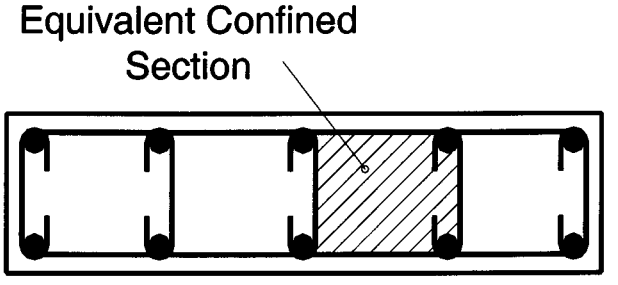

Figure 5-7 Equivalent Confined Section

Table 5-2 Modulus of Elasticity of Concrete Based on Japanese Specifications "Design 1991"[12]

Strength of unconfined concrete, MPa	Modulus of Elasticity, MPa
20.6	2.30×10^4
23.5	2.45×10^4
26.5	2.60×10^4
29.4	2.75×10^4
39.2	3.04×10^4
49.0	3.24×10^4

5.2.1.2.4 Comparison of the Confined Concrete Models

The constitutive models[13, 19, 10] for confined and unconfined concrete discussed in the previous sections were applied to pier wall 6 as an example for comparison purpose. Only 60% of the lateral reinforcement yield stress was considered. The following data were used in the analysis:

ρ_l = 0.0025 ρ_c = 0.0020

s_h = 182 mm h'' = 1450 mm

f'_c = 26.2 MPa f_{yh} = 424.0 MPa

E_s = 200,000 MPa ε_{sm} = 0.1

Table 5-3 presents the properties of the unconfined and confined concrete, and the percent difference between the confined and unconfined concrete properties. The stress-strain curves were developed and plotted (Figure 5-8). The comparison of the confined concrete properties shows that the three constitutive models led to nearly the same concrete compressive strength and corresponding strain. The ultimate strain based on the Hoshikuma model was close to that of the unconfined concrete using the Kent and Park model. The modified Kent and Park model gives nearly twice the ultimate strain as the modified Mander model. Figure 5-8 shows that the three models have nearly the same ascending segment and the difference is in the descending part. The deterioration rate predicted by modified Kent and Park model was nearly the same as that of the modified Mander et al. model. Hoshikuma model gives a deterioration rate close to that of Kent and Park for unconfined concrete. Since the results from the Hoshikuma model did

not seem to adequately reflect the effect of confinement, this model was excluded from further consideration.

Table 5-3 Calculated Unconfined and Confined Concrete Properties

Properties	Kent & Park Model[23] Unconfined Concrete	Modified Kent & Park Model[13]		Modified Mander et al. Model[19]		Hoshikuma Model[10]	
		Value	Diff. %	Value	Diff. %	Value	Diff. %
f_{cc} (MPa)	26.20	27.34	4	28.34	8	27.07	3
ε_{cc}	0.0020	0.0021	4	0.0028	41	0.0026	29
ε_{cu}	0.0040	0.0198	394	0.0097	144	0.0046	15

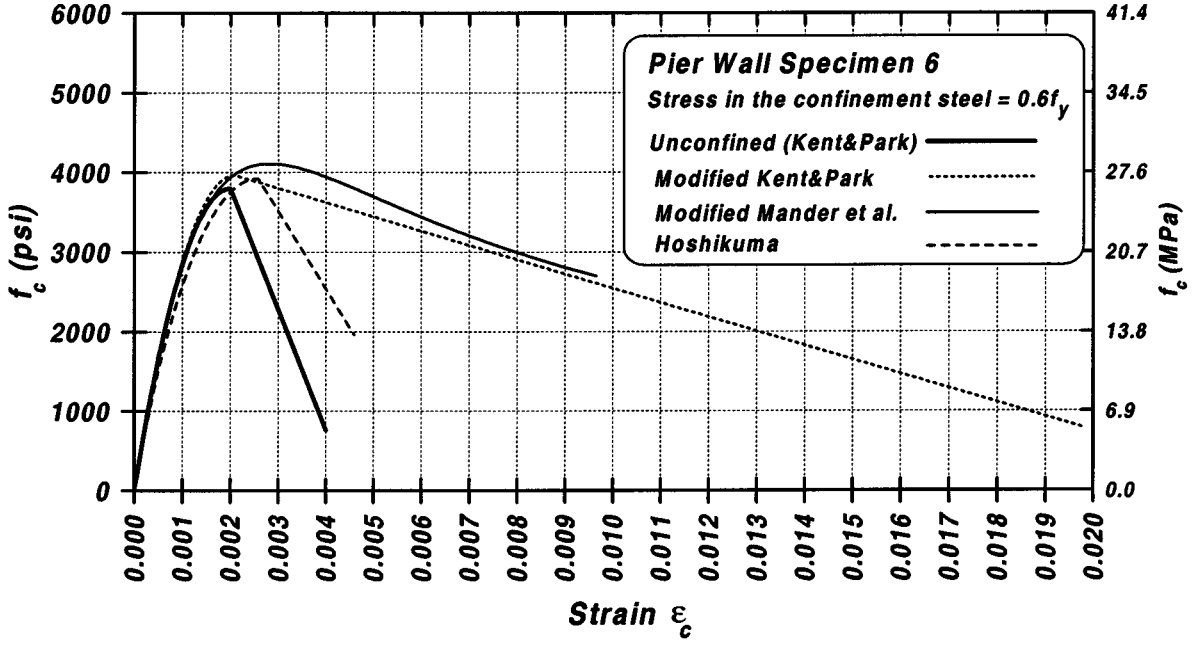

Figure 5-8 Comparison of Confined Concrete Models

5.2.1.3 Reinforcing Steel Model

The stress-strain relationship of the steel was idealized as show in figure 5-9. The first branch of the stress-strain curve is the elastic loading range at which the stress is linearly proportional to the strain (line O-A). A yield plateau (line A-B) is included. At the strain hardening stage

(curve B-C), the steel starts to gain stress at a rate that is reduced at higher strains. The ultimate strain is considered as the strain corresponding to the maximum stress. To model the strain-hardening curve, Burns and Seiss[5] proposed a single function, which was later generalized by Kent and Park[12] and also used by Leslie[16]. Based on the results of a wide range of tension and compression tests, Mander[17] proposed an improved alternative formulation. In this formulation, the start and end coordinates of the strain hardening curve, (ε_{sh}, f_y) and (ε_{su}, f_{su}) respectively, and the modulus of elasticity of the strain hardening, E_{sh}, are used to define the strain-hardening curve. The expression is in the form of a power curve with the ultimate stress-strain coordinates as origin and is given as:

$$f_s = f_{su} + (f_y - f_{su})\left[\frac{\varepsilon_{su} - \varepsilon_s}{\varepsilon_{su} - \varepsilon_{sh}}\right]^P \tag{5-21}$$

where:

f_s = Steel stress

ε_s = Steel Strain

f_y = Steel yield stress

ε_{sh} = Strain at the beginning of strain hardening

f_{su} = Maximum stress in steel

ε_{su} = Strain at maximum stress

The strain hardening power, P, is determined by differentiating Equation 5-21 to give the tangent modulus of elasticity, E_t, as follows:

$$E_t = \frac{df_s}{d\varepsilon_s} = P\left[\frac{f_{su} - f_y}{\varepsilon_{su} - \varepsilon_{sh}}\right]\left[\frac{\varepsilon_{su} - \varepsilon_s}{\varepsilon_{su} - \varepsilon_{sh}}\right]^{P-1} \tag{5-22}$$

The modulus of elasticity of the strain hardening is the tangent modulus at $\varepsilon_s = \varepsilon_{sh}$ and can be written as:

$$E_{sh} = P\left[\frac{f_{su} - f_y}{\varepsilon_{su} - \varepsilon_{sh}}\right] \tag{5-23}$$

The power factor, P, which is the ratio of the modulus of the strain hardening to the secant modulus between the start and end coordinates of the strain-hardening curve, is given by the following equation:

$$P = E_{sh}\left[\frac{\varepsilon_{su} - \varepsilon_{sh}}{f_{su} - f_y}\right] \tag{5-24}$$

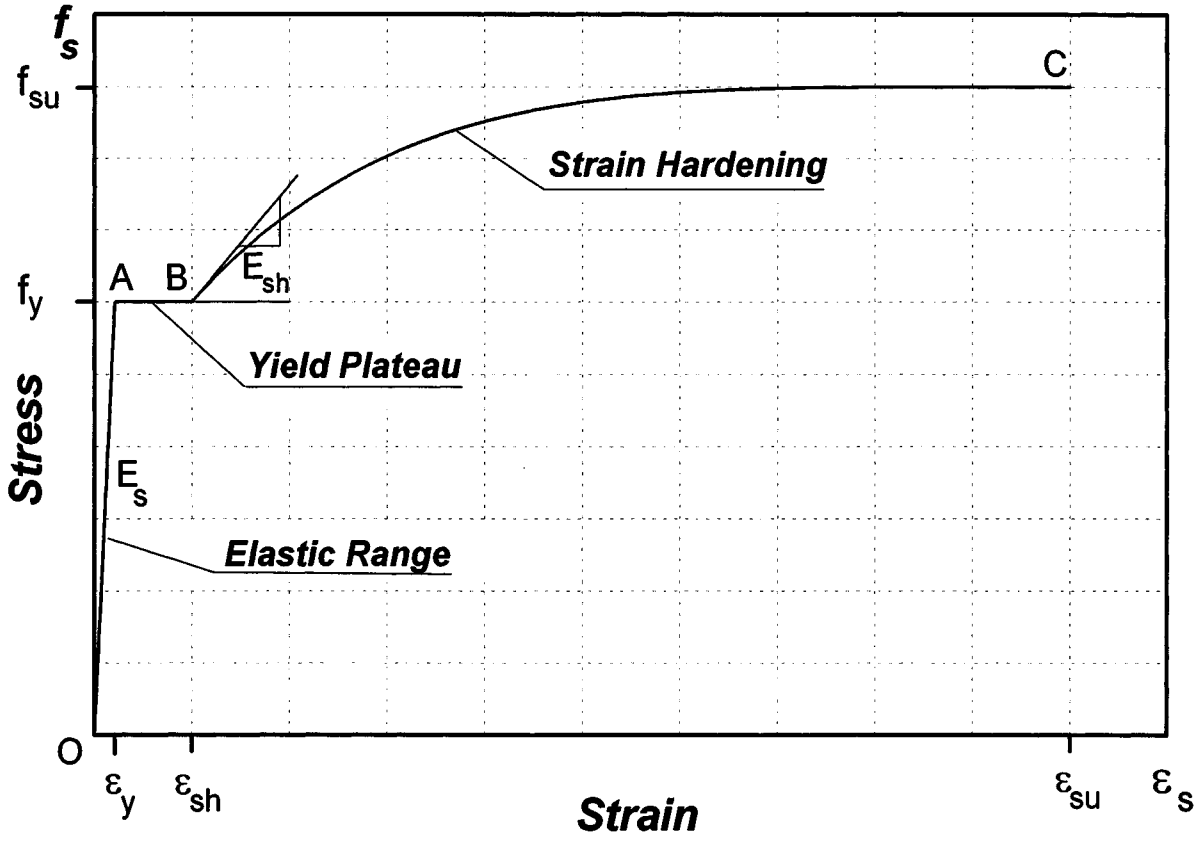

Figure 5-9 Stress-Strain Model for Steel

5.2.2 Flexural Deflection

The flexural deflection at the free end of a pier wall can be found by applying the moment area theorem as follows:

$$\Delta_f = \int_0^1 \phi x dx \tag{5-25}$$

which is the static moment of the area under the curvature profile along the height of the pier wall taken about its free end. The parameters in Equation 5-25 are shown in figure 5-1.

To calculate the deflection due to flexure, the idealized curvature along the height of the pier wall was used. The idealized curvature between the cracking and the yield points of the pier wall is presented in figure 5-10, where M_{cr} and M_y, are the cracking moment and the yield moment, respectively, and ϕ_{cr} and ϕ_y are the corresponding curvatures. The ultimate displacement can be found as[26]

$$(\Delta_f)_u = (\Delta_f)_y + (\Delta_f)_p \tag{5-26}$$

where:

$(\Delta_f)_y$ = Flexural deflection at yield

$(\Delta_f)_p$ = Additional flexural deflection due to rigid body rotation at the plastic hinge (Plastic displacement)

The idealized curvature at the ultimate state includes the effect of the plastic hinge (Figure 5-11). In this idealization, the actual plastic hinge length is replaced by an equivalent plastic hinge length that would result in the same plastic displacement at the free end[35]. Assuming that the plastic rotation is concentrated at the middle of the equivalent plastic hinge length, $(\Delta_f)_p$ can be found as:

$$(\Delta_f)_p = (\varphi_u - \varphi_y)\, l_p \left(1 - \frac{l_p}{2}\right) \tag{5-27}$$

where:

l = The length of the cantilever wall

l_p = The equivalent plastic hinge length

ϕ_u = The ultimate curvature

ϕ_y = The yield curvature

Paulay and Priestley[24] proposed an empirical expression to calculate the equivalent plastic hinge length of reinforced concrete members, which is based on the member length and the longitudinal bar diameter and given by:

$$l_p = 0.08l + 0.022 d_p f_y \tag{5-28}$$

where:

l = Length of the member between critical section and point of contraflexure, mm

d_p = Longitudinal bar diameter, mm

f_y = Yield strength of the longitudinal bars, MPa

To calculate the displacement between the yield and the ultimate, it was assumed that the plastic hinge length at $\mu_d = 1$, is equal to 50% of the calculated value using Equation 5-28, while it is equal to 100% at $\mu_d = 4$. These values are based on judgment, and they appear to be reasonable. A linear interpolation for the plastic hinge coefficient was assumed between displacement ductility levels of 1 and 4 (Figure 5-12). The plastic hinge coefficient defines the fraction of the full plastic hinge length used in the analysis (from Equation 5-28) depending on the ductility level.

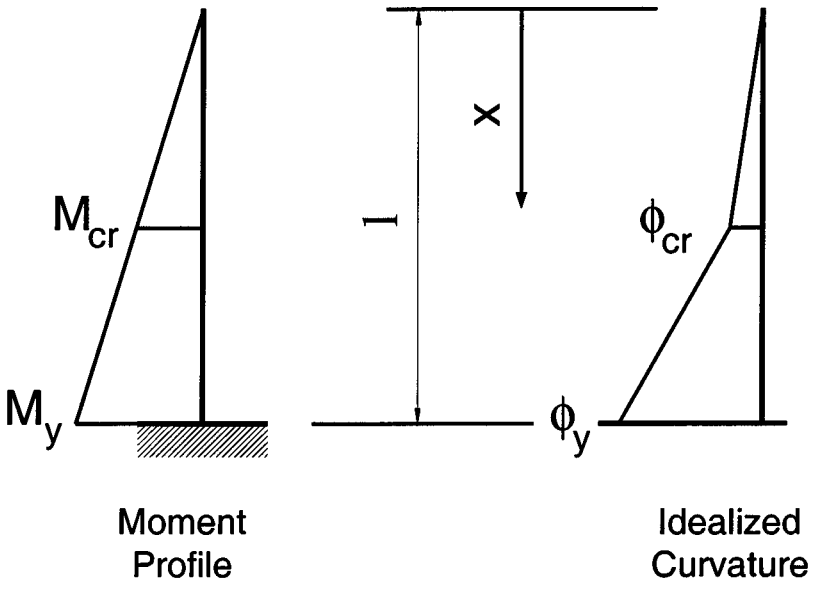

Figure 5-10 Bending Moment and Idealized Curvature at Yield

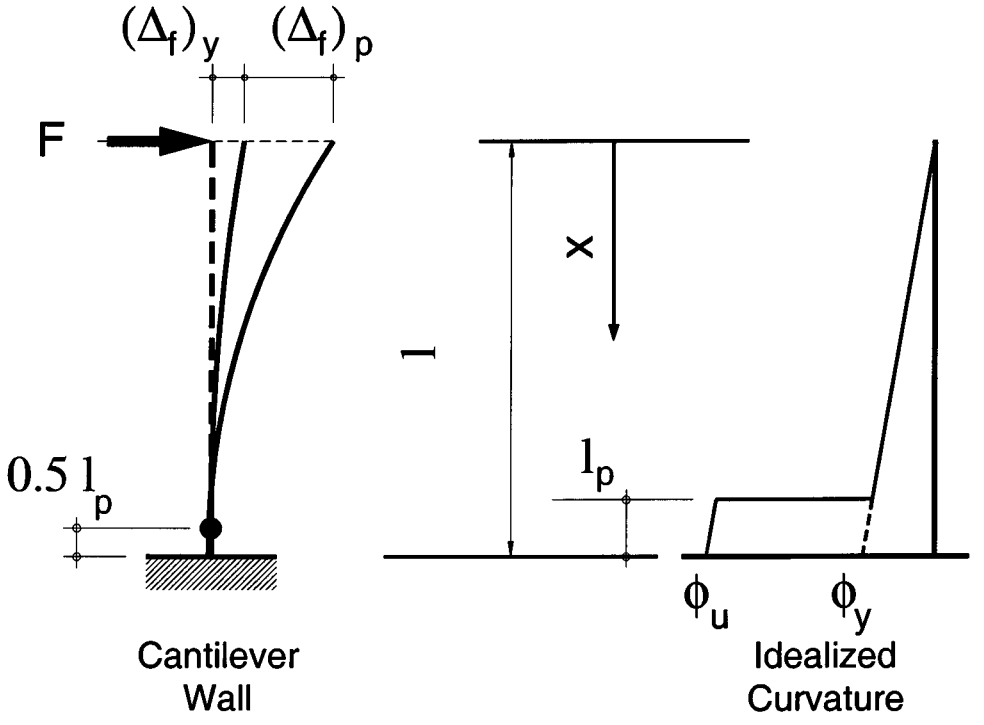

Figure 5-11 Flexural Deflection and Idealized Curvature at Ultimate

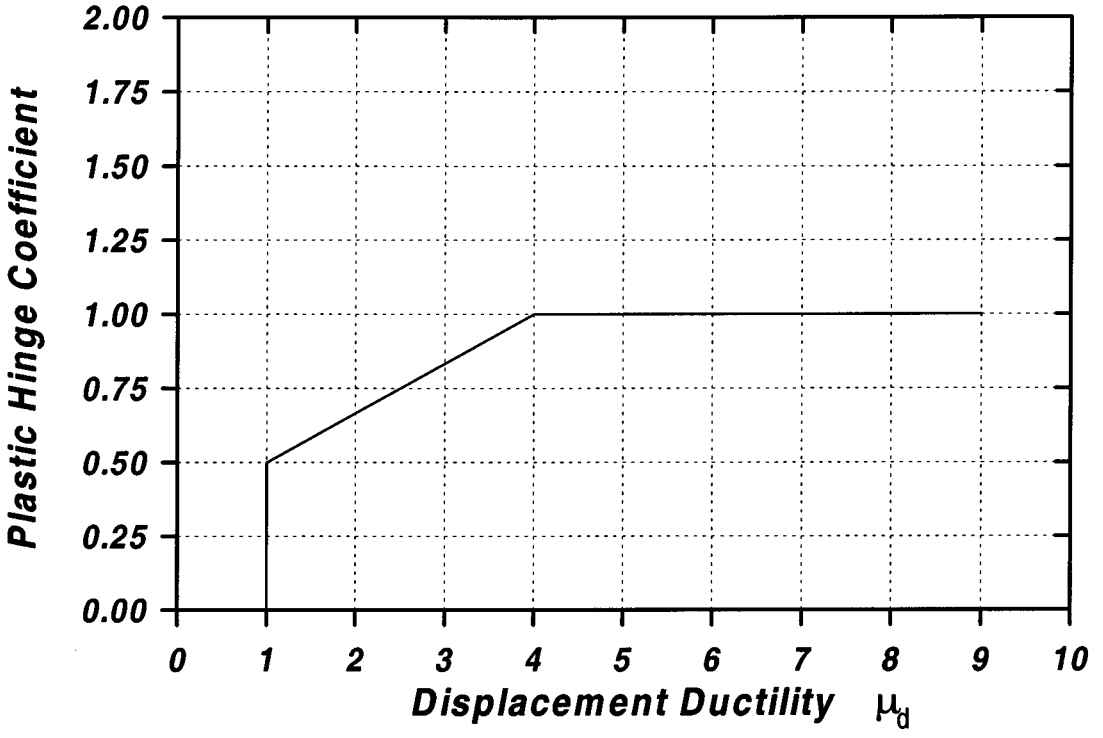

Figure 5-12 Plastic Hinge Coefficient vs. Displacement Ductility

5.2.2.1 Moment-Curvature Analysis

The moment-curvature analysis of reinforced concrete sections is based on equilibrium of forces and compatibility of strains. Therefore, it is required to find a strain profile for the cross section that would result in equilibrium between the external axial force and the internal forces in concrete and steel. This can be achieved by selecting the strain at the extreme compressive fibers of the cross section, and using an iterative procedure to find the tensile steel strain that would satisfy the equilibrium condition. Figure 5-13 shows a pier wall cross section subjected to axial load and bending, the strain profile, and the stress profile in confined and unconfined concrete. Based on the strain profile and the geometry of the cross section the curvature is calculated. The corresponding moment is found by summing the moments of forces developed in the cross section about the plastic centroid of the section. A complete moment-curvature diagram is found by repeating the process for different strain levels at the extreme fibers.

The following assumptions were made in developing the moment-curvature relationships:

- Plane sections remain plane after bending
- Perfect bond exists between steel bars and concrete
- The tensile strength of the concrete is neglected
- The cross sections used in the analysis are rectangular
- The modified Mander et al.[19] model is used to model the stress-strain relationship of the confined concrete
- The Kent and Park[23] model is used to model the stress-strain relationship of the unconfined concrete of the cover concrete part
- The reinforcing steel model proposed by Mander[17] is used
- Spalling of cover concrete is accounted for by removing the cover once the maximum strain reaches the ultimate strain of unconfined concrete
- Failure of concrete is considered when the maximum strain in the confined concrete is equal to the ultimate strain of the confined concrete
- Failure in steel occurs when the strain in the vertical bars reaches the rupture strain of the steel
- The strain in every steel bar is equal to the strain at its center

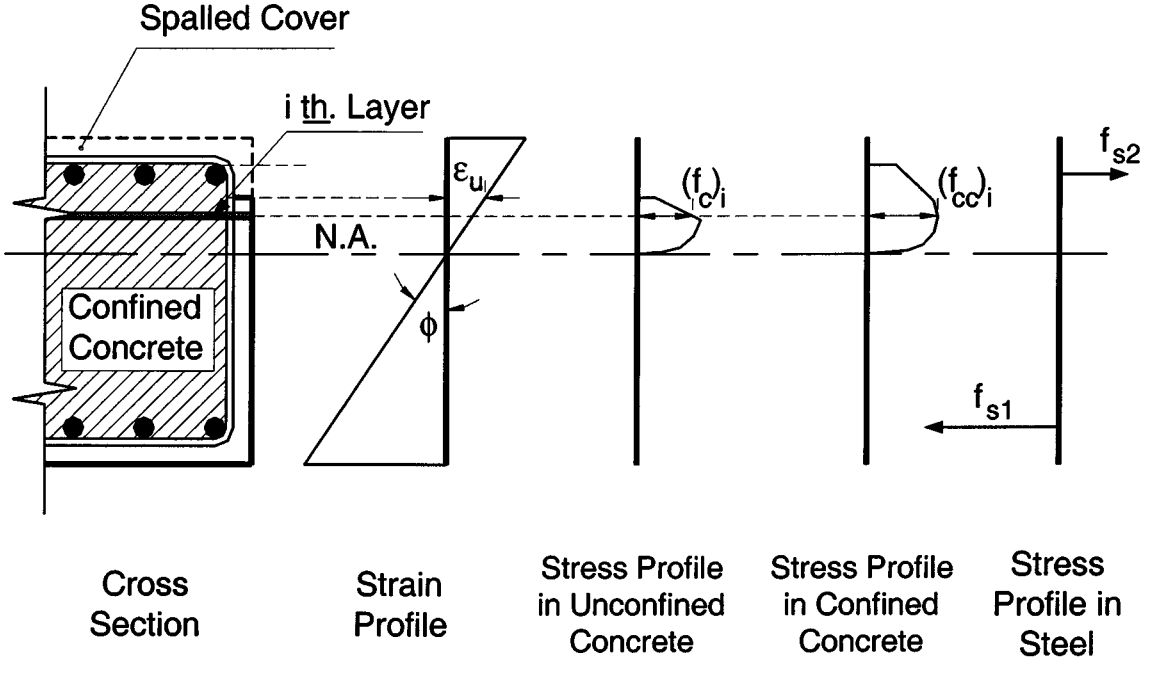

Figure 5-13 Pier Wall Cross Section Subjected to Axial Load and Bending

5.2.3 Shear Deflection

To calculate the lateral deformation at the top of a reinforced concrete pier wall, it is essential to include the shear deformation. The shear stiffness, K_v, is defined as the shear force that will cause a unit shear displacement when applied to a unit length of a reinforced concrete member. Cracks occur in pier walls when the moment exceeds the cracking moment. Some of these cracks extend into diagonal cracks and increase the shear deformation. Park and Paulay[23] derived expressions to calculate the shear stiffness of uncracked and cracked members. For uncracked members the shear stiffness is given as follows:

$$K'_v = \frac{0.4E_c b_w d}{f} \tag{5-29}$$

where:

b_w = Section width perpendicular to the applied shear force

d = Effective section depth parallel to the applied shear force

E_c = Elastic modulus of concrete

The factor, f, allows for the non-uniform distribution of the shear stresses and is equal to 1.2 for the case of rectangular sections.

The shear stiffness of a member with diagonal inclined cracks at an angle α can be calculated as:

$$K_v = \frac{\rho_v \sin^4 \alpha(\cot\alpha + 1)^2}{\sin^4 \alpha + n\rho_v} E_s b_w d \tag{5-30}$$

where:

K_v = Shear stiffness for an element with a unit length

E_s = Elastic modulus of shear reinfor

s = Spacing of shear reinforcement sets along the member longitudinal axis

In this study, the diagonal crack angle, α, was assumed to be 45°. Therefore, Equation 5-30 can be written as:

$$K_{v,45} = \frac{\rho_v}{1 + 4n\rho_v} E_s b_w d \tag{5-31}$$

Park and Paulay found that the shear stiffness of a diagonally cracked member is approximately 10 to 30% of that of the uncracked members, depending on the amount of the shear steel. For pier walls with very low or no shear reinforcement, Equation 5-31 leads to low shear stiffness and an unrealistic, large deformation due to shear. To account for these cases, a minimum cracked shear stiffness was taken as 10% of the uncracked stiffness. Having the shear stiffness for a unit length of the member, the total shear deflection, Δ_{sh} is:

$$\Delta_{sh} = \frac{VL}{K_{v,45}} \tag{5-32}$$

where:

V = The applied shear force

L = The shear span

5.2.4 Bond Slip Deflection

To attain the flexural capacity of the wall-footing interface, the vertical reinforcing bars of the wall should be developed into the footing. The development of the bars is provided through bond stress between the bars and the surrounding concrete. The strains associated with the stresses along the tensile bar development length lead to bar elongation at the wall-footing interface (Figure 5-14), which is called bond slip. The bond slip at the wall-footing interface produces relative rotation between the wall and the footing, and lateral deflection at the top of the wall.

Wehbe et al.[30] proposed a method that is applicable to members with tensile bars having sufficient development length so as to prevent bar pull out. Yield plateau was ignored in the Wehbe et al. method. This caused inaccuracy in the calculated deflection due to bond slip throughout the yield plateau. This method was modified and used in this study. The modified method is based on compatibility and equilibrium of the tensile bars. The bond slip rotation, θ_s, is assumed to occur about the neutral axis of the wall section at the connection interface. The location of the neutral axis and the strain and stress in the tensile steel are determined from moment-curvature analysis of the wall section. The additional elongation of the bars, δl, at the interface is calculated by integration of the theoretical strain profile along the development length (Figure 5-14). The relative rotation, θ_s, can be found by dividing δl by the neutral axis depth to the center of the slipped bars. The lateral deflection at the top of the wall, Δ_s, is obtained by multiplying the rotation by the shear span.

To calculate the development length, the bond stress between the bars and the concrete for bar diameter of 35 mm or smaller is given by:

$$u = \frac{20\sqrt{f'_c}}{d_b} \leq 5.5 \qquad \text{(MPa)} \tag{5-33}$$

The strain and stress profiles in the modified method are based on a tri-linear steel model with strain hardening stage represented by a linear relationship. Three sets of equations are used to calculate the development length, l, and the extension, δl, based on the strain level in the longitudinal bars as follows:

(a) Elastic loading ($\varepsilon_s \leq \varepsilon_{sh}$ and $f_s \leq f_y$)

$$l = \frac{f_s d_b}{4u} \tag{5-34}$$

$$\delta l = \frac{\varepsilon_s l}{2} \tag{5-35}$$

(b) Yield plateau ($\varepsilon_{sh} \geq \varepsilon_s > \varepsilon_y$ and $f_s = f_y$)

$$l = \frac{f_y d_b}{4u} \tag{5-36}$$

$$\delta l = \frac{\varepsilon_y l}{2} \tag{5-37}$$

(c) Strain hardening ($\varepsilon_s > \varepsilon_{sh}$ and $f_s > f_y$)

$$l_1 = \frac{(f_s - f_y) d_b}{4u} \tag{5-38}$$

$$l_2 = \frac{f_y d_b}{4u} \tag{5-39}$$

$$\delta l = \frac{\varepsilon_y l_2}{2} + \frac{(\varepsilon_s + \varepsilon_{sh})}{2} l_1 \tag{5-40}$$

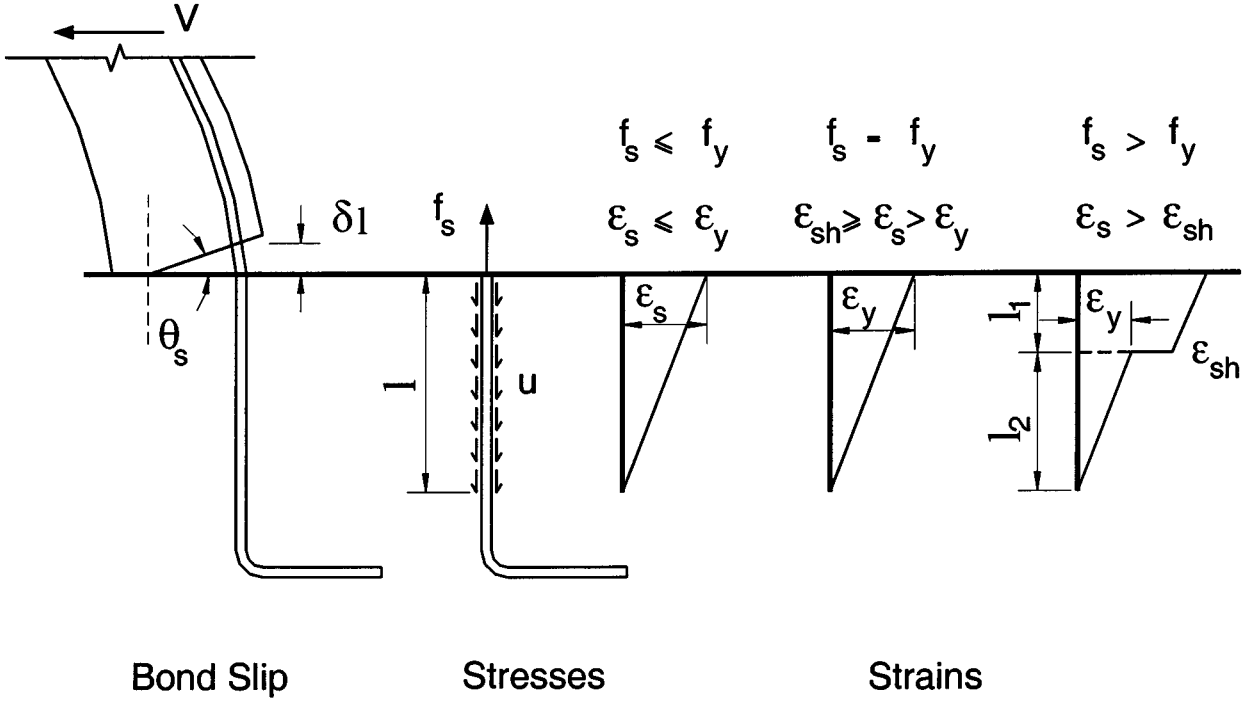

Figure 5-14 Bond Slip of Longitudinal Bars

5.2.5 Low-Cycle Fatigue

One of the limit states that can control the ultimate displacement of a pier wall is failure of the longitudinal bars in low-cycle fatigue. The plastic strain is dominant in low-cycle fatigue while the elastic strain is dominant in high-cycle fatigue[20] (Figure 5-15). Thus, in low-cycle fatigue studies, only the plastic strain is considered. The fatigue life, N_f is defined as the number of cycles to failure. The plastic strain amplitude, $\Delta\varepsilon_p/2$ is the difference between the maximum and the average plastic strains. Coffin and Manson[20] developed a linear log-log relationship between the plastic strain and the fatigue life (Figure 5-15). This relationship is given as:

$$\frac{\Delta\varepsilon_p}{2} = \varepsilon_c'(2N_f)^c \tag{5-41}$$

where:

$$\frac{\Delta\varepsilon_p}{2} = \frac{(\varepsilon_p)_{max} - (\varepsilon_p)_{min}}{2}$$

$2N_f$ = Number of reversals to failure

ε'_f = Fatigue ductility coefficient

c = Fatigue ductility exponent

$(\varepsilon_p)_{max}$ = Maximum tensile plastic strain

$(\varepsilon_p)_{min}$ = Maximum compressive plastic strain

Based on the experimental observations of low and high alloy steel, Mander et al.[18] found that, regardless of steel grade, a dependable plastic-strain life fatigue relationship can be given by:

$$\frac{\Delta\varepsilon_p}{2} = 0.08(2N_f)^{-0.5} \tag{5-42}$$

The linear damage model by Miner[21] was used in this study. In this damage model, the damage index is defined as the indicator that identifies failure in fatigue when it is equal to unity. The damage per cycle can be calculated using the following expression:

$$\text{Damage}_{\text{cycle}} = \frac{1}{N_f} \tag{5-43}$$

The damage index is given as:

$$D = \sum_{i=1}^{m} \frac{n_i}{N_{fi}} \tag{5-44}$$

where:

n_i = Number of applied cycles at $(\Delta\varepsilon_p/2)_i$

N_{fi} = Number of cycles to failure (fatigue life) at $(\Delta\varepsilon_p/2)_i$

In this study, the plastic strain amplitude was calculated based on the moment-curvature analysis of pier wall sections and was taken as one half of the difference between the tensile plastic strain and the compressive plastic strain in the vertical steel (Figure 5-16). Therefore, the corresponding fatigue life, N_f, for the plastic strain amplitude level was calculated using Equation 5-42. Knowing that two cycles were applied at each displacement ductility level during the experimental tests (described in Sections 3 and 4), Equation 5-43 and 5-44 can be rewritten to calculate the damage at each displacement ductility level and the damage index, respectively as:

$$\text{Damage}_{\mu_d} = \frac{2}{N_f} \tag{5-45}$$

$$D = \sum_{i=1}^{m} \frac{2}{N_{fi}} \tag{5-46}$$

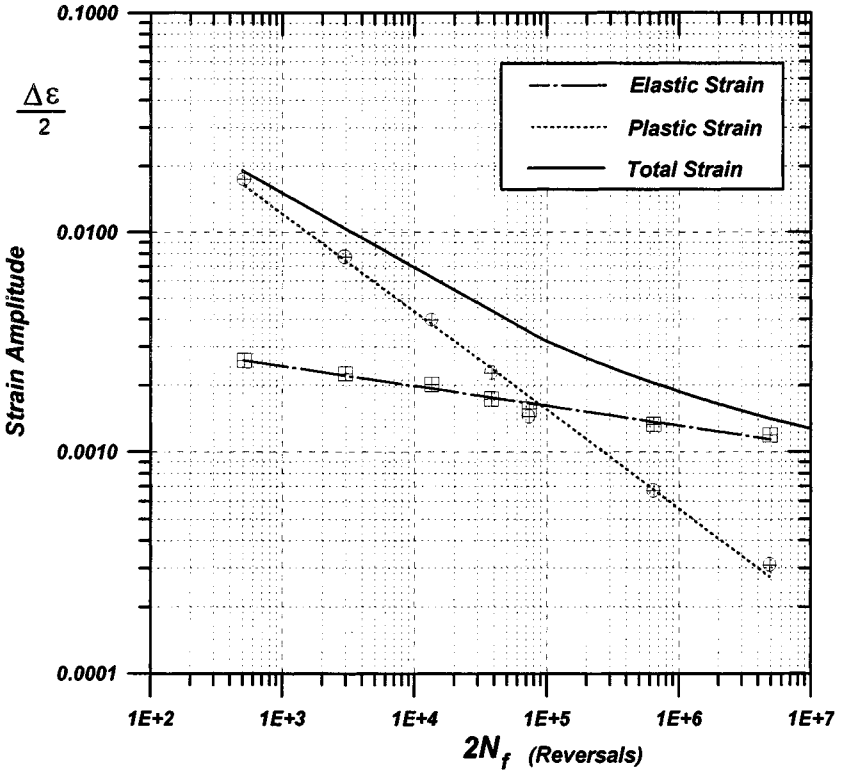

Figure 5-15 Typical Strain-Fatigue Life Curve

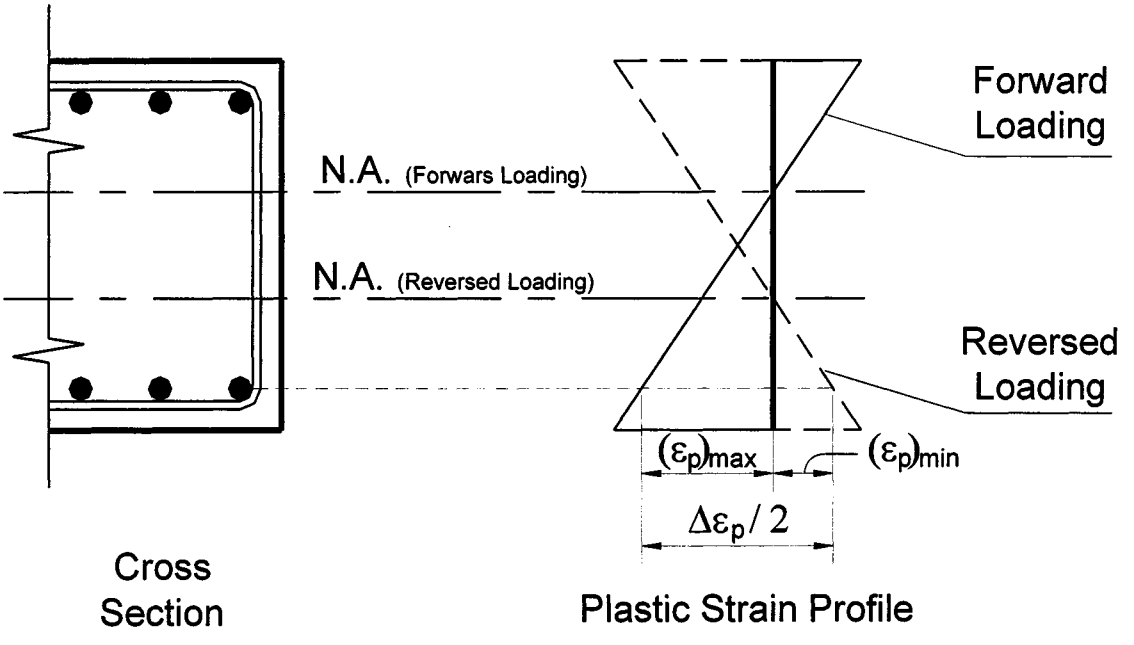

Figure 5-16 Typical Plastic Strain Profile

5.3 "PIER" Computer Program to Calculate the Deflections and the Ductility

The objective of developing the computer program "PIER"[1] was to have an efficient tool to reduce the analysis time and effort. It includes all the unconfined and confined concrete, the steel, and the low-cycle fatigue models, as discussed in Section 5. The program can analyze piers with rectangular cross section and two longitudinal steel layers. The required data to run the program are the pier geometrical properties, the vertical and confinement reinforcement, the unconfined concrete compressive strength, and the steel model parameters (as defined in Section 5.2.1.3). The program provides displacements due to flexure, shear, and bond slip at the cracking, yield, and ultimate points. Moreover, the program has the capability to define the failure mode and the displacement ductility capacity. A flow chart of the program is presented in figure 5-17. The program has the following features:

- Calculates the confined concrete properties and develops the stress-strain curves for unconfined and confined concrete using the models presented in Sections 5.2.1.1 and 5.2.1.2
- Performs the moment-curvature analysis for piers with two longitudinal steel curtains subjected to a known axial load
- Includes the effect of cover concrete spalling
- Defines the moment and curvature for cracking and yield points
- Calculates the deflections at the top of the pier due to flexure, shear, and bond slip
- Calculates the damage index to check failure of the longitudinal bars in low-cycle fatigue
- Defines the mode of failure (compression failure of the concrete or low-cycle fatigue of the longitudinal bars)
- Calculates the displacement ductility capacity of piers

5.4 Comparison of Analytical and Experimental Results

The pier wall specimens that were tested in this study and in previous studies[14, 15] were analyzed using "PIER". The confined concrete properties and stress-strain relationship was determined using the modified Mander et al.[19] model. The following sections present the analytical results for both sets of specimens. To evaluate the performance of the analytical model, the analytical results were compared with the experimental results.

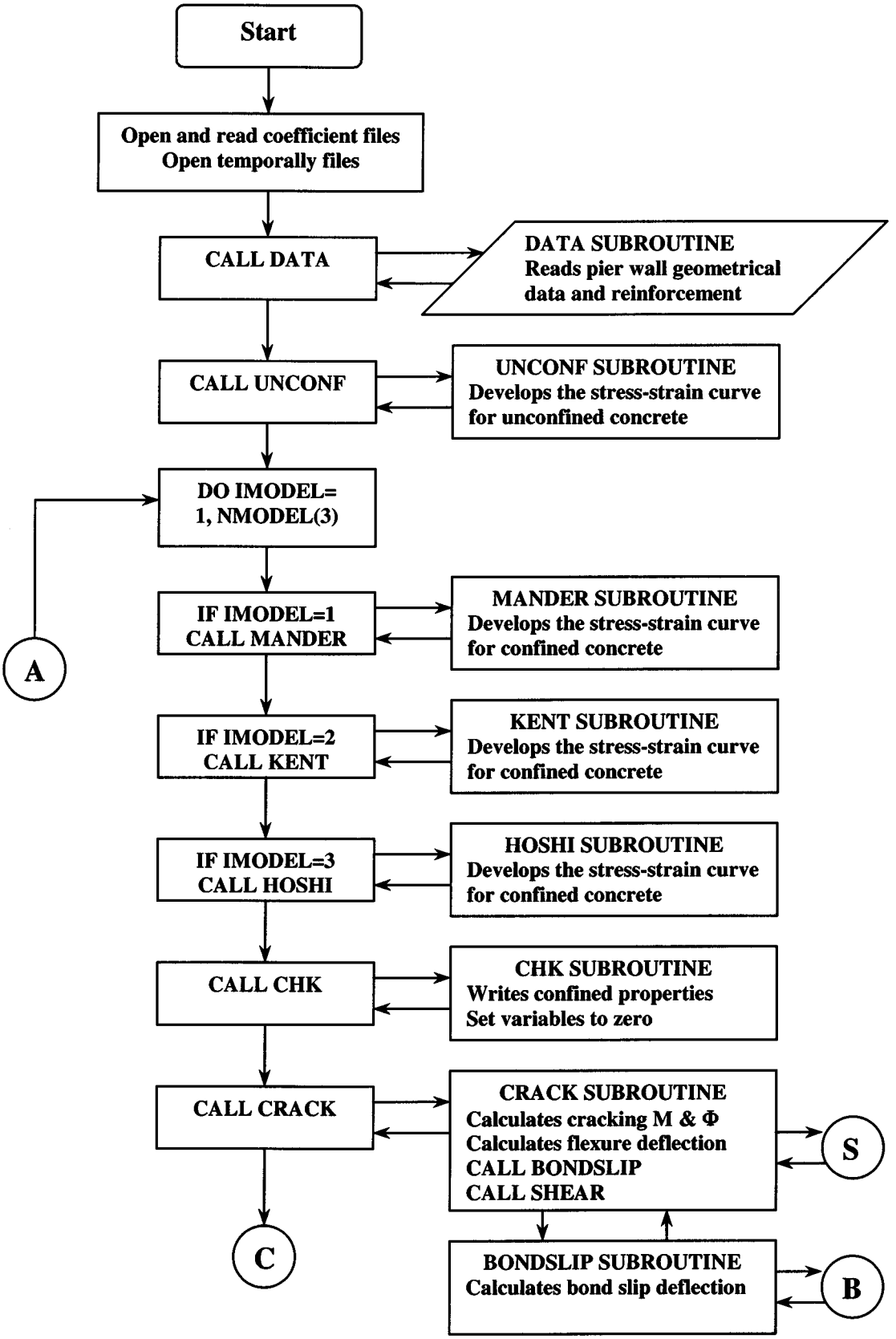

Figure 5-17(a) Flow Chart for the Computer Program "PIER"

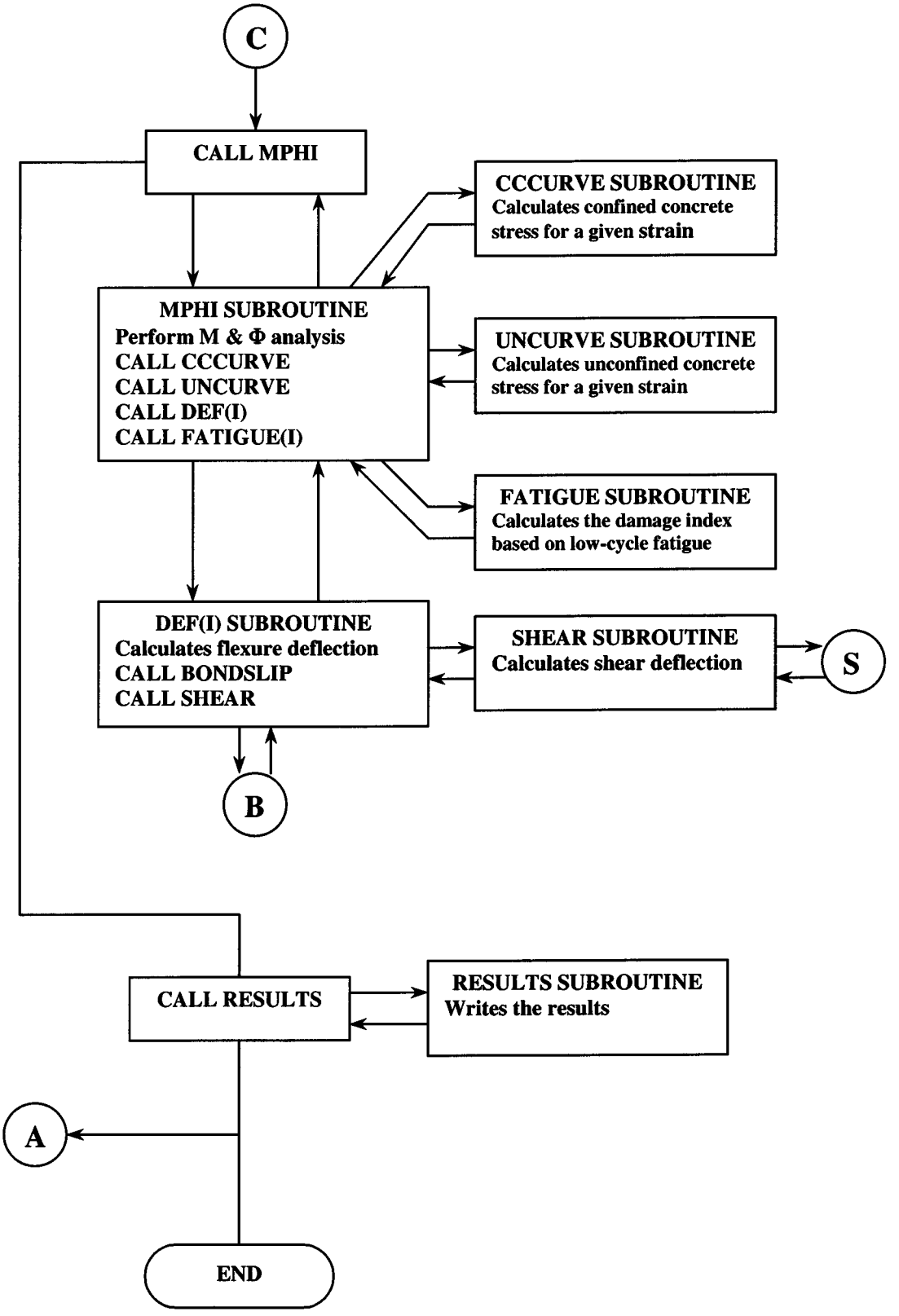

Figure 5-17(b) Flow Chart for the Computer Program "PIER"

5.4.1 Analysis of Pier Walls Tested at The University of Nevada, Reno (UNR)

Dimensions and reinforcement details of the wall specimens that were tested as a part of this study were presented in Section 3-2. The measured material properties were used in the analysis. Section 4 included the experimental test results. Figures 5-18 through 5-24 show the theoretical moment-curvature relationships of the specimens and identify the calculated yield and ultimate curvatures. Tables 5-4(a) and 5-4(b) present the calculated flexural, bond slip and shear components of the lateral deflections as absolute values and percentages of the total deflections. The measured and calculated total displacements at the yield and ultimate points, and the displacement ductility capacities are listed in table 5-5. The difference between the measured and calculated total displacements and ductilities is presented for comparison.

Table 5-4(a) Calculated Yield Displacement Components for UNR Wall Specimens

Specimen No.	Calculated Yield Displacement						
	Total Deflection (mm)	Displacement Components (mm)			Displacement Components (%)		
		Flexure	Bond Slip	Shear	Flexure	Bond Slip	Shear
1	32.6	24.5	4.9	3.2	75.3	15	9.7
2	32.2	24.1	4.9	3.2	74.9	15.2	9.9
3	30.3	24.0	4.9	1.4	79.2	16.1	4.7
4	41.9	30.1	6.3	5.5	71.8	15.1	13.1
5	42.6	31.0	6.8	4.9	72.7	15.8	11.5
6	39.7	30.7	6.5	2.6	77.2	16.4	6.4
7	19.5	13.2	3.7	2.6	68.0	18.8	13.2

Table 5-4(b) Calculated Ultimate Displacement Components for UNR Wall Specimens

Specimen No.	Calculated Ultimate Displacement						
	Total Deflection (mm)	Displacement Components (mm)			Displacement Components (%)		
		Flexure	Bond Slip	Shear	Flexure	Bond Slip	Shear
1	230.5	204.1	22.9	3.5	88.6	9.9	1.5
2	227.8	201.7	22.6	3.4	88.6	9.9	1.5
3	224.8	200.6	22.5	1.7	89.3	10.0	0.7
4	259.3	224.9	27.9	6.4	86.8	10.8	2.5
5	271.3	235.0	30.5	5.7	86.6	11.2	2.1
6	267.0	234.5	29.7	2.9	87.8	11.1	1.1
7	158.8	158.8	16.3	2.7	89.3	9.1	1.5

Table 5-5 Comparison of Measured and Calculated Displacement and Displacement Ductility for UNR Wall Specimens

Specimen No.	Yield Displacement (mm)			Ultimate Displacement (mm)			Displacement Ductility		
	Measured	Calculated	Diff. %	Measured	Calculated	Diff. %	Measured	Calculated	Diff. %
1	32.5	32.6	0.23	211.3	230.5	9.11	6.5	7.1	8.86
2	27.5	32.2	16.91	192.5	227.8	18.31	7.0	7.1	1.20
3	25.0	30.3	21.00	187.5	224.8	19.87	7.5	7.4	-0.94
4	41.5	41.9	1.02	240.7	259.3	7.71	5.8	6.2	6.61
5	42.5	42.6	0.29	242.3	271.3	11.97	5.7	6.4	11.64
6	42.5	39.7	-6.53	257.7	267.0	3.62	6.1	6.7	10.86
7	17.5	19.5	11.14	157.5	177.8	12.87	9.0	9.1	1.56
Average			6.30			11.92			5.69
σ			10.15			5.77			5.07

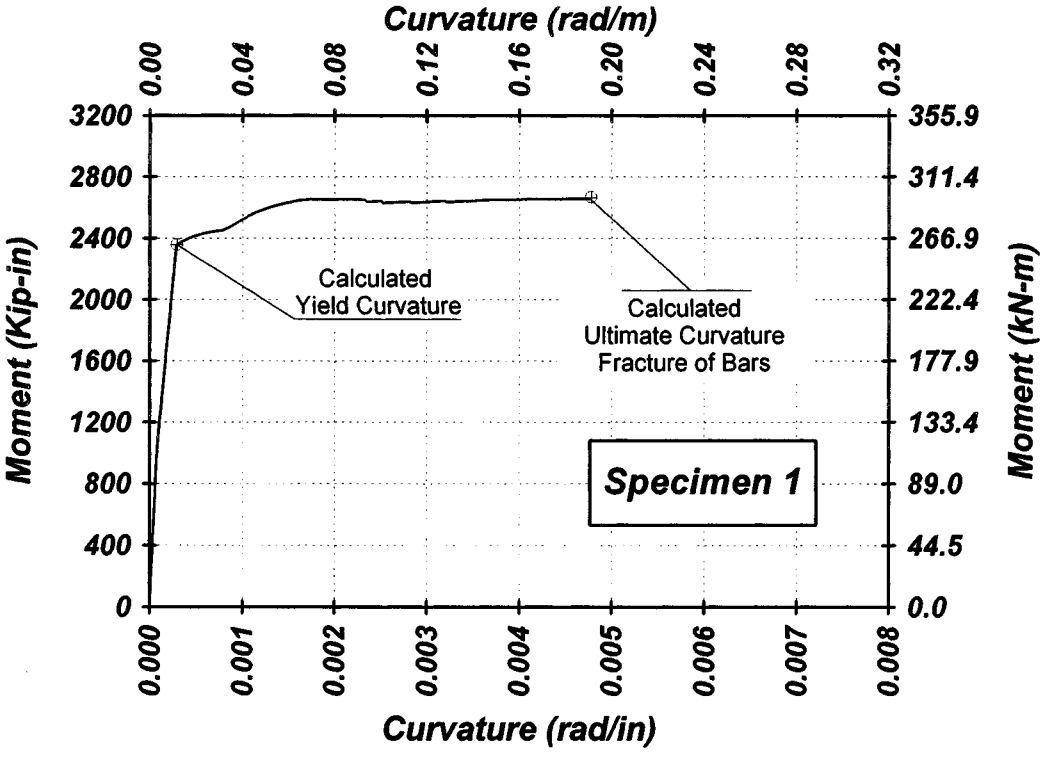

Figure 5-18 Analytical Moment-Curvature Relationship for Specimen 1

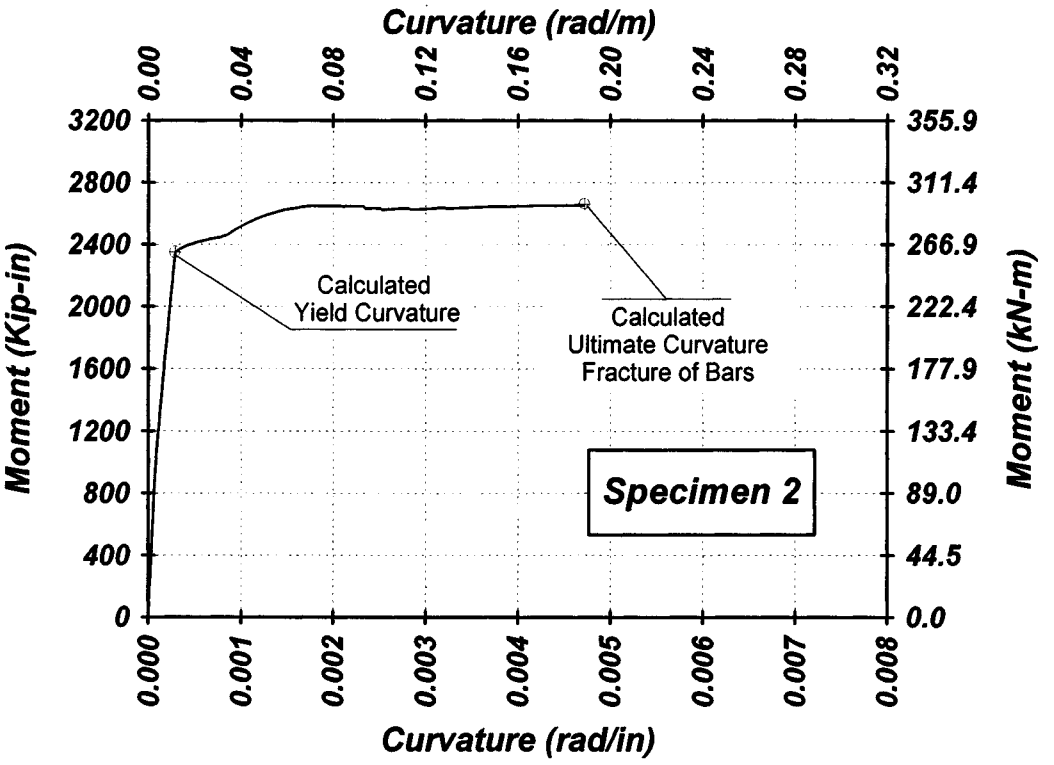

Figure 5-19 Analytical Moment-Curvature Relationship for Specimen 2

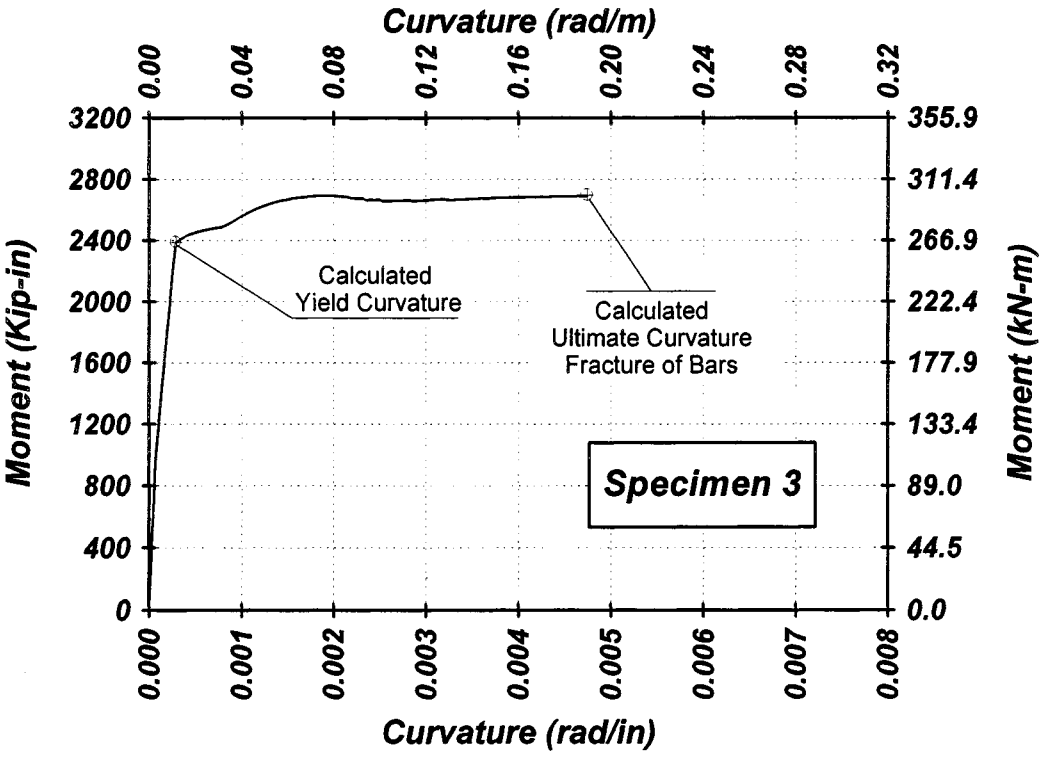

Figure 5-20 Analytical Moment-Curvature Relationship for Specimen 3

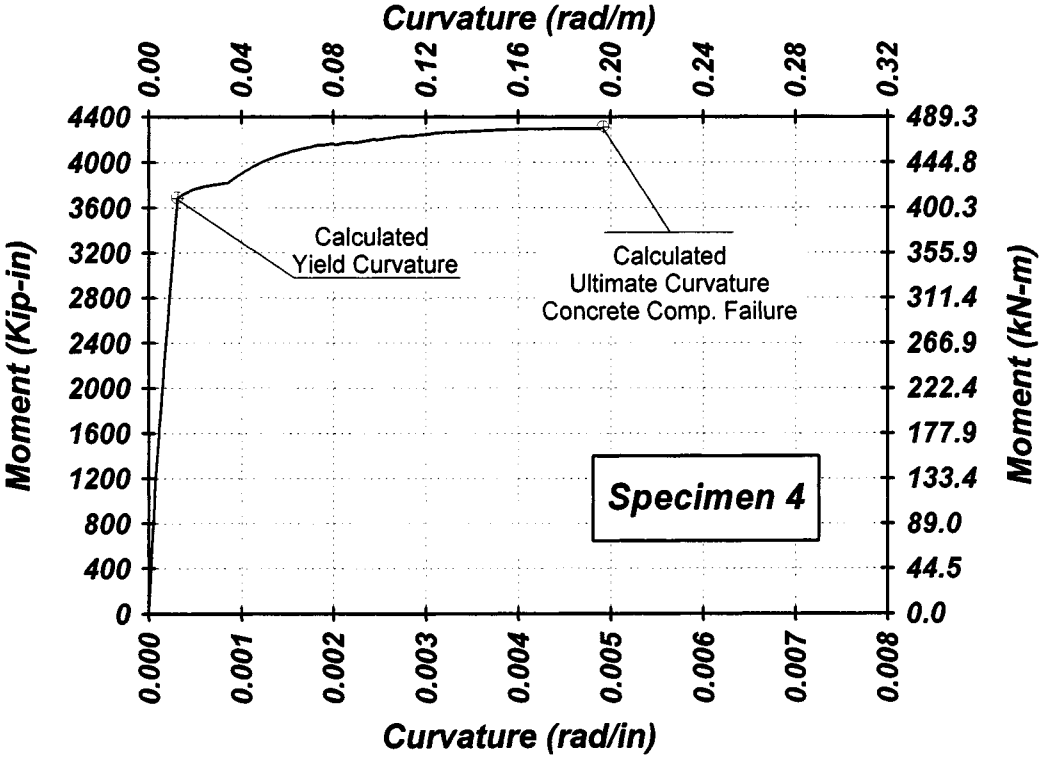

Figure 5-21 Analytical Moment-Curvature Relationship for Specimen 4

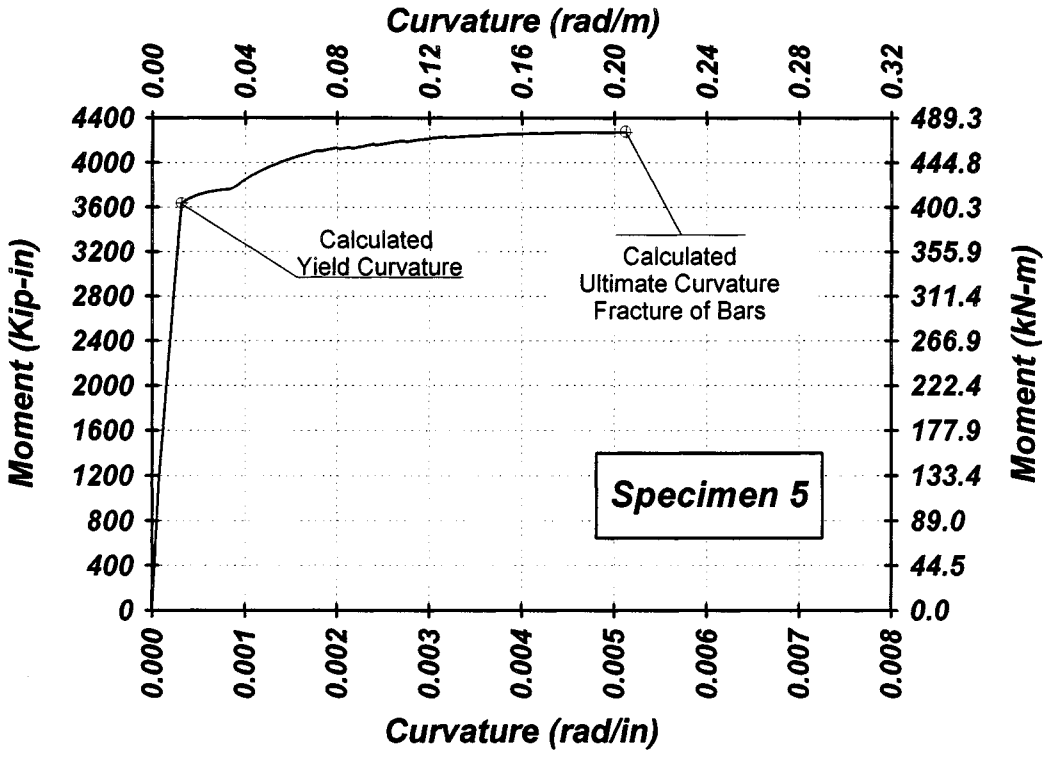

Figure 5-22 Analytical Moment-Curvature Relationship for Specimen 5

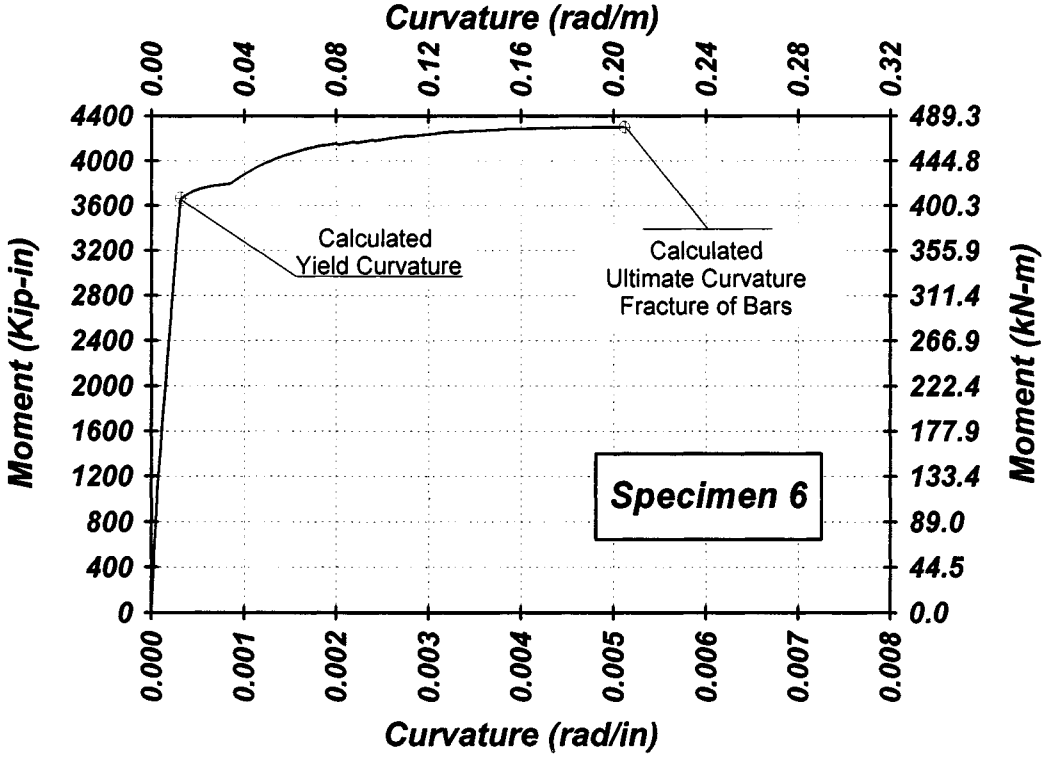

Figure 5-23 Analytical Moment-Curvature Relationship for Specimen 6

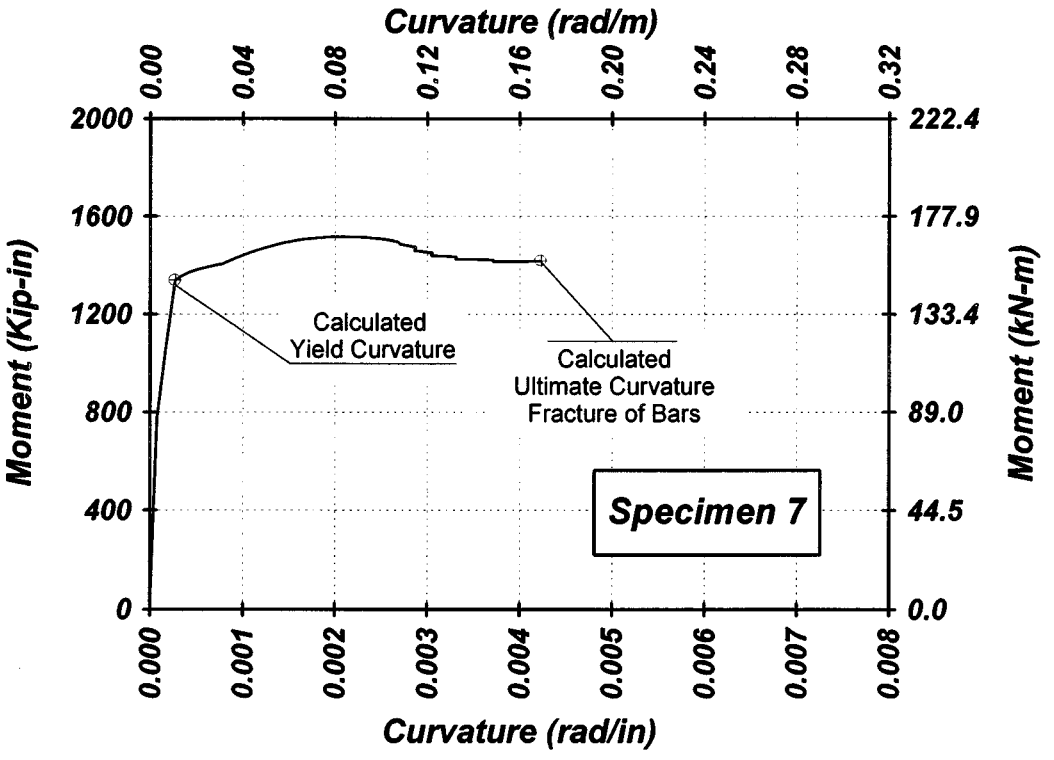

Figure 5-24 Analytical Moment-Curvature Relationship for Specimen 7

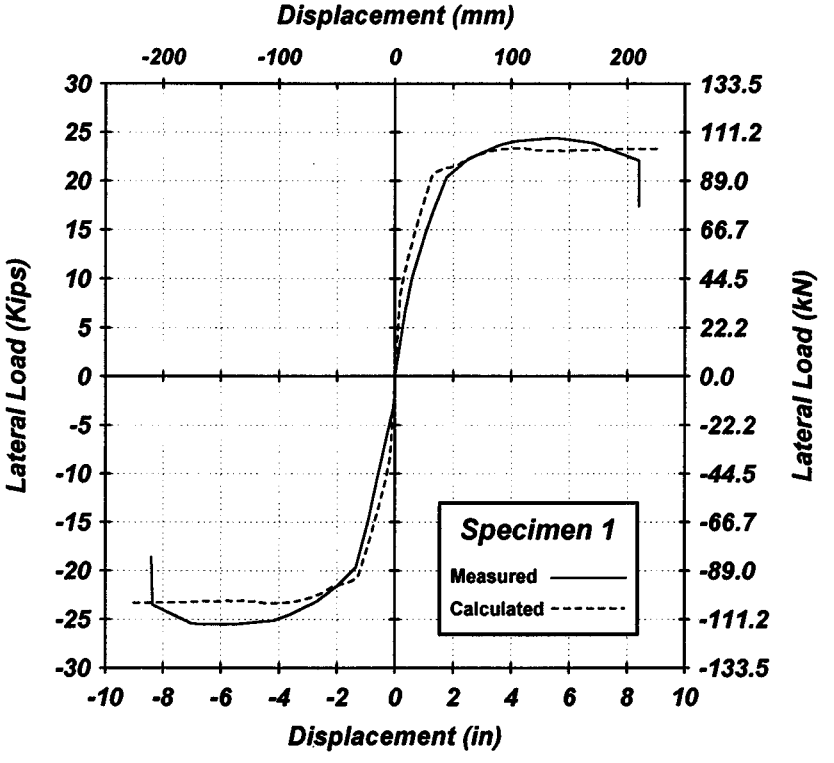

Figure 5-25 Measured and Calculated Lateral load-Displacement for Specimen 1

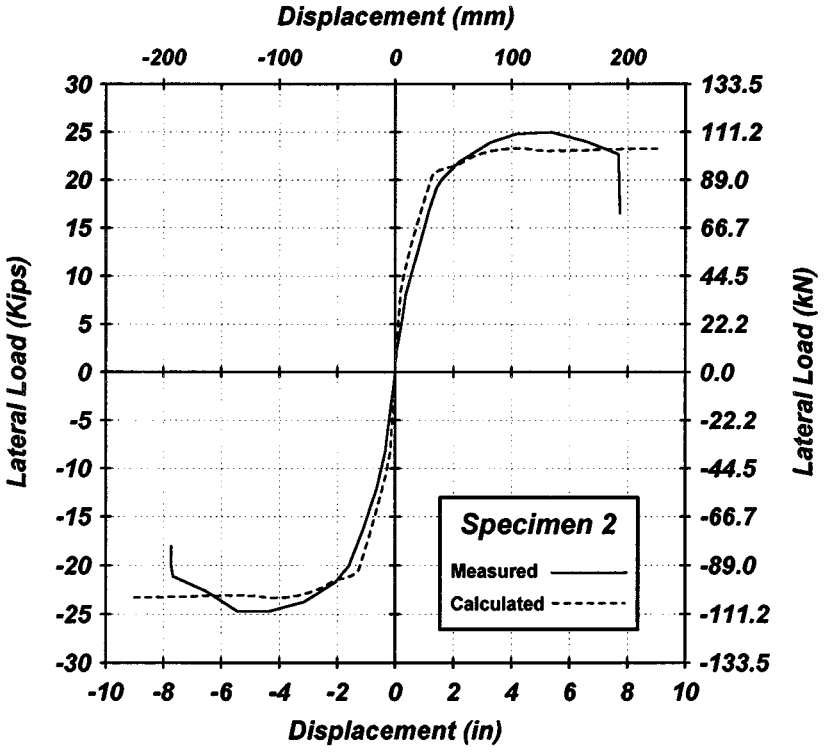

Figure 5-26 Measured and Calculated Lateral load-Displacement for Specimen 2

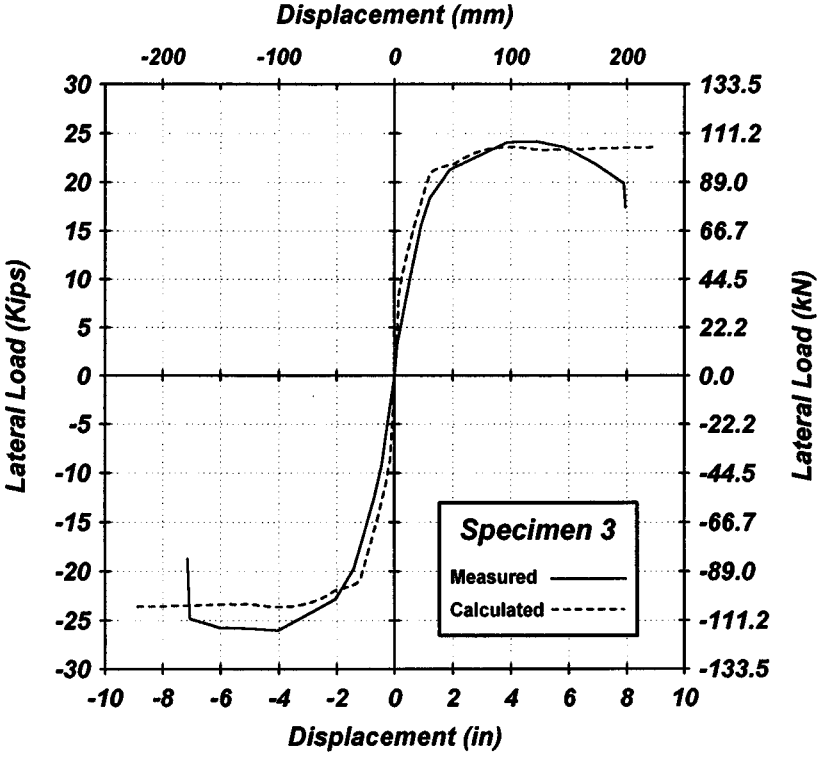

Figure 5-27 Measured and Calculated Lateral load-Displacement for Specimen 3

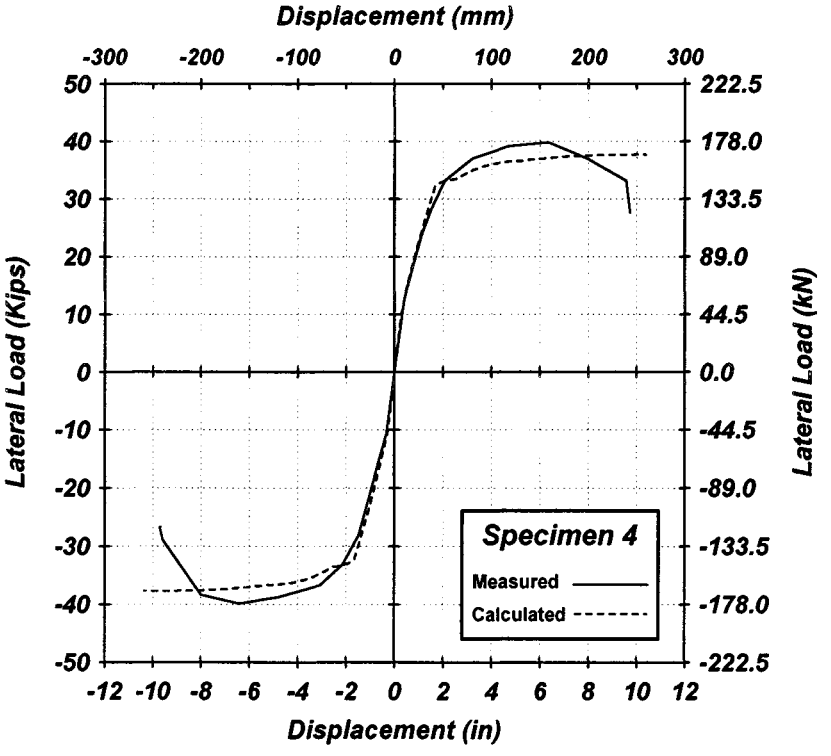

Figure 5-28 Measured and Calculated Lateral load-Displacement for Specimen 4

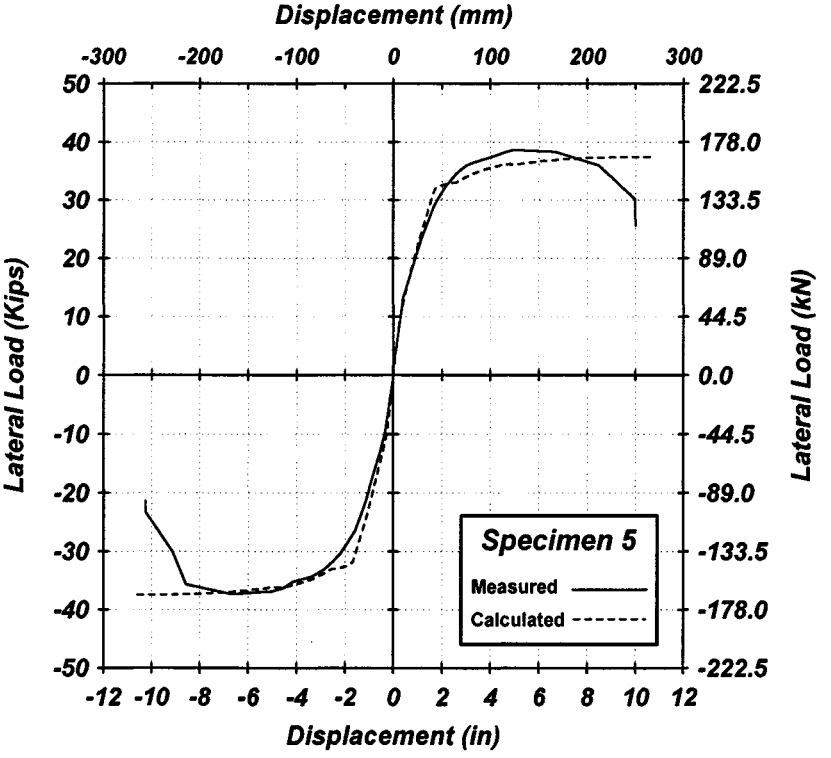

Figure 5-29 Measured and Calculated Lateral load-Displacement for Specimen 5

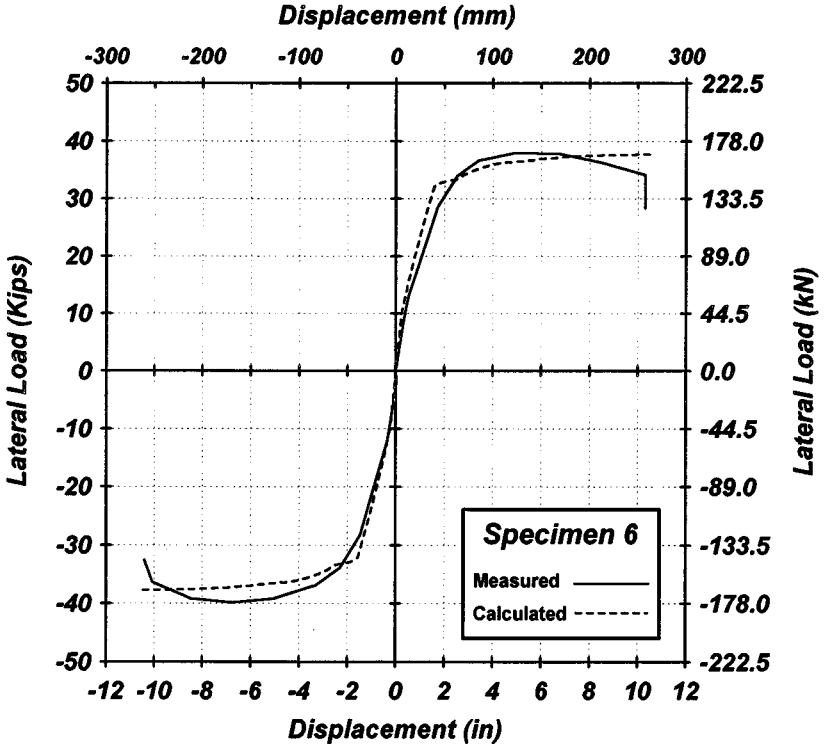

Figure 5-30 Measured and Calculated Lateral load-Displacement for Specimen 6

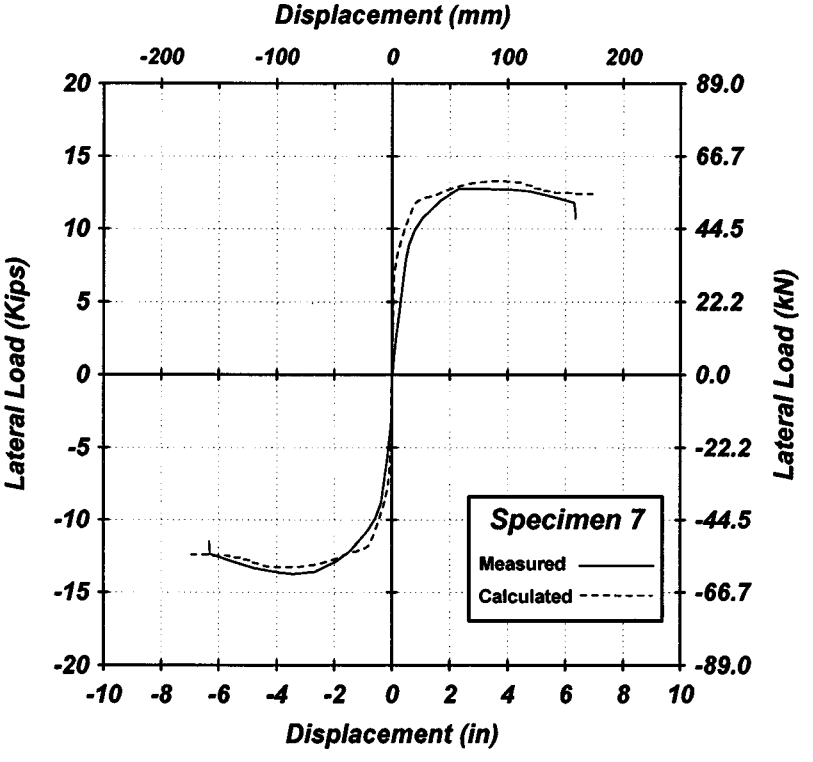

Figure 5-31 Measured and Calculated Lateral load-Displacement for Specimen 7

The predicted mode of failure (shown on the analytical moment curvature relationships, figures 5-18 through 5-24) for all wall specimens was the same as the observed mode of failure (Section 4-2). In comparing the envelope of the lateral load-displacement relationships with the calculated responses (Figures 5-25 through 5-31), good agreement was found. The calculated lateral load capacities were usually lower than the measured lateral load capacities. On the contrary, the calculated ultimate displacements were slightly higher than the measured ultimate displacements. The analytical model could not represent the deterioration of the wall specimen between the peak and the failure points. The strength deterioration of the specimens was mainly due to cyclic loading, while the loading used in the analytical model was monotonic.

The break down of the lateral displacements (Table 5-4(a) and 5-4(b)) shows that the deflection due to bond slip represented an average of 16.1% at yield while its average was 10.3% at ultimate. As for deflection due to shear, its average contributions were 9.8% and 1.6% at yield and ultimate, respectively. On the contrary, the flexure component of the total deflection was more significant at ultimate than yield. The average of the flexure components increased from 74.1% at yield to 88.1% at ultimate. This is because the flexure deflection is related to the section curvature which is significantly increased between the yield and ultimate. As expected, for walls with the same vertical reinforcement, the shear deflection components for the specimens with higher lateral reinforcement dropped since the lateral reinforcement increases the shear stiffness (Equation 5-30).

The average difference between the measured and calculated total yield displacements was 6.3% with a standard deviation, σ, of 10.2% while it was 11.9% with σ = 5.8% for the ultimate displacements (Table 5-5). An average difference of 5.7% with σ = 5.1% was found between the measured and the calculated displacement ductility capacity.

5.4.2 Analysis of Pier Walls Tested at UC-Irvine

This section includes the analysis of pier wall specimens that were tested at the University of California, Irvine[8, 9]. The as-built specimens (presented in Reference 8), that were tested in the weak direction and had class "C" splice (28 d_b) were selected for analysis. The specimens

represented one-half scale model of existing pier walls. The height and thickness of the specimens were 3175 mm, and 250 mm, respectively. The width was 913 mm in specimen WC1 while it was 950 mm for specimens WC2 and WC3. The vertical bars were 13-mm diameter at 212.5-mm spacing. The lateral steel was provided using deformed D7 wires at 175-mm spacing, placed inside the vertical bars. The wall specimens did not include lateral reinforcement or crossties in the short direction. The specified yield stress of the vertical bars was 276 MPa while it was 483 MPa for the deformed wires. The specified concrete compressive strength was 27.6 MPa. The vertical and lateral steel ratios, the measured concrete compressive strength, and the applied axial load are presented in table 5-6. Details of Specimens WC1, WC2, and WC3 are shown in figure 5-32.

The wall specimens tested in the second study[9] were approximately one-half scale model of existing pier walls. The typical dimensions of these wall specimens were 3175 mm high, 2400 mm wide, and 25 mm thick. Table 5-6 presents data for the wall specimens. Each specimen was denoted by two letters: the first is either "H" or "L" indicating high or low vertical reinforcement ratio, whereas the second letter "N", "P", or "U" indicates the crosstie distribution as no crossties, partially, or uniformly distributed crossties (Figure 5-33). Two bar diameters, 19 mm and 25 mm were used in the "L", and "H" specimens, respectively with a spacing of 175 mm for all the specimens. The lateral steel was provided using 10 mm bars placed outside the vertical bars with a vertical spacing of 225 mm, and 113 mm in the "U" and "P" specimens, respectively. Deformed D5 wires were used as crossties with a standard shape of 90° and 135° hooks. The specified concrete compressive strength was 27.6 MPa while the steel yield stress for the vertical bars and the deformed wires were 414 MPa, and 620 MPa, respectively.

The test procedure was nearly the same for the wall specimens in both studies[8, 9]. For each specimen a constant axial load was applied first, then the specimen was subjected to three cycles at each displacement ductility level in the weak direction. In the second study[9], the number of cycles was increased for a displacement ductility level of 3.5 or higher to examine the effect of the number of cycles on the deterioration of the wall specimens. The measured yield displacement was taken corresponding to a load equal to 90% and 75% of the ideal load in the first[8] and second[9] study, respectively. The ideal load was calculated from the moment capacity

of the wall section using the ACI code[3] approach in which ε_{cu}, the maximum concrete strain was set to 0.003. The ultimate displacement was assumed to have been reached when the load dropped to 80% of its maximum value.

Because neither LN nor HN specimens had shear reinforcement in the weak direction, the cracked shear stiffness was taken as 10% of the uncracked stiffness (as discussed in Section 5.2.3).

Tables 5-7(a) and 5-7(b) show the break down of the calculated yield and ultimate displacements. The bond slip component at yield in the first study[8] had an average of 12.2% while its averages in the second study[9] were 17.1% and 23.7% for the "L" and "H" specimens, respectively. At ultimate, the average of the bond slip components were 8.9%, 14.4%, and 19.3% for "WC", "L", and "H" specimens, respectively. This trend was expected because higher bond slip component is associated with larger bar diameters. The shear deflection component dropped from 2.1% at yield to 0.4% at ultimate. The flexural displacement component increased at ultimate. Its average was 80.2% at yield and 85.4% at ultimate. This is because the curvature is higher at ultimate than at yield.

The measured and calculated yield and ultimate displacements and displacement ductility are presented in table 5-8. The percentage differences between the measured and calculated values are presented for comparison. An average difference of –0.8% with σ = 7.1% was found between the measured and calculated yield displacement, while it was 0.9% with σ = 8.8% for the ultimate displacement. As for the displacement ductility capacity, the average difference was 1.5% with σ = 8.9%.

Table 5-6 Data for Wall Specimens Tested at UC-Irvine

Specimen	Vertical Steel Ratio	Lateral Steel Ratio	Crosstie Steel Ratio	Measured Concrete Strength	Axial Load
	ρ_v %	ρ_l %	ρ_c %	f'_c (MPa)	kN
WC1[8]	0.56	0.15	NA	26.6	275.8
WC2[8]	0.56	0.15	NA	36.9	275.8
WC3[8]	0.56	0.15	NA	38.6	275.8
LN[9]	1.30	0.25	NA	28.4	880.8
LP[9]	1.30	0.25	0.16%	25.3	880.8
LU[9]	1.30	0.25	0.08%	25.3	880.8
HN[9]	2.30	0.25	NA	32.2	1000.9
HP[9]	2.30	0.25	0.16%	28.4	1000.9
HU[9]	2.30	0.25	0.08%	32.2	1000.9

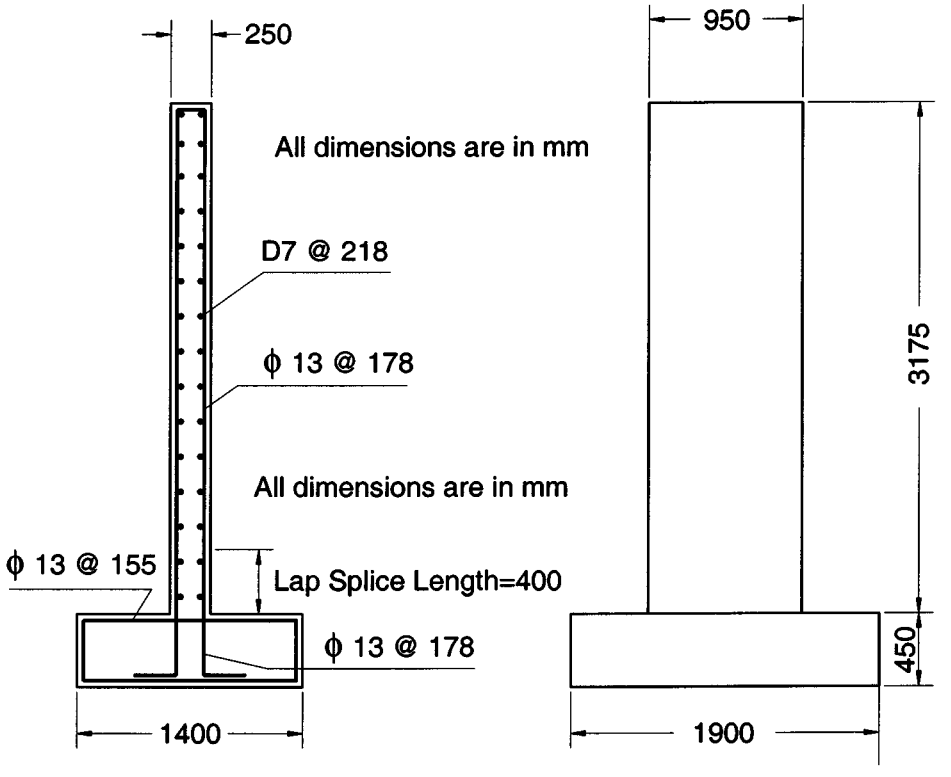

Figure 5-32 Details of Wall Specimens Tested at UC-Irvine (Reference 8)

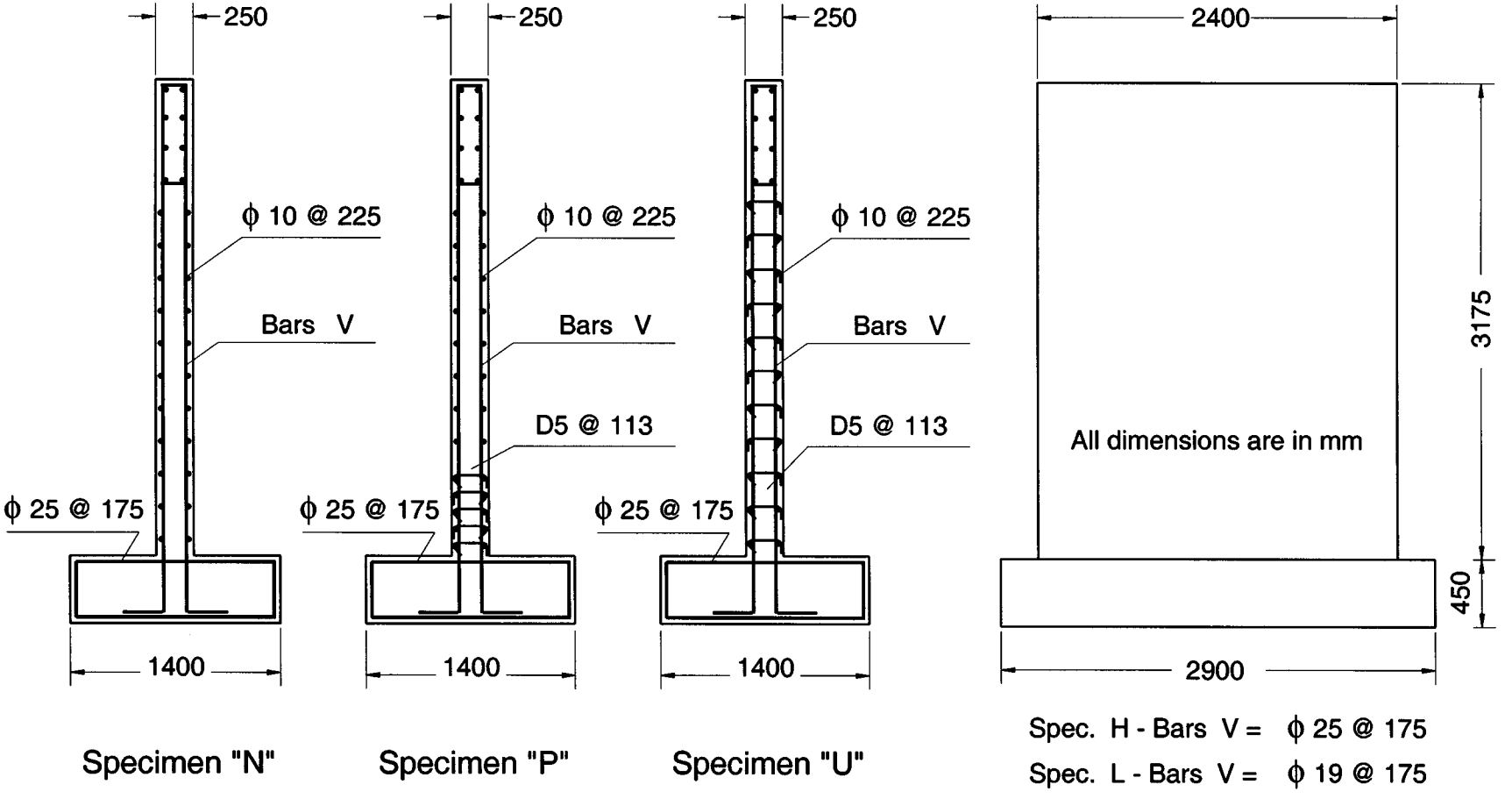

Figure 5-33 Details of Wall Specimens Tested at UC-Irvine (Reference 9)

Table 5-7(a) Calculated Yield Displacement Components for UC-Irvine Wall Specimens

Specimen No.	Calculated Yield Displacement						
	Total Deflection (mm)	Displacement Components (mm)			Displacement Components (%)		
		Flexure	Bond Slip	Shear	Flexure	Bond Slip	Shear
WC1	20.1	17.4	2.3	0.4	86.8	11.3	1.9
WC2	16.4	14.0	2.0	0.5	84.9	11.9	3.2
WC3	16.0	13.5	2.2	0.3	84.5	13.4	2.0
LN	45.7	37.2	7.7	0.9	81.4	16.8	1.9
LP	47.4	38.4	8.2	0.9	80.9	17.2	1.9
LU	47.5	38.4	8.2	0.9	81.0	17.2	1.8
HN	58.4	43.5	13.7	1.3	74.4	23.5	2.1
HP	61.3	45.1	14.9	1.3	73.6	24.3	2.2
HU	58.8	43.9	13.7	1.3	74.6	23.3	2.1

Table 5-7(b) Calculated Ultimate Displacement Components for UC-Irvine Wall Specimens

Specimen No.	Calculated Ultimate Displacement						
	Total Deflection (mm)	Displacement Components (mm)			Displacement Components (%)		
		Flexure	Bond Slip	Shear	Flexure	Bond Slip	Shear
WC1	195.6	178.1	17.1	0.4	91.1	8.7	0.2
WC2	200.8	182.5	18.0	0.4	90.9	8.9	0.2
WC3	203.6	185.0	18.3	0.3	90.9	9.0	0.2
LN	190.4	164.4	25.0	1.0	86.4	13.1	0.5
LP	252.7	214.6	37.0	1.1	84.9	14.7	0.4
LU	247.0	208.1	37.9	1.1	84.2	15.3	0.4
HN	242.9	196.9	44.5	1.5	81.1	18.3	0.6
HP	297.9	234.5	61.8	1.6	78.7	20.7	0.5
HU	260.4	209.6	49.3	1.5	80.5	18.9	0.6

Table 5-8 Comparison of Measured and Calculated Displacement and Displacement Ductility for UC-Irvine Specimens

Specimen No.	Yield Displacement (mm)			Ultimate Displacement (mm)			Displacement Ductility		
	Measured	Calculated	Diff. %	Measured	Calculated	Diff. %	Measured	Calculated	Diff. %
WC1	17.8	20.1	11.5	153.3	195.6	21.7	8.6	9.8	11.5
WC2	16.5	16.4	-0.5	195.0	200.8	2.9	11.8	12.2	3.3
WC3	16.5	16.0	-3.1	195.0	203.6	4.2	11.8	12.7	7.1
LN	46.5	45.7	-1.7	202.5	190.4	-6.4	4.4	4.2	-4.6
LP	44.8	47.4	5.6	275.0	252.7	-8.8	6.1	5.3	-15.3
LU	44.8	47.5	5.7	252.5	247.0	-2.2	5.6	5.2	-8.4
HN	62.0	58.4	-6.2	250.0	242.9	-2.9	4.0	4.2	3.1
HP	66.8	61.3	-8.8	298.8	297.9	-0.3	4.5	4.9	7.8
HU	64.3	58.8	-9.3	260.0	260.4	0.2	4.0	4.4	8.6
Average			-0.8			0.9			1.5
σ			7.1			8.8			8.9

5.5 Concluding Remarks

In this section, an analytical model was developed and evaluated. The Kent and Park[13] model and Mander et al.[19] model were used for the cover concrete and the confined concrete, respectively. To model the steel stress-strain relationship, a modified version of the model proposed by Mander[17] was used. The shear deflection was calculated using Park and Paulay[23] expressions while the bond slip deflection was calculated using a proposed method, which is a modified version of the Wehbe et al.[30] method. To determine the low-cycle fatigue ultimate point, the Manson-Coffin[20] expression and the Linear Damage model of Miner[21] were employed.

The wall specimens tested in this study and in previous studies[8, 9] were analyzed using the analytical model (described in Section 4) for the evaluation purpose. In analyzing the wall specimens that were tested at UNR, the predicted mode of failure for all wall specimens was the same as the observed mode of failure. The overall lateral load-displacement response predicted by the analytical model is reasonable. Good agreement was found when comparing the measured and calculated yield and ultimate displacements and the ductility capacity of the wall specimens that were tested at UNR and UC-Irvine. The average difference between the measured and calculated displacement ductility was 5.7% with a standard deviation σ = 5.1%, and 1.5% with σ = 5.9% for UNR and UC-Irvine wall specimens, respectively.

SECTION 6
PARAMETRIC STUDY

6.1 Introduction

A parametric study was conducted to extend the seismic response study to bridge pier walls that were not tested experimentally. The analysis was performed using the computer program that was developed in this study (Section 5). A practical approach was developed to calculate the required confinement reinforcement in the plastic hinge zones of bridge pier walls based on the desired displacement ductility level and to evaluate the displacement ductility capacity of an existing pier wall. A comparison between the proposed approach and other available methods[3, 2, 6, 4, 30] was performed. As was mentioned in Section 1, the pier walls in the Moribe Viaduct failed during the 1995 Hanshin Awaji earthquake. The proposed model was used to estimate the ductility capacity of the walls in that bridge. This section summarizes the parametric study, interpretation of results, the proposed approach, and the analysis of the Moribe Viaduct.

6.2 Analysis of the Wall Cases

To perform the parametric study, 120 different pier walls were analyzed using the computer program "PIER" presented in Section 5. The parameters included in this study were the ratio of the wall height to its thickness, the vertical steel ratio, the confinement steel ratio, and the axial load index. The selected ranges for the parameters were based on the data found in the survey (Section-2). Table 6-1 includes the range of the parameters in the survey and the selected values for the parametric study. The ratio of the wall height to its thickness ranged from 2 to 15 to represent wide range of short to high walls. Walls with higher ratio were excluded because of their very low population in the database. Four vertical steel ratios were selected between 0.5 % and 2.5 % to model pier walls with low to high vertical steel ratios, respectively. The confinement reinforcement (transverse steel or crossties) ratio ranged from 0.1% to 0.4%. The transverse and crosstie steel ratios were taken equal to each other. Two values of 5% and 10% were chosen for the axial load index. An index of 10% is believed to be the upper bound for bridge pier walls and should account for extra loads due to the vertical earthquake component.

The wall cross section was taken as 300 mm x 1500 mm. Tables B-1(a), B-1(b), and B-1(c) (Appendix B) present data for all the cases in the parametric study.

A modified version of the Mander et al.[19] model was adopted to model the confined concrete. The concrete compressive strength was taken as 31 MPa, while the steel yield stress was taken as 448.2 MPa. The yield strain, strain hardening, and ultimate strain were taken as 0.0022, 0.01, and 0.1, respectively. The ultimate steel stress was assumed as 620 MPa.

Table 6-1 The Selected Values for the Parameters

Parameter	Units	Survey Range		Selected Values
		Minimum	Maximum	
Wall height to thickness (H / t)	Ratio	2.75	18.22	2, 4, 7, 10, 15
Vertical steel ratio (ρ_v)	%	0.21	3.77	0.5, 1.0, 1.75, 2.5
Confinement steel ratio (ρ_l & ρ_c)	%	0.01	1.02	0.1, 0.25, 0.4
Axial load index ($P / (A_g . f'_c)$)	%	0.9	6.7	5, 10

6.3 Results of the Parametric Study

Details of the analysis results for all cases included in the parametric study are presented in Appendix B. Tables B-2(a), B-2(b), and B-2(c) contain the total displacements and the break down of the displacements due to flexure, bond slip, and shear at yield and ultimate for each case. Figures 6-1 through 6-6 present the relationship between the yield displacement, Δ_y, and the ratio of the wall height to thickness, H/t, at different values of axial load index and confinement reinforcement ratio. The ultimate displacement vs. H/t at different confinement steel ratios and axial load index values are shown in figures 6-7 through 6-12.

For cases with the same axial load index and confinement steel ratio, the deflection due to flexure increased when the ratio of the wall height to thickness, H/t, was increased, since the flexural deflection is obtained by integrating the curvature along the wall height. This increased the percentage contribution of the flexural deformation to the total lateral displacement and reduced that of the bond slip and shear deformation. When the vertical steel ratio, ρ_v, was

increased for cases with the same H/t and confinement reinforcement, the deflections due to flexure and shear at the yield point were increased while the displacement ductility capacity, μ_d, was reduced. This is because high yield curvature and lateral load capacity are associated with high vertical steel ratio. When failure was controlled by compression crushing of concrete, high ρ_v reduced the ultimate deflection. On the contrary, high ρ_v increases the ultimate displacement when failure is controlled by low-cycle fatigue. Nevertheless the displacement ductility capacity dropped for both failure modes because of relatively high yield displacement (the denominator in the ductility ratio). A similar trend was observed when the axial load index was increased from 5% to 10%.

The relationship between the displacement ductility capacity, μ_d, and H/t ratio is presented in figures 6-13 through figure 6-18. As expected, wall cases with higher vertical steel ratios exhibited lower displacement ductility capacity than that of walls with low vertical steel ratios. When the confinement reinforcement ratio was 0.1% (lower than 0.25%, the minimum required by AASHTO[2] and Caltrans[6]) and the axial load index was 5%, the displacement ductility capacity was nearly constant for walls with the same vertical steel ratio and H/t = 4 or higher (Figure 6-13). On the contrary, in walls with H/t $\leq$ 4, the displacement ductility capacity was sensitive to H/t ratio. Another important observation in figure 6-13 is that, despite the very low amount of confinement steel, ductile behavior is expected for walls as long as the vertical steel ratio is 1% or less. This indicates that it is the relative value of the confinement steel and the vertical steel that affects the ductility capacity. When the axial load index was raised from 5% to 10 %, the displacement ductility capacity dropped and was nearly the same for wall cases with H/t = 4 or higher (Figure 6-16).

The displacement ductility capacity was improved considerably when the confinement steel ratio was raised from 0.1% to 0.25%, particularly for high vertical steel ratios (Figures 6-13, 6-14, 6-16, and 6-17). The change in μ_d was not that significant for walls with an axial load index of 5% when the confinement steel ratio was changed from 0.25 to 0.4 % (Figures 6-14 and 6-15). When the axial load index was 10% and the vertical steel ratio was equal to 1.75% or more, μ_d was enhanced significantly by increasing the confinement reinforcement from 0.25% to 0.4% (Figures 6-17 and 6-18).

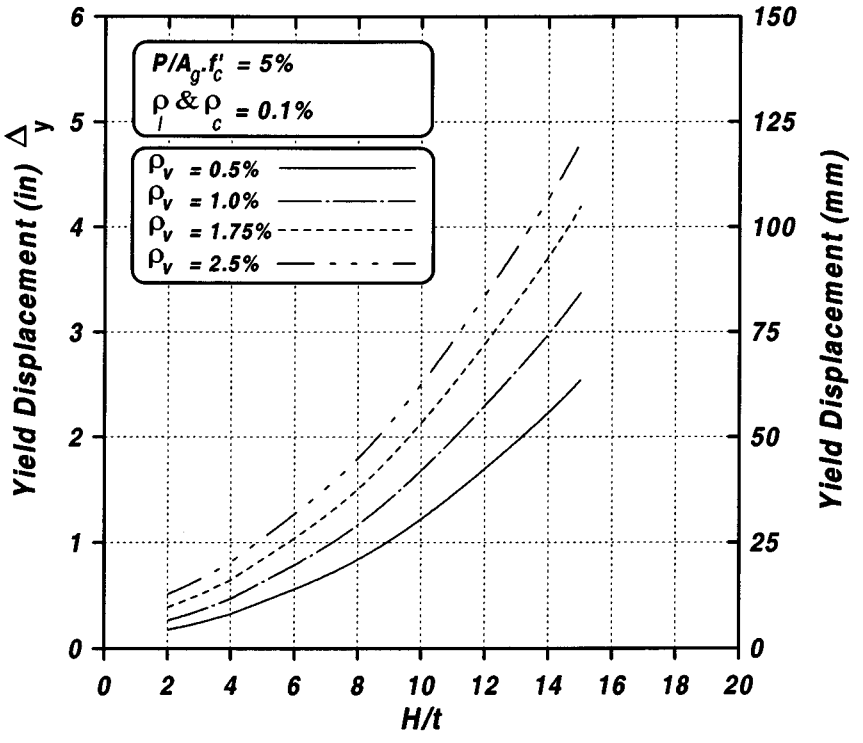

Figure 6-1 Yield Displacement vs. H/t for $P/(f'_c.A_g)$= 5% and ρ_l&ρ_c= 0.1%

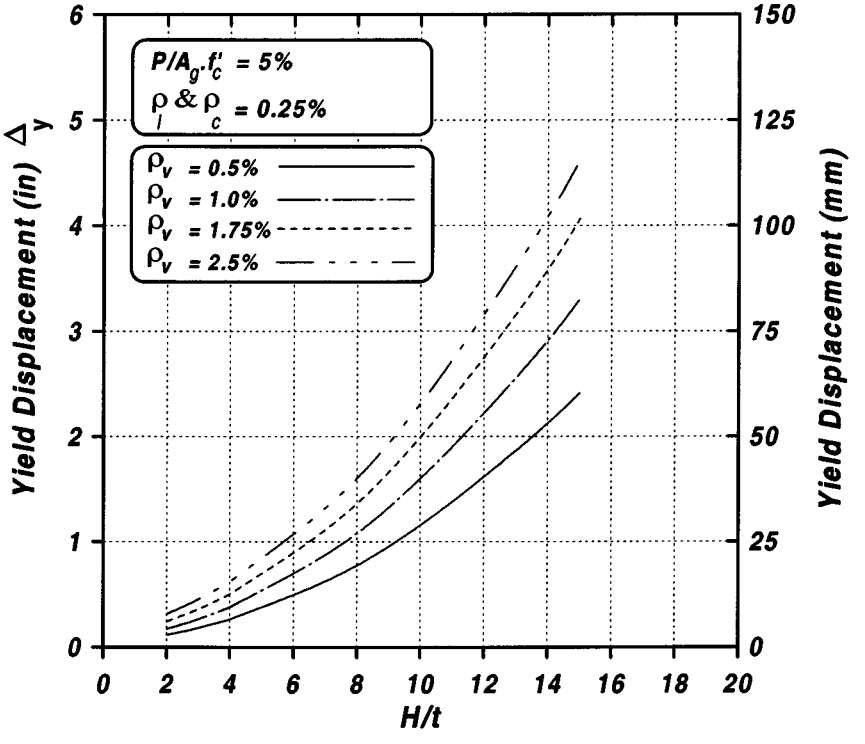

Figure 6-2 Yield Displacement vs. H/t for $P/(f'_c.A_g)$= 5% and ρ_l&ρ_c= 0.25%

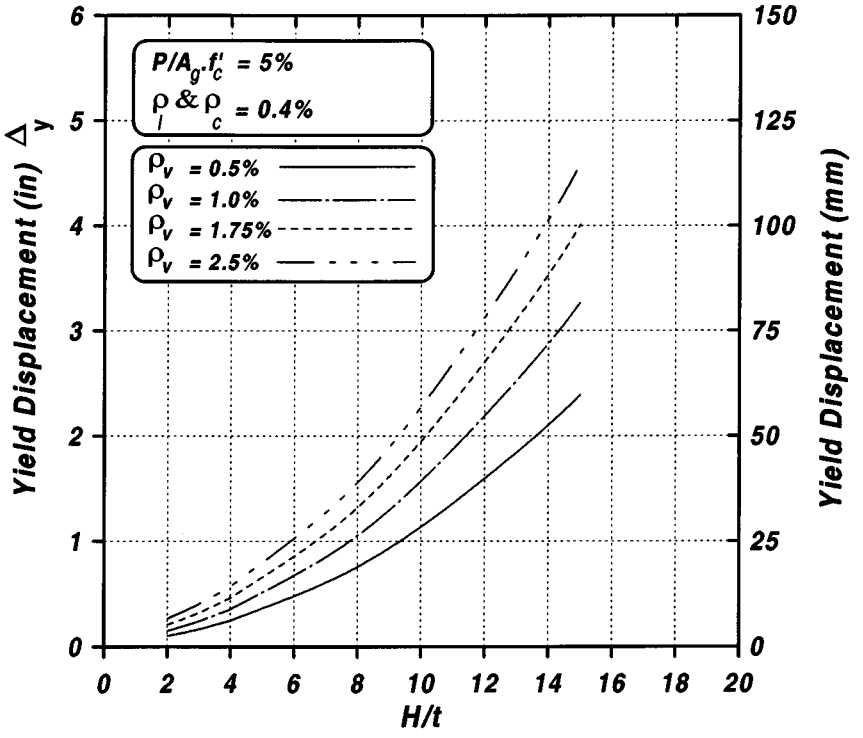

Figure 6-3 Yield Displacement vs. H/t for $P/(f'_c.A_g)$= 5% and ρ_l&ρ_c= 0.4%

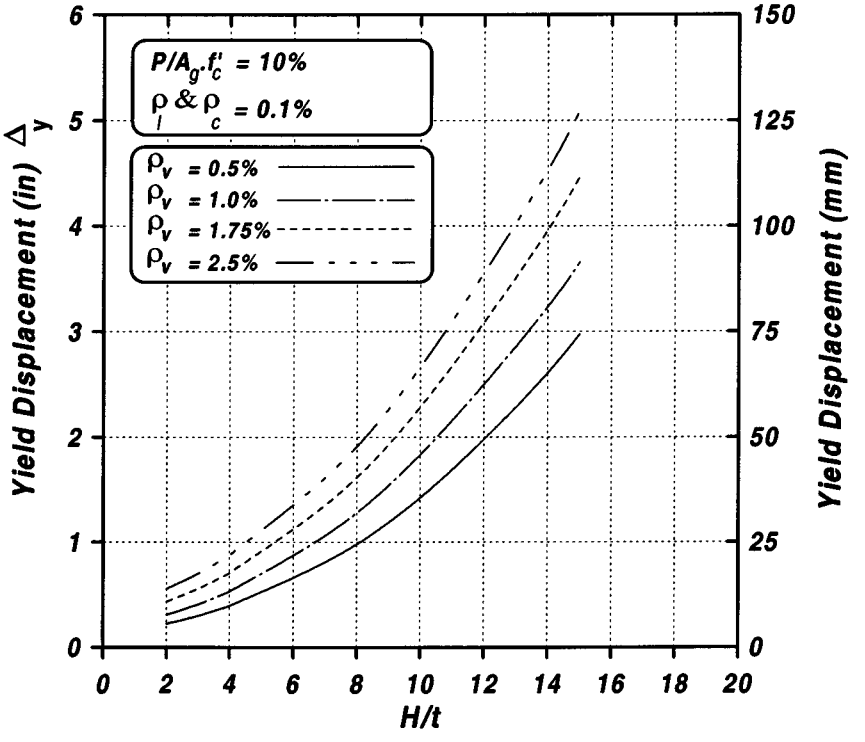

Figure 6-4 Yield Displacement vs. H/t for $P/(f'_c.A_g)$= 10% and ρ_l&ρ_c= 0.1%

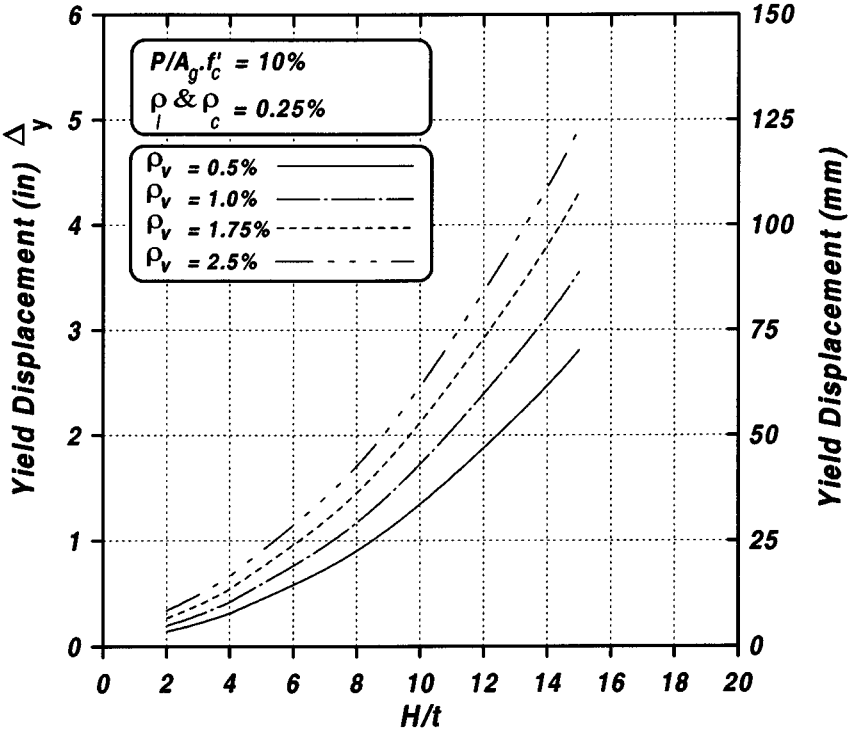

Figure 6-5 Yield Displacement vs. H/t for $P/(f'_c.A_g)$= 10% and ρ_l&ρ_c= 0.25%

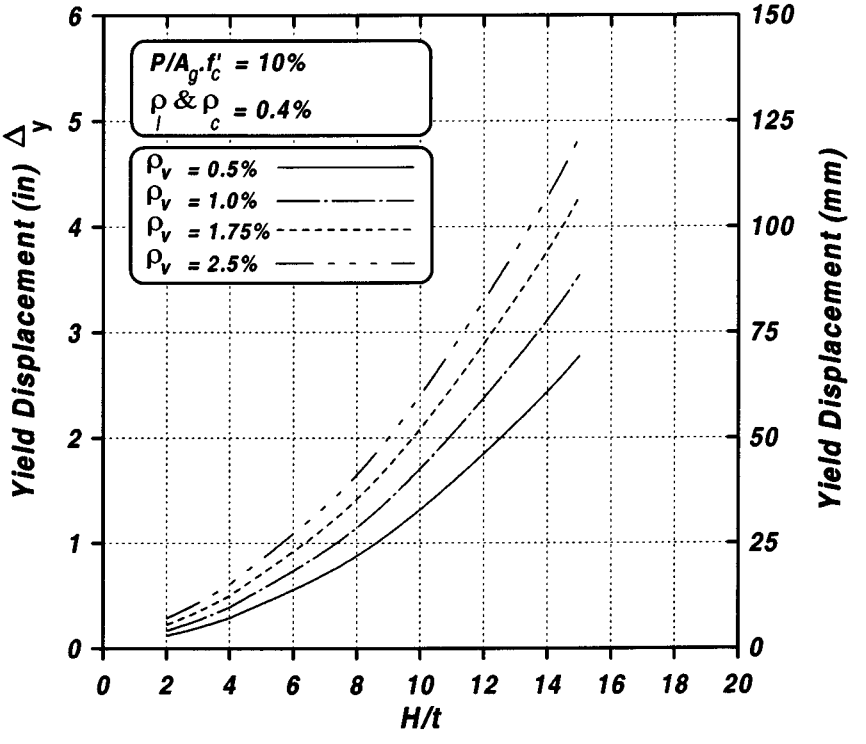

Figure 6-6 Yield Displacement vs. H/t for $P/(f'_c.A_g)$= 10% and ρ_l&ρ_c= 0.4%

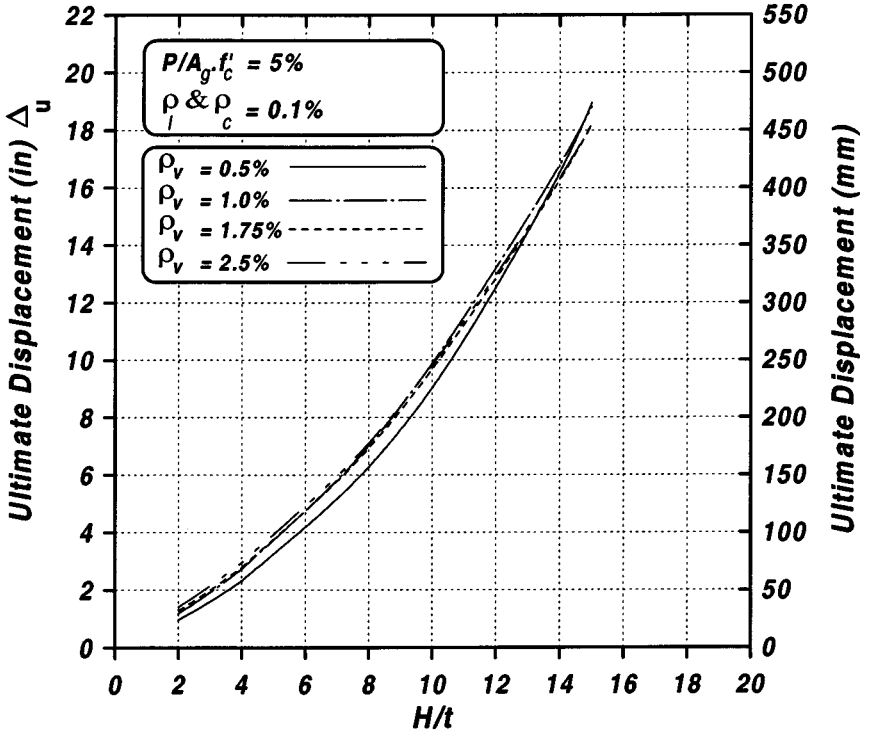

Figure 6-7 Ultimate Displacement vs. H/t for $P/(f'_c.A_g)$= 5% and ρ_l&ρ_c= 0.1%

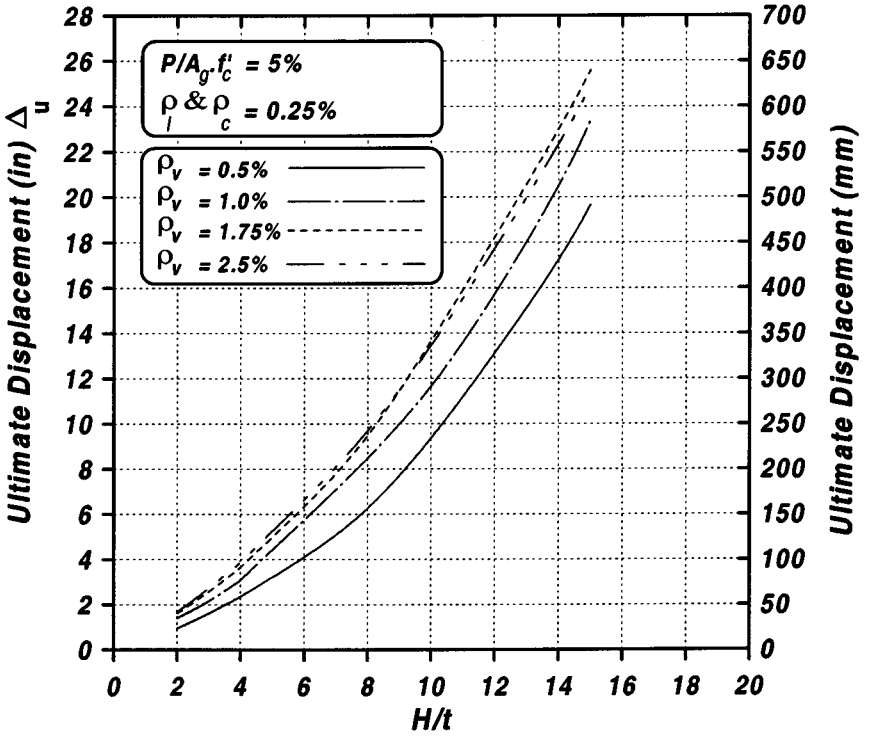

Figure 6-8 Ultimate Displacement vs. H/t for $P/(f'_c.A_g)$= 5% and ρ_l&ρ_c= 0.25%

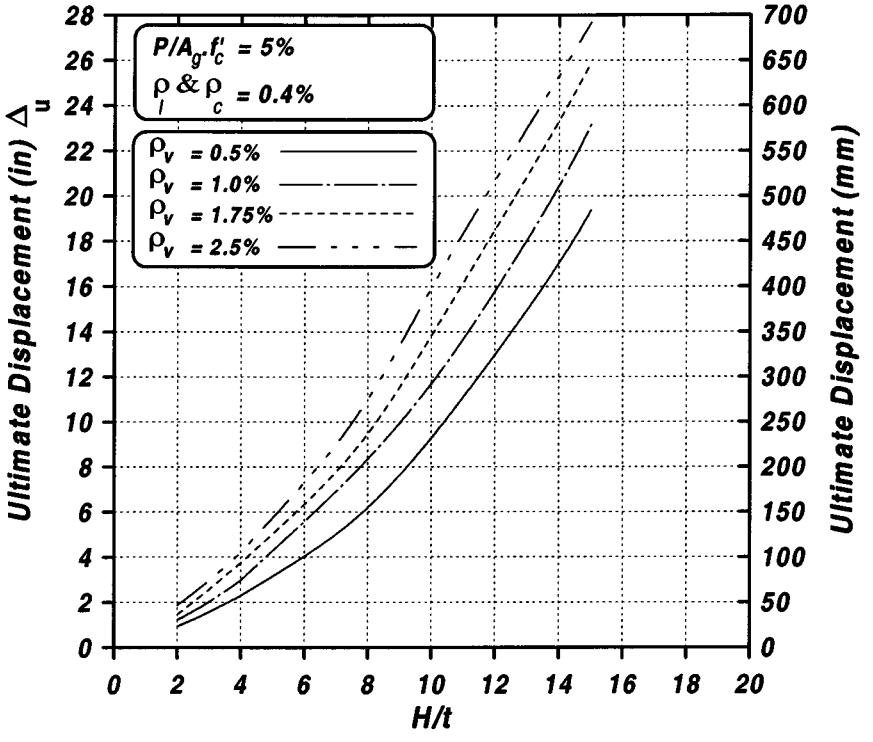

Figure 6-9 Ultimate Displacement vs. H/t for $P/(f'_c.A_g)$= 5% and ρ_l&ρ_c= 0.4%

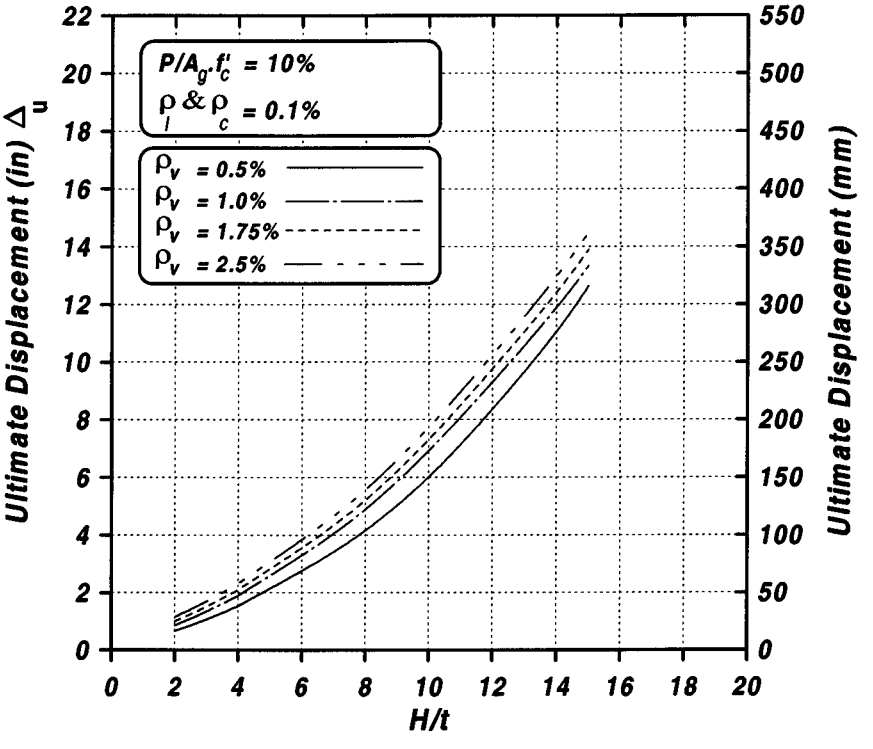

Figure 6-10 Ultimate Displacement vs. H/t for $P/(f'_c.A_g)$= 10% and ρ_l&ρ_c= 0.1%

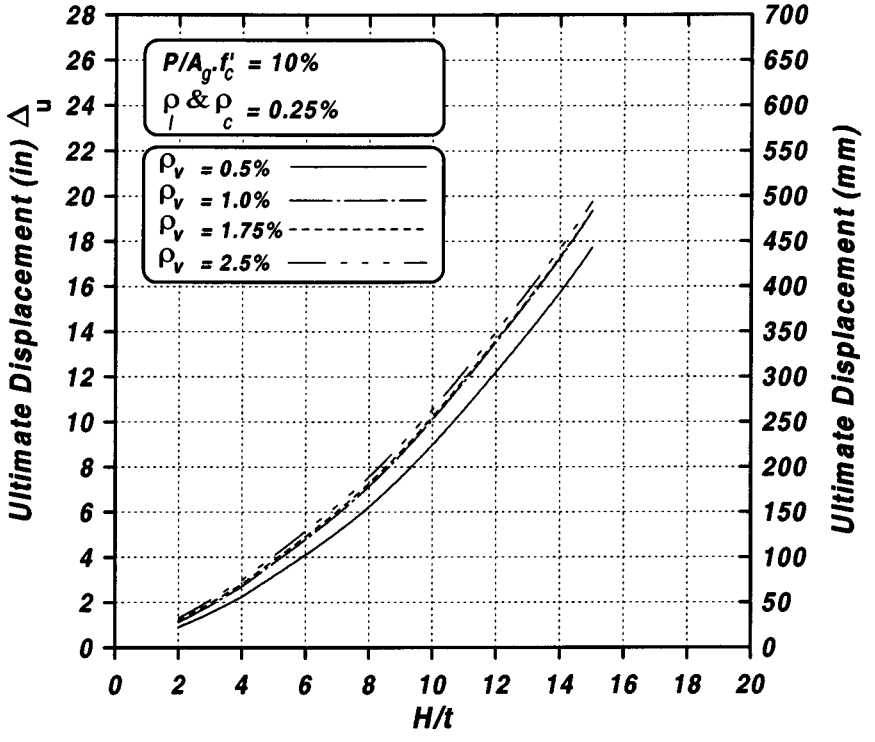

Figure 6-11 Ultimate Displacement vs. H/t for $P/(f'_c.A_g)$= 10% and ρ_l&ρ_c= 0.25%

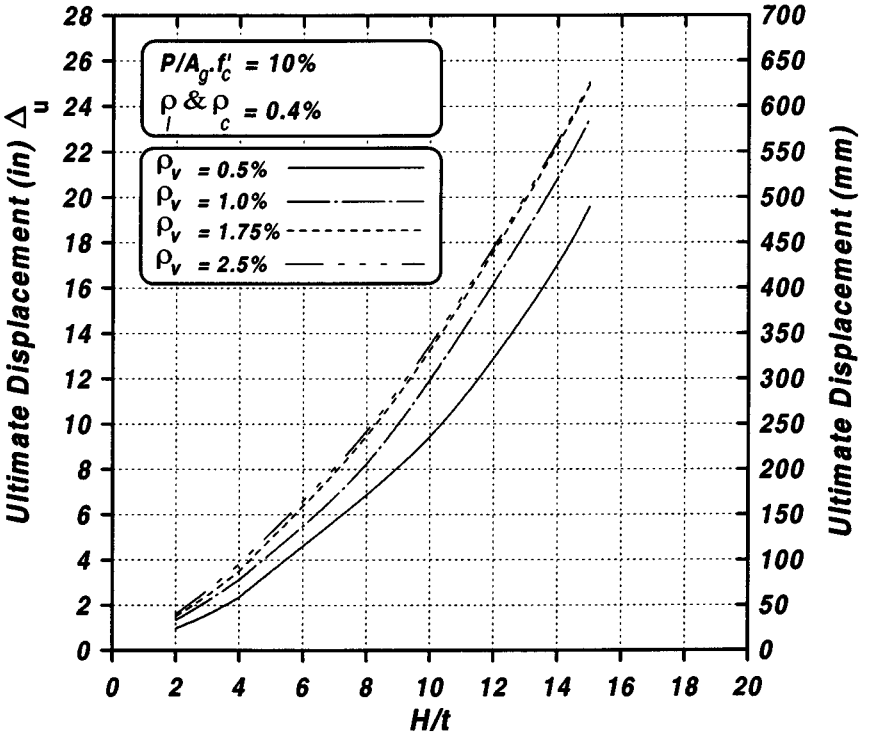

Figure 6-12 Ultimate Displacement vs. H/t for $P/(f'_c.A_g)$= 10% and ρ_l&ρ_c= 0.4%

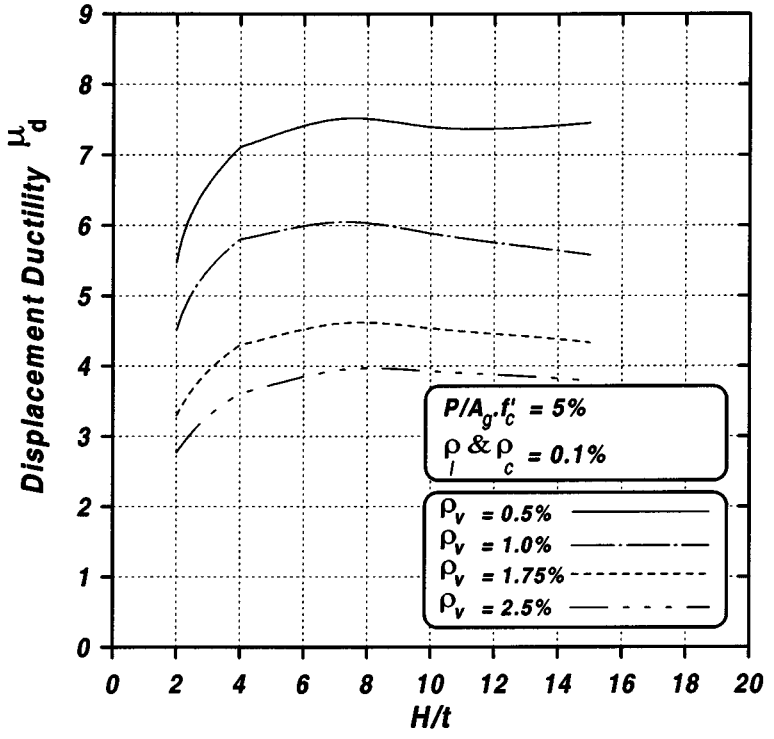

Figure 6-13 Ductility vs. H/t for $P/(f'_c.A_g)$= 5% and ρ_l&ρ_c= 0.1%

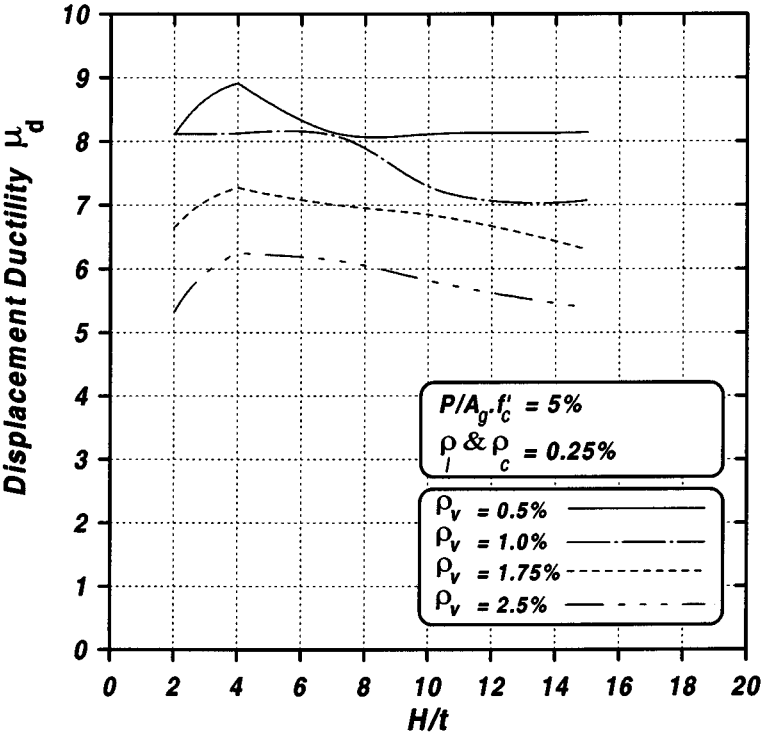

Figure 6-14 Ductility vs. H/t for $P/(f'_c.A_g)$= 5% and ρ_l&ρ_c= 0.25%

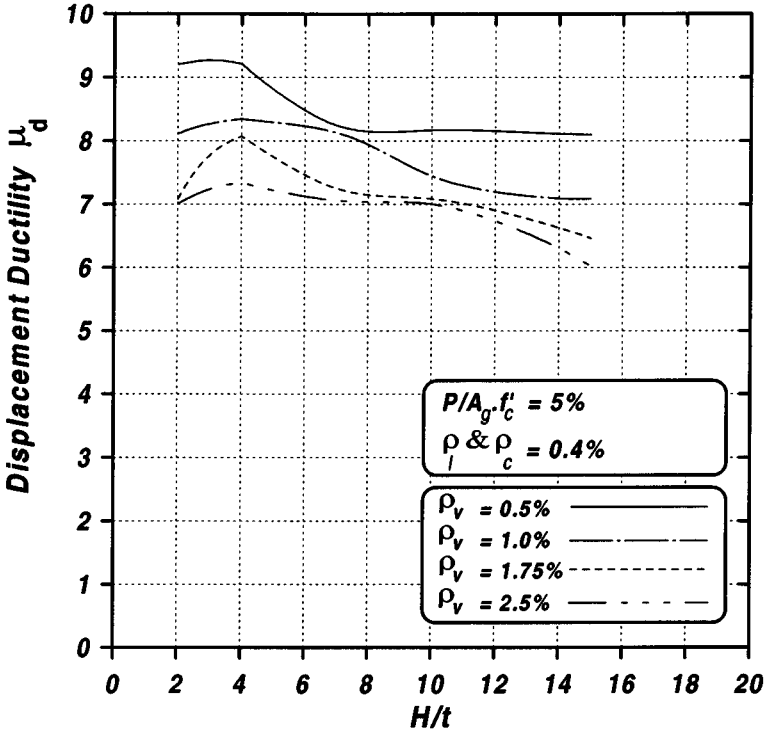

Figure 6-15 Ductility vs. H/t for $P/(f'_c.A_g)$= 5% and ρ_l&ρ_c= 0.4%

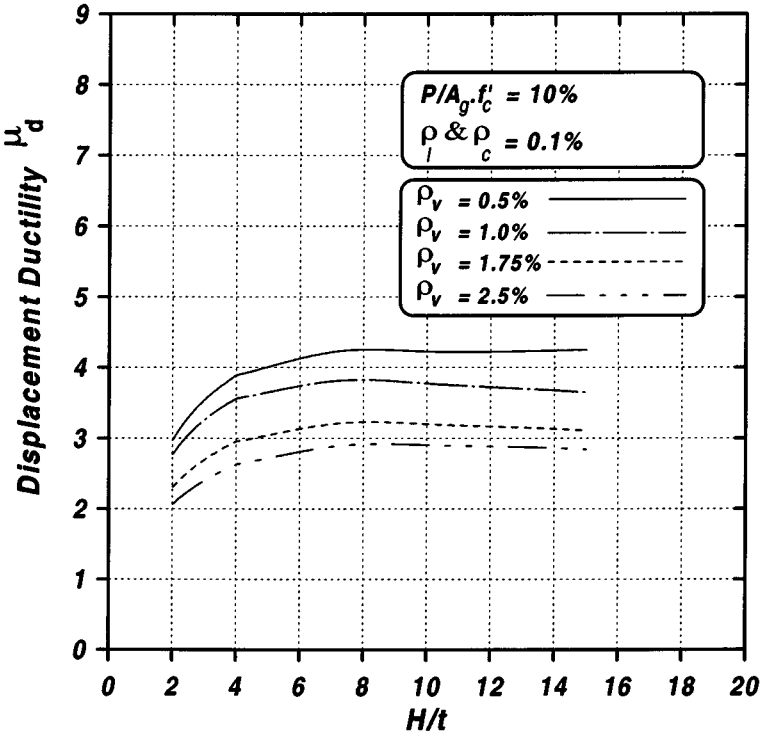

Figure 6-16 Ductility vs. H/t for $P/(f'_c.A_g)$= 10% and ρ_l&ρ_c= 0.1%

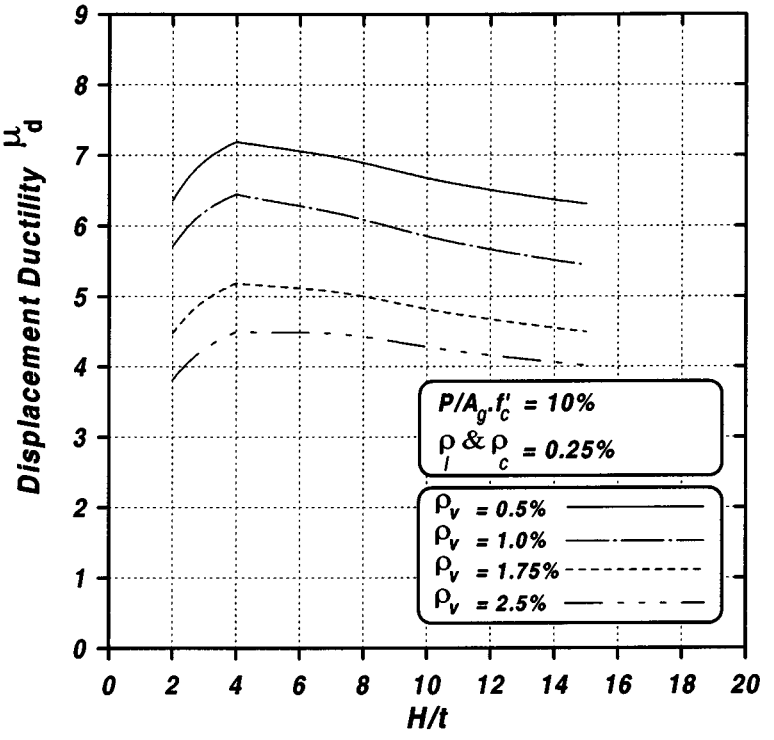

Figure 6-17 Ductility vs. H/t for $P/(f'_c.A_g)$= 10% and ρ_l&ρ_c= 0.25%

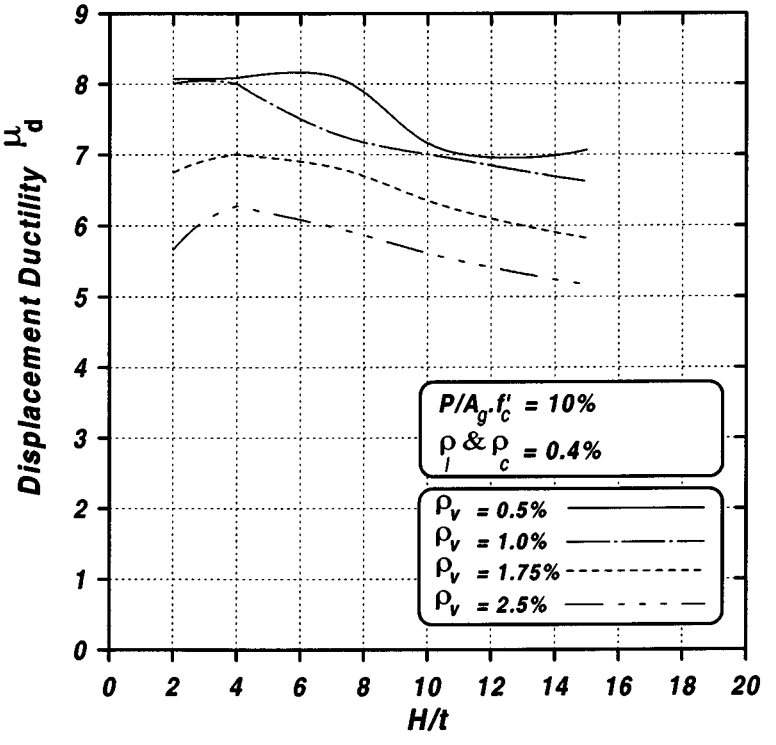

Figure 6-18 Ductility vs. H/t for $P/(f'_c.A_g)$= 10% and ρ_l&ρ_c= 0.4%

6.4 Design Implications

Current codes[3, 2, 6, 4] require a certain amount of confinement reinforcement in the plastic hinge zone to enhance the displacement ductility capacity of reinforced concrete columns. A recent study[30] introduced an equation to relate the attainable displacement ductility to the amount of lateral steel in rectangular reinforced concrete columns. Based on the results of the parametric study discussed in previous sections, a new approach to calculate the ductility of pier walls as a function of the ratio of confinement and vertical steel was developed. A comparison between the available equations and the proposed approach was performed using the wall specimens tested in this study (Section 4) and other typical pier wall examples.

6.4.1 Proposed Relationship between the Confinement Steel and Ductility

A proposed approach, which is based on the results of the parametric study to relate the confinement reinforcement to the displacement ductility capacity of pier walls, is presented in this section. The confinement steel ratio was normalized relative to the vertical steel ratio and used in the equation. Figures 6-19 through 6-28 show the relationship of the displacement ductility capacity and the normalized confinement steel ratio to the vertical steel ratio. Note that in all the analyses, the lateral and crosstie steel ratios were assumed to be the same. A log best fit approach was used for each axial load index and H/t ratio. The log curve is given by the following equation:

$$\mu_d = a + b\left[\mathrm{Ln}\left(\frac{\rho_t}{\rho_v}\right)\right] \qquad (6\text{-}1)$$

where:

ρ_t = Confinement steel ratio (in this study taken equal to ρ_l or ρ_c)

a, b = Fitting constants

Equation 6-1 was developed for ρ_t/ρ_l in the range of 0.04 and 0.8. The second term in the right hand side of Equation 6-1 is usually negative and reduces the resultant μ_d. Table 6-2 presents the fitting constants (a, b) for each axial load index and H/t ratio. For an axial load index of 5%, the

first constant, a, had an average of 9.6 with standard deviation, σ, of 0.63. The constant had an average of 8.35 with σ = 0.6 for 10% axial load index. The constant, b, had an average of 1.7 with σ = 0.33 and an average of 1.8 with σ = 0.28 corresponding to an axial load index of 5% and 10%, respectively. The low standard deviation enabled simplifying the equations and reducing their number to two, one for each axial load index. Figures 6-29 and 6-30 show the relationships between the displacement ductility capacity and the normalized steel ratio for each axial load index. Note that the effect of H/t ratio is implicitly included in the data. The following equations were developed for the best fit for each axial load index:

For axial load index of 5%:

$$\mu_d = 9.6 + 1.7\mathrm{Ln}\left(\frac{\rho_t}{\rho_v}\right) \tag{6-2}$$

For axial load index of 10%:

$$\mu_d = 8.35 + 1.8\mathrm{Ln}\left(\frac{\rho_t}{\rho_v}\right) \tag{6-3}$$

A parallel curve of μ_d - σ to the μ_d vs. ρ_t/ρ_v relationship (Figures 6-29 and 6-30) was plotted to identify the lower bound of the displacement ductility capacity. The lower bound curve can be used to design the confinement steel and to determine a conservative estimate of μ_d for pier walls.

For axial load index of 5%:

$$\mu_d = 8 + 1.7\mathrm{Ln}\left(\frac{\rho_t}{\rho_v}\right) \tag{6-4}$$

For axial load index of 10%:

$$\mu_d = 6.6 + 1.8\mathrm{Ln}\left(\frac{\rho_t}{\rho_v}\right) \tag{6-5}$$

Table 6-2 Fitting Constants

Figure (Curve)	Axial Load Index ($P/A_g.f'_c$) %	H/t ratio	a	B
6-19 (best fit)	5	2	10.12	2.20
6-20 (best fit)	5	4	10.37	1.93
6-21 (best fit)	5	7	9.48	1.52
6-22 (best fit)	5	10	9.13	1.44
6-23 (best fit)	5	15	8.91	1.50
6-24 (best fit)	10	2	8.69	2.18
6-25 (best fit)	10	4	8.98	2.02
6-26 (best fit)	10	7	8.60	1.84
6-27 (best fit)	10	10	7.92	1.60
6-28 (best fit)	10	15	7.54	1.53
6-29 (best fit)	5	All ratios	9.60	1.70
6-29 (lower bound)	5	All ratios	8.0	1.70
6-30 (best fit)	10	All ratios	8.35	1.80
6-30 (lower bound)	10	All ratios	6.60	1.80

Equations 6-4 and 6-5 are plotted in figure 6-31. The proposed approach can be used to design the confinement reinforcement or to estimate the displacement ductility capacity of given pier walls using Equations 6-4 and 6-5 or the design curve (Figure 6-31) as follows:

Design of confinement reinforcement:

1- Determine the axial load index based on the axial load, probable concrete strength, and cross section dimensions

2- Using a performance based design method, estimate the desired level of ductility

3- Using the curves in figure 6-31determine ρ_t/ρ_v. Use linear interpolation for axial load indices between 5% and 10%

4- Design the transverse steel and crossties using ρ_t for each

5- If the axial load index is less than 5%, use the 5% curve for a conservative estimate of ρ_t/ρ_v

Estimate of the displacement ductility capacity:

1- Determine the axial load index based on the axial load, probable concrete strength, and cross section dimensions

2- Determine ρ_t as the average of lateral and crosstie steel ratio

3- Determine ρ_t/ρ_v

4- Using ρ_t/ρ_v and the appropriate curve for the axial load index, determine the displacement ductility. Use linear interpolation for axial load indices between 5% and 10%

5- If the axial load index is less than 5%, use the 5% curve for a conservative estimate of μ_d

6.4.2 Transverse Steel Design Methods

Seismic design of pier walls in the weak direction is based on the provisions for rectangular columns. A summary of existing methods is presented in this section, followed by a comparison between the proposed and other methods.

6.4.2.1 American Concrete Institute (ACI)

The American Concrete Institute[3] requires a minimum confinement hoop and crosstie area to be the greater of:

$$A_{sh} = 0.3sh_c \frac{f'_c}{f_y}\left[\left(\frac{A_g}{A_{ch}}\right)-1\right] \tag{6-6}$$

$$A_{sh} = 0.09sh_c \frac{f'_c}{f_{yh}} \tag{6-7}$$

where:

s = Spacing of transverse reinforcement along the member axis

h_c = Dimension of column core measured center-to-center of confining reinforcement

A_g = Sectional gross area

A_{ch} = Cross-section area measured out-to-out of transverse reinforcement

f'_c = Specified concrete compressive strength

f_{yh} = Specified steel yield stress for lateral reinforcement

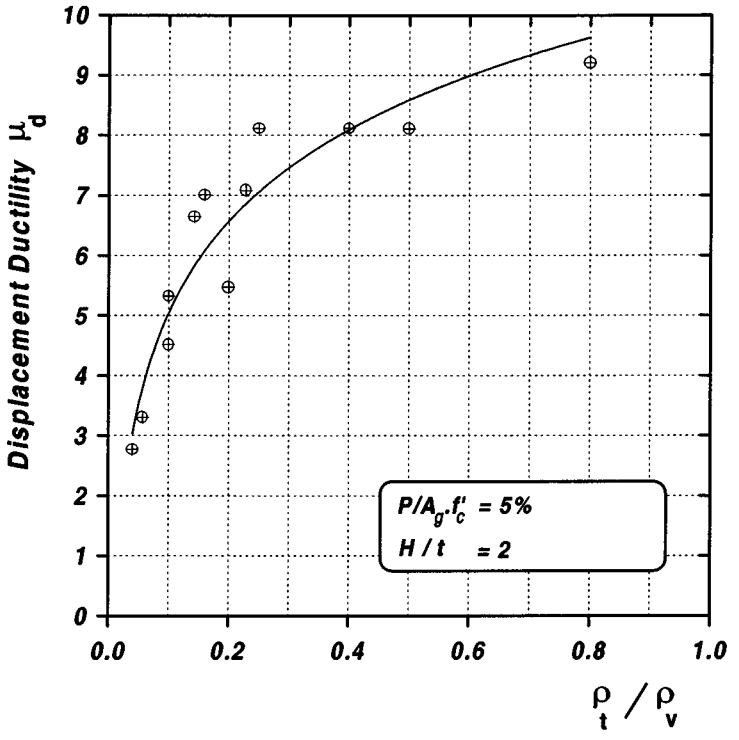

Figure 6-19 Displacement Ductility vs. ρ_t/ρ_v for $P/(f'_c.A_g)$ = 5% and H/t = 2

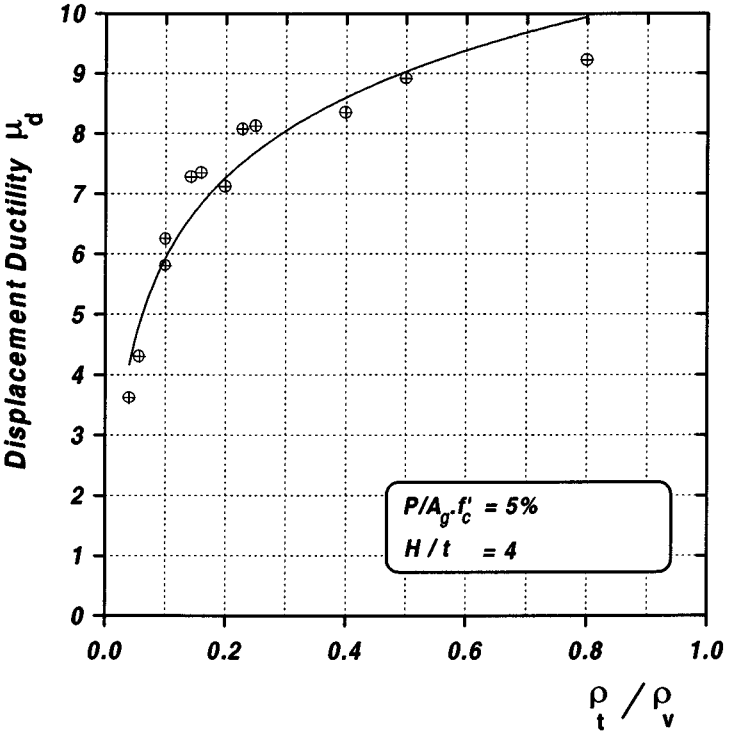

Figure 6-20 Displacement Ductility vs. ρ_t/ρ_v for $P/(f'_c.A_g)$ = 5% and H/t = 4

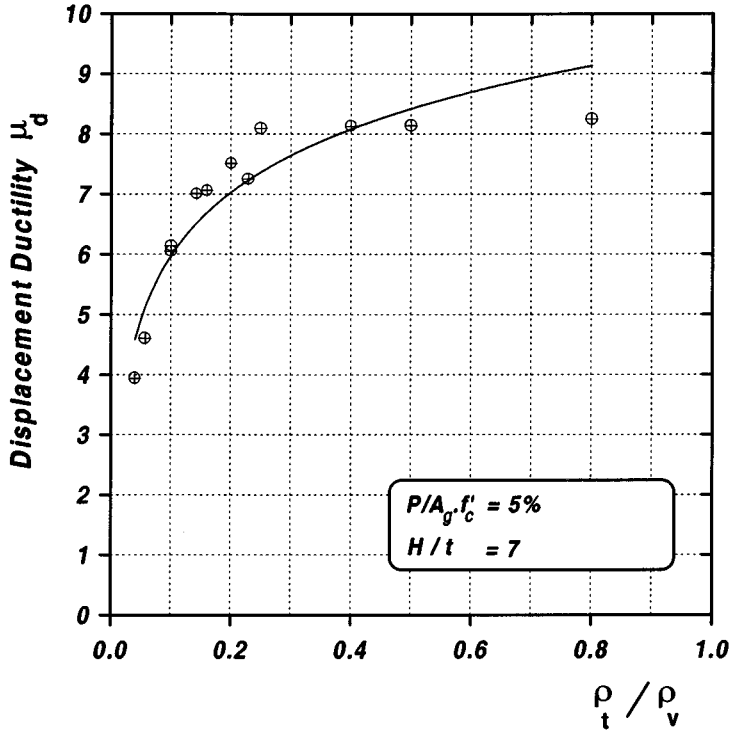

Figure 6-21 Displacement Ductility vs. ρ_t/ρ_v for $P/(f'_c.A_g) = 5\%$ and H/t = 7

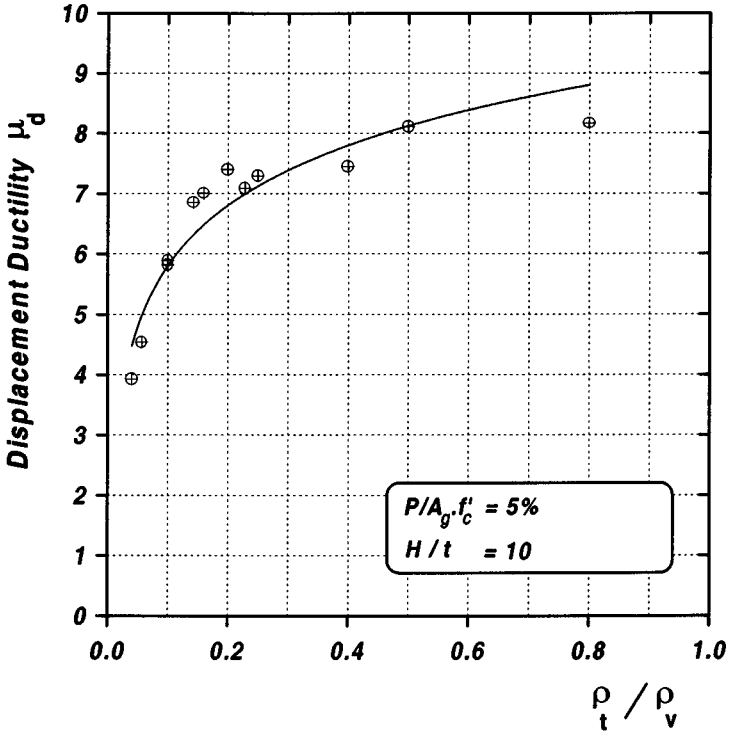

Figure 6-22 Displacement Ductility vs. ρ_t/ρ_v for $P/(f'_c.A_g) = 5\%$ and H/t = 10

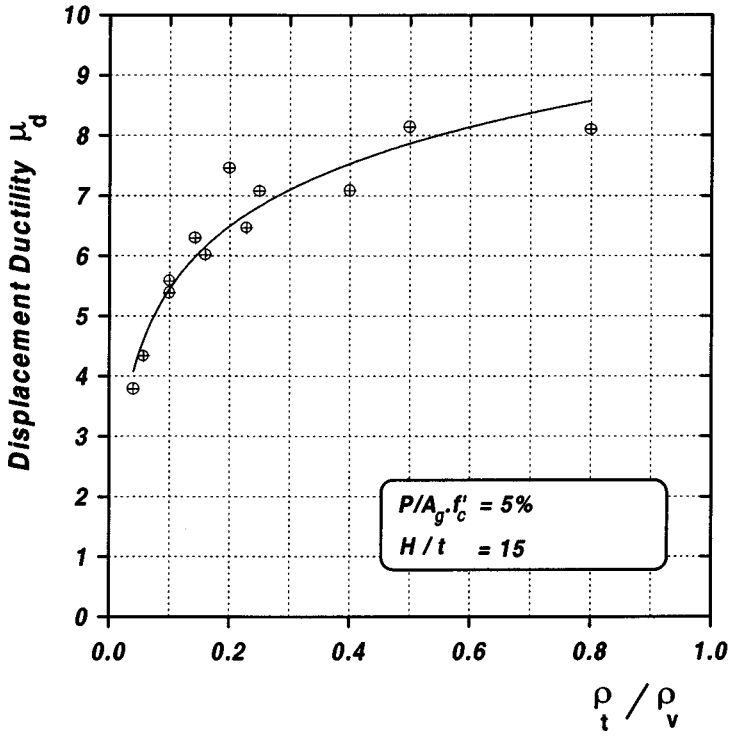

Figure 6-23 Displacement Ductility vs. ρ_t/ρ_v for $P/(f'_c.A_g) = 5\%$ and H/t = 15

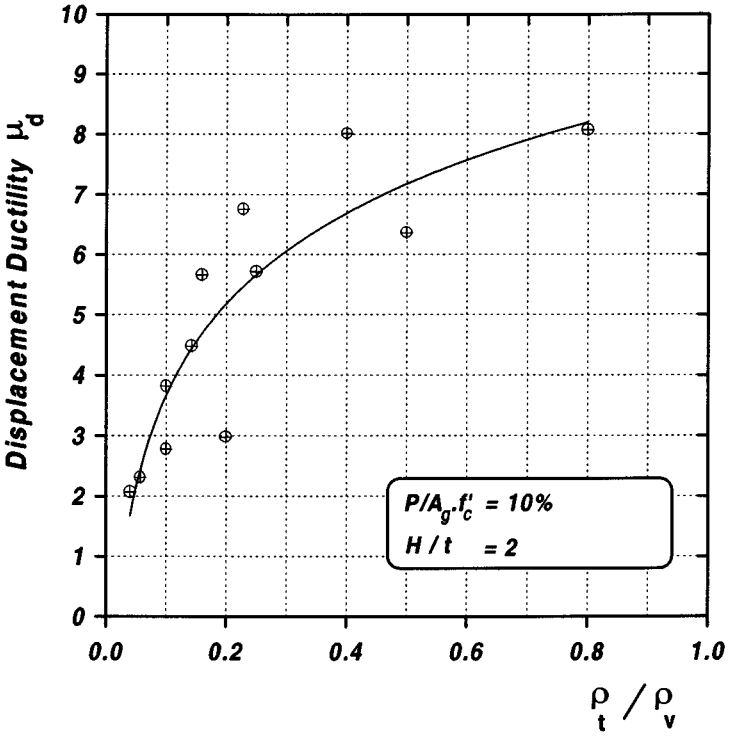

Figure 6-24 Displacement Ductility vs. ρ_t/ρ_v for $P/(f'_c.A_g) = 10\%$ and H/t = 2

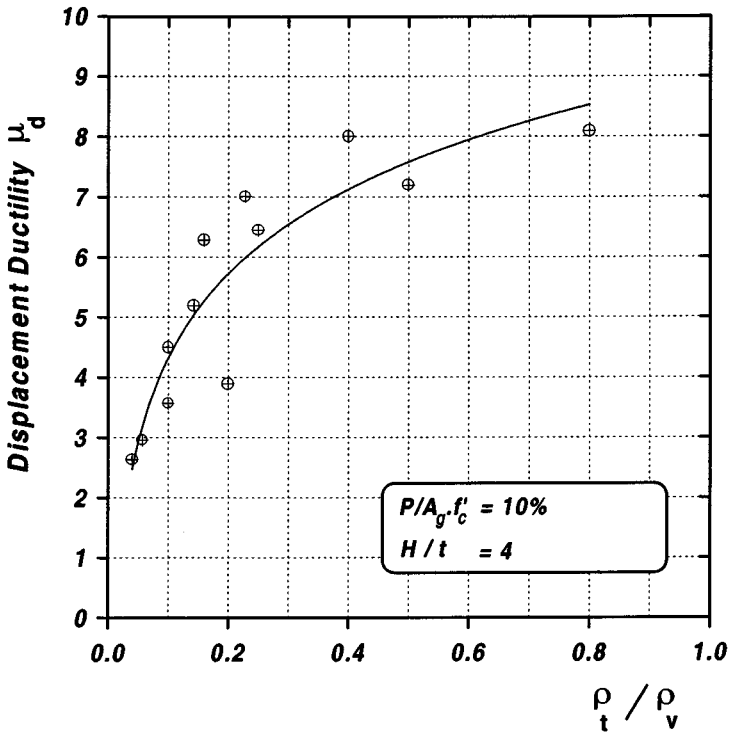

Figure 6-25 Displacement Ductility vs. ρ_t/ρ_v for $P/(f'_c.A_g) = 10\%$ and H/t = 4

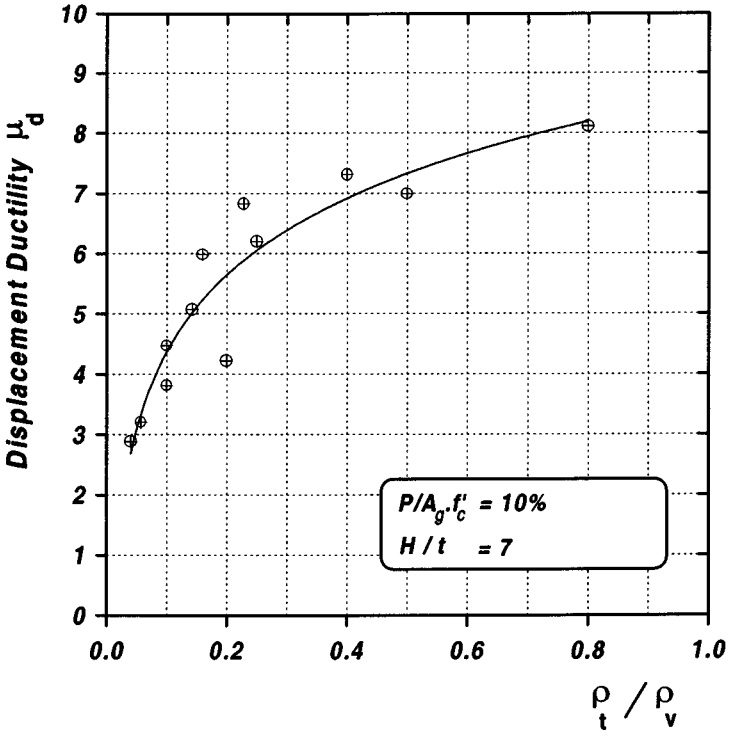

Figure 6-26 Displacement Ductility vs. ρ_t/ρ_v for $P/(f'_c.A_g) = 10\%$ and H/t = 7

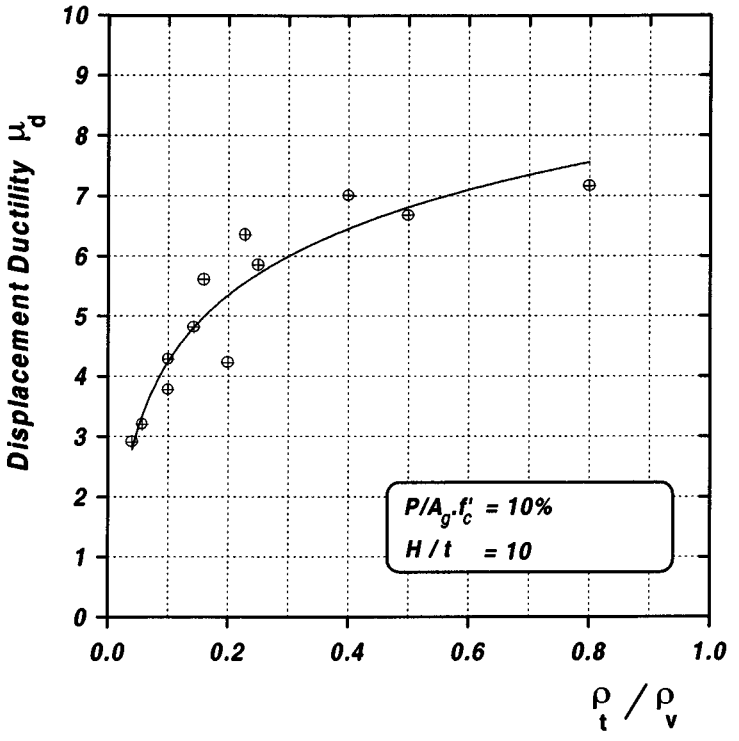

Figure 6-27 Displacement Ductility vs. ρ_t/ρ_v for $P/(f'_c.A_g)$ = 10% and H/t = 10

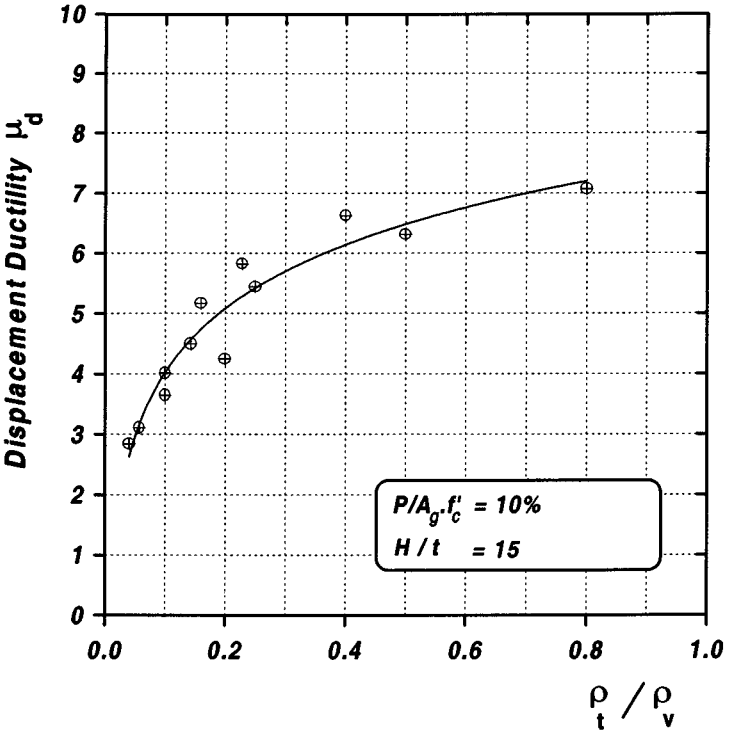

Figure 6-28 Displacement Ductility vs. ρ_t/ρ_v for $P/(f'_c.A_g)$ = 10% and H/t = 15

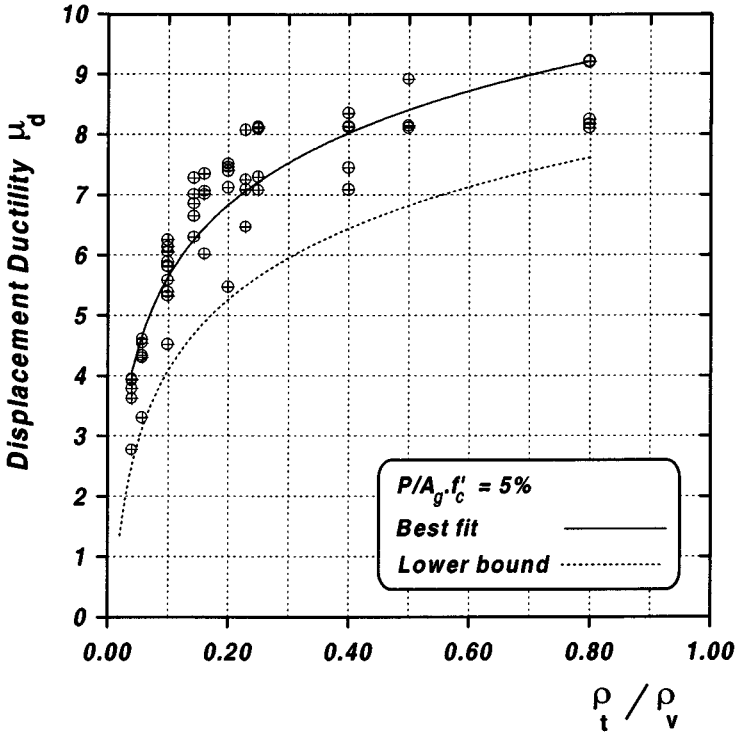

Figure 6-29 Displacement Ductility vs. ρ_t/ρ_v for $P/(f'_c.A_g) = 5\%$

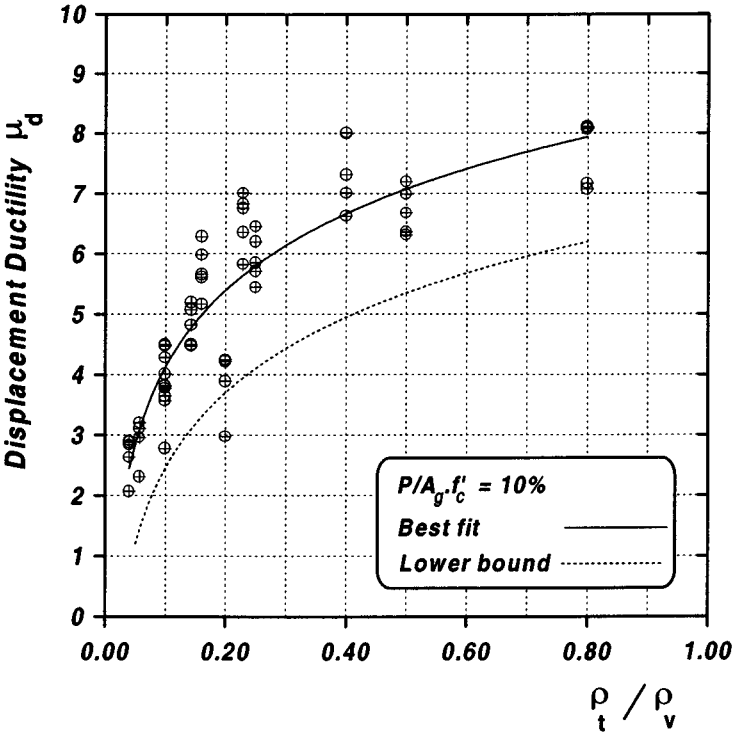

Figure 6-30 Displacement Ductility vs. ρ_t/ρ_v for $P/(f'_c.A_g) = 10\%$

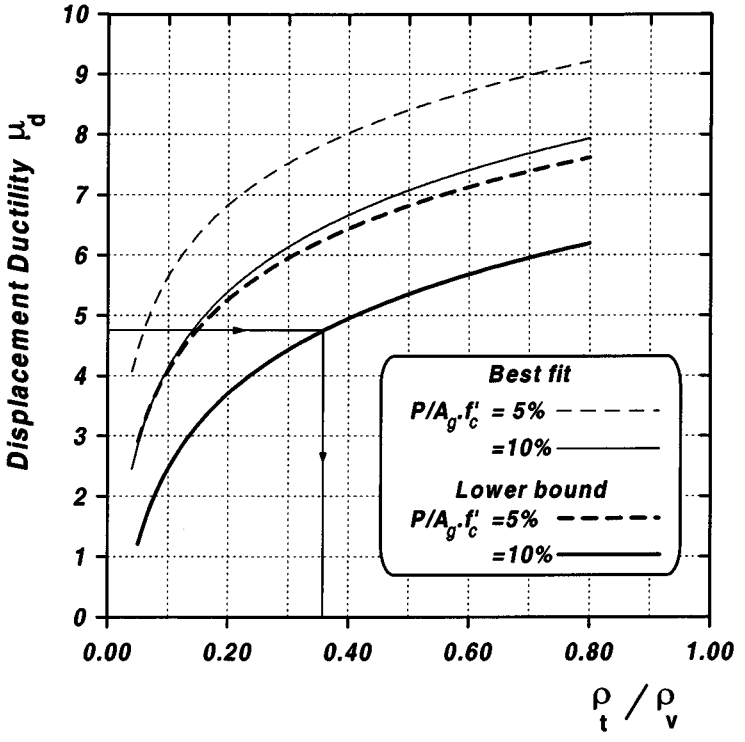

Figure 6-31 Displacement Ductility vs. ρ_t/ρ_v (Design Curve)

6.4.2.2 American Association of State Highway and Transportation Officials (AASHTO)

AASHTO[2] adopted the ACI equations to calculate the lateral reinforcement. A coefficient of 0.12 is used in Equation 6-7 instead of 0.09.

6.4.2.3 California Department of Transportation (Caltrans)

Caltrans[6] requires lateral reinforcement that is the greater of the results from Equation 6-6 and the following equation:

$$A_{sh} = 0.12 s_t h_c \frac{f'_c}{f_y}\left[0.5 + 1.25\frac{P_e}{f'_c A_g}\right] \qquad (6\text{-}8)$$

where:

s_t = Spacing of transverse steel along the member axis

P_e = Axial load

6.4.2.4 ACT-32 Method

The "Bridge Design Specifications" issued by the Applied Technology Council[4] recommends the following equation to calculate the minimum cross sectional area of lateral steel in rectangular columns:

$$A_{sh} = 0.12 s_t h_c \frac{f'_{ce}}{f_{yhe}} \left[0.5 + 1.25 \frac{P}{f'_{ce} A_g} \right] + 0.13 s_t h_c (\rho_l - 0.01) \tag{6-9}$$

where:

f'_{ce} = Expected concrete compressive strength

f_{yhe} = Expected yield stress of transverse reinforcement

ρ_l = Longitudinal reinforcement ratio

6.4.2.5 Wehbe et al. Equation

Wehbe et al.[30] proposed the following equation to calculate the amount of lateral steel in the plastic hinge zone of rectangular bridge columns with different levels of confinement based on the attainable displacement ductility.

$$\frac{A_{sh}}{s_t h_c} = 0.1 \mu_\Delta \sqrt{\frac{f_{c,n}}{f'_{ce}}} \left[0.12 \frac{f'_{ce}}{f_{ye}} \left(0.5 + 1.25 \frac{P}{f'_{ce} A_g} \right) + 0.13 \left(\rho_l \frac{f_y}{f_{s,n}} \right) - 0.01 \right] \tag{6-10}$$

where:

A_{sh} = Lateral steel area

s_t = Spacing of transverse reinforcement along the member axis

h_c = Dimension of column core measured center-to-center of confining reinforcement

μ_d = The target displacement ductility

$f_{c,n}$ = Specified concrete compressive strength

$f_{s,n}$ = Specified steel yield stress

f_{ye} = Expected yield stress of longitudinal reinforcement

P = Axial load

A_g = Sectional gross area

6.5 Comparison of the Proposed and Wehbe Methods

The required confinement reinforcement was calculated for the wall specimens, which were tested early in this study (Section 4), using the proposed approach and the Wehbe[30] method. Both methods are based on the displacement ductility capacity and can be used to design the confinement reinforcement and to evaluate the displacement ductility capacity. The confinement steel was calculated based on a displacement ductility capacity of 4 and 6. Table 6-3 contains the calculated ρ_t using the proposed and the Wehbe[30] methods, and the ratio of the latter to the former methods for each pier wall.

Table 6-3 Confinement Steel Using the Proposed and the Wehbe et al. Methods

Specimen	ρ_t % for μ_d=4		Ratio of ρ_t using Wehbe to proposed approach	ρ_t % for μ_d=6		Ratio of ρ_t using Wehbe to proposed approach
	Proposed Approach	Wehbe et al.		Proposed Approach	Wehbe et al.	
1	0.07	0.12	1.60	0.24	0.18	0.74
2	0.07	0.12	1.61	0.24	0.18	0.75
3	0.07	0.12	1.65	0.24	0.18	0.76
4	0.14	0.14	1.00	0.45	0.21	0.46
5	0.14	0.14	0.97	0.45	0.20	0.45
6	0.14	0.14	0.99	0.45	0.21	0.46
7	0.03	0.10	3.80	0.09	0.15	1.76

When the target displacement ductility capacity was 4, the Wehbe[30] method overestimated the required confinement steel ratio for pier walls with low vertical steel ratio (0.75% in walls 1 to 3 and 0.28% in wall 7). The required confinement steel using the proposed approach was nearly the same as that by the Wehbe et al. method when the vertical steel ratio was 1.5%. On the contrary, the Wehbe et al. method underestimated the required confinement steel when the target

μ_d was 6 and the vertical steel ratio, ρ_v, was 0.75% or 1.5%. Note that the Wehbe method was developed for columns and not specifically for walls where as the proposed method was developed for walls.

6.6 Comparison of the Proposed and the Wehbe Method to Estimate Ductility

The displacement ductility capacity of the pier wall specimens (considering the actual ρ_t and material properties) was evaluated using the proposed approach and the Wehbe[30] methods (Table 6-4). A comparison between the measured and the calculated displacement ductility capacity was made. Table 6-4 presents the ratio of the calculated to the measured displacement ductility capacity using both methods. When the proposed approach was used to evaluate the displacement ductility capacity of the wall specimens, the calculated μ_d ranged between 76% to 89% of the measured μ_d with an average of 80% and standard deviation, σ, of 7%. Wehbe et al.[30] method overestimated the displacement ductility capacity of Specimen 5. The calculated μ_d using Wehbe et al.[30] ranged between 58% and 106% with an average of 79% and σ of 24%.

Table 6-4 The Measured and Calculated μ_d for the Wall Specimens

Specimen	Measured μ_d	Calculated μ_d		Ratio of Calculated to Measured μ_d	
		Proposed Approach	Wehbe et al.[30]	Proposed Approach	Wehbe et al.[30]
1	6.5	5.09	3.74	0.78	0.58
2	7	6.08	6.79	0.87	0.97
3	7.5	6.08	6.65	0.81	0.89
4	5.8	4.01	3.15	0.69	0.54
5	5.6	4.99	5.95	0.89	1.06
6	6	4.99	5.86	0.83	0.98
7	9	6.84	4.39	0.76	0.49
Average				0.80	0.79
Standard Deviation σ				0.07	0.24

The proposed approach was used to evaluate the displacement ductility capacity for typical pier walls with confinement steel that was designed according to the methods discussed earlier[3, 2, 6, 4]. Six typical pier walls were selected based on three vertical steel ratios and two values for the axial load index. The vertical steel ratio, ρ_v, was taken as 0.5%, 1% and 2% while the axial load index was assumed to be 5% and 10%. The concrete compressive strength and the steel yield stress were taken as 27.6 MPa and 414 MPa, respectively. The confinement steel ratio was designed using the available methods[3, 2, 6, 4] (Section 6.4). The ACI[3] and AASHTO[2] methods consider only the gross and confined section dimensions, and the material properties. In addition to the parameters considered by these methods[3, 2], Caltrans[6] considers the axial load effect while ATC-32[4] considers the effect of both the axial load and the longitudinal reinforcement ratio. Table 6-5 presents the estimated displacement ductility capacity using Equations 6-4 and 6-5 for the typical pier walls in which the confinement steel was designed using different methods. Figures 6-32 and 6-33 show μ_d vs. ρ_v for each design code at an axial load index of 5% and 10%, respectively.

Table 6-5 Calculated Displacement Ductility Capacity for Typical Pier Walls

Pier Wall	Vertical Steel Ratio ρ_v %	Axial Load Index %	Calculated Displacement Ductility Capacity μ_d			
			ACI[3]	AASHTO[2]	Caltrans[6]	ATC-32[4]
TW 1	0.5	5	8.0	8.5	7.5	7.2
TW 2	1	5	6.8	7.3	6.3	6.3
TW 3	2	5	5.6	6.1	5.2	5.6
TW 4	0.5	10	6.6	7.1	6.3	6.0
TW 5	1	10	5.4	5.9	5.0	5.0
TW 6	2	10	4.1	4.6	3.8	4.2

The confinement steel designed based on different codes led to displacement ductilities of 5 or greater when the axial load index was equal to 5%. For typical pier walls with a vertical steel ratio greater or equal to 1.75%, and an axial load index of 10%, the displacement ductility capacity was relatively low. The upper bound of the estimated displacement ductility capacity was obtained when the confinement steel was designed according to AASHTO[2] (Figures 6-32 and 6-33). Caltrans[46] required ρ_t that produced the lower bond of μ_d when $\rho_v \geq 1\%$. On the contrary, ATC-32[4] required ρ_t that produced the lower bond of μ_d when $\rho_v < 1\%$.

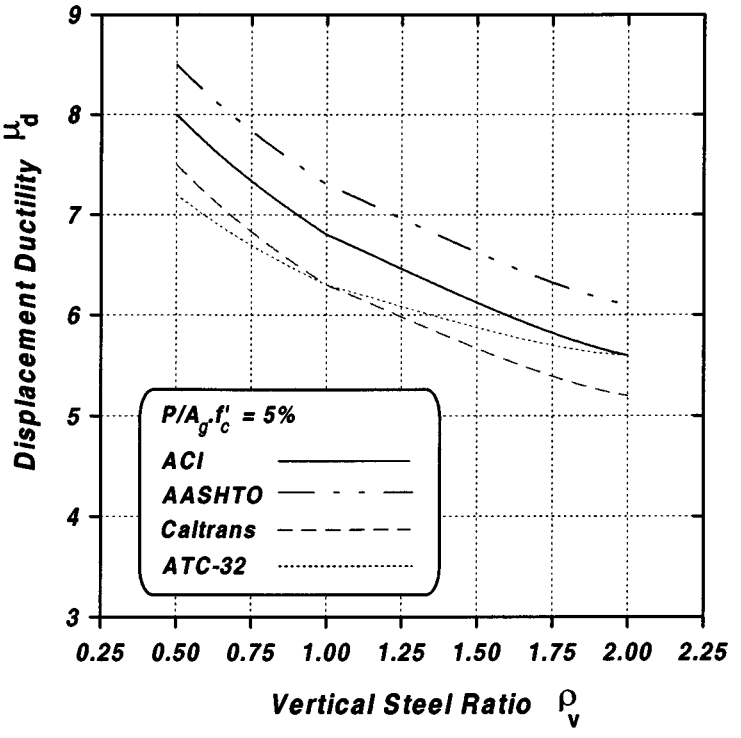

Figure 6-32 Evaluated μ_d vs. ρ_v for ρ_t Based on Different Methods at P/A_g. f'_c=5%

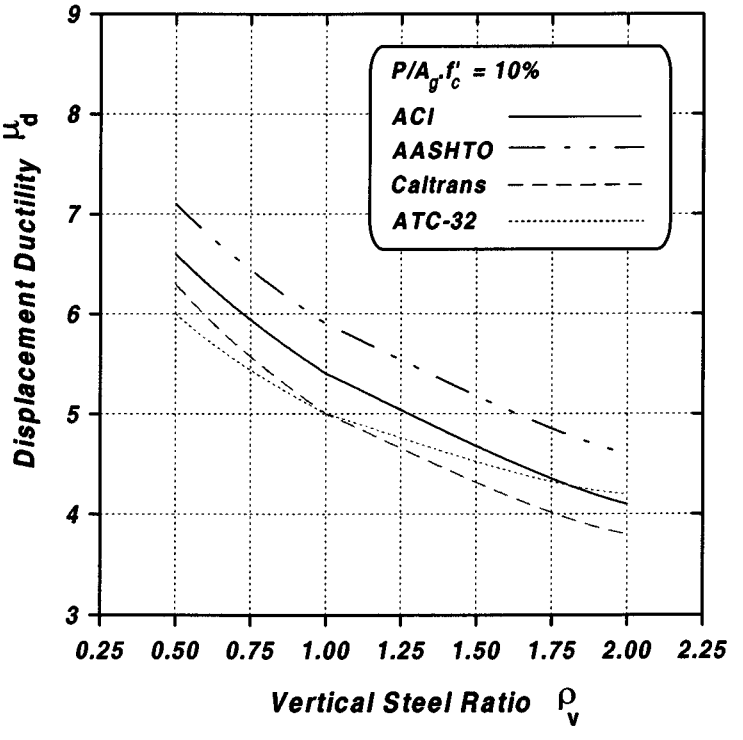

Figure 6-33 Evaluated μ_d vs. ρ_v for ρ_t Based on Different Methods at P/A_g. f'_c=10%

6.7 Evaluation of the Ductility for Pier Walls in Moribe Viaduct, Japan

The displacement ductility capacity of pier walls in Moribe Viaduct, Japan, was evaluated using the proposed approach (Section 5). The bridge was constructed in 1964. Pier walls 29 and 30 were severely damaged during the 1995 Hanshin-Awaji earthquake. The two piers were fixed at the base. The height, width, and the thickness were 7m, 5m, and 0.85m, respectively (Figure 6-34). The vertical reinforcement consisted of two layers of 32-mm diameter bar at a spacing of 250mm. The lateral reinforcement in the strong direction was steel bars of 16-mm diameter at 250-mm spacing placed inside the vertical bars. The walls had no crossties. To evaluate the displacement ductility capacity of piers 29 and 30, an axial load index of 5% (typical for pier walls) was assumed. The concrete compressive strength and the steel yield stress were assumed to be 27.6 MPa and 414 MPa, respectively.

Because the pier walls in Moribe Viaduct had no crossties, the analytical model discussed in Section 5 is not applicable to the wall. The important role of crossties in preventing the lateral deformation of horizontal bars and buckling of vertical bars is clearly demonstrated in figure 4.4. Figure 6.29 indicates that as the ratio of the crosstie steel to longitudinal steel area approaches

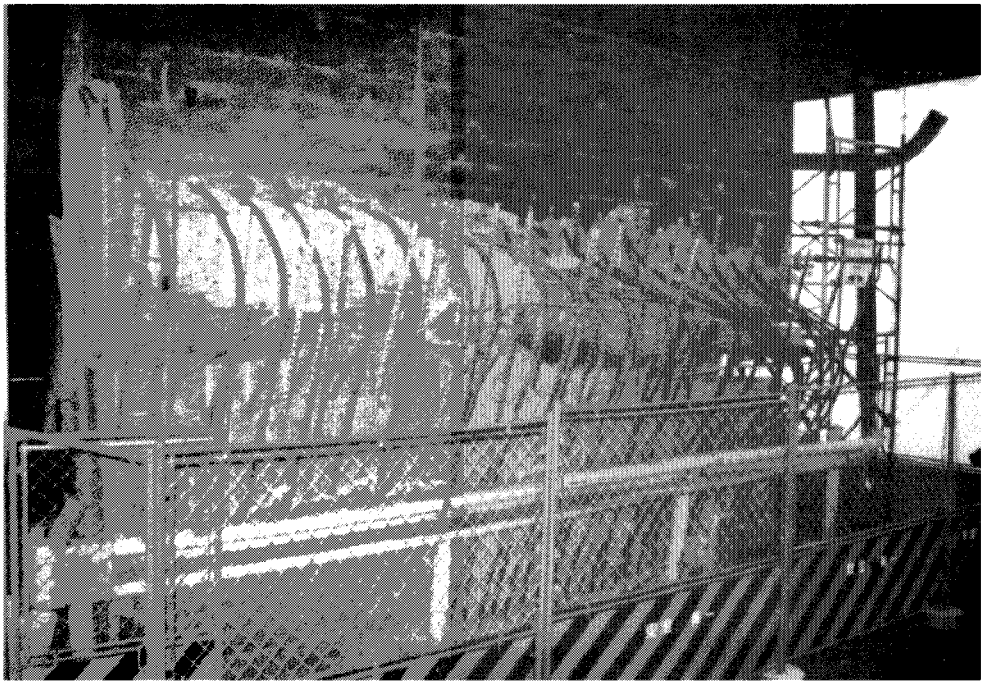

Figure 6-34 Damage to Pier Wall 29 in Moribe Viaduct, Japan, Following the 1995 Hanshin Awaji Earthquake

zero the displacement ductility capacity drops rapidly, thus explaining the failure of the walls. Had crossties of the same ratio as that of the lateral bars been used in the walls, a reasonable displacement ductility capacity would have been expected. Using program "PIER", the calculated displacement ductility in this case would be 5.8. The displacement ductility capacity using the proposed equation (Equation 6-4) would be 5.6. The calculated displacement ductility capacity is satisfactory assuming that μ_d of 5 is acceptable. The pier walls, however, had poor seismic performance in the weak direction during the earthquake because of the absence of the crossties. The lack of the crossties meant that there was no confinement for bending in the weak direction and that the vertical bars were susceptible to buckling.

6.8 Concluding Remarks

A comprehensive parametric study was performed using the analytical model presented in Section 5. The parameters were the ratio of the wall height to its thickness, the vertical steel ratio, the confinement steel ratio, and the axial load index. The selected cases intended to represent a wide range of what was found in the survey (Section 2).

As expected, μ_d was reduced when the axial load index and the vertical steel ratio were increased. It was found that the displacement ductility capacity dropped significantly when the H/t ratio was lower than 4. The displacement ductility capacity, μ_d, was nearly constant for H/t ratio of 4 or more. Assuming that a displacement ductility capacity of 5 is satisfactory, a confinement reinforcement of 0.1% (40% of the minimum required by AASHTO[2] and Caltrans[6]) was adequate for wall cases with an axial load index of 5%, $H/t \geq 4$ and $\rho_v \leq 1.5\%$. When $P/(f'_c.A_g) = 10\%$, a confinement steel ratio of 0.25% was sufficient for cases with $\rho_v \leq 1.75\%$. The change in μ_d was not as great when the confinement reinforcement was raised from 0.25% to 0.4% compared to that when ρ_t was raised from 0.1% to 0.25%. Raising ρ_t to 0.4% resulted in increasing μ_d to 6 or higher.

A practical approach to design confinement reinforcement and to evaluate the displacement ductility for an existing pier wall was developed based on the comprehensive parametric study. Relationships were established for axial load index of 5% and 10%, and H/t ratio of 2, 4, 7, 10,

and 15 (Table 6-1). The log curves were combined for each axial load index (Figures 6-29 and 6-30). The design and evaluation steps that employ Equations 6-4 and 6-5, and the design curve (Figure 6-31) are presented in Section 6.4.1.

The proposed approach and the method by Wehbe[30] were used to calculate the required confinement reinforcement for the pier wall specimens that were tested as a part of this study (Section 4). It was found that when designing for $\mu_d = 4$, the Wehbe method overestimated the required confinement steel for walls with low vertical steel ratio (0.75% and 0.28%). On the contrary, the method[30] underestimated ρ_t for walls with $\rho_v = 0.75\%$ and 1.5%, when the design displacement ductility level was equal to 6. For $\rho_v = 1.5\%$ and axial load index of 5%, both methods (the proposed and the Wehbe methods) required nearly the same confinement steel. It should be noted that the Wehbe method was developed based on data for rectangular columns.

A comparison between the measured and the calculated displacement ductility capacity of the wall specimens (Section 4) using the proposed and Wehbe methods was performed. The Wehbe equation overestimated the displacement ductility capacity in few cases. The calculated μ_d using the proposed approach was, on average, 80% of the measured data with a standard deviation of 7%. The average estimated displacement ductility using the Wehbe[30] method was 79% of the measured μ_d with $\sigma = 24\%$.

The confinement steel for six typical pier walls was designed according to different methods[1,3,4,5] as described in Section 6.4. The proposed approach was used to calculate μ_d for these typical walls. For typical pier walls with vertical steel ratio greater than or equal to 1.75%, and axial load index of 10%, the displacement ductility capacity was relatively low.

Pier walls 29 and 30 in Moribe Viaduct, Japan were analyzed using the proposed approach and the program "PIER" to evaluate the displacement ductility capacity. The calculated μ_d was found to be 5.6 and 5.8 using Equation 6-4 and "PIER", respectively. The absence of the lateral steel (crossties) reduced the confinement and increased the buckling length of the vertical bars, and is believed to be the reason for the poor seismic performance of these pier walls during the 1995 Hanshin-Awaji earthquake.

SECTION 7
SUMMARY AND CONCLUSIONS

7.1 Summary

The research presented in this report was composed of an experimental and an analytical study. The objective of the experimental study was to evaluate the out-of-plane seismic behavior of representative bridge pier walls that exist in the U.S. The analytical study had two objectives: the first was to develop and calibrate an analytical model to determine the seismic response of bridge pier walls, while the second was to develop an approach that relates the displacement ductility capacity to the amount of confinement steel.

A comprehensive bridge pier wall survey was conducted to collect information about existing typical pier walls in the U.S. (Section 2). Responses were received from 30 states. The data were well distributed geographically and states with a full range of seismicity were represented. A statistical analysis was performed on the collected data to select test parameters and specimens. Seven specimens were designed, built, and tested in the experimental study (Section 4) under slow cyclic loads. The failure mode of these wall specimens was either compression failure of the concrete or fracture of the vertical reinforcing bars due to low-cycle fatigue.

An analytical model was developed and calibrated (Section 5). A modified version of the Wehbe et al.[30] method to calculate the bond slip was introduced and used. A computer program called "PIER"[1] was developed to implement the analytical model. It included constitutive relationships for unconfined and confined concrete, and steel, in addition to a low-cycle fatigue model. Good agreement was found when comparing the calculated and measured responses of the pier wall specimens tested in the course of this study (Section 4) and at the University of California at Irvine (UC-Irvine).

A parametric study was conducted using the computer program "PIER"[1] to extend the seismic response study to bridge pier wall cases that were not tested experimentally. The parameters were the ratio of the wall height to thickness, the vertical steel ratio, the confinement steel ratio,

and the axial load index. The relationships between the displacement ductility capacity and the ratio of the wall height to thickness were established for different values of the vertical steel ratio and the axial load index.

A practical approach to correlate the confinement reinforcement in the plastic hinge zones of bridge pier walls to the displacement ductility capacity was developed based on the results of the parametric study. The proposed approach can be used to design the confinement steel or to evaluate the displacement ductility capacity of bridge pier walls for a given confinement steel ratio using the proposed set of equations or design curve. A comparison between the proposed approach and Wehbe et al.[30] was performed by evaluating the displacement ductility capacity of the wall specimens that were tested in this study.

Several other methods[3, 2, 6, 4] were investigated by designing the confinement steel in the plastic hinge zones for six typical pier walls and applying the proposed approach to evaluate the displacement ductility capacity. A comparison of the resulting ductilities was made to identify design provisions that lead to the best level of performance.

The displacement ductility capacity of pier walls 29 and 30 in Moribe Viaduct, Japan, was also calculated using the proposed approach and the computer program "PIER", and was found that the ductility capacity would be reasonable if crossties had been used. The damage and the poor seismic performance of these walls during the 1995 Hanshin-Awaji earthquake indicated that the actual ductility capacity was lower than those calculated. The likely reason for the poor seismic performance of the walls was discussed.

7.2 Conclusions

Based on the experimental and analytical studies conducted in this research, the following conclusions were reached. The conclusions are divided into those for the experimental research and those from the analytical studies.

7.2.1 Experimental Conclusions

1. As expected, pier walls with high vertical steel ratios have high lateral load capacity and high displacement capacity, but low displacement ductility capacity.

2. The seismic performance of pier walls that have axial load index, H/t ratio, and vertical steel ratios within the limits of the wall specimens (Section 3) is satisfactory even with confinement steel ratio that is 60 % lower than the minimum required by AASHTO[2] and Caltrans[6].

3. Wall specimens with higher confinement reinforcement ratios demonstrated slightly higher displacement ductility capacity.

4. The stress in the confinement steel never exceeded 60% of the steel yield stress.

5. The measured plastic hinge length of the wall specimens 1 through 6 was nearly the same (180 mm) while it was 110 mm for Specimen 7. This is because Specimen 7 had smaller bar diameter for the vertical steel.

6. The damage to the wall specimens started with spalling of the cover concrete in the potential plastic hinge zone followed by buckling of the vertical bars and opening of the 90° hook of the crossties. Failure was either due to compression failure of the concrete or fracture of the vertical reinforcing bars due to low-cycle fatigue.

7.2.2 Analytical Conclusions

1. Good agreement was found when comparing the measured and calculated yield and ultimate displacements and the ductility capacity of the wall specimens that were tested at UNR and UC-Irvine, when the computer program "PIER" was used for the analysis.

2. A simplified conservative approach to design the confinement steel in the plastic hinge zones of pier walls based on the desired displacement ductility level and to evaluate the displacement ductility capacity of existing pier walls was developed based on the results of a comprehensive parametric study on pier walls.

3. When the proposed approach was used to evaluate the ductility capacity of the wall specimens that were tested in this study (Section 4), the calculated displacement ductility capacity was nearly 80% of the measured capacity with a standard deviation of 7%.

4. The confinement steel required by the various methods[3, 2, 6, 4] produced acceptable displacement ductility when the axial load index was equal to 5% (assuming that $\mu_d = 5$ is satisfactory). For typical pier walls with vertical steel ratio greater than or equal to 1.75%, axial load index of 10% and confinement steel designed according the these methods[3, 2, 6, 4] the displacement ductility capacity was relatively low.

5. The analysis of the pier walls in Moribe Viaduct that were damaged during the 1995 Hanshin-Awaji earthquake in Japan, showed that the ductility capacity would have been adequate had crossties been used in the walls.

6. The minimum confinement steel in the walls can be reduced significantly in most cases without sacrificing ductility capacity.

7. Satisfactory seismic performance may be expected for bridge pier walls even if the lateral confinement steel is below current minimum code limits. As a result, these walls may not need retrofitting, except for relatively short walls with high vertical steel ratio and large axial load index.

SECTION 8

REFERENCES

1 Abo-Shadi, N., Saiidi, M. S., and Sanders, D., (1998), *"PIER, A Computer Program to Calculate the Displacement and Ductility for Cantilever Piers,"* Software Manual, University of Nevada, Reno, October 1998.

2 American Association of State Highway and Transportation Officials (AASHTO), (1992), *"Standard Specifications for Highway Bridges,"* Fifteenth Edition, 1992.

3 American Concrete Institute Committee 318, (1995), *"Building Code Requirements for Reinforced Concrete and Commentary,"* American Concrete Institute, Detroit, Michigan, 1995.

4 ATC-32, (1996), *"Improved Seismic Design Criteria for California Bridges: Provisional Recommendations,"* Applied Technology Council, 555 Twin Dolphin Drive, Suite 550, Redwood City, California 91065, 1996.

5 Burns, N. H. and Seiss, C. P., (1973), *"Load-Deformation Characteristics of Beam-Column Connections in Reinforced Concrete,"* Civil Engineering Studies, Structural Research Series No. 234, University of Illinois, 1973.

6 Department of Transportation, State of California, (1990), *"Bridge Design Specifications,"* June 1990.

7 Haroun, M. A., Pardoen, G. C., Bhatia, H., Shahi, S., and Kazanjy, R. P., (1997), *"Testing of Enhanced and Repaired Pier Walls of Modern Design,"* Final Report to the California Department of Transportation, November 1997.

8 Haroun, M. A., Pardoen, G. C., Shepherd, R., Hagag, H.A., and Kazanjy, R. P., (1993), *"Cyclic Behavior of Bridge Pier walls for Retrofit,"* Final Report to the California Department of Transportation, December 1993.

9 Haroun, M. A., Pardoen, G. C., Shepherd, R., Hagag, H.A., and Kazanjy, R. P., (1994), *"Assessment of Cross-Tie Performance in Bridge Pier walls,"* Final Report to the California Department of Transportation, December 1994.

10 Hoshikuma, J., Kawashima, K., Nagaya, K., and Taylor A. W., (1997), *"Stress-Strain Model for Confined Reinforced Concrete in Bridge Piers,"* ASCE Journal of Structural Engineering, Vol. 123, No. 5, May 1997, pp. 624-633.

11 Imbsen, R., Schamber R. A., and Osterkamp, T. A., (1996), *"Establish Representative Pier Types for Comprehensive Study: Western United States,"* Technical Report NCEER-96-0006, May 1996.

12 Japanese Specifications, (1991),*"Design of Foundation, Design Specifications of road Bridges (Part IV),"* Japan Road Association, Japan, 1991.

13 Kent, D. C. and Park R., (1971), *"Flexural Members with Confined Concrete,"* ASCE Journal of The Structural Division, Vol. 97, No. ST7, July 1971, pp. 1969-1990.

14 Kent, D. C. and Park R., (1973), *"Cyclic Load Behavior of Reinforcing Steel,"* Strain, Vol. 9, No. 3, July 1973, pp. 98-103.

15 Kulicki, J. and Prucz, Z., (1996), *"Establish Representative Pier Types for Comprehensive Study: Eastern United States,"* Technical Report NCEER-96-0005, May 1996.

16 Leslie, P. D., (1974), *"Ductility of Reinforced Concrete Bridge Piers,"* Master of Engineering Report, University of Canterbury, New Zealand, 1974, 147 pp.

17 Mander, J. B., (1983), *"Seismic Design of Bridge Piers,"* Ph.D. Thesis, University of Canterbury, New Zealand, 1983, 442 pp.

18 Mander, J. B., Panthaki, F. D. and Kasalanati, A., (1994),*"Low Cycle fatigue Behavior of Reinforcing Steel,"* Journal of Materials in Civil Engineering, ASCE, Vol. 6, No. 4, November 1994, pp. 453-467.

19 Mander, J. B., Priestley, M. J. N., and Park, R., (1988), *"Theoretical Stress-Strain Model for Confined Concrete Columns,"* ASCE Journal of Structural Engineering, Vol. 114, No. 8, August 1988, pp. 1804-1826.

20 Manson, S. S., (1953), *"Behavior of Materials under Conditions of Thermal Stresses,"* Heat Transfer Symposium, University of Michigan Engineering Research Institute, Ann Arbor, Michigan, 1953, pp 9-75.

21 Miner, M. A., (1945), *"Cumulative Damage in Fatigue,"* Trans. ASME, Journal of Applied Mechanics, Vol. 67, 1945, pp. A159-A164.

22 National Institute of Standards and Technology (NIST), (1996), *"The January 17, 1995 Hyogoken-Nanbu (Kobe) Earthquake, Performance of Structures, Lifelines, and Fire Protection Systems,"* NIST, Special Publications 901, July 1996.

23 Park, R. and Paulay, T., (1975), *"Reinforced Concrete Structures,"* John Wiley & Sons, New York, 1975.

24 Paulay, T. and Priestley, M. J. N., (1992), *"Seismic Design of Reinforced Concrete and Masonry Buildings,"* John Wiley & Sons, Inc., New York, 1992.

25 Popovics, S., (1973), *"A Numerical Approach to the Complete Stress-Strain Curves of Concrete,"* Cement and Concrete Research, Vol. 3, No. 5, September 1973, pp. 583-599.

26 Priestley, M. J. N., and Park, R., (1987), *"Strength and Ductility of Concrete Bridge Columns under Seismic Loading,"* ACI Structural Journal, Vol. 84, January-February 1987, pp. 61-75.

27 Saatcioglu, M., (1991), *"Deformability of Reinforced Concrete Columns,"* American Concrete Institute, SP 127, 1991, pp. 421-452.

28 Saatcioglu, M. and Razvi, R., (1992), *"Strength and Ductility of Confined Concrete,"* ASCE Journal of Structural Engineering, Vol. 118, No. 6, June 1992, pp. 1590-1607.

29 Sheikh, S., A. and Uzumeri, S. M., (1982), *"Analytical Model for Concrete Confinement in Tied Columns,"* Journal of the Structural Division, ASCE, Vol. 108, No. ST12, December 1982, pp. 2703-2722.

30 Wehbe, N., Saiidi, M. S., and Sanders, D., (1997), *"Effect of Confinement and Falres on the Seismic Performance of Reinforced Concrete Bridge Columns,"* Civil Engineering Department, Report No. CCEER-97-2, University of Nevada, Reno, September 1997.

Appendix A

MEASURED LATERAL-LOAD STRAIN IN THE REINFORCING BARS

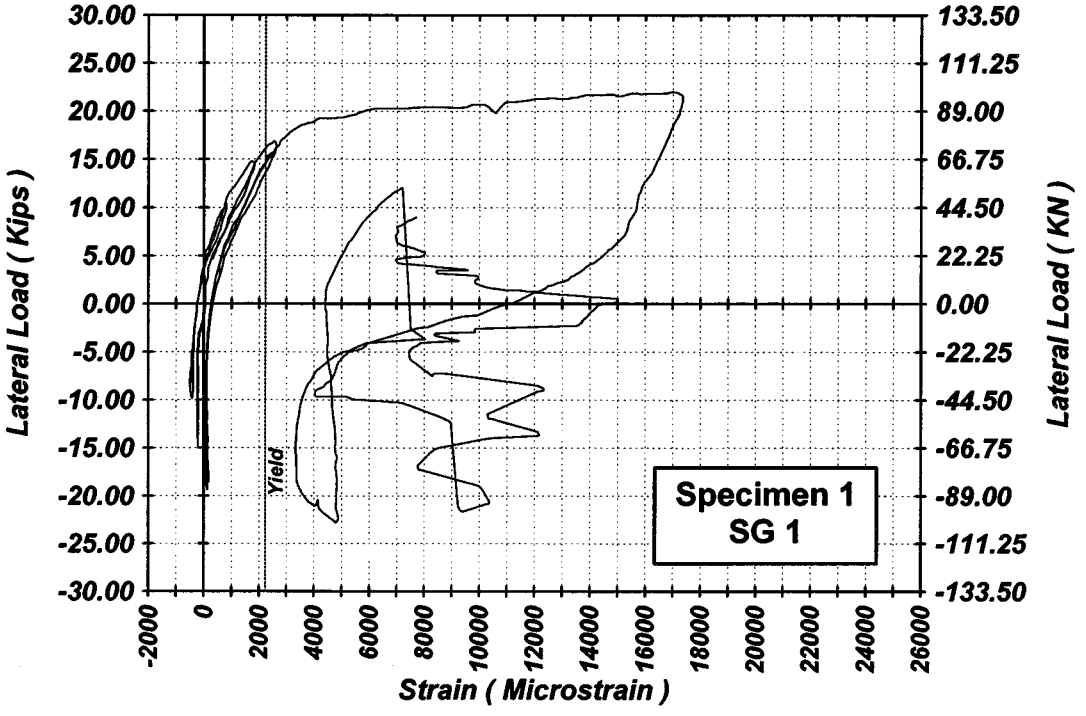

Figure A-1 Measured Lateral Load-Strain in SG-1 of Specimen 1

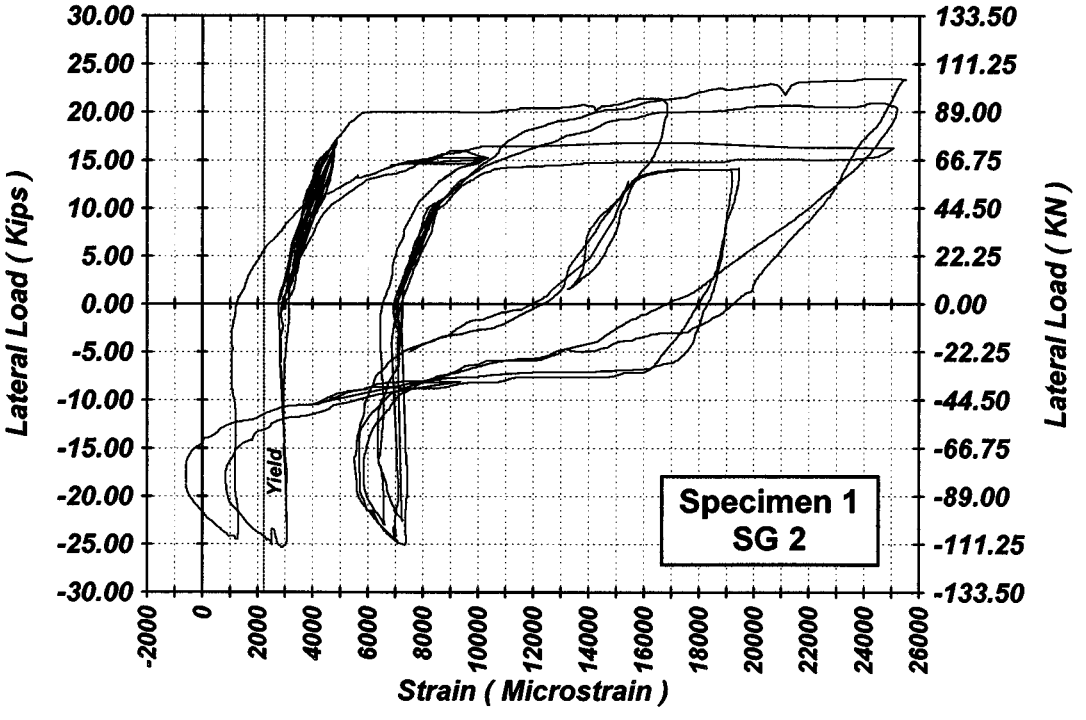

Figure A-2 Measured Lateral Load-Strain in SG-2 of Specimen 1

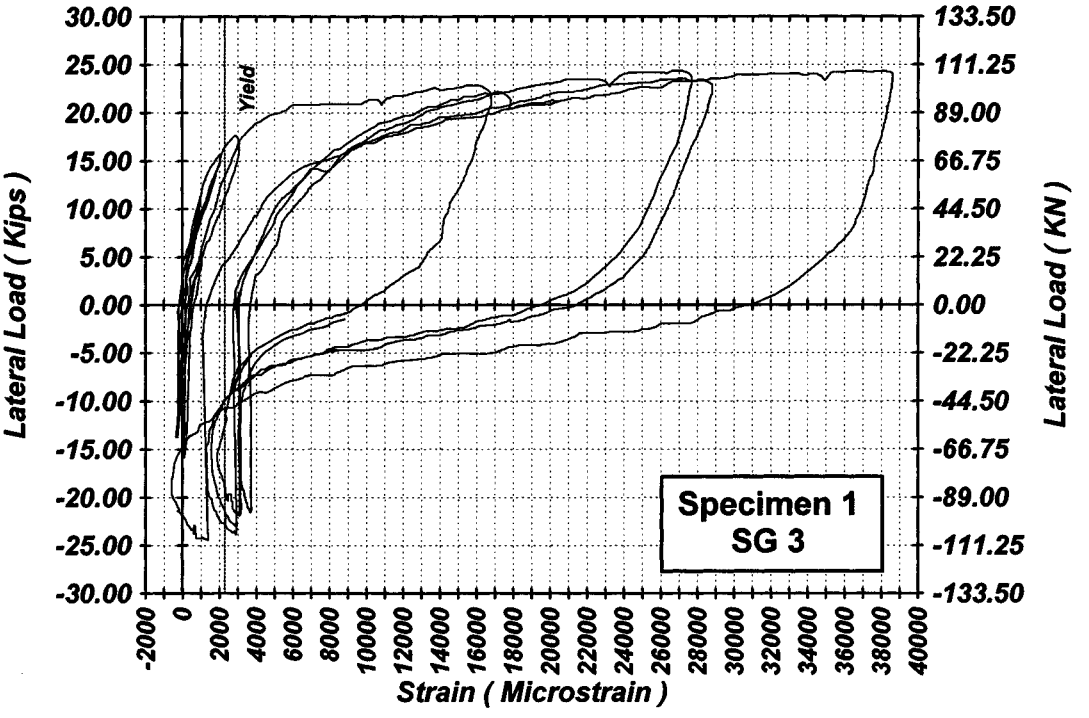

Figure A-3 Measured Lateral Load-Strain in SG-3 of Specimen 1

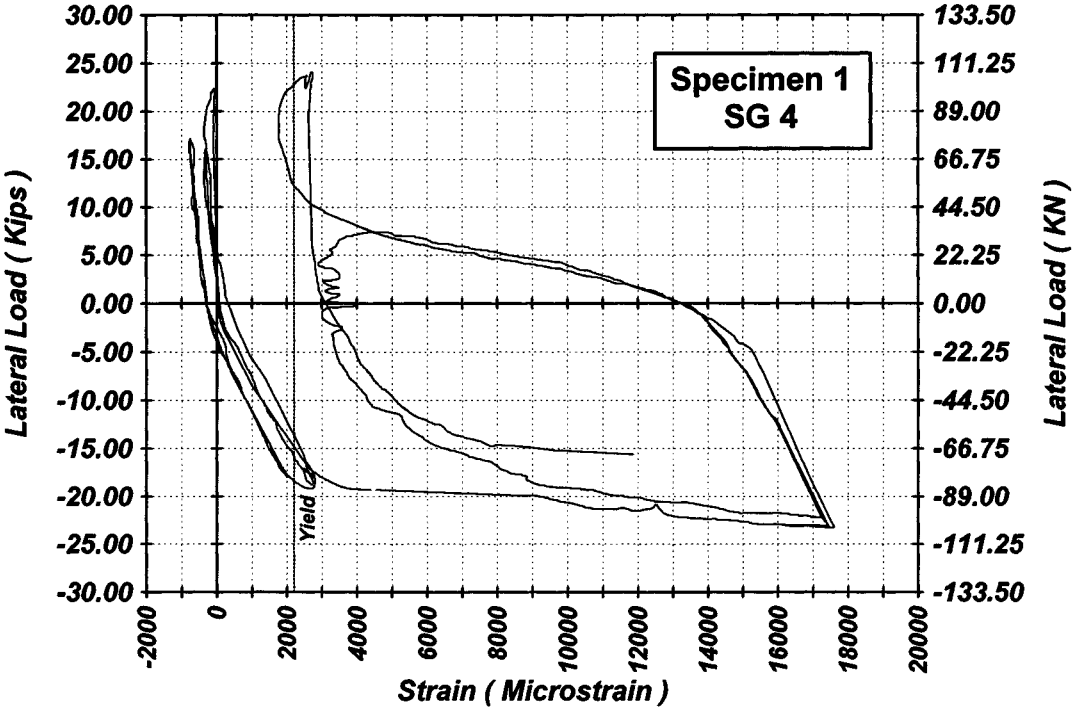

Figure A-4 Measured Lateral Load-Strain in SG-4 of Specimen 1

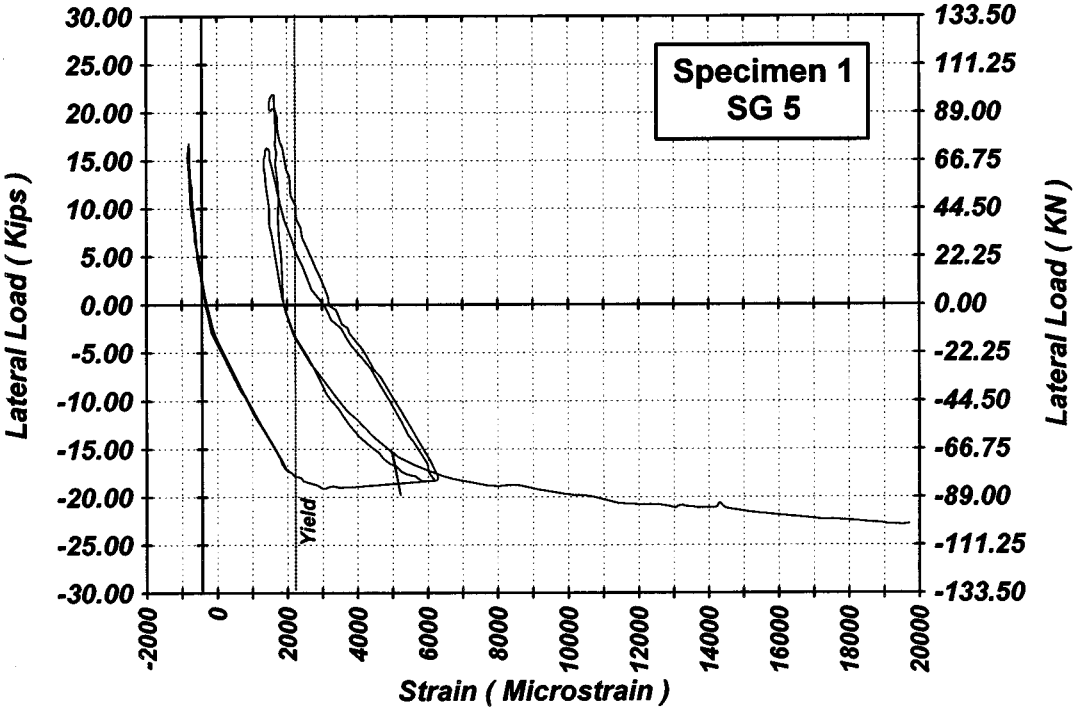

Figure A-5 Measured Lateral Load-Strain in SG-5 of Specimen 1

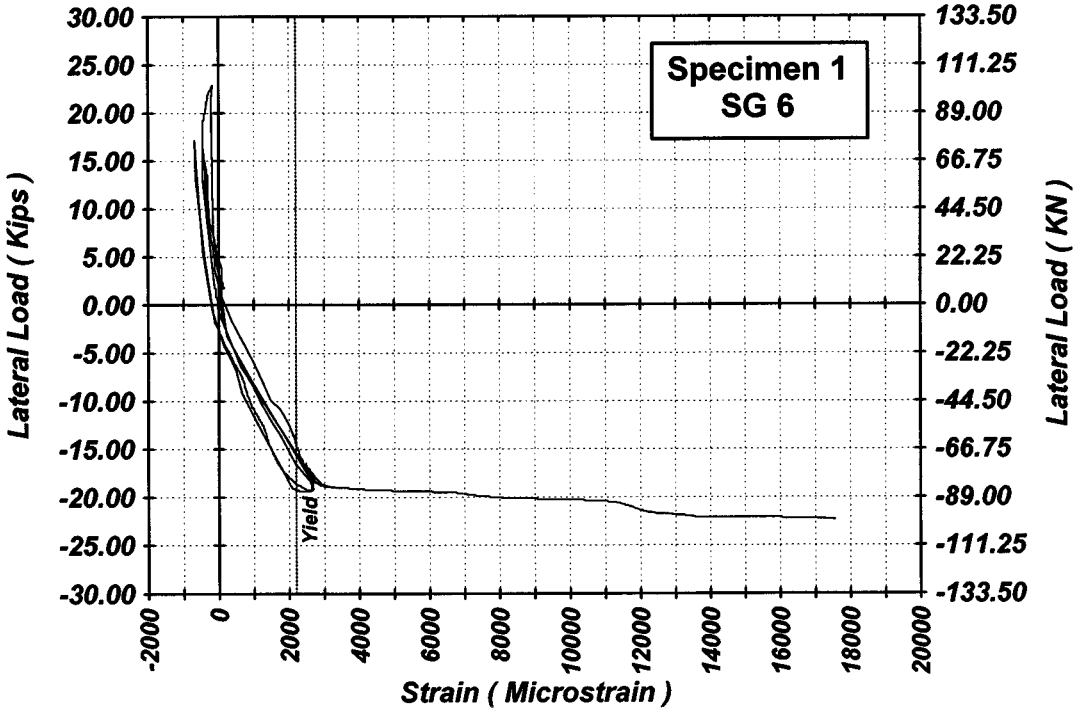

Figure A-6 Measured Lateral Load-Strain in SG-6 of Specimen 1

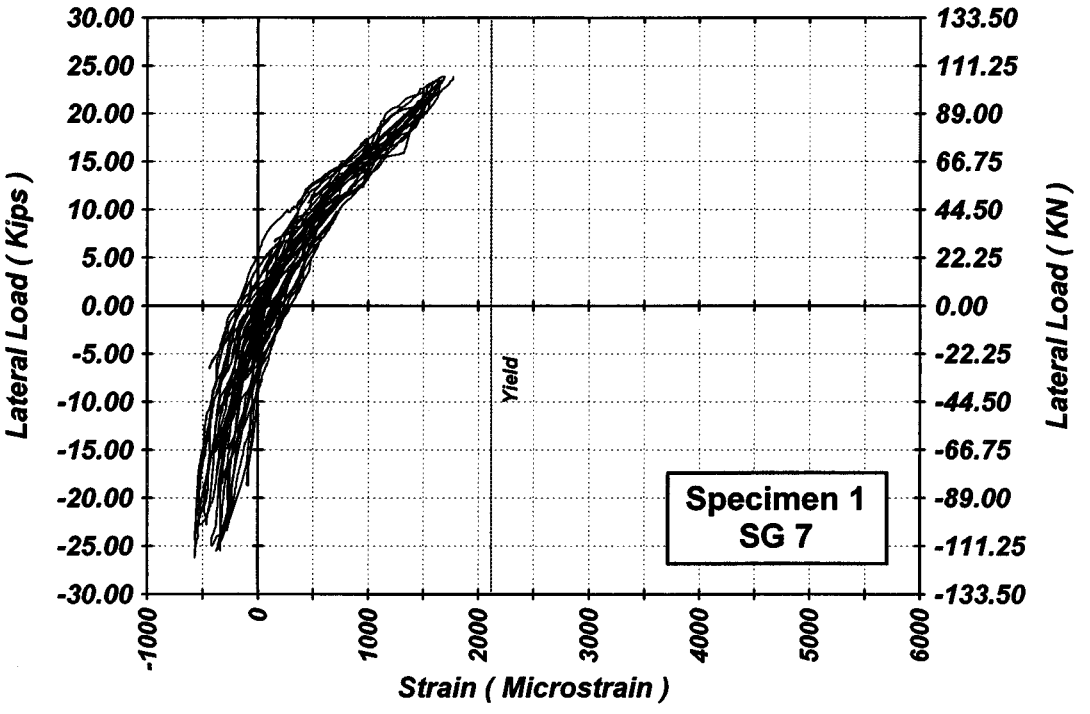

Figure A-7 Measured Lateral Load-Strain in SG-7 of Specimen 1

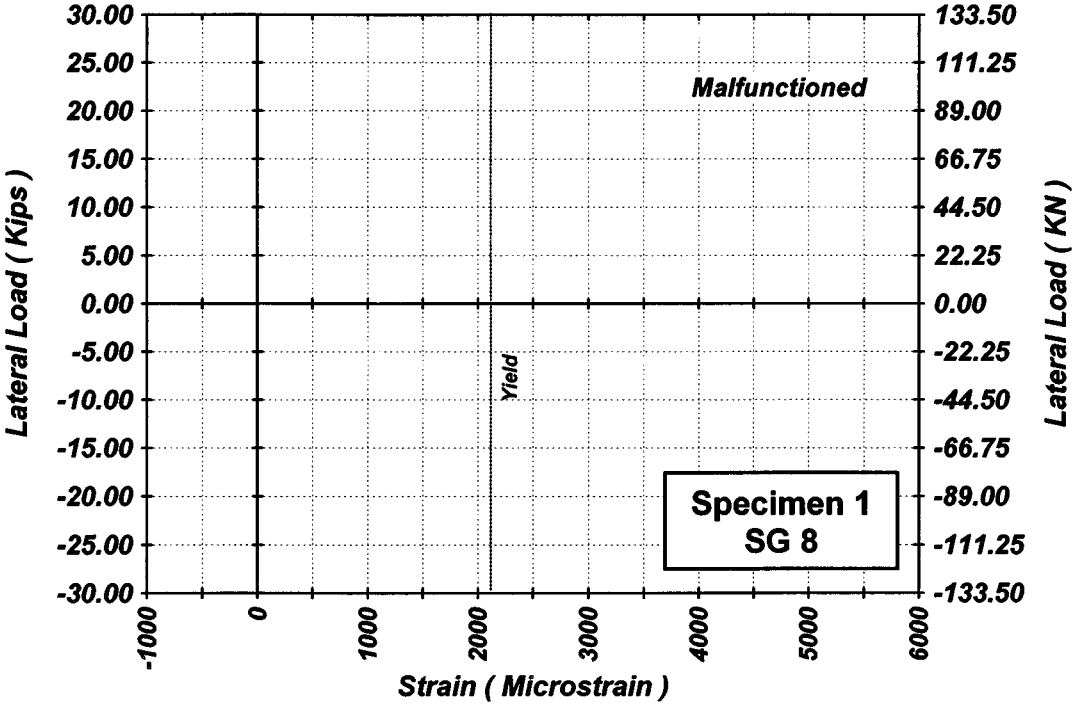

Figure A-8 Measured Lateral Load-Strain in SG-8 of Specimen 1

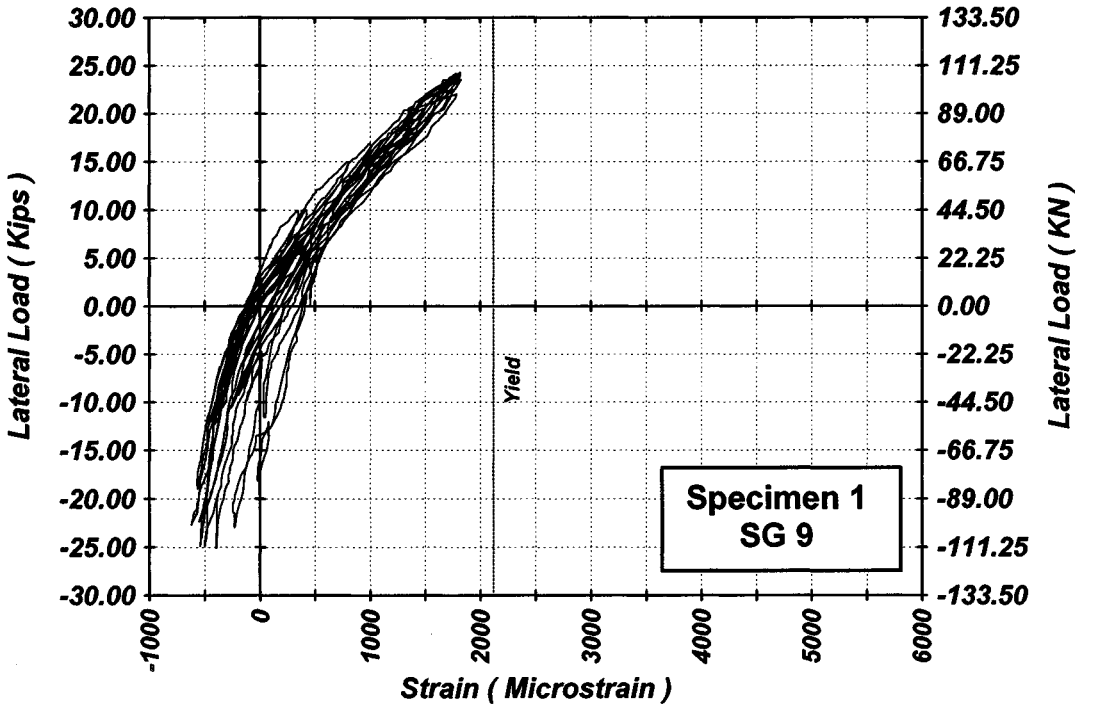

Figure A-9 Measured Lateral Load-Strain in SG-9 of Specimen 1

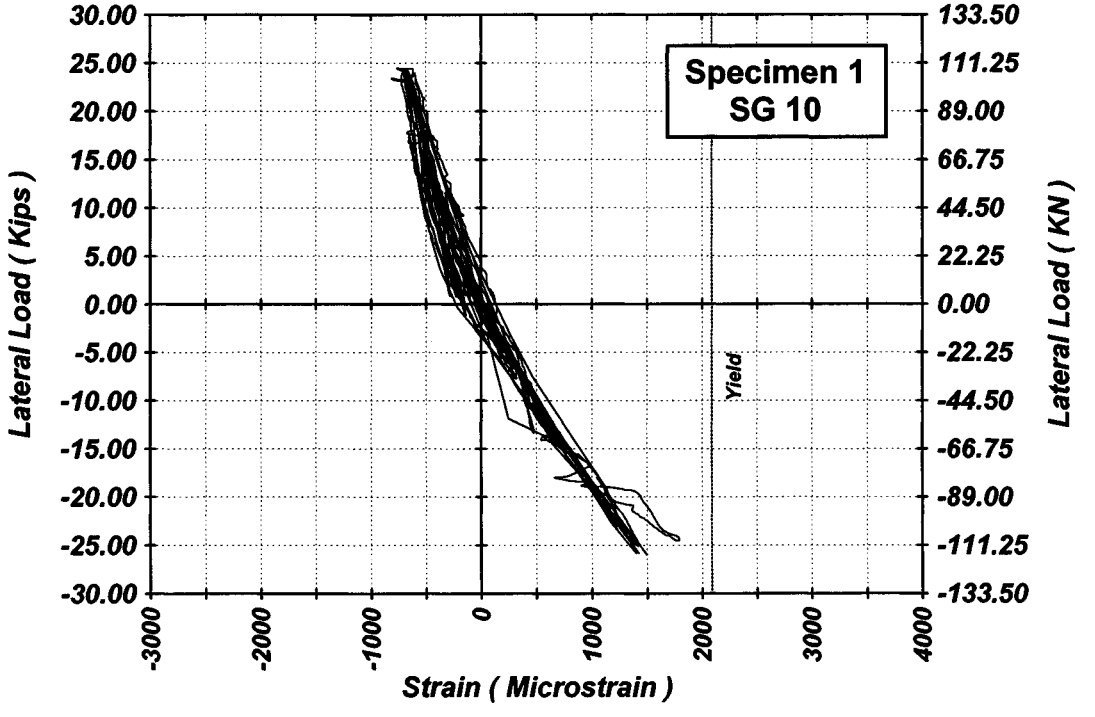

Figure A-10 Measured Lateral Load-Strain in SG-10 of Specimen 1

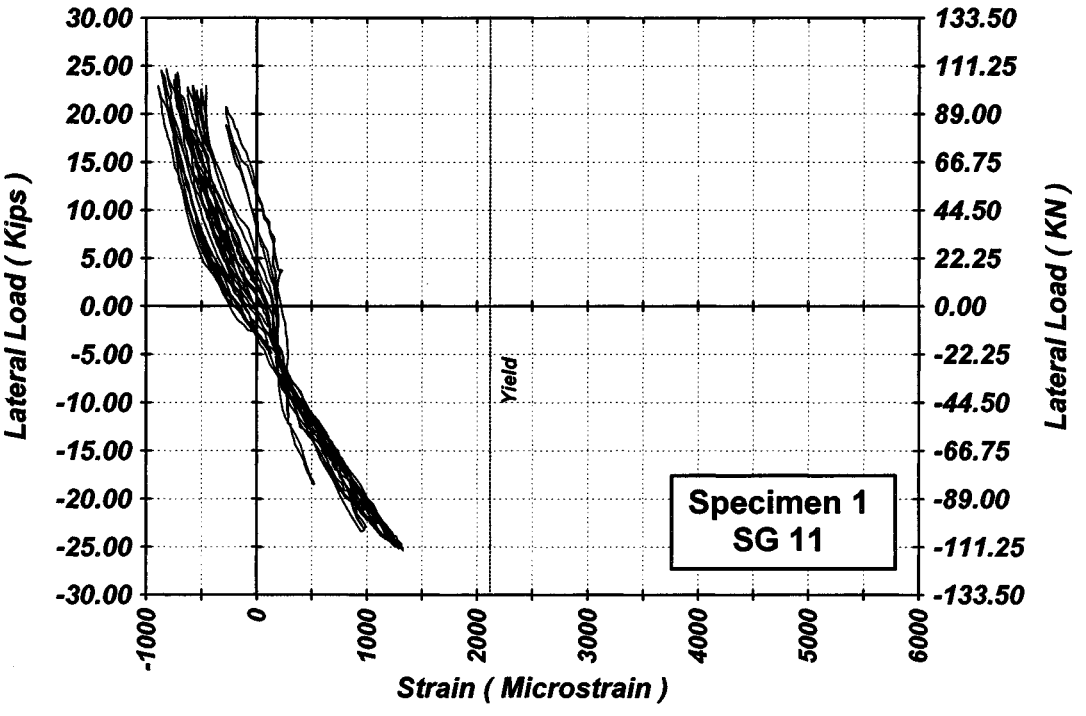

Figure A-11 Measured Lateral Load-Strain in SG-11 of Specimen 1

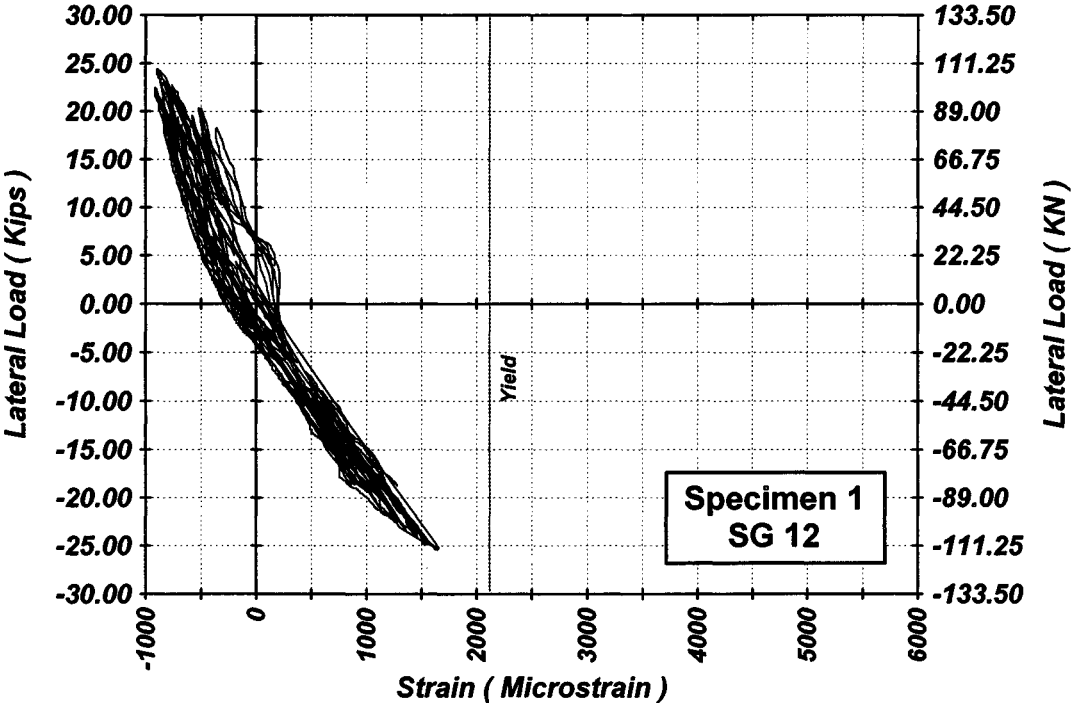

Figure A-12 Measured Lateral Load-Strain in SG-12 of Specimen 1

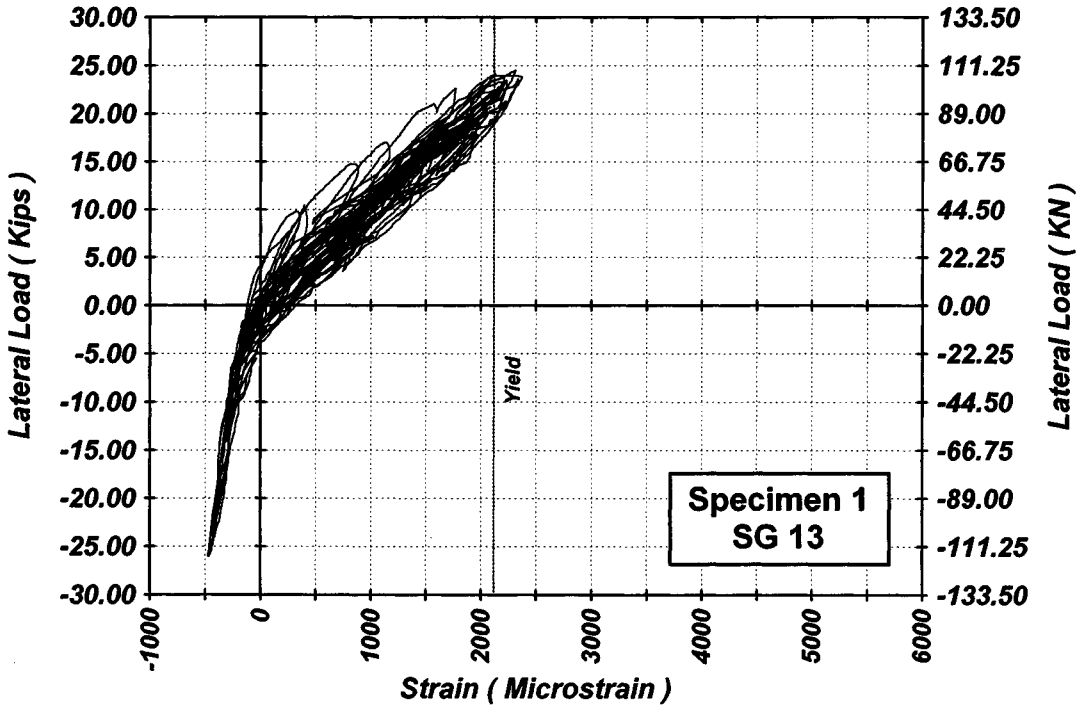

Figure A-13 Measured Lateral Load-Strain in SG-13 of Specimen 1

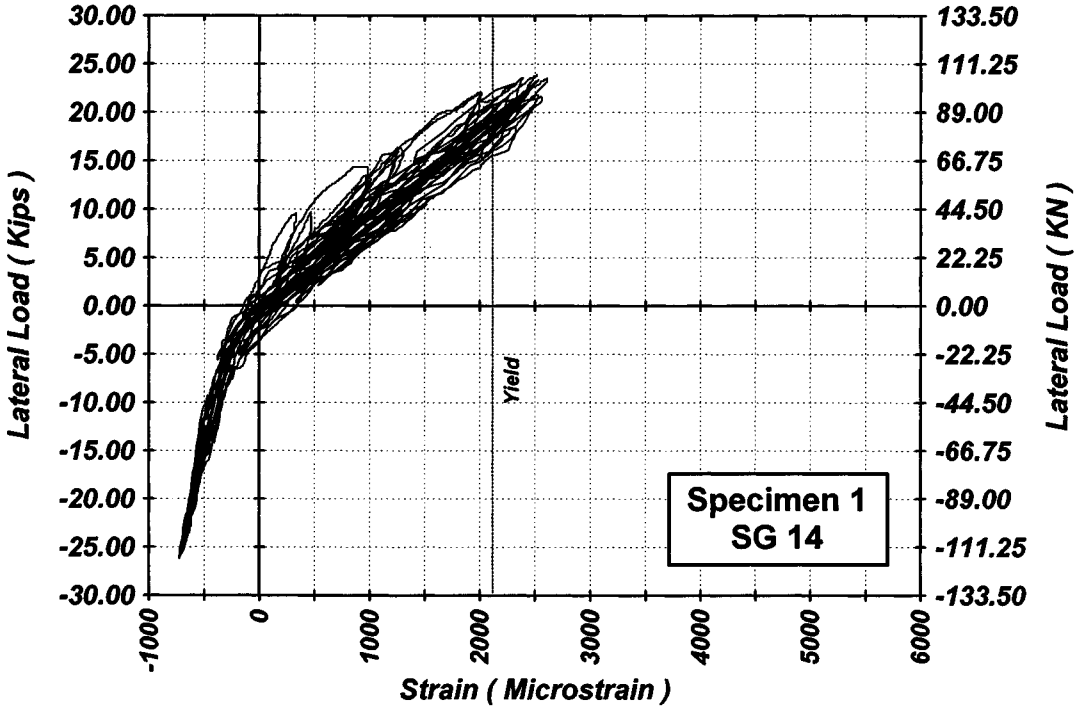

Figure A-14 Measured Lateral Load-Strain in SG-14 of Specimen 1

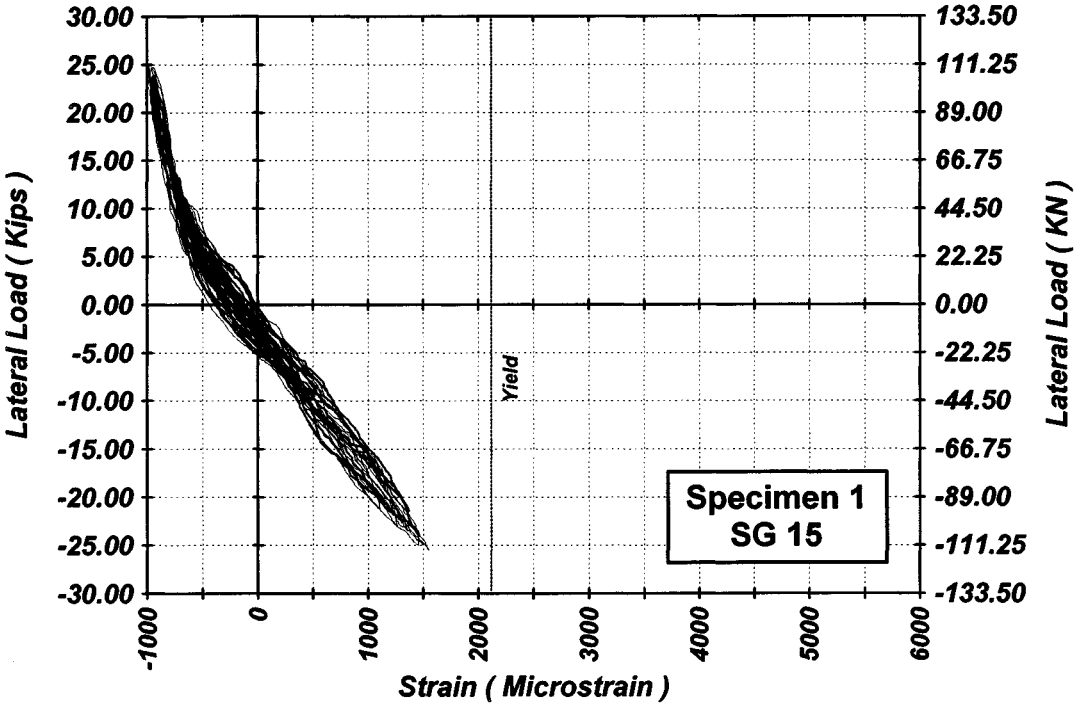

Figure A-15 Measured Lateral Load-Strain in SG-15 of Specimen 1

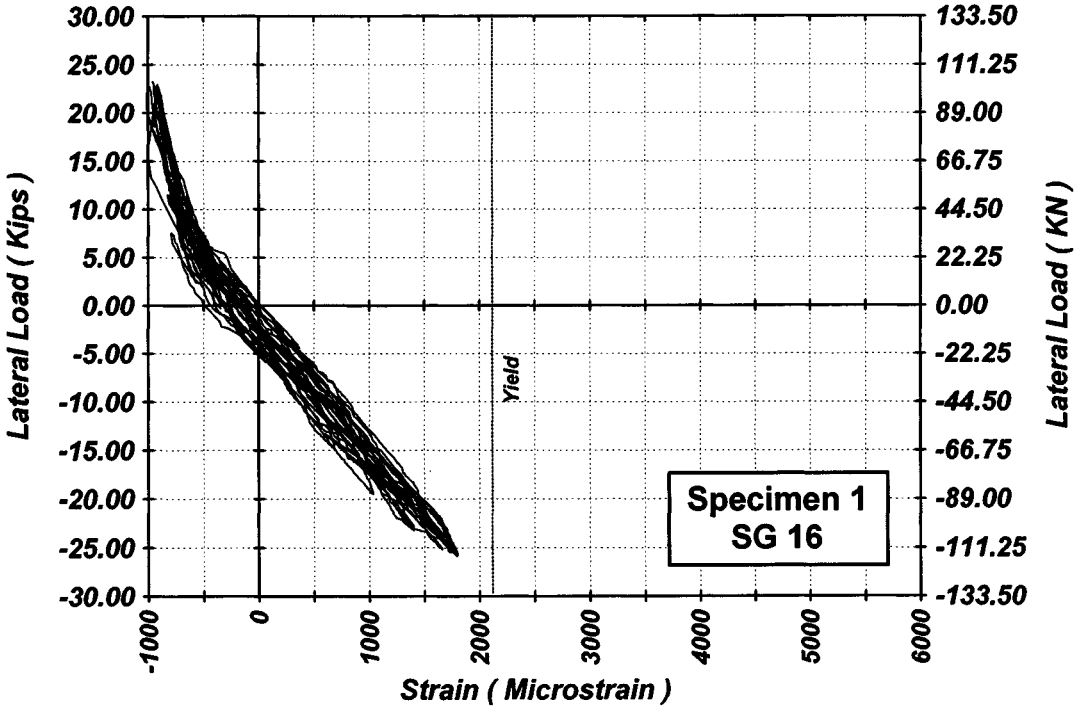

Figure A-16 Measured Lateral Load-Strain in SG-16 of Specimen 1

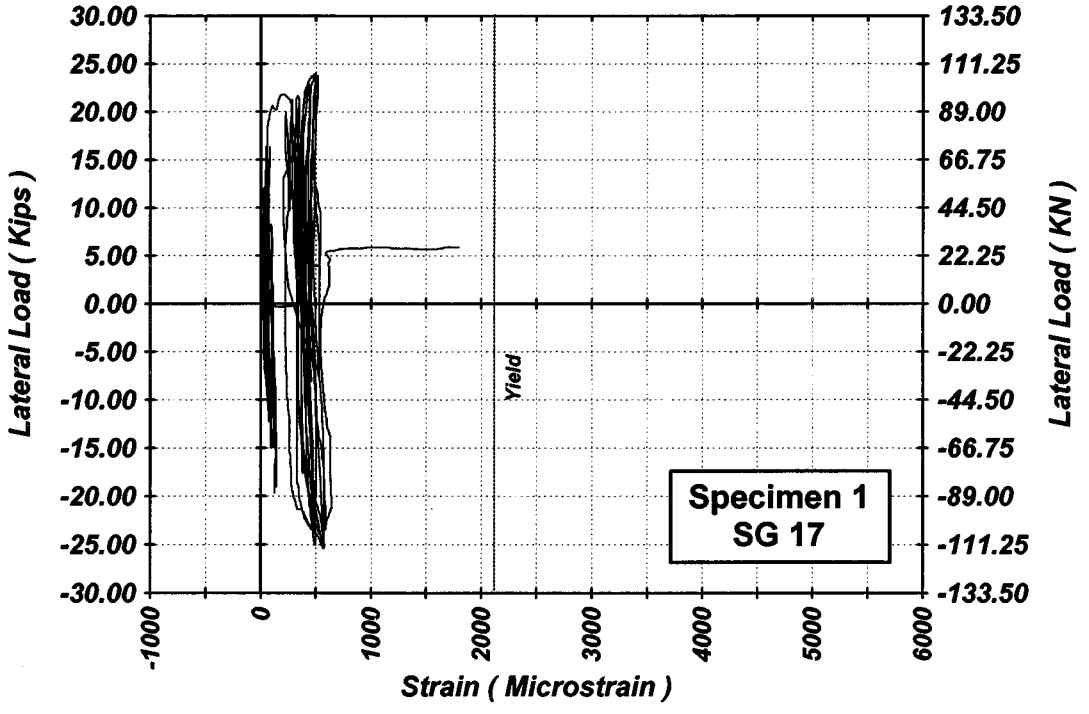

Figure A-17 Measured Lateral Load-Strain in SG-17 of Specimen 1

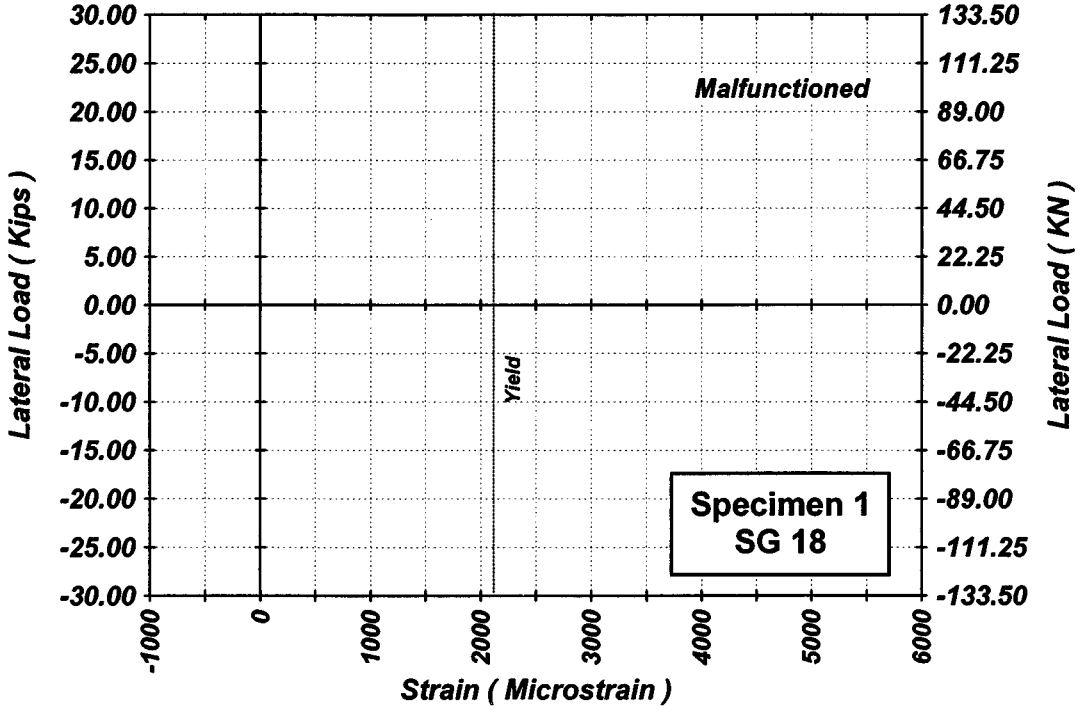

Figure A-18 Measured Lateral Load-Strain in SG-18 of Specimen 1

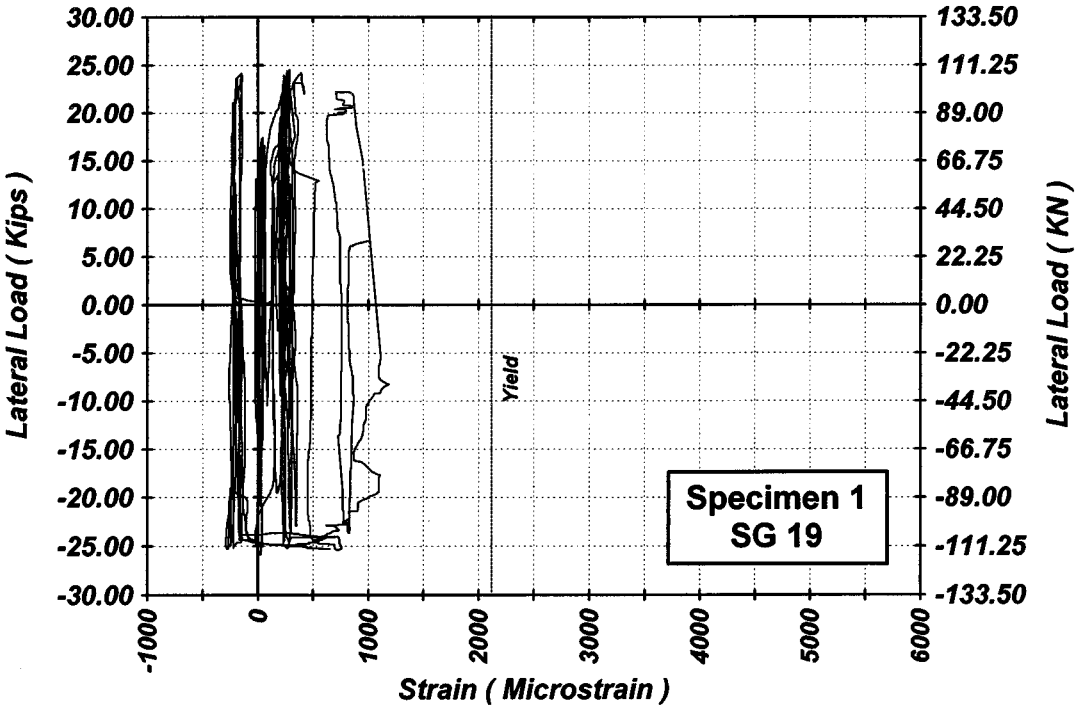

Figure A-19 Measured Lateral Load-Strain in SG-19 of Specimen 1

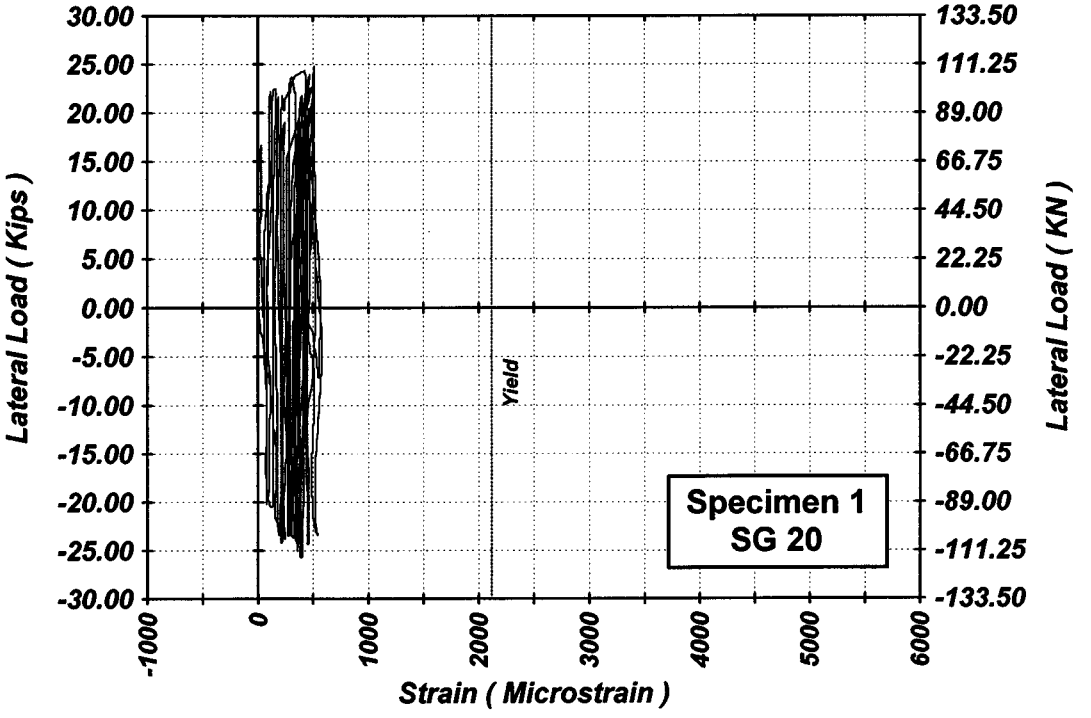

Figure A-20 Measured Lateral Load-Strain in SG-20 of Specimen 1

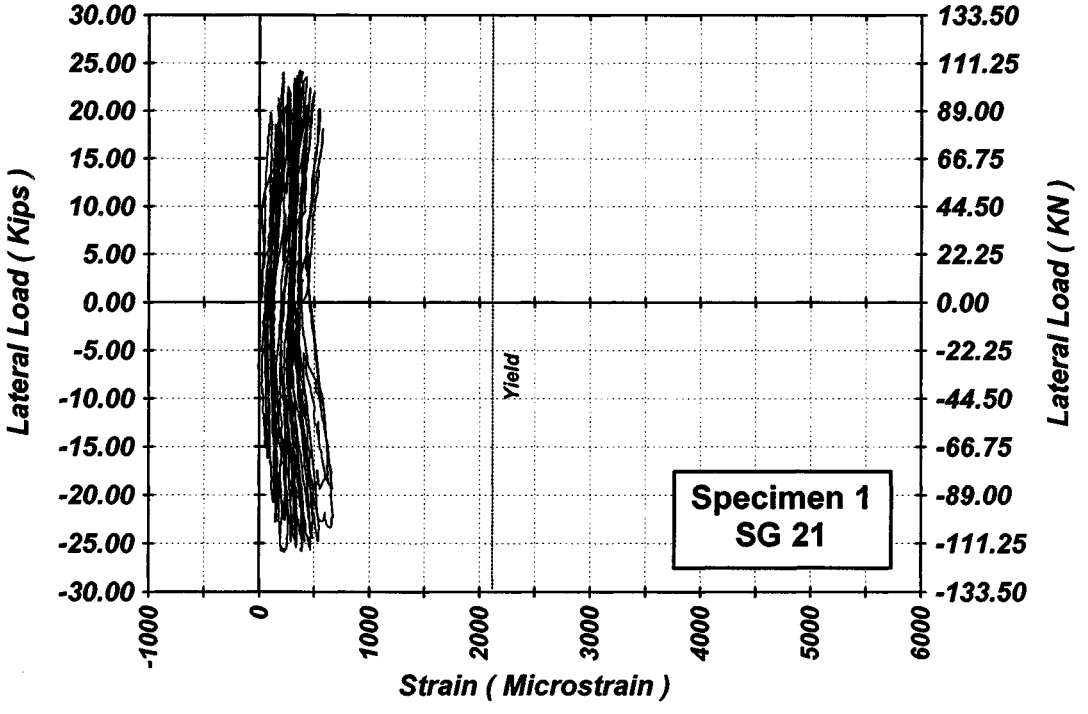

Figure A-21 Measured Lateral Load-Strain in SG-21 of Specimen 1

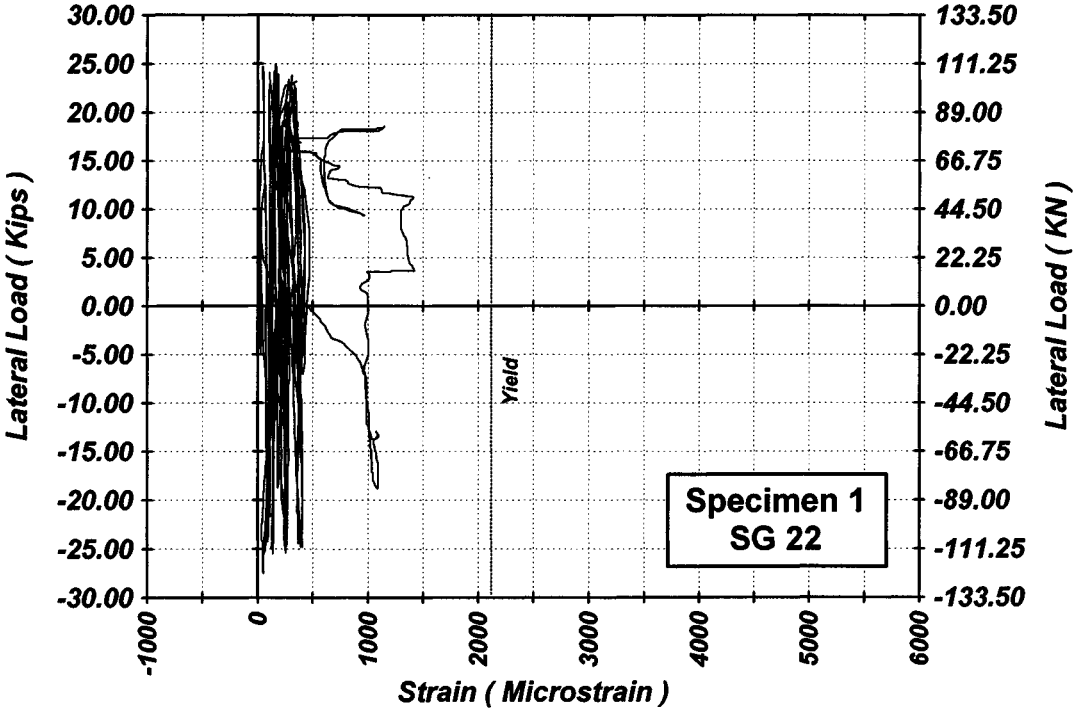

Figure A-22 Measured Lateral Load-Strain in SG-22 of Specimen 1

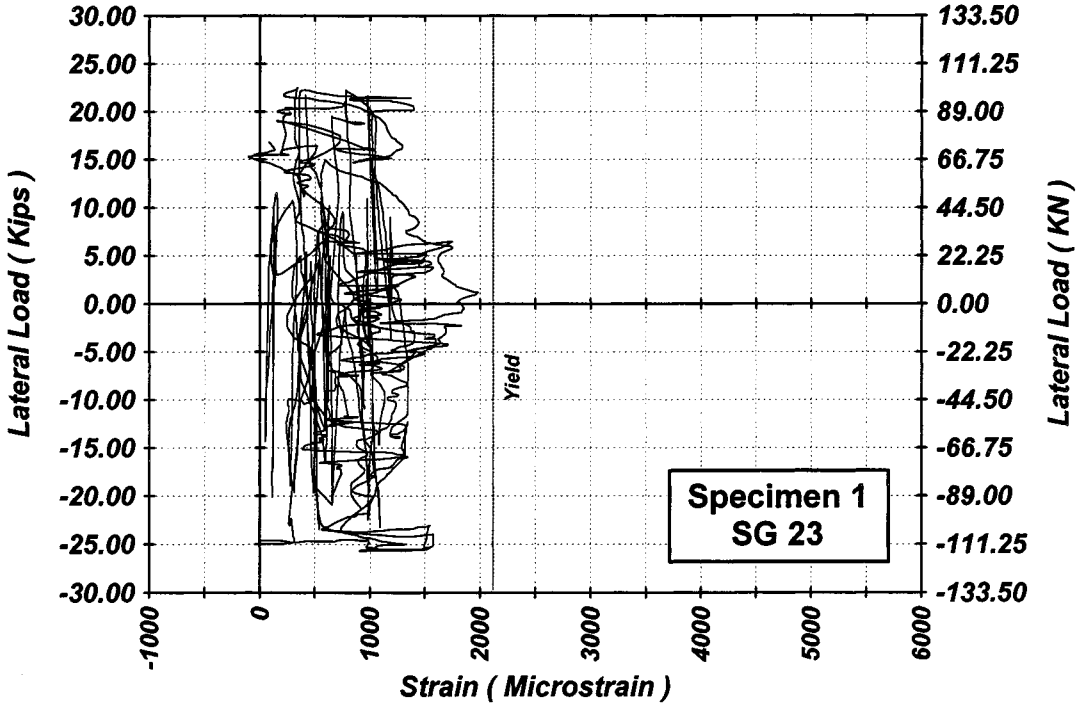

Figure A-23 Measured Lateral Load-Strain in SG-23 of Specimen 1

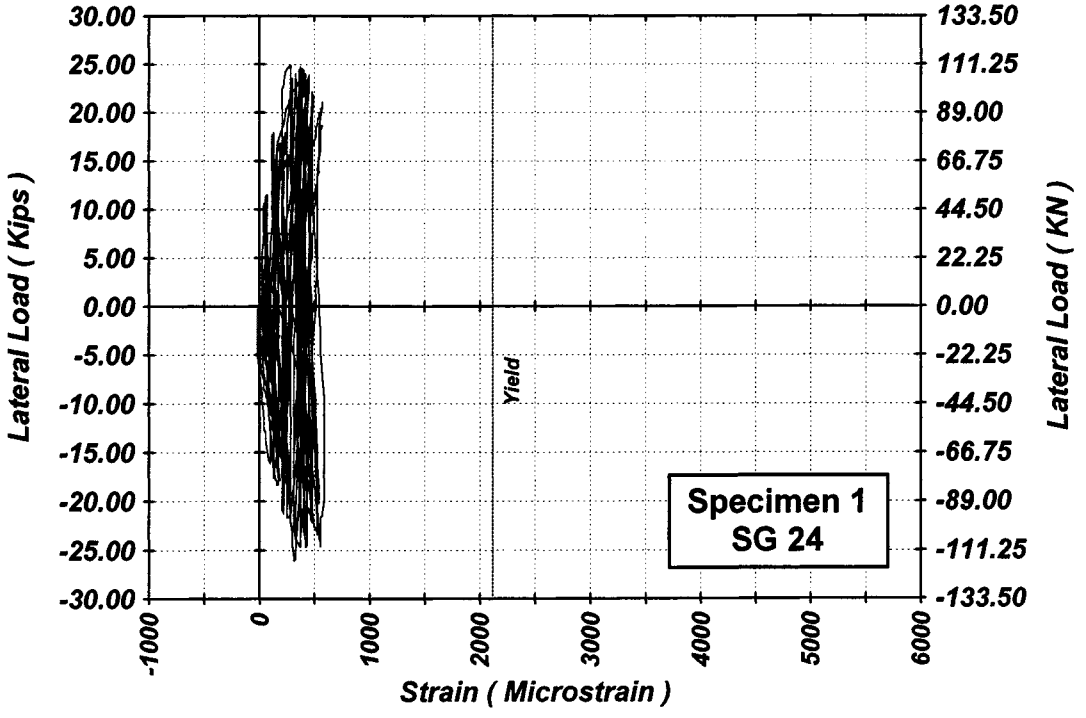

Figure A-24 Measured Lateral Load-Strain in SG-24 of Specimen 1

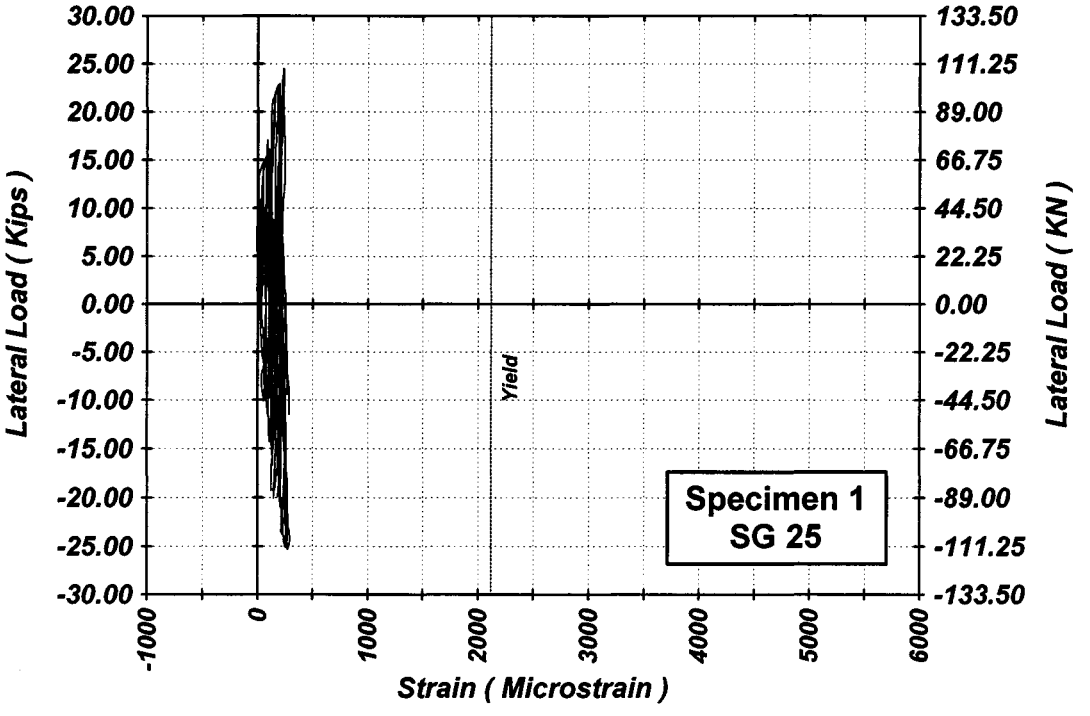

Figure A-25 Measured Lateral Load-Strain in SG-25 of Specimen 1

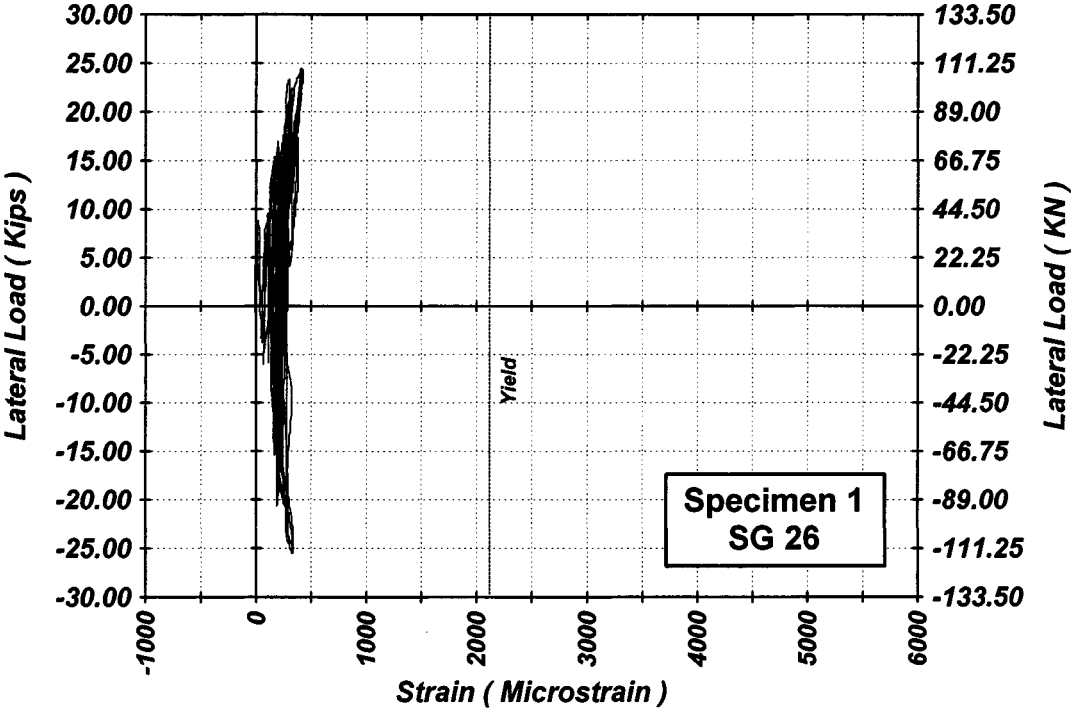

Figure A-26 Measured Lateral Load-Strain in SG-26 of Specimen 1

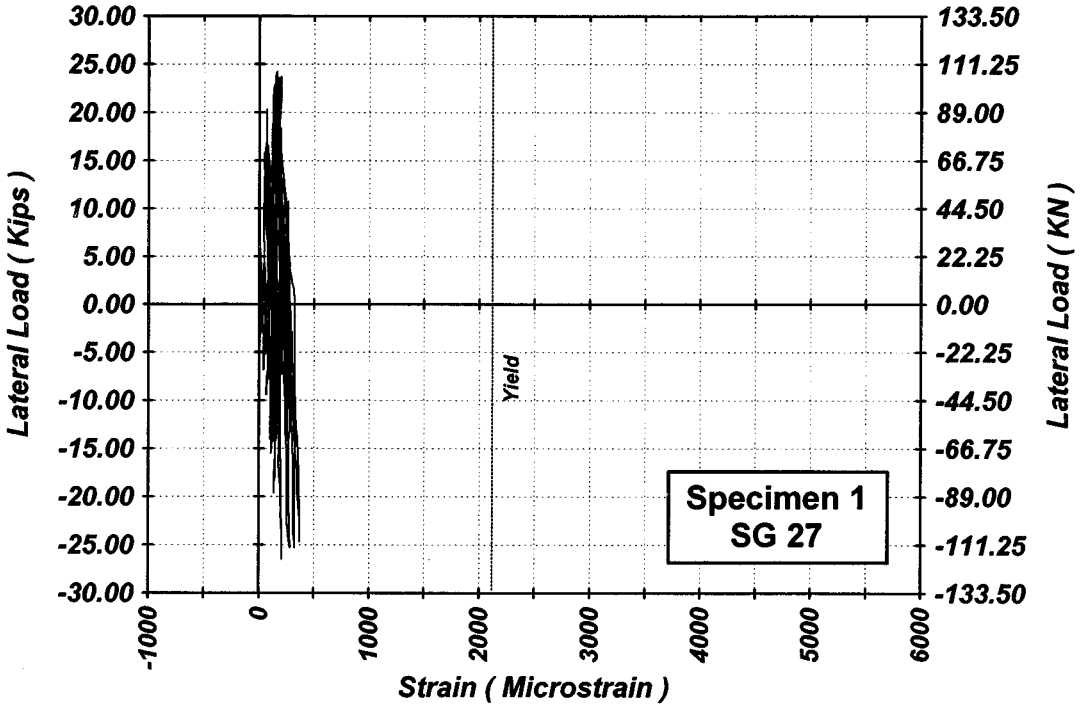

Figure A-27 Measured Lateral Load-Strain in SG-27 of Specimen 1

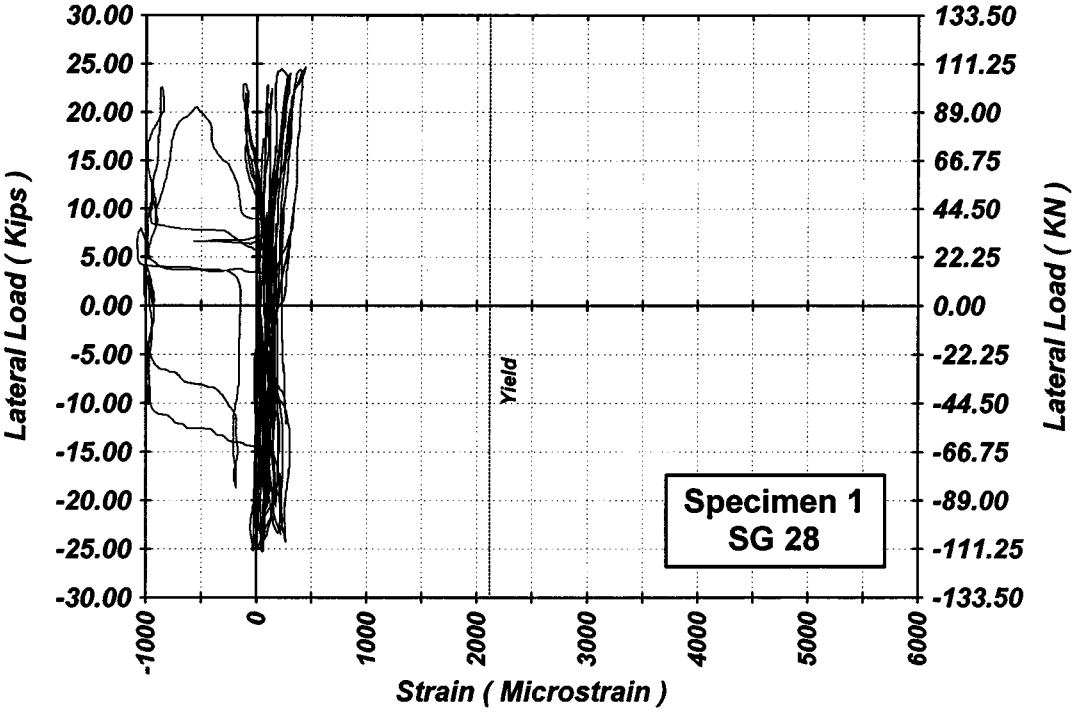

Figure A-28 Measured Lateral Load-Strain in SG-28 of Specimen 1

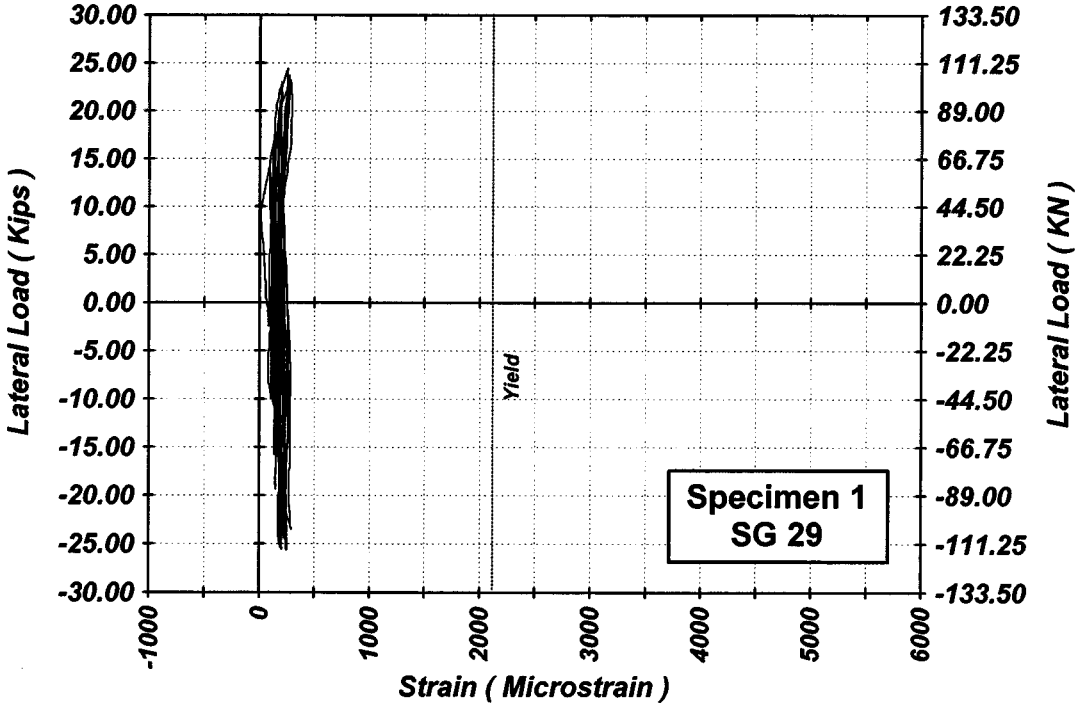

Figure A-29 Measured Lateral Load-Strain in SG-29 of Specimen 1

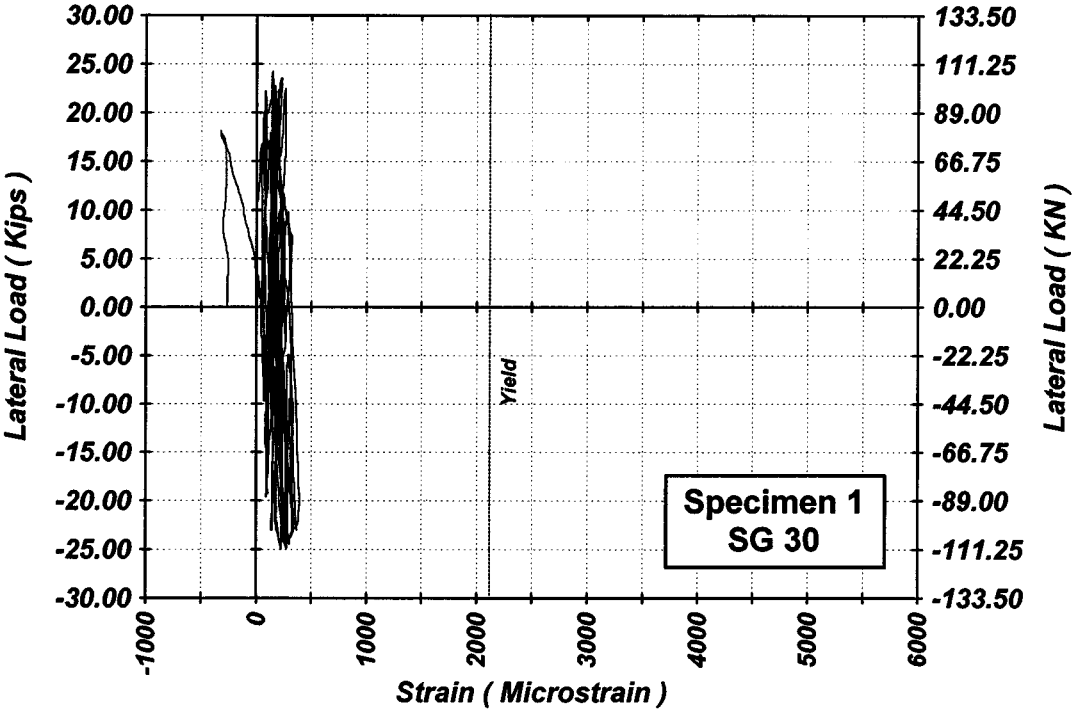

Figure A-30 Measured Lateral Load-Strain in SG-30 of Specimen 1

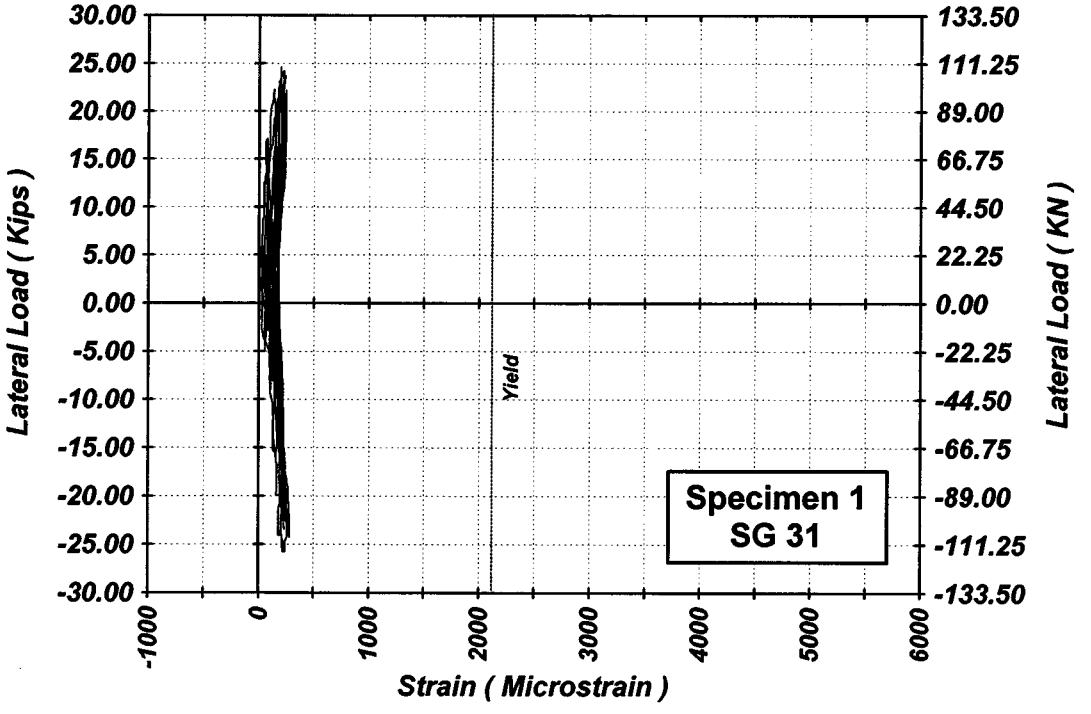

Figure A-31 Measured Lateral Load-Strain in SG-31 of Specimen 1

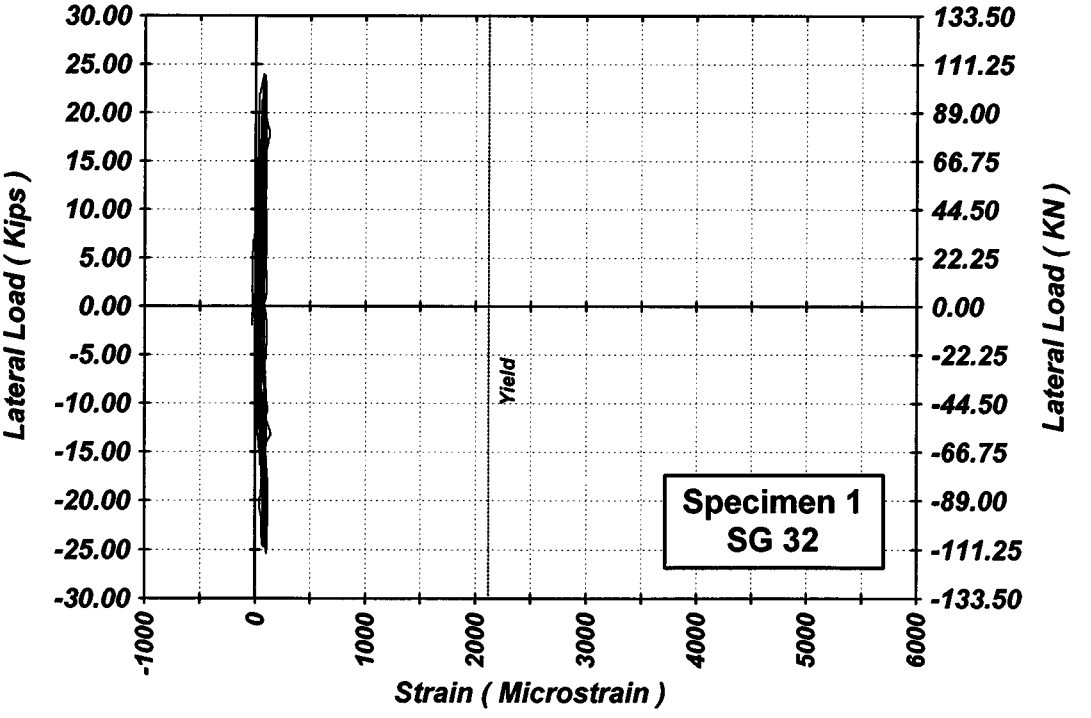

Figure A-32 Measured Lateral Load-Strain in SG-32 of Specimen 1

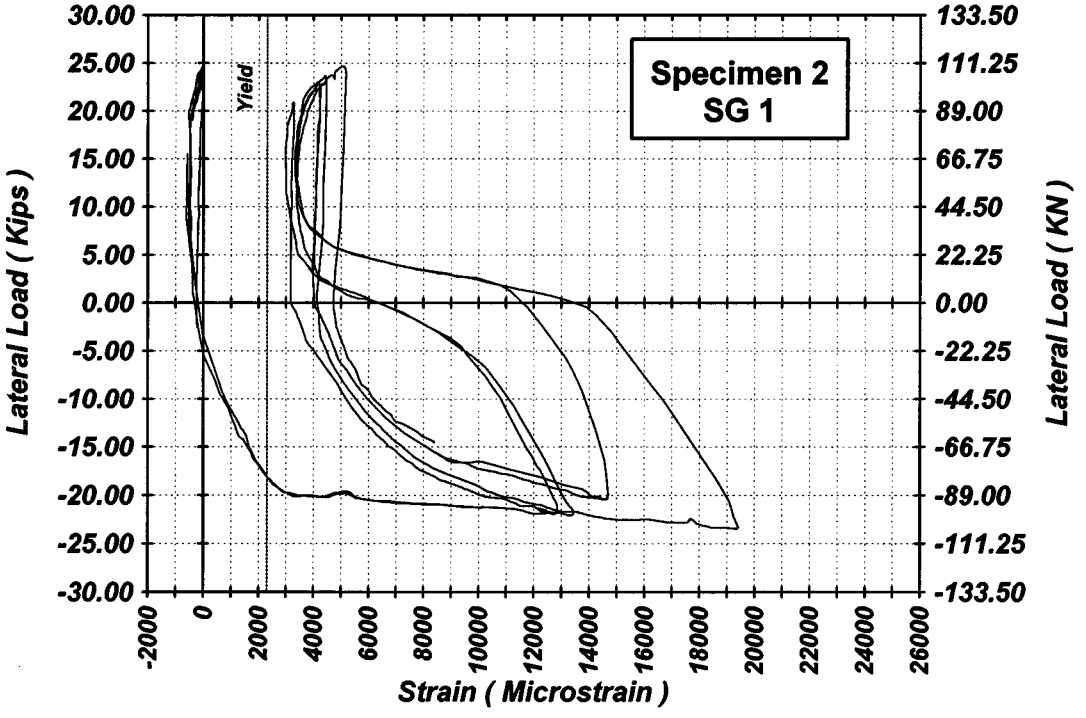

Figure A-33 Measured Lateral Load-Strain in SG-1 of Specimen 2

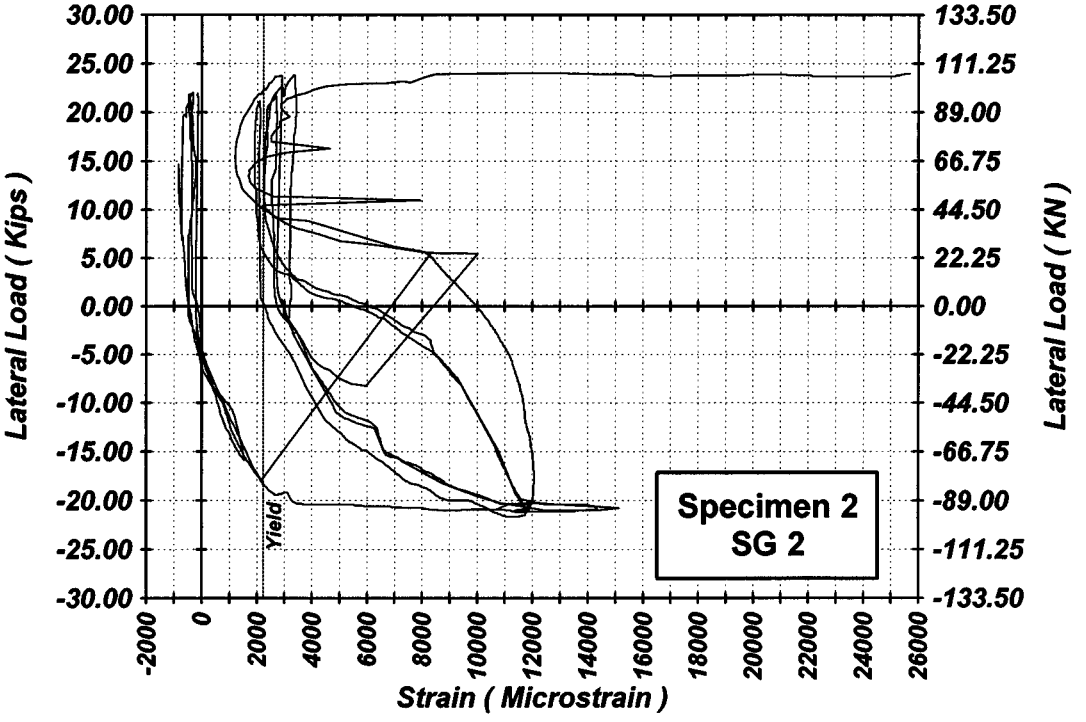

Figure A-34 Measured Lateral Load-Strain in SG-2 of Specimen 2

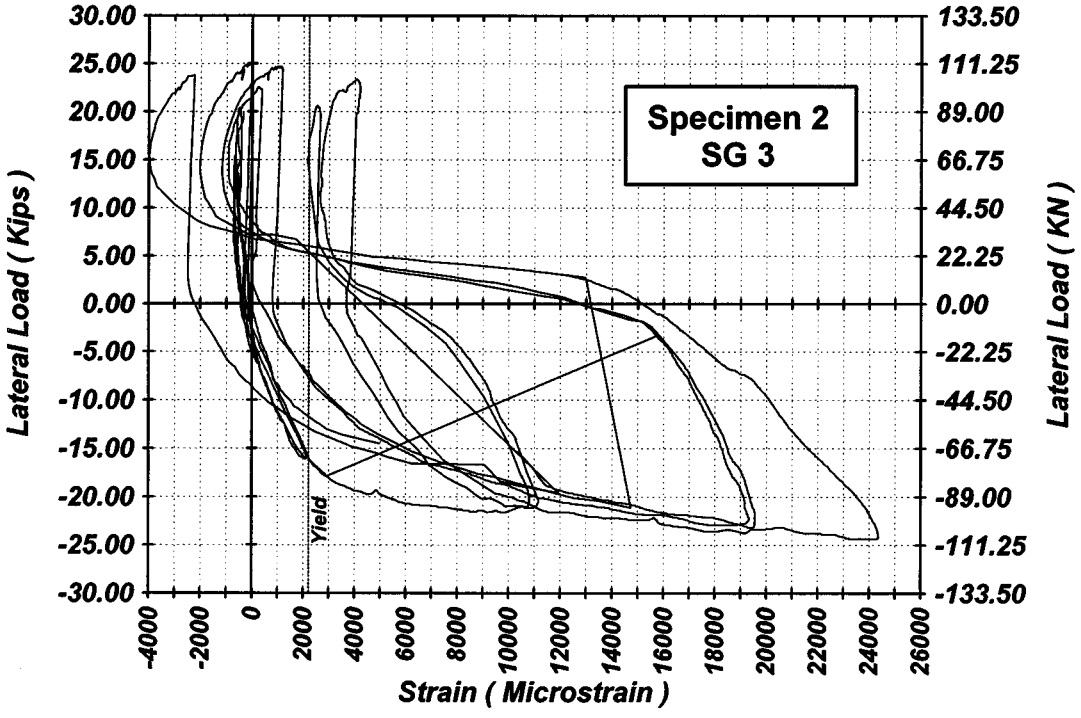

Figure A-35 Measured Lateral Load-Strain in SG-3 of Specimen 2

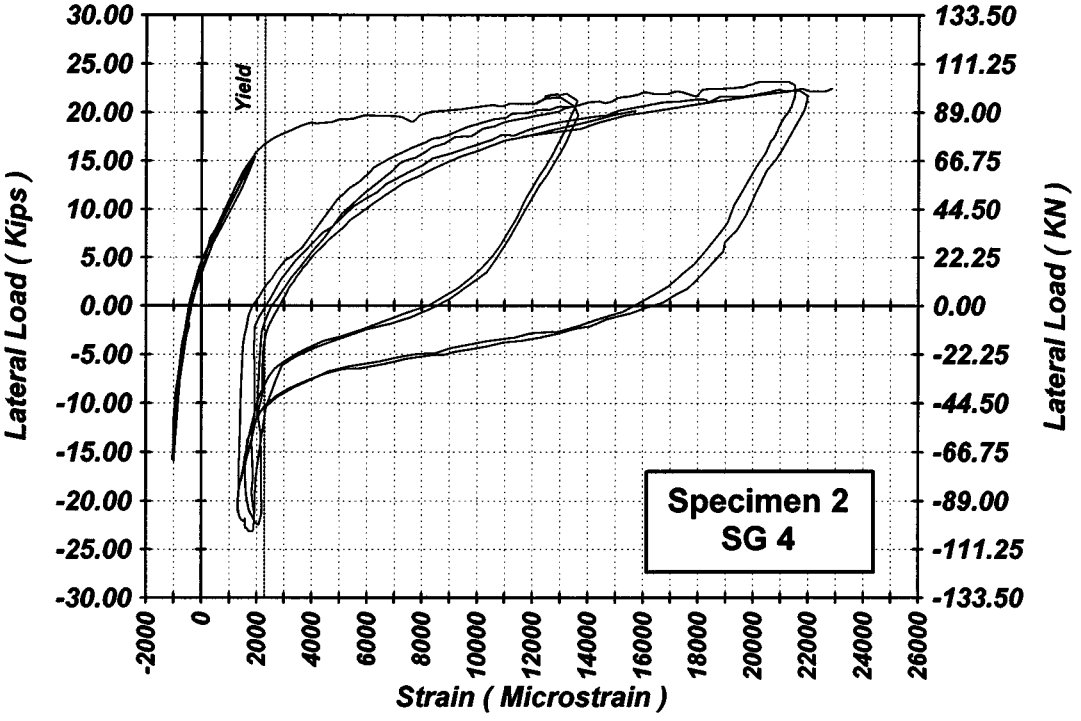

Figure A-36 Measured Lateral Load-Strain in SG-4 of Specimen 2

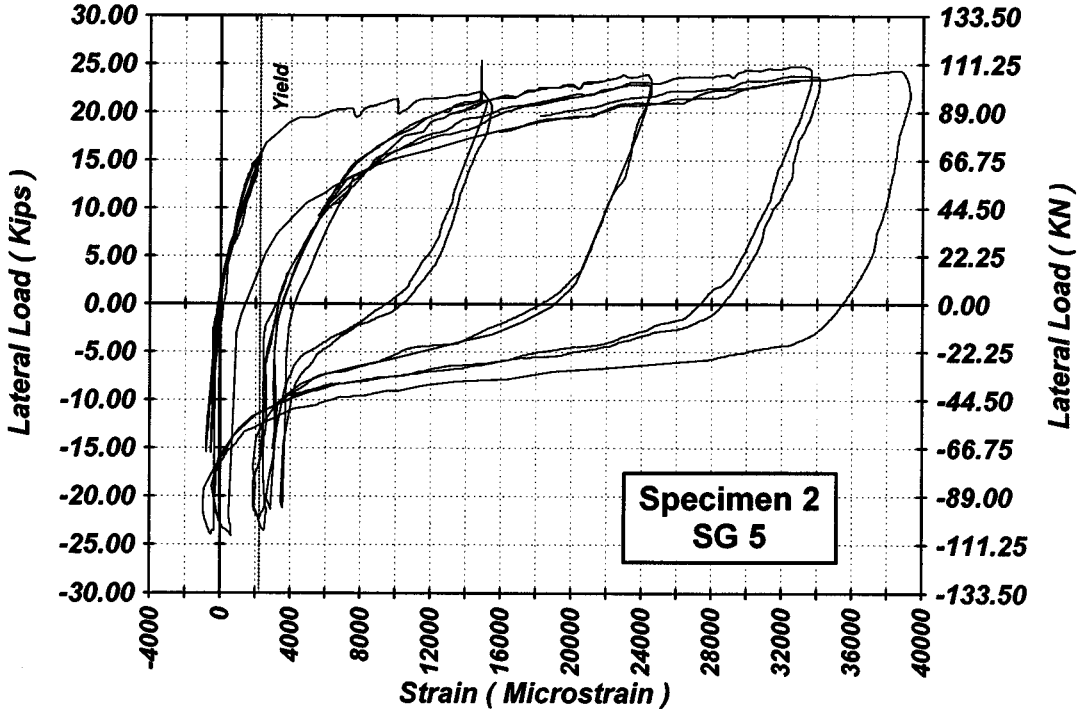

Figure A-37 Measured Lateral Load-Strain in SG-5 of Specimen 2

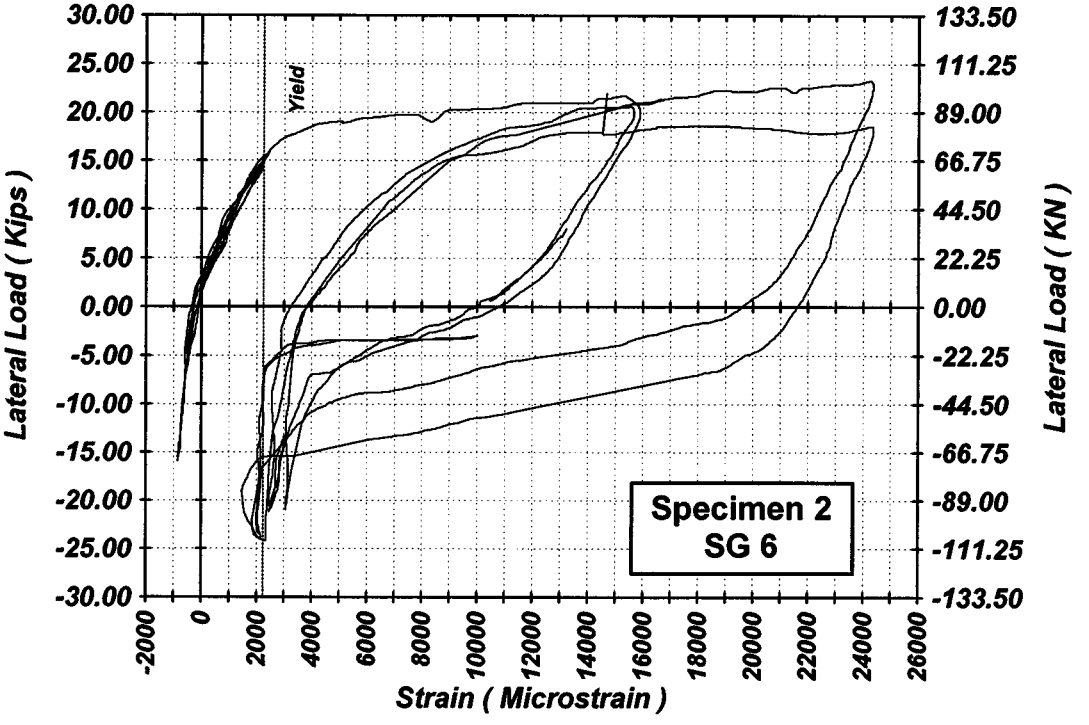

Figure A-38 Measured Lateral Load-Strain in SG-6 of Specimen 2

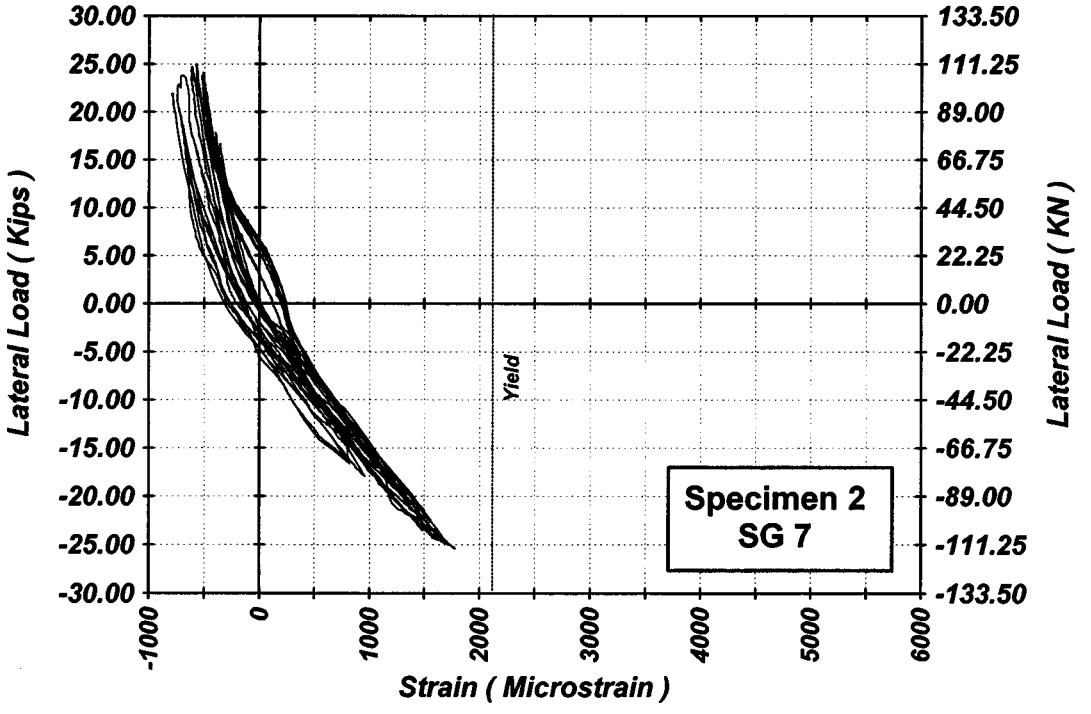

Figure A-39 Measured Lateral Load-Strain in SG-7 of Specimen 2

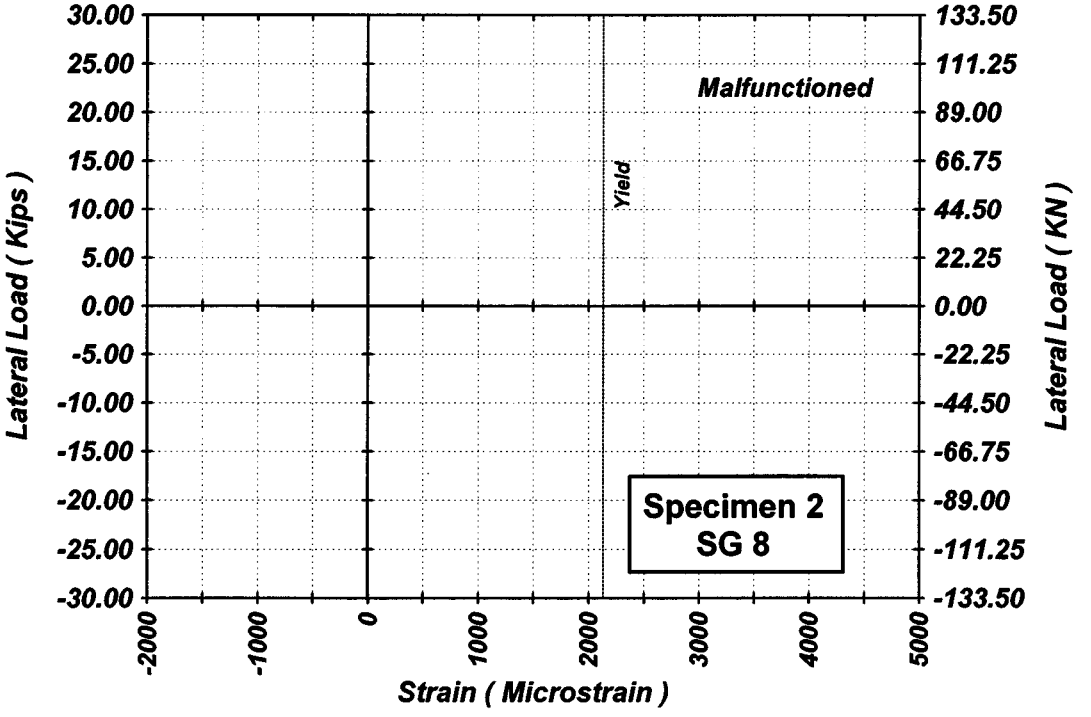

Figure A-40 Measured Lateral Load-Strain in SG-8 of Specimen 2

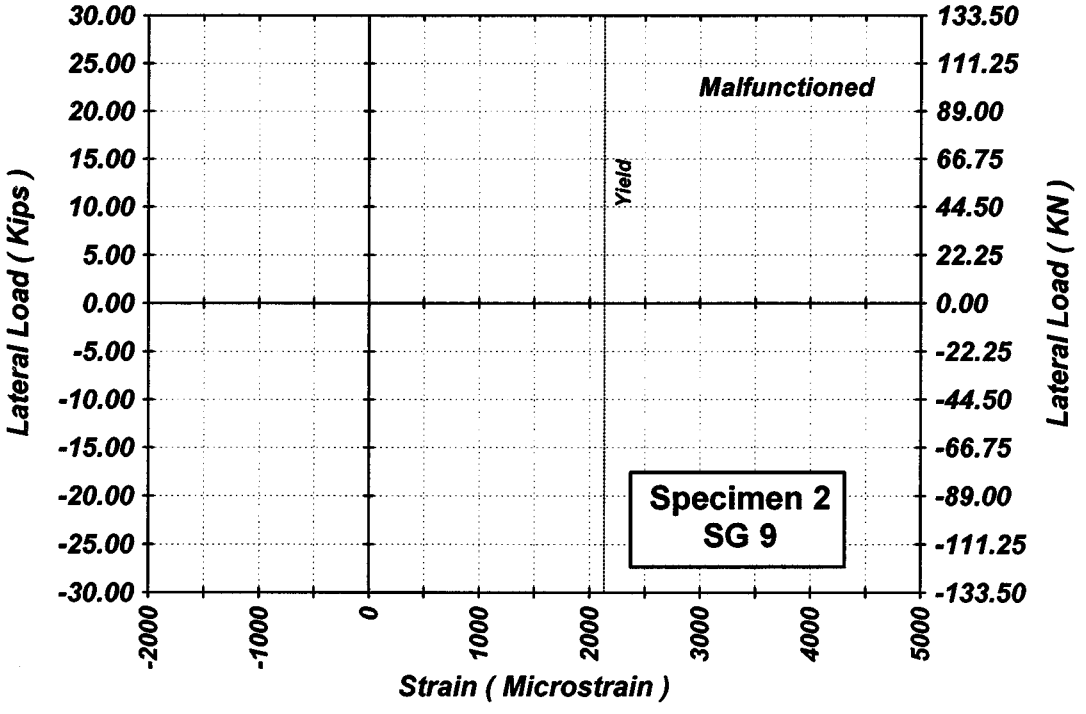

Figure A-41 Measured Lateral Load-Strain in SG-9 of Specimen 2

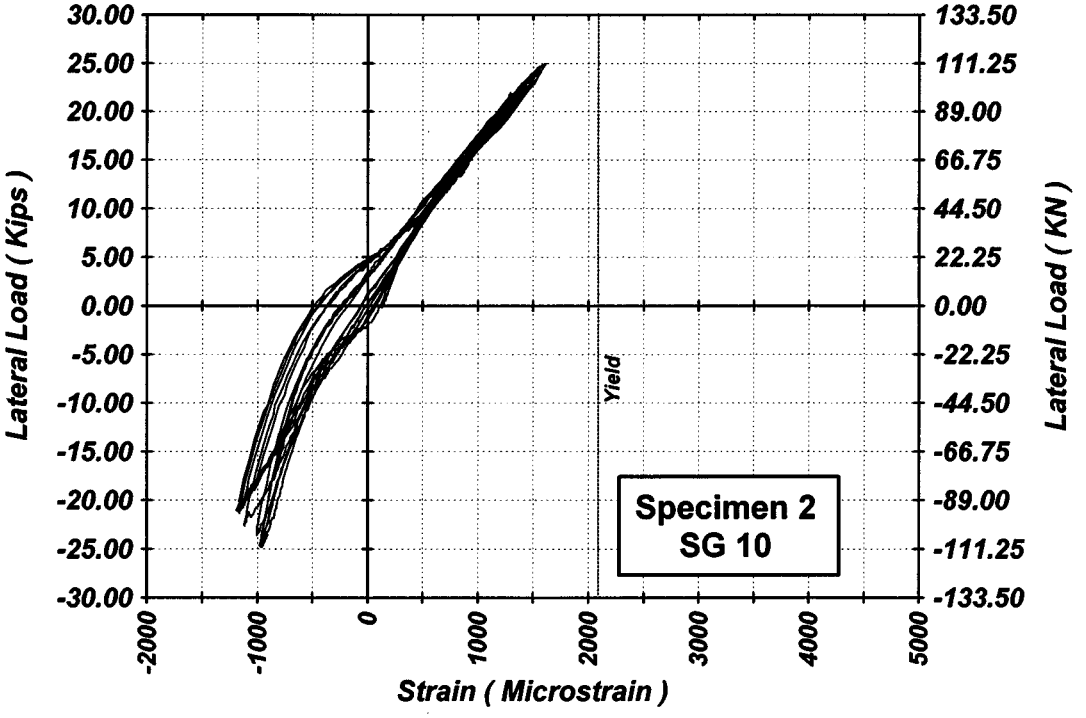

Figure A-42 Measured Lateral Load-Strain in SG-10 of Specimen 2

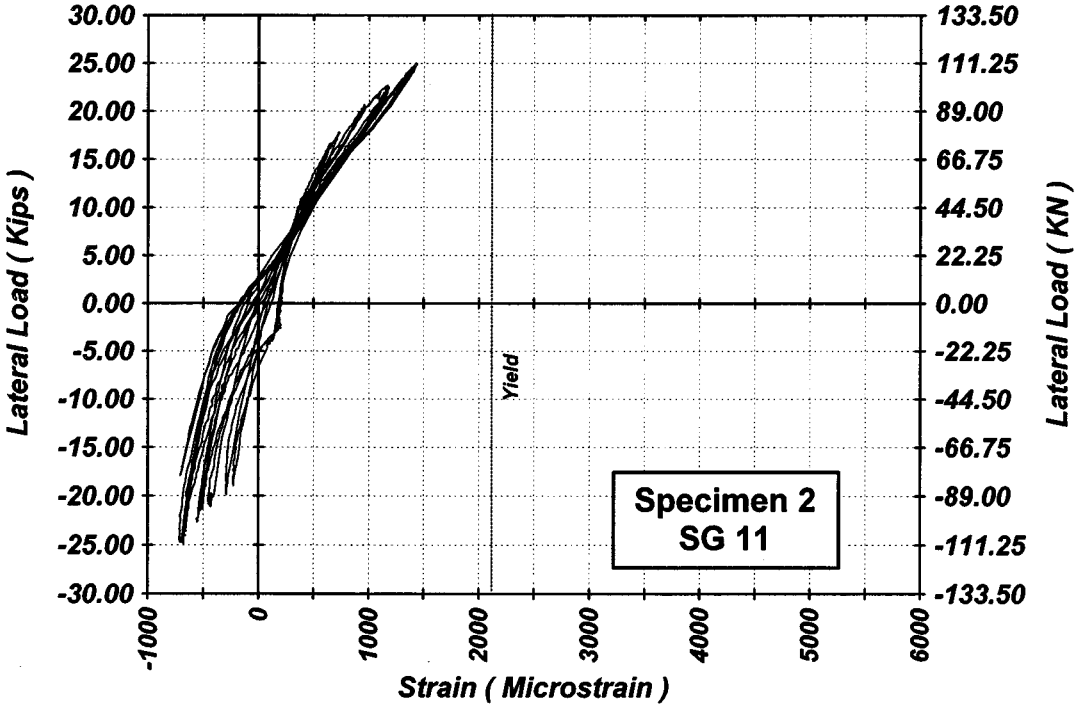

Figure A-43 Measured Lateral Load-Strain in SG-11 of Specimen 2

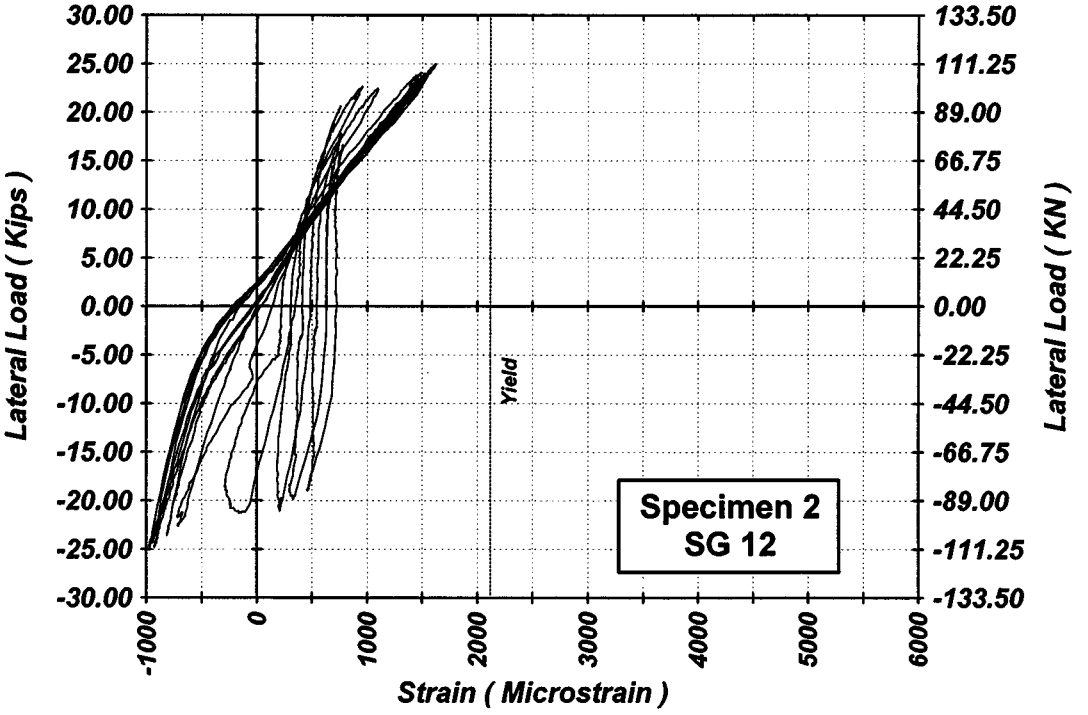

Figure A-44 Measured Lateral Load-Strain in SG-12 of Specimen 2

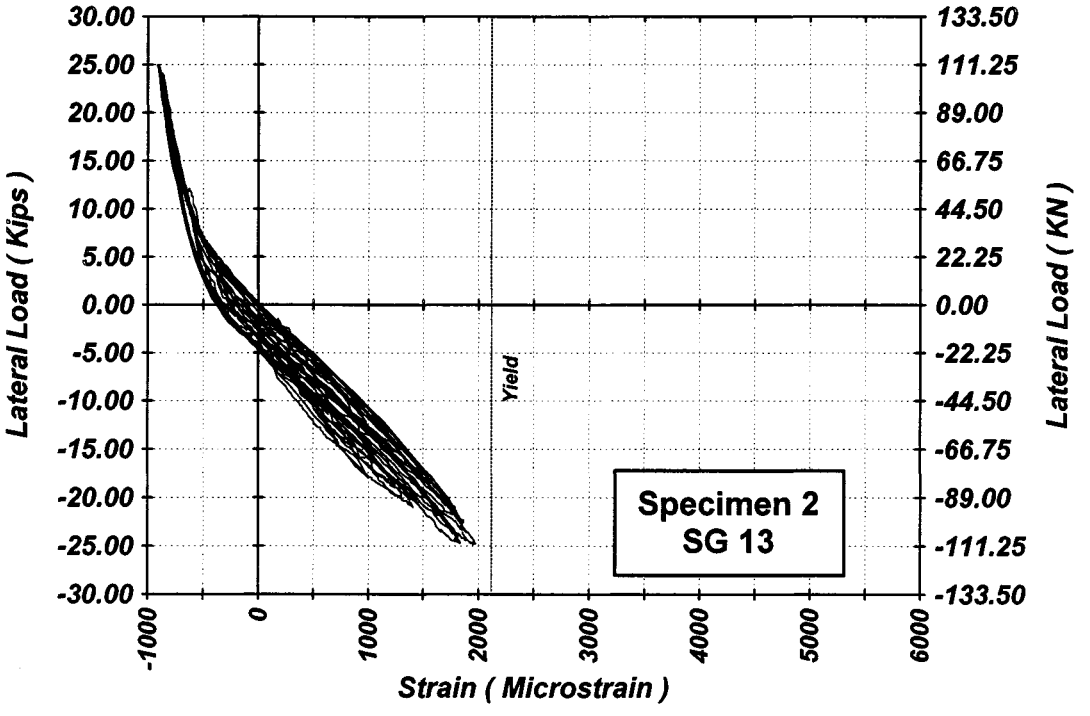

Figure A-45 Measured Lateral Load-Strain in SG-13 of Specimen 2

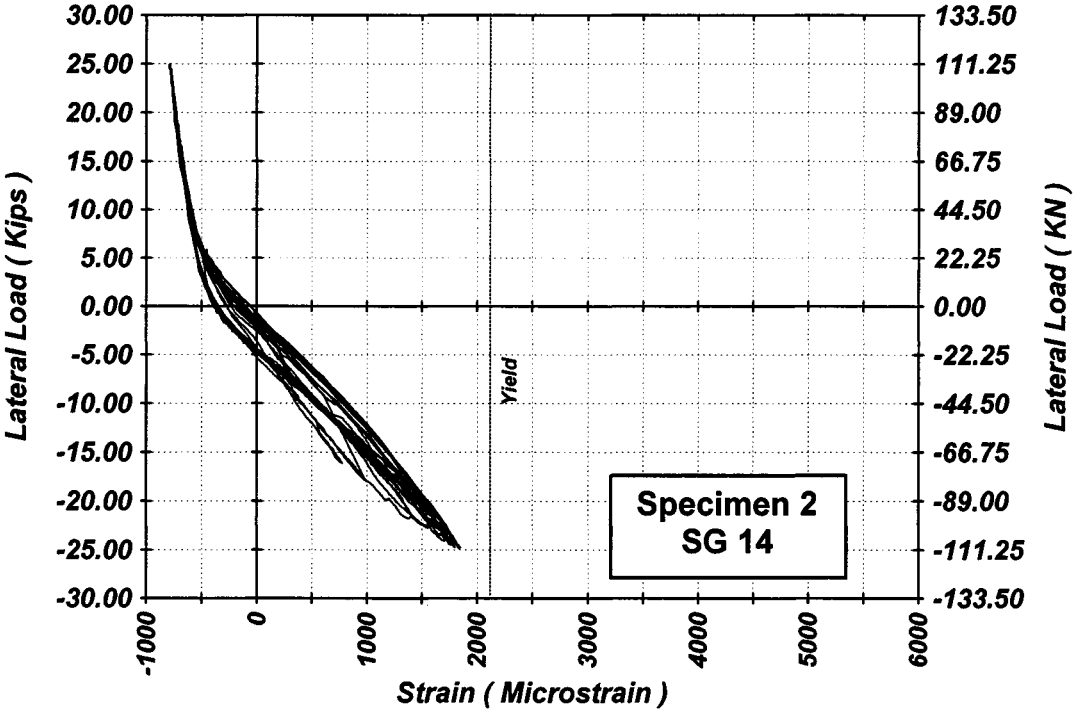

Figure A-46 Measured Lateral Load-Strain in SG-14 of Specimen 2

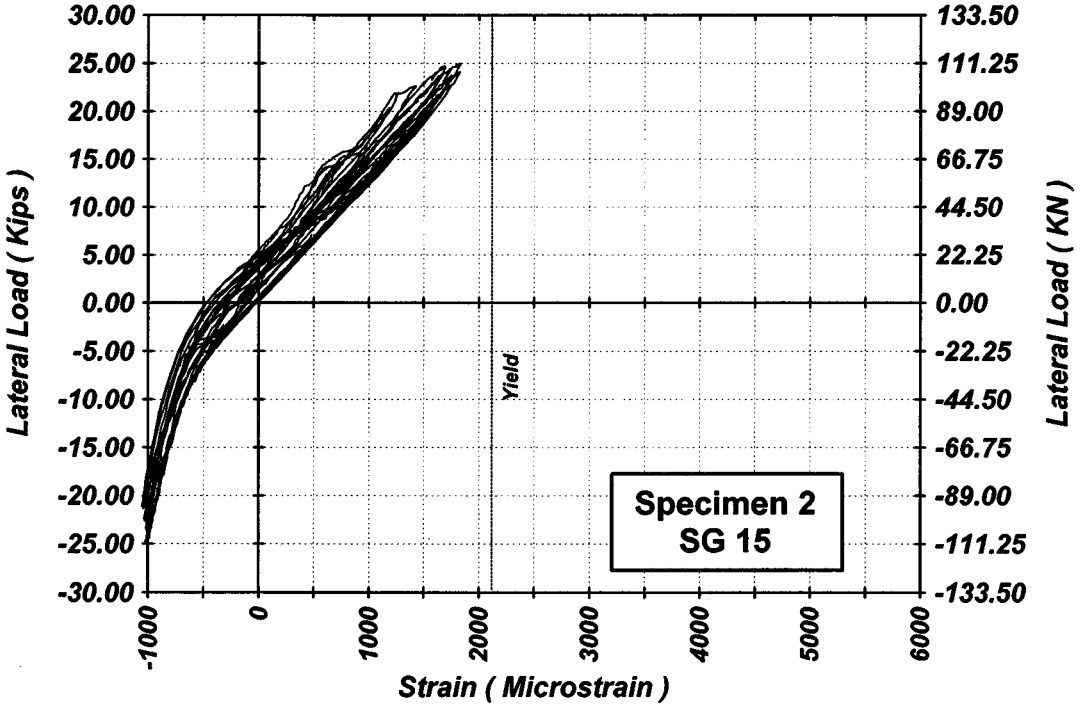

Figure A-47 Measured Lateral Load-Strain in SG-15 of Specimen 2

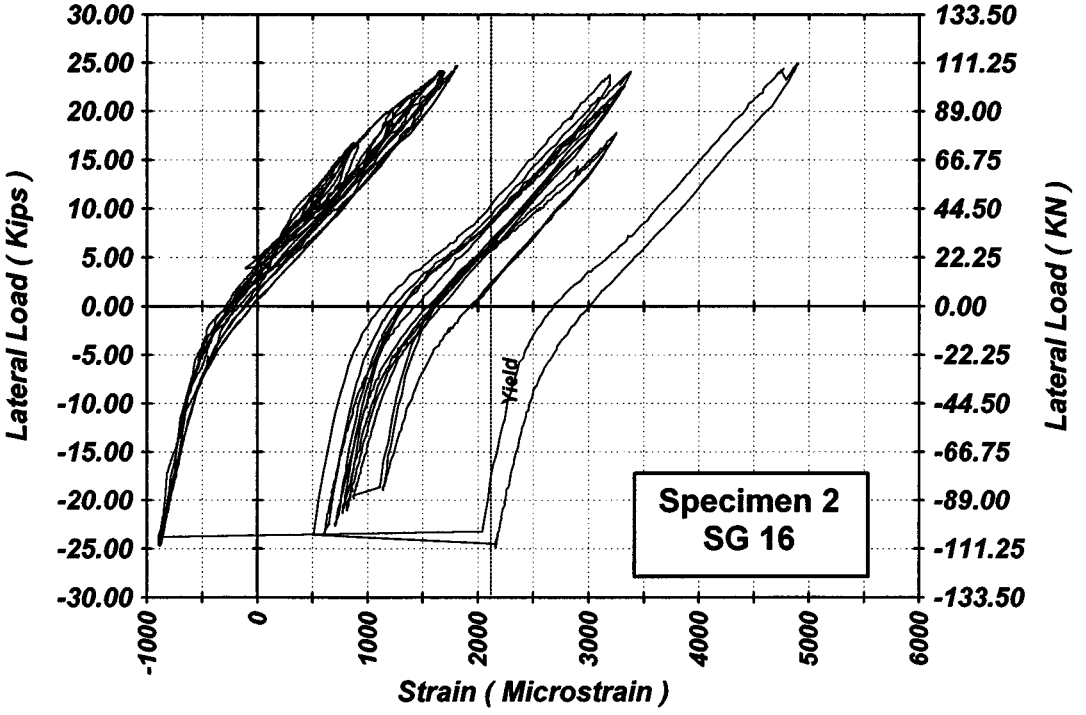

Figure A-48 Measured Lateral Load-Strain in SG-16 of Specimen 2

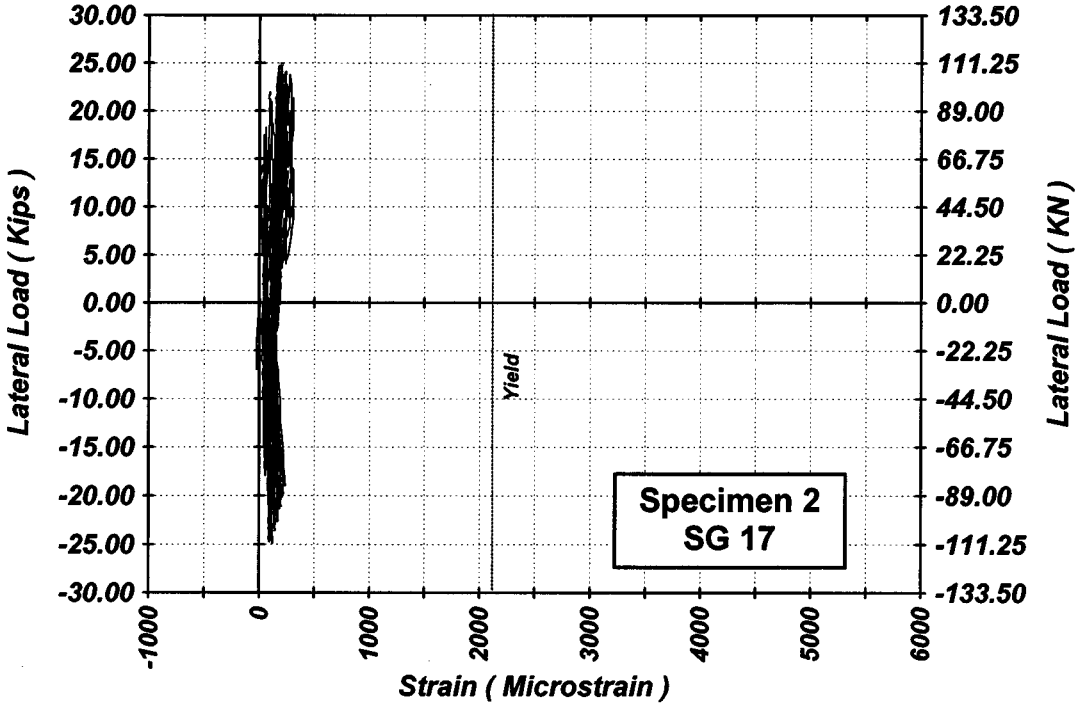

Figure A-49 Measured Lateral Load-Strain in SG-17 of Specimen 2

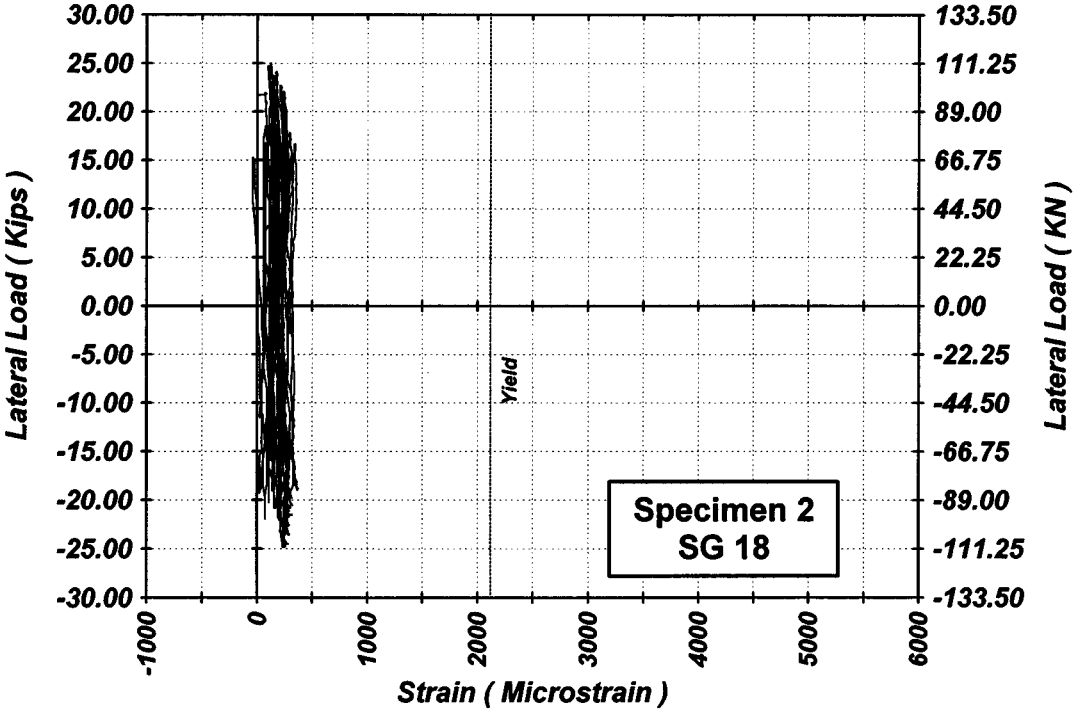

Figure A-50 Measured Lateral Load-Strain in SG-18 of Specimen 2

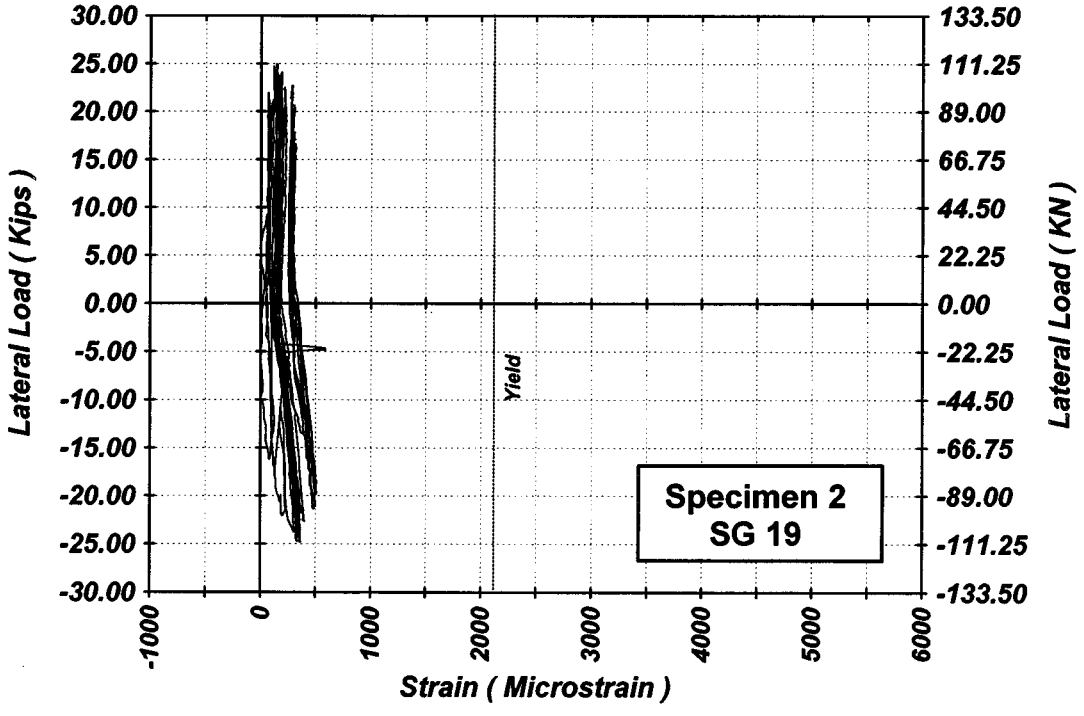

Figure A-51 Measured Lateral Load-Strain in SG-19 of Specimen 2

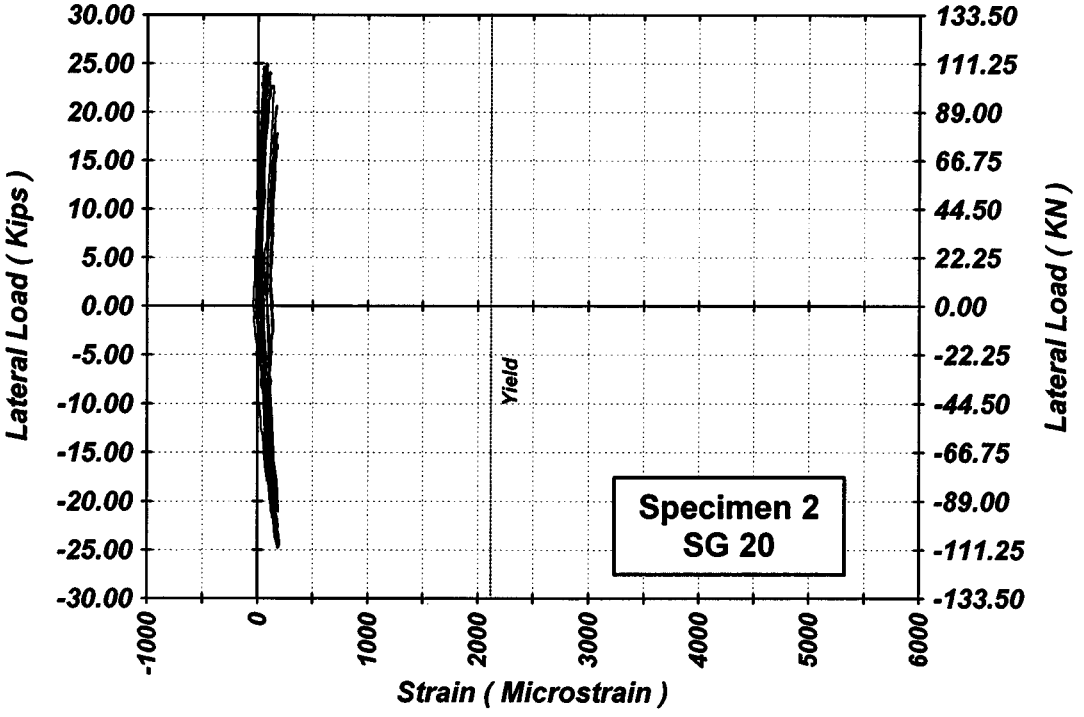

Figure A-52 Measured Lateral Load-Strain in SG-20 of Specimen 2

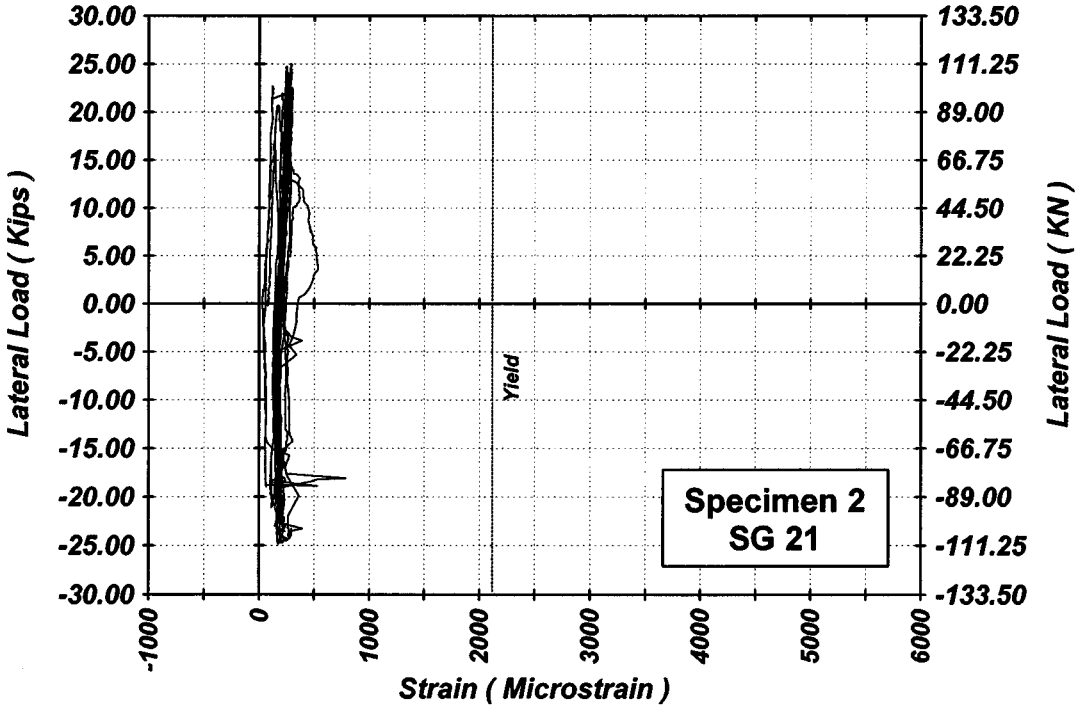

Figure A-53 Measured Lateral Load-Strain in SG-21 of Specimen 2

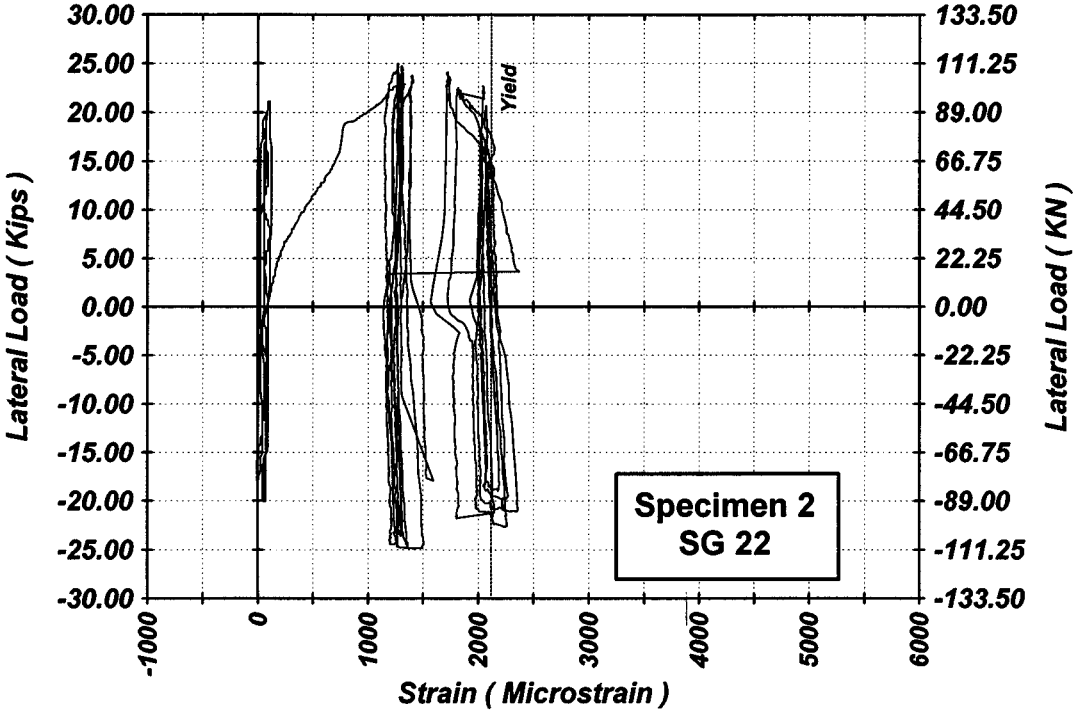

Figure A-54 Measured Lateral Load-Strain in SG-22 of Specimen 2

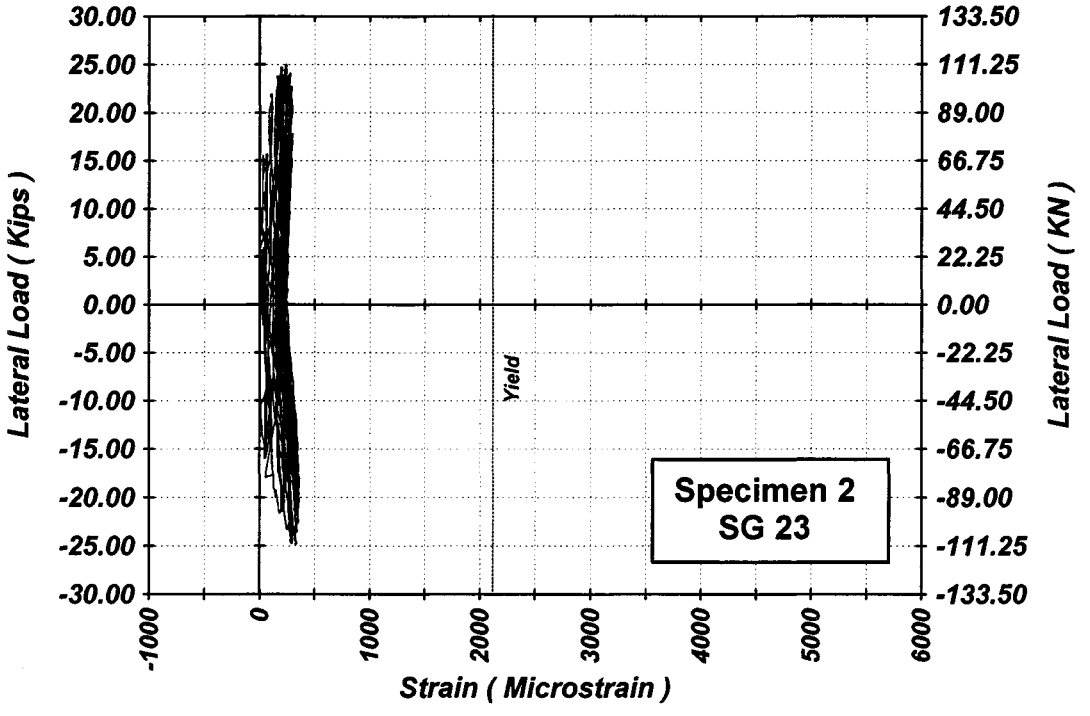

Figure A-55 Measured Lateral Load-Strain in SG-23 of Specimen 2

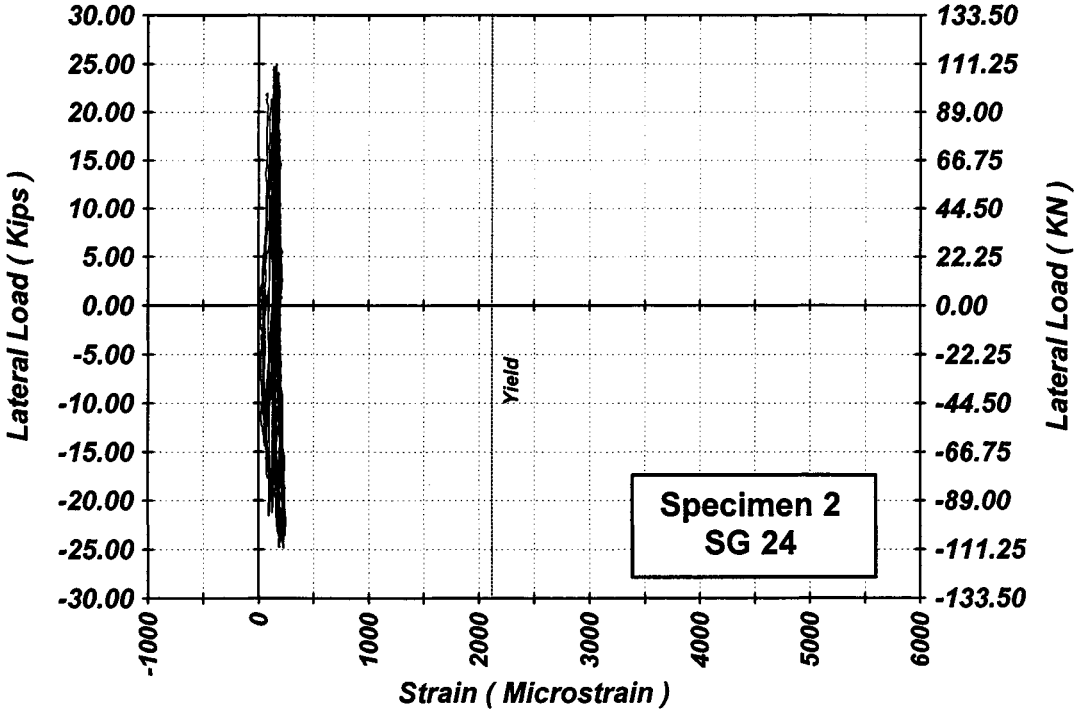

Figure A-56 Measured Lateral Load-Strain in SG-24 of Specimen 2

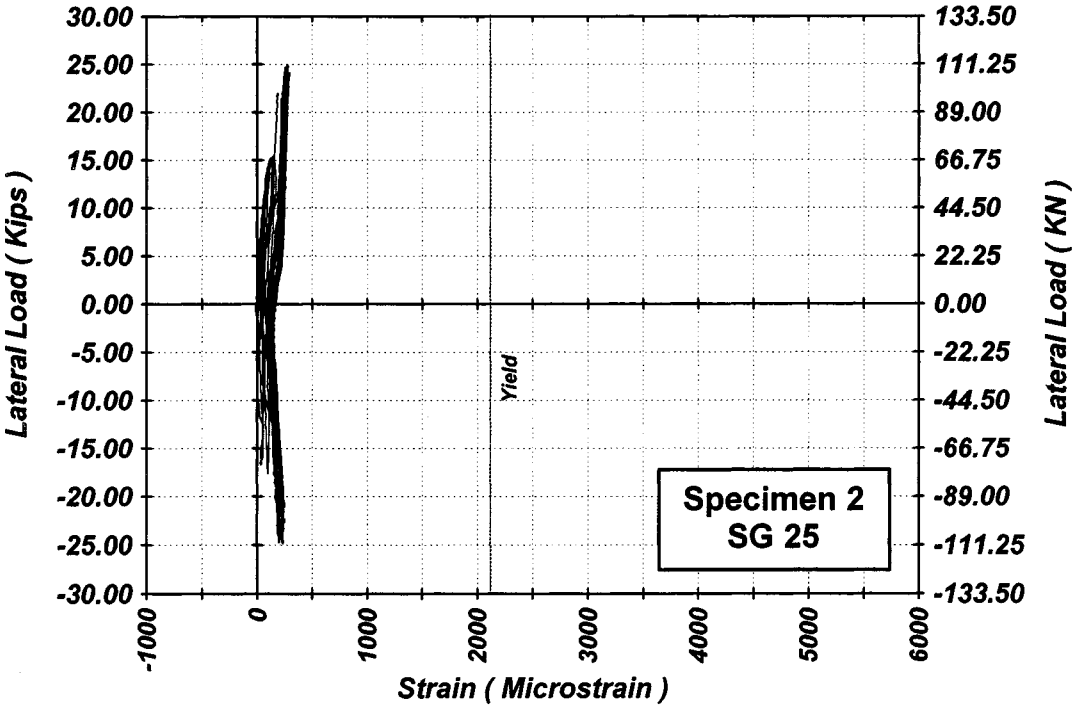

Figure A-57 Measured Lateral Load-Strain in SG-25 of Specimen 2

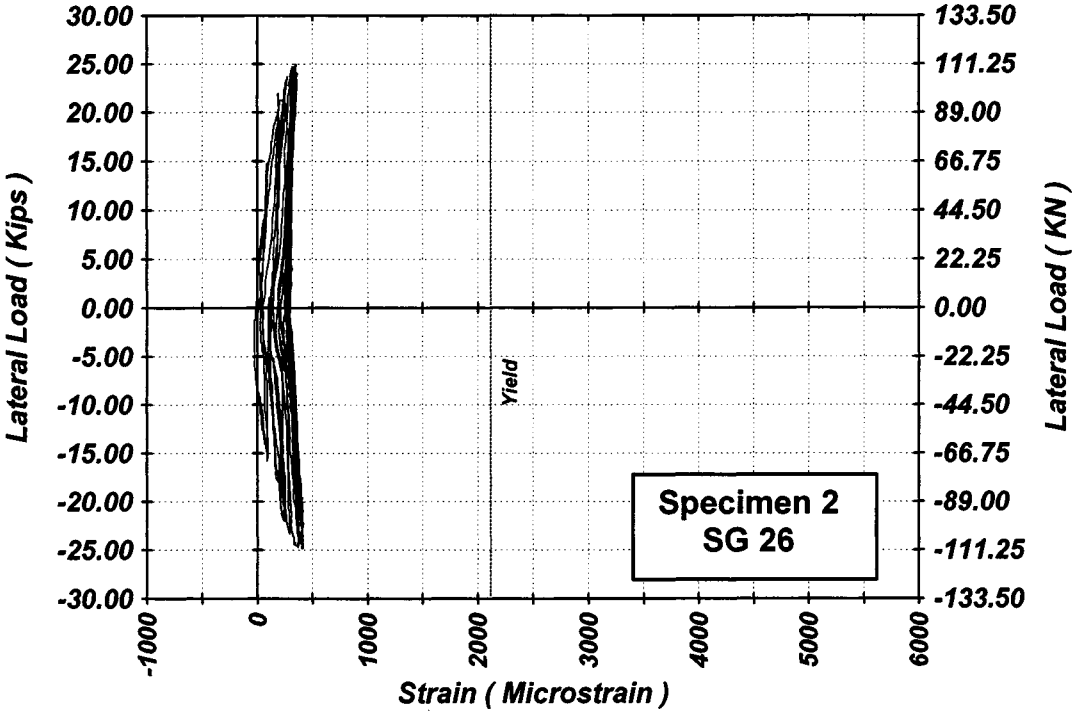

Figure A-58 Measured Lateral Load-Strain in SG-26 of Specimen 2

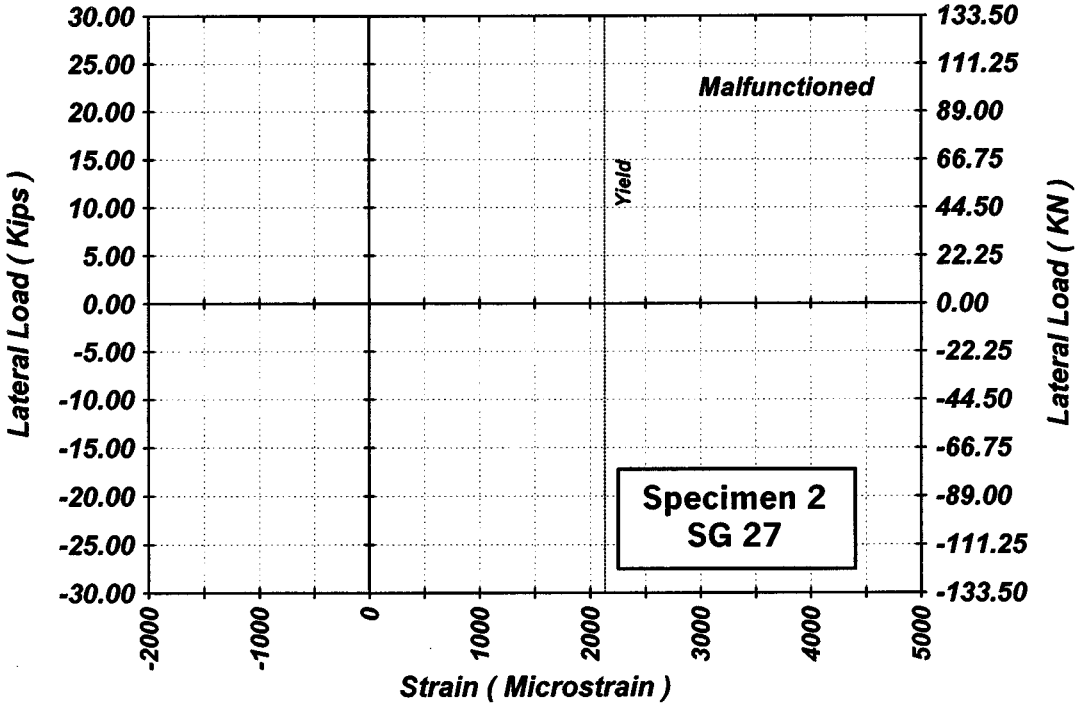

Figure A-59 Measured Lateral Load-Strain in SG-27 of Specimen 2

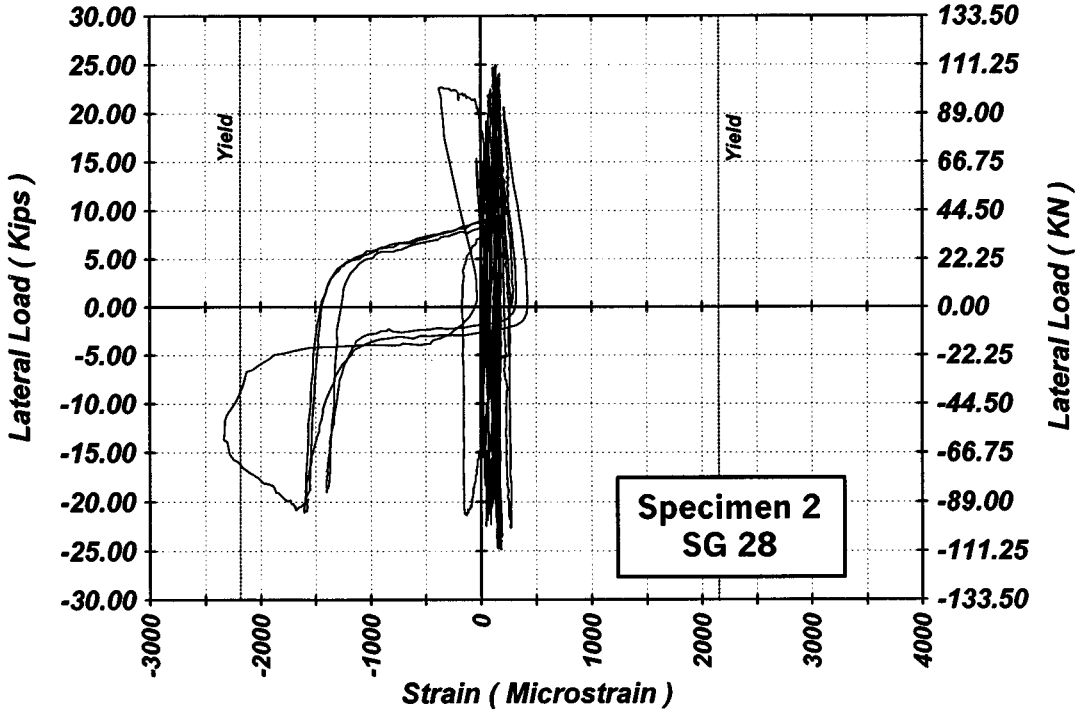

Figure A-60 Measured Lateral Load-Strain in SG-28 of Specimen 2

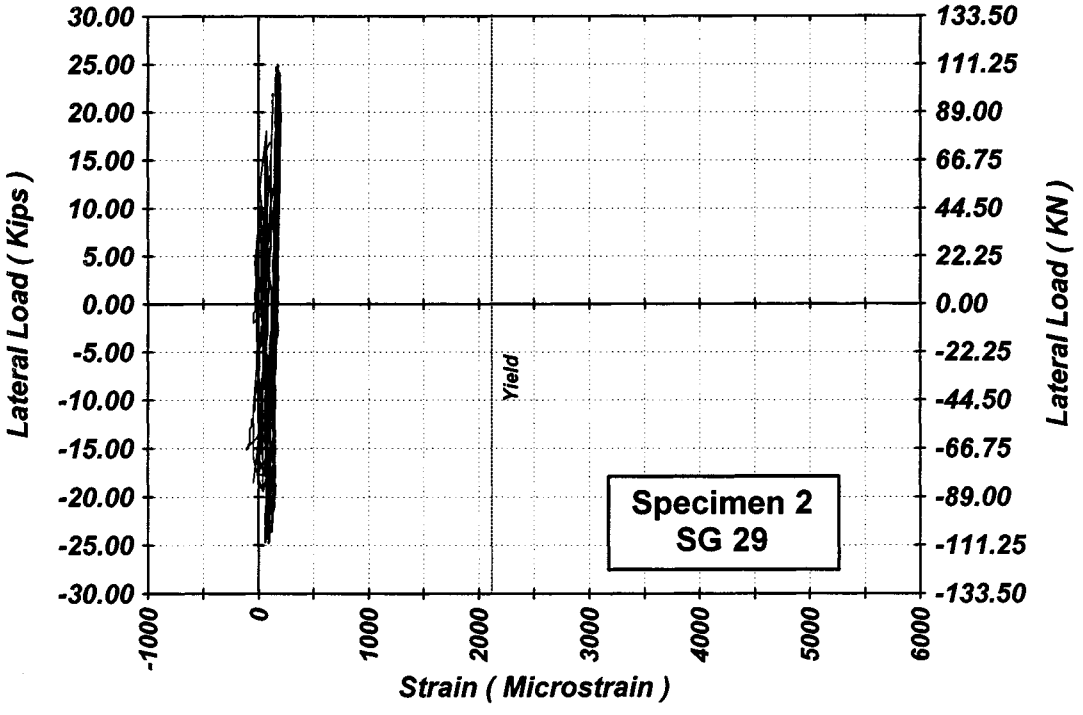

Figure A-61 Measured Lateral Load-Strain in SG-29 of Specimen 2

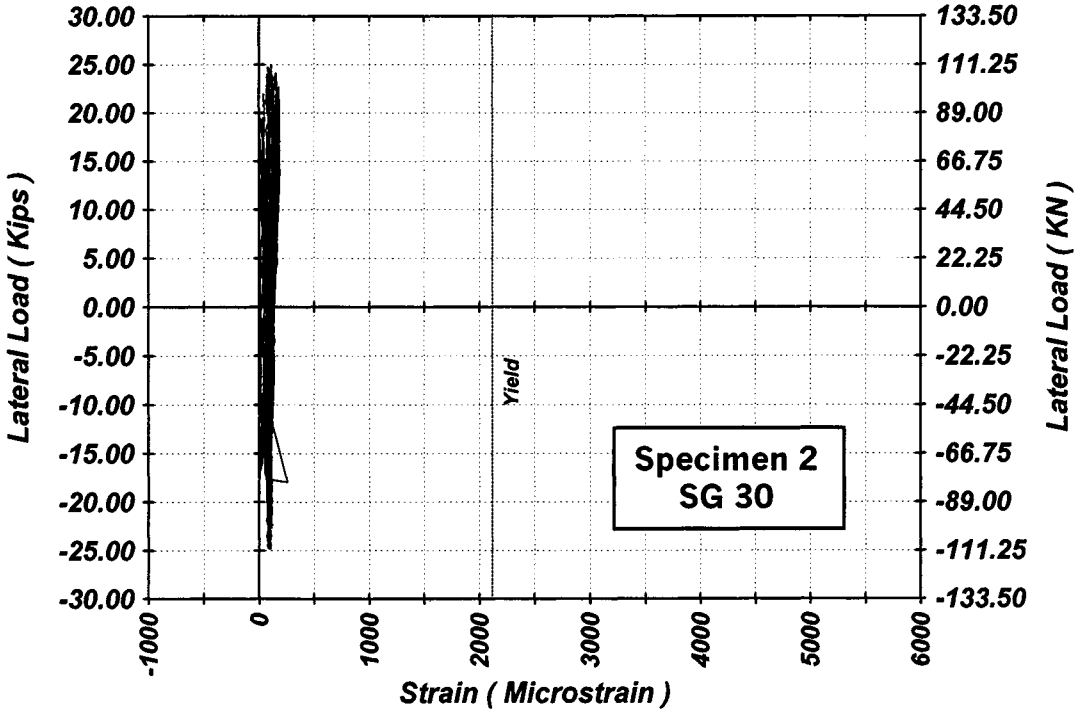

Figure A-62 Measured Lateral Load-Strain in SG-30 of Specimen 2

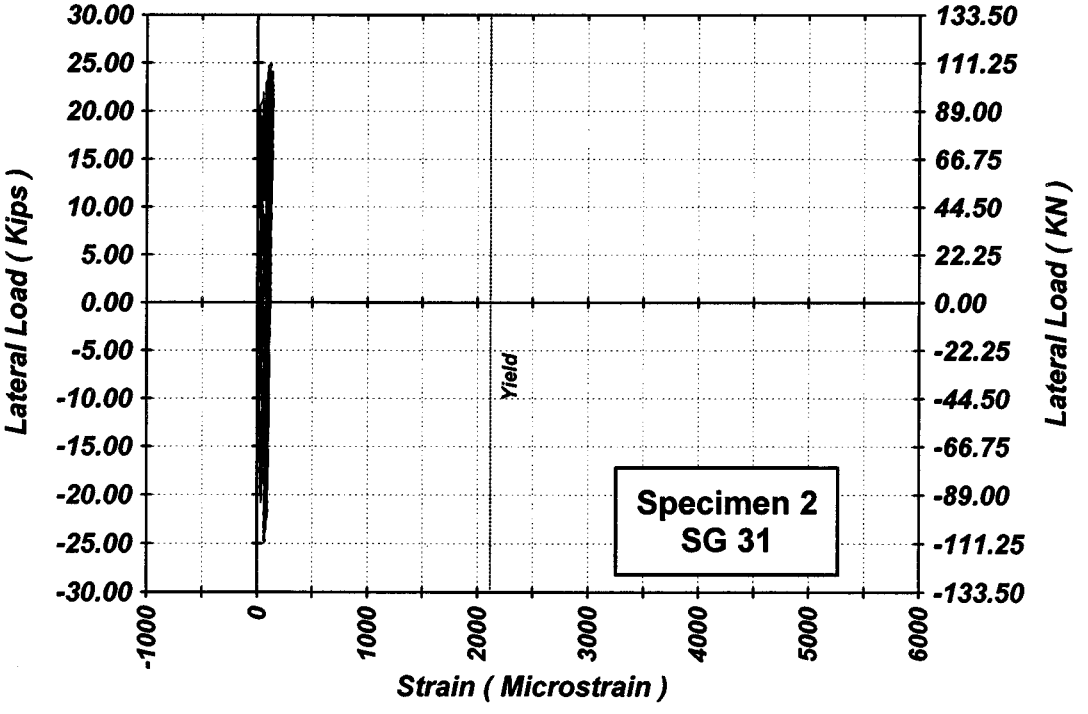

Figure A-63 Measured Lateral Load-Strain in SG-31 of Specimen 2

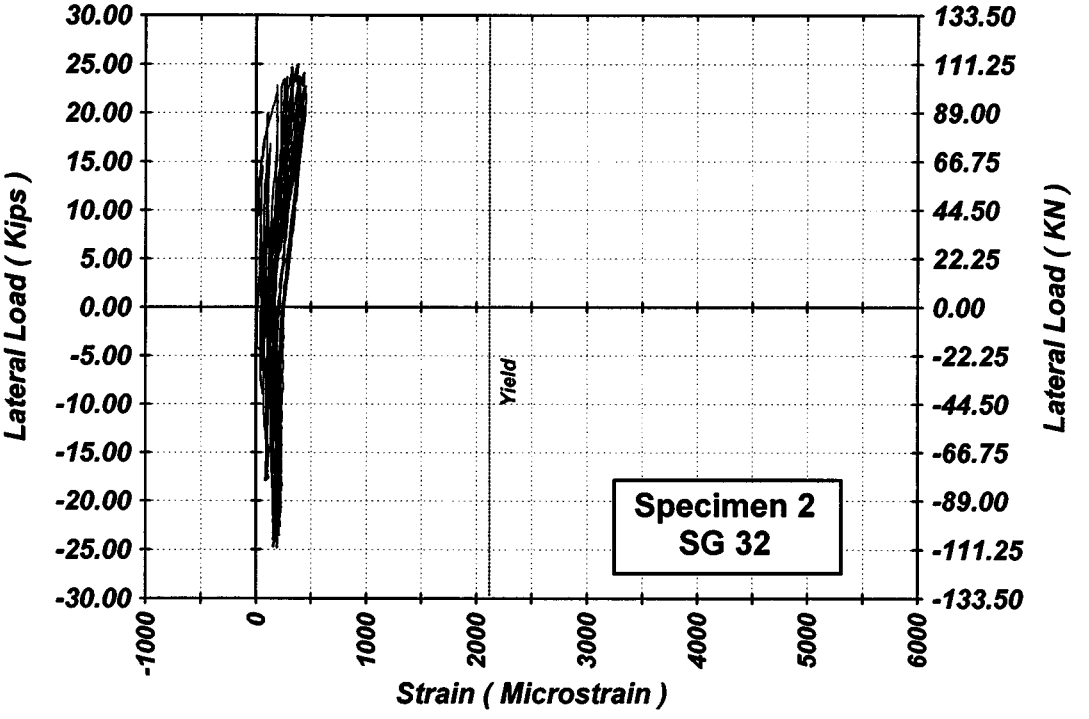

Figure A-64 Measured Lateral Load-Strain in SG-32 of Specimen 2

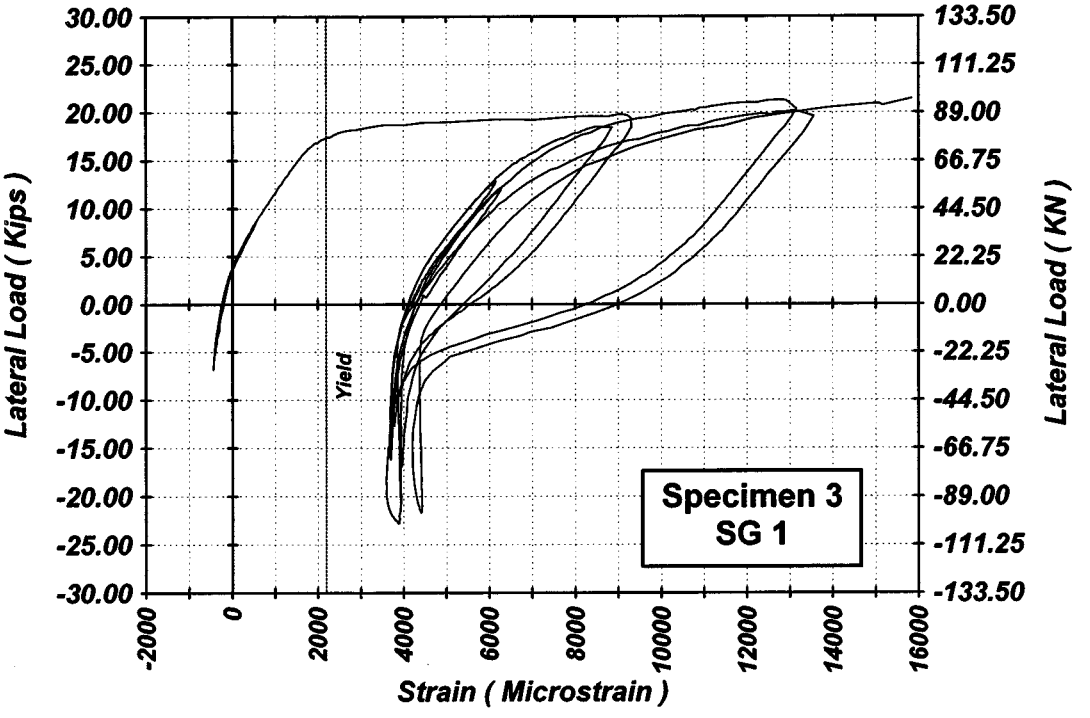

Figure A-65 Measured Lateral Load-Strain in SG-1 of Specimen 3

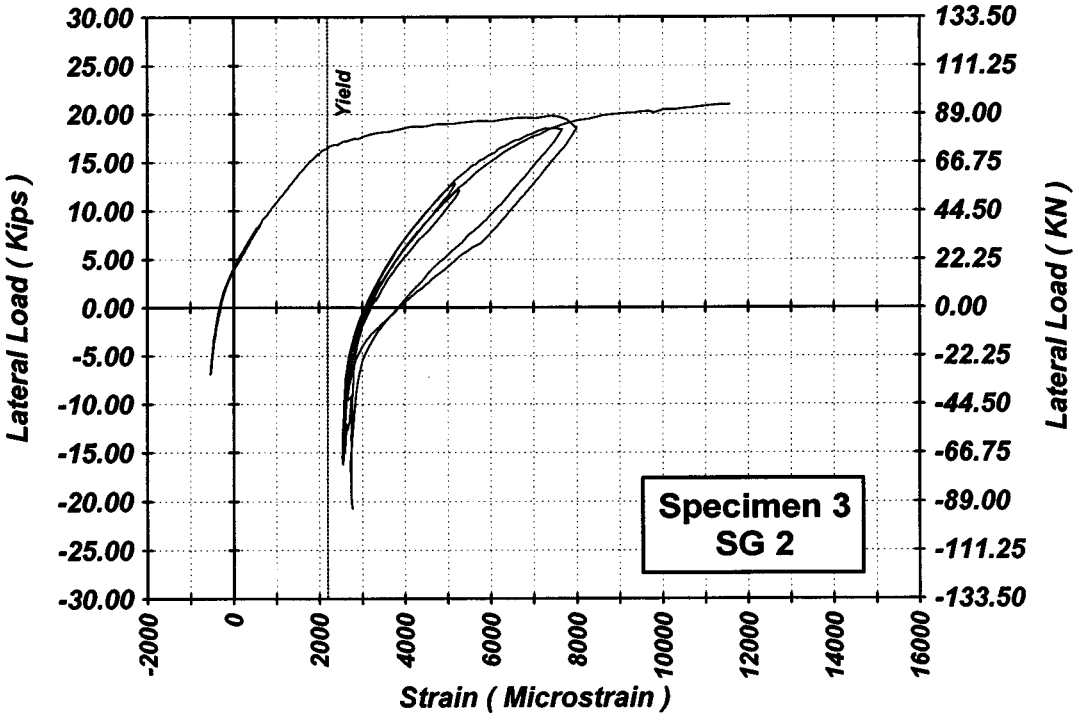

Figure A-66 Measured Lateral Load-Strain in SG-2 of Specimen 3

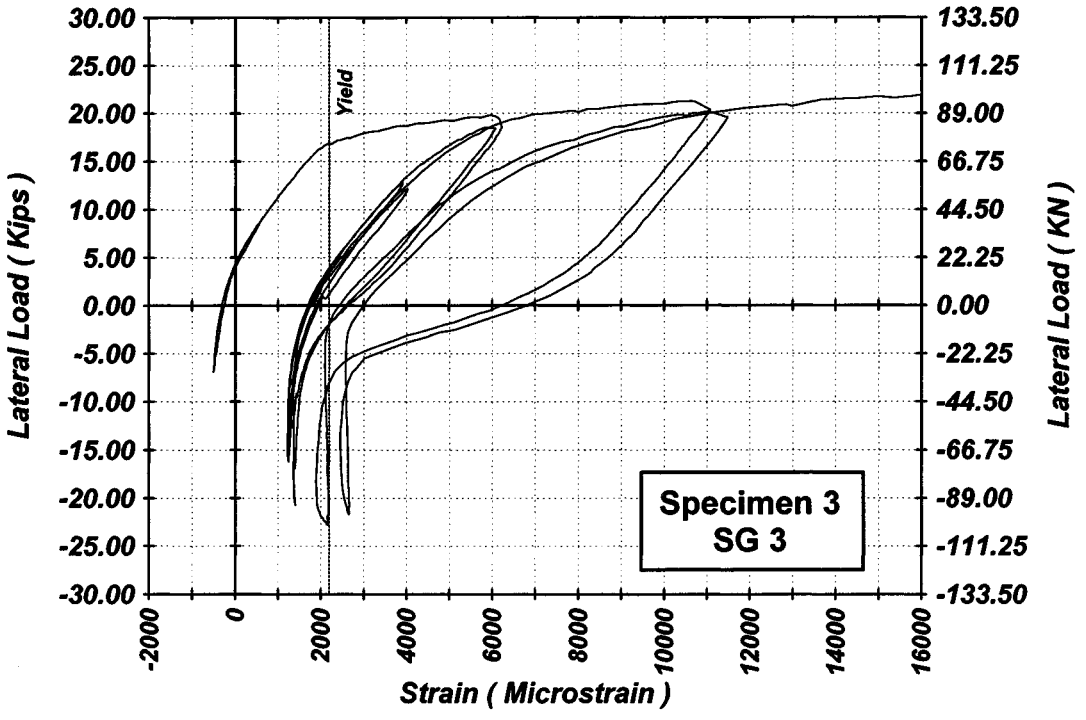

Figure A-67 Measured Lateral Load-Strain in SG-3 of Specimen 3

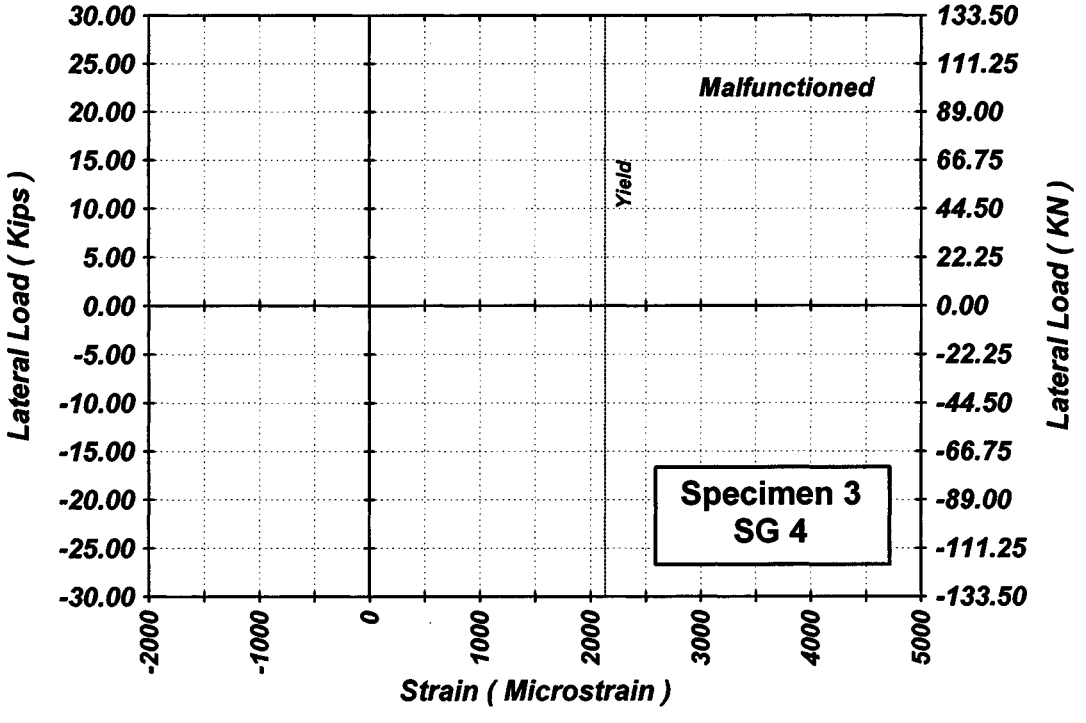

Figure A-68 Measured Lateral Load-Strain in SG-4 of Specimen 3

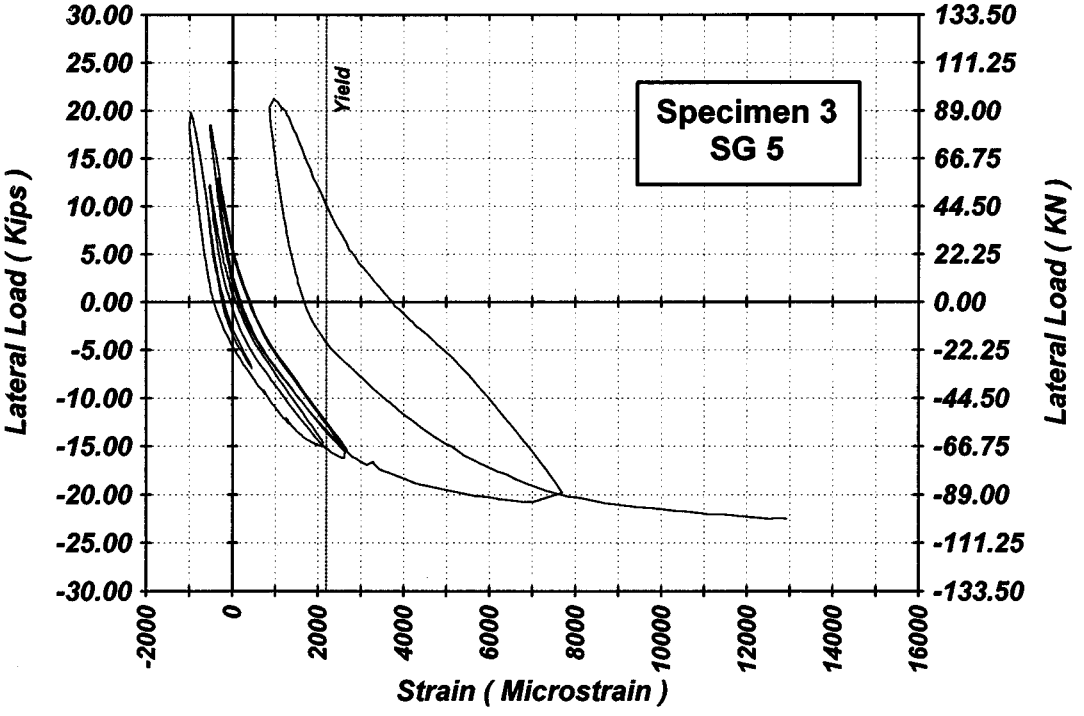

Figure A-69 Measured Lateral Load-Strain in SG-5 of Specimen 3

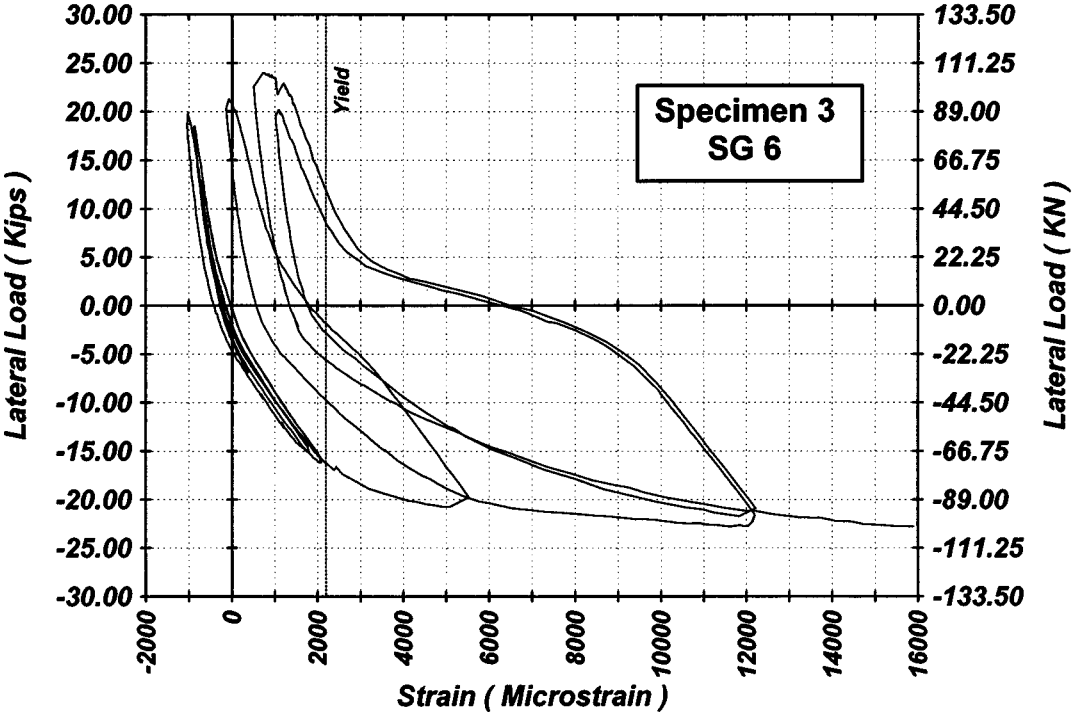

Figure A-70 Measured Lateral Load-Strain in SG-6 of Specimen 3

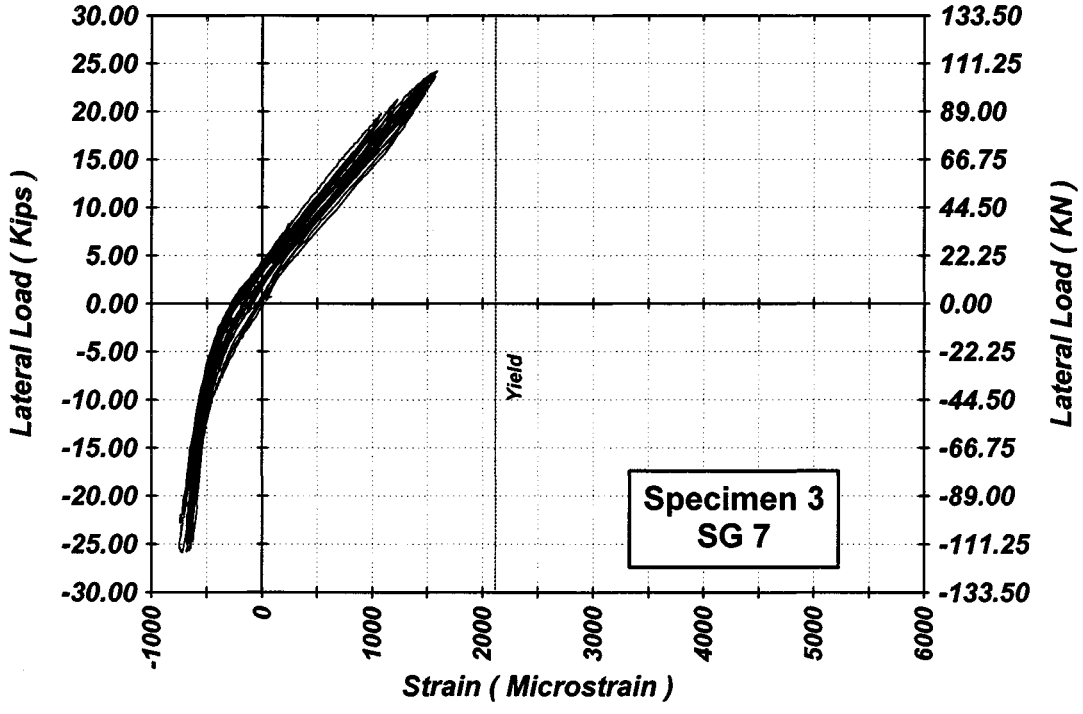

Figure A-71 Measured Lateral Load-Strain in SG-7 of Specimen 3

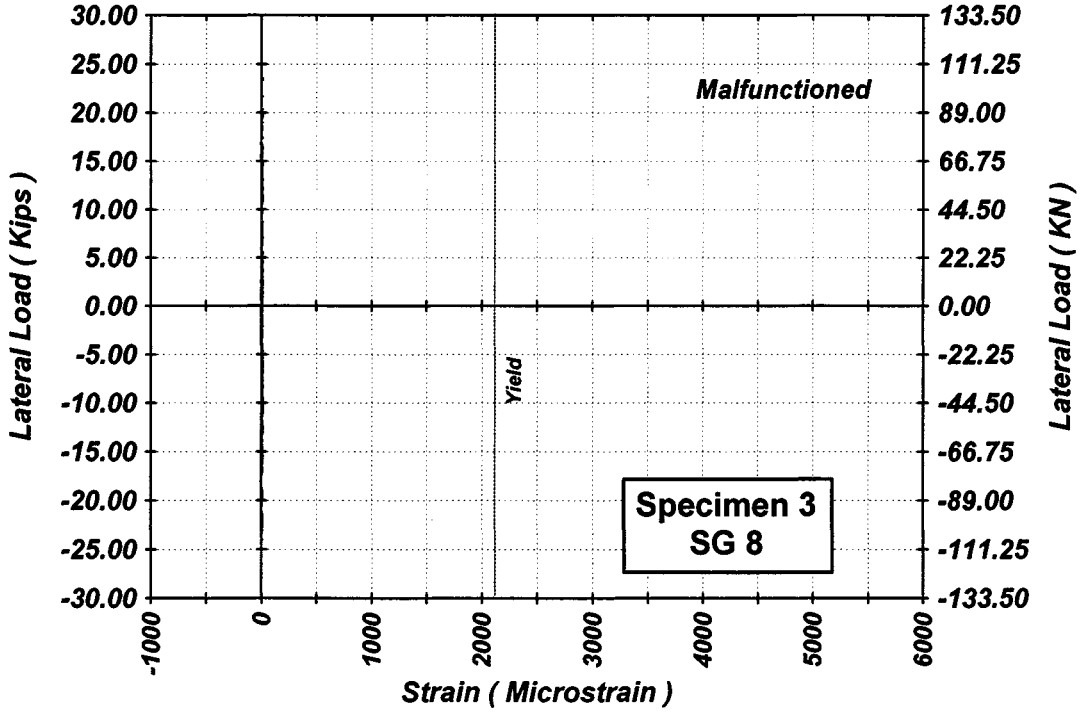

Figure A-72 Measured Lateral Load-Strain in SG-8 of Specimen 3

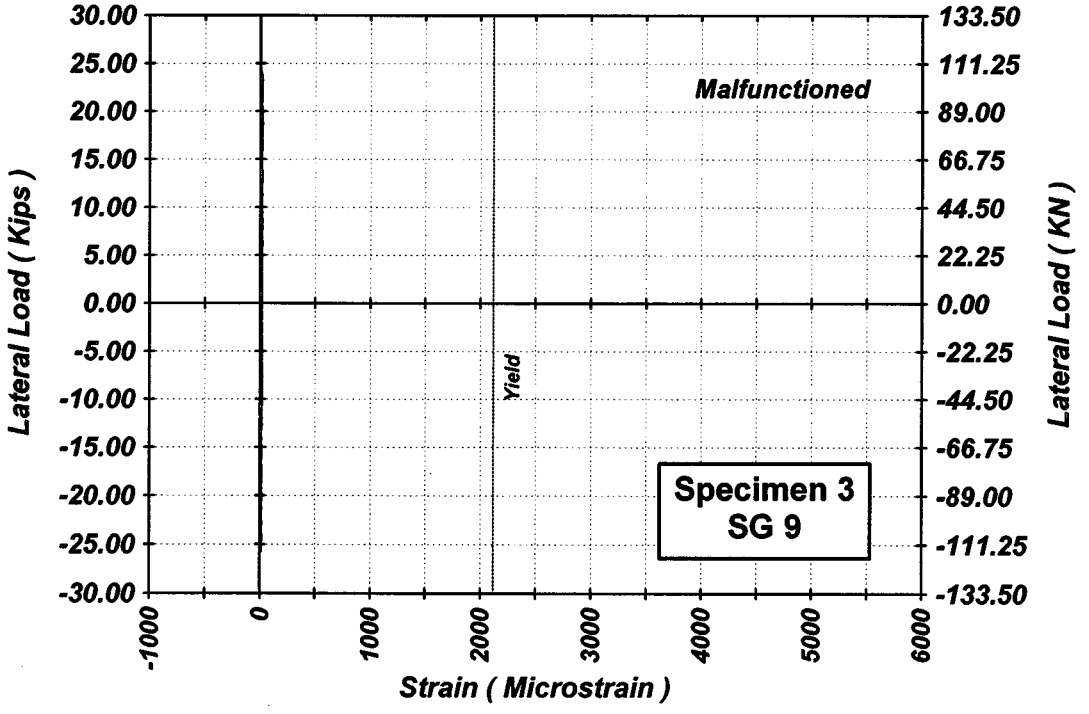

Figure A-73 Measured Lateral Load-Strain in SG-9 of Specimen 3

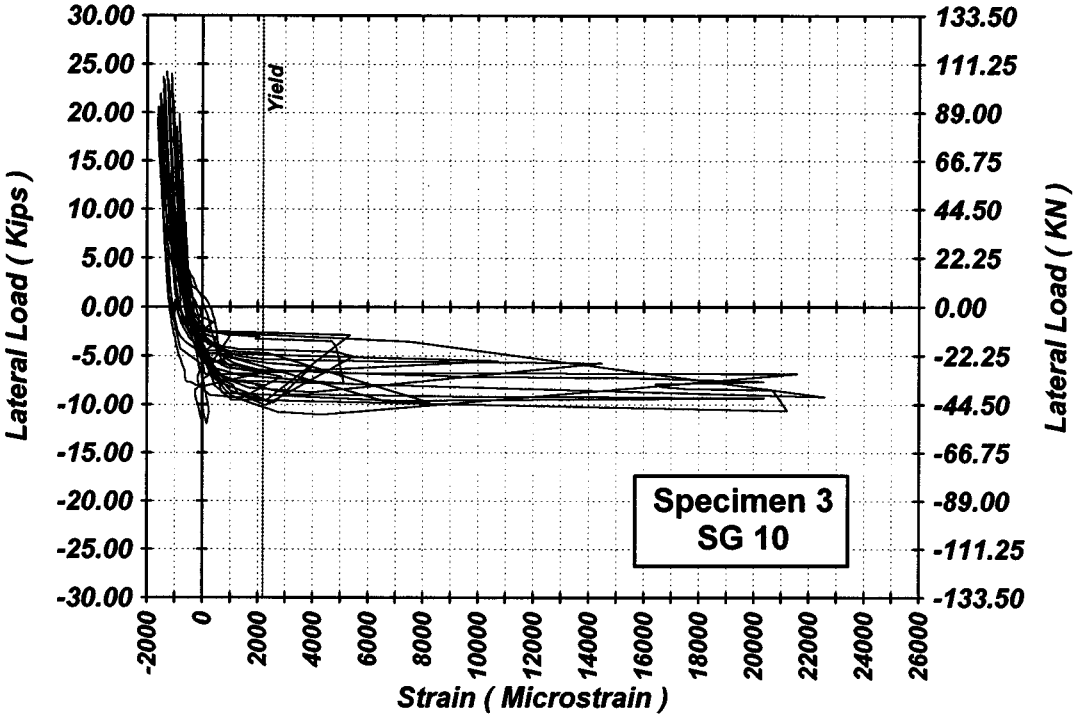

Figure A-74 Measured Lateral Load-Strain in SG-10 of Specimen 3

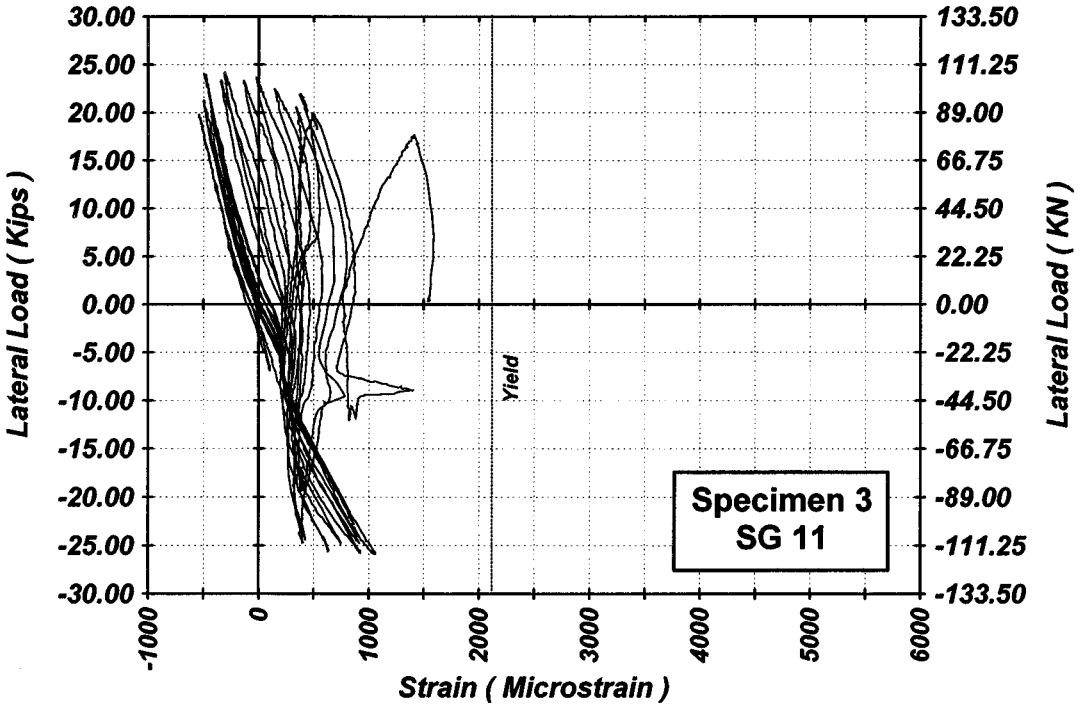

Figure A-75 Measured Lateral Load-Strain in SG-11 of Specimen 3

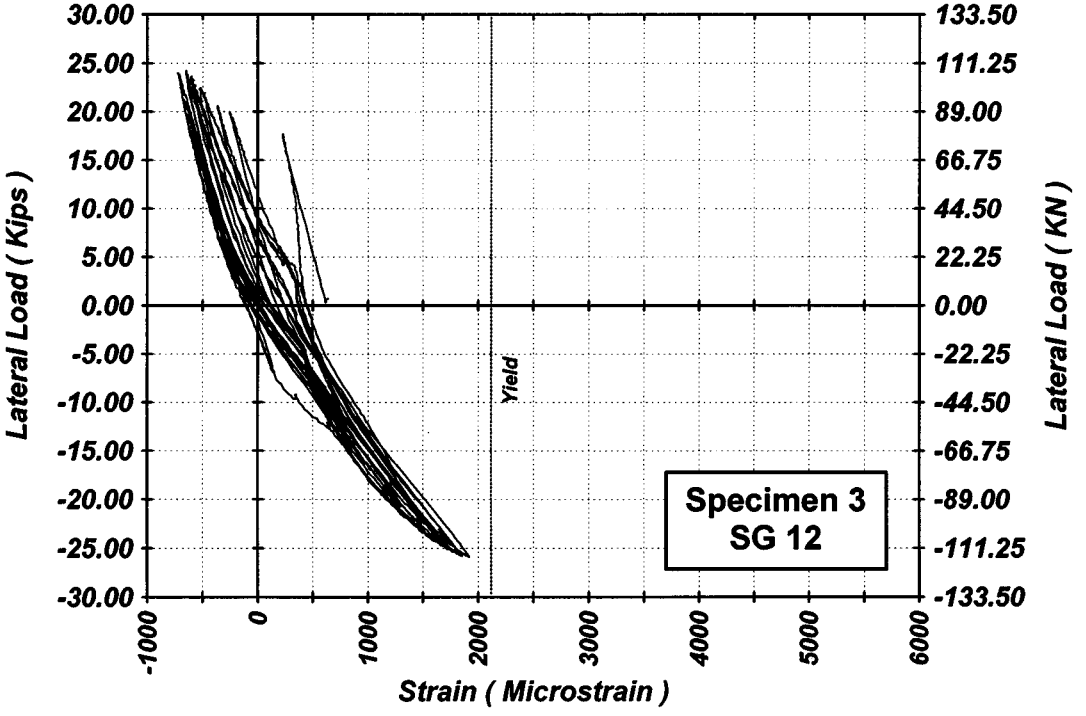

Figure A-76 Measured Lateral Load-Strain in SG-12 of Specimen 3

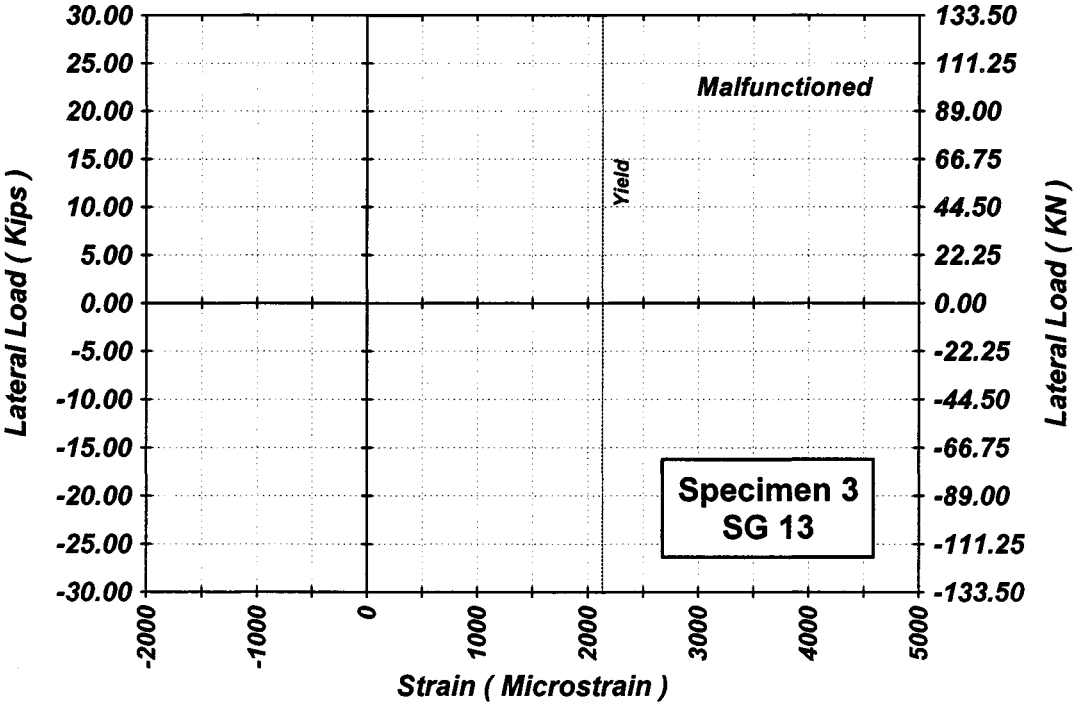

Figure A-77 Measured Lateral Load-Strain in SG-13 of Specimen 3

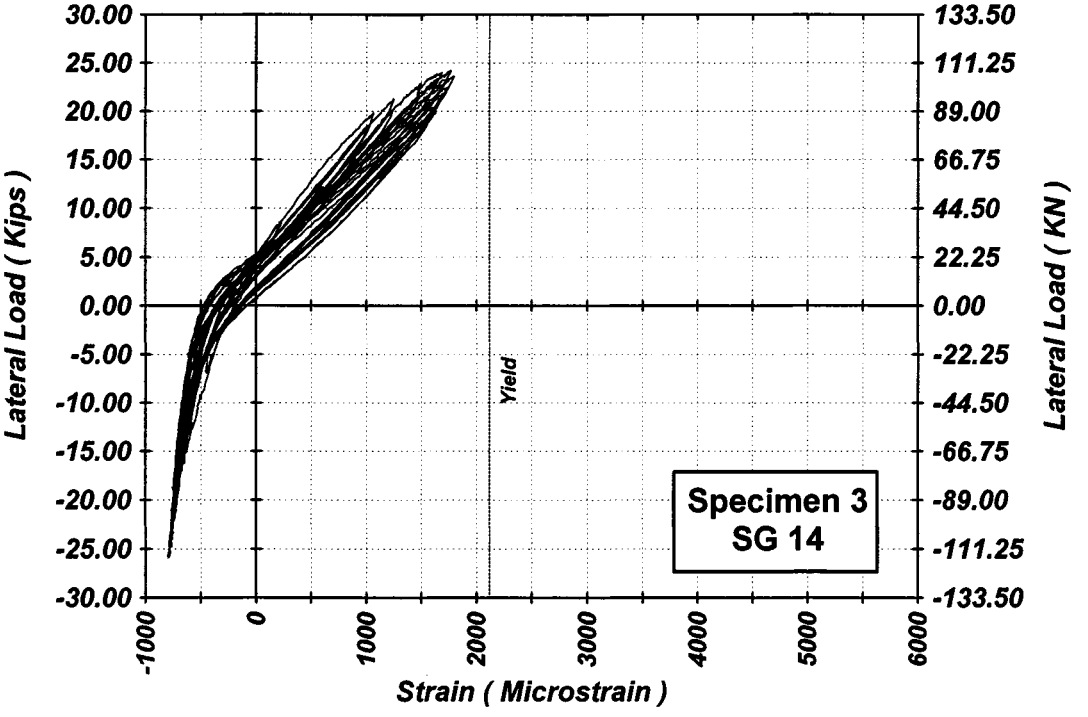

Figure A-78 Measured Lateral Load-Strain in SG-14 of Specimen 3

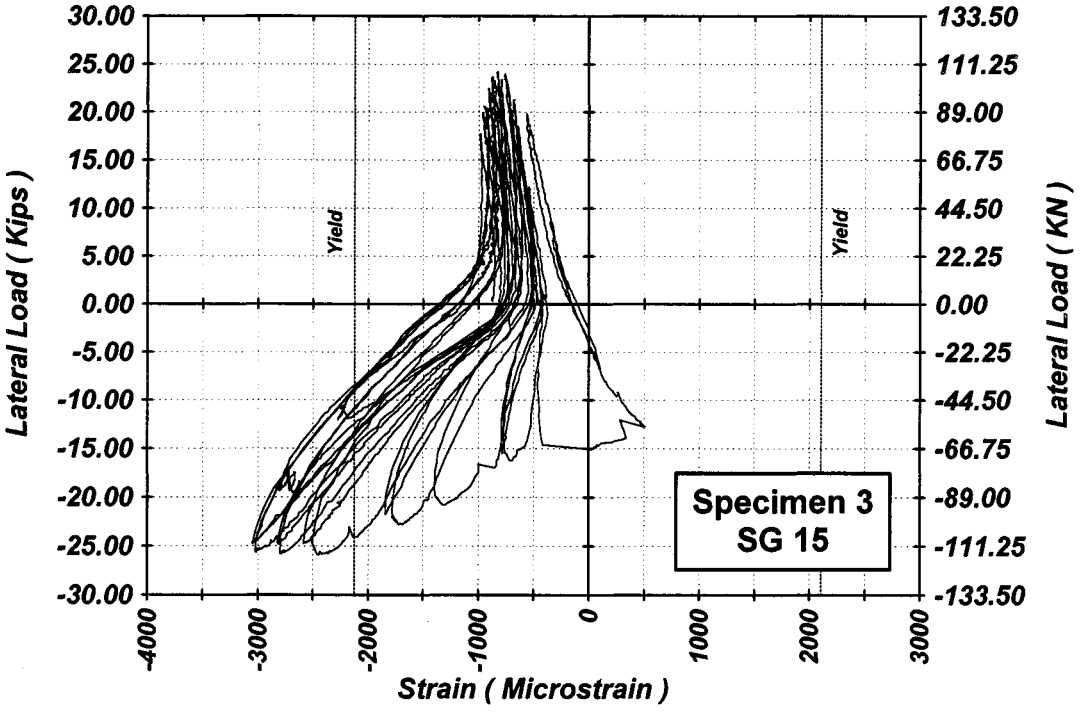

Figure A-79 Measured Lateral Load-Strain in SG-15 of Specimen 3

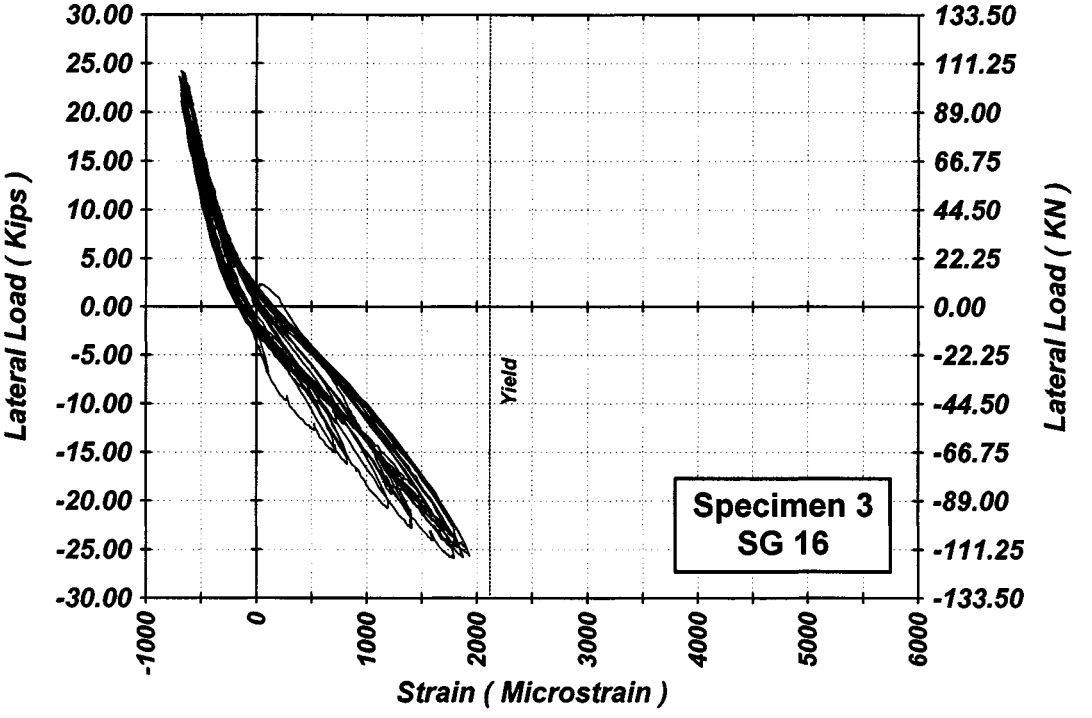

Figure A-80 Measured Lateral Load-Strain in SG-16 of Specimen 3

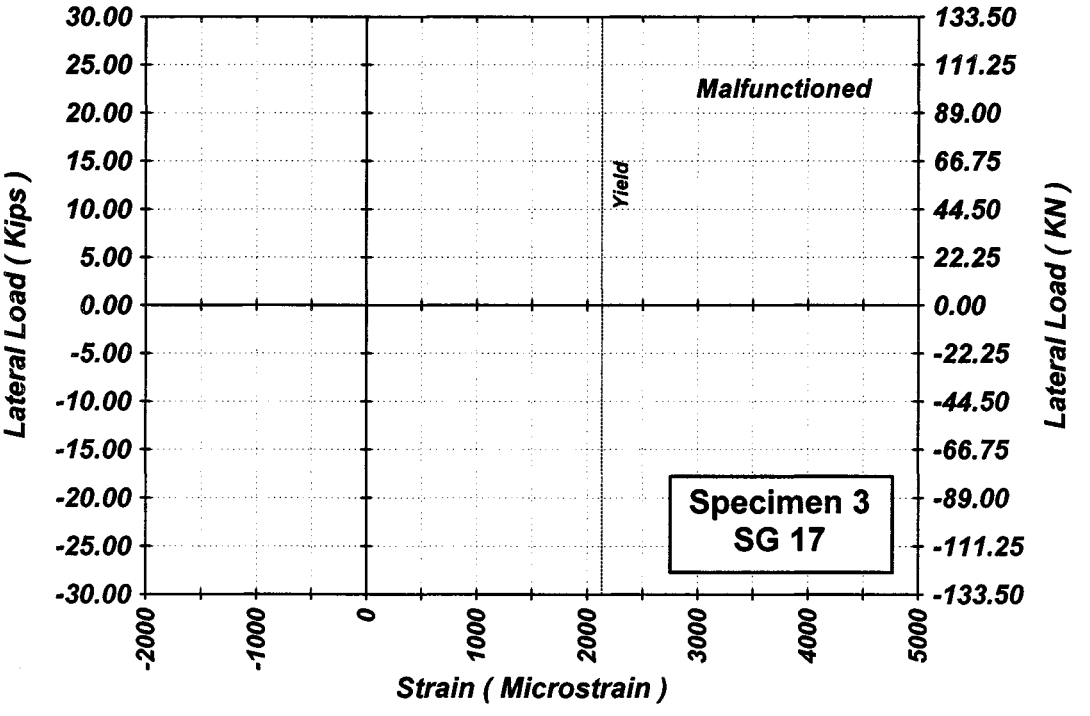

Figure A-81Measured Lateral Load-Strain in SG-17 of Specimen 3

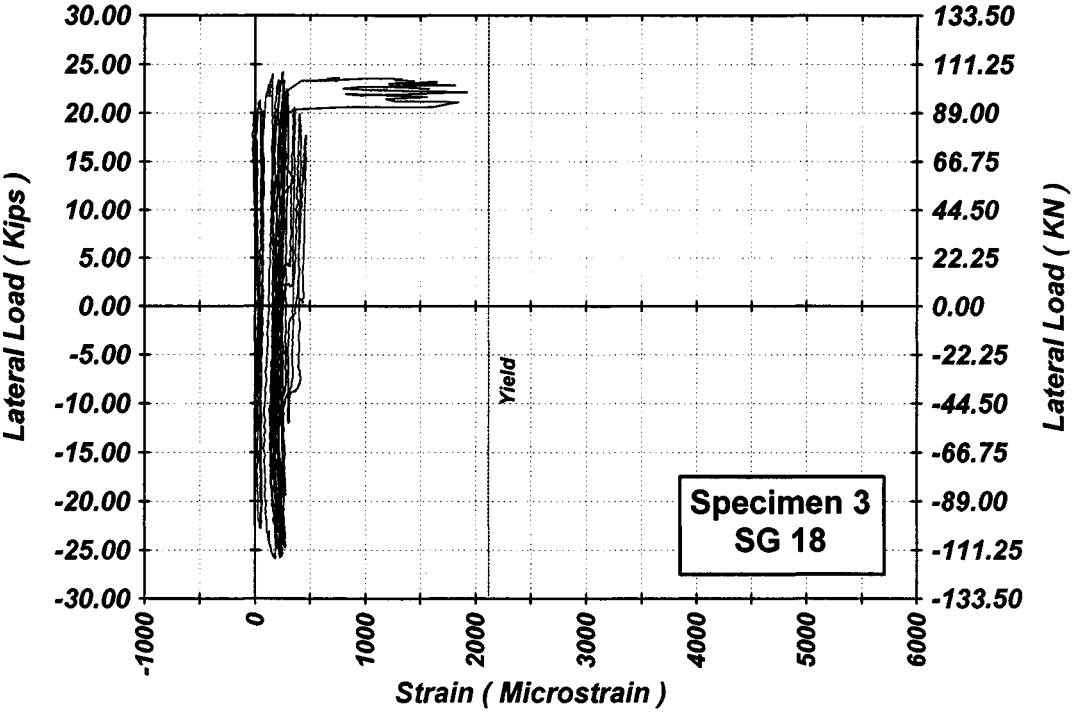

Figure A-82 Measured Lateral Load-Strain in SG-18 of Specimen 3

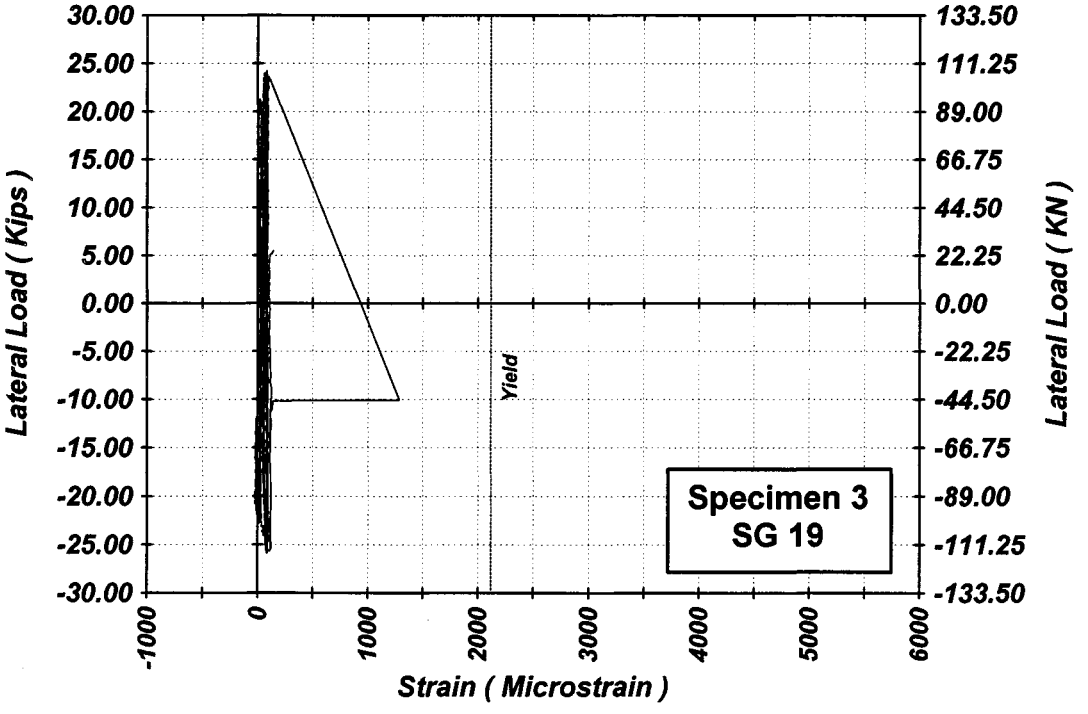

Figure A-83 Measured Lateral Load-Strain in SG-19 of Specimen 3

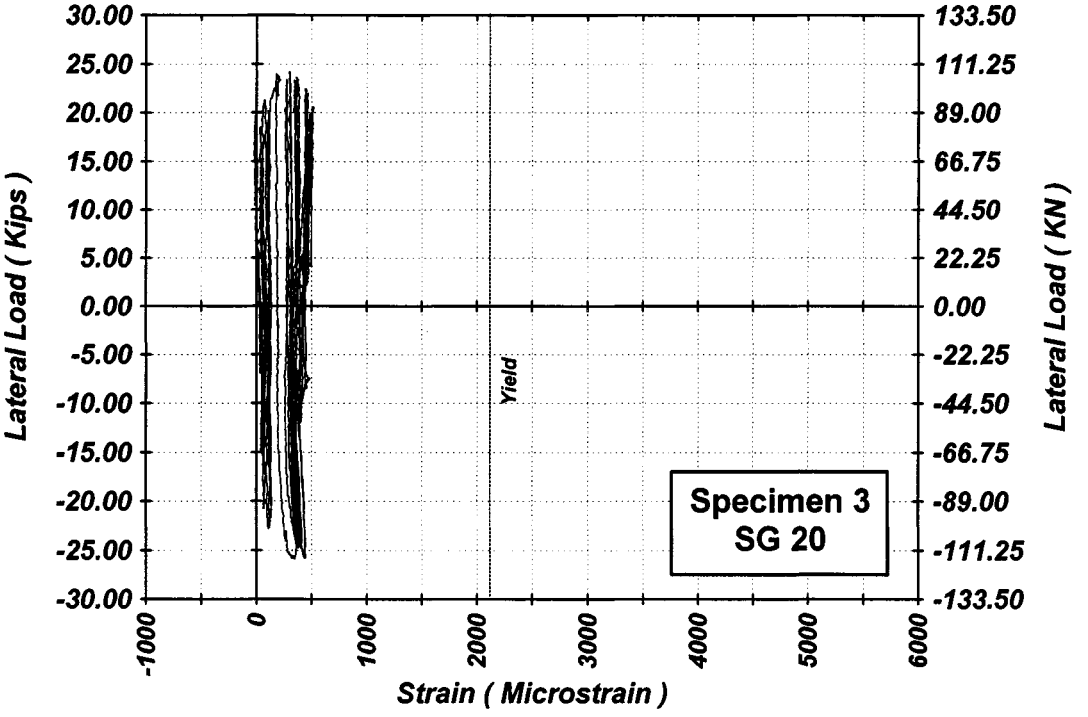

Figure A-84 Measured Lateral Load-Strain in SG-20 of Specimen 3

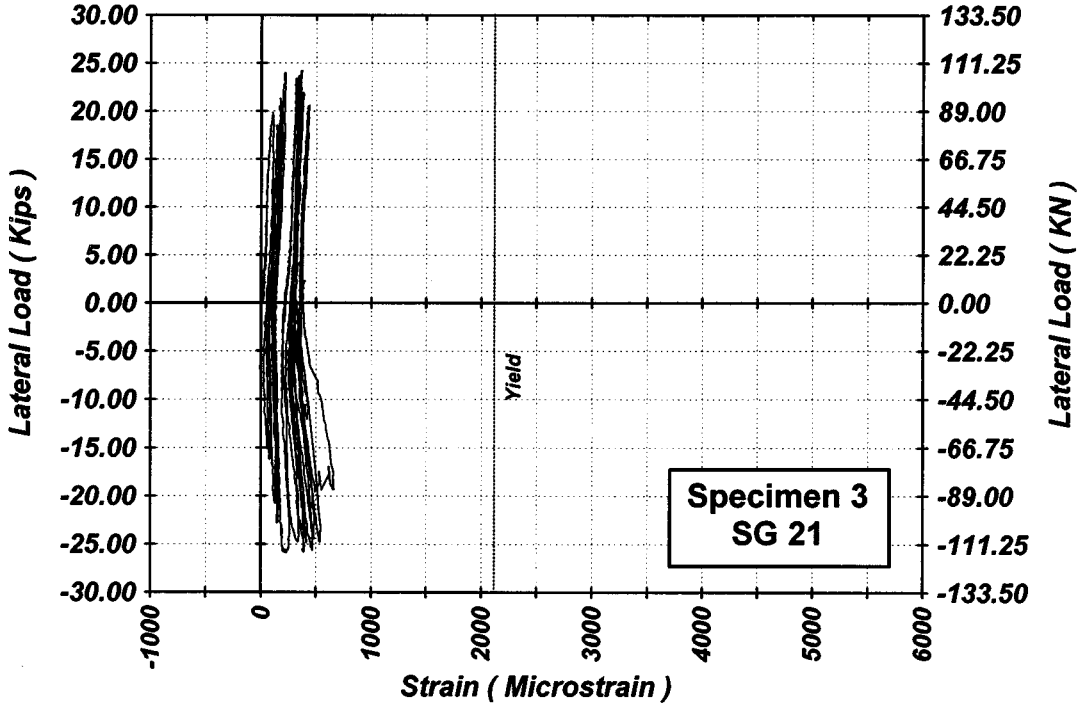

Figure A-85 Measured Lateral Load-Strain in SG-21 of Specimen 3

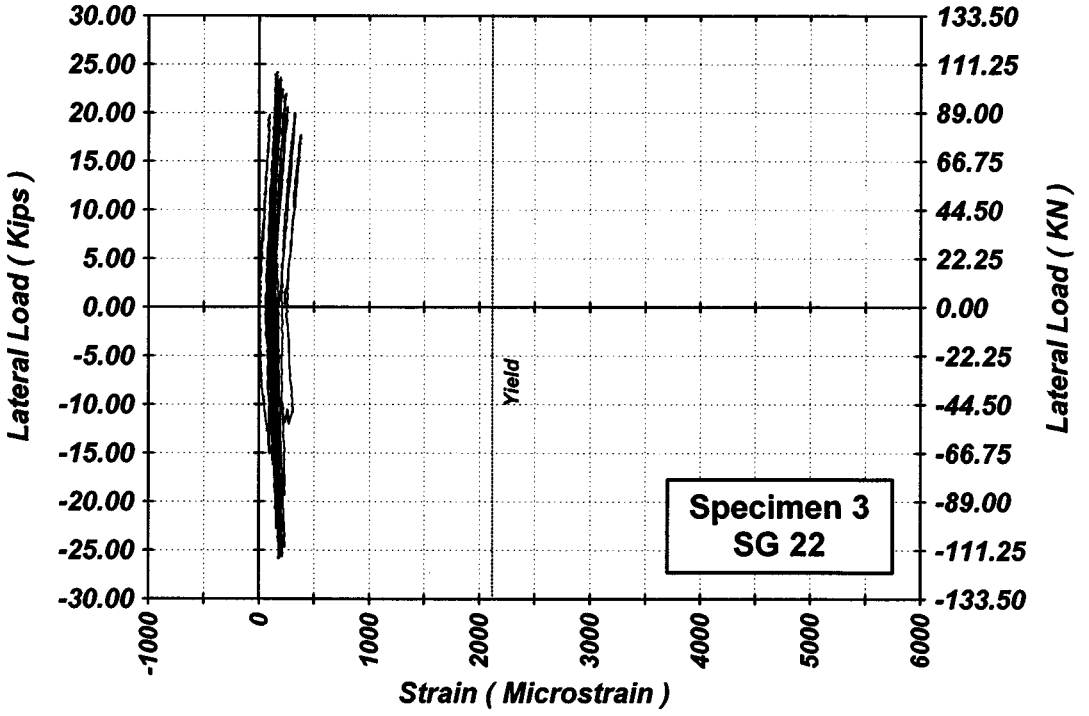

Figure A-86 Measured Lateral Load-Strain in SG-22 of Specimen 3

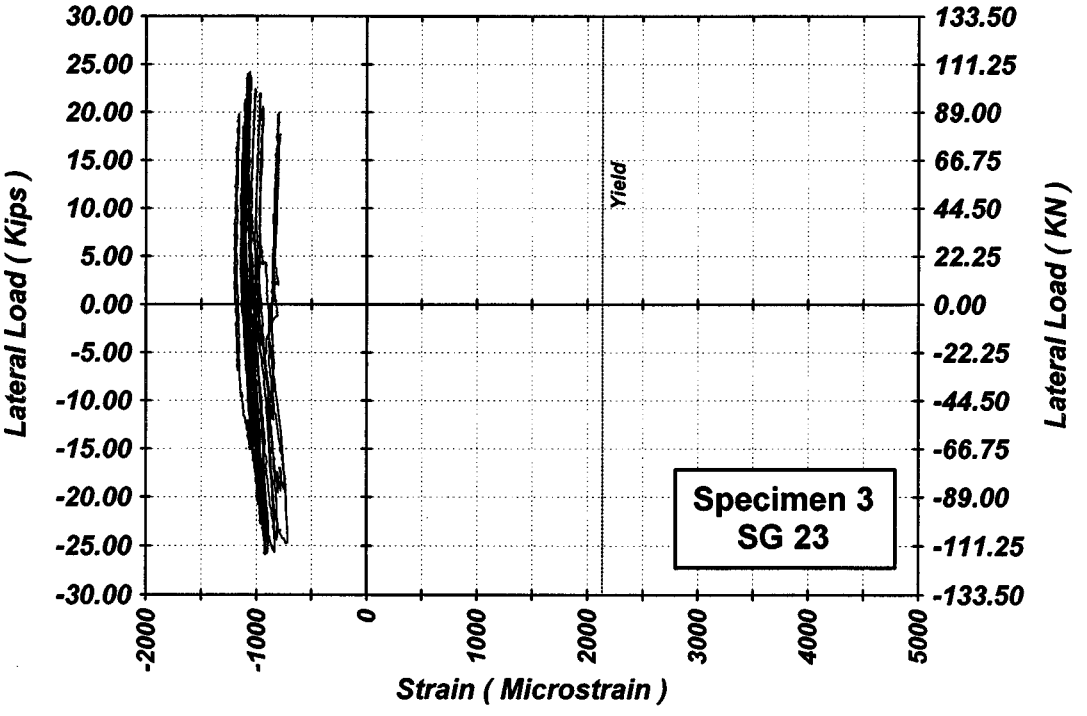

Figure A-87 Measured Lateral Load-Strain in SG-23 of Specimen 3

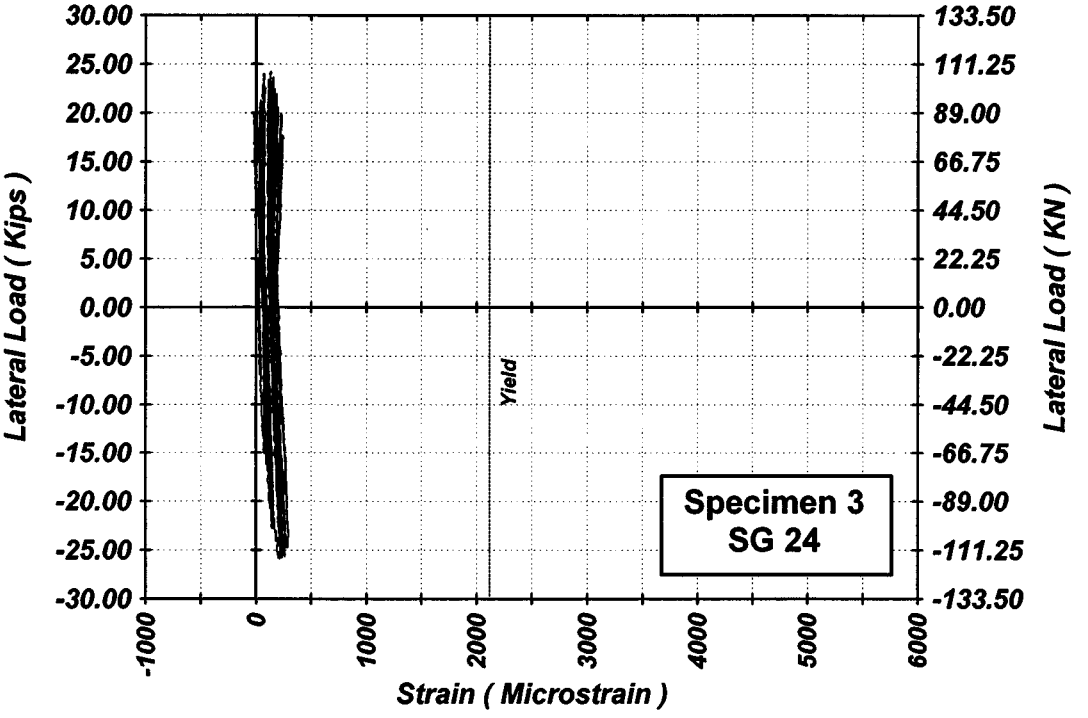

Figure A-88 Measured Lateral Load-Strain in SG-24 of Specimen 3

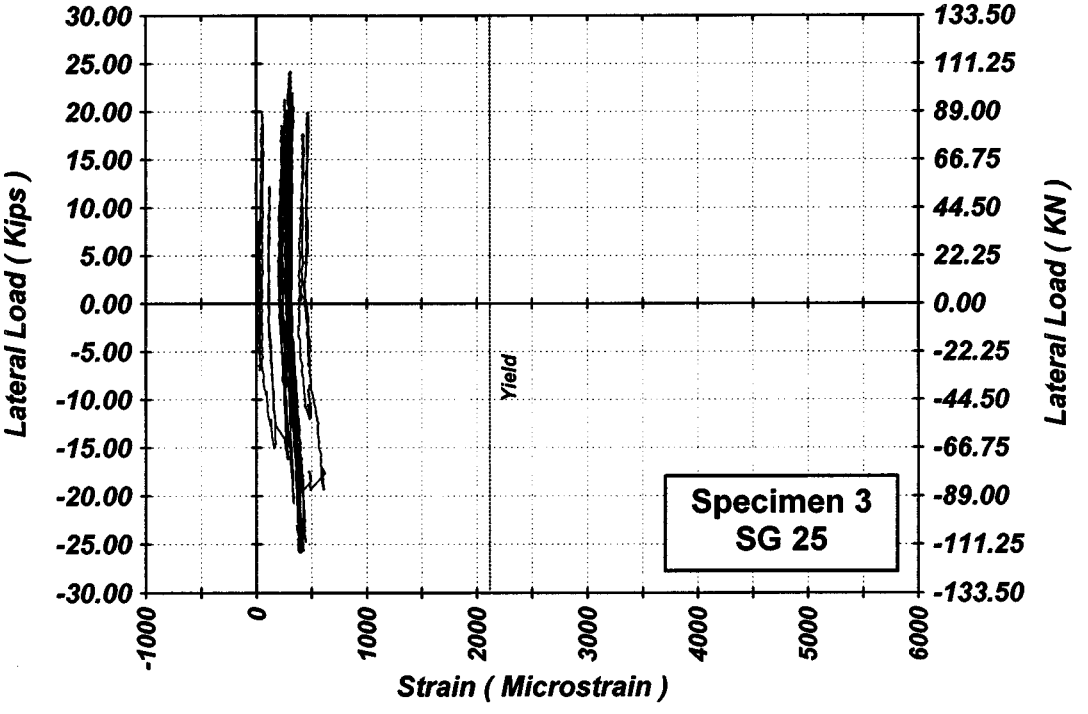

Figure A-89 Measured Lateral Load-Strain in SG-25 of Specimen 3

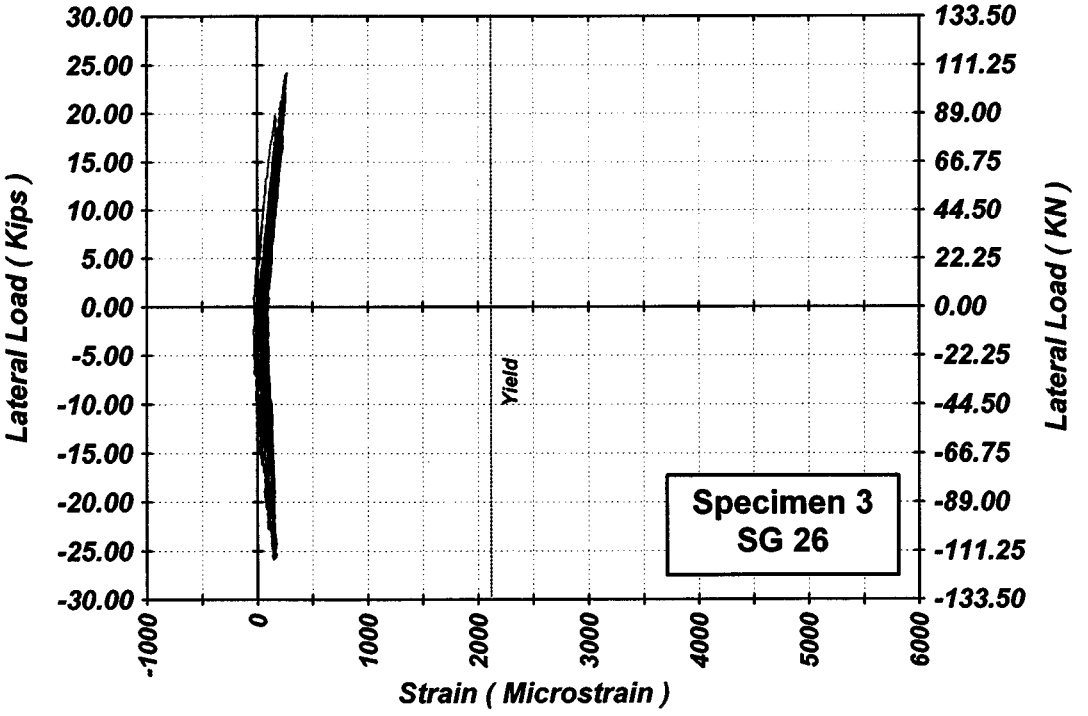

Figure A-90 Measured Lateral Load-Strain in SG-26 of Specimen 3

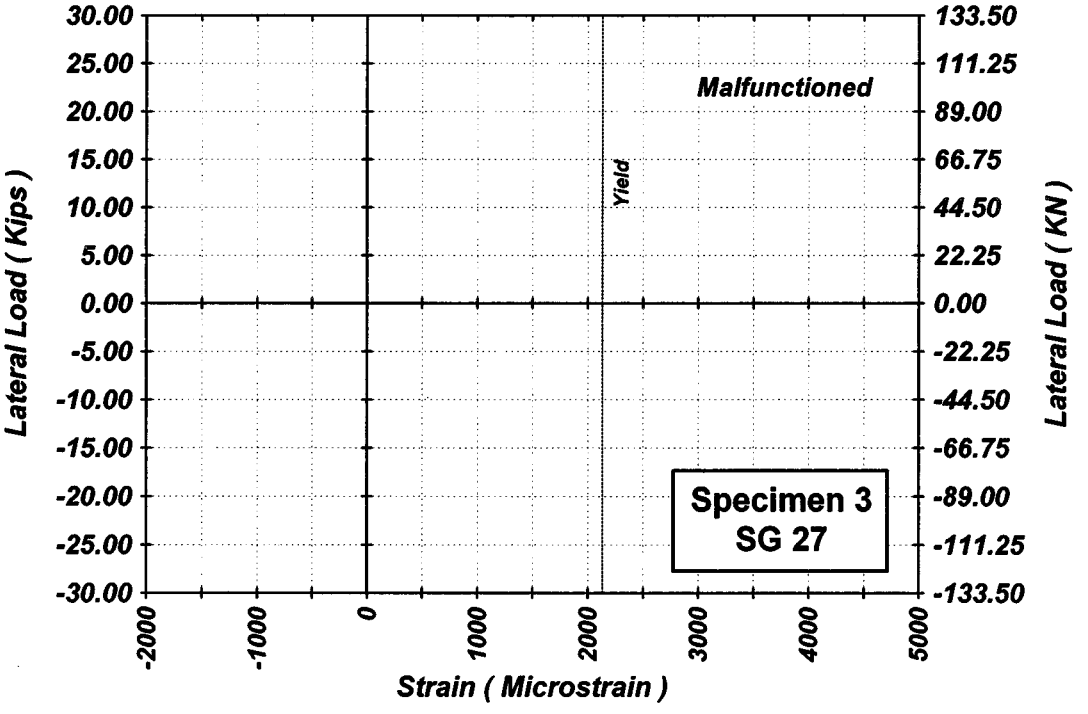

Figure A-91 Measured Lateral Load-Strain in SG-27 of Specimen 3

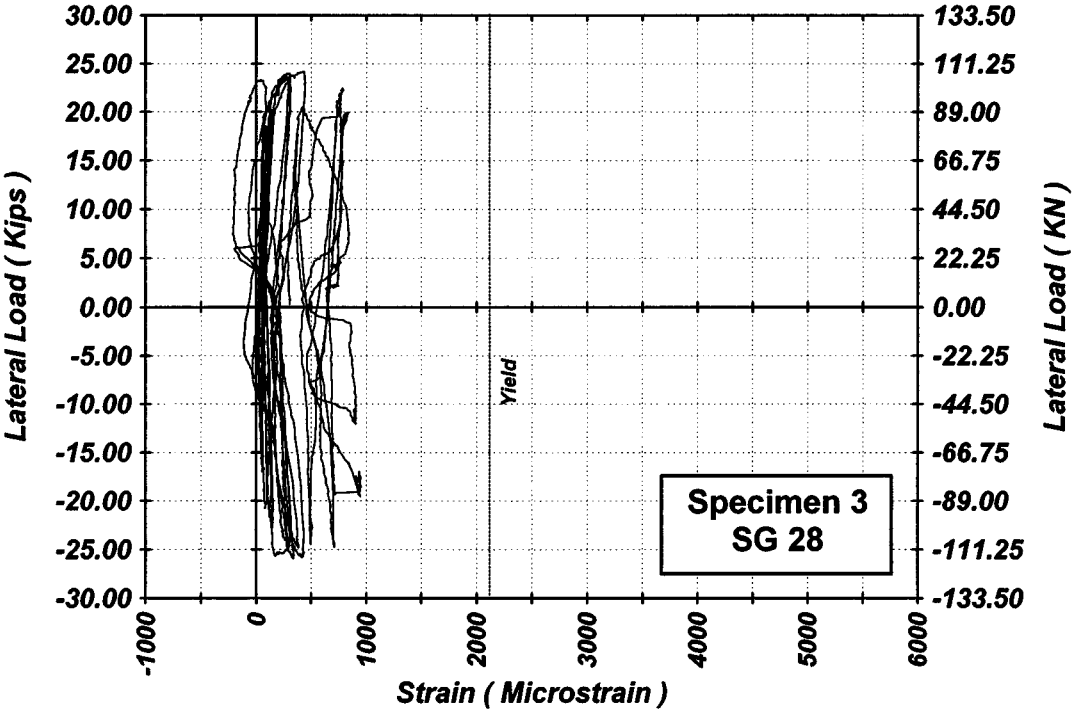

Figure A-92 Measured Lateral Load-Strain in SG-28 of Specimen 3

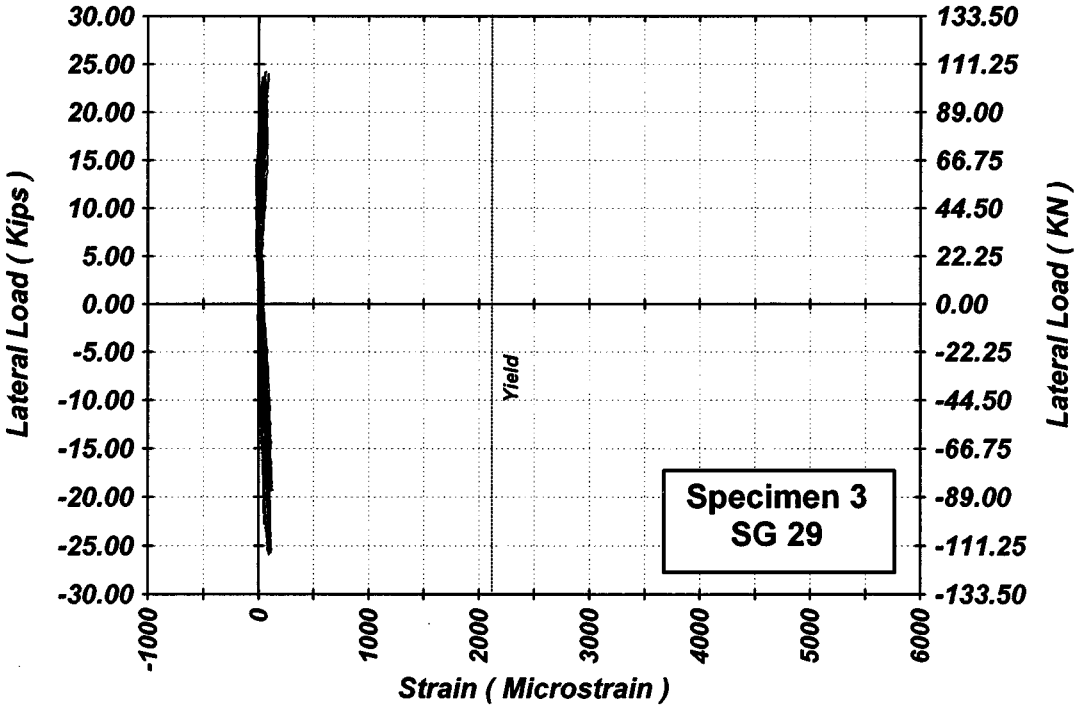

Figure A-93 Measured Lateral Load-Strain in SG-29 of Specimen 3

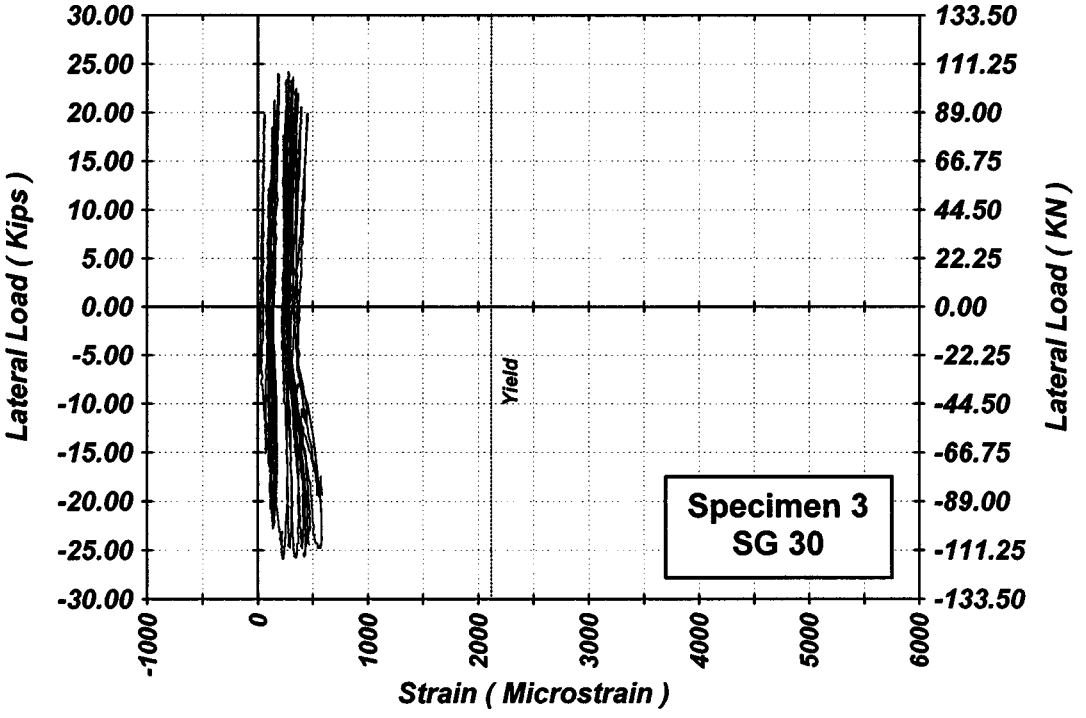

Figure A-94 Measured Lateral Load-Strain in SG-30 of Specimen 3

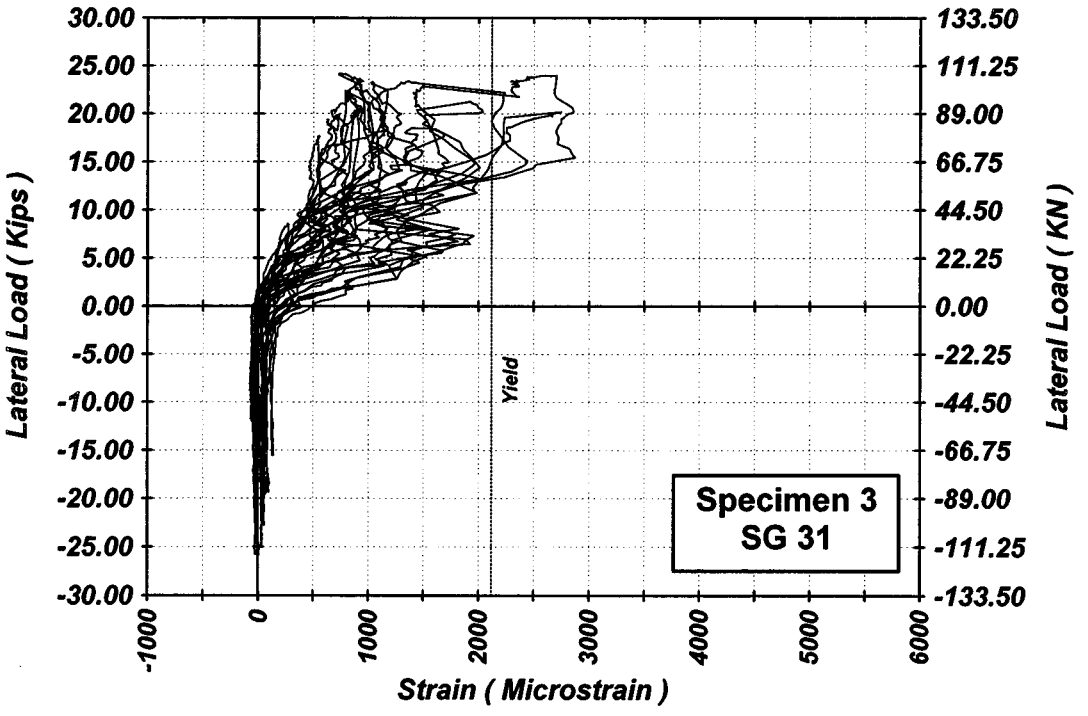

Figure A-95 Measured Lateral Load-Strain in SG-31 of Specimen 3

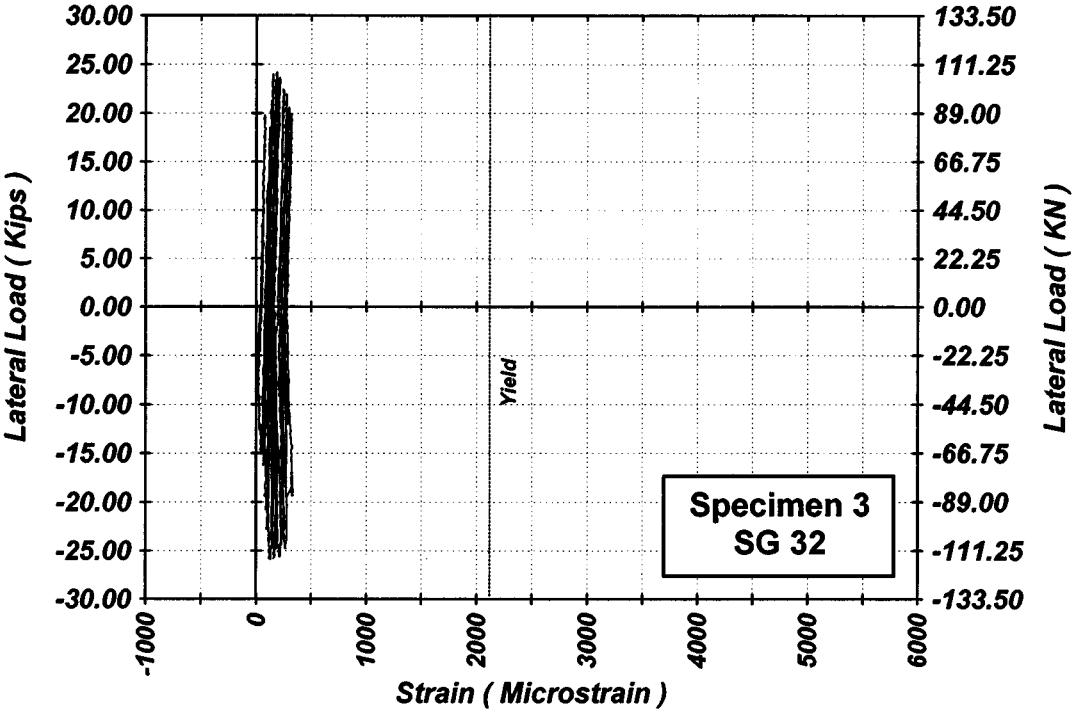

Figure A-96 Measured Lateral Load-Strain in SG-32 of Specimen 3

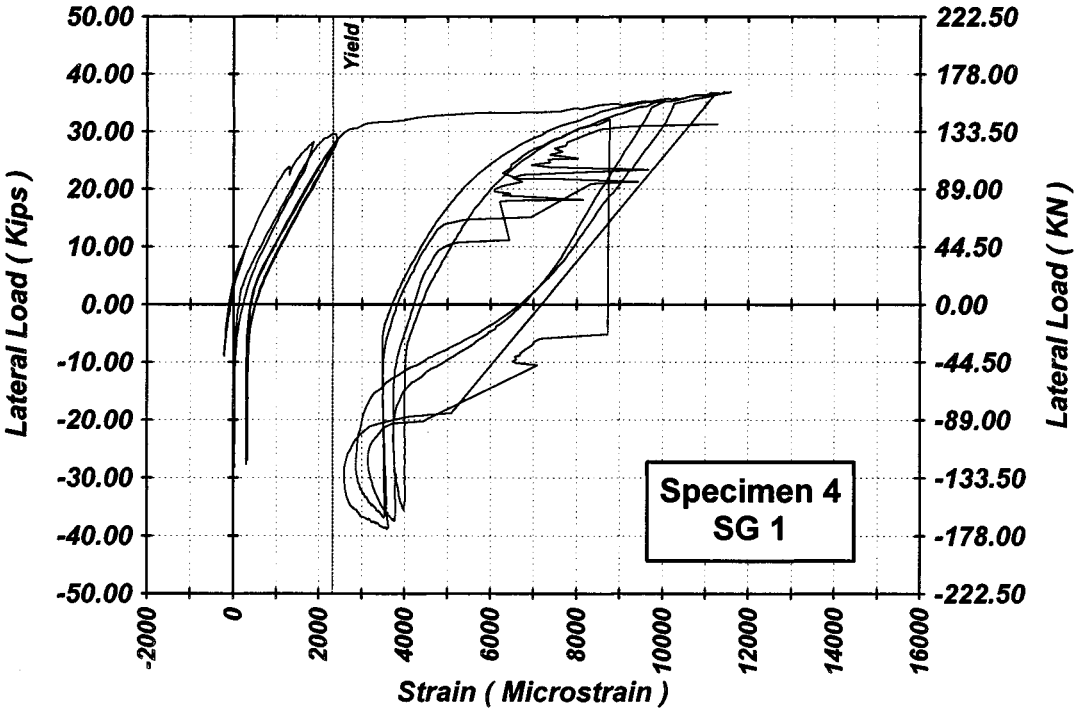

Figure A-97 Measured Lateral Load-Strain in SG-1 of Specimen 4

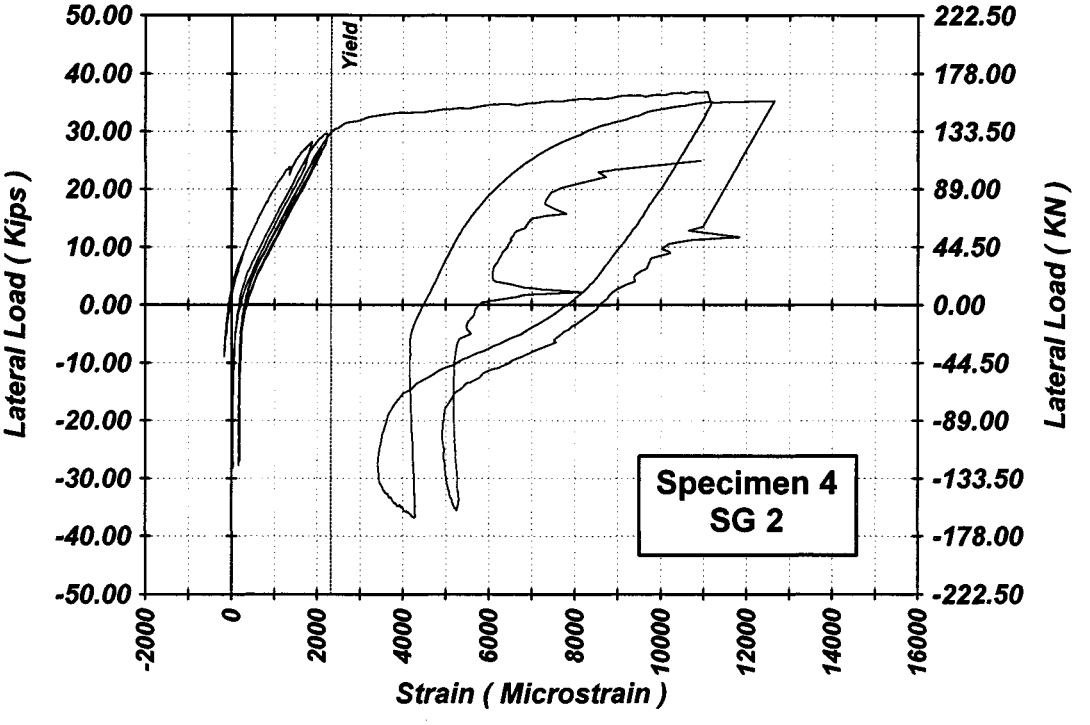

Figure A-98 Measured Lateral Load-Strain in SG-2 of Specimen 4

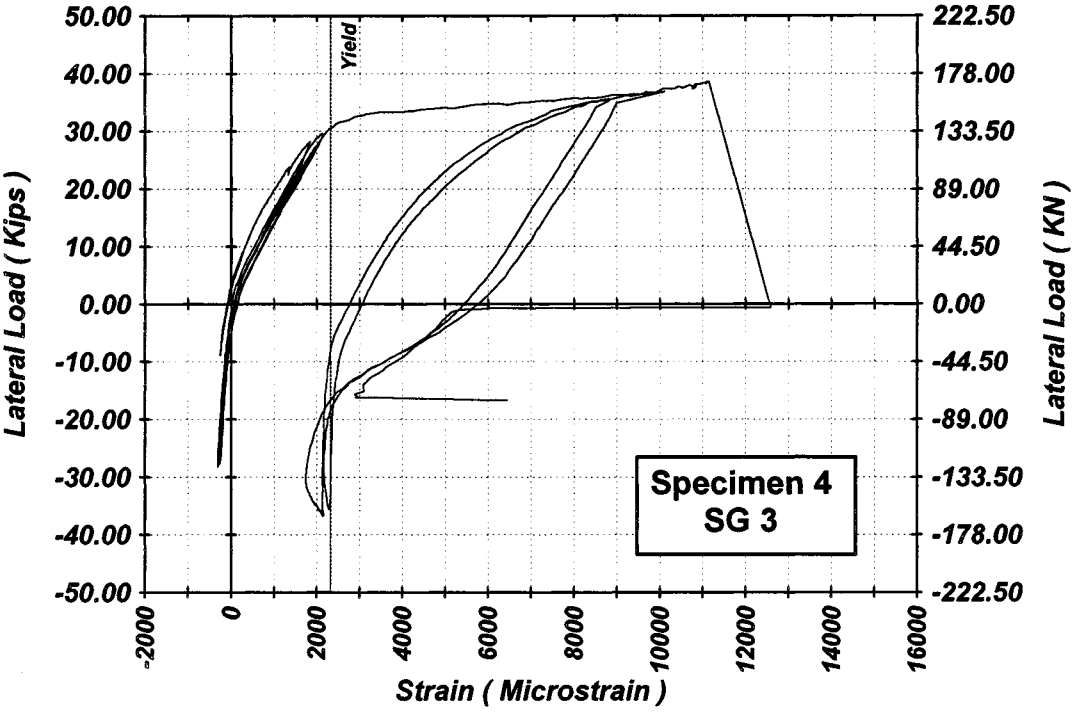

Figure A-99 Measured Lateral Load-Strain in SG-3 of Specimen 4

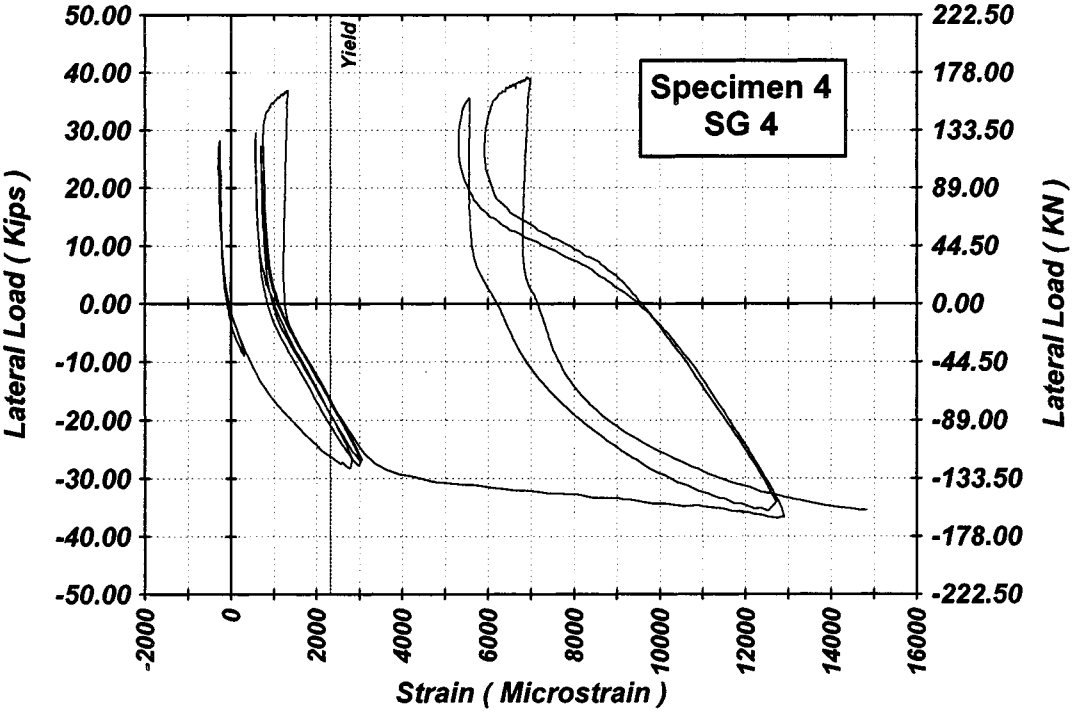

Figure A-100 Measured Lateral Load-Strain in SG-4 of Specimen 4

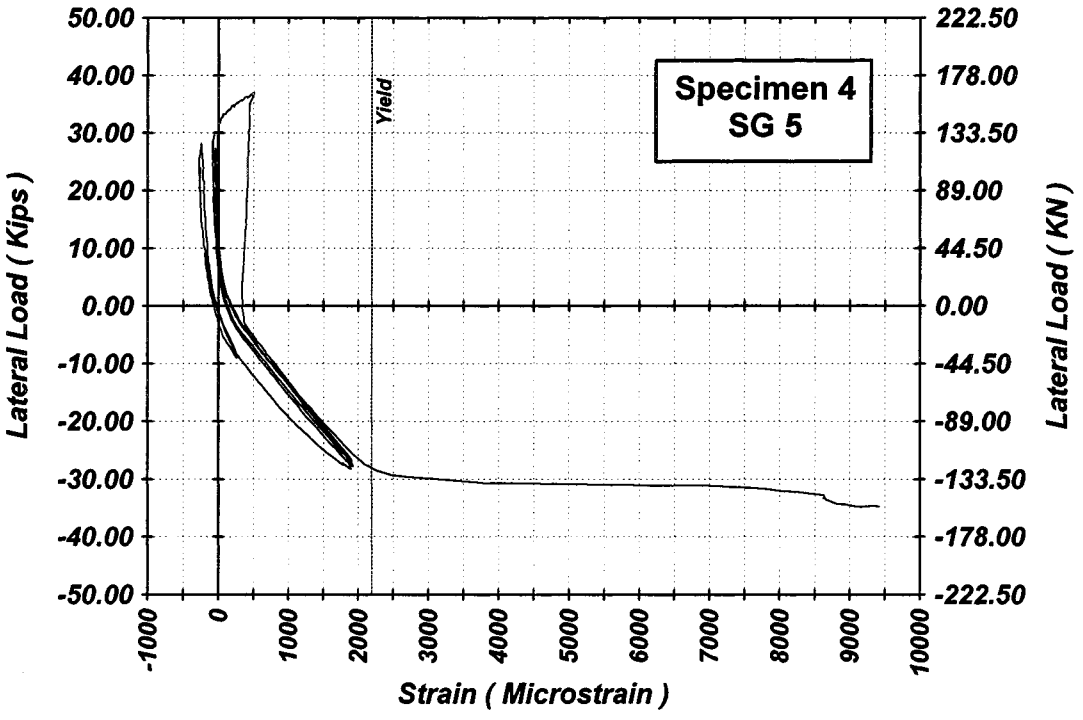

Figure A-101 Measured Lateral Load-Strain in SG-5 of Specimen 4

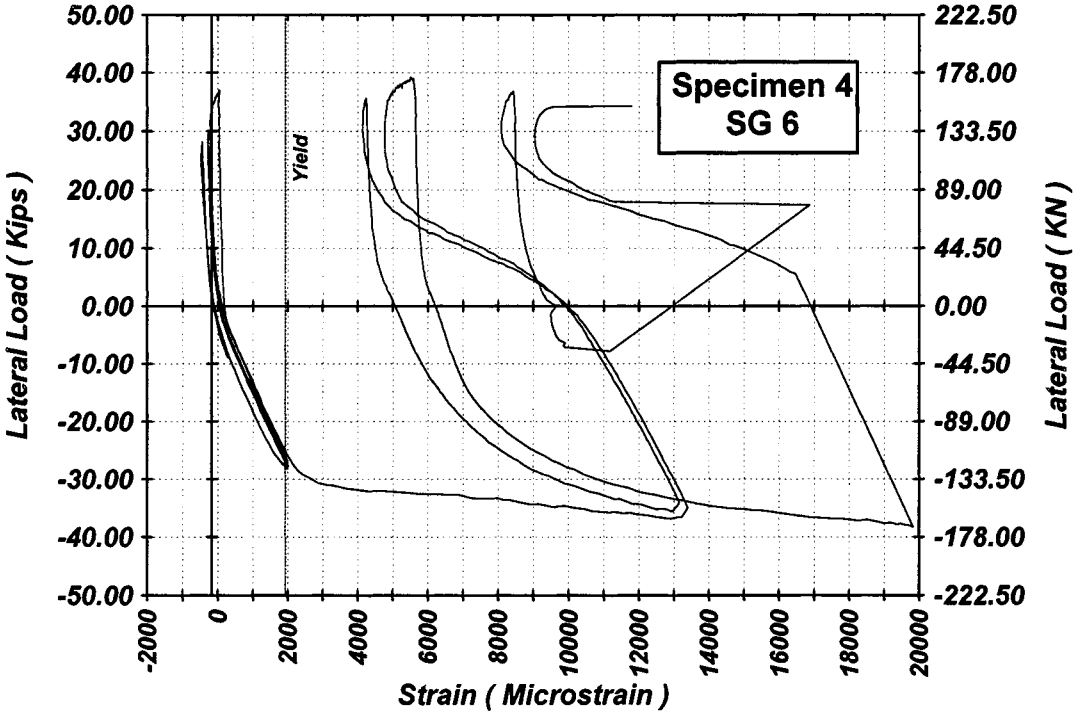

Figure A-102 Measured Lateral Load-Strain in SG-6 of Specimen 4

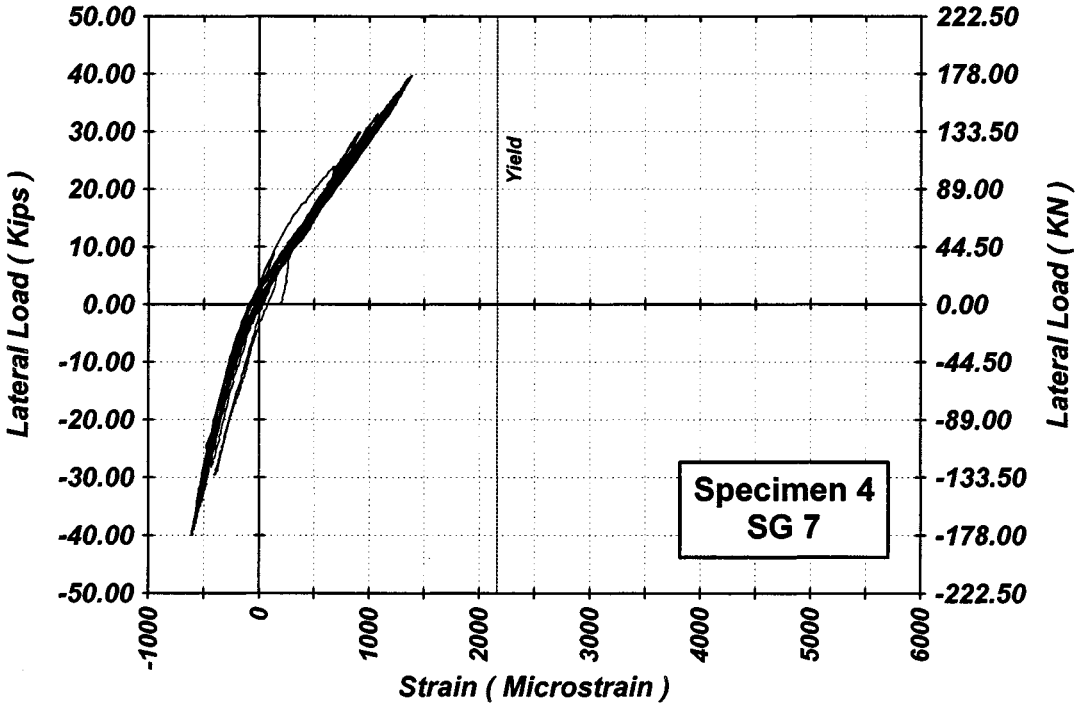

Figure A-103 Measured Lateral Load-Strain in SG-7 of Specimen 4

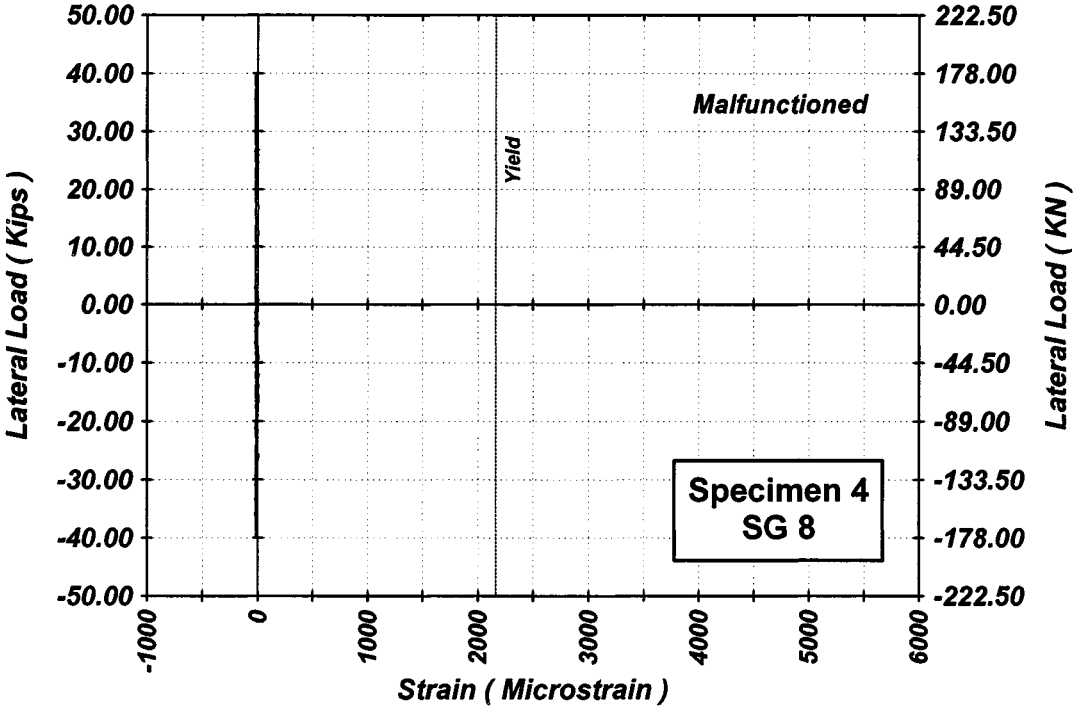

Figure A-104 Measured Lateral Load-Strain in SG-8 of Specimen 4

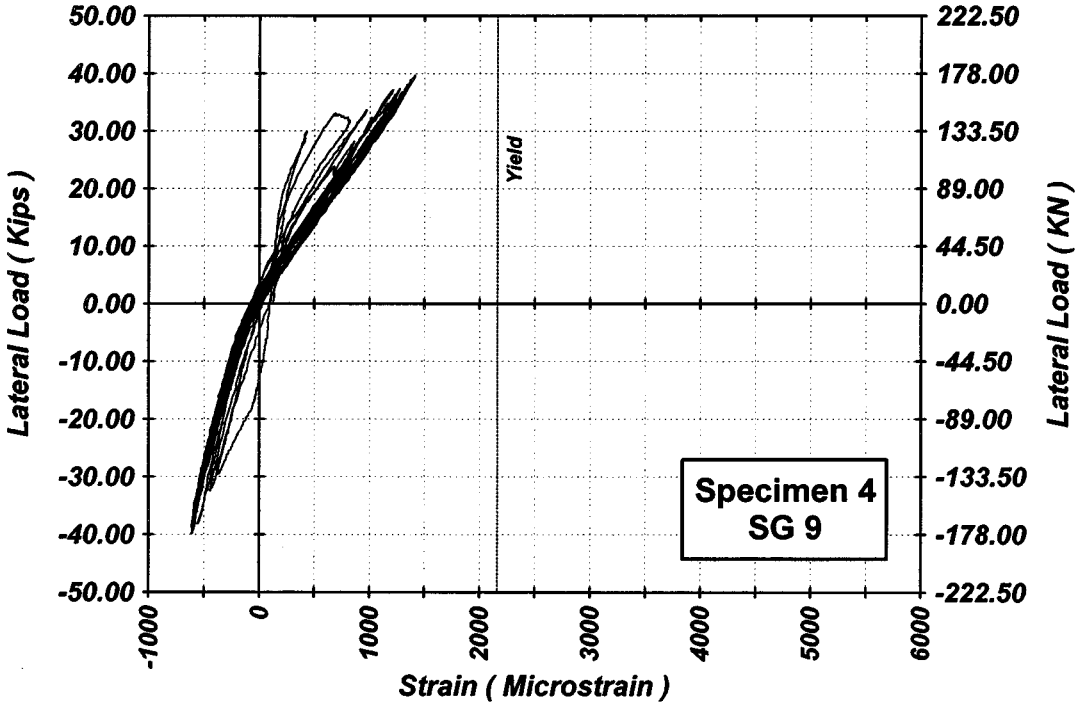

Figure A-105 Measured Lateral Load-Strain in SG-9 of Specimen 4

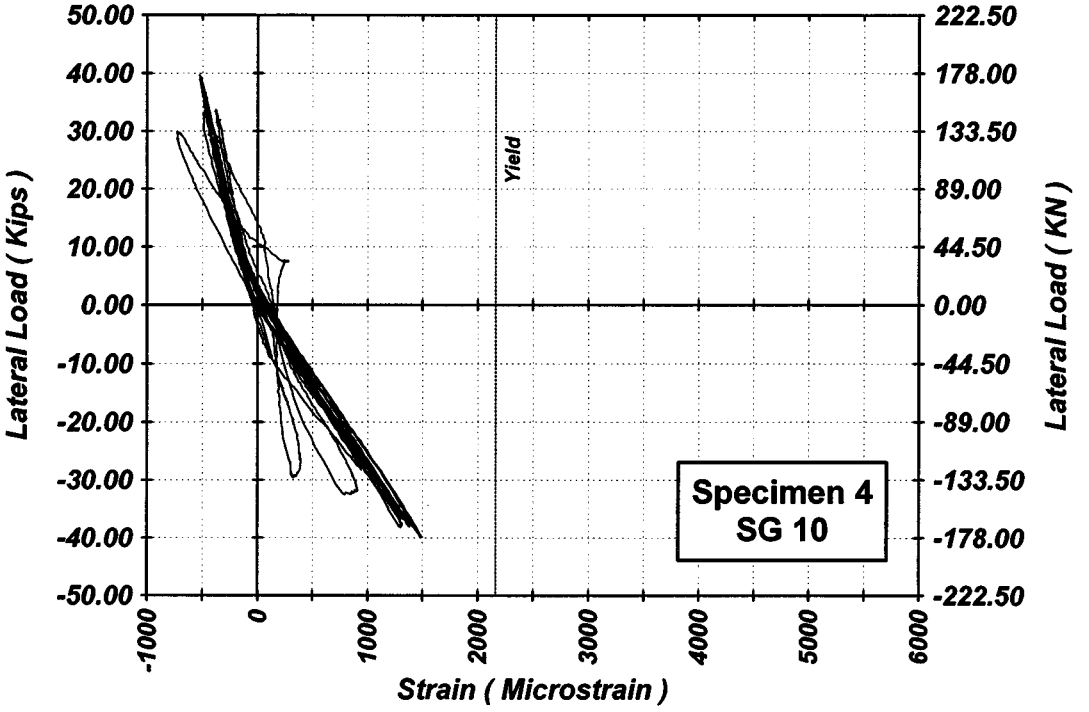

Figure A-106 Measured Lateral Load-Strain in SG-10 of Specimen 4

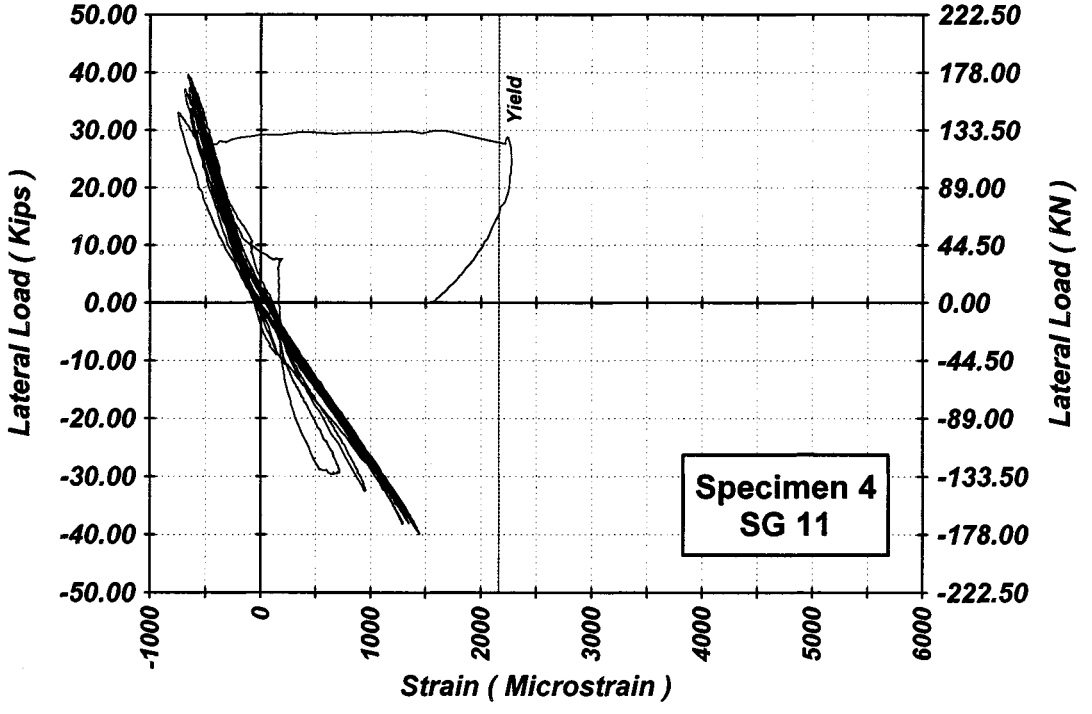

Figure A-107 Measured Lateral Load-Strain in SG-11 of Specimen 4

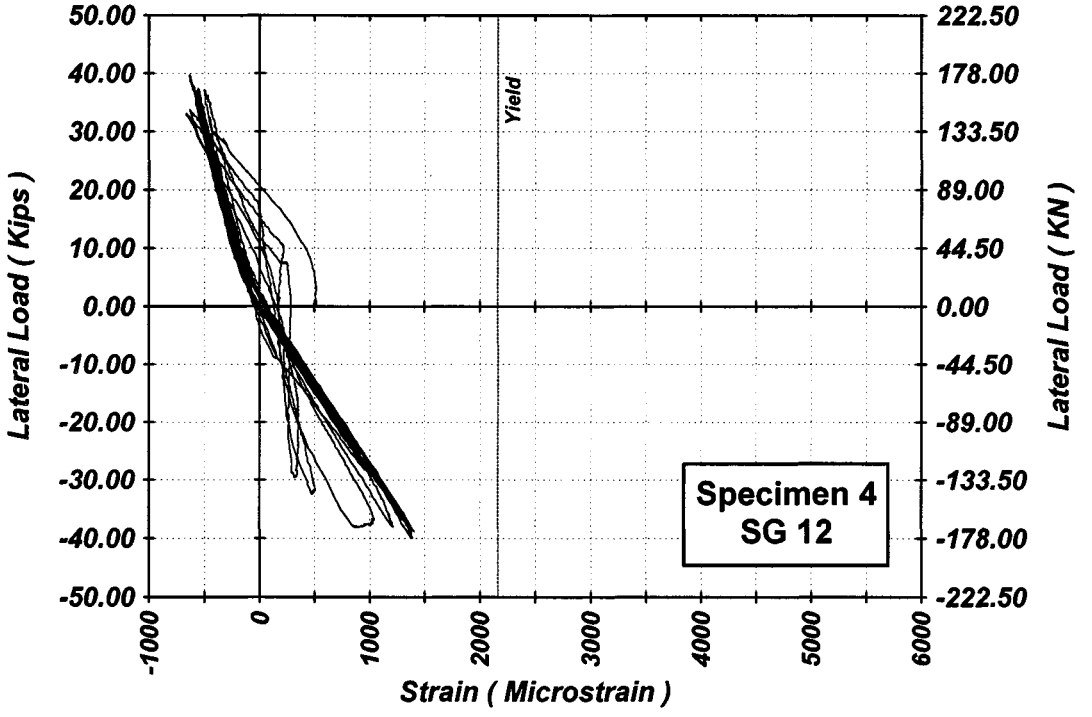

Figure A-108 Measured Lateral Load-Strain in SG-12 of Specimen 4

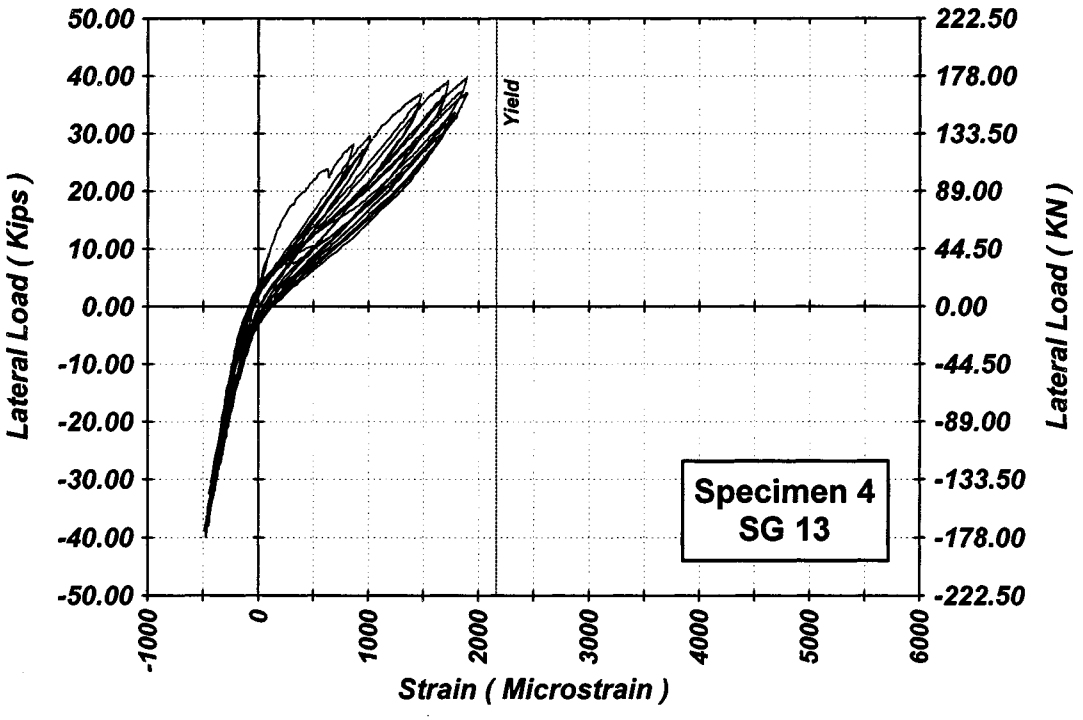

Figure A-109 Measured Lateral Load-Strain in SG-13 of Specimen 4

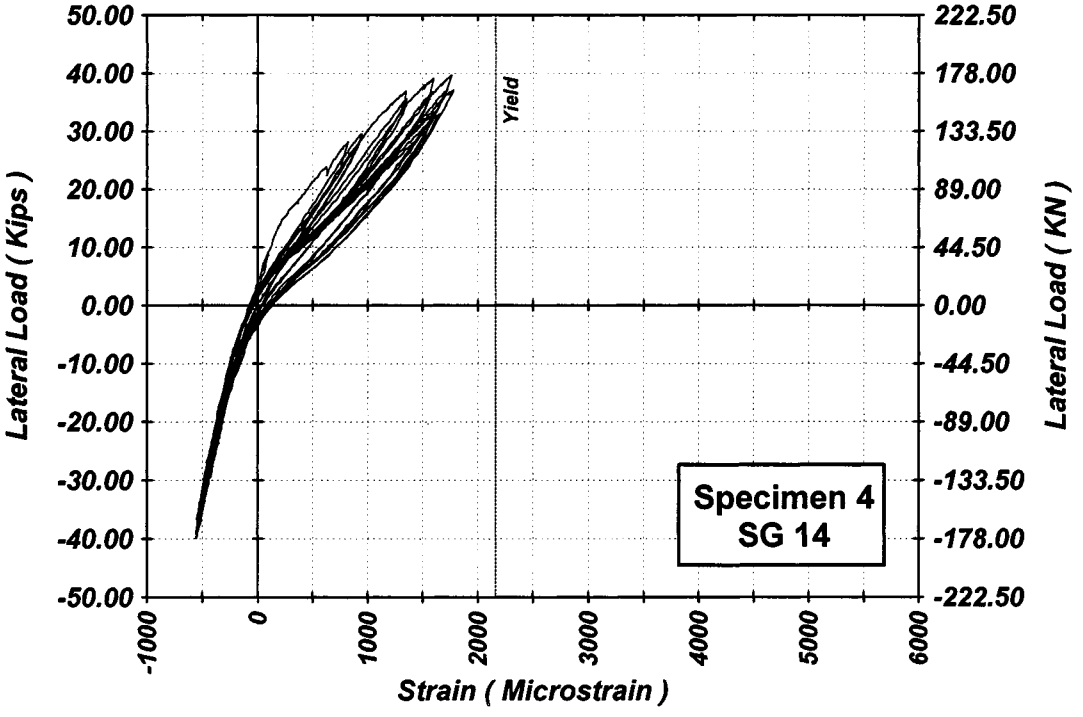

Figure A-110 Measured Lateral Load-Strain in SG-14 of Specimen 4

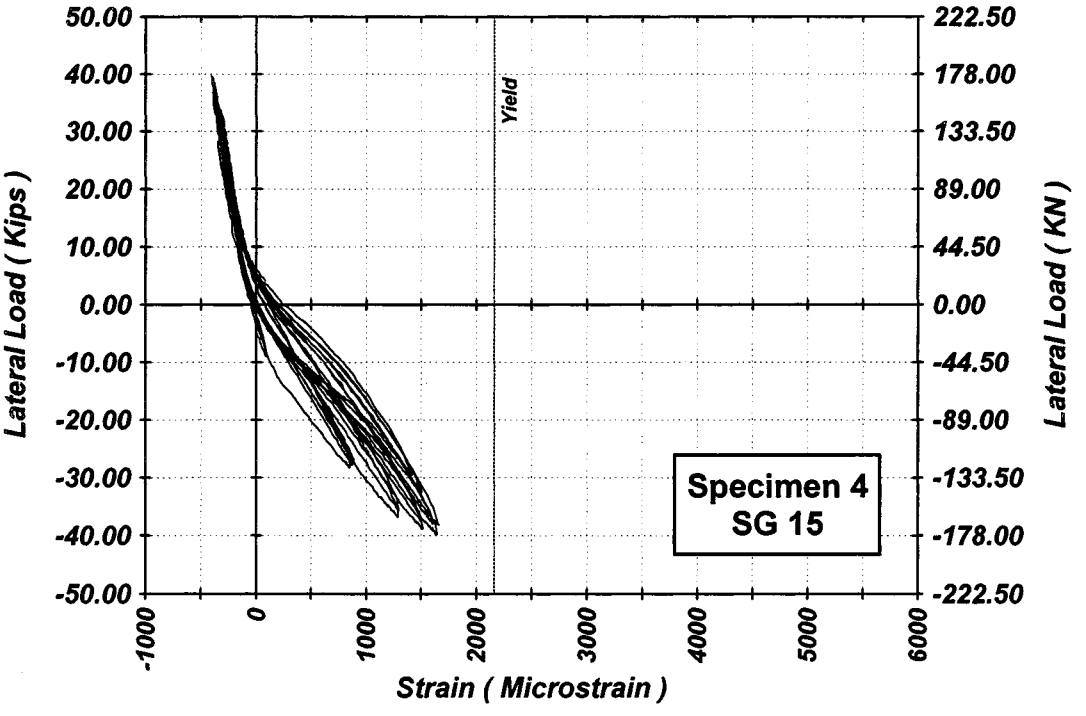

Figure A-111 Measured Lateral Load-Strain in SG-15 of Specimen 4

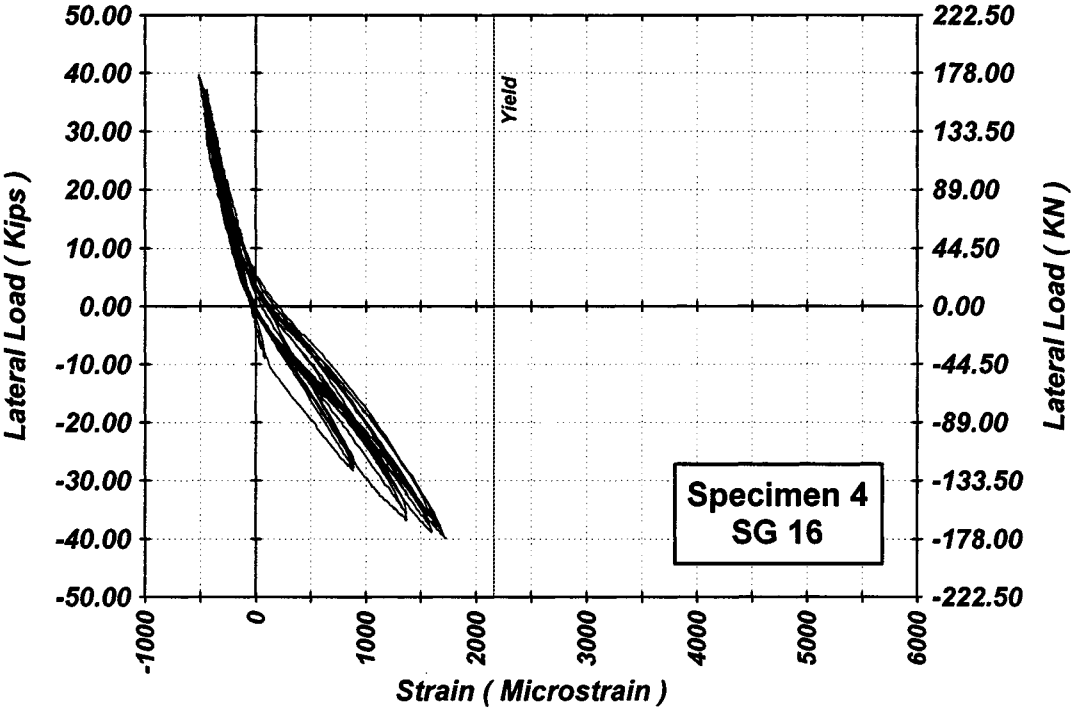

Figure A-112 Measured Lateral Load-Strain in SG-16 of Specimen 4

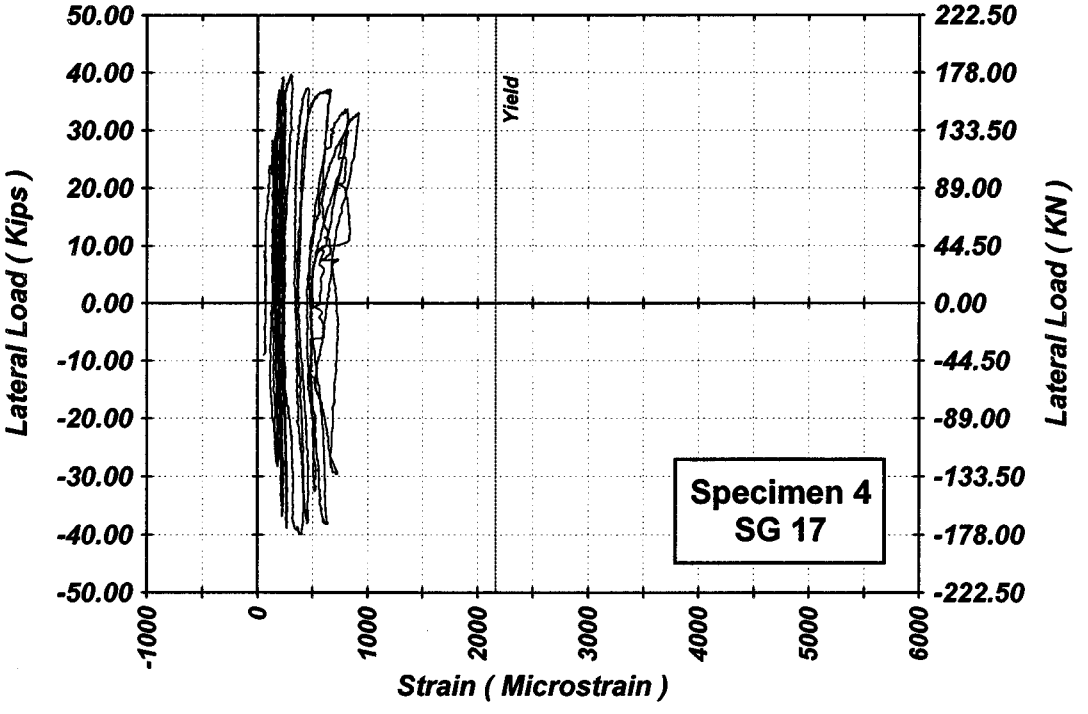

Figure A-113 Measured Lateral Load-Strain in SG-17 of Specimen 4

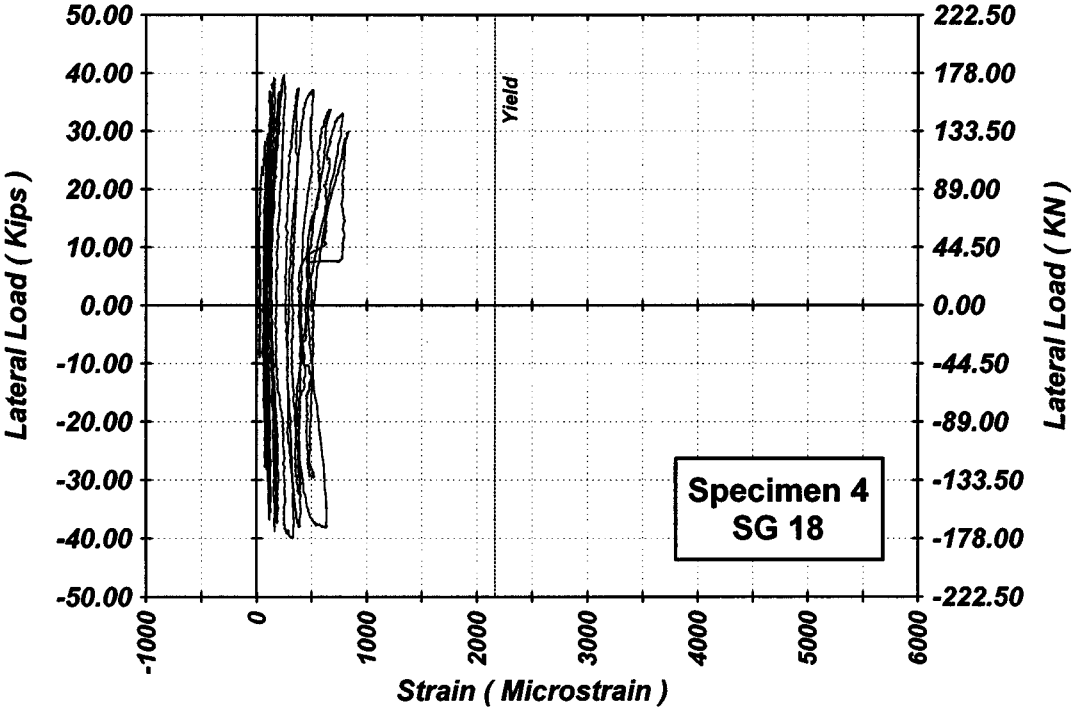

Figure A-114 Measured Lateral Load-Strain in SG-18 of Specimen 4

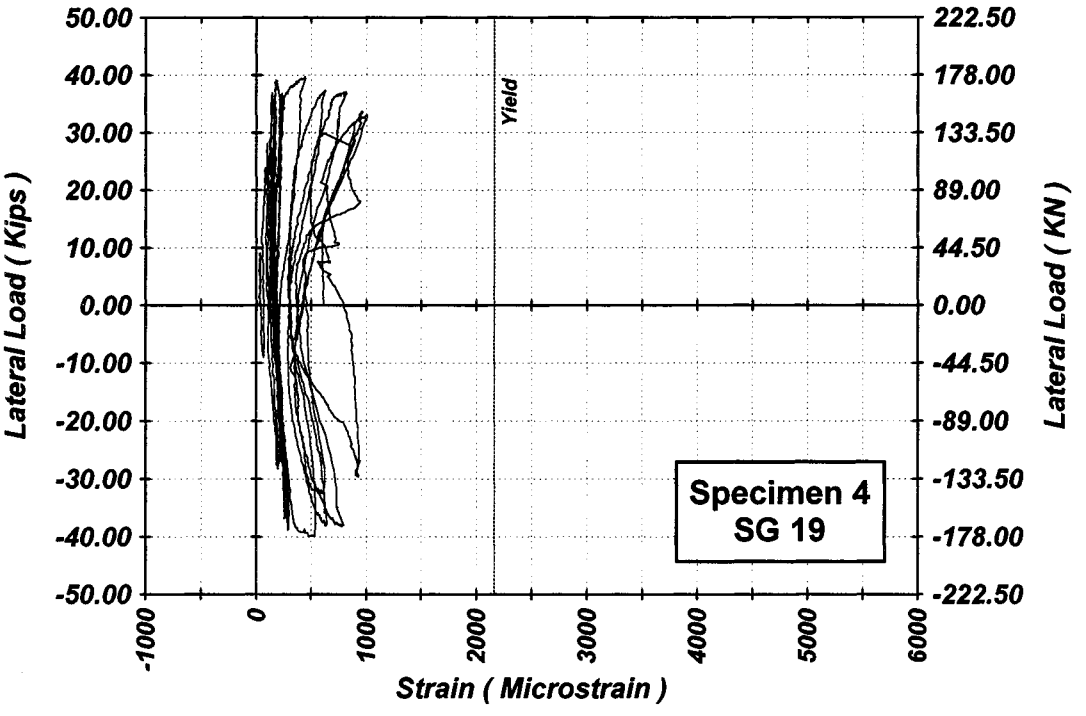

Figure A-115 Measured Lateral Load-Strain in SG-19 of Specimen 4

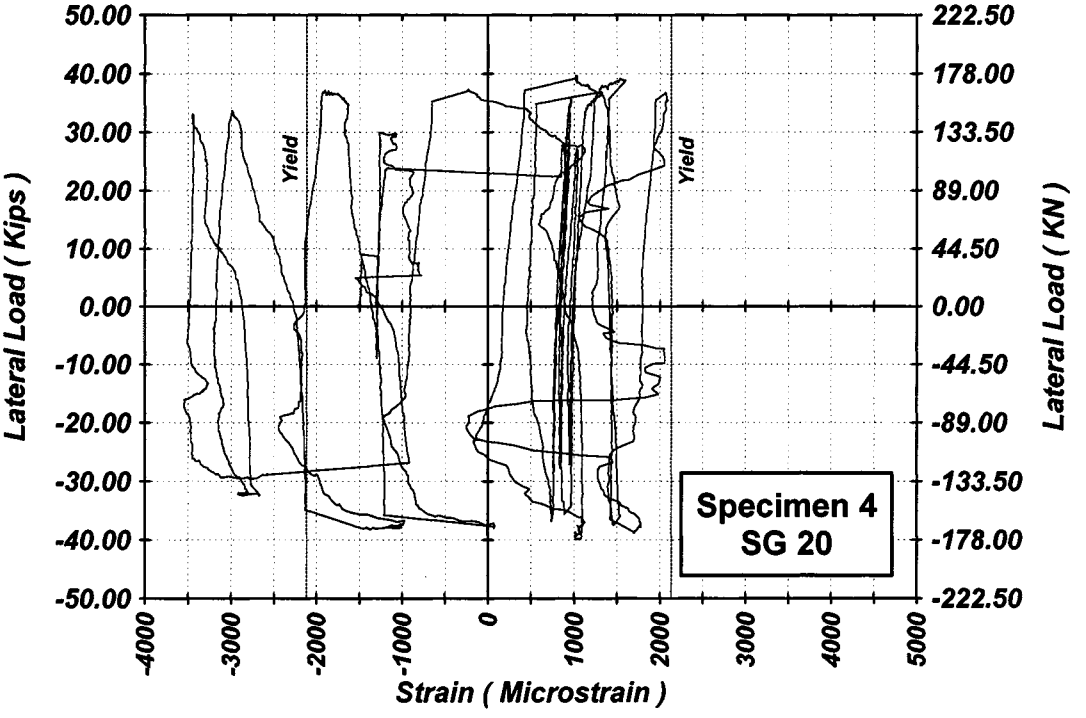

Figure A-116 Measured Lateral Load-Strain in SG-20 of Specimen 4

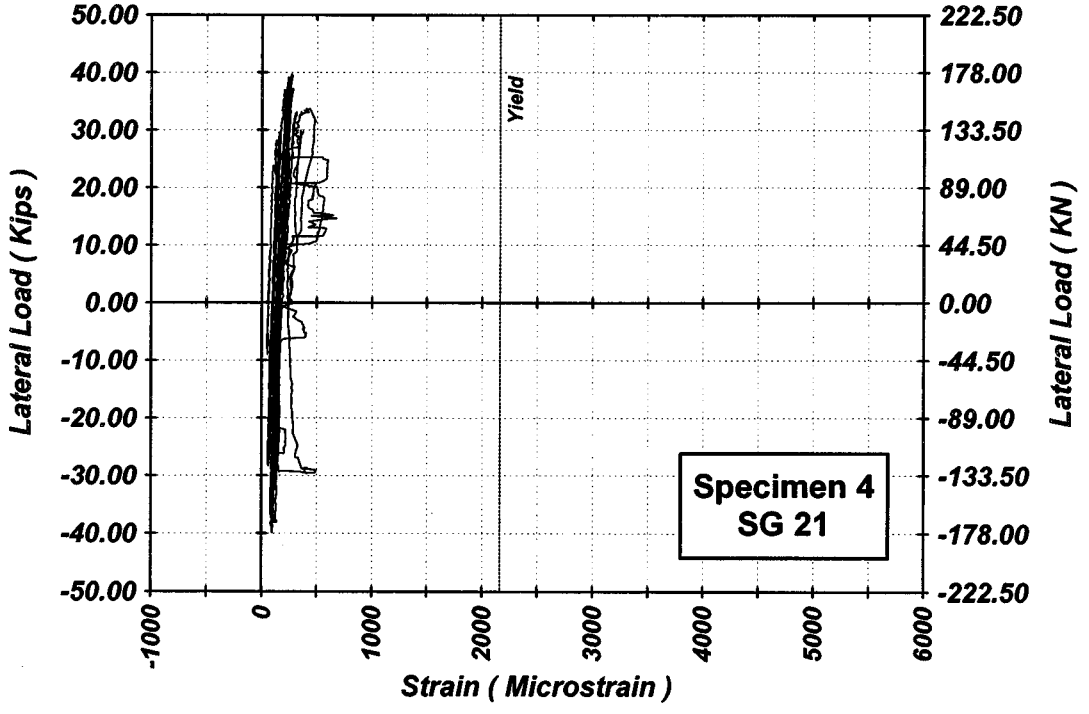

Figure A-117 Measured Lateral Load-Strain in SG-21 of Specimen 4

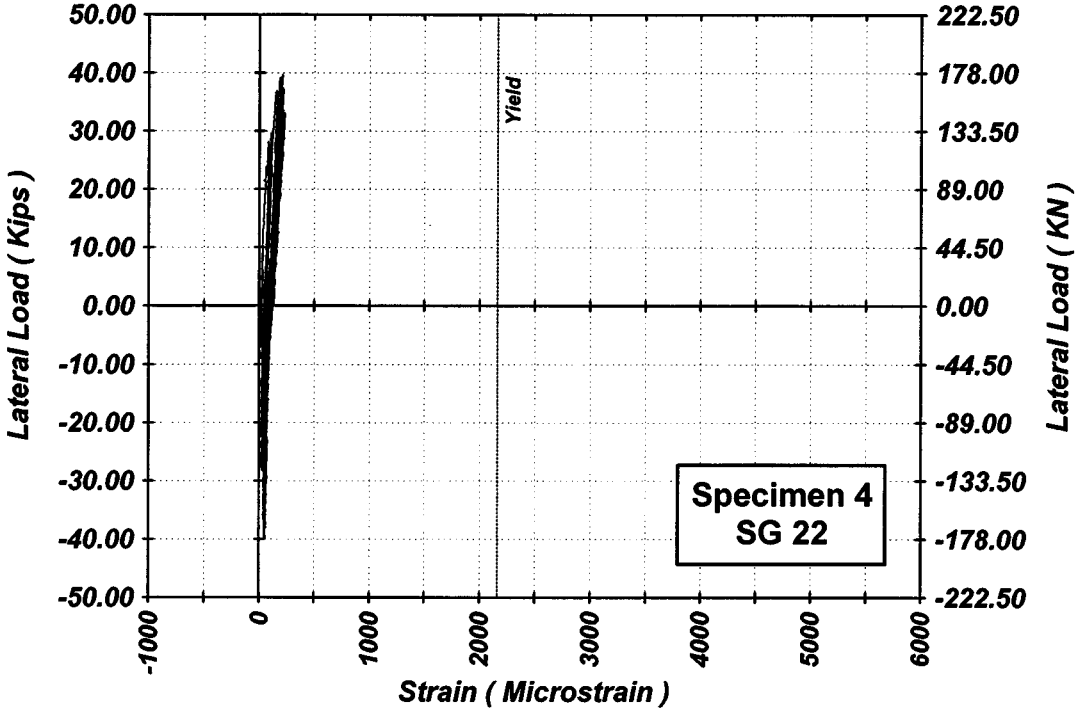

Figure A-118 Measured Lateral Load-Strain in SG-22 of Specimen 4

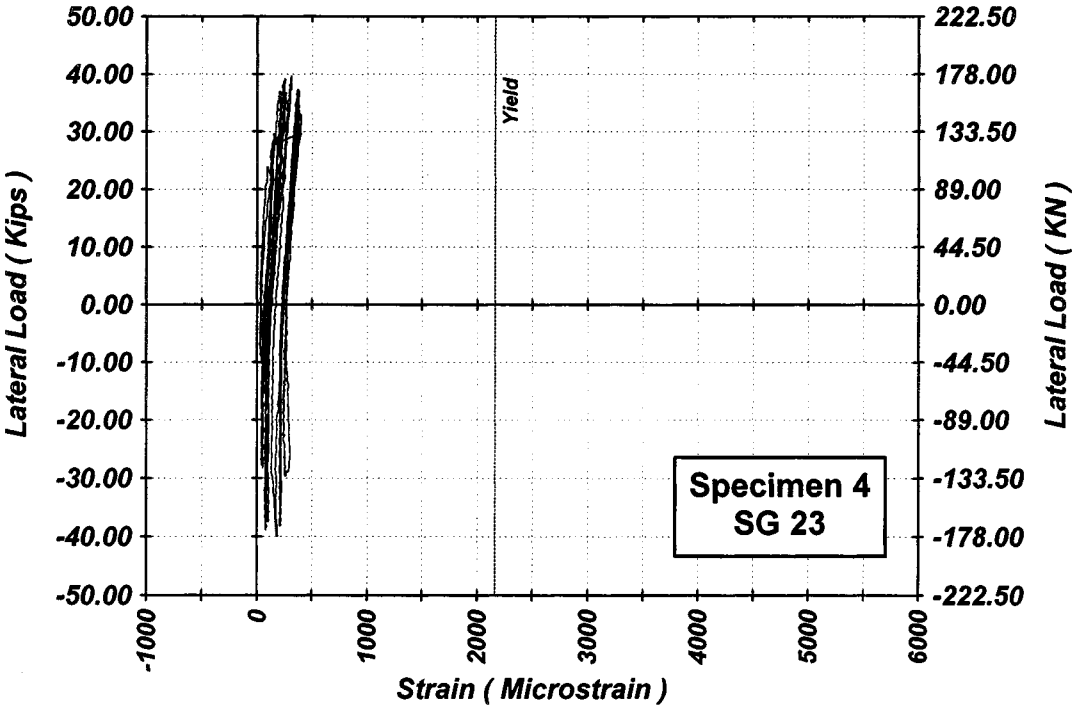

Figure A-119 Measured Lateral Load-Strain in SG-23 of Specimen 4

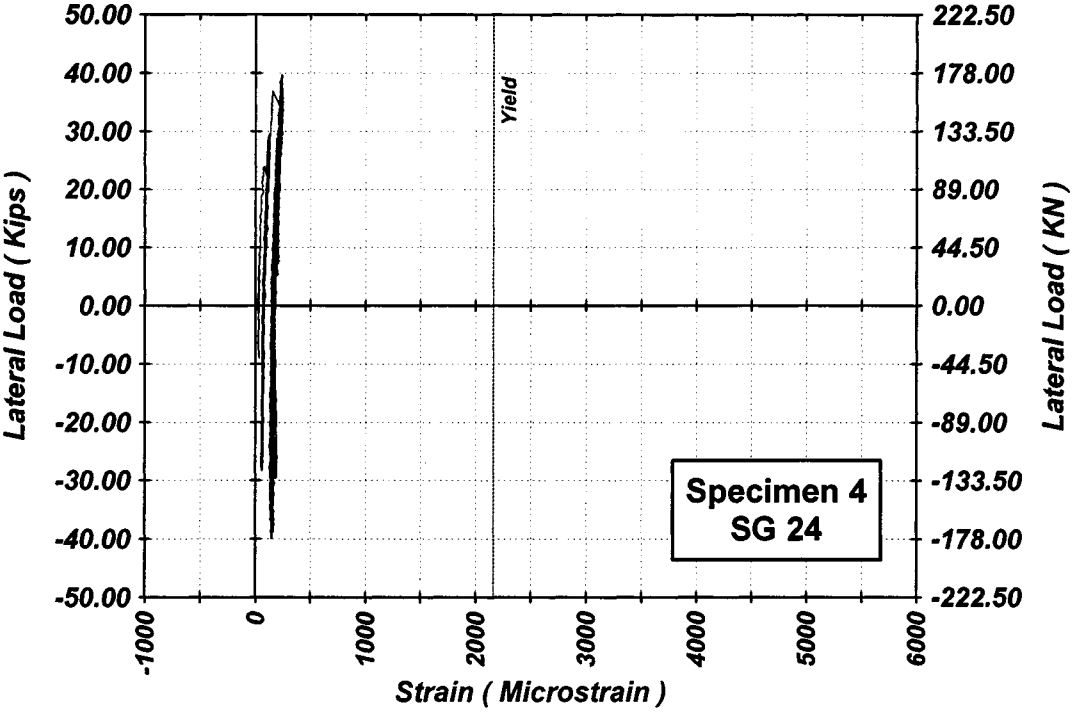

Figure A-120 Measured Lateral Load-Strain in SG-24 of Specimen 4

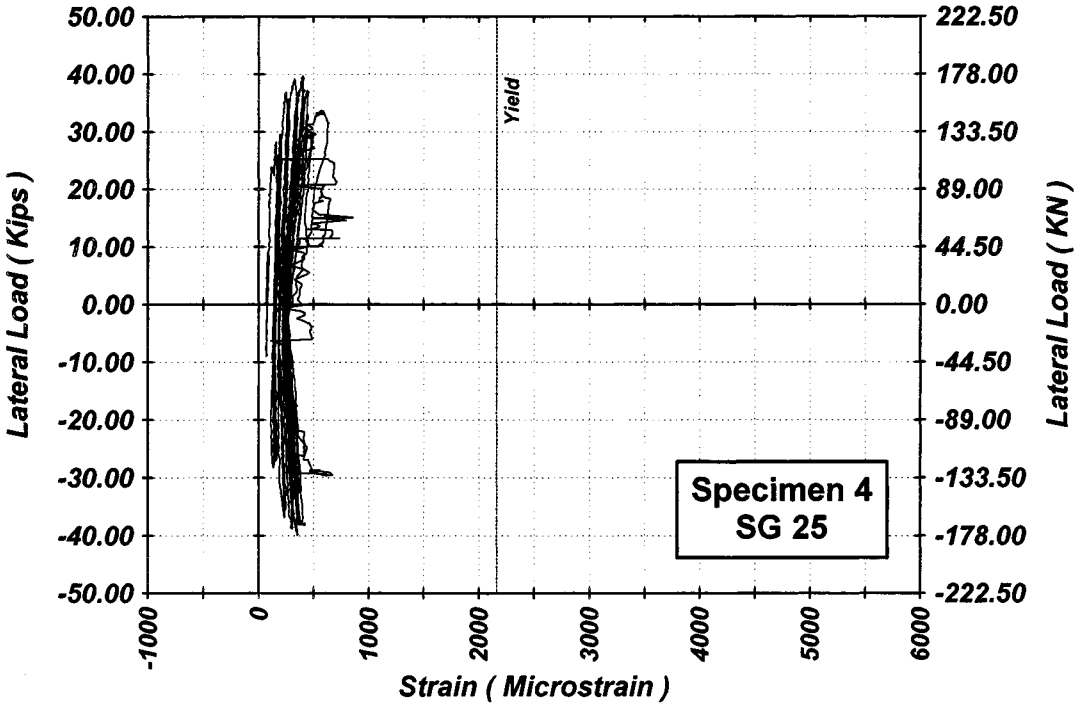

Figure A-121 Measured Lateral Load-Strain in SG-25 of Specimen 4

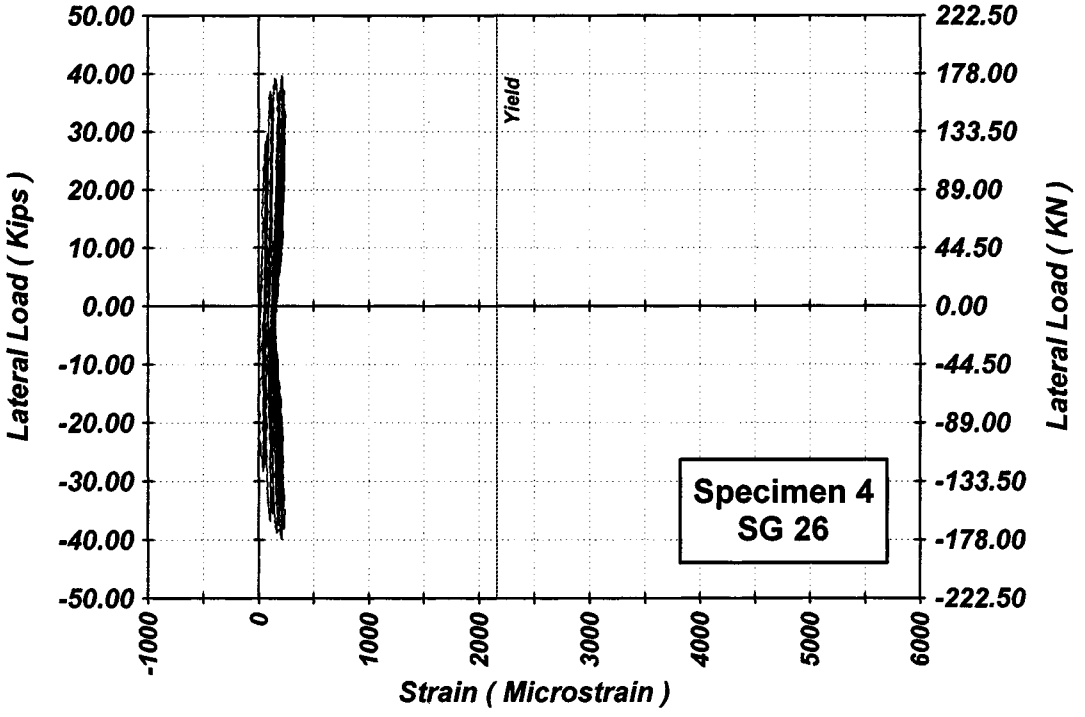

Figure A-122 Measured Lateral Load-Strain in SG-26 of Specimen 4

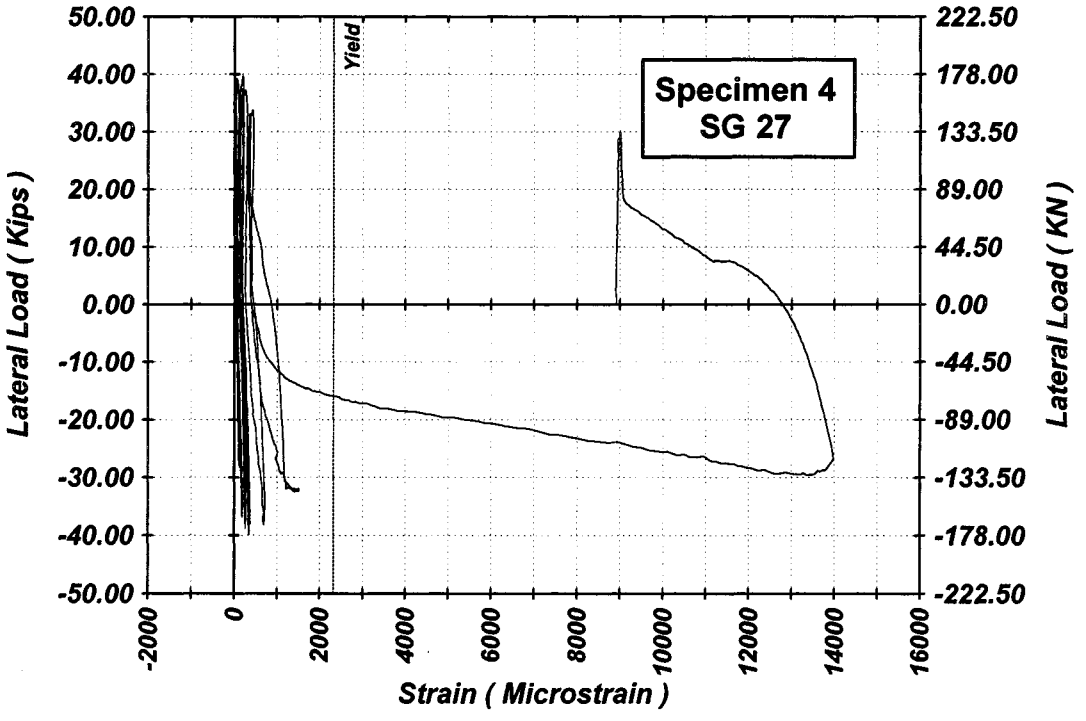

Figure A-123 Measured Lateral Load-Strain in SG-27 of Specimen 4

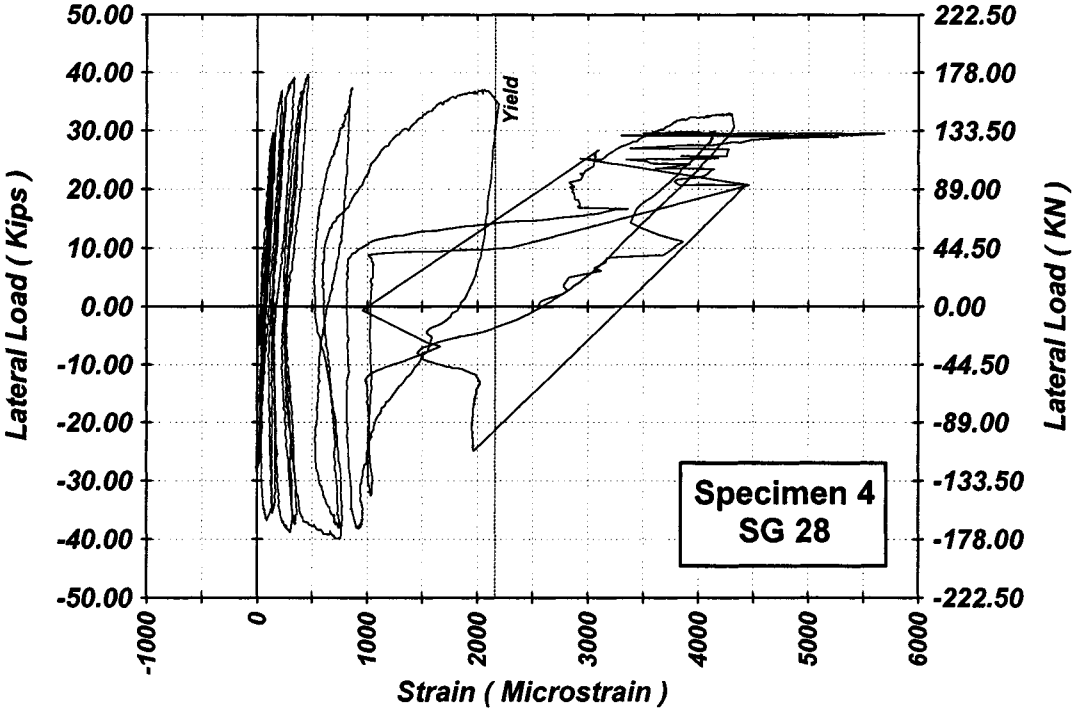

Figure A-124 Measured Lateral Load-Strain in SG-28 of Specimen 4

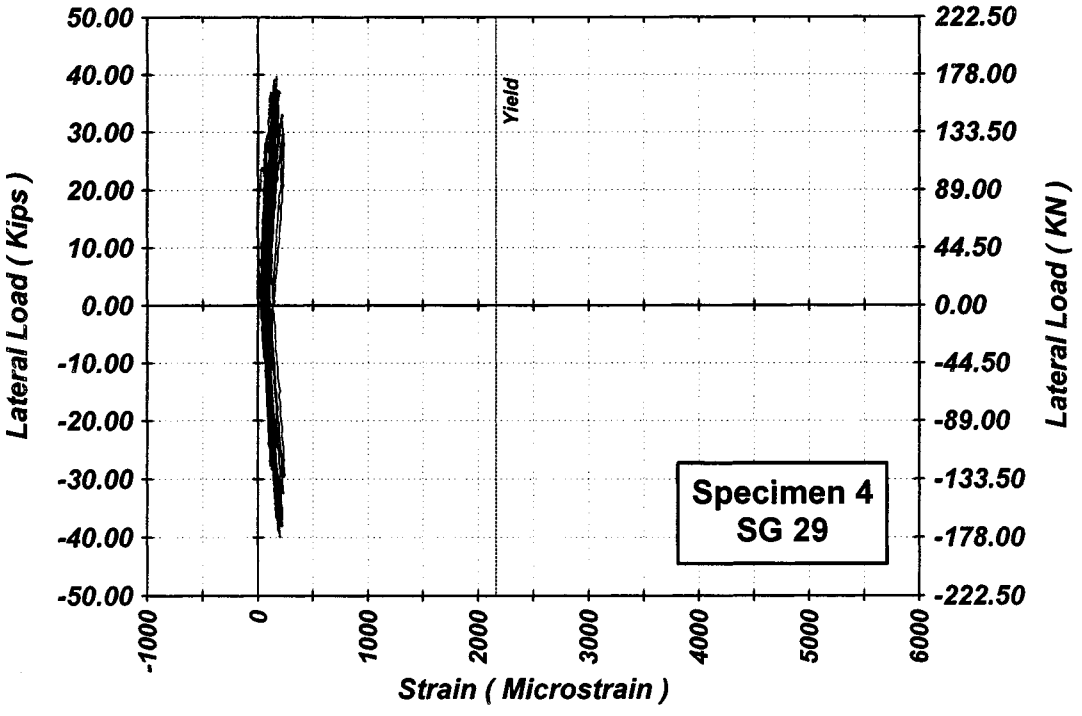

Figure A-125 Measured Lateral Load-Strain in SG-29 of Specimen 4

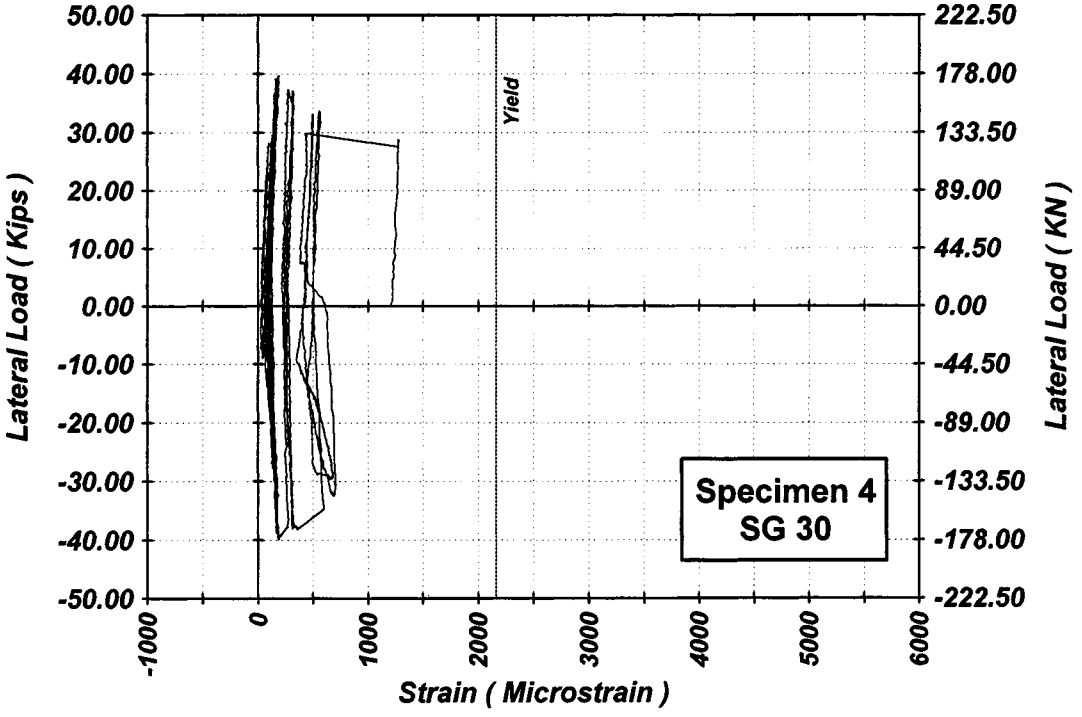

Figure A-126 Measured Lateral Load-Strain in SG-30 of Specimen 4

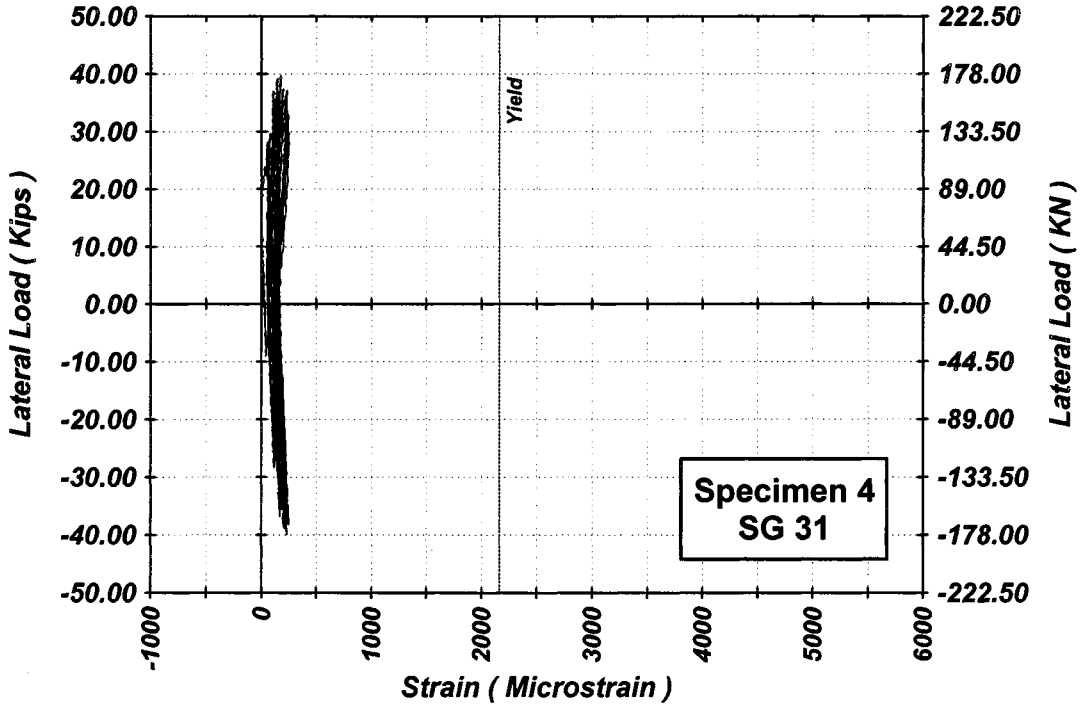

Figure A-127 Measured Lateral Load-Strain in SG-31 of Specimen 4

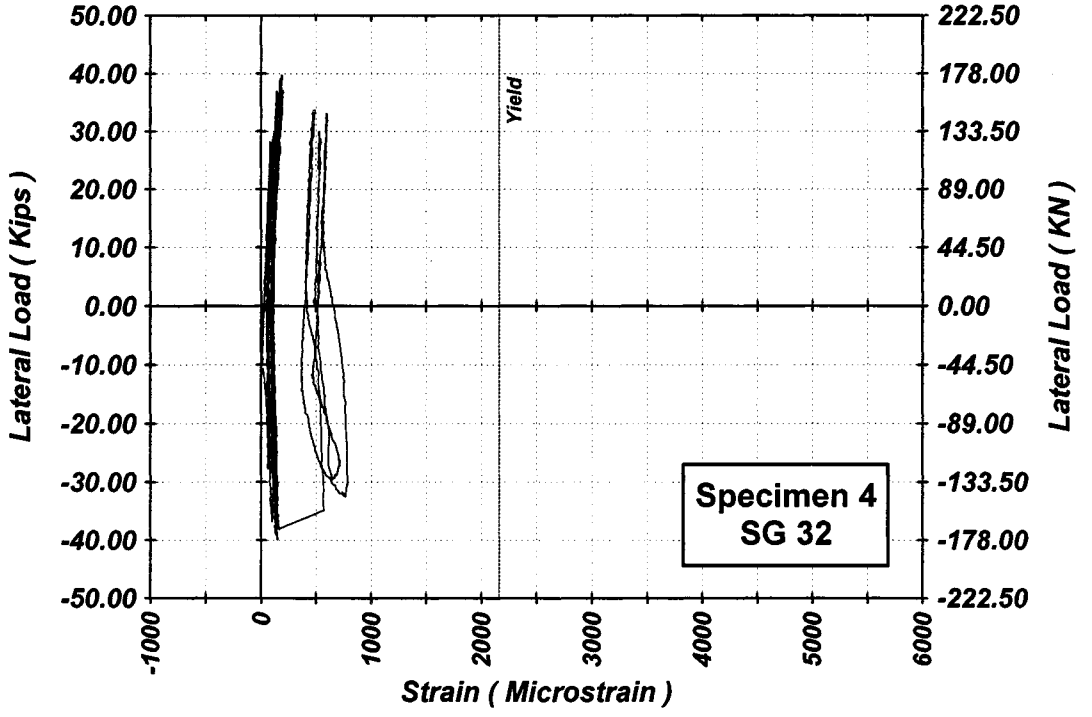

Figure A-128 Measured Lateral Load-Strain in SG-32 of Specimen 4

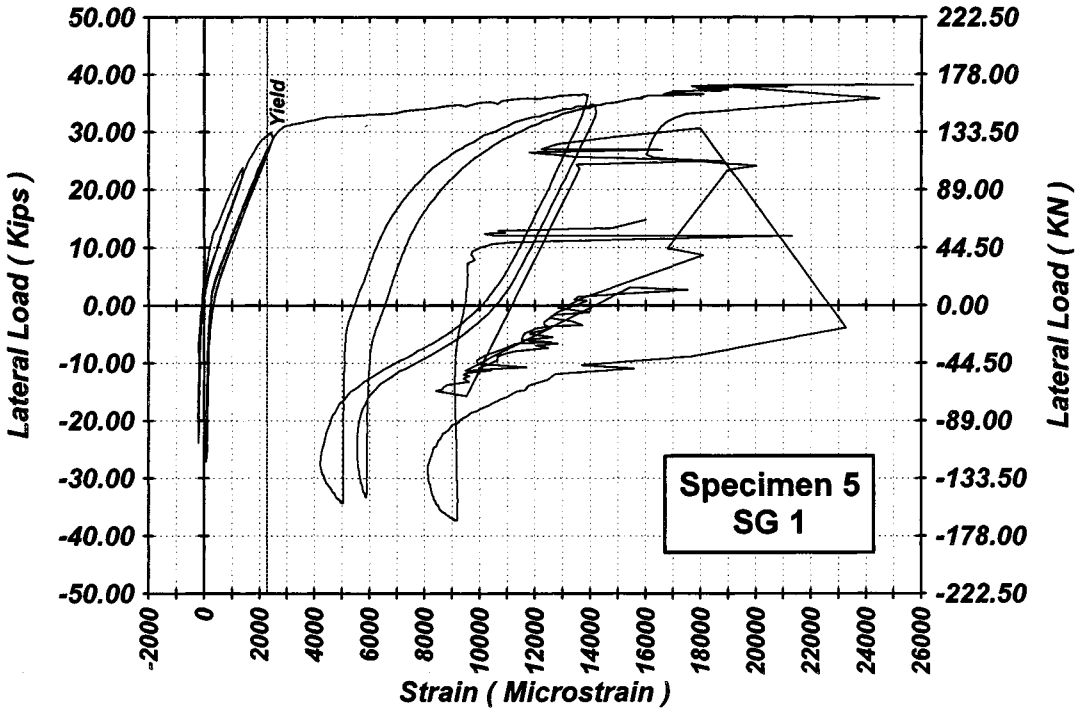

Figure A-129 Measured Lateral Load-Strain in SG-1 of Specimen 5

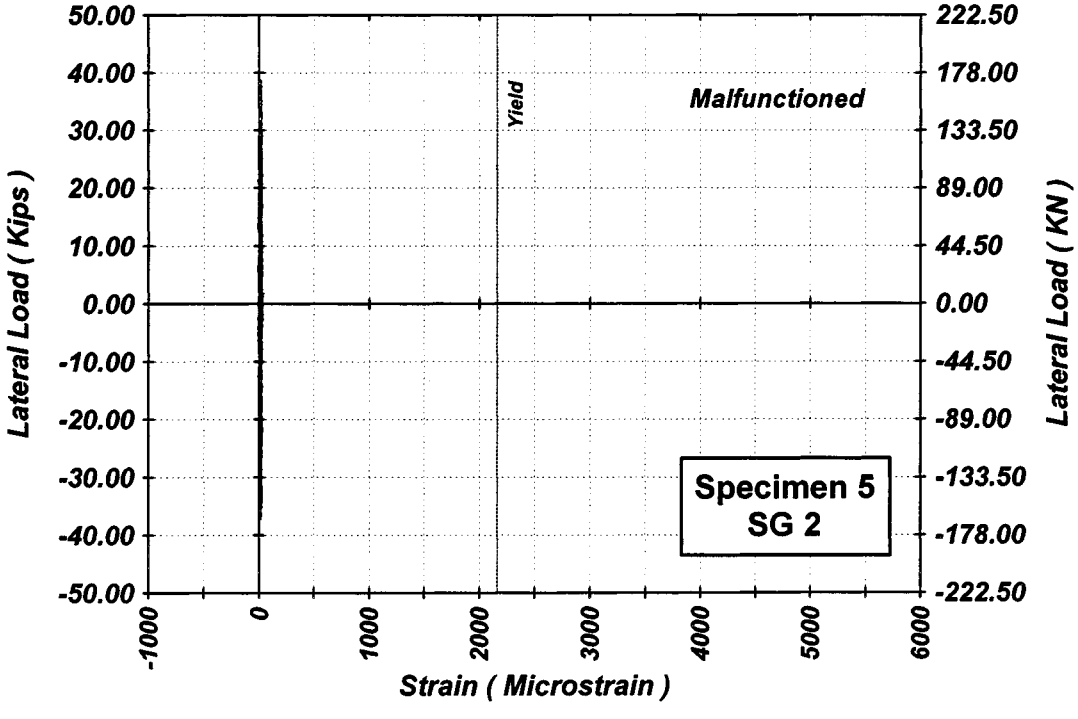

Figure A-130 Measured Lateral Load-Strain in SG-2 of Specimen 5

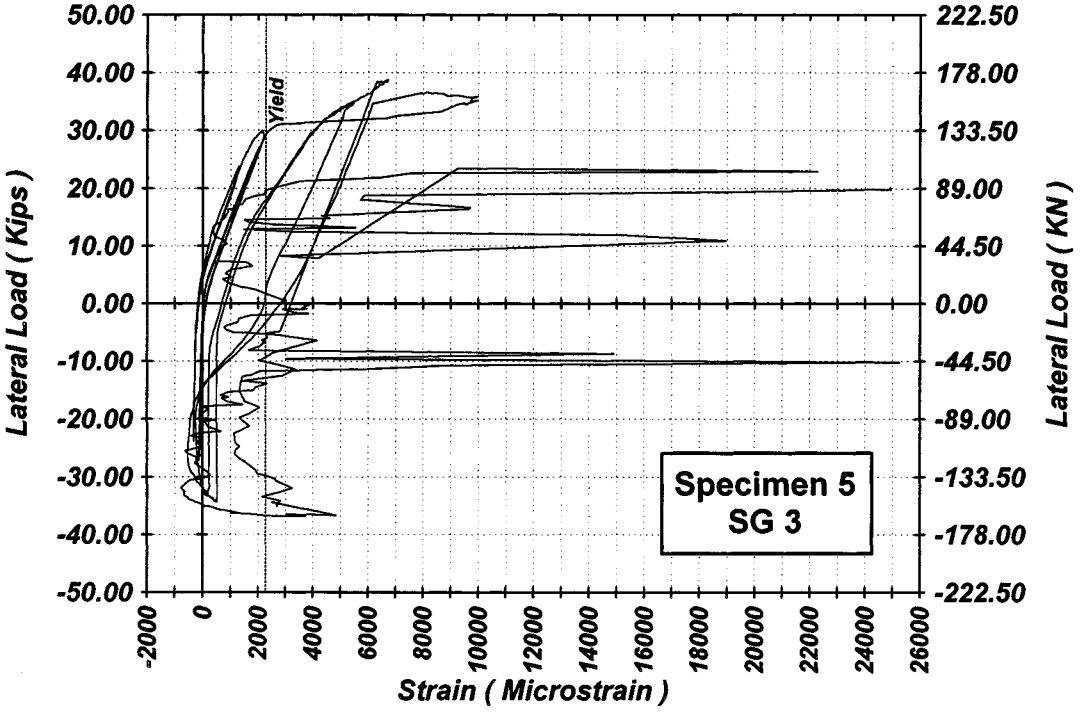

Figure A-131 Measured Lateral Load-Strain in SG-3 of Specimen 5

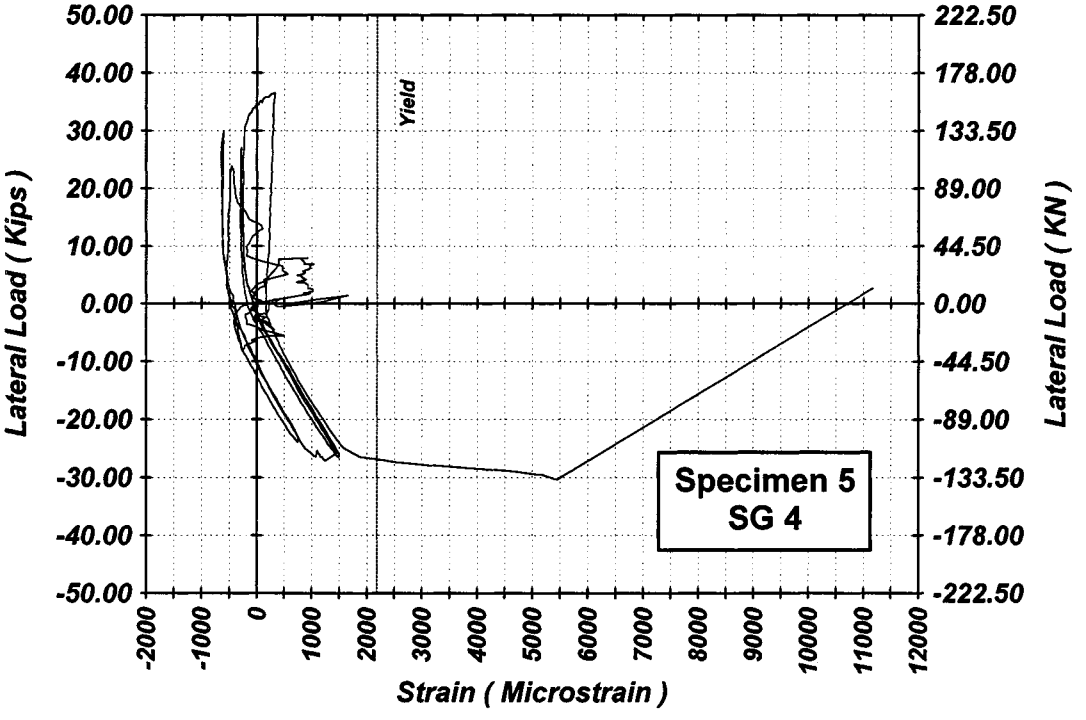

Figure A-132 Measured Lateral Load-Strain in SG-4 of Specimen 5

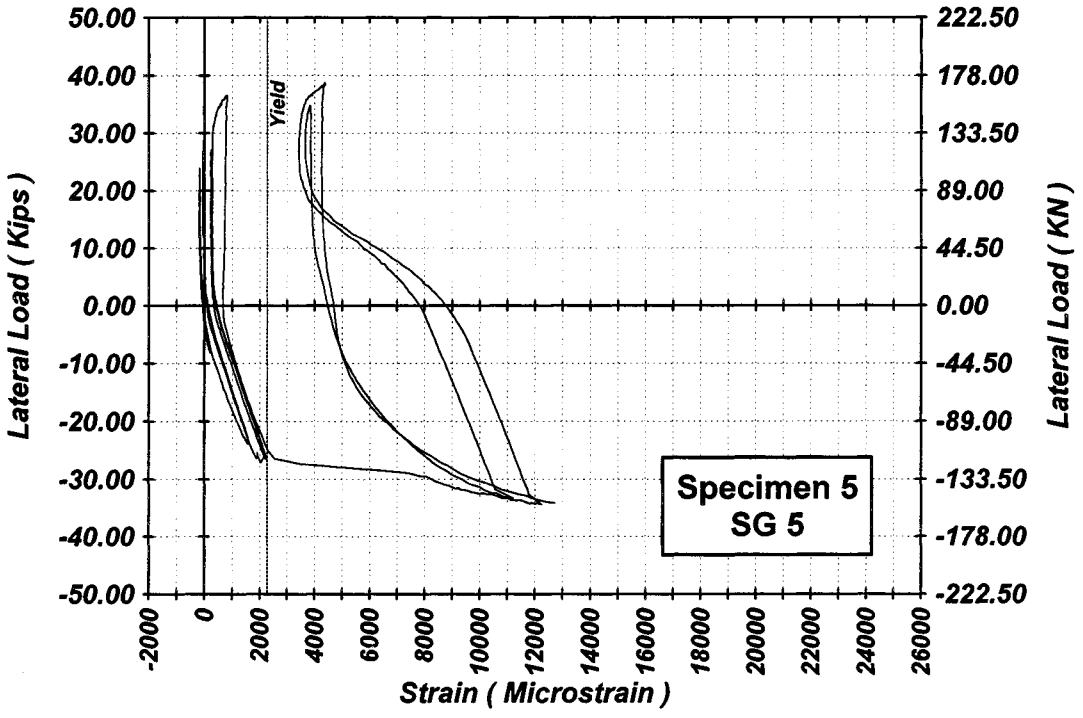

Figure A-133 Measured Lateral Load-Strain in SG-5 of Specimen 5

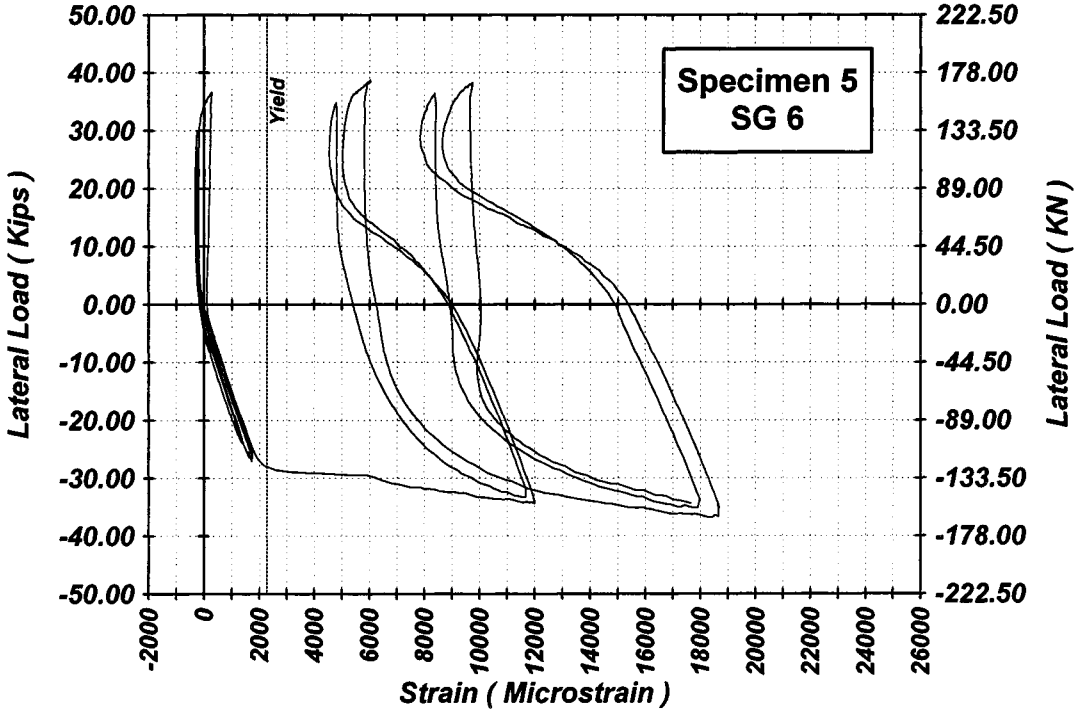

Figure A-134 Measured Lateral Load-Strain in SG-6 of Specimen 5

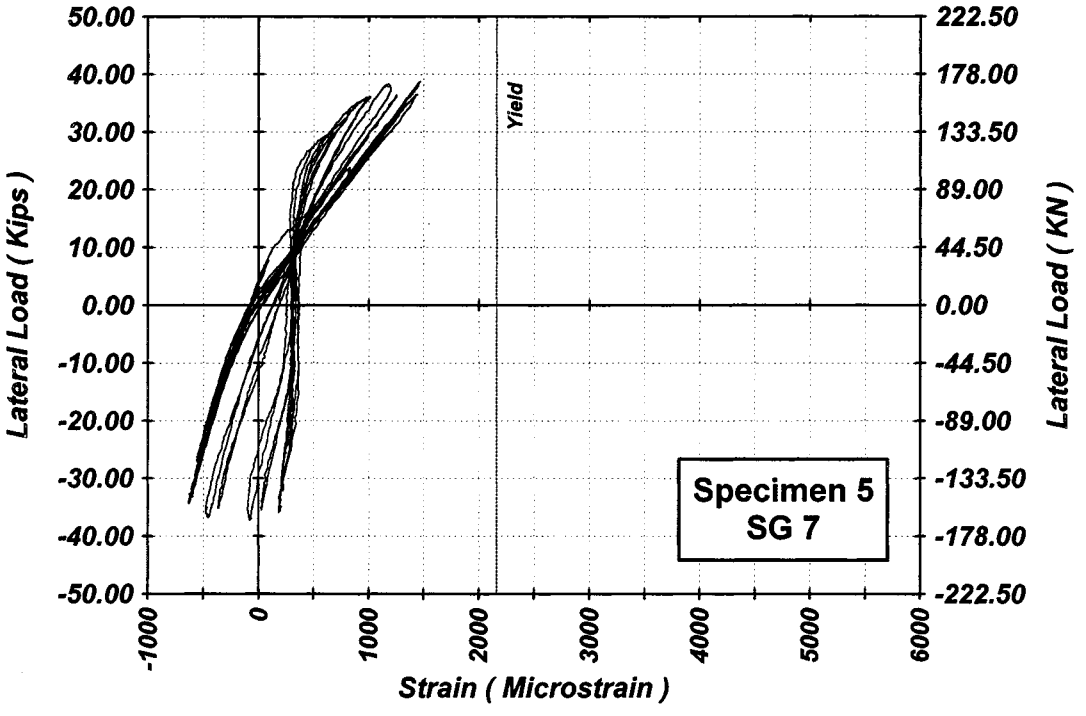

Figure A-135 Measured Lateral Load-Strain in SG-7 of Specimen 5

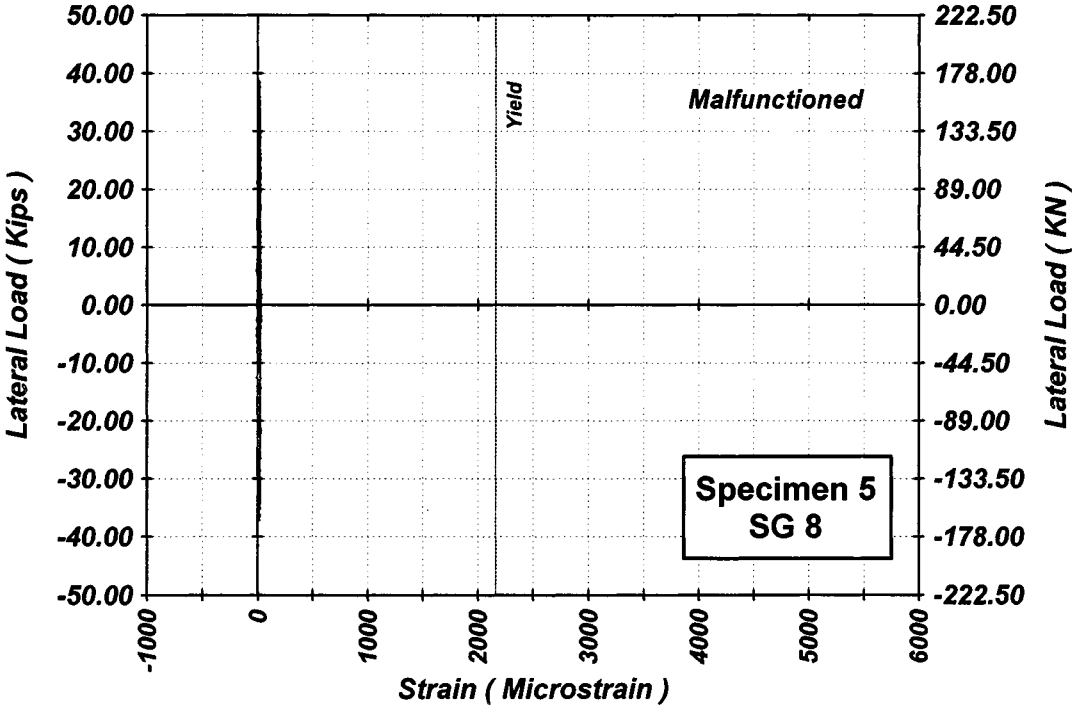

Figure A-136 Measured Lateral Load-Strain in SG-8 of Specimen 5

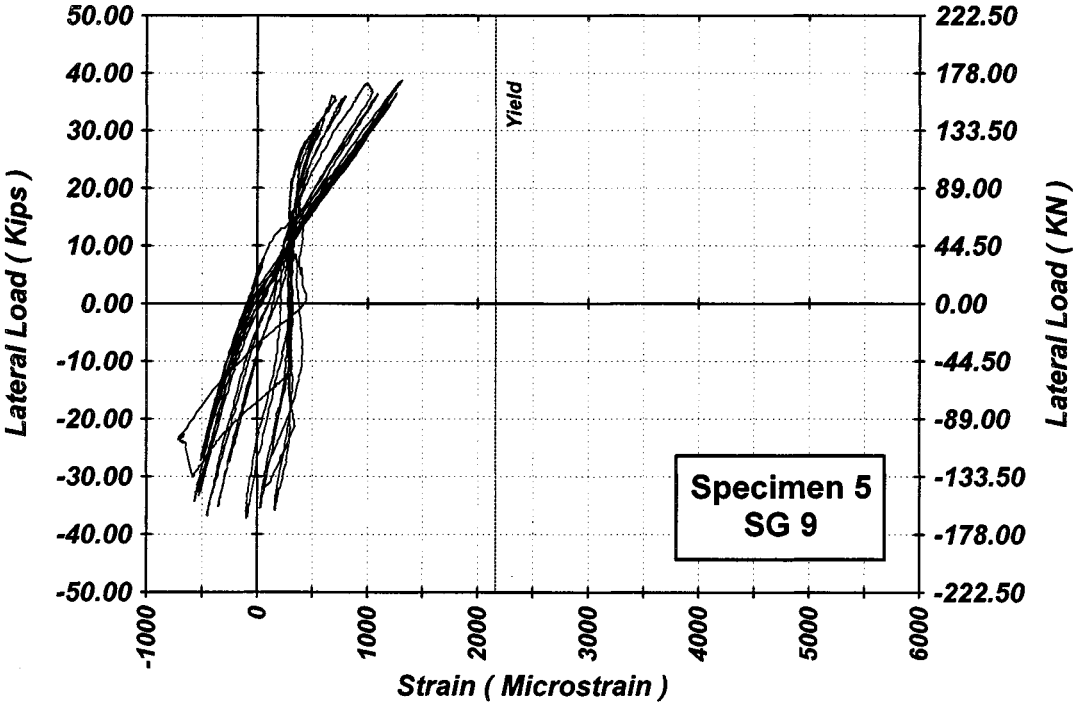

Figure A-137 Measured Lateral Load-Strain in SG-9 of Specimen 5

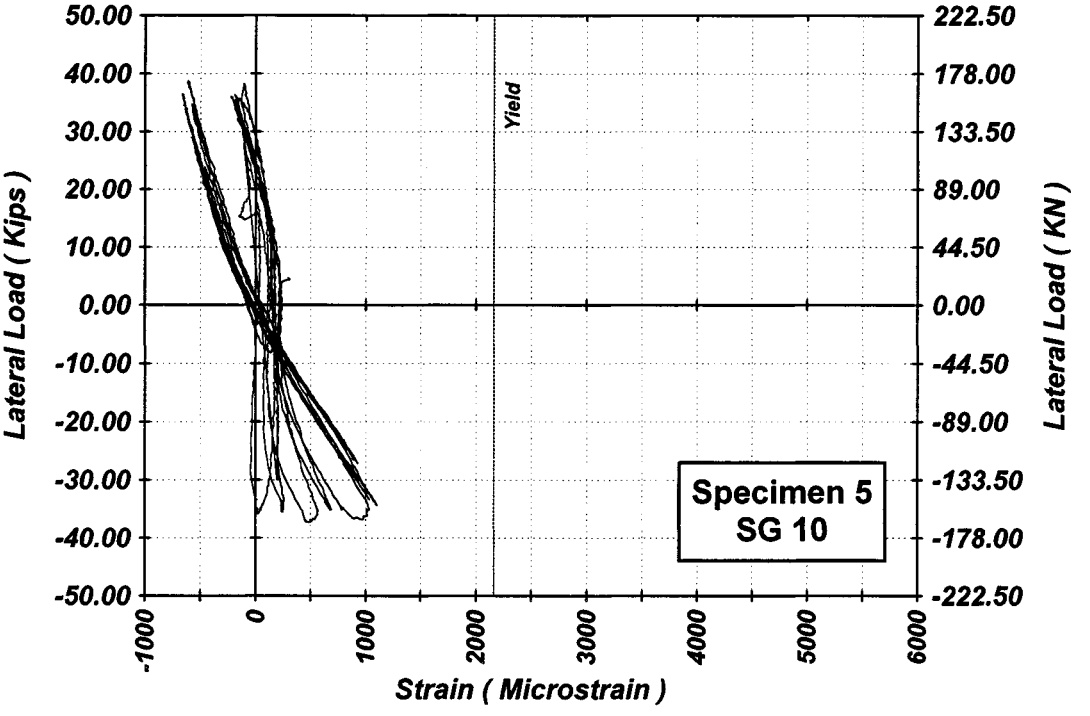

Figure A-138 Measured Lateral Load-Strain in SG-10 of Specimen 5

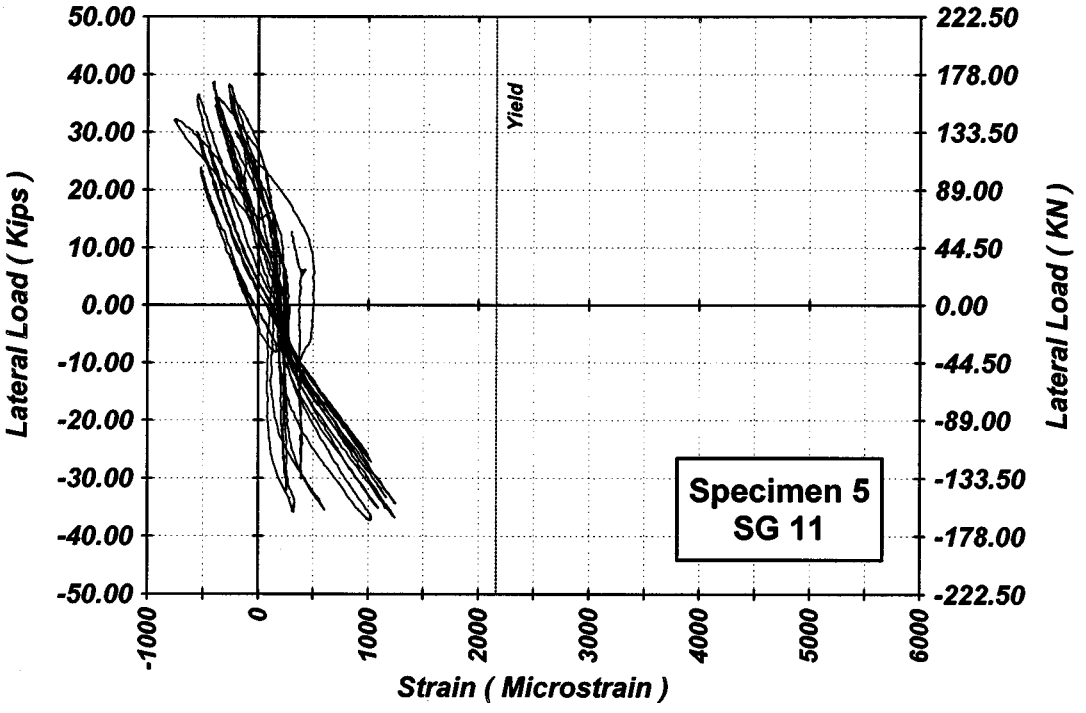

Figure A-139 Measured Lateral Load-Strain in SG-11 of Specimen 5

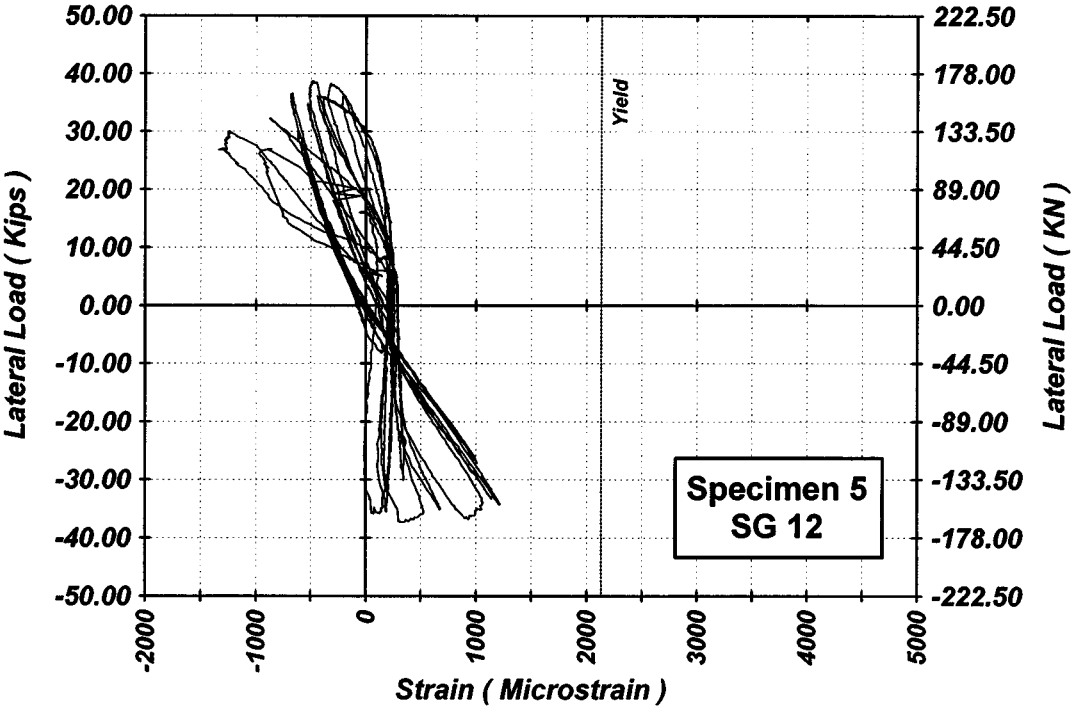

Figure A-140 Measured Lateral Load-Strain in SG-12 of Specimen 5

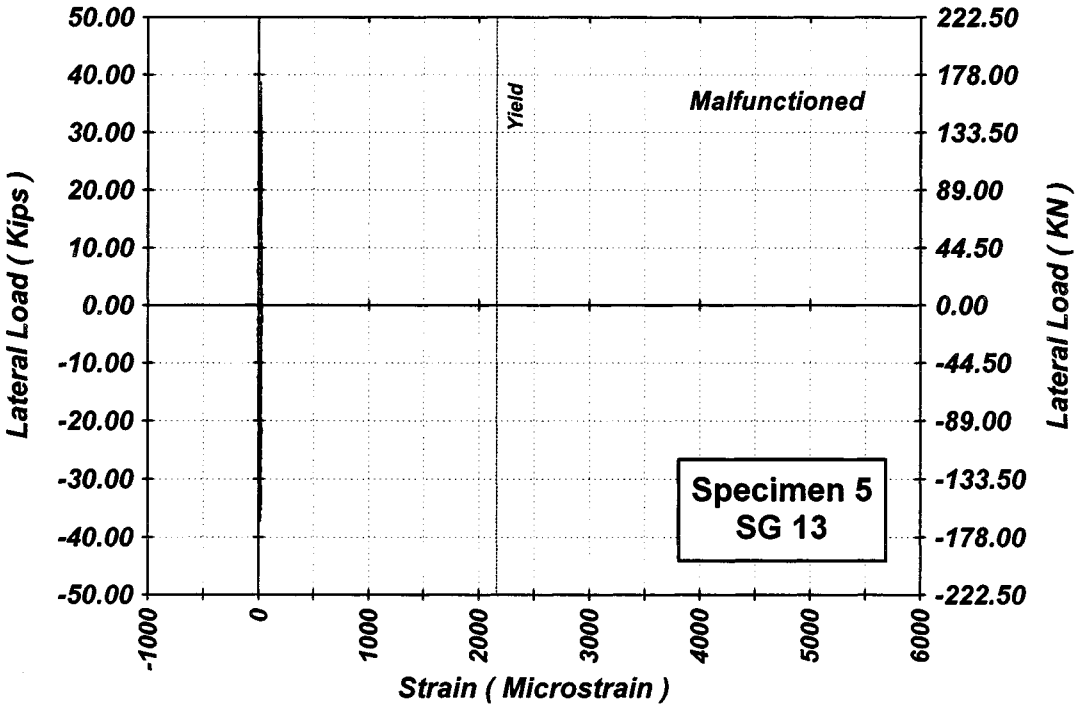

Figure A-141 Measured Lateral Load-Strain in SG-13 of Specimen 5

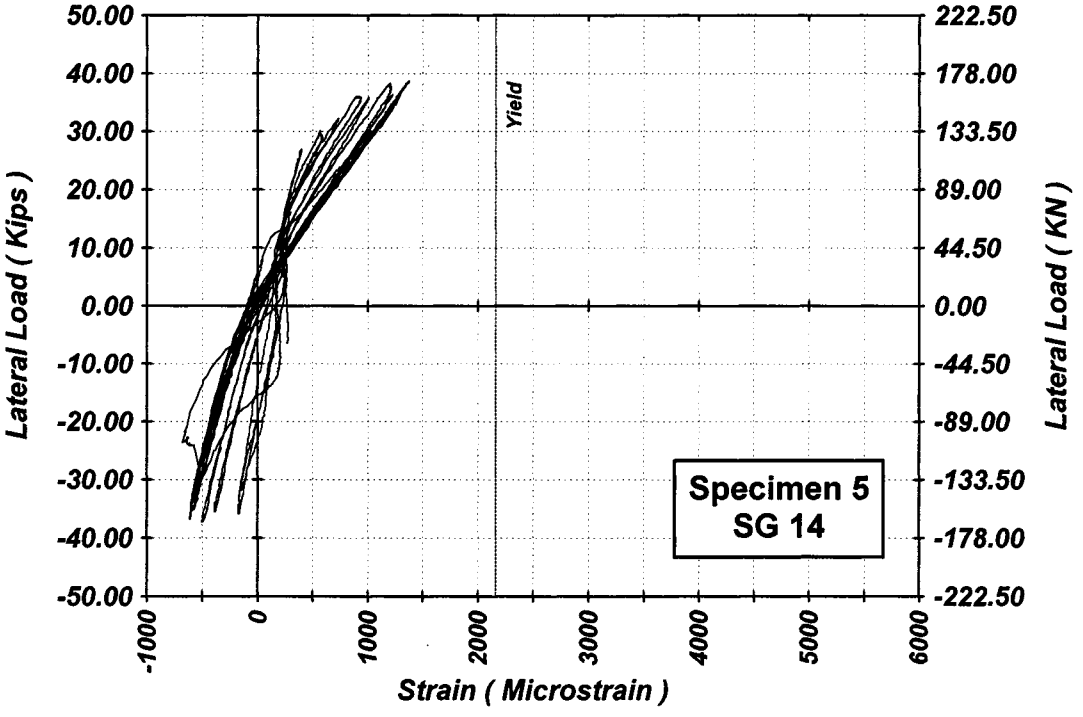

Figure A-142 Measured Lateral Load-Strain in SG-14 of Specimen 5

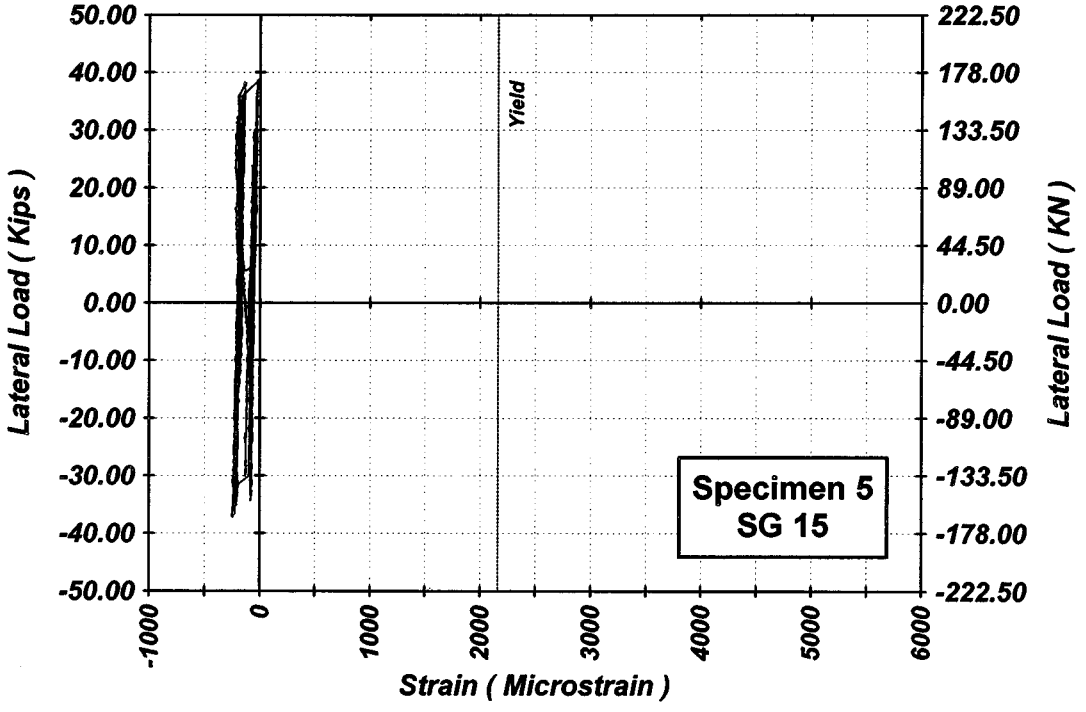

Figure A-143 Measured Lateral Load-Strain in SG-15 of Specimen 5

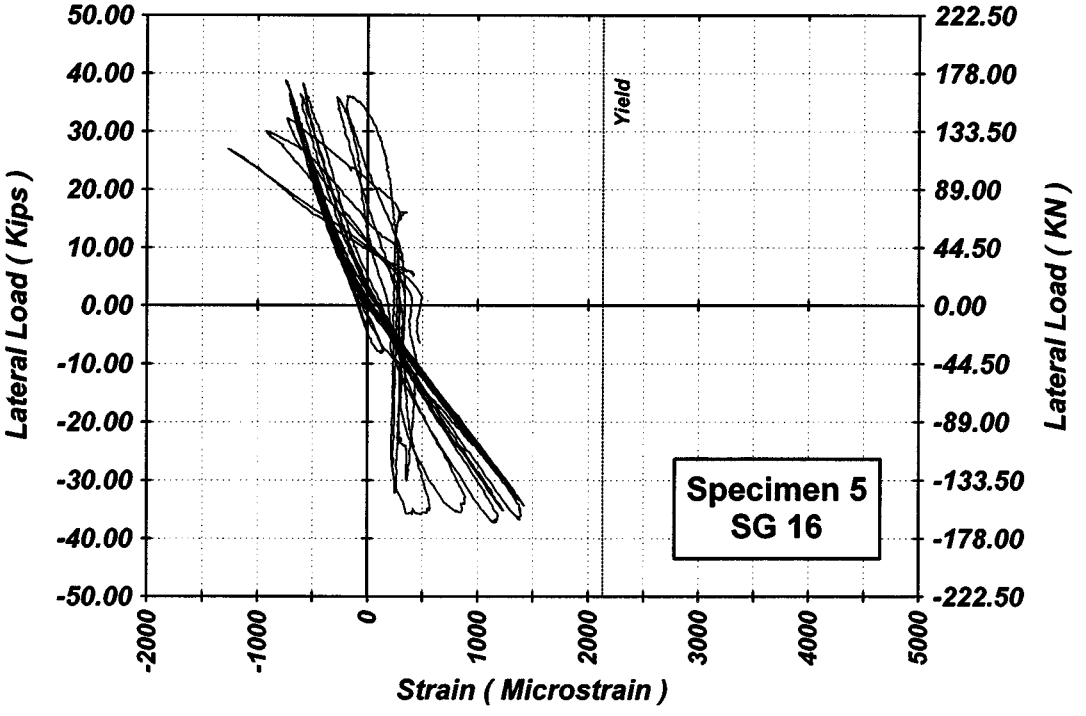

Figure A-144 Measured Lateral Load-Strain in SG-16 of Specimen 5

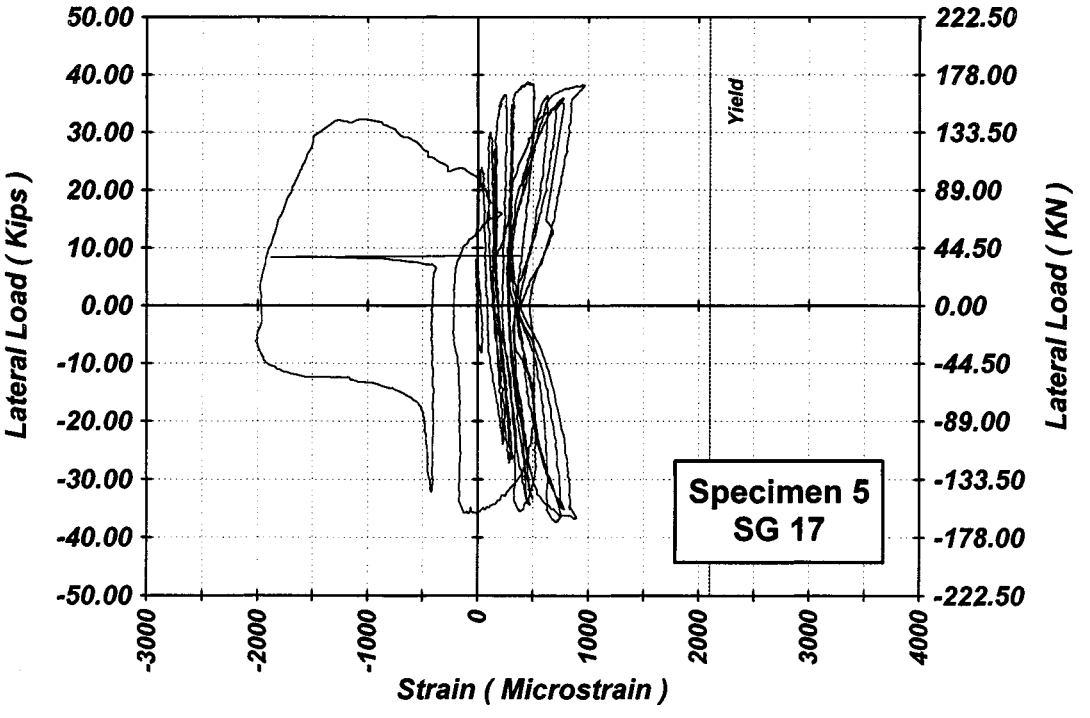

Figure A-145 Measured Lateral Load-Strain in SG-17 of Specimen 5

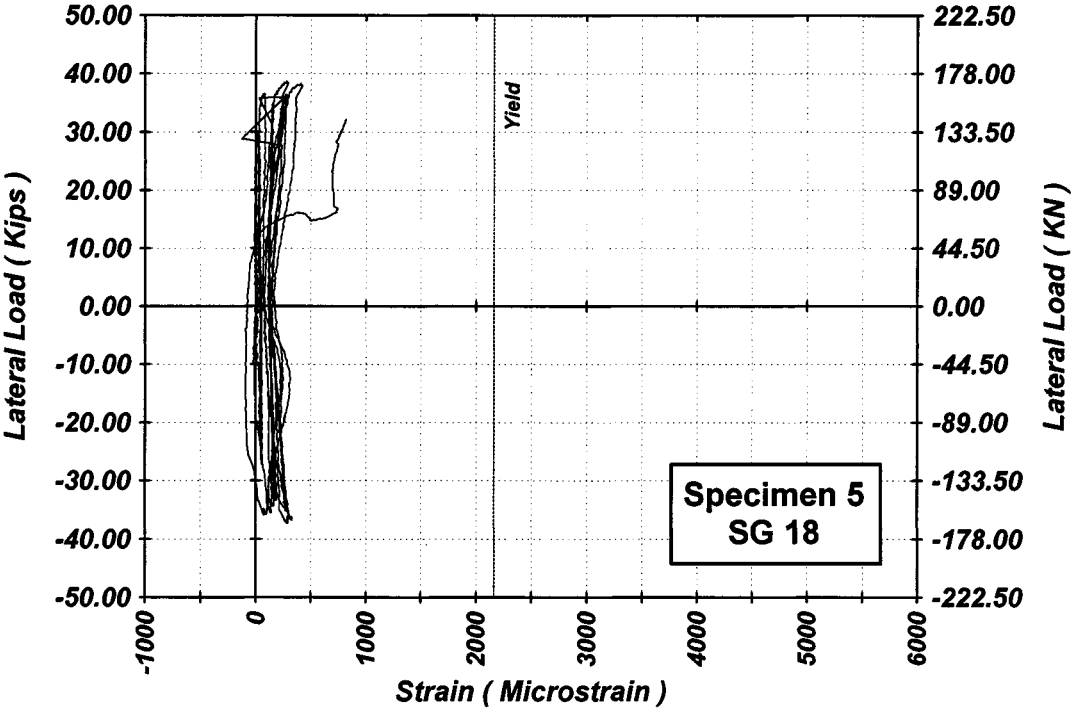

Figure A-146 Measured Lateral Load-Strain in SG-18 of Specimen 5

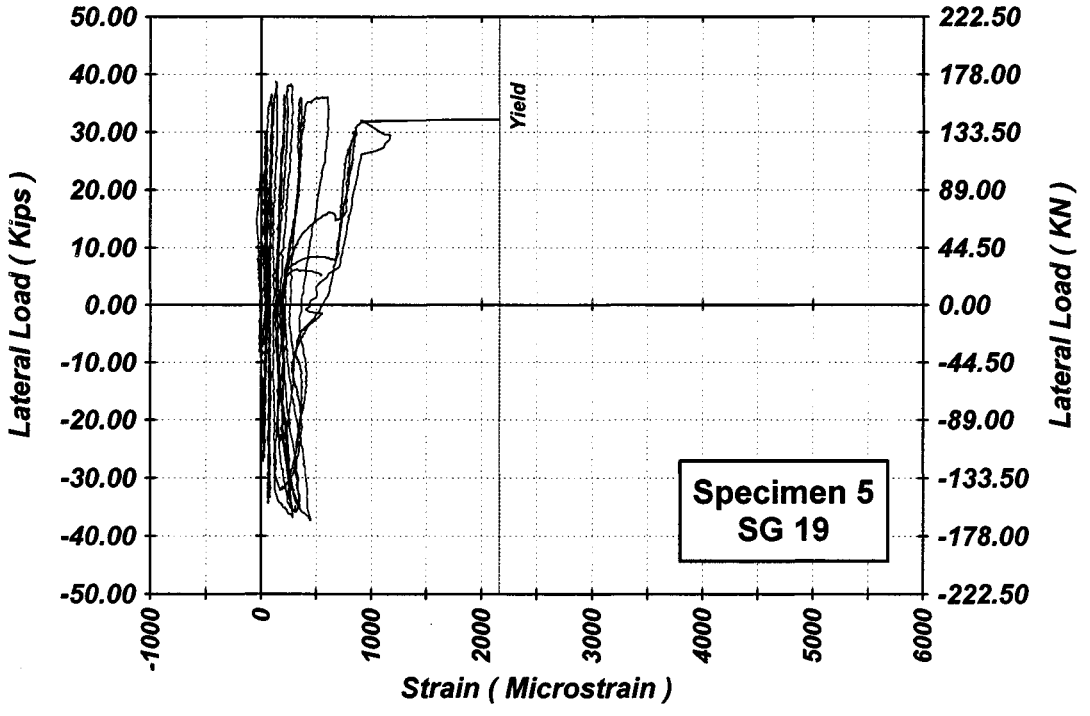

Figure A-147 Measured Lateral Load-Strain in SG-19 of Specimen 5

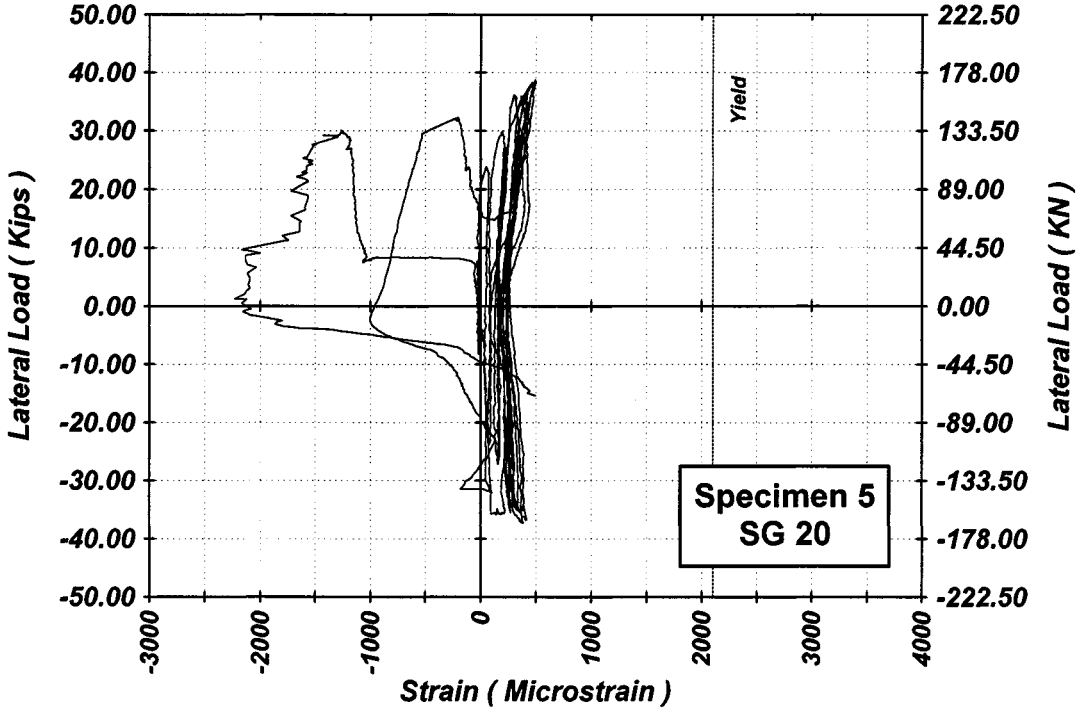

Figure A-148 Measured Lateral Load-Strain in SG-20 of Specimen 5

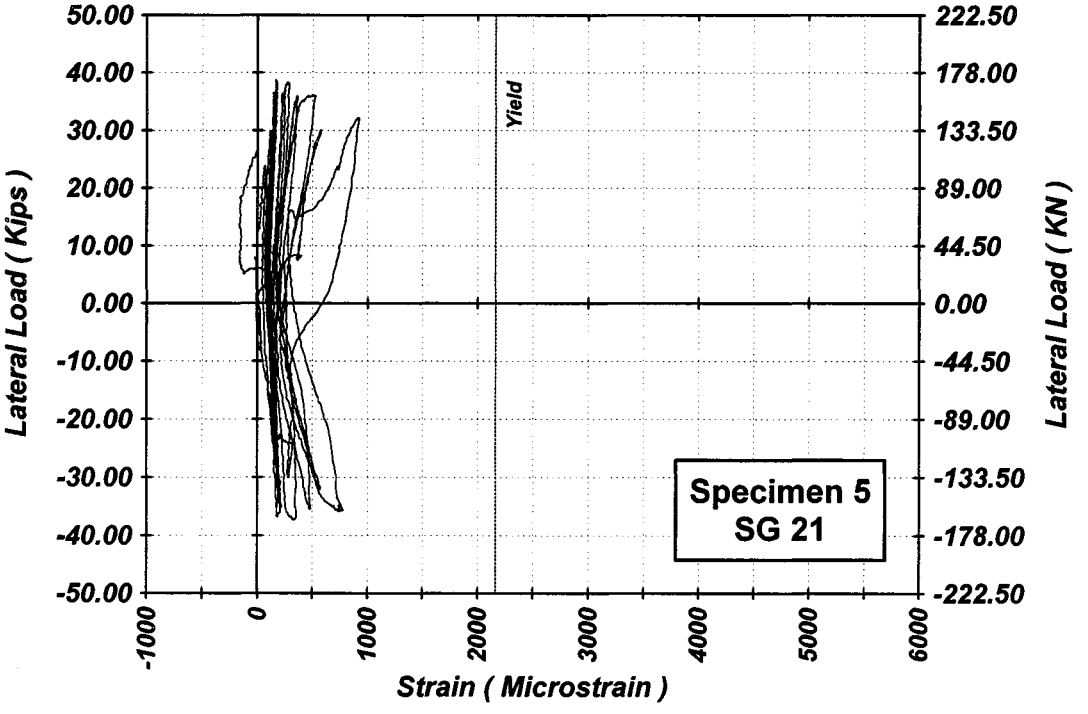

Figure A-149 Measured Lateral Load-Strain in SG-21 of Specimen 5

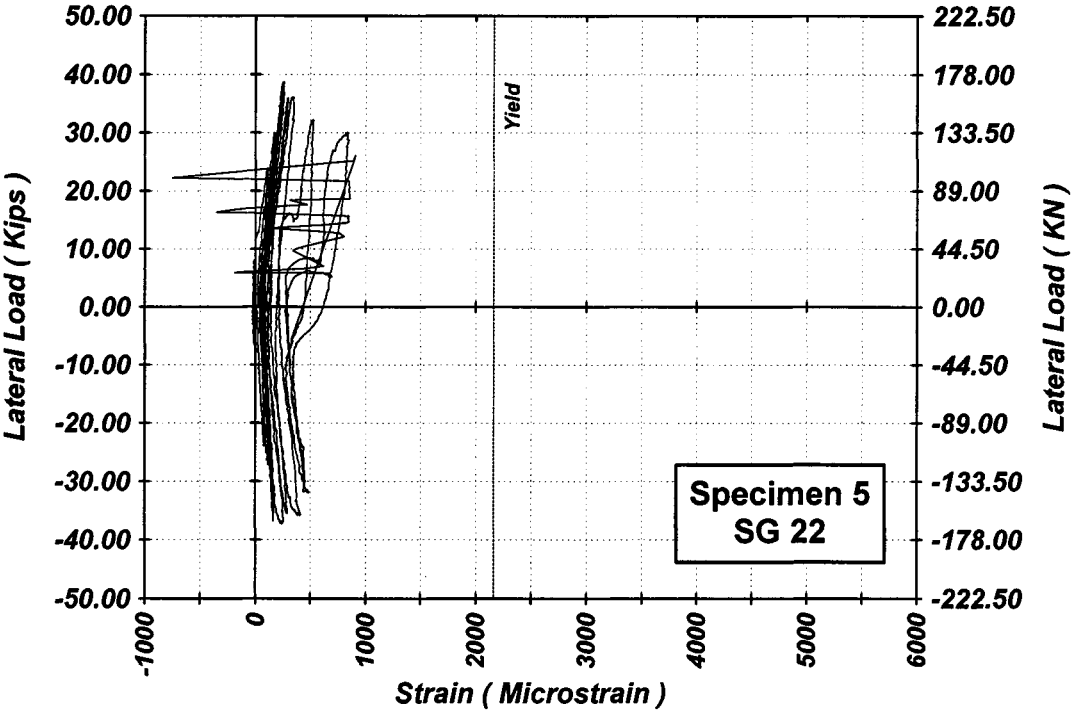

Figure A-150 Measured Lateral Load-Strain in SG-22 of Specimen 5

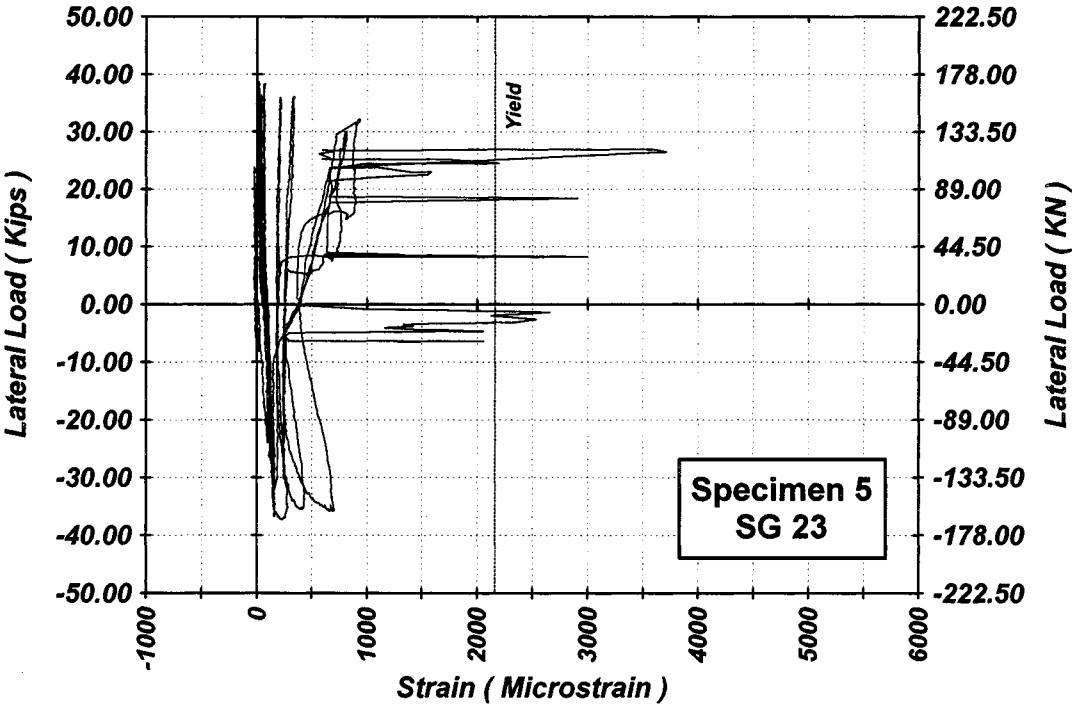

Figure A-151 Measured Lateral Load-Strain in SG-23 of Specimen 5

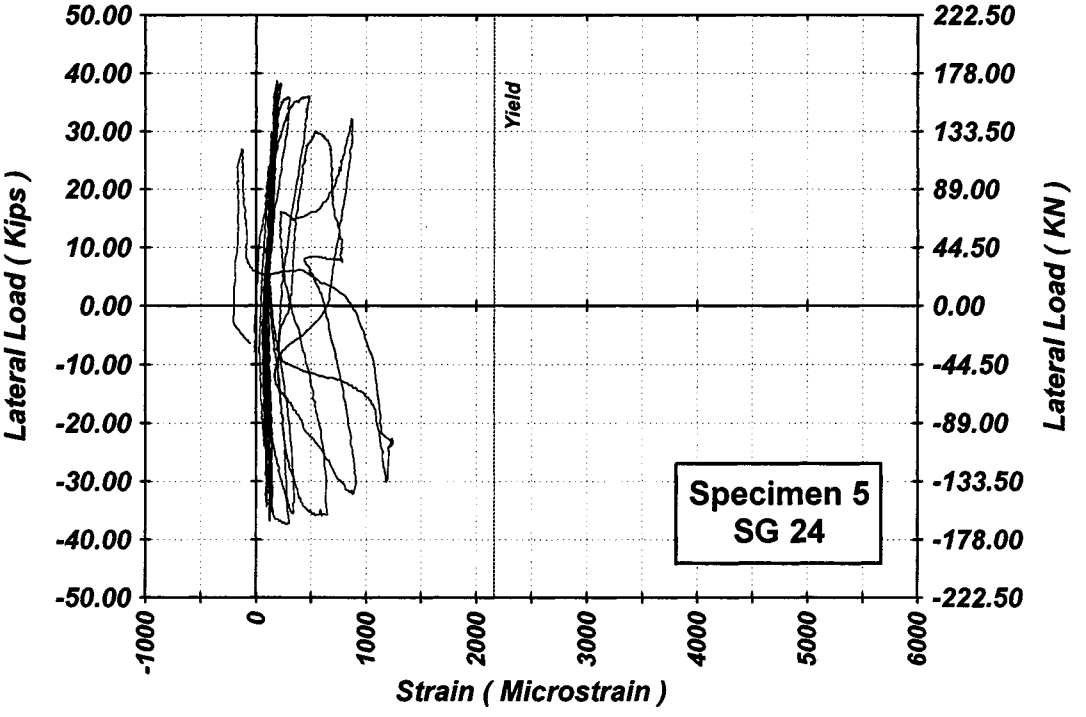

Figure A-152 Measured Lateral Load-Strain in SG-24 of Specimen 5

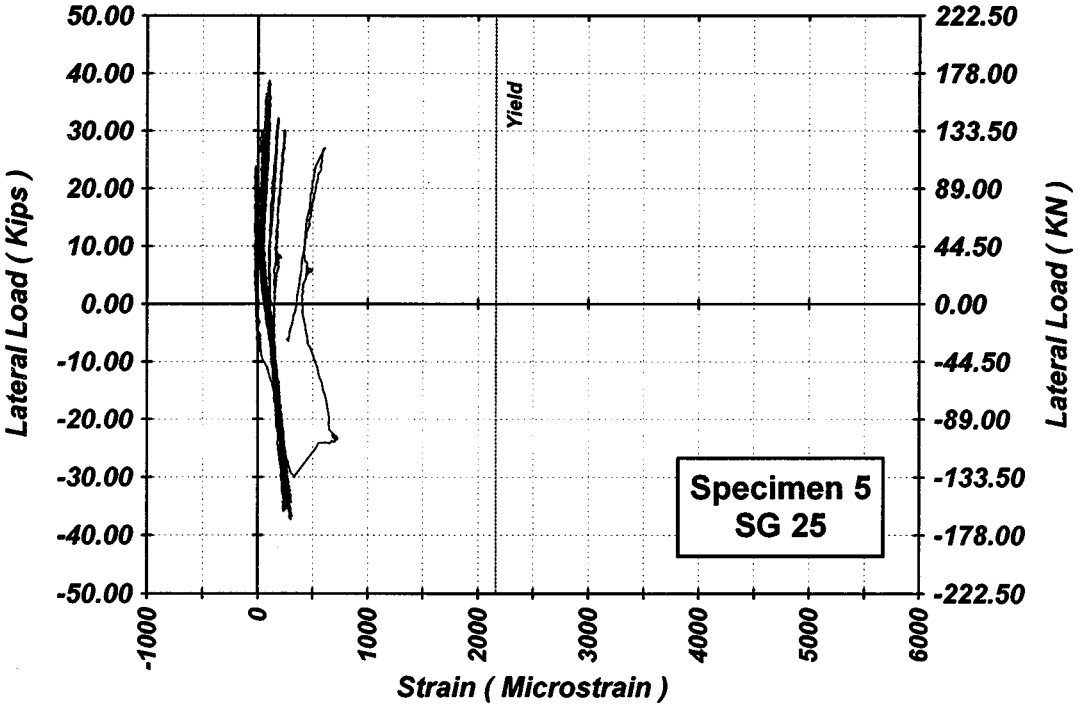

Figure A-153 Measured Lateral Load-Strain in SG-25 of Specimen 5

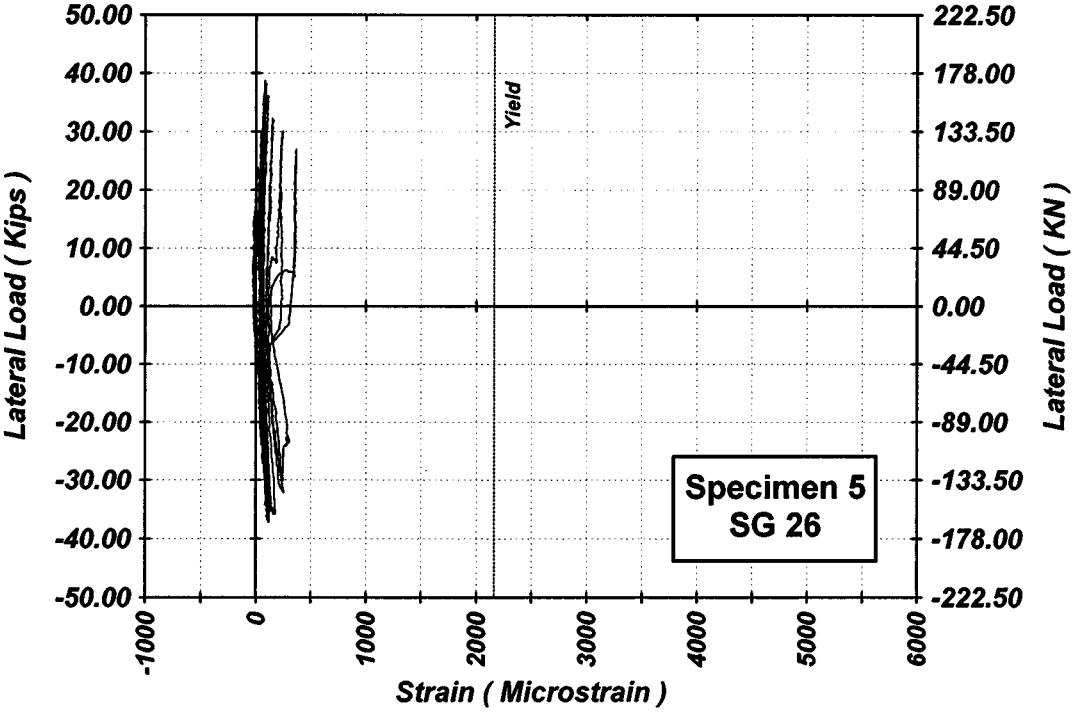

Figure A-154 Measured Lateral Load-Strain in SG-26 of Specimen 5

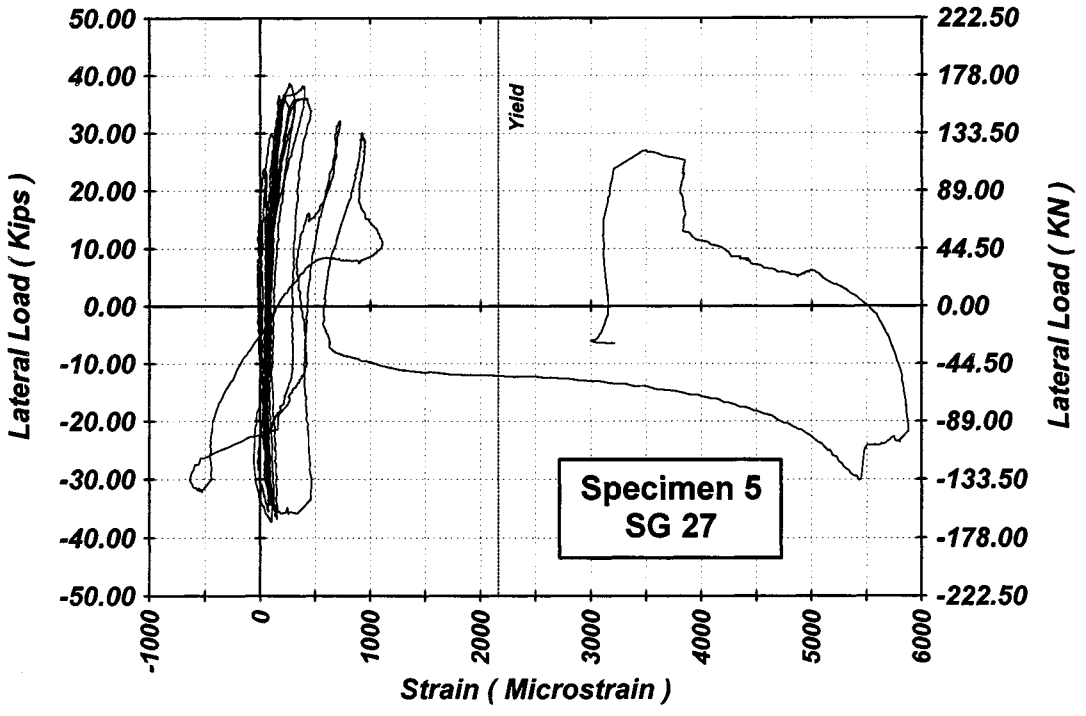

Figure A-155 Measured Lateral Load-Strain in SG-27 of Specimen 5

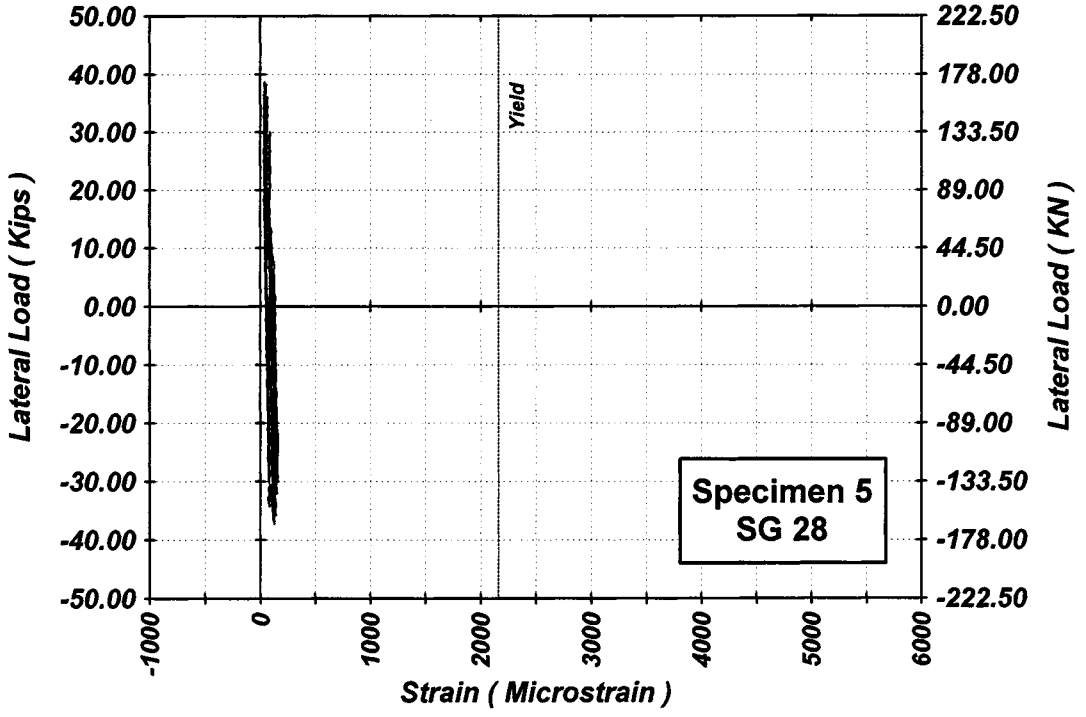

Figure A-156 Measured Lateral Load-Strain in SG-28 of Specimen 5

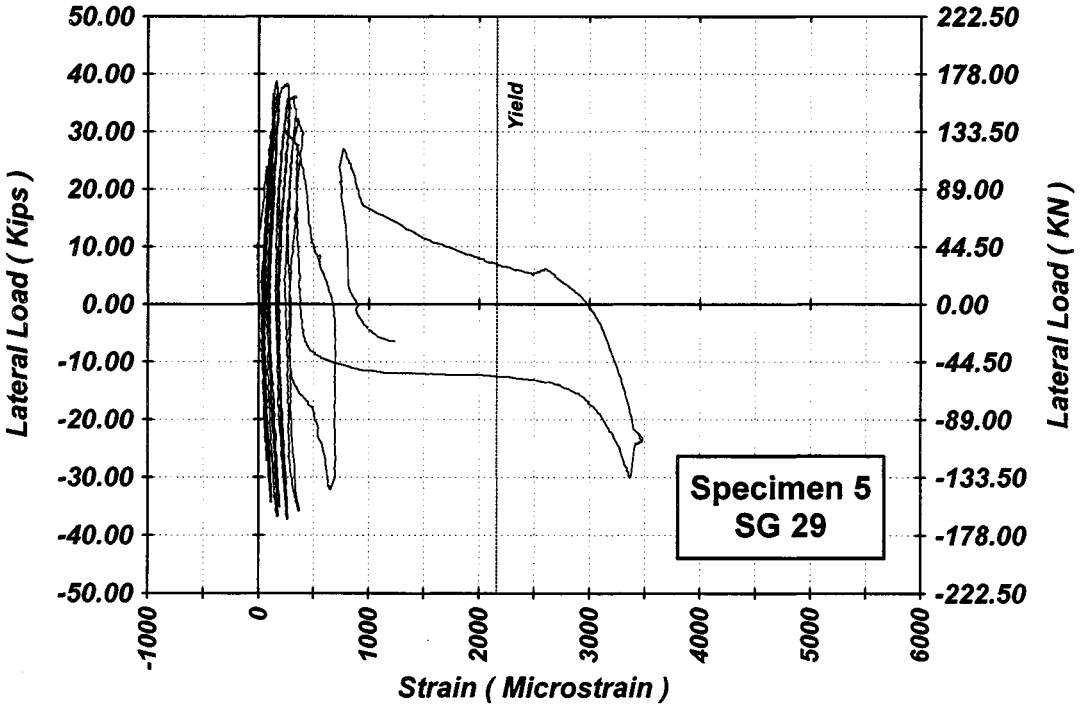

Figure A-157 Measured Lateral Load-Strain in SG-29 of Specimen 5

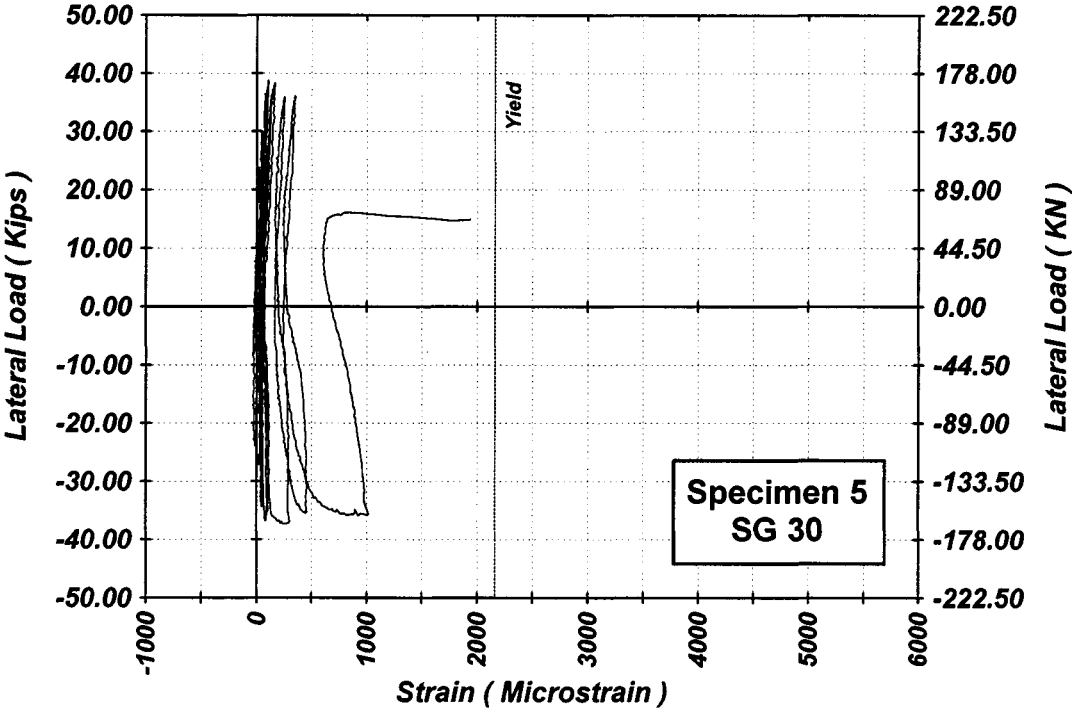

Figure A-158 Measured Lateral Load-Strain in SG-30 of Specimen 5

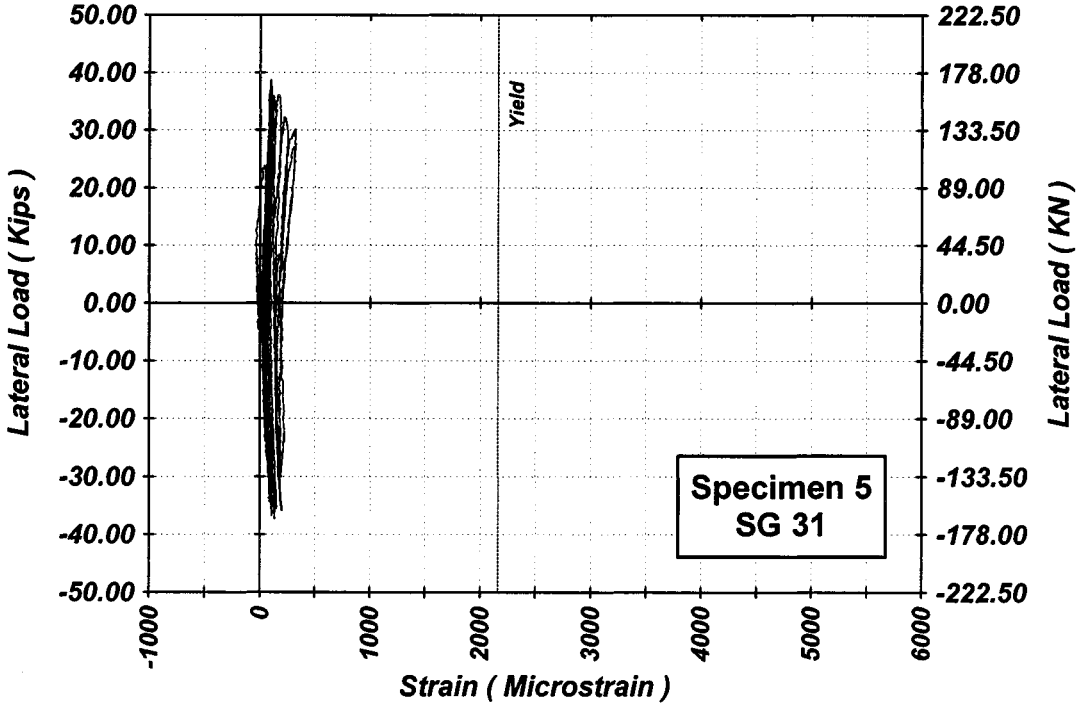

Figure A-159 Measured Lateral Load-Strain in SG-31 of Specimen 5

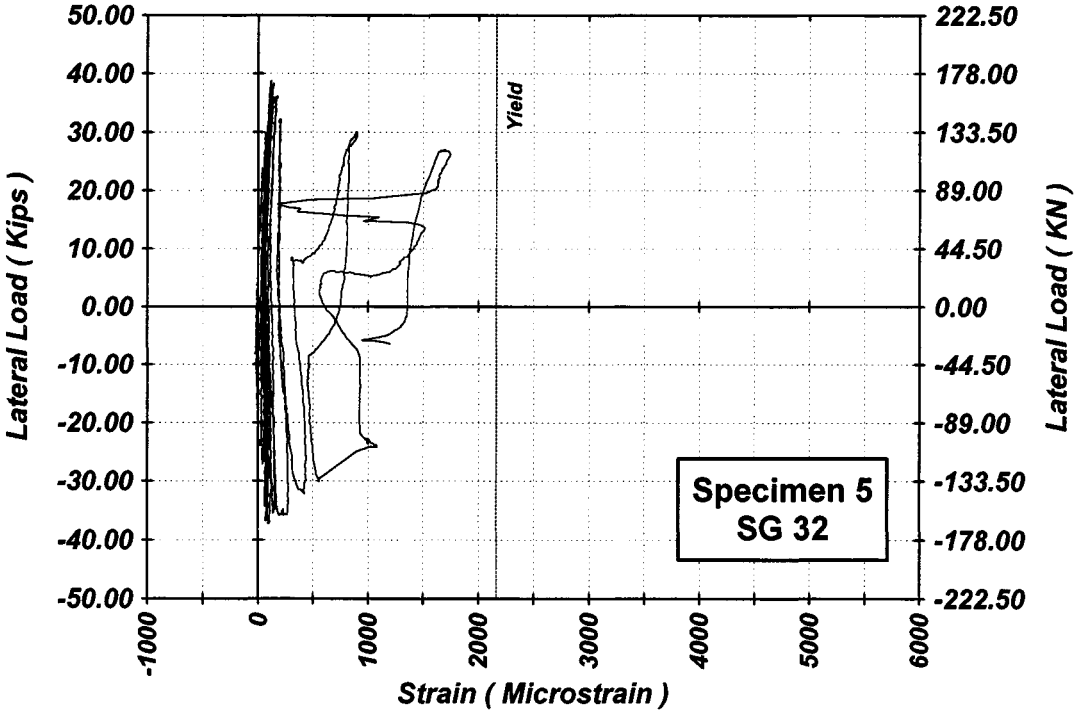

Figure A-160 Measured Lateral Load-Strain in SG-32 of Specimen 5

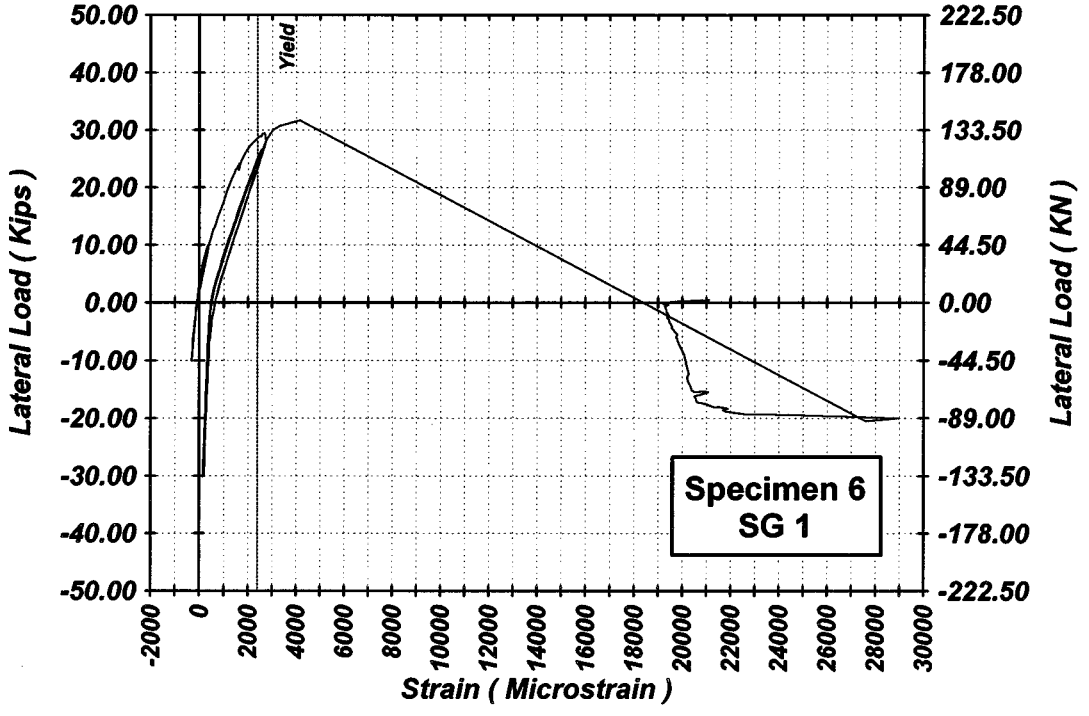

Figure A-161 Measured Lateral Load-Strain in SG-1 of Specimen 6

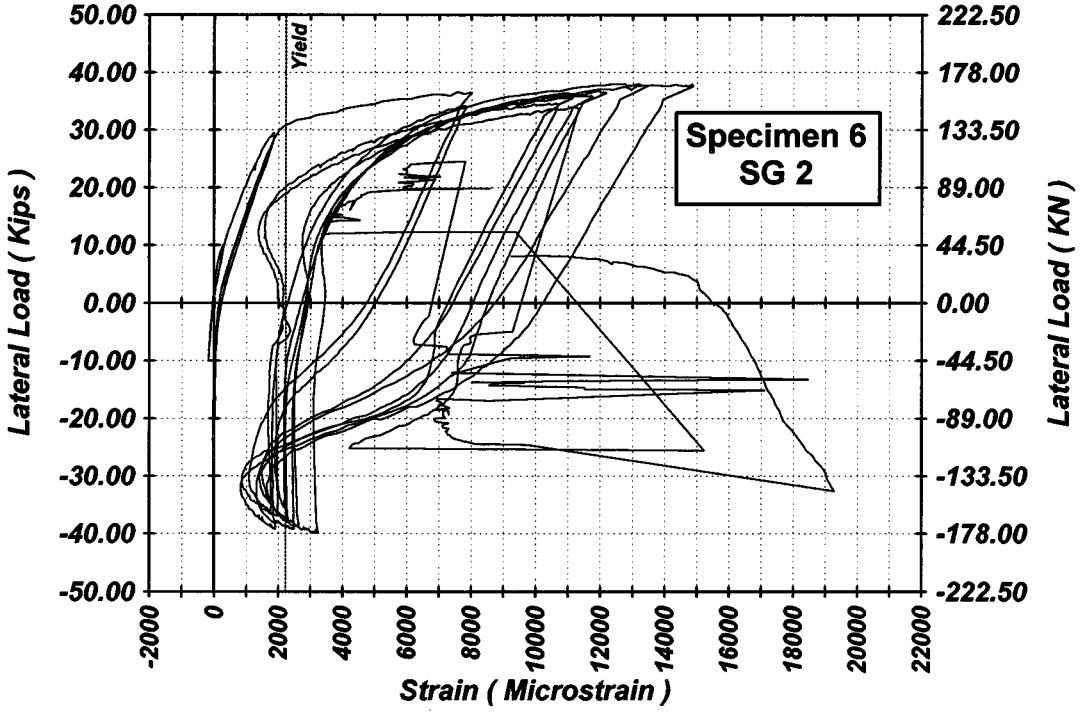

Figure A-162 Measured Lateral Load-Strain in SG-2 of Specimen 6

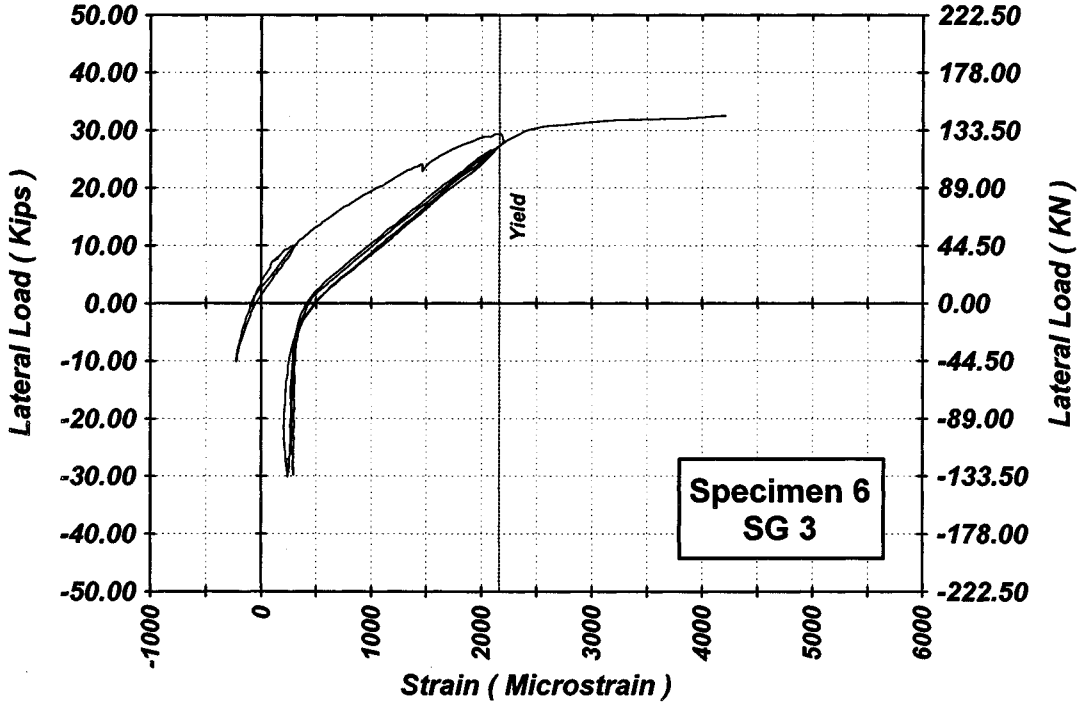

Figure A-163 Measured Lateral Load-Strain in SG-3 of Specimen 6

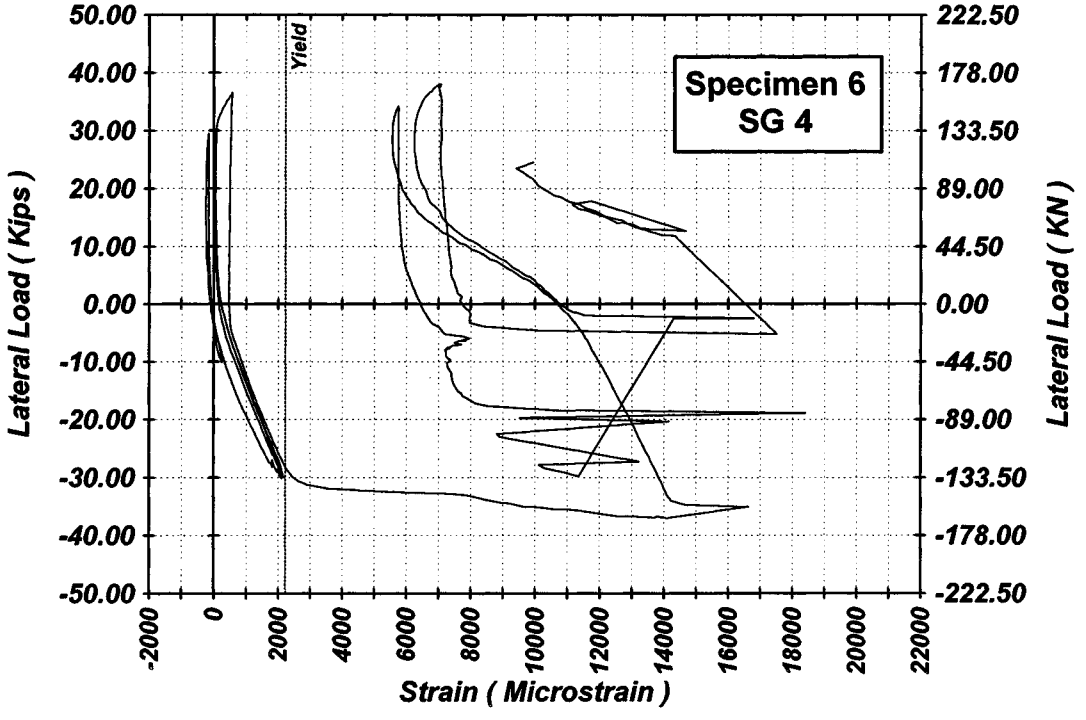

Figure A-164 Measured Lateral Load-Strain in SG-4 of Specimen 6

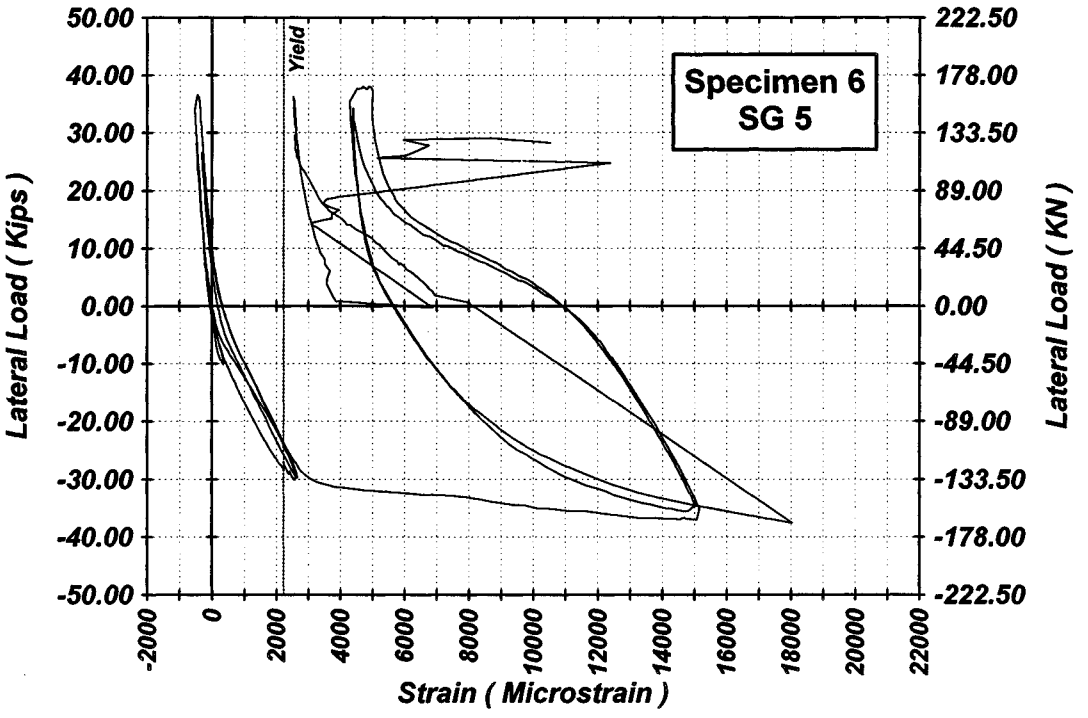

Figure A-165 Measured Lateral Load-Strain in SG-5 of Specimen 6

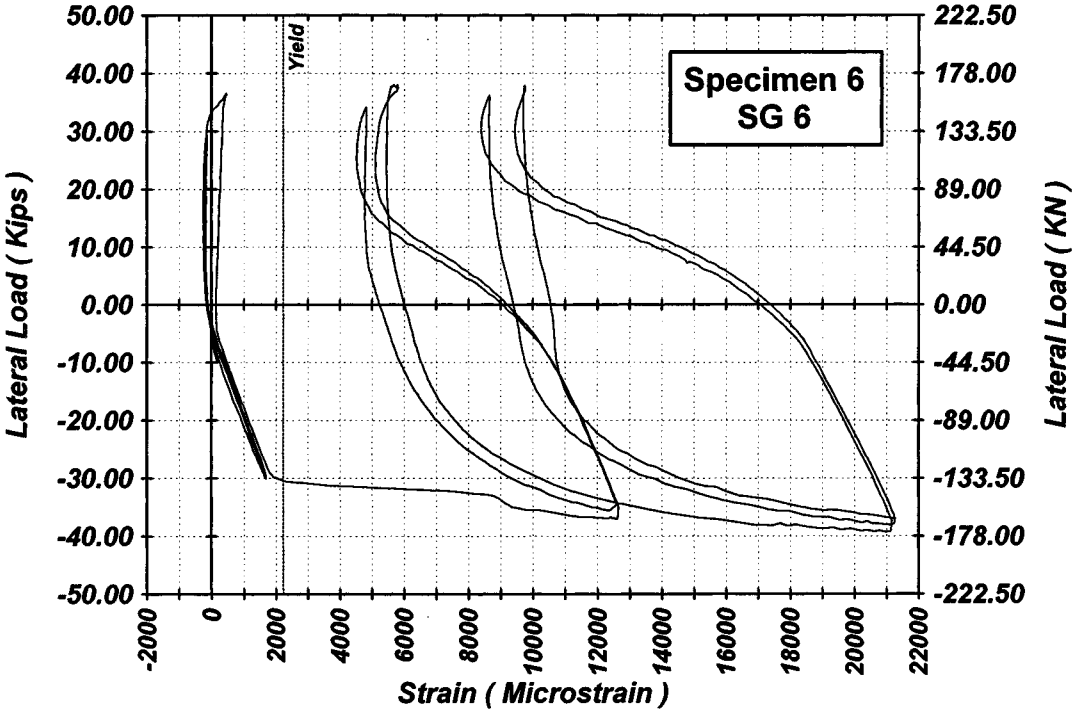

Figure A-166 Measured Lateral Load-Strain in SG-6 of Specimen 6

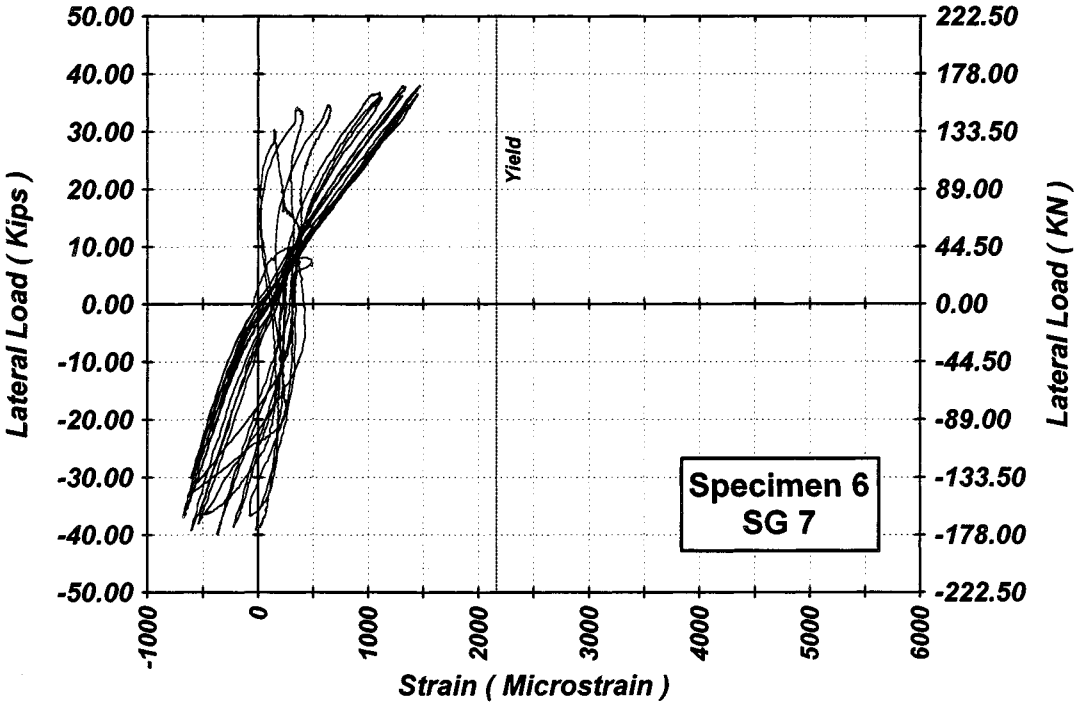

Figure A-167 Measured Lateral Load-Strain in SG-7 of Specimen 6

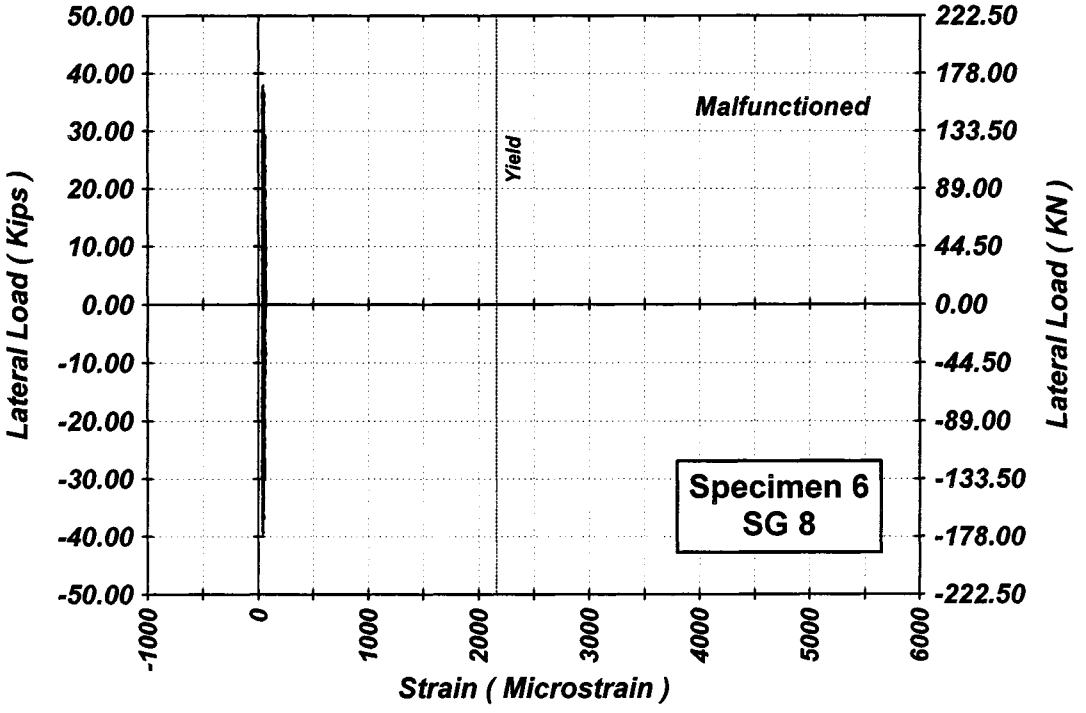

Figure A-168 Measured Lateral Load-Strain in SG-8 of Specimen 6

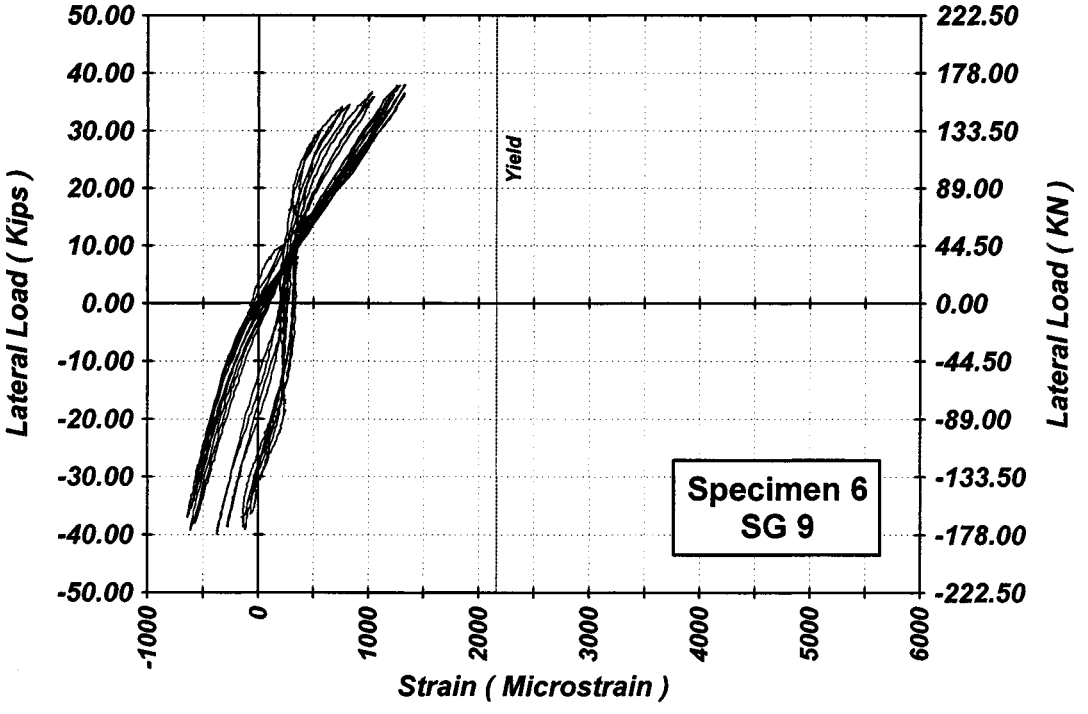

Figure A-169 Measured Lateral Load-Strain in SG-9 of Specimen 6

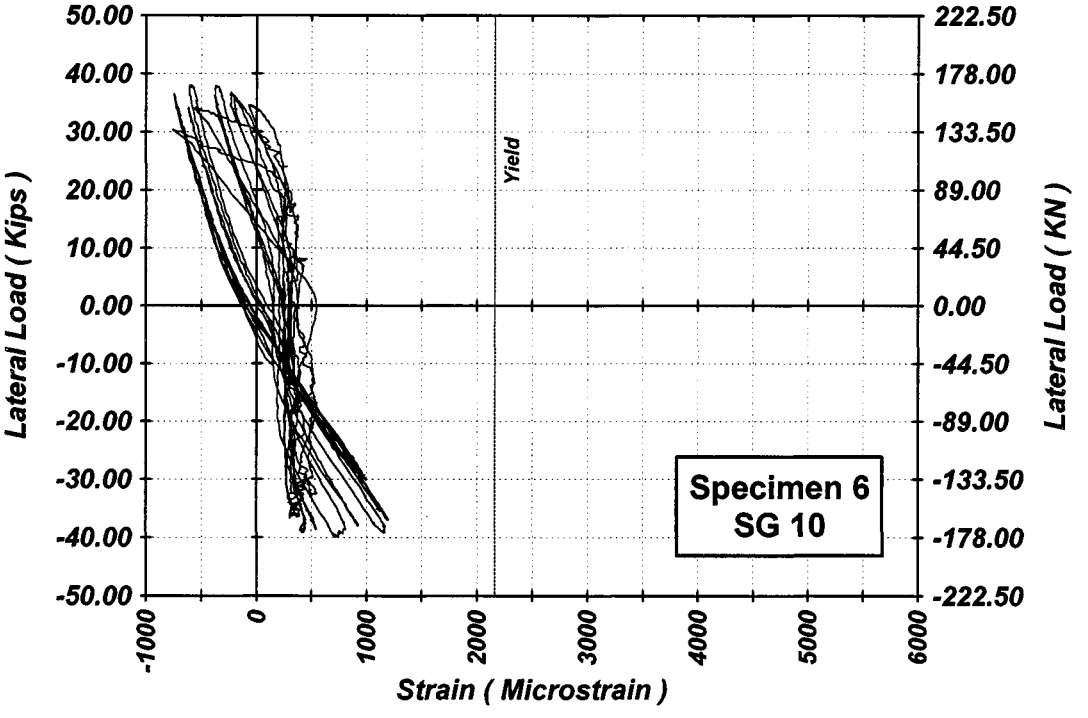

Figure A-170 Measured Lateral Load-Strain in SG-10 of Specimen 6

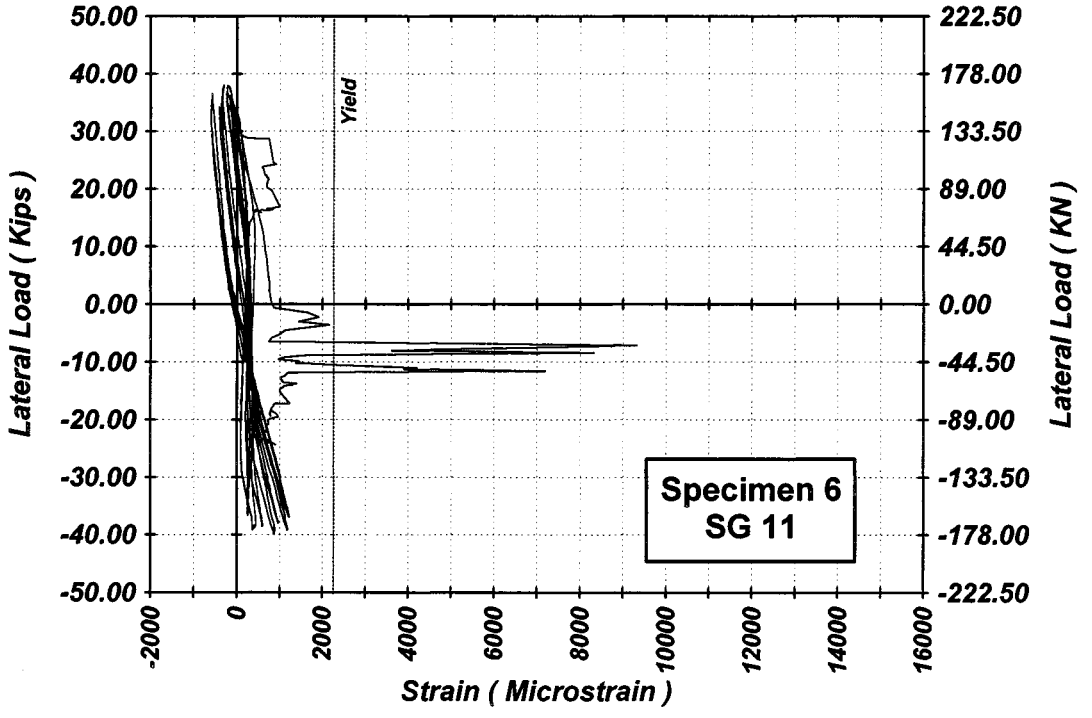

Figure A-171 Measured Lateral Load-Strain in SG-11 of Specimen 6

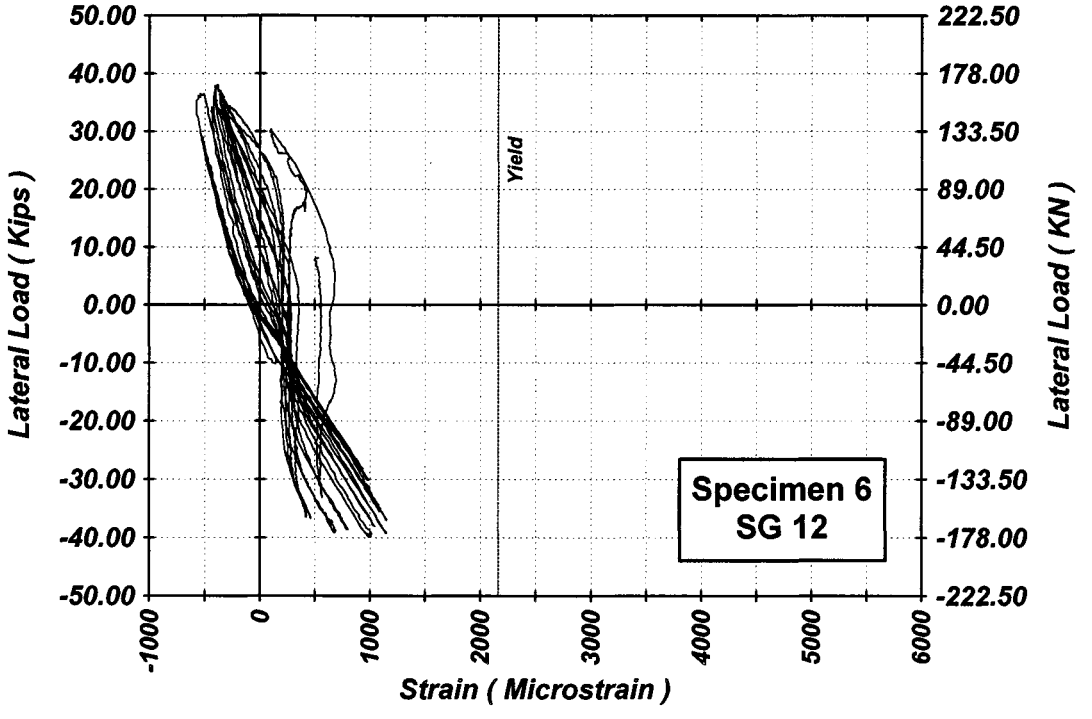

Figure A-172 Measured Lateral Load-Strain in SG-12 of Specimen 6

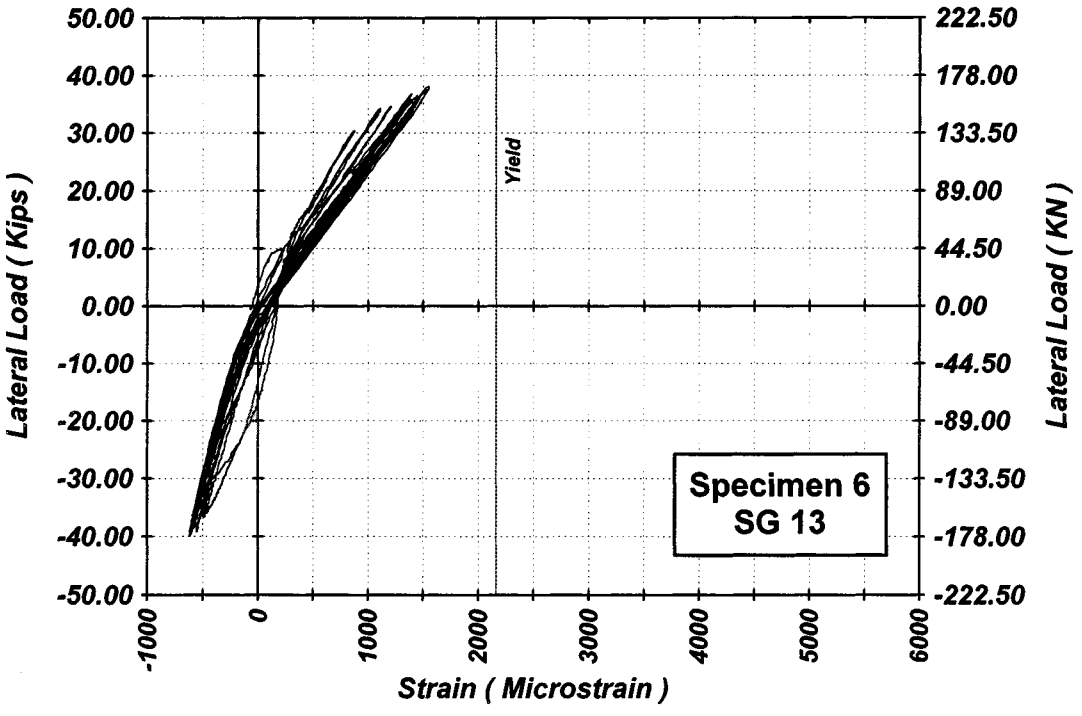

Figure A-173 Measured Lateral Load-Strain in SG-13 of Specimen 6

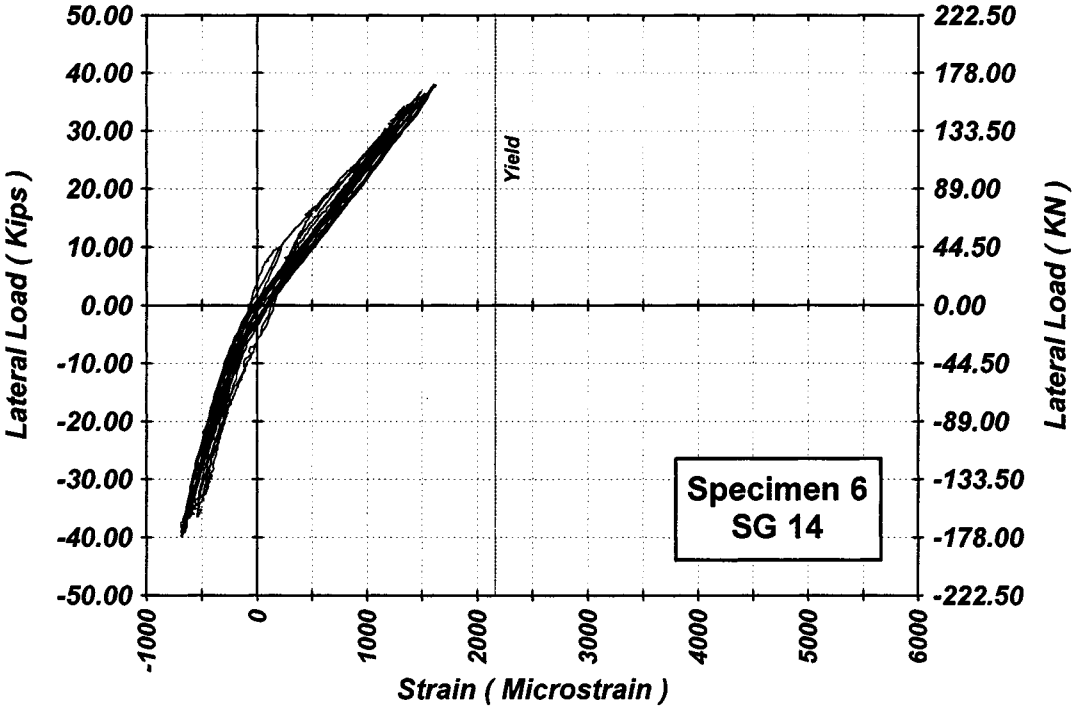

Figure A-174 Measured Lateral Load-Strain in SG-14 of Specimen 6

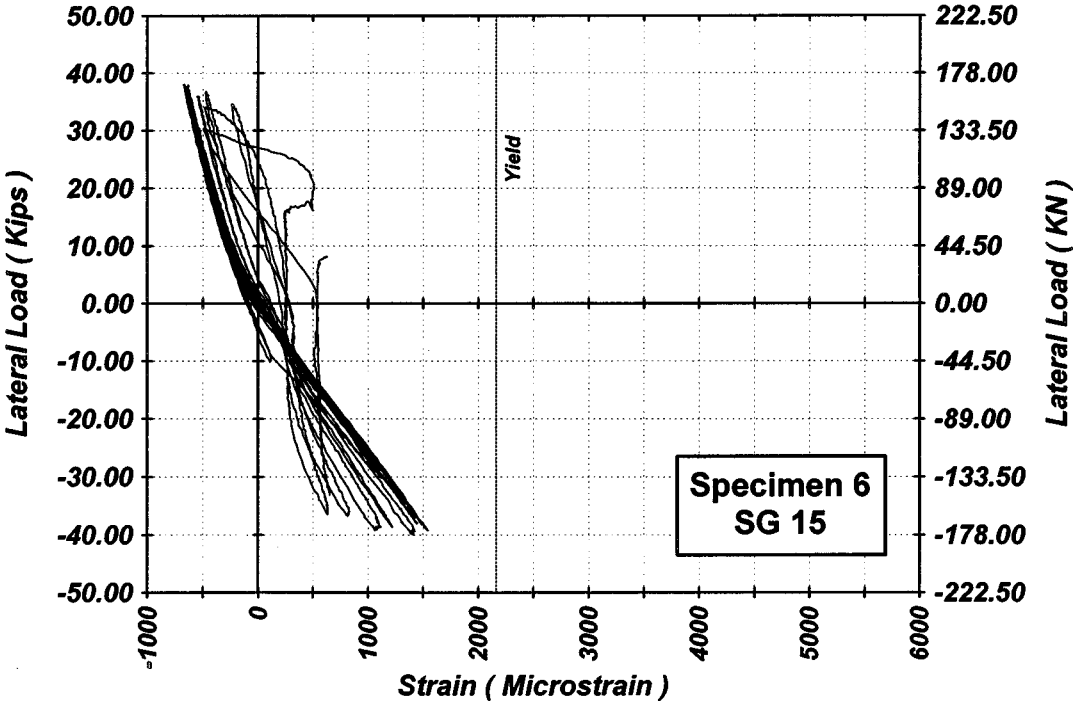

Figure A-175 Measured Lateral Load-Strain in SG-15 of Specimen 6

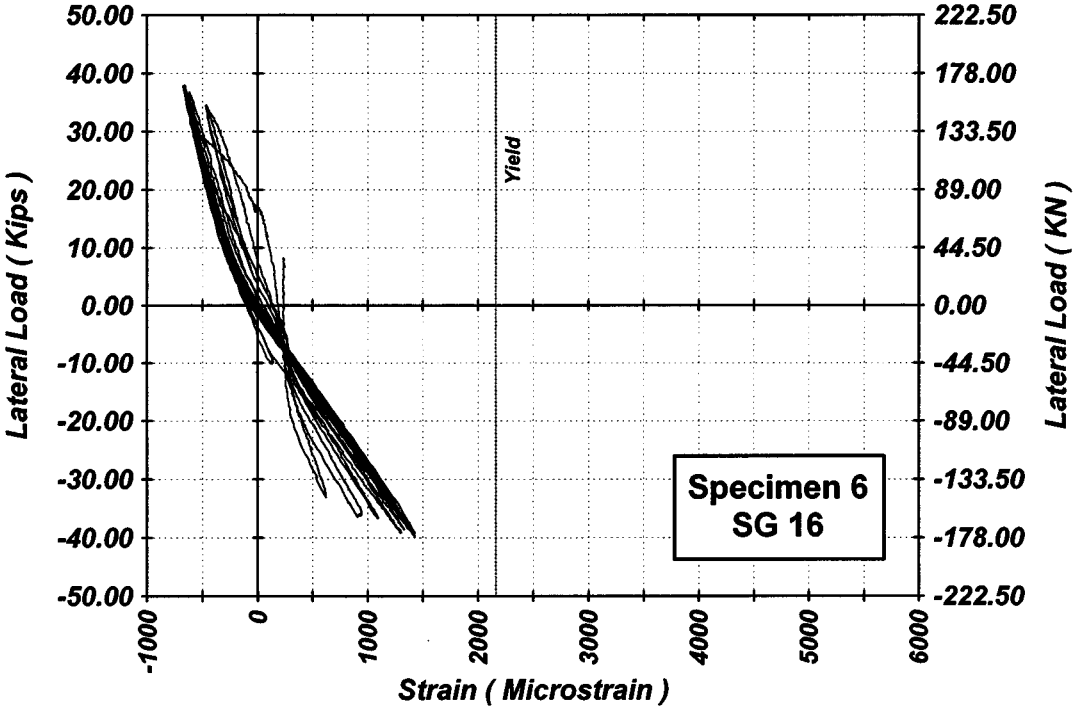

Figure A-176 Measured Lateral Load-Strain in SG-16 of Specimen 6

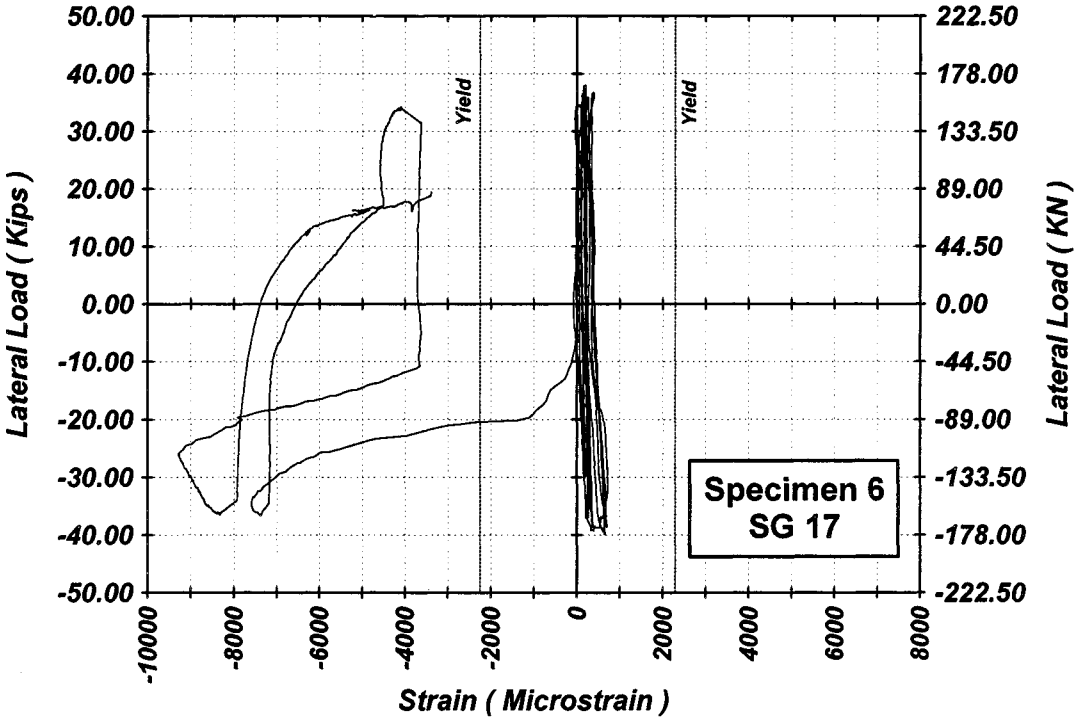

Figure A-177 Measured Lateral Load-Strain in SG-17 of Specimen 6

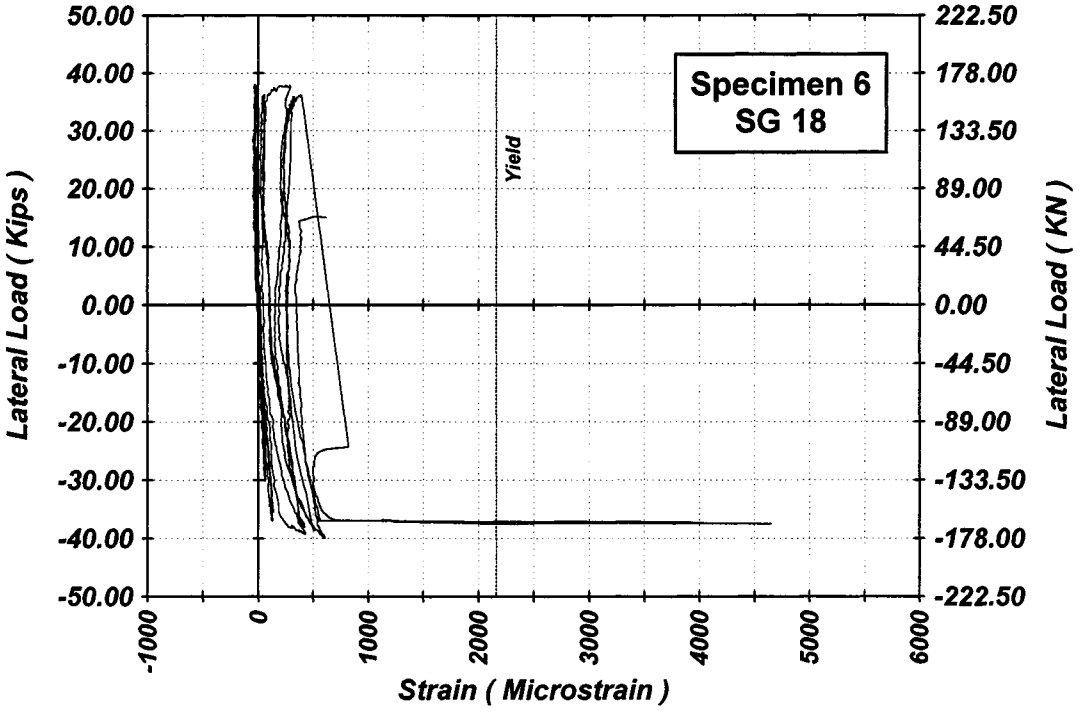

Figure A-178 Measured Lateral Load-Strain in SG-18 of Specimen 6

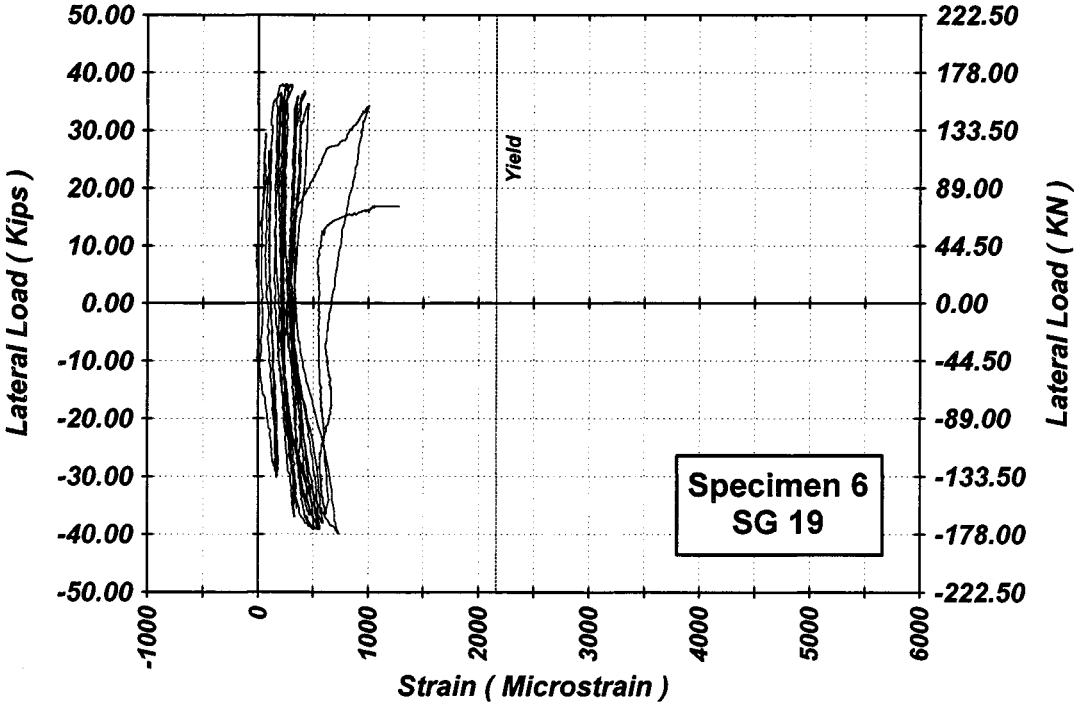

Figure A-179 Measured Lateral Load-Strain in SG-19 of Specimen 6

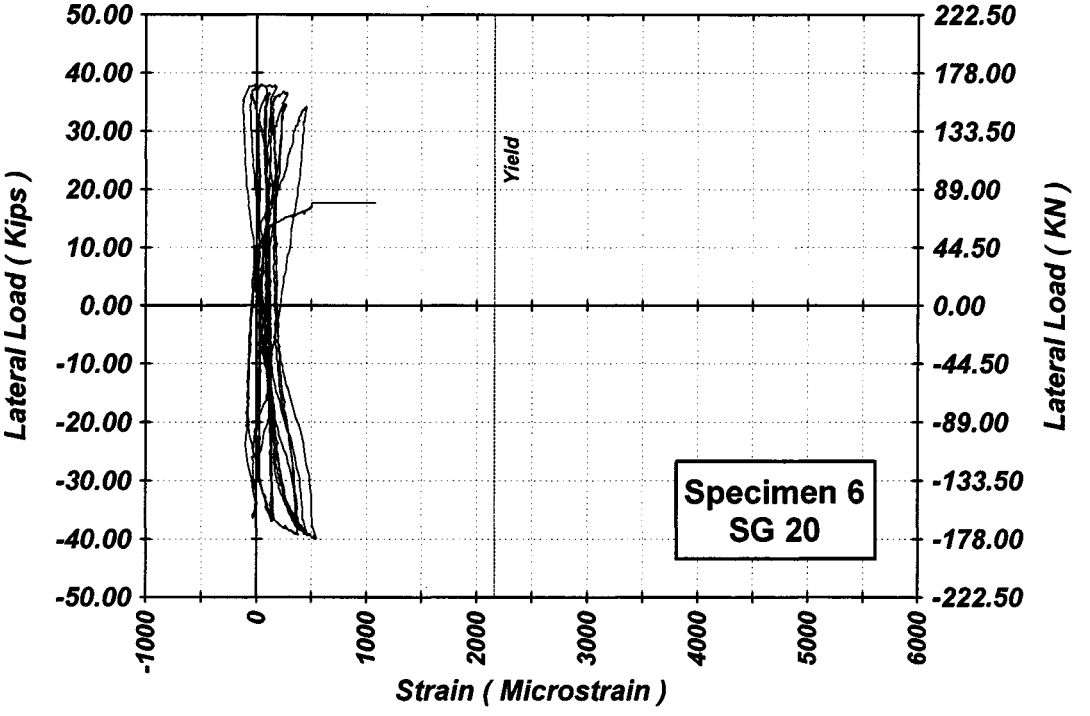

Figure A-180 Measured Lateral Load-Strain in SG-20 of Specimen 6

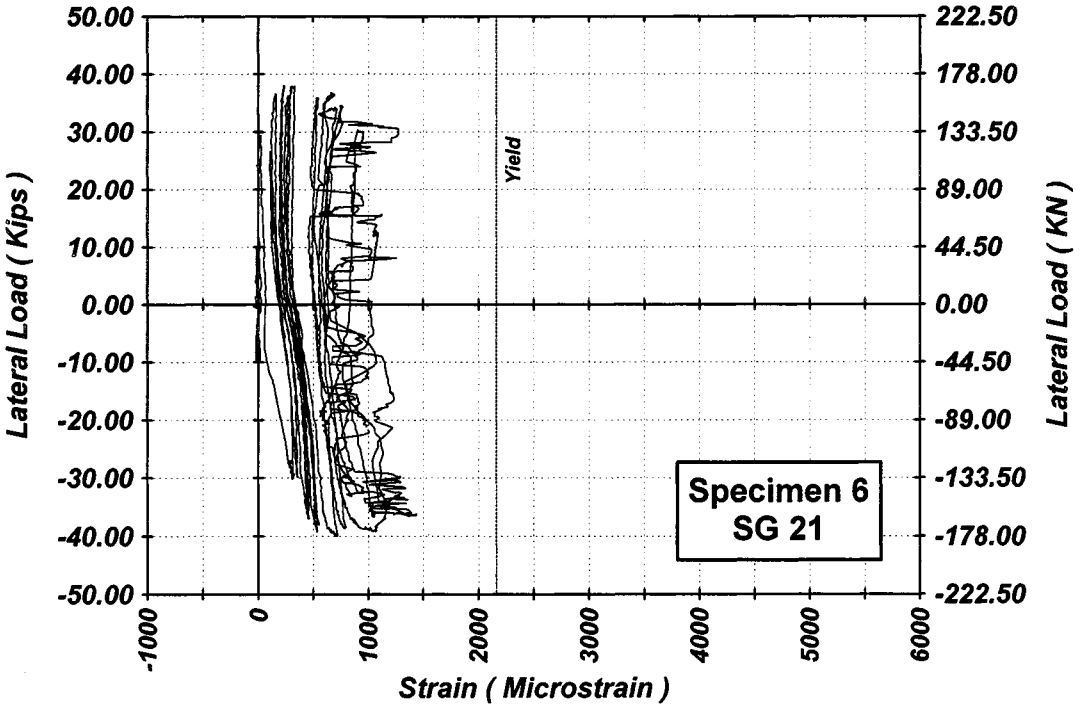

Figure A-181 Measured Lateral Load-Strain in SG-21 of Specimen 6

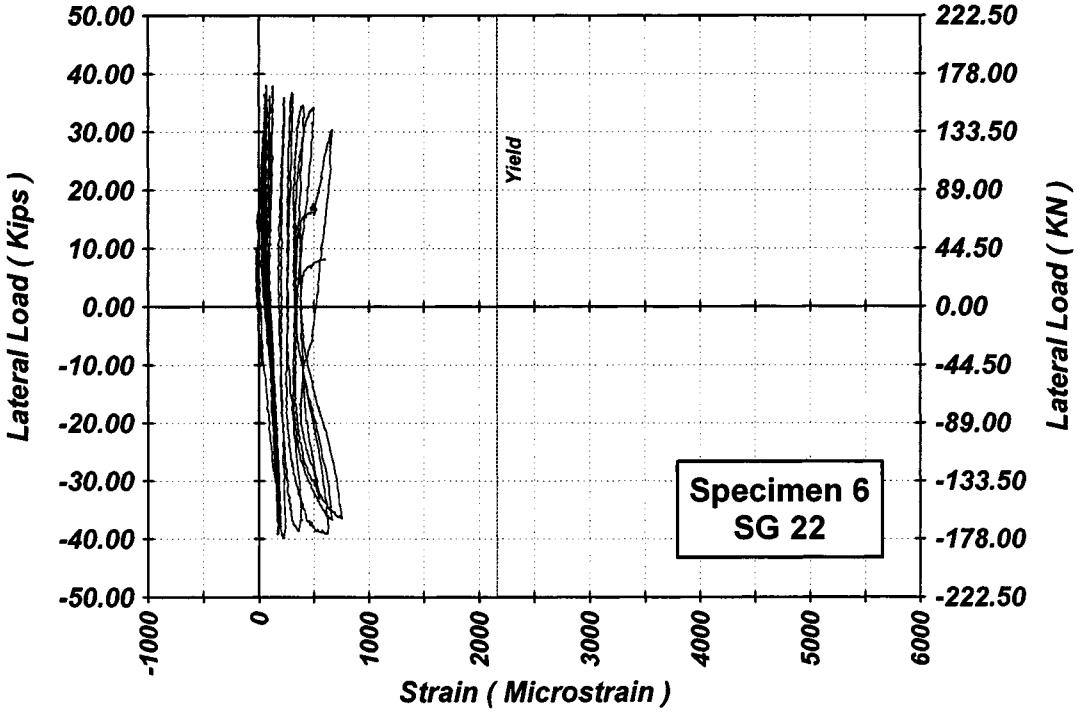

Figure A-182 Measured Lateral Load-Strain in SG-22 of Specimen 6

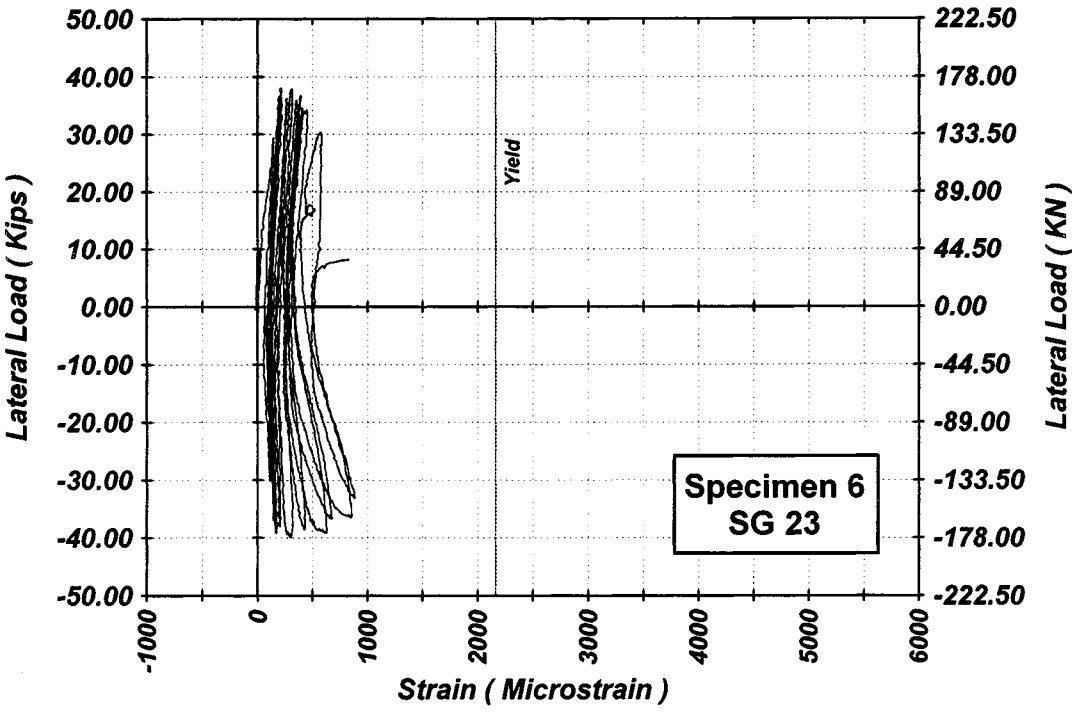

Figure A-183 Measured Lateral Load-Strain in SG-23 of Specimen 6

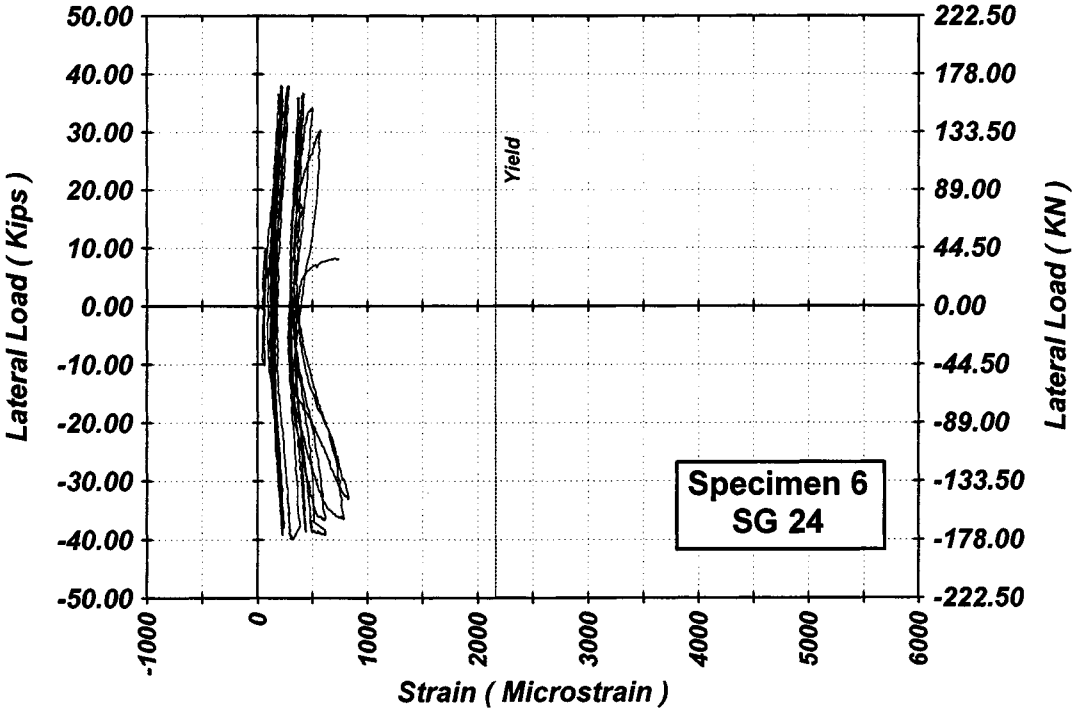

Figure A-184 Measured Lateral Load-Strain in SG-24 of Specimen 6

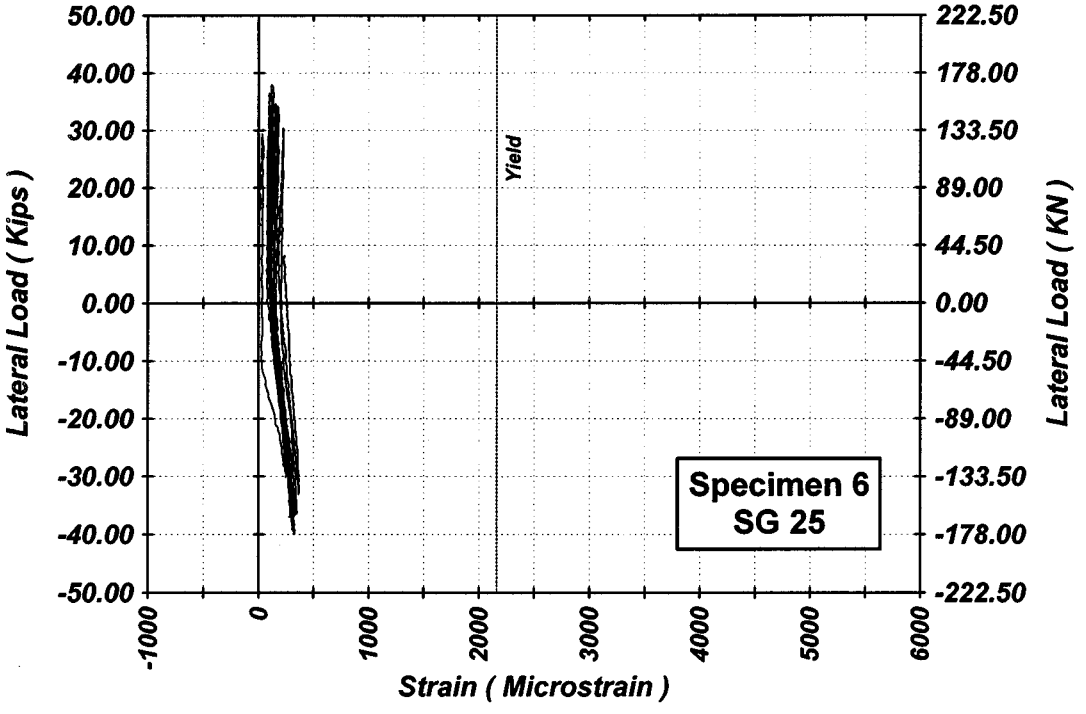

Figure A-185 Measured Lateral Load-Strain in SG-25 of Specimen 6

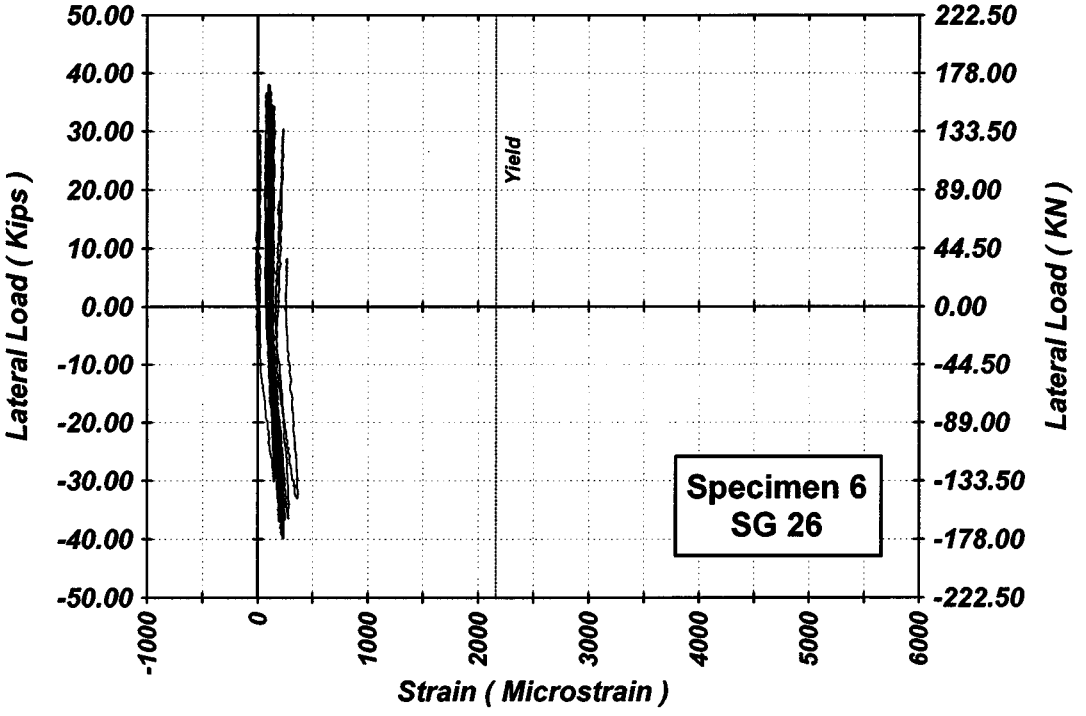

Figure A-186 Measured Lateral Load-Strain in SG-26 of Specimen 6

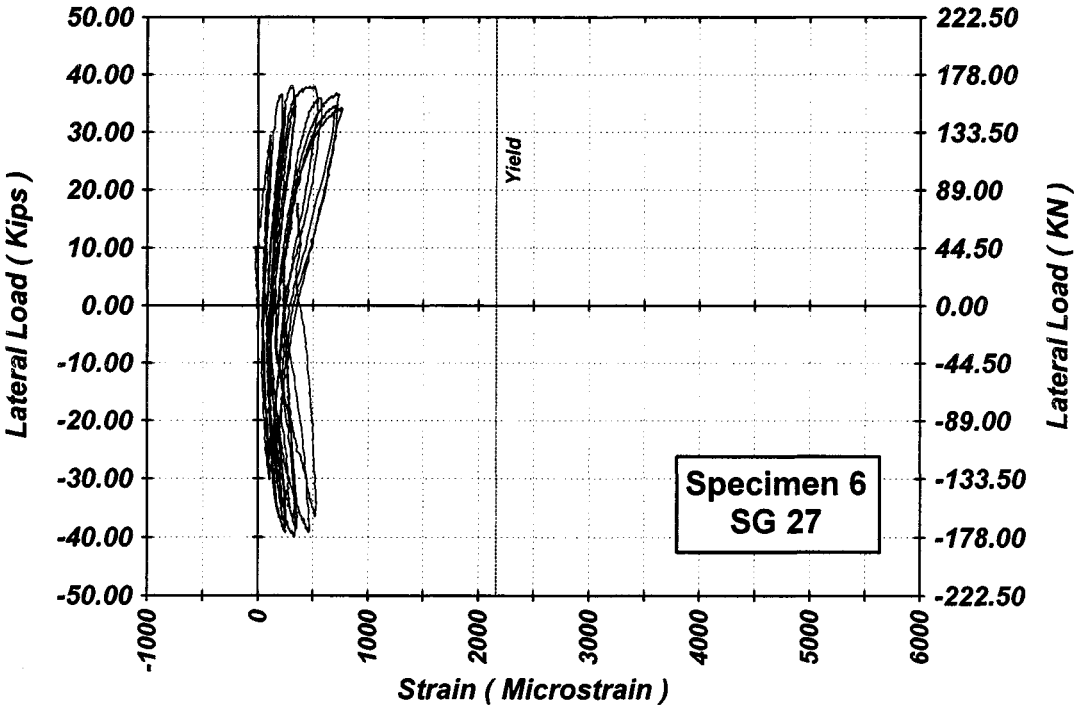

Figure A-187 Measured Lateral Load-Strain in SG-27 of Specimen 6

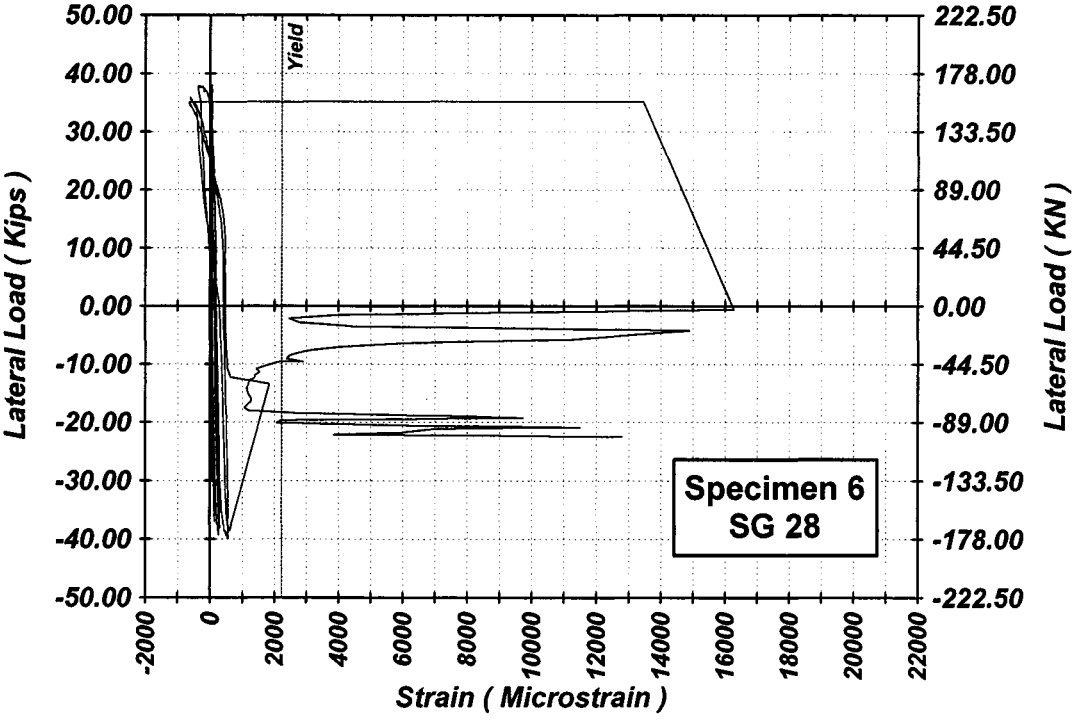

Figure A-188 Measured Lateral Load-Strain in SG-28 of Specimen 6

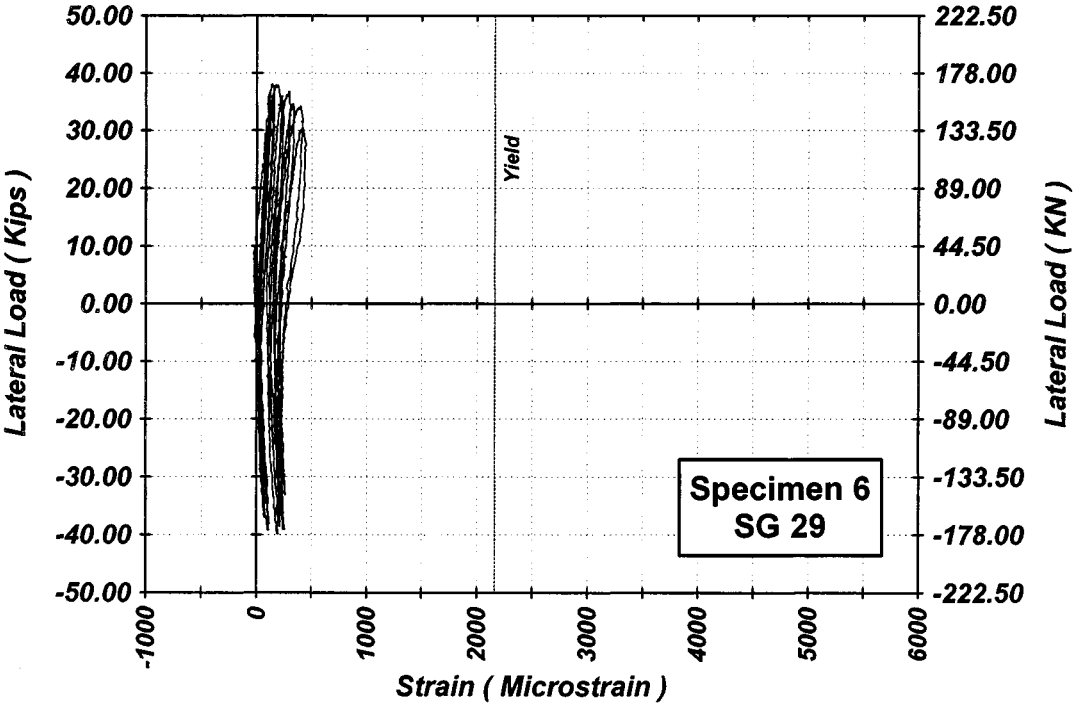

Figure A-189 Measured Lateral Load-Strain in SG-29 of Specimen 6

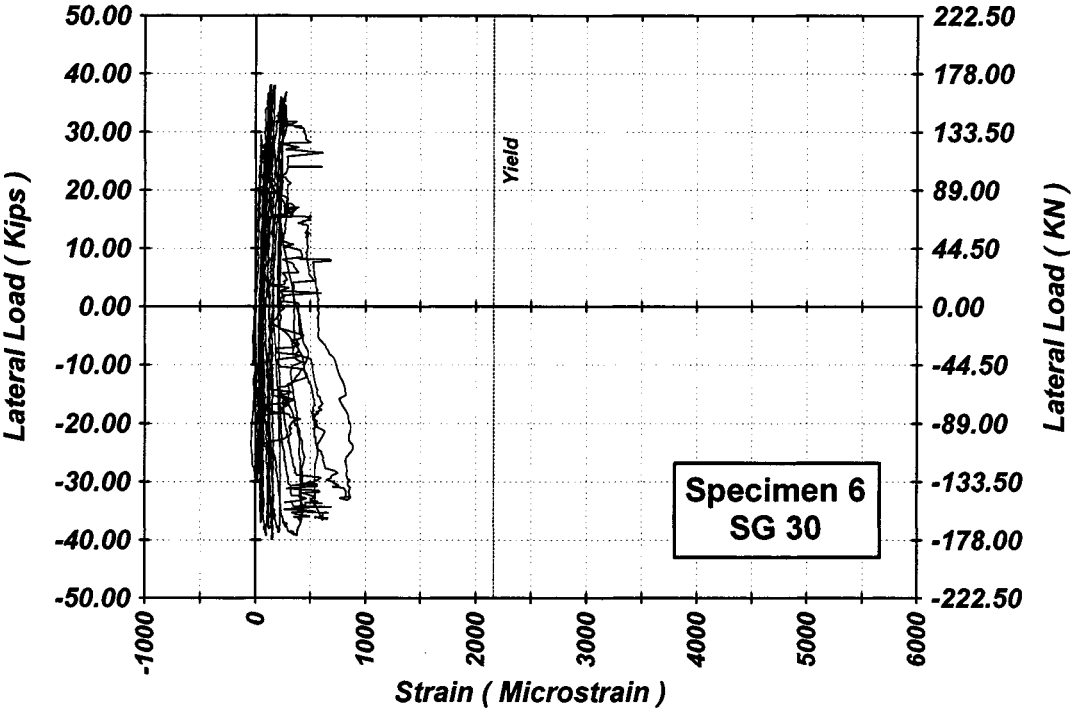

Figure A-190 Measured Lateral Load-Strain in SG-30 of Specimen 6

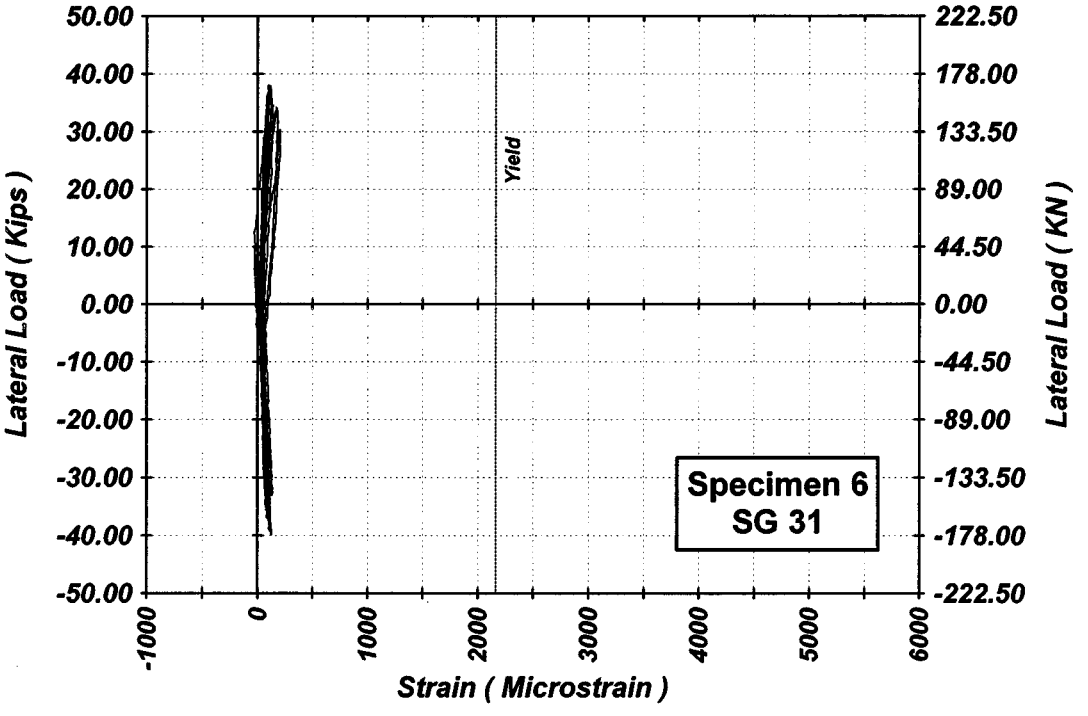

Figure A-191 Measured Lateral Load-Strain in SG-31 of Specimen 6

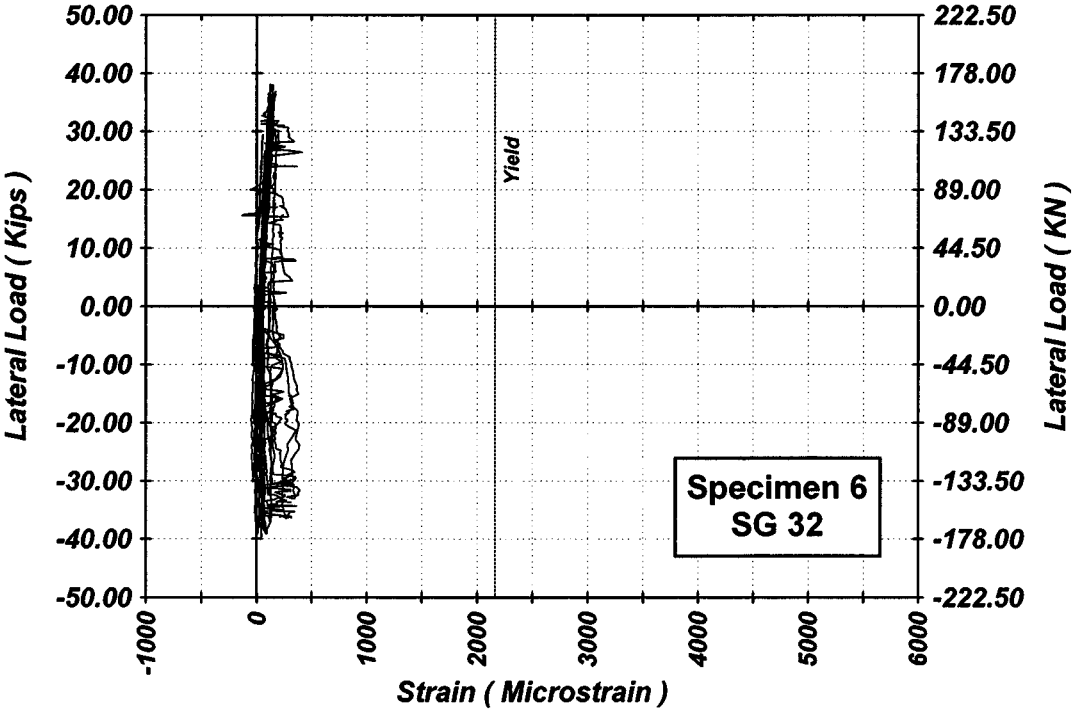

Figure A-192 Measured Lateral Load-Strain in SG-32 of Specimen 6

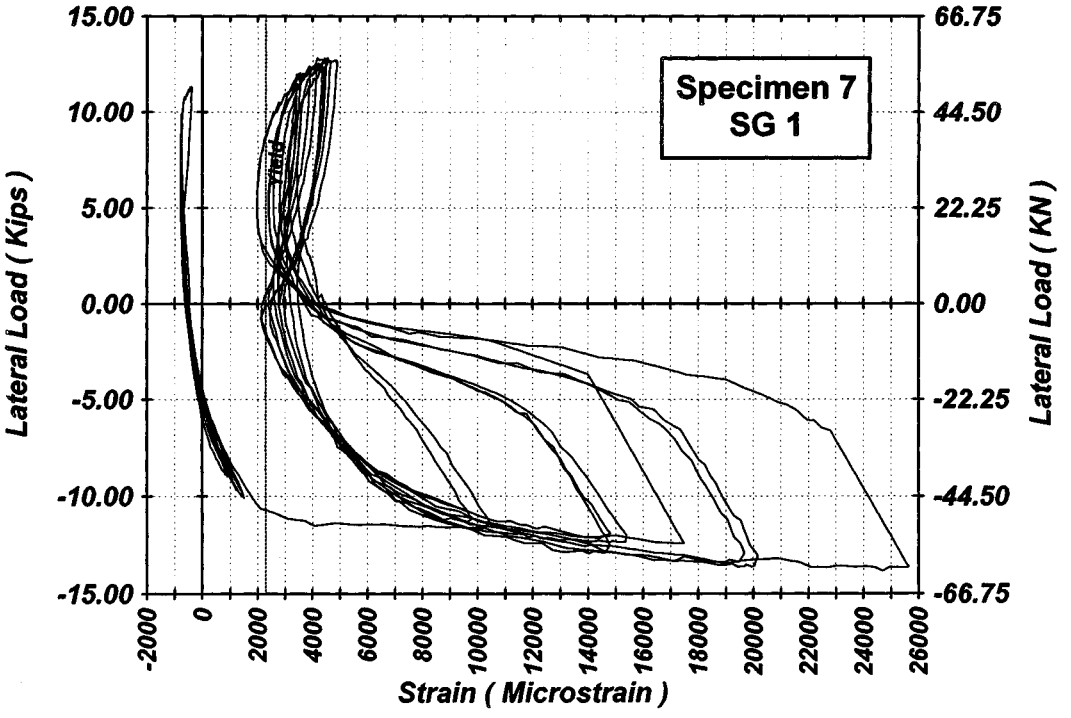

Figure A-193 Measured Lateral Load-Strain in SG-1 of Specimen 7

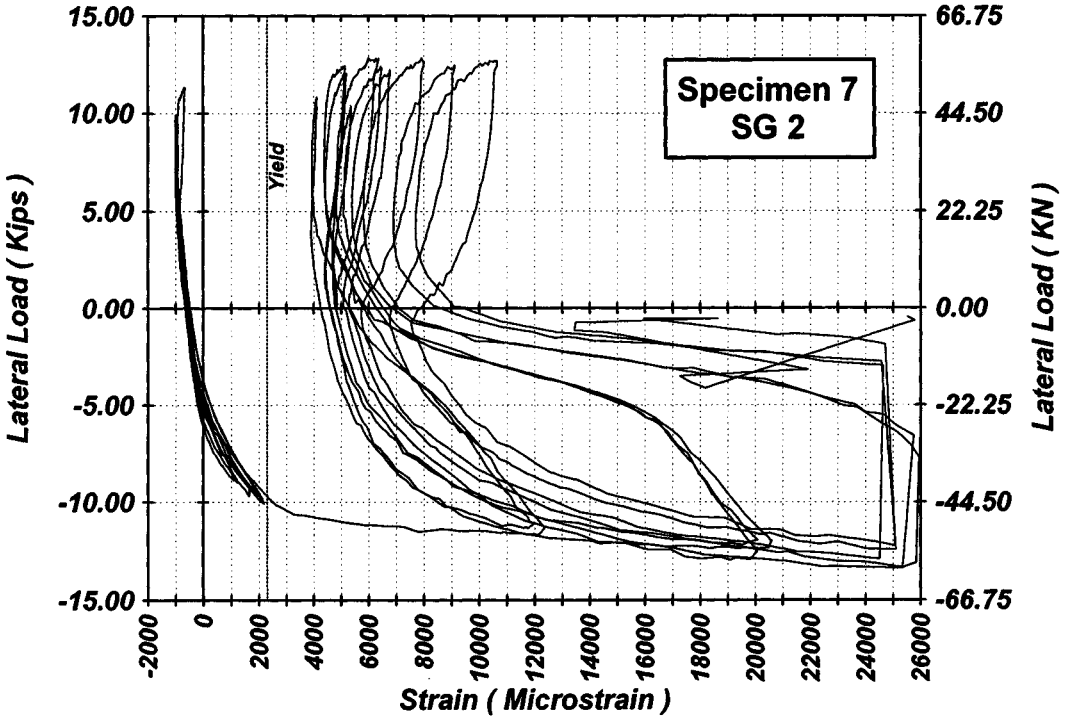

Figure A-194 Measured Lateral Load-Strain in SG-2 of Specimen 7

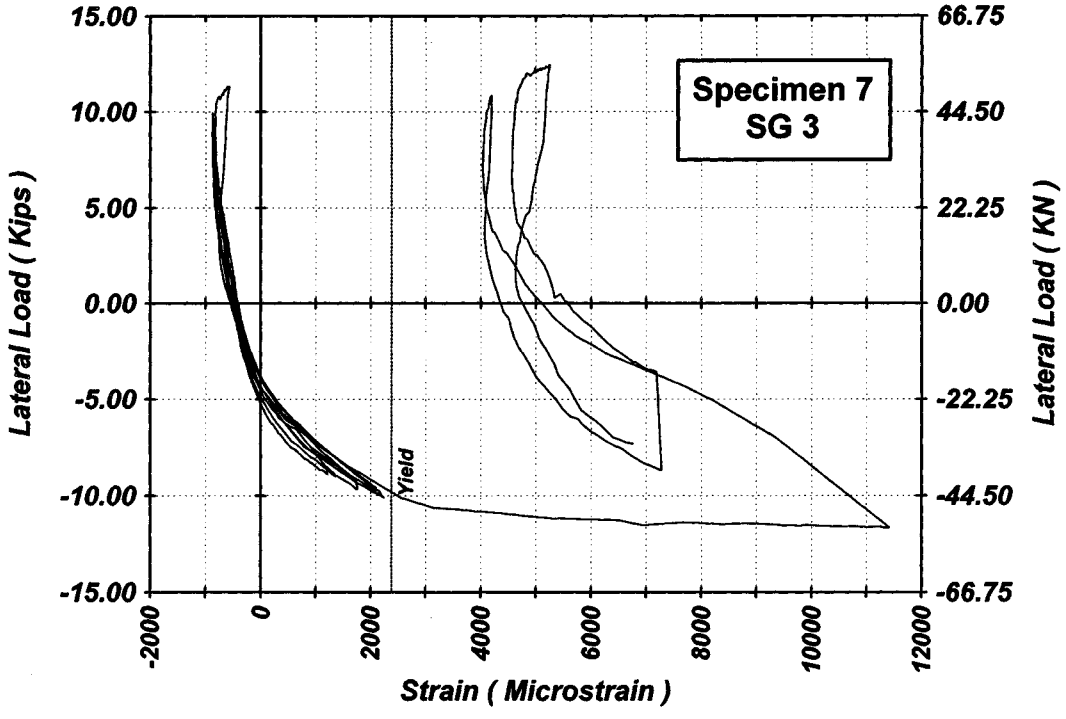

Figure A-195 Measured Lateral Load-Strain in SG-3 of Specimen 7

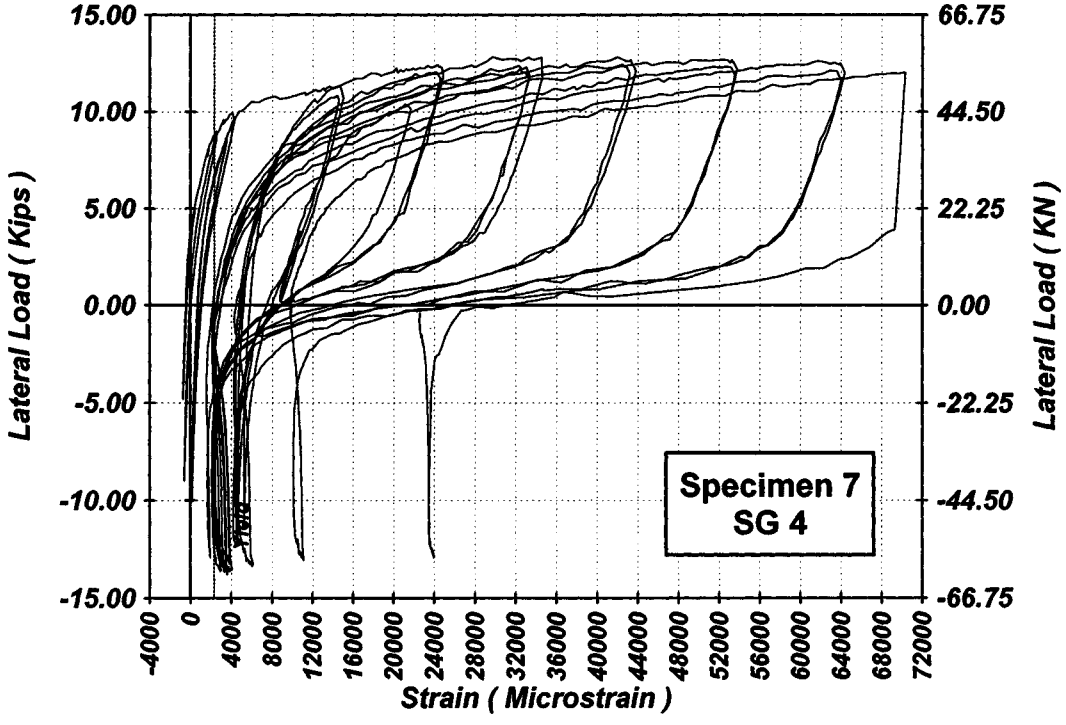

Figure A-196 Measured Lateral Load-Strain in SG-4 of Specimen 7

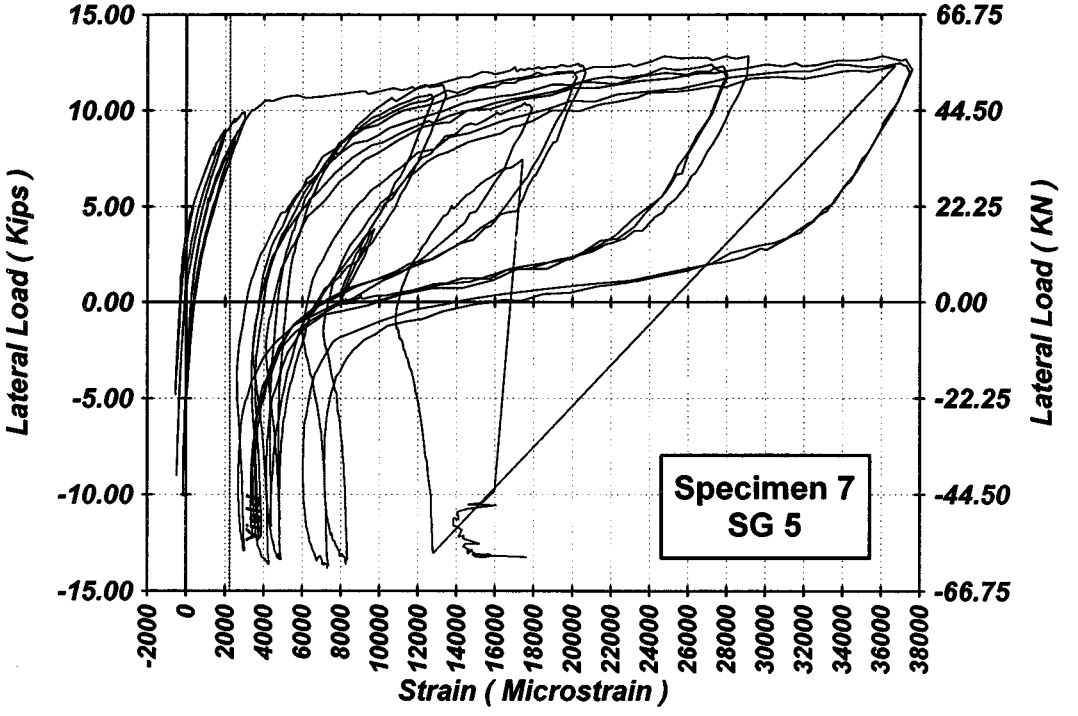

Figure A-197 Measured Lateral Load-Strain in SG-5 of Specimen 7

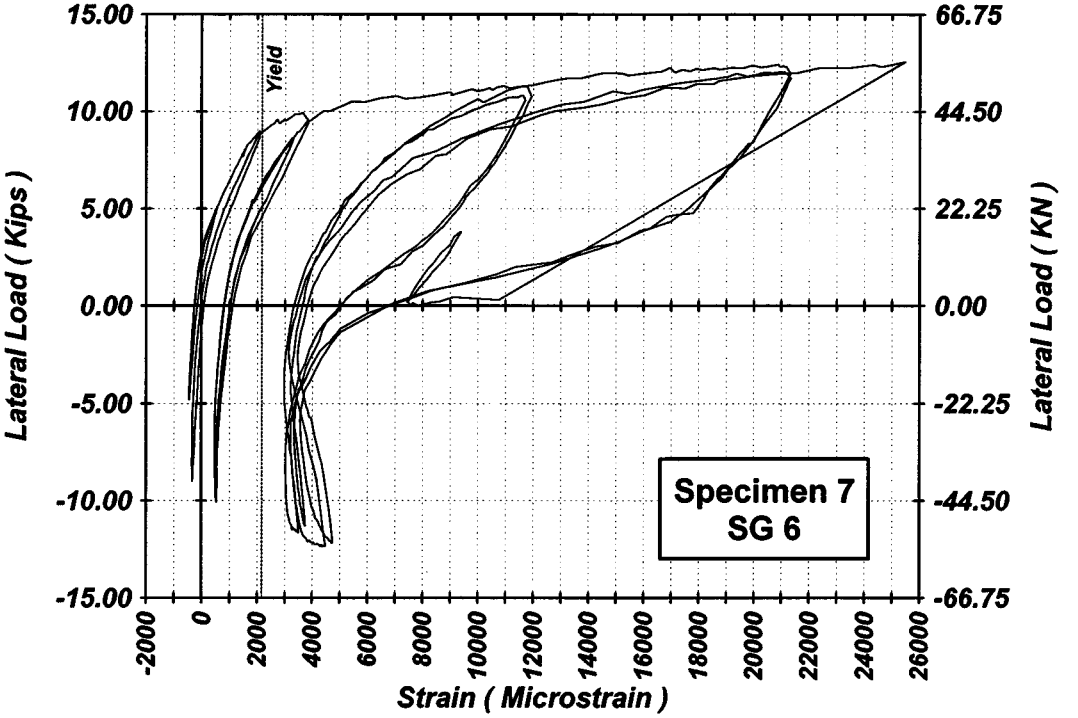

Figure A-198 Measured Lateral Load-Strain in SG-6 of Specimen 7

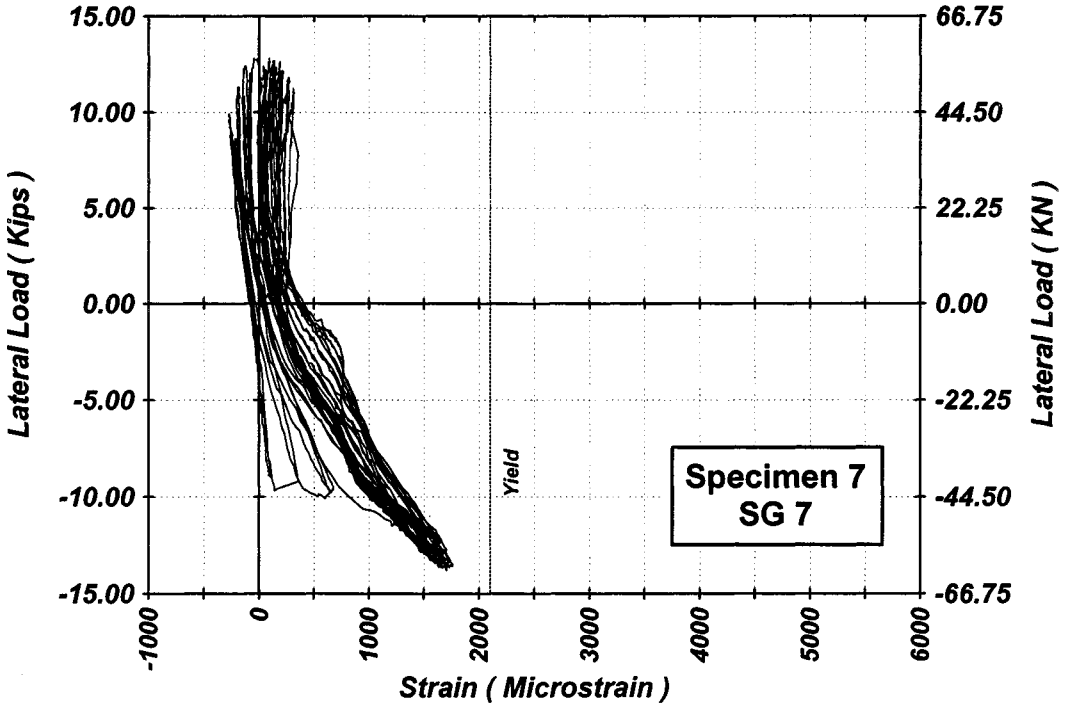

Figure A-199 Measured Lateral Load-Strain in SG-7 of Specimen 7

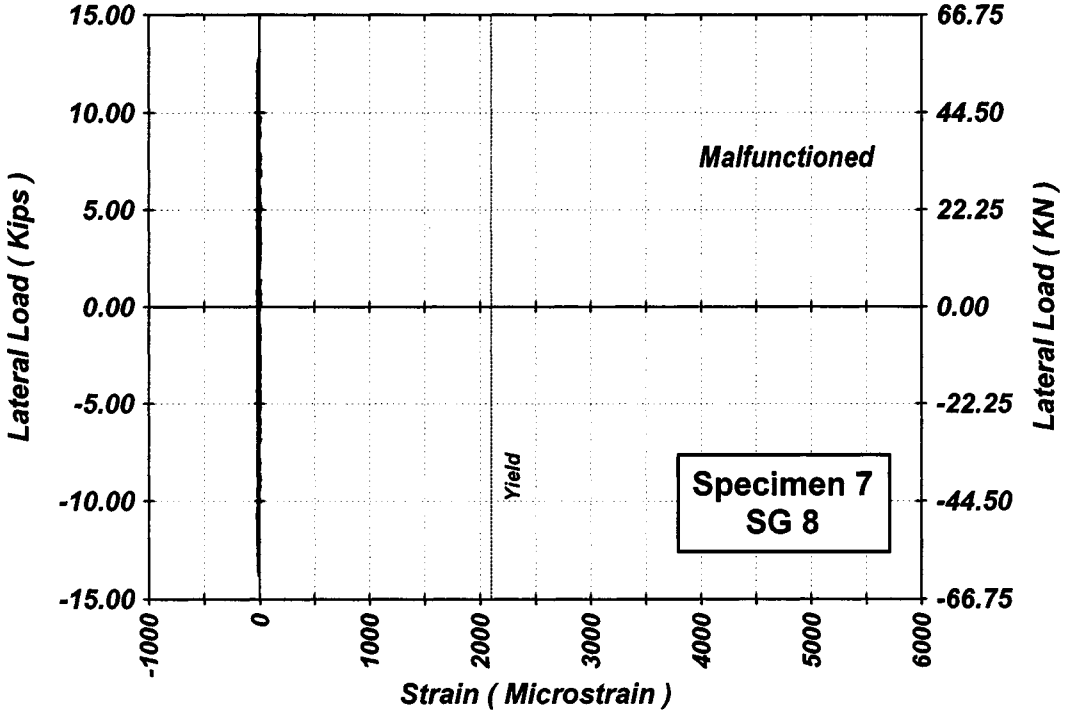

Figure A-200 Measured Lateral Load-Strain in SG-8 of Specimen 7

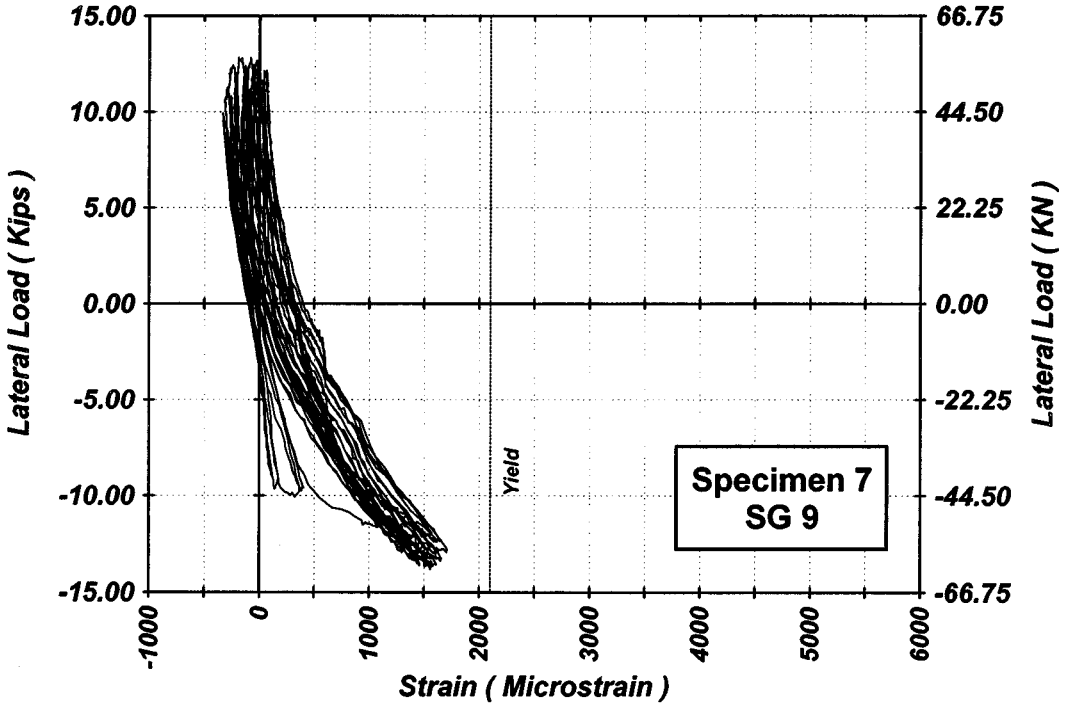

Figure A-201 Measured Lateral Load-Strain in SG-9 of Specimen 7

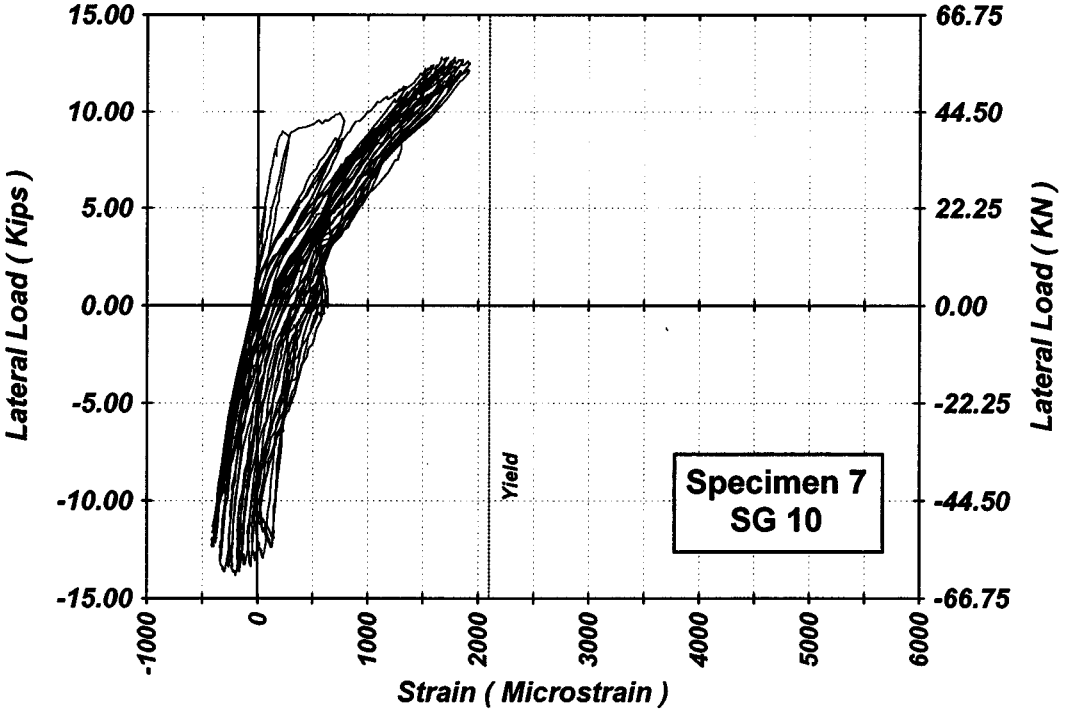

Figure A-202 Measured Lateral Load-Strain in SG-10 of Specimen 7

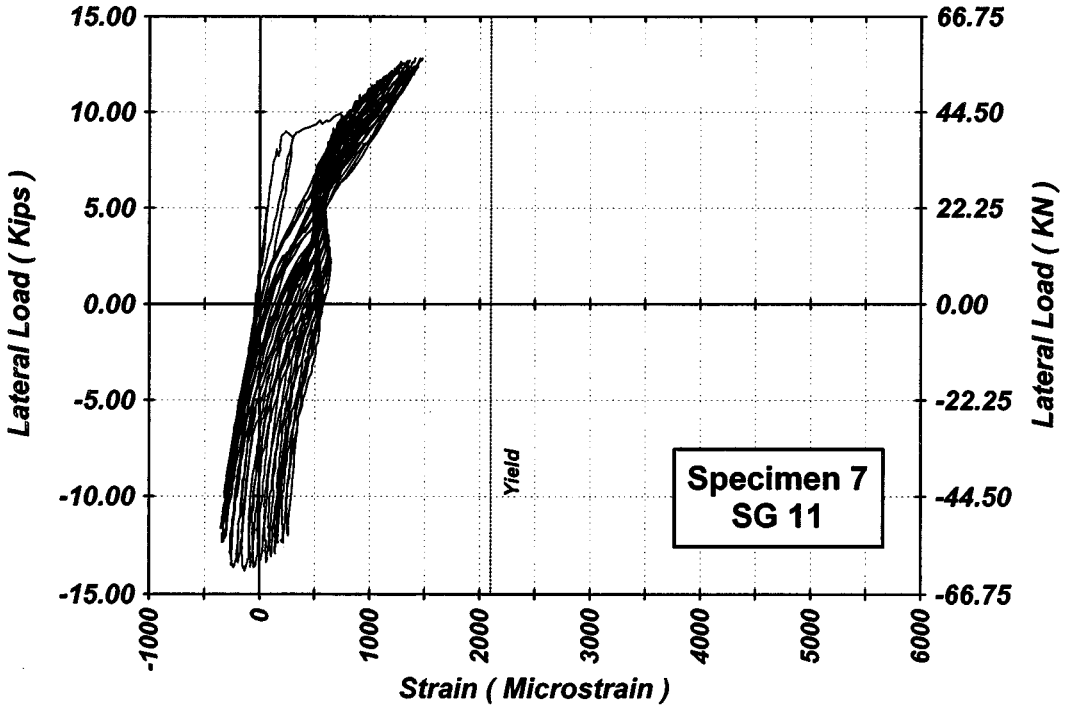

Figure A-203 Measured Lateral Load-Strain in SG-11 of Specimen 7

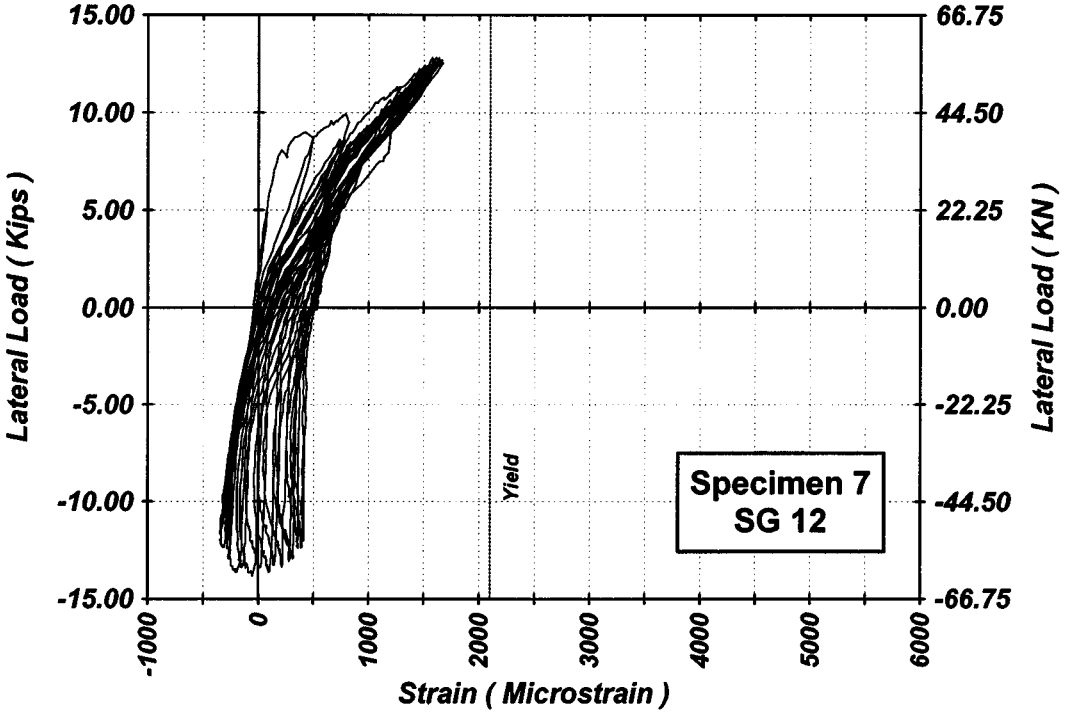

Figure A-204 Measured Lateral Load-Strain in SG-12 of Specimen 7

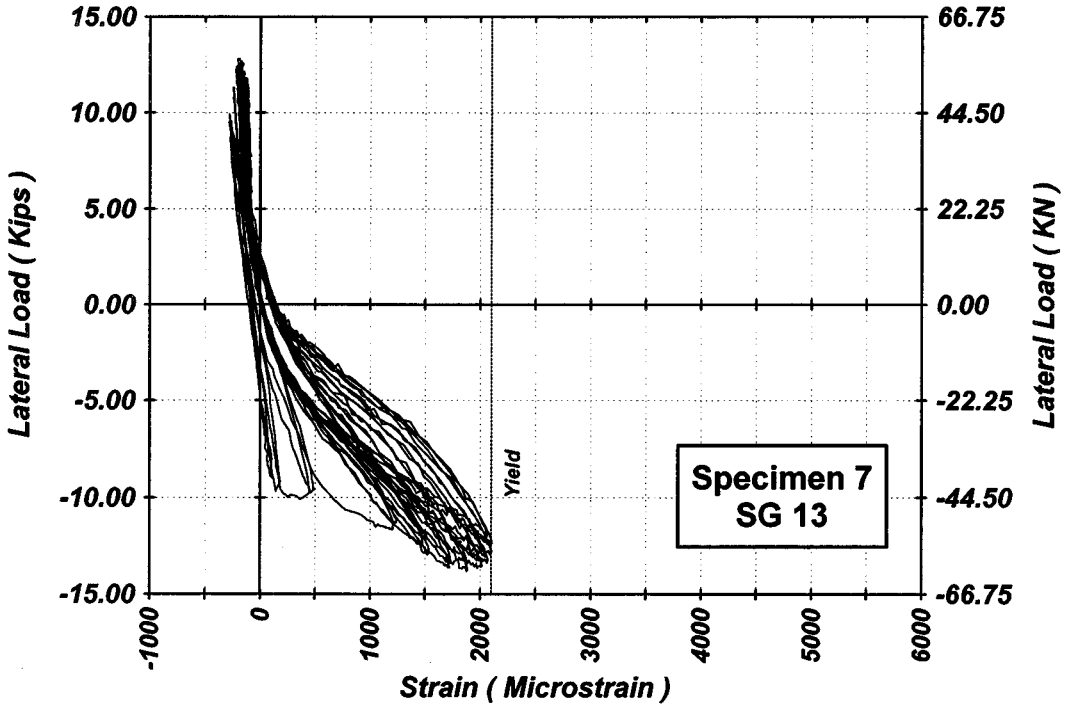

Figure A-205 Measured Lateral Load-Strain in SG-13 of Specimen 7

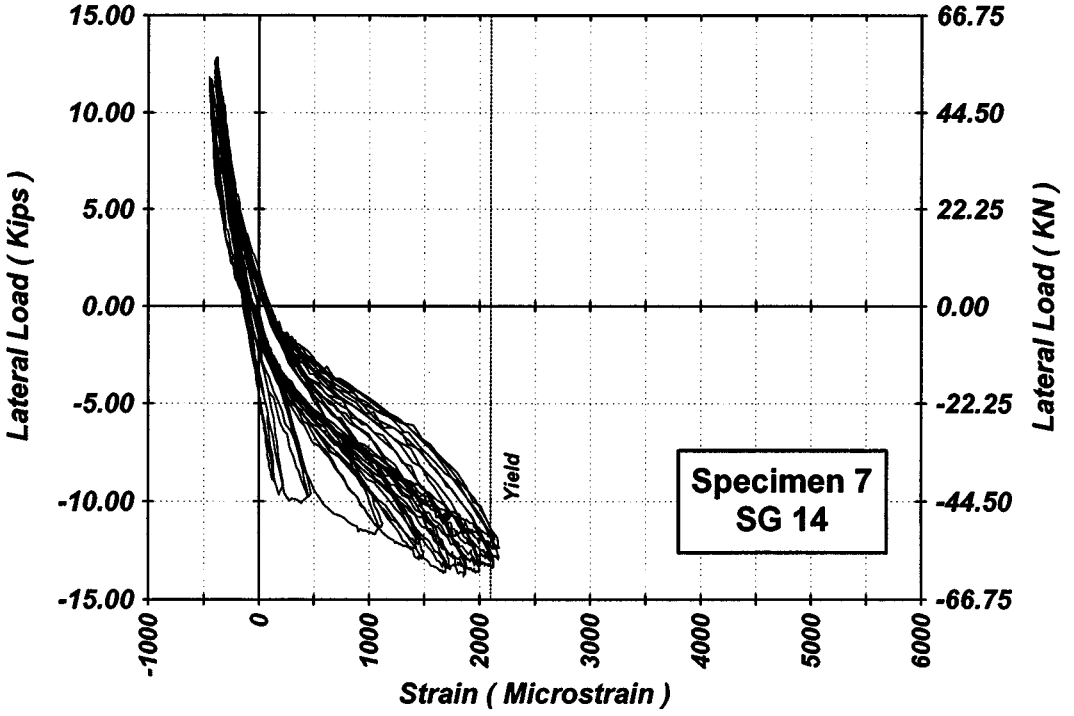

Figure A-206 Measured Lateral Load-Strain in SG-14 of Specimen 7

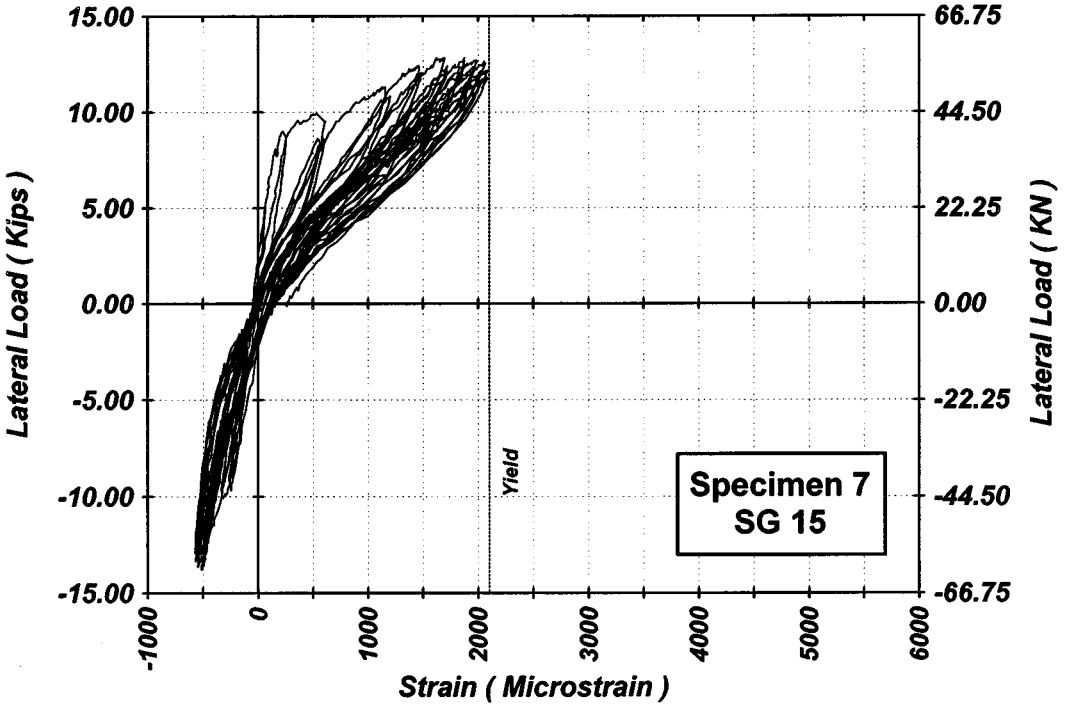

Figure A-207 Measured Lateral Load-Strain in SG-15 of Specimen 7

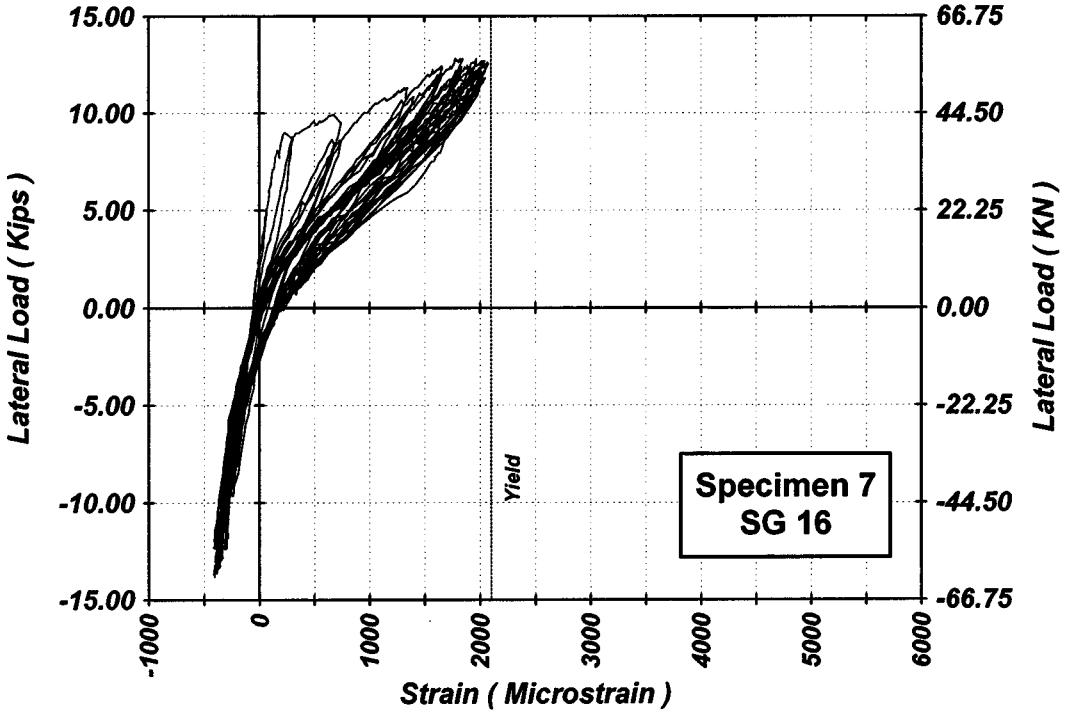

Figure A-208 Measured Lateral Load-Strain in SG-16 of Specimen 7

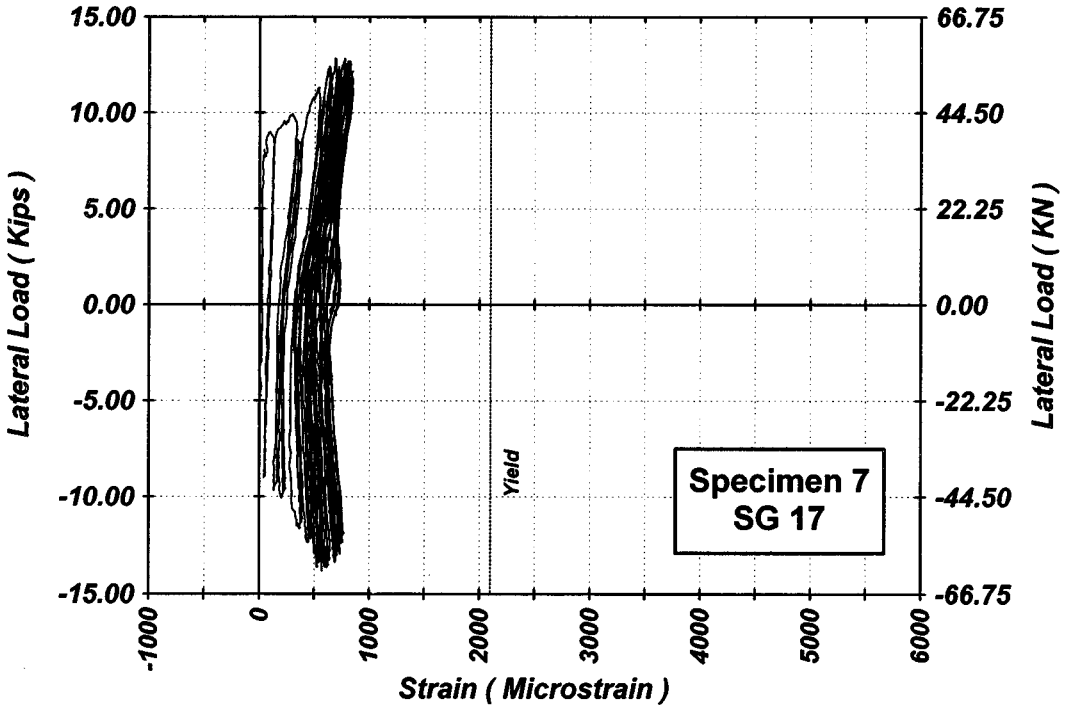

Figure A-209 Measured Lateral Load-Strain in SG-17 of Specimen 7

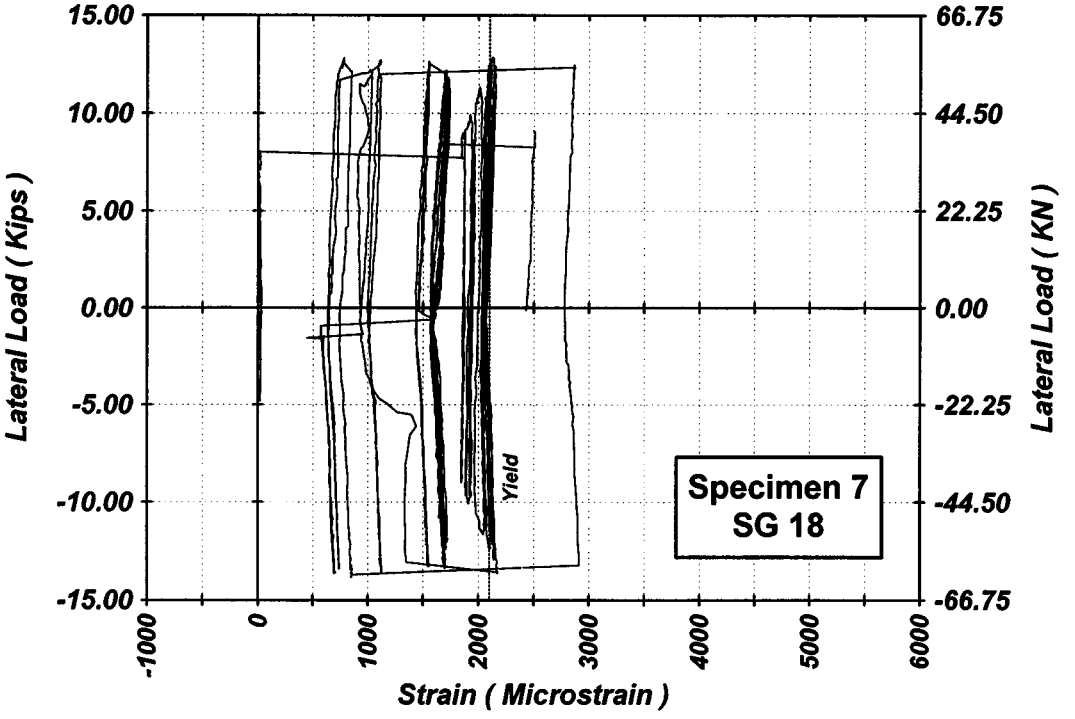

Figure A-210 Measured Lateral Load-Strain in SG-18 of Specimen 7

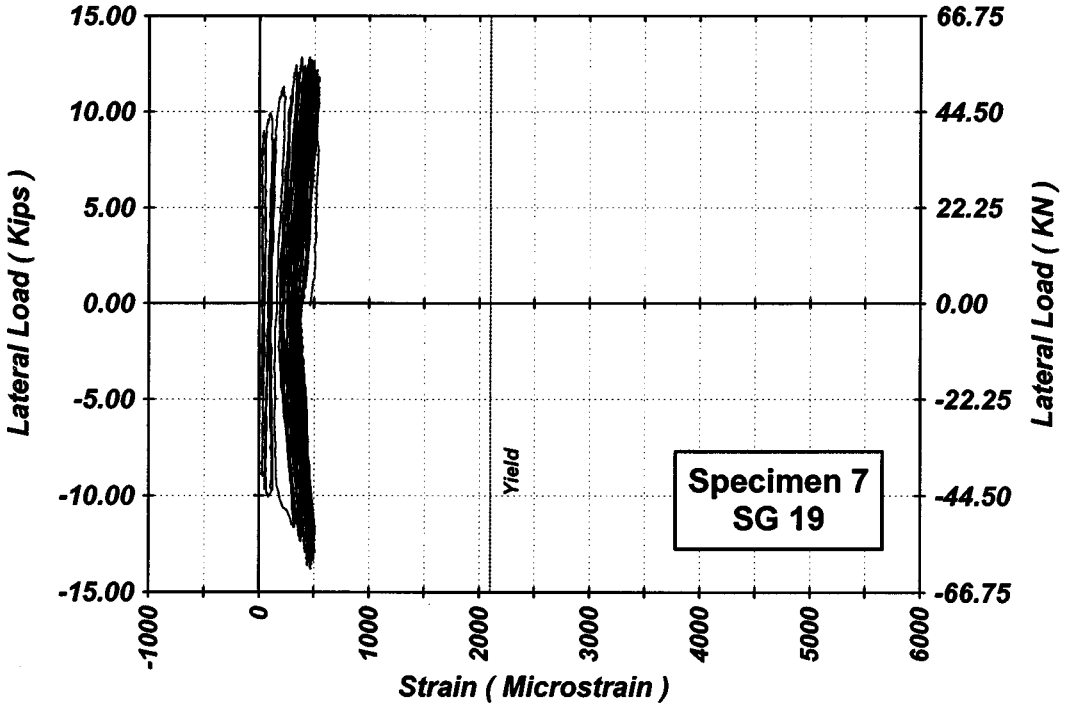

Figure A-211 Measured Lateral Load-Strain in SG-19 of Specimen 7

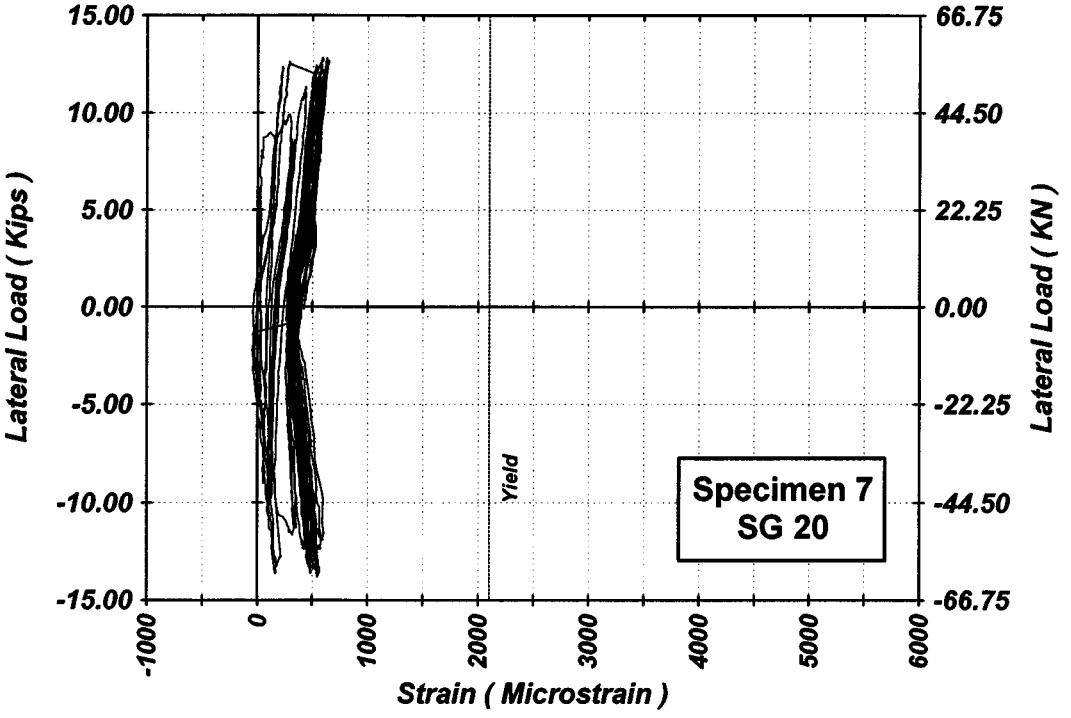

Figure A-212 Measured Lateral Load-Strain in SG-20 of Specimen 7

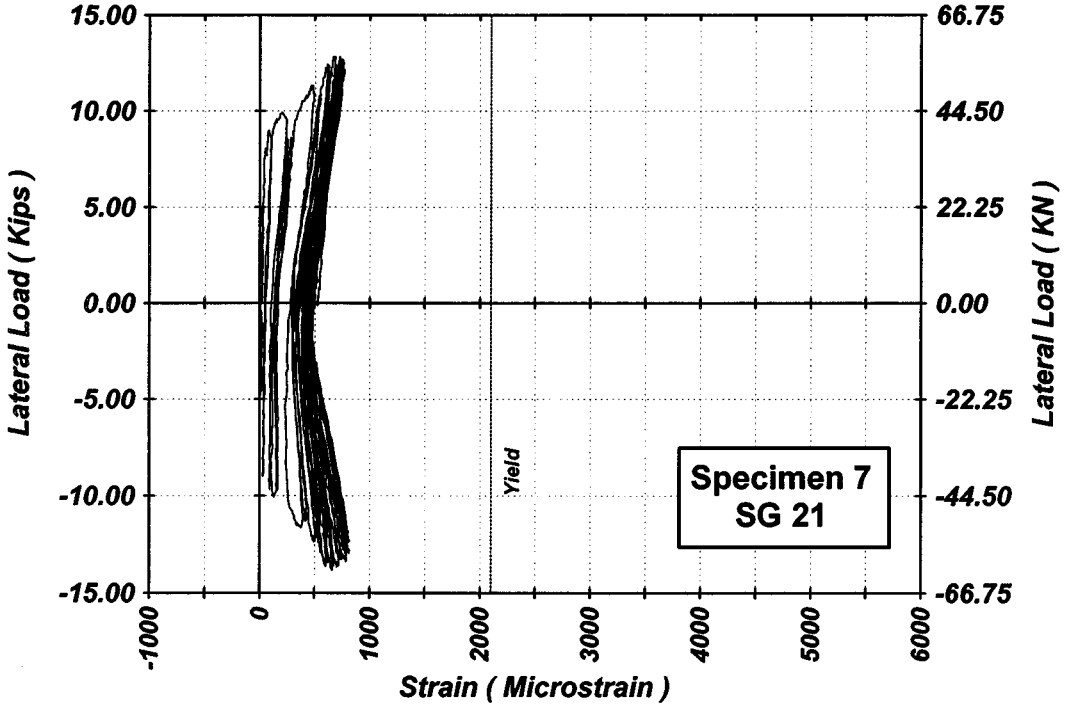

Figure A-213 Measured Lateral Load-Strain in SG-21 of Specimen 7

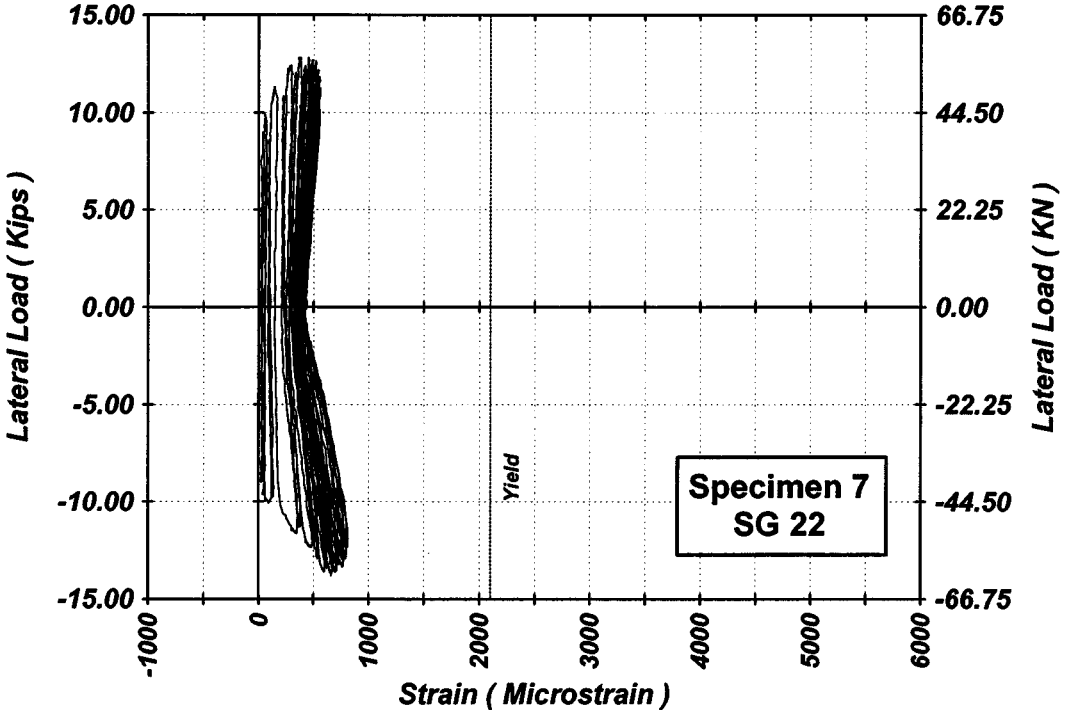

Figure A-214 Measured Lateral Load-Strain in SG-22 of Specimen 7

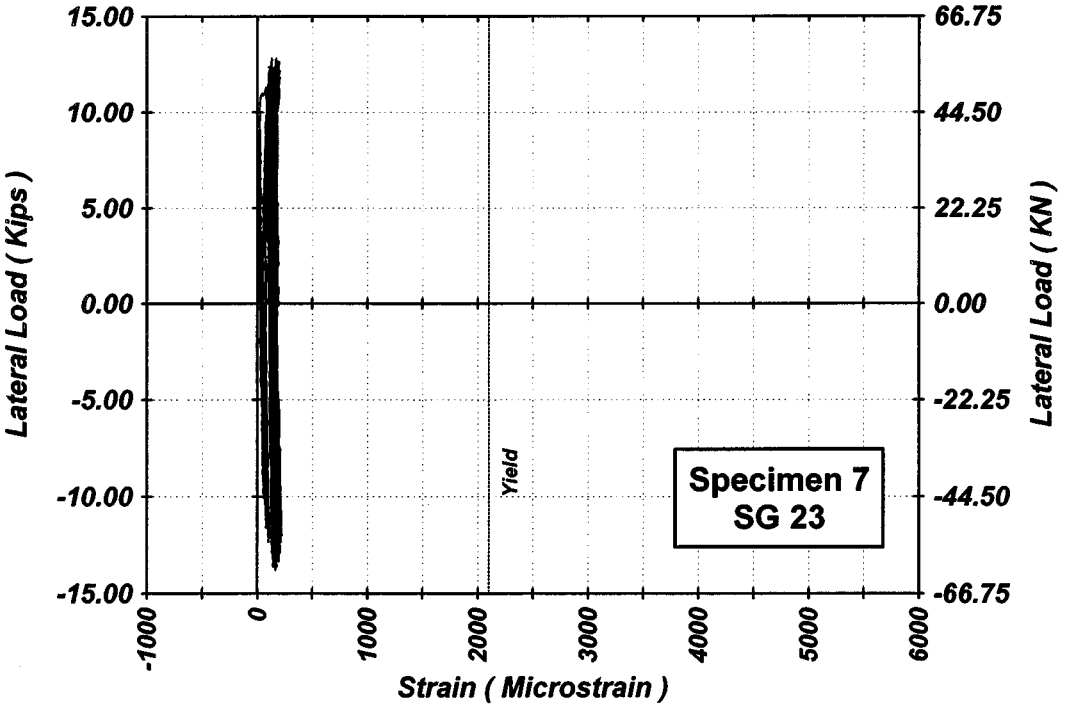

Figure A-215 Measured Lateral Load-Strain in SG-23 of Specimen 7

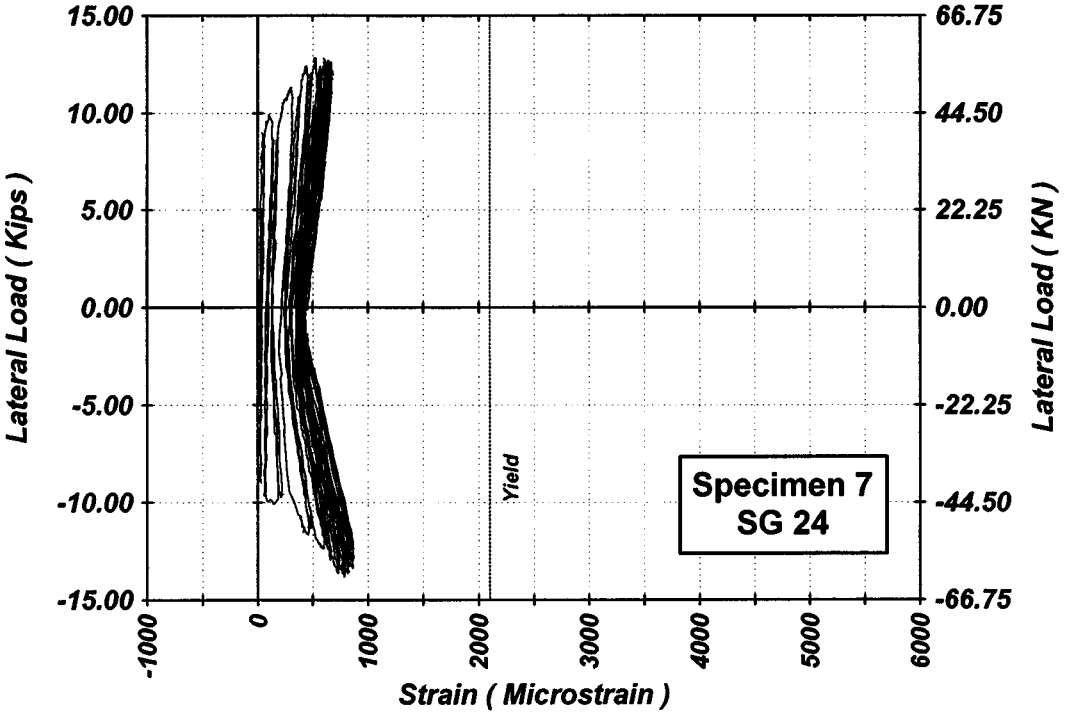

Figure A-216 Measured Lateral Load-Strain in SG-24 of Specimen 7

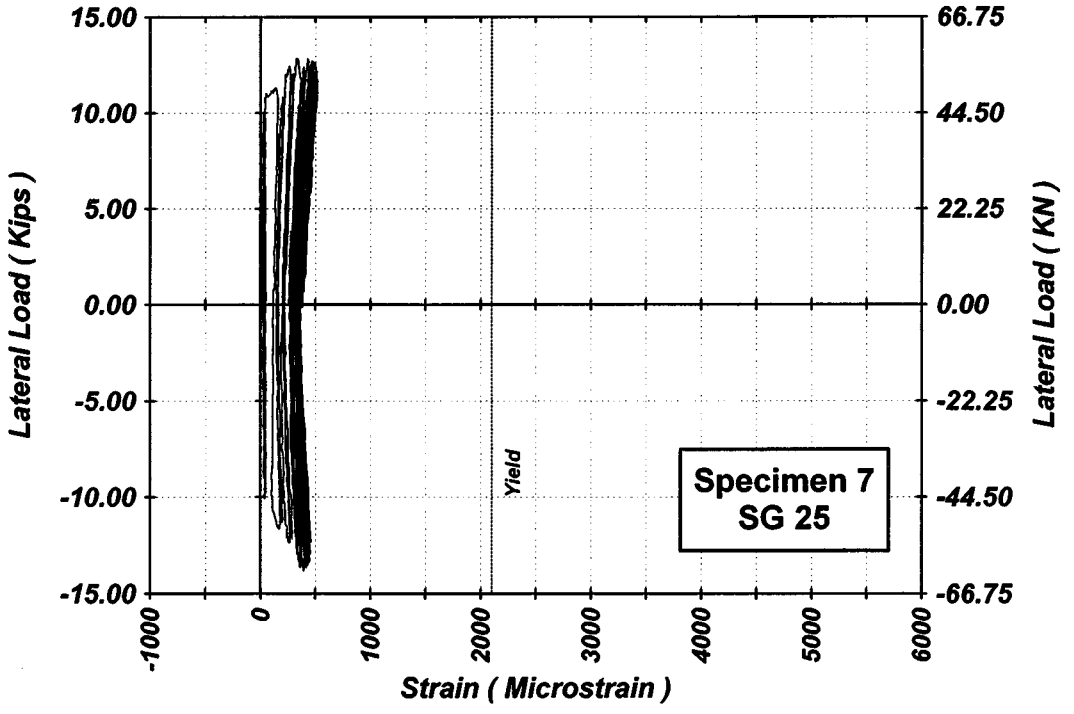

Figure A-217 Measured Lateral Load-Strain in SG-25 of Specimen 7

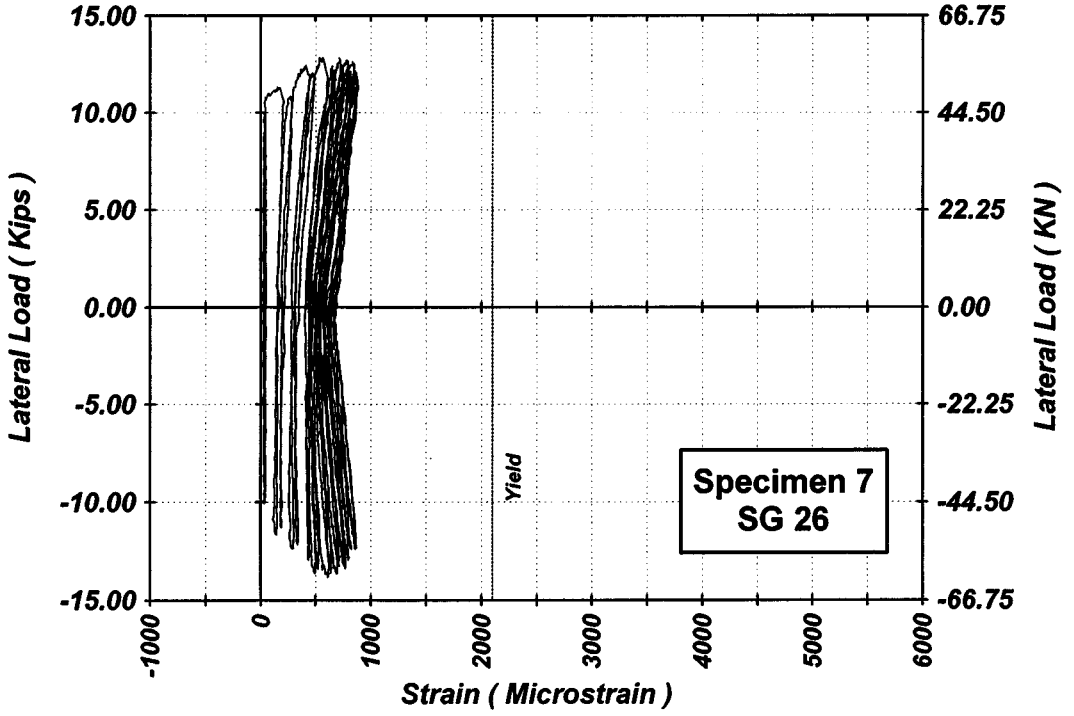

Figure A-218 Measured Lateral Load-Strain in SG-26 of Specimen 7

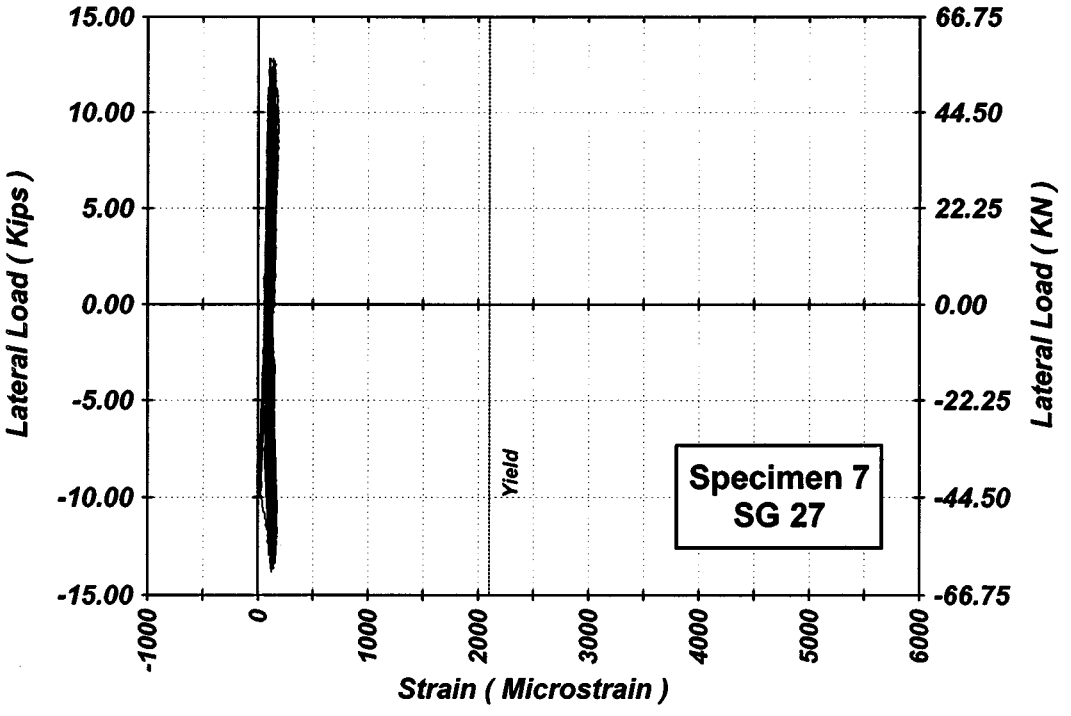

Figure A-219 Measured Lateral Load-Strain in SG-27 of Specimen 7

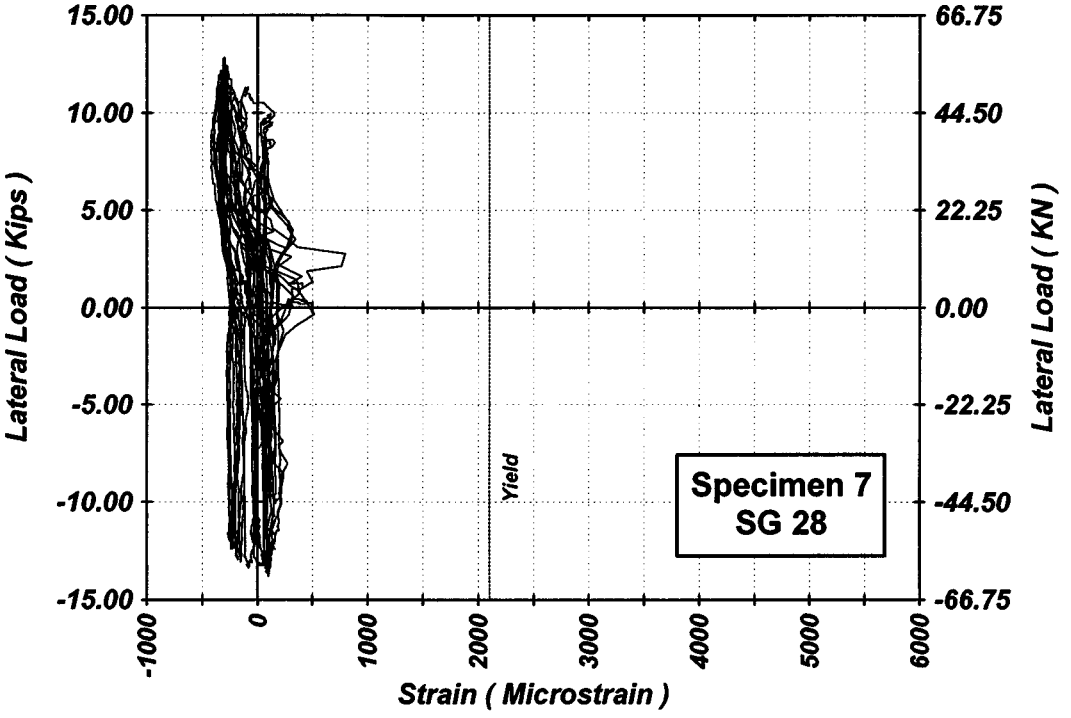

Figure A-220 Measured Lateral Load-Strain in SG-28 of Specimen 7

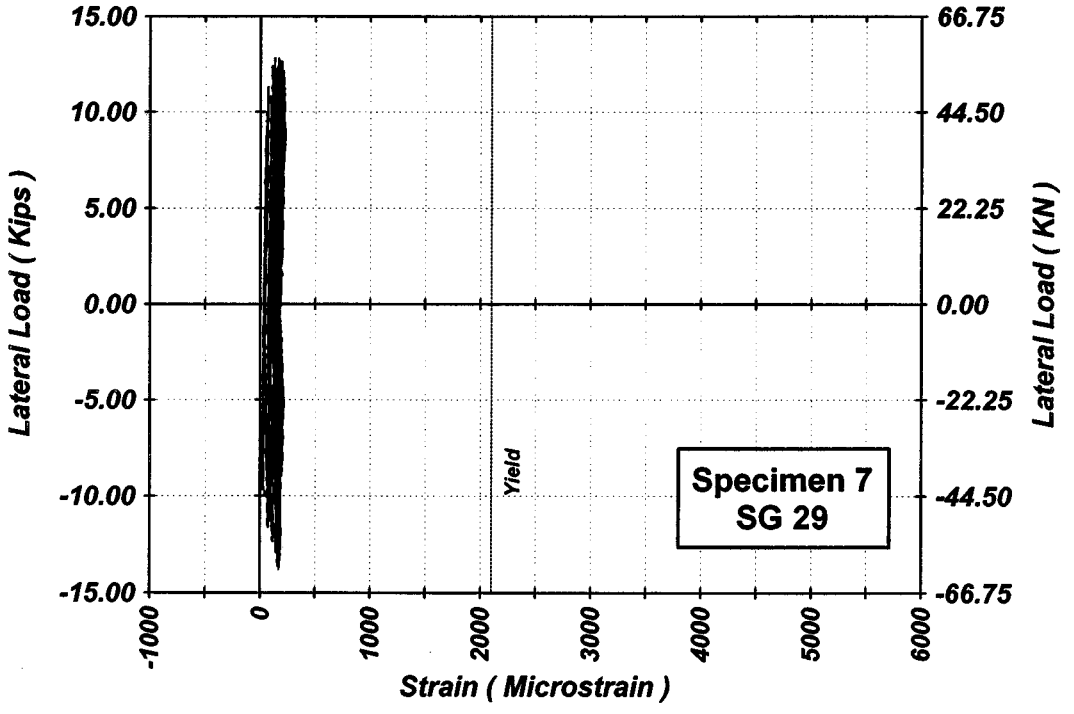

Figure A-221 Measured Lateral Load-Strain in SG-29 of Specimen 7

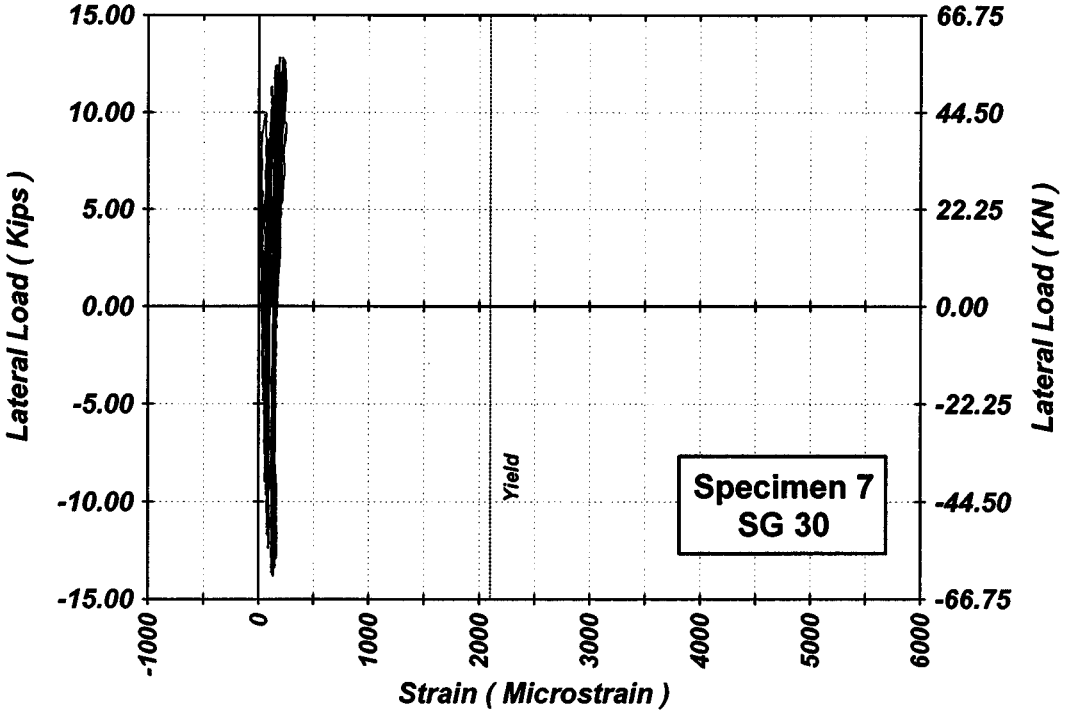

Figure A-222 Measured Lateral Load-Strain in SG-30 of Specimen 7

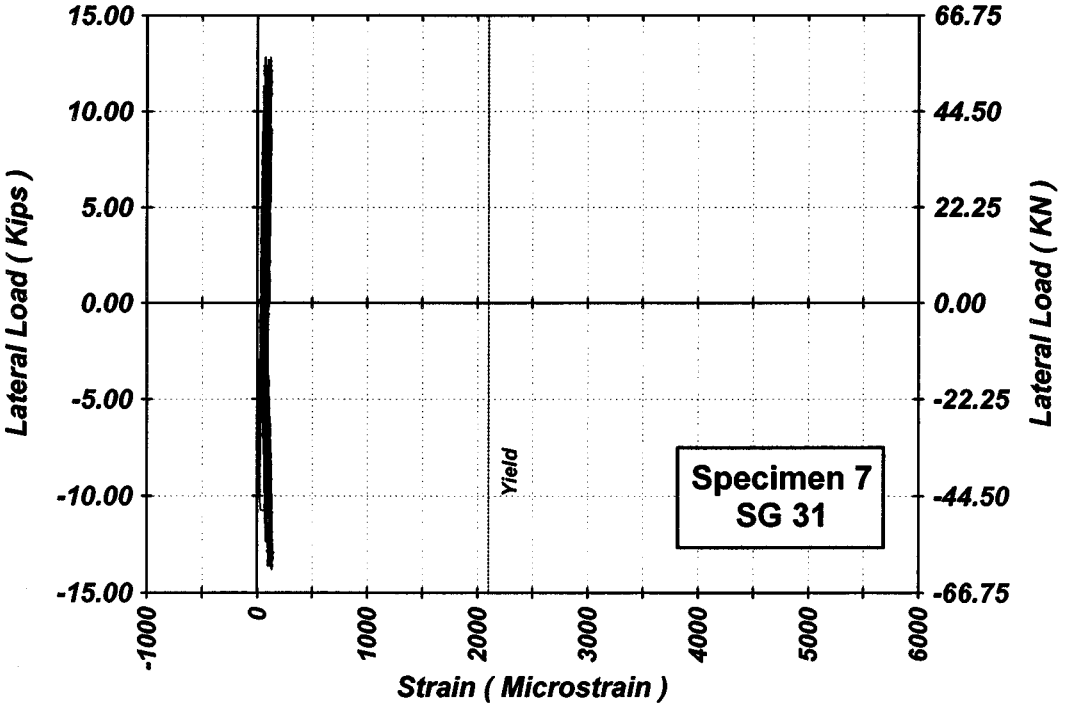

Figure A-223 Measured Lateral Load-Strain in SG-31 of Specimen 7

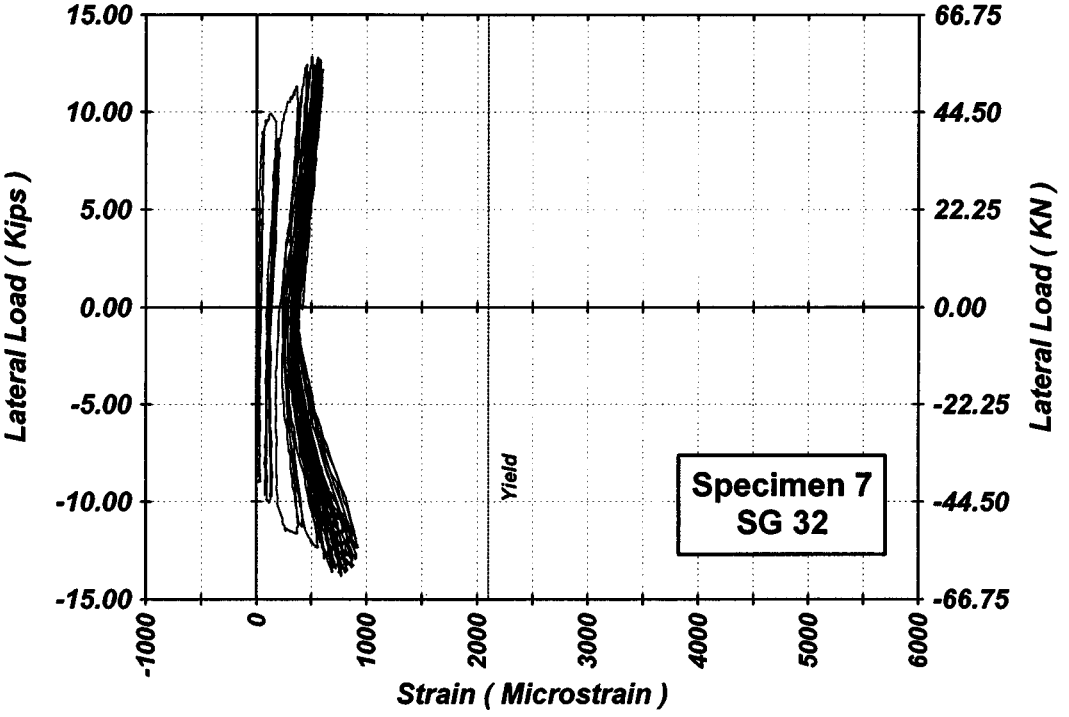

Figure A-224 Measured Lateral Load-Strain in SG-32 of Specimen 7

Appendix B

DATA AND RESULTS FOR THE PARAMETRIC STUDY

Table B-1(a) Data for Cases in the Parametric Study

Wall Case	Wall Height to its thickness (H / t)	Wall Height (mm)	Vertical Steel ratio (ρ_v) %	Confinement Steel Ratio (ρ_l & ρ_c) %	Axial Load Index $P/(A_g.f'_c)$ %
C-1	2	600	0.50	0.10	5
C-2	4	1200	0.50	0.10	5
C-3	7	2100	0.50	0.10	5
C-4	10	3000	0.50	0.10	5
C-5	15	4500	0.50	0.10	5
C-6	2	600	1.00	0.10	5
C-7	4	1200	1.00	0.10	5
C-8	7	2100	1.00	0.10	5
C-9	10	3000	1.00	0.10	5
C-10	15	4500	1.00	0.10	5
C-11	2	600	1.75	0.10	5
C-12	4	1200	1.75	0.10	5
C-13	7	2100	1.75	0.10	5
C-14	10	3000	1.75	0.10	5
C-15	15	4500	1.75	0.10	5
C-16	2	600	2.50	0.10	5
C-17	4	1200	2.50	0.10	5
C-18	7	2100	2.50	0.10	5
C-19	10	3000	2.50	0.10	5
C-20	15	4500	2.50	0.10	5
C-21	2	600	0.50	0.25	5
C-22	4	1200	0.50	0.25	5
C-23	7	2100	0.50	0.25	5
C-24	10	3000	0.50	0.25	5
C-25	15	4500	0.50	0.25	5
C-26	2	600	1.00	0.25	5
C-27	4	1200	1.00	0.25	5
C-28	7	2100	1.00	0.25	5
C-29	10	3000	1.00	0.25	5
C-30	15	4500	1.00	0.25	5
C-31	2	600	1.75	0.25	5
C-32	4	1200	1.75	0.25	5
C-33	7	2100	1.75	0.25	5
C-34	10	3000	1.75	0.25	5
C-35	15	4500	1.75	0.25	5
C-36	2	600	2.50	0.25	5
C-37	4	1200	2.50	0.25	5
C-38	7	2100	2.50	0.25	5
C-39	10	3000	2.50	0.25	5
C-40	15	4500	2.50	0.25	5

Table B-1(b) Data for Cases in the Parametric Study (Continue)

Wall Case	Wall Height to its thickness (H / t)	Wall Height (mm)	Vertical Steel ratio (ρ_v) %	Confinement Steel Ratio (ρ_l & ρ_c) %	Axial Load Index $P/(A_g.f'_c)$ %
C-41	2	600	0.50	0.40	5
C-42	4	1200	0.50	0.40	5
C-43	7	2100	0.50	0.40	5
C-44	10	3000	0.50	0.40	5
C-45	15	4500	0.50	0.40	5
C-46	2	600	1.00	0.40	5
C-47	4	1200	1.00	0.40	5
C-48	7	2100	1.00	0.40	5
C-49	10	3000	1.00	0.40	5
C-50	15	4500	1.00	0.40	5
C-51	2	600	1.75	0.40	5
C-52	4	1200	1.75	0.40	5
C-53	7	2100	1.75	0.40	5
C-54	10	3000	1.75	0.40	5
C-55	15	4500	1.75	0.40	5
C-56	2	600	2.50	0.40	5
C-57	4	1200	2.50	0.40	5
C-58	7	2100	2.50	0.40	5
C-59	10	3000	2.50	0.40	5
C-60	15	4500	2.50	0.40	5
C-61	2	600	0.50	0.10	10.00
C-62	4	1200	0.50	0.10	10.00
C-63	7	2100	0.50	0.10	10.00
C-64	10	3000	0.50	0.10	10.00
C-65	15	4500	0.50	0.10	10.00
C-66	2	600	1.00	0.10	10.00
C-67	4	1200	1.00	0.10	10.00
C-68	7	2100	1.00	0.10	10.00
C-69	10	3000	1.00	0.10	10.00
C-70	15	4500	1.00	0.10	10.00
C-71	2	600	1.75	0.10	10.00
C-72	4	1200	1.75	0.10	10.00
C-73	7	2100	1.75	0.10	10.00
C-74	10	3000	1.75	0.10	10.00
C-75	15	4500	1.75	0.10	10.00
C-76	2	600	2.50	0.10	10.00
C-77	4	1200	2.50	0.10	10.00
C-78	7	2100	2.50	0.10	10.00
C-79	10	3000	2.50	0.10	10.00
C-80	15	4500	2.50	0.10	10.00

Table B-1(c) Data for Cases in the Parametric Study (Continue)

Wall Case	Wall Height to its thickness (H / t)	Wall Height (mm)	Vertical Steel ratio (ρ_v) %	Confinement Steel Ratio (ρ_l & ρ_c) %	Axial Load Index $P/(A_g.f'_c)$ %
C-81	2	600	0.50	0.25	10.00
C-82	4	1200	0.50	0.25	10.00
C-83	7	2100	0.50	0.25	10.00
C-84	10	3000	0.50	0.25	10.00
C-85	15	4500	0.50	0.25	10.00
C-86	2	600	1.00	0.25	10.00
C-87	4	1200	1.00	0.25	10.00
C-88	7	2100	1.00	0.25	10.00
C-89	10	3000	1.00	0.25	10.00
C-90	15	4500	1.00	0.25	10.00
C-91	2	600	1.75	0.25	10.00
C-92	4	1200	1.75	0.25	10.00
C-93	7	2100	1.75	0.25	10.00
C-94	10	3000	1.75	0.25	10.00
C-95	15	4500	1.75	0.25	10.00
C-96	2	600	2.50	0.25	10.00
C-97	4	1200	2.50	0.25	10.00
C-98	7	2100	2.50	0.25	10.00
C-99	10	3000	2.50	0.25	10.00
C-100	15	4500	2.50	0.25	10.00
C-101	2	600	0.50	0.40	10.00
C-102	4	1200	0.50	0.40	10.00
C-103	7	2100	0.50	0.40	10.00
C-104	10	3000	0.50	0.40	10.00
C-105	15	4500	0.50	0.40	10.00
C-106	2	600	1.00	0.40	10.00
C-107	4	1200	1.00	0.40	10.00
C-108	7	2100	1.00	0.40	10.00
C-109	10	3000	1.00	0.40	10.00
C-110	15	4500	1.00	0.40	10.00
C-111	2	600	1.75	0.40	10.00
C-112	4	1200	1.75	0.40	10.00
C-113	7	2100	1.75	0.40	10.00
C-114	10	3000	1.75	0.40	10.00
C-115	15	4500	1.75	0.40	10.00
C-116	2	600	2.50	0.40	10.00
C-117	4	1200	2.50	0.40	10.00
C-118	7	2100	2.50	0.40	10.00
C-119	10	3000	2.50	0.40	10.00
C-120	15	4500	2.50	0.40	10.00

Table B-2(a) Results for Cases in the Parametric Study

Case	Yield Deflections (mm)				Ultimate Deflections (mm)				μ_d
	d_f	d_b	d_{sh}	d_t	d_f	d_b	d_{sh}	d_t	
C-1	1.0	0.9	2.6	4.4	15.7	5.6	3.0	24.3	5.47
C-2	3.8	1.8	2.6	8.2	43.8	11.2	3.0	58.0	7.12
C-3	11.5	3.1	2.6	17.2	106.9	19.6	3.0	129.4	7.51
C-4	23.5	4.4	2.6	30.6	195.1	28.0	3.0	226.1	7.40
C-5	52.6	8.4	2.6	63.5	418.5	52.3	3.0	473.8	7.46
C-6	1.3	1.4	4.0	6.6	17.9	7.2	4.7	29.8	4.52
C-7	5.0	2.8	4.0	11.8	49.0	14.4	4.7	68.2	5.81
C-8	15.2	5.0	4.0	24.1	115.8	25.2	4.7	145.7	6.05
C-9	31.0	7.1	4.0	42.0	206.7	36.0	4.7	247.4	5.89
C-10	69.7	10.6	4.0	84.3	411.7	54.0	4.7	470.5	5.58
C-11	1.5	2.0	6.3	9.8	17.1	7.5	7.7	32.2	3.30
C-12	6.0	3.9	6.3	16.2	47.1	15.0	7.7	69.7	4.30
C-13	18.3	6.9	6.3	31.4	110.8	26.3	7.7	144.7	4.60
C-14	37.3	9.8	6.3	53.4	197.1	37.5	7.7	242.2	4.54
C-15	83.9	14.7	6.3	104.9	390.9	56.3	7.7	454.8	4.34
C-16	1.6	2.7	8.5	12.8	16.8	8.5	10.2	35.5	2.77
C-17	6.5	5.4	8.5	20.4	46.6	17.0	10.2	73.7	3.62
C-18	19.9	9.5	8.5	37.9	109.2	29.7	10.2	149.1	3.94
C-19	40.7	13.6	8.5	62.7	193.4	42.4	10.2	246.0	3.93
C-20	91.5	20.3	8.5	120.3	381.7	63.6	10.2	455.5	3.79
C-21	0.9	0.9	1.1	2.9	16.4	5.9	1.3	23.6	8.11
C-22	3.8	1.8	1.1	6.6	45.8	11.9	1.3	58.9	8.92
C-23	11.5	3.1	1.1	15.7	106.6	19.6	1.3	127.4	8.14
C-24	23.4	4.4	1.1	28.9	203.7	29.6	1.3	234.6	8.11
C-25	52.7	6.7	1.1	60.4	442.2	48.2	1.3	491.7	8.14
C-26	1.3	1.4	1.7	4.3	23.1	9.9	2.0	35.0	8.12
C-27	5.0	2.8	1.7	9.5	57.3	17.8	2.0	77.1	8.13
C-28	15.3	5.0	1.7	21.9	142.2	33.3	2.0	177.5	8.10
C-29	31.3	7.1	1.7	40.0	244.2	45.5	2.0	291.7	7.29
C-30	70.4	10.6	1.7	82.7	510.0	72.9	2.0	585.0	7.08
C-31	1.5	2.0	2.7	6.1	24.9	12.3	3.4	40.5	6.65
C-32	6.0	3.9	2.7	12.6	64.7	23.3	3.3	91.4	7.28
C-33	18.4	6.9	2.7	27.9	150.9	41.0	3.3	195.2	7.01
C-34	37.5	9.8	2.7	49.9	276.9	61.6	3.4	341.8	6.85
C-35	84.3	14.7	2.7	101.7	544.3	92.4	3.4	640.0	6.30
C-36	1.6	2.7	3.5	7.9	23.8	13.7	4.5	41.9	5.32
C-37	6.5	5.4	3.5	15.5	65.0	27.4	4.5	96.9	6.26
C-38	20.0	9.5	3.5	33.0	150.4	47.9	4.5	202.8	6.14
C-39	40.8	13.6	3.5	57.9	263.8	68.5	4.5	336.8	5.82
C-40	91.8	20.4	3.5	115.7	515.5	102.7	4.5	622.6	5.38

Table B-2(b) Results for Cases in the Parametric Study (Continue)

Case	Yield Deflections (mm)				Ultimate Deflections (mm)				μ_d
	d_f	d_b	d_{sh}	d_t	d_f	d_b	d_{sh}	d_t	
C-41	0.9	0.9	0.7	2.5	16.5	6.0	0.8	23.3	9.21
C-42	3.7	1.8	0.7	6.2	44.9	11.6	0.8	57.3	9.22
C-43	11.4	3.1	0.7	15.2	105.5	19.3	0.8	125.6	8.25
C-44	23.3	4.4	0.7	28.5	202.2	29.4	0.8	232.4	8.17
C-45	52.4	6.7	0.7	59.8	436.2	47.4	0.8	484.5	8.10
C-46	1.3	1.4	1.1	3.8	20.5	8.6	1.3	30.4	8.12
C-47	5.0	2.9	1.1	8.9	55.8	17.2	1.3	74.2	8.35
C-48	15.3	5.0	1.1	21.3	139.3	32.5	1.3	173.2	8.13
C-49	31.1	7.1	1.1	39.3	245.4	45.9	1.3	292.6	7.45
C-50	70.0	10.7	1.1	81.8	505.6	72.3	1.3	579.2	7.09
C-51	1.5	2.0	1.7	5.2	23.1	11.3	2.2	36.6	7.08
C-52	6.0	3.9	1.7	11.6	67.1	24.5	2.2	93.8	8.08
C-53	18.3	6.9	1.7	26.9	151.3	41.3	2.2	194.8	7.25
C-54	37.3	9.8	1.7	48.8	280.8	63.0	2.2	345.9	7.09
C-55	83.8	14.8	1.7	100.3	551.7	94.4	2.2	648.4	6.47
C-56	1.7	2.7	2.3	6.7	27.3	16.4	3.0	46.7	7.01
C-57	6.6	5.4	2.3	14.3	71.2	31.0	3.0	105.1	7.35
C-58	20.1	9.5	2.3	31.9	167.0	55.5	3.0	225.4	7.06
C-59	41.1	13.6	2.3	56.9	310.2	85.6	3.0	398.8	7.01
C-60	92.4	20.4	2.3	115.0	570.0	118.9	3.0	691.9	6.02
C-61	1.1	1.0	3.6	5.6	10.1	2.9	3.7	16.7	2.97
C-62	4.4	2.0	3.6	9.9	28.8	5.8	3.7	38.3	3.89
C-63	13.3	3.4	3.6	20.3	71.7	10.1	3.7	85.5	4.22
C-64	27.2	4.9	3.6	35.6	132.3	14.5	3.7	150.4	4.23
C-65	61.7	9.2	3.5	74.4	285.4	27.0	3.7	316.1	4.25
C-66	1.3	1.6	4.9	7.7	12.2	4.0	5.2	21.4	2.77
C-67	5.3	3.1	4.9	13.3	34.1	8.0	5.2	47.3	3.57
C-68	16.3	5.4	4.9	26.6	82.0	14.0	5.2	101.2	3.81
C-69	33.3	7.7	4.9	45.9	148.1	20.0	5.2	173.2	3.77
C-70	75.0	11.6	4.9	91.4	298.4	29.9	5.2	333.5	3.65
C-71	1.6	2.1	7.2	10.9	12.6	4.6	7.9	25.1	2.31
C-72	6.3	4.2	7.2	17.7	35.3	9.1	7.9	52.4	2.96
C-73	19.4	7.4	7.2	33.9	84.6	16.0	7.9	108.5	3.20
C-74	39.5	10.5	7.2	57.2	152.2	22.9	7.9	182.9	3.20
C-75	88.9	15.8	7.2	111.8	305.3	34.3	7.9	347.5	3.11
C-76	1.7	2.9	9.3	13.9	12.9	5.5	10.3	28.8	2.07
C-77	6.9	5.8	9.3	21.9	36.5	11.0	10.3	57.8	2.63
C-78	21.0	10.1	9.3	40.4	86.9	19.3	10.3	116.5	2.88
C-79	42.9	14.4	9.3	66.6	155.7	27.5	10.3	193.5	2.91
C-80	96.6	21.6	9.3	127.5	310.8	41.3	10.3	362.4	2.84

Table B-2(c) Results for Cases in the Parametric Study (Continue)

Case	Yield Deflections (mm)				Ultimate Deflections (mm)				μ_d
	d_f	d_b	d_{sh}	d_t	d_f	d_b	d_{sh}	d_t	
C-81	1.1	1.0	1.5	3.6	15.6	5.4	1.6	22.6	6.36
C-82	4.4	2.0	1.5	7.8	43.7	10.8	1.6	56.1	7.19
C-83	13.4	3.4	1.5	18.3	107.2	18.9	1.6	127.7	6.99
C-84	27.3	4.9	1.5	33.7	196.2	27.0	1.6	224.7	6.68
C-85	61.4	7.3	1.5	70.2	401.2	40.4	1.6	443.2	6.31
C-86	1.3	1.6	2.0	4.9	18.5	7.3	2.3	28.1	5.71
C-87	5.4	3.1	2.0	10.5	50.7	14.6	2.3	67.5	6.45
C-88	16.4	5.4	2.0	23.8	119.8	25.5	2.3	147.6	6.20
C-89	33.4	7.7	2.0	43.2	214.1	36.4	2.3	252.7	5.85
C-90	75.2	11.6	2.0	88.8	426.8	54.6	2.3	483.7	5.45
C-91	1.6	2.1	3.0	6.7	18.4	8.0	3.5	29.9	4.48
C-92	6.3	4.2	3.0	13.5	50.7	16.1	3.5	70.3	5.19
C-93	19.4	7.4	3.0	29.8	119.3	28.1	3.5	150.9	5.07
C-94	39.5	10.5	3.0	53.1	212.1	40.1	3.5	255.7	4.82
C-95	88.9	15.8	3.0	107.7	420.5	60.2	3.5	484.2	4.49
C-96	1.7	2.9	3.9	8.5	18.5	9.4	4.6	32.5	3.82
C-97	7.0	5.8	3.9	16.6	51.3	18.8	4.6	74.6	4.50
C-98	21.3	10.1	3.9	35.2	120.2	32.8	4.6	157.5	4.47
C-99	43.4	14.4	3.9	61.7	212.6	46.9	4.6	264.0	4.28
C-100	97.6	21.6	3.9	123.1	419.0	70.3	4.6	493.9	4.01
C-101	1.1	1.0	1.0	3.0	17.2	6.2	1.1	24.4	8.07
C-102	4.4	2.0	1.0	7.3	46.1	11.6	1.1	58.7	8.09
C-103	13.3	3.4	1.0	17.7	120.3	22.1	1.1	143.4	8.11
C-104	27.1	4.9	1.0	33.0	206.2	29.1	1.1	236.3	7.16
C-105	61.0	7.4	1.0	69.3	442.4	46.6	1.1	490.0	7.07
C-106	1.4	1.6	1.3	4.2	22.7	9.6	1.5	33.7	8.01
C-107	5.4	3.1	1.3	9.8	58.9	18.0	1.5	78.4	8.01
C-108	16.5	5.4	1.3	23.2	137.2	31.0	1.5	169.7	7.31
C-109	33.6	7.8	1.3	42.7	251.5	46.0	1.5	299.0	7.01
C-110	75.6	11.6	1.3	88.6	513.4	71.6	1.5	586.6	6.62
C-111	1.6	2.1	2.0	5.7	24.2	11.7	2.4	38.2	6.75
C-112	6.4	4.2	2.0	12.5	63.3	22.1	2.4	87.8	7.01
C-113	19.5	7.4	2.0	28.8	153.5	40.8	2.4	196.6	6.83
C-114	39.7	10.6	2.0	52.2	271.2	58.2	2.4	331.7	6.35
C-115	89.4	15.8	2.0	107.1	534.1	87.3	2.4	623.7	5.82
C-116	1.7	2.9	2.5	7.2	24.0	13.5	3.1	40.5	5.66
C-117	6.9	5.8	2.5	15.2	65.7	26.9	3.1	95.6	6.28
C-118	21.1	10.1	2.5	33.8	152.0	47.1	3.1	202.2	5.98
C-119	43.1	14.5	2.5	60.1	267.1	67.3	3.1	337.4	5.61
C-120	97.0	21.7	2.5	121.2	522.5	100.9	3.1	626.4	5.17

MULTIDISCIPLINARY CENTER FOR EARTHQUAKE ENGINEERING RESEARCH

A National Center of Excellence in Advanced Technology Applications

University at Buffalo, State University of New York
Red Jacket Quadrangle ▪ Buffalo, New York 14261-0025
Phone: 716/645-3391 ▪ Fax: 716/645-3399
E-mail: mceer@acsu.buffalo.edu ▪ WWW Site: http://mceer.buffalo.edu

University at Buffalo *The State University of New York*

ISSN 1520-295X